Electrochemical Anion Sensing in Solution and at Receptive Interfaces

Robert Hein

Lady Margaret Hall, University of Oxford



A thesis submitted for the degree of Doctor of Philosophy

University of Oxford

Trinity Term 2020

“If you want to have good ideas you must have many ideas. Most of them will be wrong, and what you have to learn is which ones to throw away.”

Linus Pauling

This thesis is dedicated to my late grandma and my family.

Electrochemical Anion Sensing in Solution and at Receptive Interfaces

Robert Hein, Lady Margaret Hall, University of Oxford

Abstract of thesis submitted for the degree of D.Phil., Trinity Term 2020.

This thesis describes the investigation of halogen bonding and hydrogen bonding anion receptors for the electrochemical sensing of anions in solution and at receptor-modified electrodes.

Chapter 1 introduces the general concepts of supramolecular host-guest chemistry and electrochemical anion sensing. A range of voltammetric, impedimetric and potentiometric anion sensors and their basic operational principles are discussed.

Chapter 2 describes redox-active ferrocene- or osmium (II) bipyridyl-containing anion receptors for the voltammetric detection of anions in aqueous-organic solvent systems. This includes detailed studies and comparisons of voltammetric sensing under diffusive as well as surface-confined conditions.

Chapter 3 explores the unprecedented use of non-Faradaic capacitance spectroscopy for the sensing of anions in pure water. This is demonstrated at surface-immobilised foldamer receptors enabling the selective sensing of ReO_4^-, SCN^- and I^-.

Chapter 4 expands on the use of the capacitive methodology developed in Chapter 3 for the enantioselective detection of anions at chiral molecular films.

Chapter 5 investigates the sensing of ion-pairs *via* non-Faradaic capacitance spectroscopy at surface-confined heteroditopic receptors.

Chapter 6 summarises the main conclusions from Chapters 2−5.

Chapter 7 details experimental and synthetic procedures used throughout this thesis and provides characterisation of all novel compounds.

Chapter 8 contains the full list of all references cited in this thesis.

The appendices contain a variety of supplementary information, such as raw data and further sensor and surface characterisation.

Acknowledgements

With this amazing journey coming to an end after almost four years, I would like to express my sincere gratitude to everyone who has helped me on my way to not only grow as a researcher but also as a person. Having worked in two different research groups and on multiple collaborative projects this list will be rather long but without all of you amazing people I would not have made it this far and I am very grateful for all contributions to my work and life. I have truly enjoyed my time in Oxford which I can largely attribute to my friends and great colleagues. Both the Beer and Davis groups were always welcoming and provided a friendly, warm and collaborative work environment. Thus I would first like to thank all present and previous members of the Beer and Davis groups. Of course all of this was enabled by Prof. **Paul Beer** and Prof. **Jason Davis**, who have both been great mentors. They gave me the freedom to pursue my own ideas while always providing support and useful input when needed. Paul´s positive attitude and encouraging comments were always a nice morale boost and made the many failed experiments much more bearable. I am also very grateful that both always made time for "quick" chats and were always available; Jason once proof-read a 30000 word review within one day!

Almost all of the work that I carried out during my DPhil was collaborative and I am extremely thankful to everyone who contributed to my projects or who enabled me to contribute to theirs. Firstly, I have to thank the people without whom this thesis would not have been possible and who hugely contributed to my work by providing multiple crucial synthons or receptors investigated in this thesis: **Andrew Docker**, **Arseni Borissov** and **Thanthapatra "Valentine" Bunchuay**. I am also indebted to **Hena Bagha**, **Sophie Patrick**, **Xiaoxiong "George" Li**, **Julia Piccoli**, **Adriano Santos**, **Amol Patil, Ausra Baradoke**, **Clare**

Megarity, **Cheng Jiang**, **Richard Tse**, **Edward "TJ" Mitchell**, **Asha Brown, Robert Jacobs, Candan Catli, Philip Holdway** and **Qian Li** for discussions/help/collaborations.

While we never worked on any major projects together, I would like to explicitly thank **Jane Liew, Jessica Pancholi, Laura Bickerton**, **Timothy Barendt** and **Connor Ellis**, for being amazing lab mates and friends who significantly improved my time here. Similarly, I am grateful to everyone who had the unenviable? honour of proof-reading this thesis including Paul, Jason, Sophie, Jane, Amol, Jess, Andrew, Connor and **Felix Fleschhut**.

A special thanks also to Prof. **Paulo Bueno** and his research group in Araraquara, Brazil. As a result of multiple research collaborations Paulo has become a friend and mentor and I am very happy that he gave me the opportunity to work in his lab. My short research trip to Brazil was amazing and I would like to thank everyone who helped me there, especially Julia (+family), Adriano and **Bea**, muito obrigado!

I would have never made it this far without the many great mentors I had before coming to Oxford. My time at Jacobs University was extremely formative and I am certain that I would not have become the researcher I am today without the great supervision I received in Prof. **Werner Nau**´s lab, especially from **Andreas Hennig** and **Khaleel Assaf**. Similarly, I have to thank everyone who supervised me during my internships and studies abroad, especially **Matthew Rowland**, Prof. **Oren Scherman**, **Anne LaPointe** and Prof. **Geoffrey Coates**.

Lastly, I have to acknowledge my friends (from home and Oxford), including **Ben**, **Lizy**, **Peter** and **Helena** and my family and who were extremely supportive throughout my studies.

List of Publications

Arising from work discussed in this thesis:

Chapter 1:

R. Hein, P. D. Beer, J. J. Davis, "Electrochemical Anion Sensing: Supramolecular Approaches", *Chem. Rev., **2020**, 120, 1888-1935*.

***Chapter 2**:*

R. Hein, X. Li, P. D. Beer, J. J. Davis, "Enhanced Interfacial Voltammetric Anion Sensing at Halogen and Hydrogen Bonding Ferrocenyl SAMs", *To be submitted.*

***Chapter 3**:*

P. R. Bueno, **R. Hein**, A. Santos, J. J. Davis, "The Nanoscopic Principles of Capacitive Ion Sensing Interfaces", *Phys. Chem. Chem. Phys., **2020**, 22, 3770-3774.*

R. Hein, A. Borissov, M. D. Smith, P. D. Beer, J. J. Davis, "A halogen-bonding foldamer molecular film for selective reagentless anion sensing in water", *Chem. Commun., **2019**, 55, 4849-4852.*

Others:

C. Jiang, F. Hopfner, A. Katsikoudi, **R. Hein**, S. Evetts, Y. Huang, H. Wang, J. W. Ryder, G. Kuhlenbäumer, G. Deuschl, A. Padovani, D. Berg, B. Borroni, M. T. Hu, J. J. Davis, G. K. Tofaris, "*a*-Synuclein in serum neuronal exosomes precedes and predicts Parkinson's disease ", *J. Neurol. Neurosurg. Psychiatry, **2020**, 91, 720-729.*

C. Jiang[†], G. Wang[†], **R. Hein**[†], N. Liu, X. Luo, J. J. Davis, "Antifouling Strategies for Selective In Vitro and In Vivo Sensing" *Chem. Rev., **2020**, 120, 3852-3889.*

[†] - equal contribution.

A. Baradoke, **R. Hein**, X. Li, J. J. Davis, "Reagentless Redox Capacitive Assaying of C-Reactive Protein at a Polyaniline Interface", *Anal. Chem., **2020**, 92, 3508-3511.*

J. Piccoli, **R. Hein**, A. H. El-Sagheer, T. Brown, E. M. Cilli, P. R. Bueno, J. J. Davis, "Redox Capacitive Assaying of CRP at a Peptide Supported Aptamer Interface", *Anal. Chem., **2018**, 90, 3005-3008.*

M. J. Rowland, C. C. Parkins, J. H. McAbee, A. Kolb, **R. Hein**, X. J. Loh, O. A. Scherman, "An Adherent Tissue-inspired Hydrogel Delivery Vehicle Utilized in Primary Human Glioma Models", *Biomat., **2018**, 179, 199-208.*

M. A. Alnajjar, J. Bartelmeß, **R. Hein**, P. Ashokkumar, M. Nilam, W. M. Nau, K. Rurack, A. Hennig, "Rational design of boron-dipyrromethene (BODIPY) reporter dyes for cucurbit[7]uril", *Beilstein J. Org. Chem., **2018**, 14, 1961-1971.*

R. Hein, C. Uzundal, A. Hennig, "Simple and rapid quantification of phospholipids for supramolecular membrane transport assays", *Org. Biomol. Chem., **2016**, 14, 2182-2185.*

Abbreviations

δ	chemical shift
λ	wavelength
μ	micro
Δ	change in (a measurement), heat
°	degree
°C	degrees Celsius
Å	Ångstrom
A^-	anion
aq.	aqueous
a.u.	arbitrary units
AC	alternating current
ACN	acetonitrile
Ar	aromatic
ATP	adenosine triphosphate
ATR-FTIR	attenuated total reflectance Fourier transform infrared
BEF	binding enhancement factor
bipy/bpy	2,2'-bipyridine
Boc	di-*tert*-butyl dicarbonate
BODIPY	Boron-dipyrromethene
br	broad
BSA	bovine serum albumin
Bu	butyl

C	capacitance
cat.	catalytic
C_{dl}	double layer capacitance
conc.	concentrated
CPE	constant phase element
CuAAC	copper(I)-catalysed azide–alkyne cycloaddition
d	doublet
DBU	1,8-diazabicycloundec-7-ene
DC	direct current
DCM	dichloromethane
dd	doublet of doublets
DIPEA	*N*,*N*-di-*iso*-propylethylamine
DMF	*N*,*N*-dimethylformamide
DMSO	dimethyl sulfoxide
DNA	deoxyribonucleic acid
e.g.	*exempli gratia*
ECS	electrochemical capacitance spectroscopy
EIS	electrochemical impedance spectroscopy
em	emission
emf	electromotive force
eq., equiv.	equivalent
ESI	electrospray ionisation
Et	ethyl

EWG	electron-withdrawing group
ex	excitation
Fc	ferrocene
F.I.	fluorescence intensity
FRA	frequency response analyser
FWHM	full width at half maximum
g	gram
G	guest
GC	glassy carbon
H	host
HB	hydrogen bonding
Hz	hertz
I	Intensity/current
i_{pa}	anodic peak current
i_{pc}	cathodic peak current
i.e.	*id est*
ISE	ion-selective electrode
J	Joule
J	coupling constant
k	kilo
K	Kelvin
K	binding constant
L	litre

LOD	limit of detection
M	molar, mega, molecular ion
m	milli, multiplet
m	*meta*
m/z	mass-to-charge ratio
max.	maximum
Me	methyl
min	minute
MLCT	metal-to-ligand charge transfer
mol	mole
MS	mass spectrometry
Ms, mesyl	methanesulfonyl chloride
n	nano
NMR	nuclear magnetic resonance
OAc^-	acetate
OBz^-	benzoate
p	*para*
PEG	polyethylene glycol
PET	photoinduced electron transfer
pH	$-\log_{10}[H^+]$
Ph	phenyl
pK_a	$-\log_{10}K_a$
ppm	parts per million

Pr	propyl
q	quartet
quin.	quintet
R	chemical substituent
R_{ct}	charge transfer resistance
R_s	solution resistance
rt	room temperature
s	second, singlet
SAM	self-assembled monolayer
sat.	saturated
sept.	septet
t	triplet
t, tert	tertiary
TBA	tetrabutyl ammonium
TBTA	tris[(1-benzyl-1*H*-1,2,3-triazol-4-yl)methyl]amine
TEG	triethylene glycol
TLC	thin layer chromatography
Ts, tosyl	*para*-toluenesulfuonyl chloride
UV	ultra-violet
V	volt
v/v	volume/volume
vis.	visible
vs.	*versus*

wt.	weight
X	halogen atom
XB	halogen bonding
XPS	X-ray photoelectron spectroscopy
Z	impedance

Table of Contents

ABSTRACT iv

ACKNOWLEDGEMENTS v

LIST OF PUBLICATIONS vii

ABBREVIATIONS ix

CHAPTER 1: INTRODUCTION 2

1.1 Anion Supramolecular Chemistry 2
1.1.1 Relevance of Anion Recognition and Sensing 2
1.1.2 Design Principles of Synthetic Supramolecular Anion Receptors 3
1.1.2.1 Complementarity and Preorganisation 4
1.1.2.2 Non-covalent Interactions in Anion Recognition 7

1.2 Anion Sensing *via* Host-Guest Chemistry 11
1.2.1 Potentiometric Anion Sensing 12
1.2.1.1 General Experimental and Theoretical Considerations 12
1.2.1.2 Ionophores for Anion-selective Electrodes 13
1.2.2 Voltammetric Anion Sensing 16
1.2.2.1 Redox Transducers 19
1.2.2.2 Solution-Phase Voltammetric Anion Sensing 23
1.2.2.3 Surface-Confined Voltammetric Sensors 41
1.2.3 Faradaic Impedimetric Anion Sensing 45
1.2.4 Other Anion Sensors 48

1.3 Thesis Aims 50

CHAPTER 2: VOLTAMMETRIC ANION SENSING IN SOLUTION AND AT RECEPTIVE SAMS 53

2.1 Introduction and Chapter Aims 53

2.2 Electrochemical Anion Sensing at Ferrocenyl Hydrogen and Halogen Bonding SAMs 58
2.2.1 Receptor Design and Synthesis 58
2.2.2 Solution-Phase Binding Studies 61
2.2.2.1 ^{1}H NMR Titrations 61
2.2.2.2 Voltammetric Studies 64
2.2.3 Voltammetric Anion Sensing at Redox-Active SAMs 75
2.2.3.1 SAM Formation and Characterisation 75
2.2.3.2 Interfacial Anion Sensing 84

2.2.4 Comparison of Diffusive and Surface-Confined Sensor Response 95

2.3 Acyclic Osmium(II) Bipyridyl-Containing Receptors 101
2.3.1 Previous Work 101
2.3.2 Receptor Design and Synthesis 103
2.3.3 Electrochemical Properties of 2.7 and 2.8 105
2.3.4 Voltammetric Anion Binding Studies 108

2.4 Conclusions and Future Work 113
2.4.1 Conclusions 113
2.4.2 Future work 114
2.4.2.1 Further Exploration of Signal Transduction Principles at Redox-Active Interfaces 114
2.4.2.2 Redox Capacitive Anion Sensing 116

CHAPTER 3: NON-FARADAIC CAPACITIVE ANION SENSING AT FOLDAMER SAMS 122

3.1 Introduction and Chapter Aims 122

3.2 Molecular Design and Synthesis 124

3.3 Film Formation and Characterisation 128
3.3.1 X-ray Photoelectron Spectroscopy (XPS) 129

3.4 Anion Sensing *via* Non-Faradaic Capacitance Spectroscopy 135
3.4.1 Voltammetric and Impedimetric Investigation of the SAMs 135
3.4.2 Capacitive Investigation of the SAMs and Anion Sensing 137
3.4.3 Capacitive Measurements at Different Potentials 147

3.5 Elucidation of the Signal Transduction Mechanism 151
3.5.1 Equivalent Circuit Analysis 152
3.5.2 Dielectric Model 159
3.5.3 Mesoscopic Model 161

3.6 Conclusions and Future Work 166
3.6.1 Conclusions 166
3.6.2 Future work 168
3.6.2.1 Exploring Other Anion Receptive Interfaces 168
3.6.2.2 Further Investigations of the Capacitive Transduction Principles 169

CHAPTER 4: NON-FARADAIC CAPACITIVE ENANTIOSELECTIVE ANION SENSING AT CHIRAL SAMS 172

4.1 Introduction and Chapter Aims 172

4.2 Anion Sensing at Chiral SAMs 176

4.2.1 Receptor Design and Synthesis 176
4.2.2 SAM Formation and Characterisation 178
4.2.2.1 ATR-FTIR Spectroscopy 181
4.2.2.2 X-ray Photoelectron Spectroscopy (XPS) 182
4.2.3 Chiral Anion Sensing 186
4.2.3.1 Capacitive Properties of $4.4XB_{SAM}$ 186
4.2.3.2 Non-Faradaic Capacitive BINOL-PO_4^- Sensing 189
4.2.3.3 Faradaic Impedimetric BINOL-PO_4^- Sensing 199

4.3 Conclusions and Future Work 203
4.3.1 Conclusions 203
4.3.2 Future work 204
4.3.2.1 Further Exploration of Impedimetric/Capacitive Chiral Anion Sensing 204
4.3.2.2 Anion Sensing at Dicationic Chiral SAMs 205
4.3.2.3 More Advanced Chiral Receptors 206

CHAPTER 5: NON-FARADAIC CAPACITIVE ION-PAIR SENSING AT HETERODITOPIC SAMS 210

5.1 Introduction 210
5.1.1 Ion-Pair Recognition 210
5.1.2 Ion-Pair Sensing 213
5.1.3 Chapter Aims 215

5.2 Ion-Pair Sensing at Heteroditopic SAMs 216
5.2.1 Receptor Design and Synthesis 216
5.2.2 SAM Formation and Characterisation 217
5.2.2.1 X-ray Photoelectron Spectroscopy (XPS) 219
5.2.2.2 Atomic Force Microscopy (AFM) 223
5.2.3 Ion-Pair Sensing 225
5.2.3.1 General Considerations and Capacitive Properties of $5.5XB_{SAM}$ 225
5.2.3.2 Capacitive Cation Sensing 227
5.2.3.3 Capacitive Anion Sensing 232
5.2.3.4 Capacitive Ion-Pair Sensing 233

5.3 Conclusions and Future Work 238
5.3.1 Conclusions 238
5.3.2 Future work 240
5.3.2.1 Further Capacitive Ion-Pair Sensing Studies in Aqueous-Organic Media 240
5.3.2.2 Development of Appropriate Models 240
5.3.2.3 Capacitive Investigations at lower Ionic Strength 241
5.3.2.4 Amino Acid Sensing 243
5.3.2.5 Control Experiments at Non-Receptive SAMs 244
5.3.2.6 Switching Surface Wettability 245

CHAPTER 6: SUMMARY AND CONCLUSIONS 248

CHAPTER 7: EXPERIMENTAL 254

7.1 General Considerations 254
7.1.1 Chemicals and Solvents 254
7.1.2 NMR and MS 254

7.2 Electrochemical Experiments 255
7.2.1 Electrode Cleaning 256
7.2.2 Cyclic Voltammetry (CV) 257
7.2.3 Square Wave Voltammetry (SWV) 257
7.2.4 Electrochemical Impedance Spectroscopy (EIS) 258
7.2.5 Determination of Molecular Surface Coverage (Γ) 261
7.2.6 Reductive Thiol Stripping 261
7.2.7 Electrochemical Sensing Studies 262
7.2.7.1 General Considerations and Terminology 262
7.2.7.2 Electrochemical Titrations 264

7.3 SAM Formation and Surface Characterisation 265
7.3.1 SAM Formation 265
7.3.2 ATR-FTIR Spectroscopy 266
7.3.3 X-ray Photoelectron Spectroscopy (XPS) 267
7.3.4 Water Contact Angle Measurements 267
7.3.5 Ellipsometry 268
7.3.6 Atomic Force Microscopy (AFM) 268

7.4 Data Analysis and Fitting 269

7.5 Synthesis 272
7.5.1 Synthesis for Chapter 2 273
7.5.2 Synthesis for Chapter 3 280
7.5.3 Synthesis for Chapter 4 303
7.5.4 Synthesis for Chapter 5 310

CHAPTER 8: REFERENCES 316

APPENDICES 335

A2: Supplementary Information for Chapter 2 335

A3: Supplementary Information for Chapter 3 346

A4: Supplementary Information for Chapter 4 353

A5: Supplementary Information for Chapter 5 358

Chapter 1

Introduction

Chapter 1: Introduction

1.1 Anion Supramolecular Chemistry

1.1.1 Relevance of Anion Recognition and Sensing

Ubiquitous in Nature, anions play a pivotal role in a wide range of environmental, physiological and technical applications. For example, phosphate species are crucial components of many biomolecules including DNA, RNA and ATP, and are vital for many cellular processes. As a fundamental constituent of amino acids (and proteins) carboxylates are another class of anionic species with large structural diversity and physiological relevance. Similarly, bicarbonate acts as an important buffer to maintain the pH of blood, while chloride plays a crucial role in membrane transport processes. The study of such anion mediated processes is thus of high medical relevance, for example, cystic fibrosis is linked to the misregulation of chloride channels,[1] while iodide is important for thyroid function.[2]

Furthermore, anions are of major interest environmentally where they are important components of water streams, (acid) rain or soil. The presence of certain anions in these environments is of concern when concentrations are elevated above critical levels; high concentrations of phosphate and nitrate species, often applied as agricultural fertilisers, can lead to eutrophication of water bodies.[3] Other anions highly toxic to the environment at much lower concentrations include azide, cyanide and the radioactive pertechnetate, a by-product of the nuclear industry.[4]

These observations highlight the critical need to not only fundamentally understand the specific role of anions in such systems, but also to have the capability to sense them in diverse environments. This has spurred on the development of synthetic anion receptors

and sensors,[5] often inspired by biotic analogues such as the sulfate and phosphate-binding proteins.[6,7]

The objective of this thesis is to develop novel electrochemical anion sensors based on supramolecular host-guest interactions (as detailed in "Thesis aims", Section 1.3). In this chapter the basic concepts relevant to this goal will be introduced, commencing with an overview of the design principles of synthetic supramolecular anion receptors before discussing electrochemical anion sensors in more detail.

1.1.2 Design Principles of Synthetic Supramolecular Anion Receptors

Supramolecular host-guest chemistry has long been utilised for the recognition of various guest species at (synthetic) host molecules. The exploitation of different non-covalent interactions enables the construction of host systems that interact with specific guest analytes in a reversible manner, whereby the association (binding) of the guest can be fine-tuned *via* modulation of, for example, receptor geometry as well as the number and nature of binding sites. This was first exploited by Pederson, Lehn and Cram in the development of crown ethers, cryptands and other macrocyclic multidentate hosts for alkali metal cation recognition. It was shown that through synthetic modifications of these hosts (*i.e.* specific substitutions or ring expansion) a high degree of selectivity for specific cations can be achieved. These groundbreaking results were later recognised with a 1987 Nobel Prize and have often been considered the birth of the field of modern supramolecular chemistry. Importantly, the design principles that were exploited in the synthesis of these cation receptors also translate to the design of anion hosts and will be briefly introduced in the following sections.

1.1.2.1 Complementarity and Preorganisation

In order to maximise the intermolecular interactions (attraction) between a (synthetic) host and a guest, both species need to complement electrostatically and in terms of size and shape. The former is dictated by the nature of the guest (*i.e.* charge) and the favourable non-covalent interaction(s) employed to drive guest binding, as discussed in more detail in Section 1.1.2.2. The latter is dictated by the geometry and size of both the host and guest and is often described by the lock and key principle. It should however be noted that a large number of host molecules possess a significant degree of flexibility allowing the adoption of certain conformations in which guest binding is enhanced. This "induced fit" model is often a more realistic description of host-guest interactions. Importantly, these size and/or shape considerations are often much more relevant in anion supramolecular chemistry; in contrast to metal cations, all of which are small, spherical guests, anions possess a much larger range of different geometries (Figure 1.1).

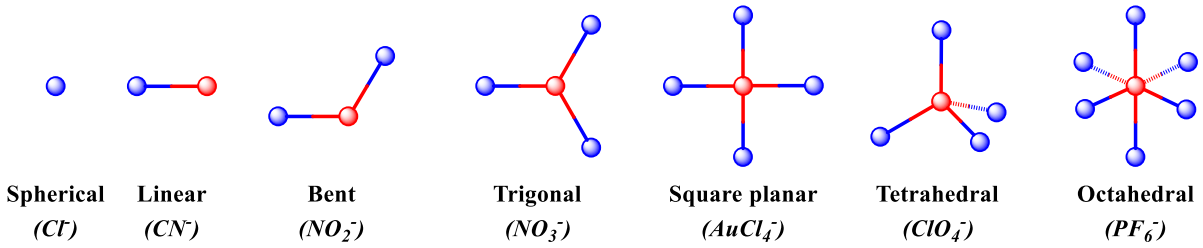


Figure 1.1. Examples of geometries adopted by anions.

This requires the preparation of host systems that are not only complementary in size but ideally possess a specific binding pocket that accommodates the anion guest *via* non-covalent interactions that are optimised for the anions' geometry.

In addition to these complementarity considerations, the recognition of anions is influenced by a variety of other factors. Perhaps most important is the strong hydration of anions by

water (typically stronger than that of cations). This hydration has to be overcome (*i.e.* removed) when anion binding is sought in aqueous media. The hydration enthalpy of an anion is strongly dependent on its charge density, rendering anions with high charge density, such as SO_4^{2-} or F^-, highly hydrated (hydrophilic), while less hydrates anions such as I^- or ClO_4^- are more hydrophobic. This is reflected in the Hofmeister series, as depicted in Figure 1.2.[8]

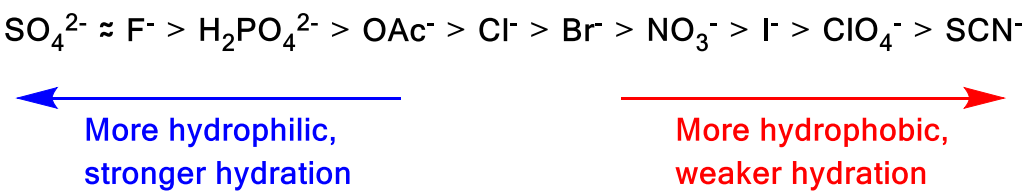
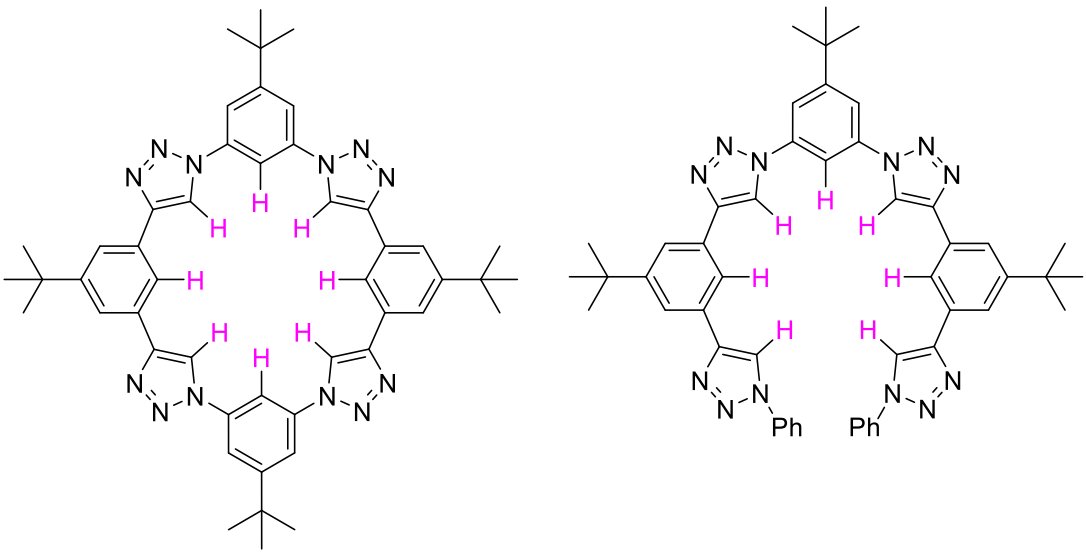


Figure 1.2. The Hofmeister series for common anions.

In predominantly aqueous media the more hydrophobic anions are usually bound more strongly, due to a decreased enthalpic energy penalty that is associated with anion dehydration upon binding. Conversely, in non-polar, organic solvents these considerations are much less relevant and anion binding is largely driven by electrostatic interactions (*vide infra*). However in these media ion-pairing effects between the anion of interest and its counter cation are often significant.[9]

Another important consideration in anion supramolecular chemistry is their pH sensitivity; many anions are protonated under sufficiently acidic conditions. In addition, some anions can be (de)protonated more than once, where depending on the pH of the solution multiple (negatively charged) species can coexist. These effects are particularly relevant for the recognition and sensing of phosphates and sulfates in aqueous media.

In order to maximise the interaction energy between a host and a guest, multiple convergent binding sites are often incorporated into the host molecule. As mentioned previously, these sites should be spatially arranged such that the number of contacts with the guest can be maximised. This can theoretically be achieved by employing a flexible host, however this flexibility results in a large entropic penalty upon guest binding and thus a diminished binding strength. If the host is preorganised or rigidified such that the binding sites inherently adopt a conformation that is conducive to guest binding, then this can be avoided.[10] Most commonly this concept is exploited in macrocyclic cation hosts such as crown ethers and in particular spherands. In anion receptive systems this macrocyclic effect is significant as well; for example Flood and co-workers demonstrated that tetra-triazole macrocycle **1.1** is capable of strong Cl^- recognition in DCM ($K = 130000\ M^{-1}$), while the analogous acyclic host **1.2** displayed negligible binding ($K = 7\ M^{-1}$, Figure 1.3).[11]



1.1

strong Cl^- binding in DCM
$K = 130000\ M^{-1}$

1.2

negligible Cl^- binding in DCM
$K = 7\ M^{-1}$

Figure 1.3. Flood's macrocyclic and acyclic tetra-triazole hosts.

1.1.2.2 Non-covalent Interactions in Anion Recognition

Electrostatic Interactions

Perhaps the most archetypical, electrostatic interactions are ubiquitous and, predictably, play a major role in the recognition of guests, in particular charged ones. They can be divided into three major categories: ion-ion, ion-dipole as well as dipole-dipole interactions. While they can be very potent (on the order of covalent bonds), their strength of interaction is strongly dependent on the distance between both interacting species as well as the dielectric constant of the surrounding medium. One final note of caution is their often non-directional nature; the incorporation of positive charges into synthetic hosts can increase anion binding strength but not necessarily imparts a significant degree of selectivity.

Hydrogen Bonding

Prevalent in biology, chemistry and physics, hydrogen bonding (HB) plays a crucial role in almost all natural and man-made (chemical) systems. HB is known as the attractive interaction between a positively polarised H-atom (*i.e.* when bonded to an electron-withdrawing group (EWG)) and a Lewis base (neutral or anionic), see Figure 1.4A. It is often considered a special case of dipole-dipole or ion-dipole interactions, but also contains other contributions that can be significant.[12] Due to its strength and ease of incorporation into synthetic receptors, HB has long been the most commonly exploited non-covalent interaction in anion recognition. A large variety of motifs are exploited as HB donors, with N–H HB donors such as amides or ureas being used most commonly. More recently, C–H HB donors, such as the 1,2,3-triazole motif, have been investigated as potent anion binding

sites.[13] Importantly, HB is directional, where R−H····A$^-$ bond angles of 180° form the strongest interactions.

Halogen Bonding and Sister Sigma Hole Interactions

Analogous to HB interactions, halogen bonding (XB) has recently emerged as a potent non-covalent interaction in anion supramolecular chemistry (Figure 1.4A).[14] The polarisation of an R−X covalent bond (where X is a halogen and R an EWG) induces the formation of an electropositive region at the halogen atom called a σ-hole (Figure 1.4B). This σ-hole forms along the axis of the R−X bond, at the polar end of the halogen atom. The magnitude of this anisotropy depends on the inductive electron withdrawing strength of the R-group as well as the polarisability of the halogen atom. The more polarisable halogens, such as iodine and bromine form larger σ-holes and are thus better XB donors, with the following general trend I > Br > Cl (fluorine, due to its low polarisability, usually does not form halogen bonds). Generally, XB strengths lie in a similar range to those of HB interactions (10-200 kJ/mol), however, XB interactions display a larger tendency to strictly adhere to a 180° R−X····A$^-$ geometry.[14] These properties are increasingly exploited in anion recognition where often XB receptors exhibit improved or complementary performance over analogous HB systems.[15,16]

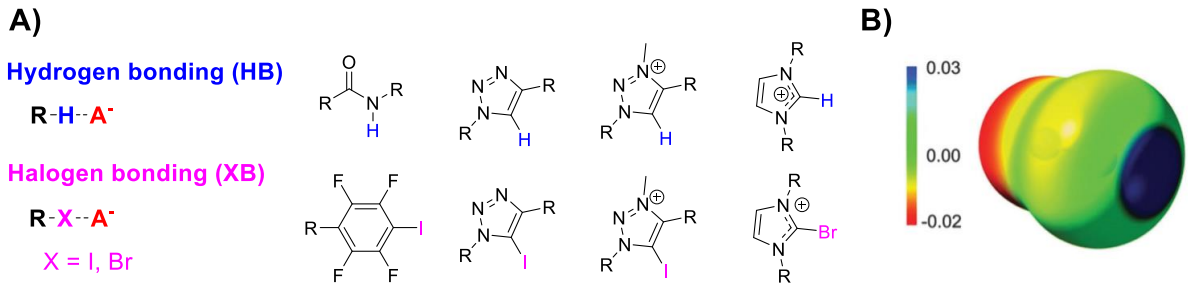


Figure 1.4. A) Commonly utilised binding motifs in anion recognition based on HB and XB donors. B) Calculated electrostatic potential of BrF showing the electropositive σ-hole as the blue region on the Br atom. Reproduced from ref.[17] with permission from the Royal Society of Chemistry 2015.

A variety of other σ-hole interactions have been reported and utilised in anion supramolecular chemistry, most notably chalcogen bonding (ChB), but very recently also pnictogen bonding.[18] In comparison to halogens, chalcogens can, depending on their hybridisation, develop one (sp^2) or two σ-holes (sp^3) giving rise to a larger range of binding geometries. In spite of this, ChB anion receptors remain rare, which can be largely attributed to synthetic challenges and chemical stability.

Anion-π Interactions

While cation-π interactions are well understood and frequently employed, anion-π interactions are underexplored and, due to their relatively poor binding strength, are not in general solely employed for anion recognition.[19] However, in tandem with HB or electrostatic interactions they have been utilised in various anion receptors, for example, a perfluorophenyl-appended sulfonamide receptor[20] or a range of ammonium-based cyclophanes.[21] Advantageously, the large electron-deficient π-aromatic surfaces that are often utilised in anion-π-based receptors can often be utilised to transduce the binding event *via* optical means as demonstrated for the sensing of fluoride by naphthalene diimide (NDI) tweezers.[22]

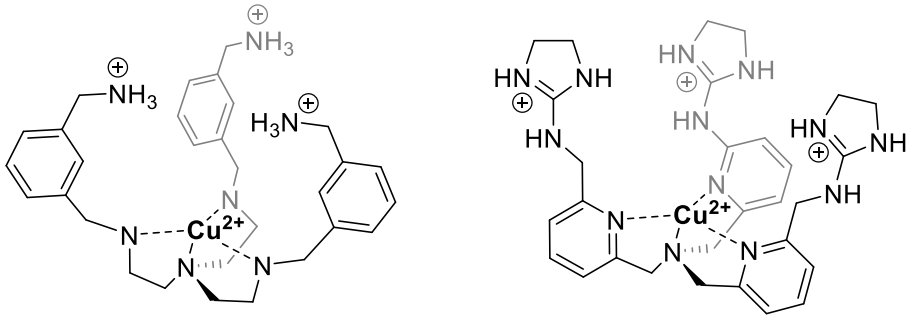
Solvophobic Interactions

Other explored interactions in anion supramolecular chemistry are solvophobic interactions such as the hydrophobic effect. This is classically an entropically-driven interaction between non-polar molecules, which, upon aggregation, release some of their hydration shell. However, the binding of large, charge-diffuse anions, for example perchlorate, to

hydrophobic hosts, such as bambusuril has been shown to be largely driven by the non-classical hydrophobic effect[23], *i.e.* the release of "high-energy" water from the hosts´ binding cavity (enthalpy-driven).[24]

Dative Anion Coordination

While not being strictly a non-covalent interaction, dative bonding of anions to various metal centres enables very strong binding with often high selectivity for small, charge-dense anions. This methodology is often limited either by the high stability of the anion-metal interaction (*i.e.* irreversibility of binding) or by the kinetic or thermodynamic instability of the host complexes. In particular the combination of dative bonding with other interactions (*e.g.* HB) can however be utilised to prepare potent anion receptors, as, for example, demonstrated by Anslyn, who reported tripodal copper complexes with pendant ammonium (receptor **1.3**) or guanidinium groups (receptor **1.4**) to enable phosphate binding in water (Figure 1.5).[25]



1.3 **1.4**

Figure 1.5. Anslyn´s ammonium- or guanidium-containing tripodal copper complexes.

Other non-metal Lewis acids that are often used are boron derivatives which are often potent receptors for diols (*e.g.* sugars) or hard inorganic anions (*e.g.* fluoride or cyanide). For example with boronic acids, formation of a negatively charged, tetrahedral boronate results: $ArB(OH)_2 + F^- \rightleftharpoons ArB(OH)_2F^-$. This equilibrium usually lies far to the right and there is a high degree of selectivity for F^- over halides and other anions. However, depending on reaction conditions and pH, multiple equilibria need to be considered, whereby further substitution can occur to yield $ArB(OH)F_2^-$ or $ArBF_3^-$.[26] These complications, together with strong, irreversible binding, limit the use of these motifs in receptors and sensors. Recently, Gabbaï and coworkers also demonstrated the utility of heavier main group elements, specifically pnictogen cations, as potent F^- hosts.[27]

1.2 Anion Sensing *via* Host-Guest Chemistry

The sensing of anions using reversible host-guest interactions at synthetic hosts has gained significant attention in the past three decades and can be achieved *via* multiple approaches.[5,28] Most commonly optical or electrochemical read-outs are employed, whereby the latter is of particular relevance because electrochemical sensors are innately sensitive, scalable and flexible and can be fabricated at low cost.[29] As a result of these favourable characteristics, electrochemical sensors have arguably become the most commonly used sensors for the detection of a wide range of analytes, including anions, which are the focus of this thesis. In the following the three main electrochemical methodologies (potentiometry, voltammetry and impedance spectroscopy) that are employed for the sensing of anions are introduced. Section 1.2.4 then briefly highlights examples of other anion sensors.

1.2.1 Potentiometric Anion Sensing

1.2.1.1 General Experimental and Theoretical Considerations

In potentiometry the electromotive force (emf; a potential) is measured between a reference electrode and an indicator electrode immersed in the analytical solution. As the simplest electroanalytical technique it has witnessed widespread use and has been investigated in detail. In its most common format ion-selective electrodes (ISEs) are used, which, through chemical means, respond selectively to the activity of the analyte.[30-37] The selectivity is often imparted by a membrane containing ionophores (ion receptors/carriers) (Figure 1.6).

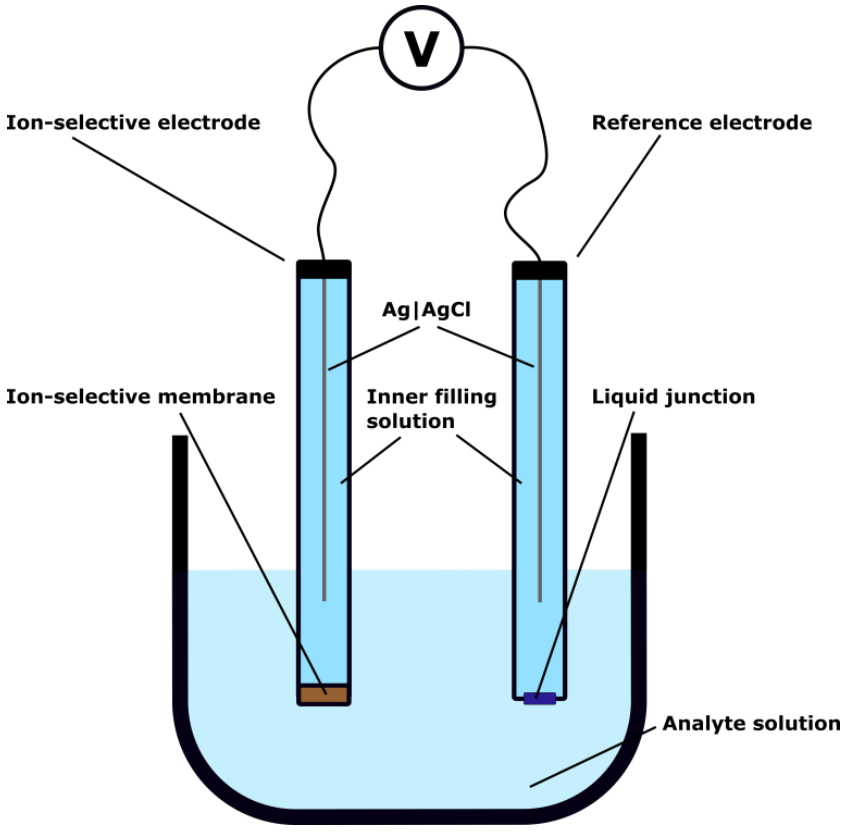


Figure 1.6. Schematic depiction of a membrane-based ion-selective electrode.

Upon ion migration (*i.e.* binding) into the membrane a potential develops which can be easily measured and accurately described by the Nernst equation:

$$E = E^0 + \frac{RT}{z_I F} \ln a_I$$

where E^0 is a constant and a_I and z_I the activity and charge of the ion, respectively, where a ten-fold increase in the activity of the analyte ion generates a potential change of 59.2 mV/z_I ("Nernstian response").

Of crucial importance is that only the desired ion partitions into the membrane and thus induces a response. This can be achieved with various membrane types including glass membranes (used in pH-probes), crystalline membranes as well as liquid or polymeric membranes containing ionophores.

1.2.1.2 Ionophores for Anion-selective Electrodes

Anionophore design largely follows the principles established for solution-phase anion hosts (*i.e.* complementarity as described above). Rather than strong ion binding, the selectivity of the ionophore is the most important parameter that needs to be optimised. This has resulted in the investigation of different receptor topologies using a myriad of reversible dative, covalent or non-covalent interactions to impart selectivity for the desired ionic species. However, a rational design of this selectivity remains cumbersome, especially because the translation of solution-phase binding data (*i.e.* binding constants/selectivities) to the performance of the receptors in ISEs is difficult (largely as a result of the difference in the chemical environment in a solvent in comparison to the (polymeric) membrane).[38] An additional impediment to potentiometric techniques is that their simple signal output (*i.e.*

the conversion of ion activity into a single signal (a potential)) does not allow for the extraction of additional information on binding processes, such as binding geometries/stoichiometries, and is hence of low relevance for fundamental studies. In spite of this, ISEs are particularly useful real-life relevant sensors with widespread applications in many fields.

Most ionophores based on non-covalent host-guest systems are HB donor systems and have been in use for decades. A range of potent anion ISEs were already well established in the 1990's (**1.5-1.8**, Figure 1.7).[39-46]

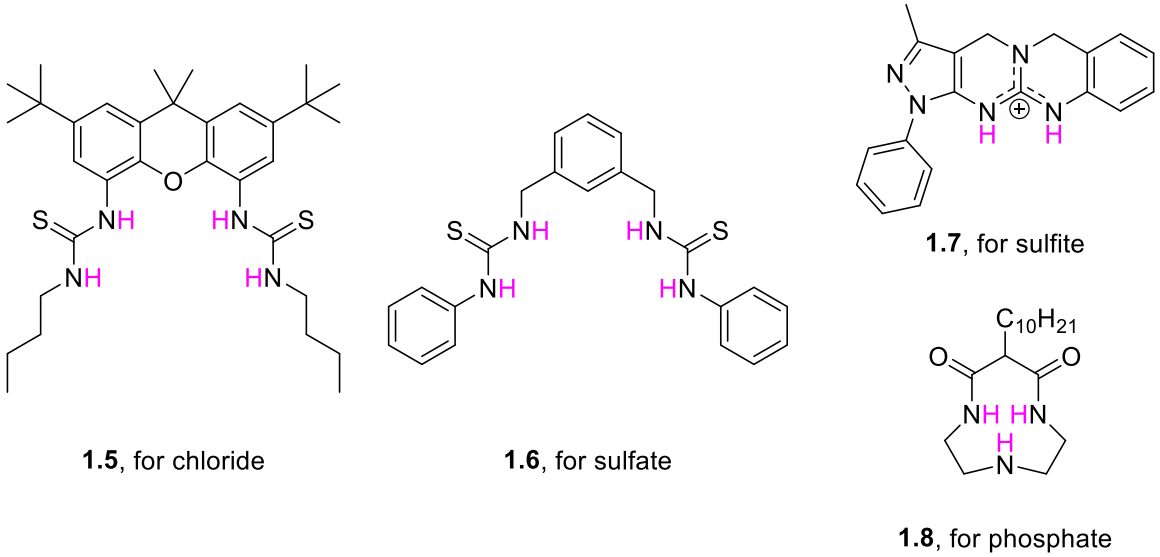
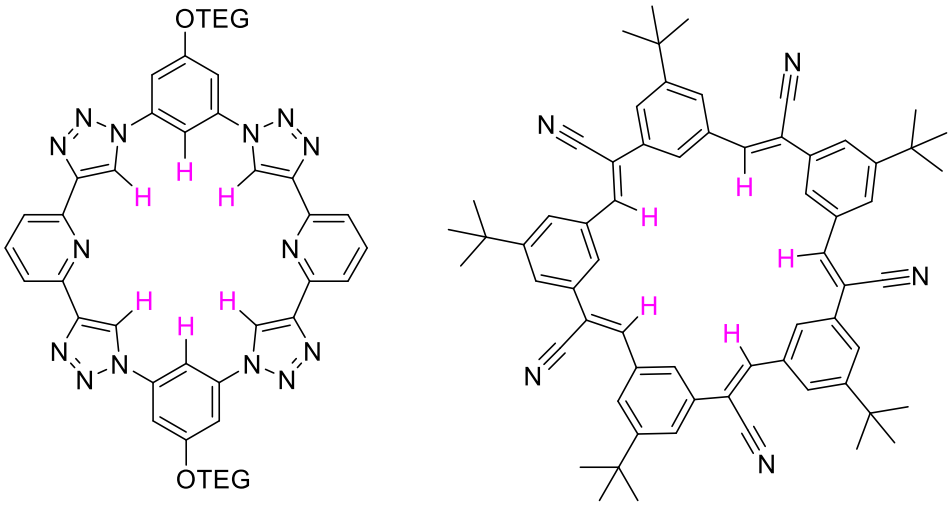


Figure 1.7. Representative examples of early anion-ionophores for potentiometric sensing of the highlighted anions.

The continued exploration of anionophores in the following two decades has resulted in a variety of simple acyclic and cyclic HB anionophores such as amides,[47] (thio)ureas,[48,49] guanidiniums,[50] free-base porphyrins,[51-53] hydrazides,[54,55] dithioxamides[56] and pyrroles/carbazoles.[57-59] Special attention has also been directed at the exploration of receptors with more elaborate topologies and scaffolds, such as tripodal amides, ureas and

squaramides[60-62] as well as ionophores based on calixarene[63-67] and calixpyrrole-scaffolds.[38,68]



1.9 **1.10**

Figure 1.8. C–H HB-based anion ionophores. TEG = triethylene glycol.

A more recent development is the investigation of C–H bond donors in anionophores as pioneered by the groups of Bachas and Flood.[69-71] In their first study the authors reported on triazolophane **1.1** (see above; Figure 1.3) as a potent halide-selective receptor with anti-Hofmeister selectivity and a Nernstian response towards bromide.[69] The good selectivity over potentially interfering anions, in particular the hydrophobic salicylate, enabled Br^- quantification in spiked horse serum. A high iodide selectivity was later achieved with a very similar pyridyl-triazolophane **1.9** (Figure 1.8).[71] The lone pairs of the two central pyridine units disfavour the formation of a 1:1 complex with halides in favour of a 2:1 host-guest complex. Similarly, a ClO_4^--selective electrode based on the 2:1 host-guest formation of cyanostar **1.10** was recently reported by the same groups.[70]

Continued efforts are directed at further improving the selectivity of ISEs[36] as well as the development of more sensitive, real-life relevant, and compact devices, including the investigation of new transduction formats.[33,72-77]

1.2.2 Voltammetric Anion Sensing

Voltammetric techniques such as cyclic voltammetry (CV), differential pulse voltammetry (DPV) or square wave voltammetry (SWV) are some of the most commonly employed electrochemical techniques to study anion binding in solution or at interfaces. Transduction of the binding event at a receptor is achieved with the help of an integrated redox transducer, whose electrochemical properties are modulated in the presence of the bound anion (Figure 1.9). In almost all cases this modulation is a cathodic shift of the transducers´ half-wave potential ($E_{1/2}$), as a result of a stabilisation of the higher oxidation state. A variety of mechanisms for this stabilisation have been proposed, with through-bond and through-space communication between the anion binding site and the redox transducer being the most important ones.[78,79] In all cases the effective transduction of the binding event is reliant on effective spatial and/or electronic coupling of the binding site and the transducer.

In contrast to simple host-guest systems, where the binding can be described by $K = \frac{[HG]}{[H][G]}$ (for a 1:1 stoichiometric host-guest system), the (an)ion binding affinity to redox-active hosts is strongly dependent on the charge (*i.e.* redox state) of the receptor.

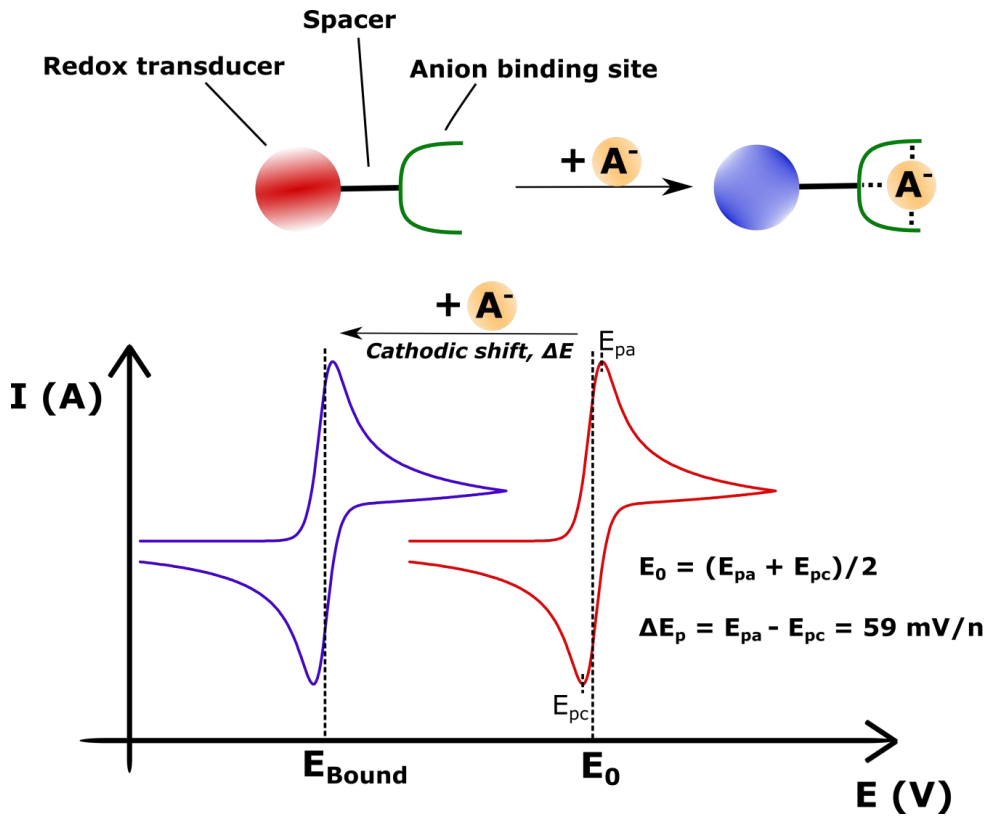


Figure 1.9. Schematic depiction of the general sensing principle of voltammetric anion sensors. Anion binding induces a cathodic perturbation of the redox transducer that is measureable *via* voltammetric techniques such as CV. The depicted voltammograms represent an ideal, reversible case in which the initial half-wave potential of the transducer E_0 as well as the peak separation ΔE_p can be described by the depicted equations.

These equilibria are depicted in the square scheme shown in Figure 1.10. Specifically, anion binding is enhanced in the higher oxidation state. Of particular importance is the fact that the voltammetric response (shift, ΔE) is largely dependent on the difference in binding strength between the different oxidation states. In its most general form, this response can be described by eqn. 1.1.[78,80] The ratio of K_{Ox}/K_{Red} (often called binding enhancement factor (BEF)) where K_{Ox} and K_{Red} are the (an)ion binding constants to the oxidised and reduced host, respectively, can be obtained directly from the maximum shift of the transducer in the presence of the target guest G. For $[G] >> [H]$ a special case has been derived (eqn. 1.2) from which both K_{Ox} and K_{Red} can be extracted *via* non-linear least square fitting of the voltammetric binding isotherms.[81]

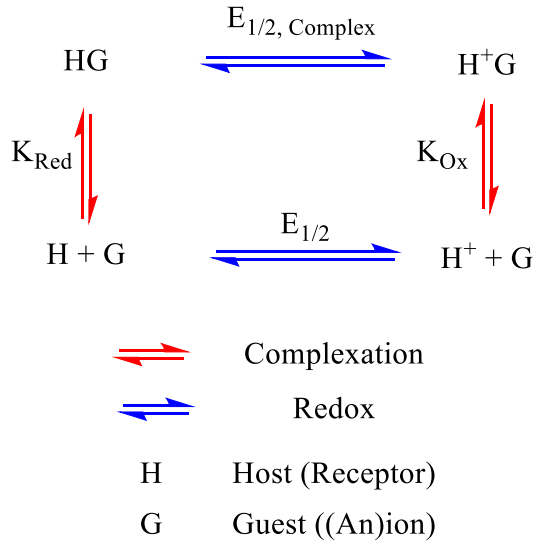


Figure 1.10. Square scheme for the host-guest equilibria involved in voltammetric (an)ion sensing.

$$\Delta E = -\frac{RT}{nF} * \ln\left(\frac{K_{Ox}}{K_{Red}}\right) \quad \text{eqn. 1.1}$$

$$\Delta E = -\frac{RT}{nF} * \ln\left(\frac{1+K_{Ox}*[G]}{1+K_{Red}*[G]}\right) \quad \text{eqn. 1.2}$$

As discussed above, in all cases the shift of the receptor's half-wave potential is dependent on the relative change in anion binding constants between the different oxidation states (K_{Ox}/K_{Red}), with a larger response in systems where the (an)ion binding is strongly affected by the electrochemical generation of a different species. This, again, highlights why efficient spatial and/or electronic coupling between binding and transducing sites is of paramount importance. These concepts are also discussed in more detail in Chapter 2, Section 2.1.

In most cases the voltammetric response of the sensor is a continuous cathodic shift of the transducers' formal potential upon anion binding, though in some instances a so-called "two-wave" behaviour, the progressive disappearance of the initial wave with a

concomitant emergence of a new wave at lower potential, is observed. This is the case in a slow exchange regime (slow ligation on/off rates), usually when anion binding is very strong, *i.e.* in non-competitive solvents. In this case the BEF (K_{Ox}/K_{Red}) can be directly obtained from the potential difference of these couples (eqn. 1.1), while under fast exchange, continuous shift conditions the BEF can only be obtained at a plateauing response or from explicit fitting of the binding isotherms. A further consideration is that in the slow exchange regime the magnitude of the shift is not dependent on anion concentration; the analyte concentration can only be inferred from the ratio of the peak currents of the two waves.

Further details about these principles as well as more detailed experimental considerations (*e.g.* electrolyte effects) are discussed in Section 2.1.

1.2.2.1 Redox Transducers

A variety of different redox-active groups can be used to report on anion binding. The most common of these redox transducers are introduced in the following and Table 1.1 provides a brief summary of their advantages and disadvantages for applications as anion sensors.

Ferrocene

Since its discovery in the early 1950s ferrocene (Fc) has been utilised in a broad range of electrochemical systems and derived sensors,[82] due largely to its availability, ease of synthetic modification and favourable electrochemical properties. Most importantly, the Fc/Fc^+ couple displays a well-defined, reversible one electron redox couple at moderate potentials and is compatible with a wide range of solvents, electrolytes and analytes. Furthermore it is particularly favourable as a transducer in anion receptors due to the

'switch-on' of binding upon oxidation to the cationic ferrocenium and together with the related isoelectronic metallocene, cobaltocenium, was one of the very first redox transducers employed in anion receptors, as reported by Beer.[83] In fact, the first synthetic redox-active anion sensor, reported in 1989, was based on a cobaltocenium macrocyclic receptor.[84] The cobaltocene/cobaltocenium (Cp_2Co/Cp_2Co^+) couple displays very similar redox-properties as the Fc/Fc^+ couple, with the most marked difference being a significantly lower $E_{1/2}$ (approx. −1.3 V *vs.* Fc/Fc^+). Notably, this can facilitate the sensing of anions whose oxidation potential is incompatible with the Fc/Fc^+ couple (such as I^-), however, this low potential can be incompatible with a variety of solvents. In addition to this, the challenging synthetic manipulation of charged cobaltocenium (derivatives) renders Fc a much more commonly employed transducer.

Tetrathiafulvalene

Tetrathiafulvalene (TTF) is another redox-active molecule that has received considerable attention as a transducer in synthetic anion receptors. In contrast to Fc, TTF exhibits three stable, reversible redox states (TTF, the radical cation $TTF^{+\bullet}$ and the dication TTF^{2+}) allowing for additional tuning of the anion-receptor interaction.[85] However, while the first redox couple ($TTF/TTF^{+\bullet}$) is accessible at potentials similar to those of Fc/Fc^+, the second couple ($TTF^{+\bullet}/TTF^{2+}$) has a half-wave potential that is more anodic by ≈350 mV. Depending on the electron-density at the TTF derivative and the solution-phase conditions, this second couple often overlaps with anions possessing a low oxidation potential (*e.g.* Br^-, I^- or N_3^-). As a consequence, usually only the first couple is exploited to transduce an anion binding event. In comparison to Fc, TTF is much less synthetically accessible and has only rarely been

applied within more complex receptive architectures such as those based on macrocyclic, interlocked or dendrimeric systems.

Porphyrin

Free base and metallo-porphyrins represent an interesting motif for sensing applications due to their rich photophysical and electrochemical properties; the latter is manifested by two quasi-reversible oxidative couples ($P/P^{+\bullet}$ and $P^{+\bullet}/P^{2+}$) at potentials more anodic than that of Fc/Fc^{+} both of which are strongly dependent on the specific substitution/metalation of the porphyrin.[86] Whilst synthetically non-trivial to manipulate, porphyrins possess rich chemistry with respect to substitution patterns and the nature of the coordinated metal. Advantageously, the metal-centre of the metallo-porphyrin can act as an anion binding site which is strongly coupled to the porphyrin resulting in efficient signal transduction. Similarly, anions can directly engage in HB to the central N−H donors of the free base porphyrin. In spite of this, only very few porphyrin-based voltammetric anion sensors have been developed.

Other Complexed Metals

Different metal complexes, in particular those of the first and second row transition metals have been utilised as transducers in electrochemical sensors. Most commonly nitrogenous ligands such as bipyridine (bpy) or terpyridine (tpy) are used to form stable and electrochemically well-behaved transducer complexes. The derivatisation of these ligands facilitates the introduction of binding sites into the organic scaffold and further allows tuning of the redox properties of the complex by variation of the electron density. Most

commonly the redox couples are reversible one-electron metal-centred oxidative couples at moderate to high potentials. It is worth noting that at, very low potentials, additional ligand-centred reductive couples are often observed, albeit rarely used to transduce anion binding. If the metal is coordinatively unsaturated, an anionic analyte may directly bind to the metal, which may result in an increased voltammetric response. Additionally, different types of ligands can be incorporated *via* sequential complexation, enabling, for example, a tuning of the number of receptive sites or incorporation of additional functionalities.[87]

Other Organic transducers

A diverse class of redox-transducers are those based on organic redox-active functionalities. While these are arguably the most synthetically adaptable and tuneable transducers they have received considerably less attention. This may be attributed to their complex electrochemical behaviour, which is often solvent and/or pH dependent. One such transducer are the tri(alkyl/aryl)amines which can be (reversibly) oxidised at moderate to high potentials and have found some application in anion sensors.[88] Similarly, (hydro)quinones have received considerable attention in various electrochemical studies, but their use in anion sensors has been limited by their relatively complex solvent and pH dependent electrochemistry which arises from two proton coupled one-electron reductions. Indeed, early studies of quinone-based anion sensors produced responses that were difficult to rationalise[89,90] impeding their further use.[91] Another solely organic electrochemically active motif that has been extensively studied in switches and interlocked structures, but has found little use in anion sensors, is the bipyridinium motif found in diquat(DQ)/paraquat(PQ).[92] This dicationic transducer can be reversibly reduced at low

potentials in two one-electron steps ($DQ^{2+}/DQ^{+\bullet}$ and $DQ^{+\bullet}/DQ$) thus deactivating anion binding. While this facilitates sensing of anions with low half-wave potentials, such as iodide, it has found limited use in voltammetric sensors most likely because of the demanding synthetic pathways required.

Examples of anion sensors based on these different transducers are discussed in the following section.

Table 1.1. Comparison of different redox transducers for application in derived voltammetric (anion) sensors.

Transducer	Advantages	Disadvantages
Ferrocene	-Well-defined, reversible redox couple -Synthetically very adaptable	
TTF	-Two-stage oxidation -Rich spectro(electro)chemistry -Conducting[a]	-Synthetically challenging -Moderate/high oxidation potential -Reversibility often compromised[b]
Porphyrin	-Highly tuneable by metal substitution -Rich photophysical properties -Biomimetic	-High oxidation potential(s) -Reversibility often compromised[b]
Metal complexes	-Highly adaptable through metal or ligand substitution -Often luminescent (double readout)	- Synthetically often challenging
Organic	-Tuneable redox potentials	-Solvent or pH-dependent redox properties -Synthetically can be challenging

a – Relevant for molecular electronics. b – In particular for the second oxidation process; reversibility often solvent dependent.

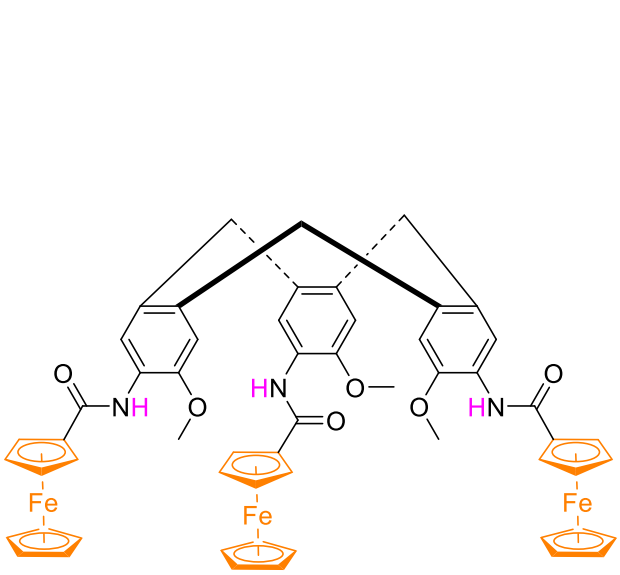
1.2.2.2 Solution-Phase Voltammetric Anion Sensing

1.2.2.2.1 Redox-Active Receptors Based on N–H Hydrogen Bond Donors

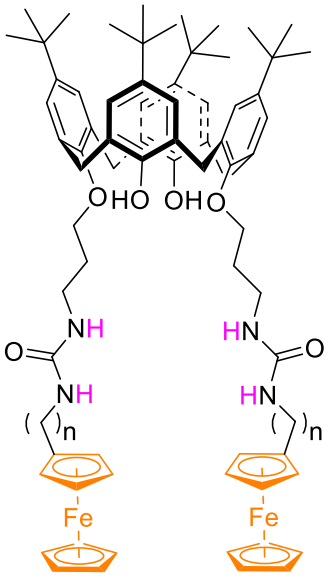
Almost invariably early voltammetric anion sensors, but also recent examples, are based on N–H hydrogen bond donors. A large variety of such systems, mainly containing amide and urea binding sites, were reported in the 1990s.[28,93] Many of these early systems and the

majority of more recent examples in the last two decades utilise an integrated Fc redox transducer with amine,[94-97] amide,[98-102] imidazole,[103-107] amide/urea macrocycle,[108,109] thiourea,[110] amidine,[111] guanidine,[112,113] cyclotriveratrylene-amide,[101] calix[4]pyrrole,[114] calix[4]arene-amide,[115,116] calix[4]arene-urea,[117,118] or calix[4]arene-amine/imine[119] conjugates (see Figure 1.11 for examples). Their sensory performance does not significantly deviate from those of earlier systems; most display a progressive cathodic shift of the respective Fc/Fc^+ redox couple upon anion addition with some displaying a "two-wave" behaviour, of which a representative example, as assessed by SWV, is shown in Figure 1.12. Furthermore, the majority of these sensors are electrochemically reversible and their anion selectivity largely dictated by the nature of the N−H HB binding site as well as anion basicity. In 2001 Reynes *et al.* reported a detailed comparison of acyclic and cyclic ferrocenylamide based sensors including the cyclotriveratrylene receptor **1.11** (Figure 1.11)**.**[101] As in almost all of the sensors discussed in the following, **1.11** displayed only one redox couple indicating that all three ferrocene transducer groups were simultaneously, independently oxidised. This system displayed a particularly interesting response to 1 equiv. of anions. F^- and HSO_4^- induced only small perturbations with one-wave (progressive shift) behaviour. This was also highly solvent dependent where F^- only perturbed the Fc/Fc^+ couple in ACN (-60 mV) and no perturbation in the less competitive DCM. Conversely, HSO_4^- induced a small response in DCM (-20 mV) while no shifts were measured in ACN. In contrast, **1.11** responded to the biologically relevant oxoanions $H_2PO_4^-$ and ATP^{2-} in both ACN (−140 mV and −160 mV, respectively) and DCM (-230 mV for both anions) displaying "two-wave" behaviour. A similar system based on bis-Fc-containing calix[4]arene-urea receptors **1.12** was later studied where the cathodic perturbations (≈−100 mV) induced in the presence of 2 equiv. of $H_2PO_4^-$ in DCM were independent of linker length (n = 1,3).[52] Additionally, the replacement

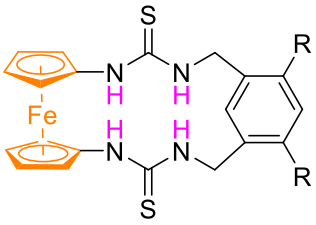
of the urea motif in **1.12** with an amide, a poorer HB donor, elicited a similar electrochemical response, indicating that binding in this non-competitive solvent was driven almost entirely by electrostatic interactions between the anion and the Fc^{+} moieties.



1.11

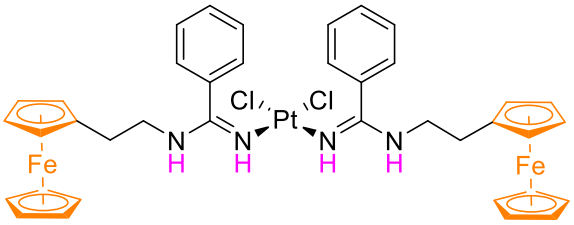


1.12: n = 1, 3



1.13a: R = $CH(CH_3)_2$

1.13b: R = H



1.14

Figure 1.11. Representative voltammetric anion sensors based on Fc and typical N−H anion binding sites.

Apart from the ubiquitously used amide and urea binding sites, thioureas have been incorporated into various Fc-based voltammetric sensors, such as **1.13a** and **1.13b**.[110] Both displayed significant responses to the basic F^{-}, OAc^{-}, $H_2PO_4^{-}$ and $HP_2O_7^{3-}$ (1 equiv. in DMSO) of between −90 to −150 mV for **1.13a** and −120 to −200 mV for **1.13b**. The response of the

less electron-rich **1.13b** was larger by at least −20 mV in all cases. Neither receptor showed any response to 10 equiv. of Cl^-, Br^-, HSO_4^- and NO_3^-.

In a more recent study Nieto *et al.* assembled a bis(ferrocenyl-amidine) receptor **1.14** *via* Pt(II)-mediated nucleophilic addition.[111] The Fc/Fc^+ couple of this sensor displayed a "two-wave" behaviour upon addition of $H_2PO_4^-$ in ACN/DCM 5:1, as shown in Figure 1.12. In this slow-exchange, strong binding regime, these voltammograms can be used to infer the stoichiometry of the receptor-anion complex. In this case the new wave at lower potential (-90 mV more cathodic) is only fully developed at 2 equiv. of $H_2PO_4^-$, indicative of formation of a 1:2 stoichiometric host-guest complex.

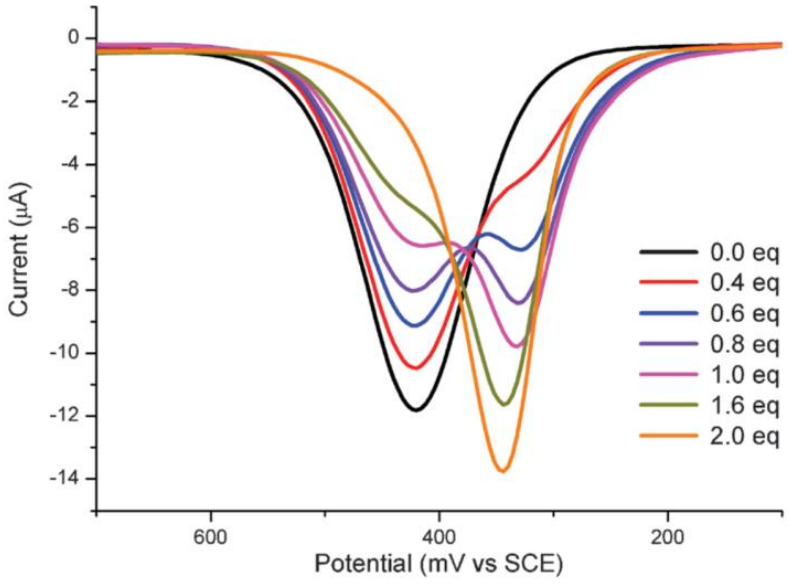
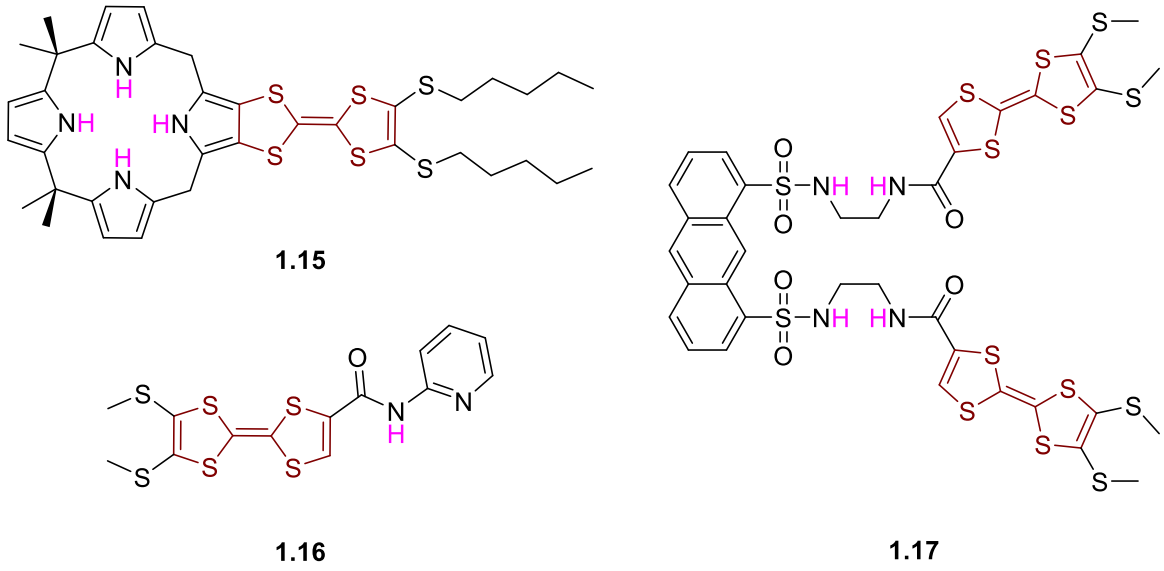


Figure 1.12. Representative evolution of a SWV upon addition of anions (two wave behaviour). In this specific case receptor **1.14** was titrated with $H_2PO_4^-$ in ACN/DCM 5:1. Reproduced from ref.[111] with permission from The Royal Society of Chemistry.

Another commonly utilised redox transducer, TTF, was first investigated in detail by Becher and co-workers in 2003.[120] A calix[4]pyrrole receptor was employed which was directly linked to TTF at one of the pyrrole units (**1.15**, Figure 1.13). Voltammetric anion sensing was

then carried out in ACN by monitoring the perturbations of the first redox couple (TTF/$TTF^{+\bullet}$). Both Br^- (−34 mV) and Cl^- (−43 mV) induced significant cathodic shifts at low concentrations (0.5 mM, 1 equiv.).



1.15 **1.16** **1.17**

Figure 1.13. Early examples of TTF voltammetric anion sensors based on calix[4]pyrrole and amide binding sites.

Other early examples were published by Zhu's group, who directly conjugated amide-binding sites to the TTF core to afford the simple mono-amide TTF receptor **1.16**[121] as well as the more complex amide-sulfonamide receptor **1.17** (Figure 1.13).[122] The presence of the anthracene backbone of the receptor additionally enabled fluorescent anion sensing. This dual signalling approach was also employed in a TTF-monoamide-BODIPY system for the sensing of fluoride in DCM.[123] It should be noted that the "selective" sensing of fluoride, or other basic anions, in many of the systems discussed arises from receptor deprotonation rather than a specific hydrogen bonding interaction. Precisely this behaviour was exploited by Xiong *et al.* who reported a 2,4-dinitrophenylhydrazone-TTF sensor. Upon addition of F^-

in DCM large *anodic* shifts of up to 400 mV (both couples) were observed. This interesting behaviour arises because deprotonation of the hydrazone leads to conjugation and subsequent intramolecular electron transfer from the electron rich TTF to the electron deficient dinitrophenyl group. This latter moiety furthermore allows optical fluoride detection whereby both electrochemical and optical sensing of F^- was achieved with good selectivity over OAc^-, $H_2PO_4^-$, Br^-, Cl^- and NO_3^-. Other TTF-containing N−H HB anion sensors include systems based on diindolylquinoxaline,[124] calix[4]arene[125] and diamino-diamido receptors.[126,127]

While an early study[128] demonstrated the potential of porphyrin as a transducer for anion sensing, its use has been, as noted above, limited. One rare example was reported in the "picket fence" tetra-amide-imidazolium Zn-porphyrin **1.18** (Figure 1.14).[129] Addition of 5 equiv. of Cl^- (−180 mV), HSO_4^- (−140 mV) and NO_3^- (−95 mV) led to the expected cathodic perturbation of the $P/P^{+\bullet}$ couple in ACN while ClO_4^- induced no shifts and $H_2PO_4^-$ led to precipitation. In a later study similar systems based on the tetra-amide-porphyrin scaffold were investigated, whereby the specific influence of the nature of the metal-centres (Fe(Cl), Co(PF_6), Ni, Cu, Zn, Cd or Hg) on the sensory performance was systematically investigated.[130] The photophysical and electrochemical properties of **1.19** are strongly dependent on the nature of the metal. For example, the half-wave potential for the first couple differed by 360 mV between the **1.19Cd** (lowest $E_{1/2}$) and **1.19Fe(Cl)** (highest) in 1:1 DCM/ACN. While addition of 5 equiv. of ClO_4^- resulted in no perturbations, addition of Cl^-, $H_2PO_4^-$ or NO_3^- induced significant cathodic shifts in almost all systems. The largest shifts for all anions were observed for **1.19Hg** with some significant variance between receptors for different anions. Interestingly, the addition of these anions to the unmodified tetraphenylporphyrin (TPP) compounds TPP.Cu, TPP.Zn and TPP.Cd led to significantly larger cathodic perturbation for

all anions. While the anion binding constants (and selectivity) to the amide-containing receptors **1.19** is certainly larger than those of the TPPs this importantly demonstrates that the response of these systems is not driven by the magnitude of the binding strength but the *relative difference* in binding between the differently charged states (*i.e.* the BEF), which, apparently, in the case of the metallated TPPs, is larger.

The sensory properties of the free-base porphyrinogen derivative **1.20** have also been investigated.[131] In ortho-dichlorobenzene both porphyrin couples were cathodically perturbed upon addition of anions (up to 3 equiv.) with maximum shifts of −600 mV (F^-), −580 mV (OAc^-), −570 mV ($H_2PO_4^-$), −70 mV (NO_3^-) and −60 mV (ClO_4^-). These substantial responses can most likely be attributed to the choice of the extremely apolar solvent, the good electronic communication (coupling) between the binding site and the transducer and potentially deprotonation of the receptor.

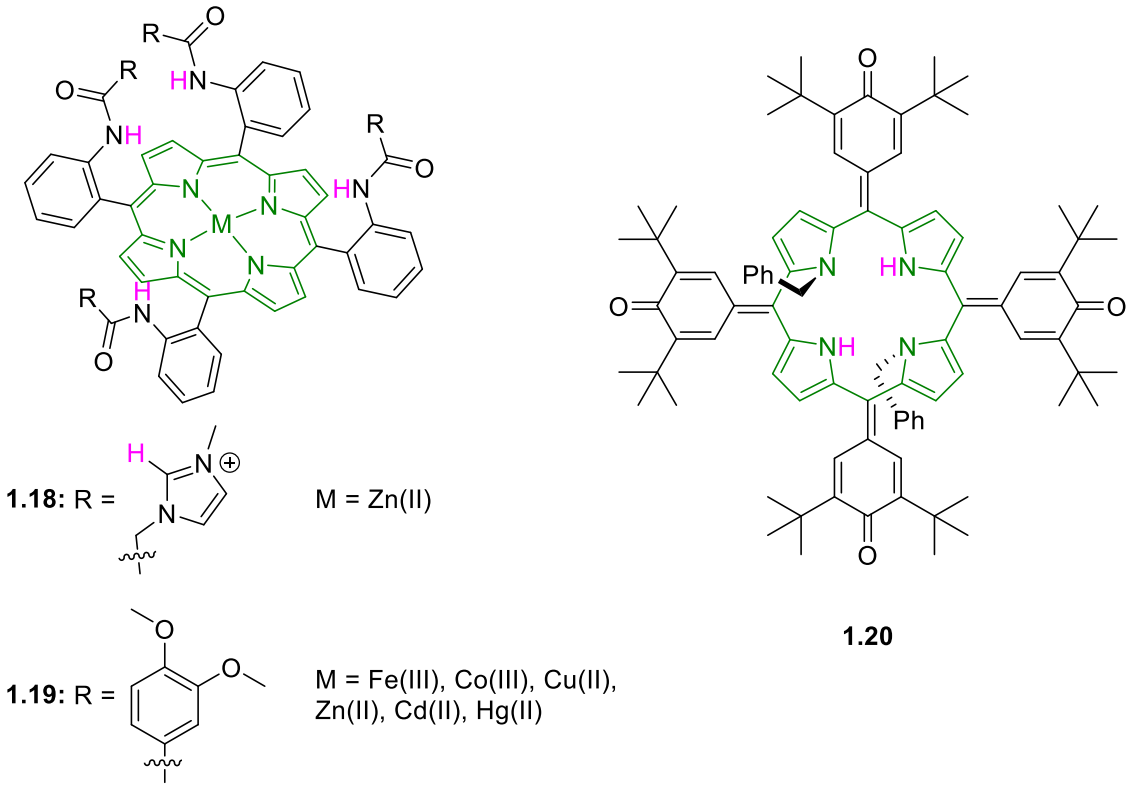


Figure 1.14. Porphyrin-based receptors for voltammetric anion sensing.

Other voltammetric anion sensors based on N−H HB donors and purely organic redox transducers include phenylenediamine-urea receptors.[132]

A variety of other redox-receptors based on metals have also been reported, whereby an advantageous double readout (electrochemical, luminescent) is often feasible. Most of these receptors are based on transition metal complexes of ruthenium or osmium with receptor modified nitrogenous ligands, such as bipy, terpy, imidazole or pyrazole, for example receptors **1.21** and **1.22**, Figure 1.15, in which anion sensing was reported *via* the M^{2+}/M^{3+} couple.[133-137]

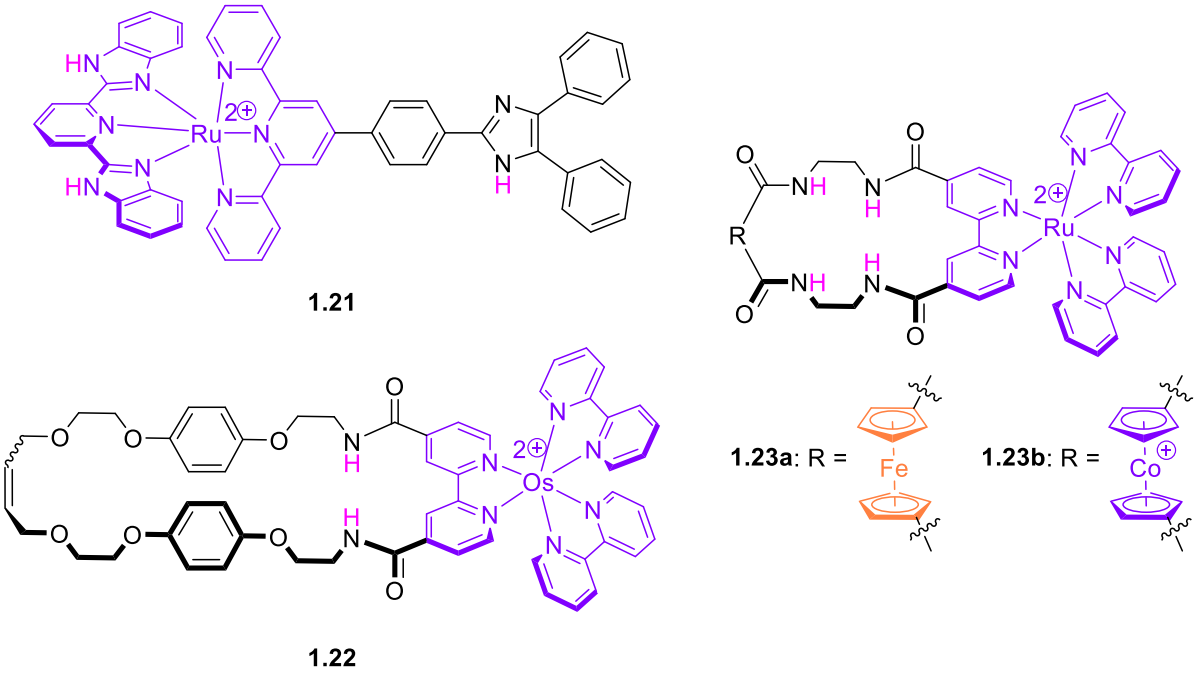


Figure 1.15. Ruthenium- and osmium-containing voltammetric anion sensors.

In a rare example of a receptor containing two redox transducers Beer and co-workers reported tetraamide macrocycles **1.23a-b** containing both a $Ru(bpy)_3^{2+}$ as well as either a Fc or a Cp_2Co^+ transducer.[138] Cl^- sensing in ACN was achieved both *via* the metallocene as well

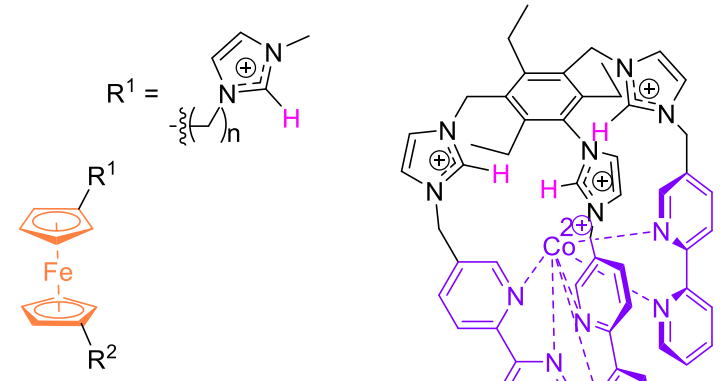
as bpy redox couples, with cathodic perturbation of **1.23a** of −40 mV and −60 mV for the couples, respectively (anion in excess). Interestingly, the cobaltocenium analogue **1.23b** exhibited an even larger perturbation of both couples of −90 mV and −110 mV, respectively. Another metal-complex redox transducer that has received some attention is the dithio carbamate-metal motif, which has been investigated by Beer and co-workers in a variety of acyclic and macrocyclic receptors.[139-141]

1.2.2.2.2 Redox-Active Receptors Based on C−H Hydrogen Bond Donors

While often weaker than N−H bond donors, C−H bonds are much less prone to deprotonation, a problem that is often observed for N−H bond donors in less-competitive media in the presence of more basic anions such as F^- or OAc^-. A prominent C−H HB motif is provided by imidazolium. The first example of an imidazolium-based C−H HB voltammetric sensor was published as early as 2000 in which simple Fc-imidazolium receptors were shown to respond to anions.[142] More systematic investigations of acyclic[143-147] and cyclic[148] imidazolium-based sensors have only been conducted more recently. For example, Jin and co-workers reported in-depth studies of a series of mono-and bis(imidazolium)-substituted ferrocenes **1.24a-f** with varying ferrocene-methylene- imidazolium group linker length (Figure 1.16).[143,147] Unsurprisingly, the magnitude of the cathodic shifts of **1.24a-d** were strongly dependent on the methylene linker length, whereby the magnitude of the Fc/Fc^+ cathodic shift response upon F^-, Cl^- and HSO_4^- addition (10 equiv. in ACN) diminished significantly with increasing distance between the ferrocene and imidazolium binding sites. Interestingly, this attenuation was observed to be dependent on the nature of the anion; for example, the response of **1.24a-d** towards F^- decreased from −230 mV, to −160 mV, −28 mV

to −12 mV while the Cl^- response magnitude was significantly lowered from −65 mV, to −21 mV, −13 mV, to −10 mV.

The incorporation of imidazolium into a bipy-ligand allowed the facile assembly of the highly-preorganised cage-like-receptor **1.25** after complexation with Co(II) (Figure 1.16).[149] Initial experiments in ACN revealed significant cathodic perturbation of the Co^{2+}/Co^{3+} couple upon addition of up to 1.5 equiv. Cl^- (−140 mV) or Br^- (−120 mV). Due to the relatively high half-wave potential of the receptor (+100 mV *vs.* Fc/Fc^+) the analysis of other anions with moderate oxidation potentials was not possible in ACN prompting the use of ACN/H_2O 4:1 for further studies. In this solvent system a significant response was observed for a wider range of anions in the order $Cl^- > Br^- \approx OCN^- > SCN^- \approx I^-$ with shifts of up to −120 mV.



1.24a-d: n = 0,1,3,4, R^2 = H

1.24e-f: n = 0 or 4, $R^2 = R^1$

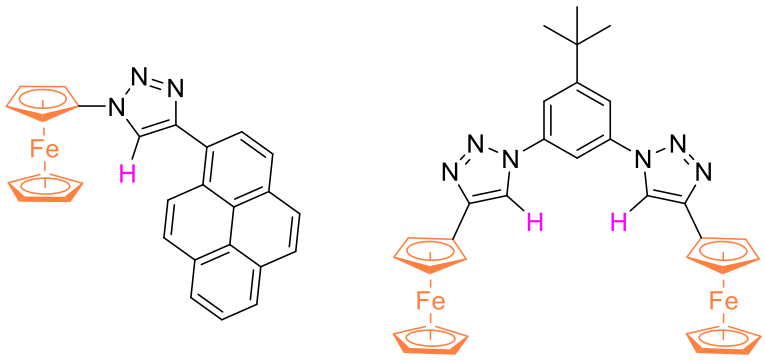
1.25

Figure 1.16. Imidazolium C−H bond donors in Fc- and $Co(bpy)_3$-containing sensors.

Another potent C−H bond donor motif recently investigated is 1,2,3-triazole.[150] The heterocycle's widespread use can largely be attributed to the ease of preparation (*via* "click" chemistry from an azide and alkyne) and the potent polarised C−H bond in the 5-position.

Furthermore the C–H hydrogen bond donor potency can be easily enhanced *via* methylation at the 3-position, yielding the cationic triazolium.

Early examples of triazole-containing voltammetric anion sensors were reported by Tárraga and Molina. The simple Fc-triazole-pyrene receptor **1.26** (Figure 1.17) exhibited a cathodic shift of −100 mV in DCM only for $HP_2O_7^{3-}$, while $H_2PO_4^-$, HSO_4^-, OAc^-, NO_3^-, F^-, Cl^- and Br^- elicited no response.[151] Kim's group utilised the bis(Fc-triazole) receptor **1.27** to also selectively sense $H_2PO_4^-$ and $HP_2O_7^{3-}$ with selectivity over all halides, PF_6^-, ClO_4^-, HSO_4^- and OAc^- (2 equiv. in DCM).[152] The phosphorus oxoanions induced cathodic shifts of the Fc/Fc^+ transducer of ≈−200 and ≈−180 mV, respectively. This design was later elaborated on by the introduction of additional amide binding sites between the triazole and Fc moieties.[153] Under equivalent conditions as for the aforementioned system this sensor responded to $H_2PO_4^-$ more weakly with a cathodic shift of −130 mV.



1.26 **1.27**

Figure 1.17. Early examples of simple Fc-triazole based voltammetric anion sensors.

Tárraga and Molina also conducted an in depth study on a range of related ferrocene triazole receptors **1.28-1.35** (Figure 1.18).[154] All receptors displayed Fc/Fc^+ cathodic shifts in the presence of $HP_2O_7^{3-}$, $H_2PO_4^-$, F^- and OAc^- in ACN (**1.30** and **1.33** in ACN/DCM 1:1 due to

solubility issues) with no response to HSO_4^-, NO_3^-, Cl^- and Br^- in almost all cases (a response was observed for Cl^- and Br^- for receptor **1.29**). The receptors **1.28**, **1.29** and **1.32** exhibited two redox waves where the more anodic one was assigned to the N-substituted Fc (N-Fc) and the other to the C-substituted Fc (C-Fc). Interestingly, the anion-receptor complexes of **1.28** and **1.29** displayed only one wave at a significantly more cathodic potential (with the exception of the **1.28**-F^- adduct). The overall magnitude of anion binding induced cathodic perturbation of N-Fc in **1.28**, **1.29** and **1.32** was comparatively much larger than that of the C-Fc (by up to one order of magnitude in some cases). For example, the C-Fc of **1.32** was not responsive to OAc^-, while the N-Fc exhibited a −100 mV response in the presence of the same anion.

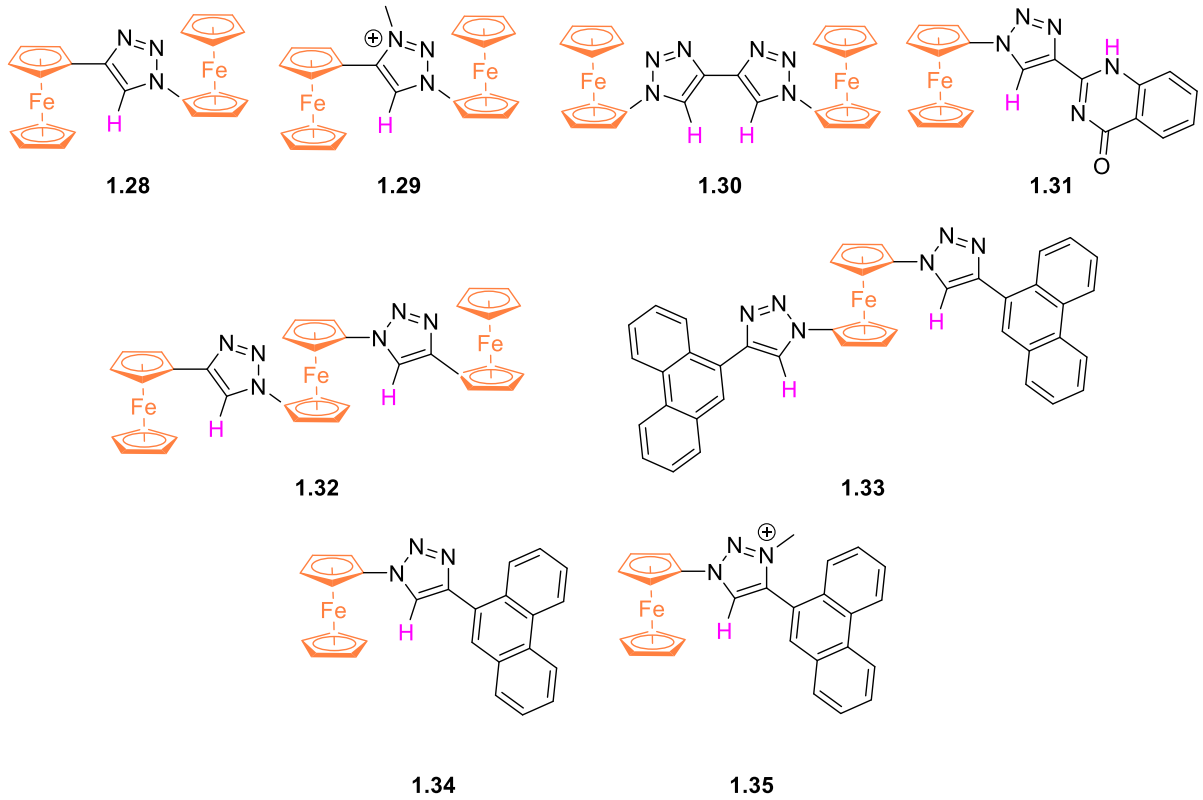


Figure 1.18. Chemical structures of various Fc-triazole receptors.

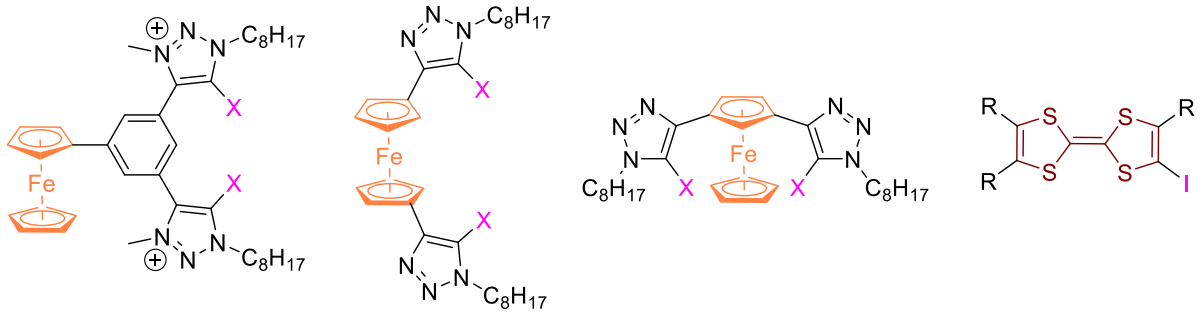
It should be noted that this contrasting responsive behaviour most likely does not arise from a better "communication" between the binding site and the N-Fc but from a pronounced "anion binding switch-on from **1.32**$^{2+}$ to **1.32**$^{3+}$" when all three Fc moieties are oxidised.

The authors furthermore showed that the response of **1.31** to the basic anions $HP_2O_7^{3-}$, $H_2PO_4^-$, F^- and OAc^- arises from deprotonation and the positively charged triazolium receptors **1.29** and **1.35** exhibited larger cathodic shift magnitudes towards all tested anions in comparison to their neutral analogues **1.28** and **1.34**. The incorporation of Fc and triazoles has also been achieved in various other architectures including macrocyclic receptors[155,156] as well as calix[4]arenes.[157]

1.2.2.2.3 Redox-Active Receptors Based on C–I Halogen Bond Donors

The proto-triazole/triazolium motifs can be modified to the XB 5-iodo-1,2,3-triazole and corresponding charge assisted XB triazolium donor analogues which have recently been utilised in anion receptors.[15,16] Based on this motif, Beer and co-workers reported the first example of a XB-receptive voltammetric anion sensor in 2015 wherein a range of neutral and cationic XB and HB receptors were prepared (Figure 1.19) and studied in ACN.[158] Both receptors **1.36XB** and **1.37XB** displayed moderate cathodic perturbations in the presence of 10 equiv. Cl^- (−32 and −30 mV, respectively) and Br^- (−19 and −18 mV, respectively) the magnitudes of which were notably much larger in comparison to the responses of the HB analogues **1.36HB** (−17 and −11 mV) and **1.37HB** (−6 and 0 mV), for Cl^- and Br^-, respectively. The XB 1,3-bis-triazole-ferrocene receptor **1.38XB**, an analogue of receptor **1.37XB**, demonstrated selectivity for N_3^- (−40 mV) over Cl^-, Br^- and OAc^- (max −22 mV for Br^-) in ACN/H_2O 99:1 at 10 equiv.[159] Importantly, the enhanced cathodic responses for all the XB

ferrocene receptors mentioned above (in comparison to their HB analogues), was attributed to better electronic communication of anion binding through the XB interaction and/or stronger binding. Molina and co-workers also studied the XB analogue of their previously discussed HB receptor **1.32** (Figure 1.18) in ACN/DCM 1:1 where the cathodic response of the XB-sensor in the presence of anions (*vide supra*) was comparatively smaller in all cases, which is not necessarily a reflection of weaker binding (see also Section 1.2.2.2.5).[160]



1.36XB: X = I **1.37XB:** X = I **1.38XB:** X = I **1.39a**: R = H

1.36HB: X = H **1.37HB:** X = H **1.38HB:** X = H **1.39b**: R = Me

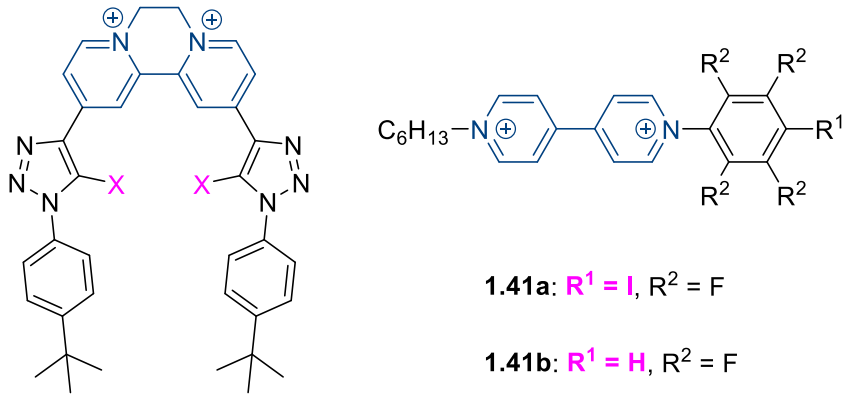
Figure 1.19. Halogen bonding voltammetric anion sensors based on Fc or TTF.

Recently, Schöllhorn and Fave used halogen bonding to drive anion recognition at iodo-modified TTFs **1.39**.[81,161] The simple substitution of a C–H bond by C–I in the TTF core enabled voltammetric sensing of Cl^- and Br^- in DMF *via* cathodic perturbations of both TTF couples.[81] Importantly, this work is one of the rare examples of a rigorous analysis of electrochemical binding isotherms and binding constants as described above (eqn. 1.2) with determination of both K_{Ox} and K_{Red} rather than just their ratio. Data fitting revealed binding constants of 20 (**1.39a**), 425 (**1.39a**$^{+\bullet}$) and 6730 M^{-1} (**1.39a**$^{2+}$) for Cl^- as well as 5 (**1.39a**) and 131 M^{-1} (**1.39a**$^{+\bullet}$) for Br^-. No perturbations of the TTF redox couples were observed in the presence of NO_3^-, OTf^-, ClO_4^- or for the parent TTF with any of the studied anions. Later in depth studies of the methylated iodo-TTF **1.39b** conclusively proved that

the observed behaviour can be attributed to the specific XB interaction between the receptors and anions.[161] Furthermore the authors assessed the influence of various other parameters, such as solvent and electrolyte influences and electrode nature and size, all of which are rarely studied, on the binding and sensing performance of **1.39b**. For example, it is often assumed that non-coordinating electrolyte anions do not interfere with anion sensing/binding. However, the authors demonstrated that the electrochemical voltammetric anion sensing performance of the system using different "non-coordinating" electrolyte anions such as BF_4^-, MsO^-, TfO^-, NO_3^-, ClO_4^-, PF_6^- or $BArF^-$ ([tetrakis[3,5-bis(trifluoromethyl)phenyl]borate) can vary significantly. For example, the magnitude of the cathodic shift for Cl^- (100 equiv.) in the presence of different electrolytes ranged between −36 and −49 mV while K_{Ox} ($K_{TTF+\bullet}$) ranged between 180 and 470 M^{-1}. The best performance (*i.e.* largest response) was observed for $BArF^-$ indicating that smaller, commonly used "non-coordinating" anions such as BF_4^- or PF_6^- can indeed compete with binding/signal transduction under these conditions.[161]

XB donors have also been investigated in viologen-based sensors (Figure 1.20). For example, Beer and co-workers incorporated XB and HB triazoles into the diquat motif to afford **1.40** which allowed for facile sensing of halides in ACN.[162] Unsurprisingly, in light of the XB ferrocene receptors, the XB receptor generally outperformed the HB receptor, with cathodic shifts of the $DQ^{2+}/DQ^{+\bullet}$ couple of −80, −30 and −10 mV as well as −40, −15 and −20 mV for Cl^-, Br^- and I^- for **1.40XB** and **1.40HB**, respectively (at 10 equiv.). Recently, Schöllhorn and co-workers reported the examination of a similar paraquat-based system **1.41** which exhibited Cl^- and Br^- induced cathodic shifts of the $PQ^{2+}/PQ^{+\bullet}$ of −31 and −20 mV for **1.41a** in DMF (100 equiv.), respectively.[100] The HB analogue **1.41b** showed smaller responses of −19 and −10 mV, while interestingly the perfluorinated **1.41c** outperformed

1.41b with shifts of −25 and −12 mV. Even phenyl substituted **1.41d** responded to Cl^- (−19 mV), but not to Br^-. These observations suggest that HB interactions are minimal and that the response is mainly driven by electrostatic, anion-π and, in the case of **1.41a**, XB interactions.



1.40XB: **X = I**

1.40HB: **X= H**

1.41a: **R^1 = I**, R^2 = F

1.41b: **R^1 = H**, R^2 = F

1.41c: $R^1 = R^2$ = F

1.41d: **$R^1 = R^2$ = H**

Figure 1.20. Redox-active halogen and hydrogen bonding bipyridinium anion receptors.

1.2.2.2.4 Redox-Active Receptors Based on other Anion Binding Motifs

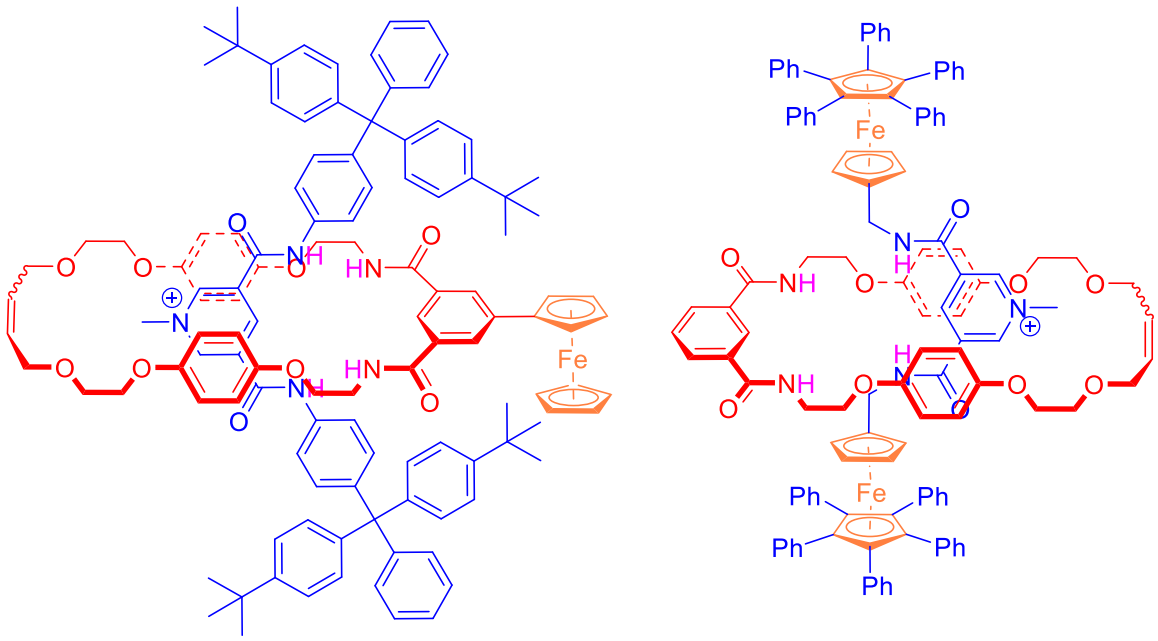
Boronic acids have long been employed in various sensors for hard inorganic anions and diols. The first example of a voltammetric sensor was the simple ferroceneboronic acid reported in 1995.[163] This system displayed a cathodic perturbation upon exposure to F^- in water (up to −150 mV at 1 M). Importantly, no significant shifts were observed in the presence of 1 M Cl^-, Br^-, SCN^-, HSO_4^- or $H_2PO_4^-$. Later a large variety of boronic acids and other boron-based Lewis acids were studied, whereby a wide range of redox-transducers were employed, including Fc,[164-167] TTF,[168,169] metal complexes[170-172] and others.[88] Interestingly, the dual use of boranes as both anion binding site as well as redox transducer has been demonstrated.[173,174]

Even in the absence of any specific binding site, anion sensing can be achieved based on electrostatic interactions. A particularly impressive example is the sensing of ATP^{2-} in water employing highly charged viologen-functionalised Fc receptors.[175] Similarly, a range of receptors based on the trimethylammonium cation have been studied.[176,177]

1.2.2.2.5 Redox-Active Mechanically Interlocked Receptors

In recent years mechanically interlocked receptors such as rotaxanes or catenanes, have been increasingly studied in the field of anion recognition.[178-180] This can mainly be attributed to their unique 3-dimensional binding cavities, which often not only leads to enhanced anion binding strength, but, importantly, imbues enhanced selectivity over simpler acyclic or macrocyclic systems. The first example of a solution-phase redox-tagged interlocked structure for anion sensing was reported by Evans and Beer in 2011, whereby rotaxane **1.42** was employed, comprising a pyridinum-bisamide axle and a 5-ferrocenylisophthalamide-based macrocycle (Figure 1.21).[181] Voltammetric studies in ACN revealed significant cathodic perturbations for Cl^-, $H_2PO_4^-$, BzO^- and HSO_4^- of up to −100 mV (for $H_2PO_4^-$ at 10 equiv.) while the maximum shift for Cl^- (−20 mV) was already observed at 1 equiv. indicative of strong binding. The Fc-transducer has not only been incorporated into the macrocyclic component but has also been used as a stopper in the axle component of a [2]rotaxane **1.43**.[182] This system displayed a similar behaviour to **1.42**, whereby addition of 1 equiv. Cl^- in ACN/DCM 1:1 was sufficient to induce plateauing of the response (−20 mV shift), which was not observed for the axle alone. The relatively small shifts that are observed in these systems are most likely a reflection of the strong binding in the neutral

state (K_{Red} large) which is not significantly modified through the introduction of an additional charge upon oxidation of the Fc moiety (*i.e.* small BEF).



1.42 **1.43**

Figure 1.21. Fc-containing [2]rotaxanes.

The incorporation of a Fc-transducer into the axle of a [3]rotaxane has also been achieved.[183] This system displays much larger cathodic perturbation in the presence of Cl^- (−55 mV at 2 equiv. with negligible further shifts at higher equiv.) indicating that a 1:2 stoichiometric host-guest complex is formed whereby one anion is bound in each of the cavities (quantitative binding). A much more complex behaviour was observed in the presence of SO_4^{2-} where, depending on the anion concentration, "two-wave" behaviour (slow exchange) was observed, with shifts of up to −270 mV (5 equiv.). A similar sensory behaviour towards Cl^- as in the previous examples was also observed for a Fc-containing [2]catenane.[184] Other examples of such interlocked systems include a recent report on Fc-

tagged neutral rotaxanes,[185] an all-halogen bonding rotaxane[186] as well as a porphyrin-containing rotaxane.[187]

1.2.2.2.6 Redox-Active Dendritic and Nanoparticle Based Sensing Configurations

Dendrimers have found numerous applications in a myriad of fields including catalysis, medicine, imaging and sensing.[188-190] In 1997 Astruc and co-workers reported the first use of Fc-amide functionalised dendrimers for voltammetric anion sensing.[191] The authors demonstrated that the cathodic shift of these dendrimers in the presence of $H_2PO_4^-$, HSO_4^-, Cl^- and NO_3^- was strongly dependent on the number of dendrimer branches, with a significantly increased response observed on increasing the number of branches from 1 to 3, 9 and 18, attributed to cooperative effects. Based on these promising results a large variety of redox-active dendrimer sensors were developed employing not only Fc-termini[192-197] but also biferrocene,[198,199] cobaltocene,[200,201] or other redox-transducers.[202] Related nanoparticle (NP) systems, in which analogous cooperative effects can often enhance the performance of the sensor, have been explored as well. Advantageously, a large number of closely-spaced redox-receptors can easily be introduced into these NPs without additional synthetic steps that are required to form large, higher generation, dendrimers.[203-206]

1.2.2.3 Surface-Confined Voltammetric Sensors

The immobilisation of redox-active anion receptors onto conducting electrode surfaces is of interest because it facilitates not only continuous anion sensing under flow, but also multiplexed sensing which can be very difficult to achieve in solution, and the facile integration into various device formats. Anion sensing has also been shown to benefit from

surface confinement through a combination of receptor preorganisation and cooperative effects.[207,208] Furthermore, these interfaces can usually be reused after a simple washing step, utilise a much lower receptor-to-target ratio and require a lower quantity of the receptor. Another advantage over solution-phase sensing is that surface-confined receptors do not need to be soluble in the sensing medium. This is particularly relevant when seeking to sense anions in pure water, which, under diffusive conditions, necessitates the introduction of hydrophilic solubilising groups or the use of highly charged receptors, both of which are often synthetically challenging or otherwise undesired, and is reflected in the low number of such sensors that operate in water. However, synthetic efforts have to be invested to facilitate immobilisation of receptors onto electrode surfaces, often by incorporation of suitable anchor groups into the redox-tagged receptors. Additionally, the characterisation of the receptive interface or processes thereat (*e.g.* binding events) is considerably more difficult than solution-phase studies, where a variety of other techniques (NMR, UV/Vis, fluorescence) are available to obtain supplementary information. Another impediment to voltammetric studies at interfaces is the increased impact of any (redox) instability of immobilised redox groups given the small number of molecules that are being repeatedly probed in any experiment and which cannot be diffusively replenished.

Despite some of these complications a variety of redox-active anion receptive films have been successfully utilised as potent voltammetric anion sensors. Most commonly the immobilisation of redox-active receptors is achieved by formation of self-assembled monolayers (SAMs) on gold electrodes through Au-S bonds (from thiols or disulfides), but other approaches have also been employed. As has been the case for solution-phase voltammetric sensors, the most commonly used transducer is Fc.

1.2.2.3.1 SAMs of Redox-Active Anion Receptors

The first example of a SAM-based redox-active anion sensor was reported by Astruc and co-workers in 1999, where a simple amide-containing Fc receptor was self-assembled on gold (**1.44$_{SAM}$**, Figure 1.22).[209] This system showed significant cathodic perturbation (−290 mV) in the presence of 1 mM $H_2PO_4^-$ in DCM. However, it was reported that these interfaces were voltammetrically unstable (loss of Fc redox signal after repetitive scanning) and that reversibility was further compromised in the presence of the target anion.

In another early example, sensing of Cl^-, Br^- and $H_2PO_4^-$ was achieved in DCM/ACN 2:1 at **1.45$_{SAM}$** containing a Fc transducer and amide anion binding sites.[210] Notably, the presence of 8-9 mM $H_2PO_4^-$ induced large cathodic shifts of −300 mV, with smaller, but significant, perturbations being observed for Cl^- and Br^- (−100 and −30 mV, respectively).

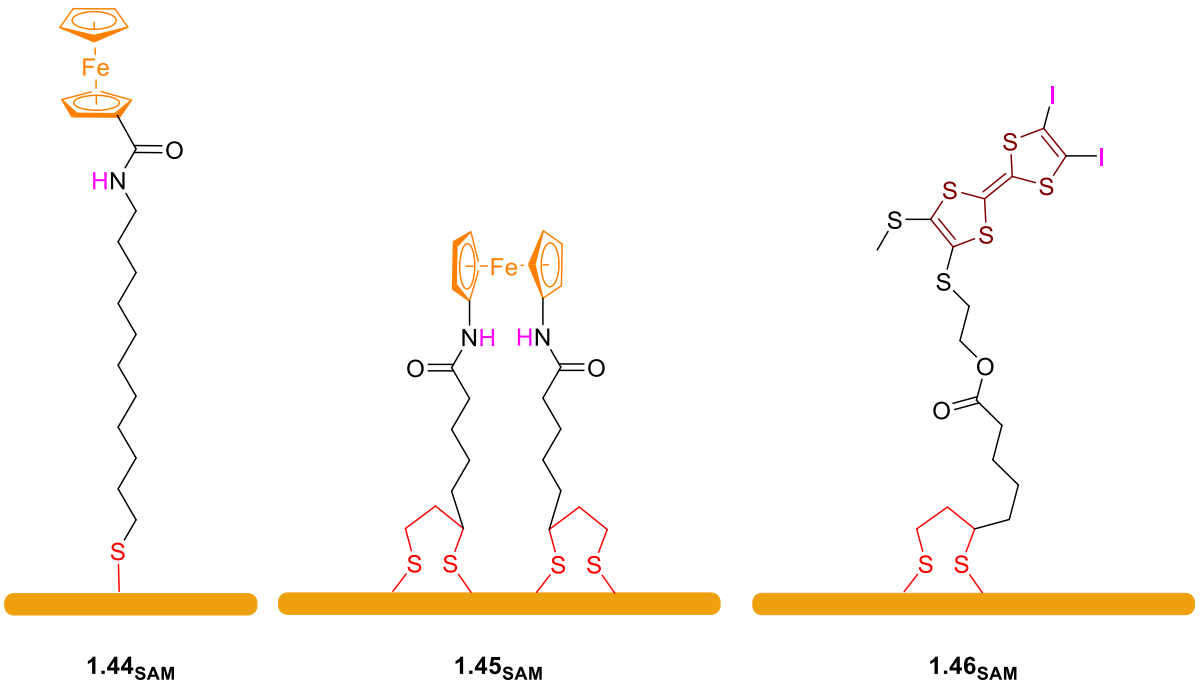


Figure 1.22. Early redox-active anion receptive interfaces.

Importantly, these responses were significantly larger in magnitude than those observed under diffusive conditions (*i.e.* in solution), which is commonly observed in these interfacial sensors and, in analogy to the previously discussed dendrimeric sensors, often attributed to cooperative or topological effects that arise from the high density of adsorbed receptor molecules.

Other Fc-containing receptive SAMs include those based on trialkylammonium,[211] urea- and amide-modified calix[4]arene,[212] peptide[213] and rotaxane[214] receptors.

Non-Fc transducers are significantly rarer in SAM-based architectures than in solution, which can most likely be attributed to the stringent reversibility requirements at interfaces (no replenishment of redox probe *via* diffusion). Nevertheless, metal-complexes[87,137,215,216] and TTF have been successfully employed as redox transducers in such a configuration, whereby the latter was appended to calix[4]pyrrole[217] and amide-foldamer receptors.[218] Another recent example reports on one of the first XB-mediated interfacial anion sensors, **1.46$_{SAM}$**, whereby a bidentate bis(iodo)TTF receptor was employed.[219] This interface was utilised for the sensing of Cl^- and Br^- in ACN, where, notably, "two-wave" behaviour was observed.

Another commonly employed strategy to modify (conducting) interfaces, so as to be specifically responsive, is (electro)polymerisation. The incorporation of electropolymerisable groups, such as pyrrole- or thiophene-derivatives allows facile generation of polymeric films on any electrode surface and is thus more versatile than self-assembly on gold. This has been exploited in the generation of a wide range of voltammetric anion sensors based on different anion binding sites and different redox transducers including metal complexes,[220] metallocenes[221-225] and organic transducers.[226-228] An even more straight-forward, but less

well-defined, approach to functionalise electrode interfaces is physisorption or dropcasting, both of which have been exploited to form (voltammetric) anion sensors. The receptors employed in such a format are almost exclusively redox-active dendrimers.[229-232]

1.2.3 Faradaic Impedimetric Anion Sensing

Of all electroanalytical techniques electrochemical impedance spectroscopy (EIS) stands out as one which is particularly sensitive to interfacial events. The application of a small amplitude AC perturbation at a fixed bias potential (and varying AC frequencies) allows for facile extraction of a range of interfacial parameters (*e.g.* resistance and capacitance) with minimal perturbations of the interface. EIS is commonly exploited for sensing of large biomolecules whereby the charge transfer resistance (R_{ct}) of a receptor (*e.g.* antibody) modified electrode in the presence of a solution-phase redox probe (most commonly $[Fe(CN)_6]^{3-/4-}$) is utilised as transducer for analyte binding.[233] This concept has been expanded to the sensing of small molecules and ions also. In particular impedimetric cation sensing at crown ether modified electrodes has received some attention,[234-237] though impedimetric anion sensing remains rare.

Early work in this field was conducted by Echegoyen *et al.* who exploited SAMs of cyclotriveratrylene (CTV)[238] and calixarene-based[239] anion receptors on gold electrodes (**1.47$_{SAM}$** and **1.48$_{SAM}$**, Figure 1.23). Sensing of various anions such as $H_2PO_4^-$, OAc^-, F^- and others was achieved in the presence of either $[Ru(NH_3)_6]^{2+/3+}$ or $[Fe(CN)_6]^{3-/4-}$; a decrease or increase in R_{ct}, respectively, was observed upon anion binding (Figure 1.24). These altered charge-transfer characteristics can be attributed to electrostatic interactions between the surface-captured anion and the solution-phase redox probe, whereby electrostatic

attraction facilitates electron transfer, *i.e.* leads to a lower R_{ct}, and, conversely, repulsion results in an increased R_{ct}.

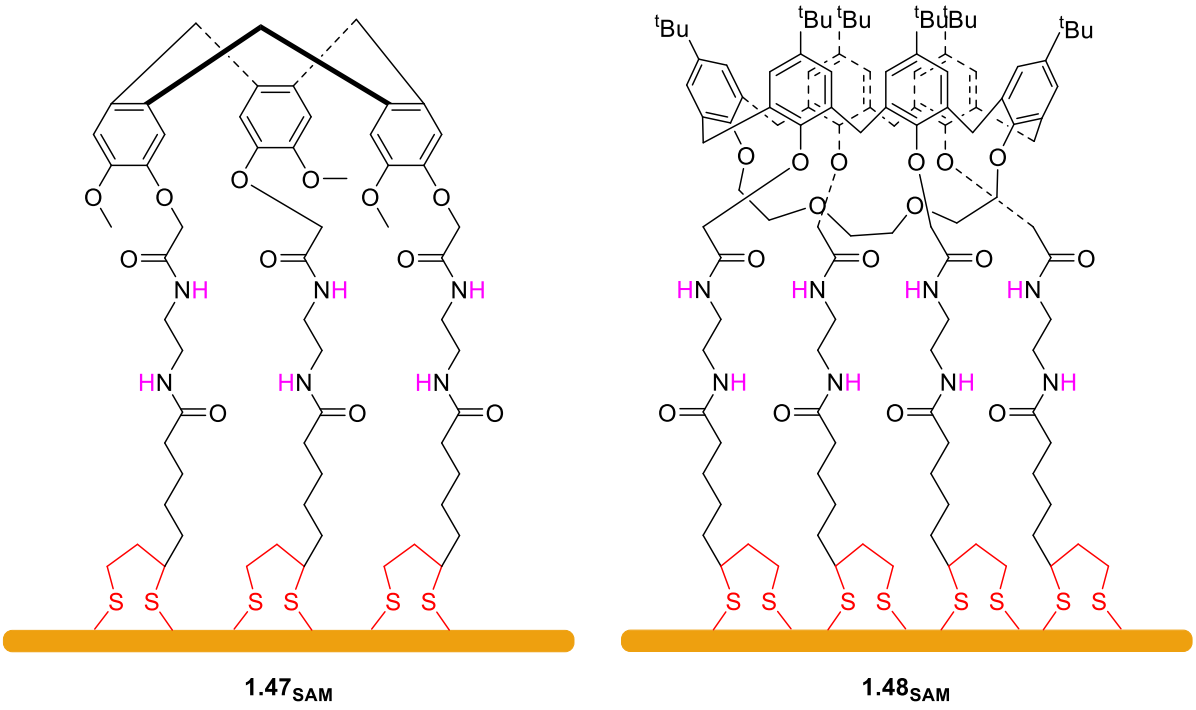


Figure 1.23. SAMs of CTV and calix[6]arene-based anion receptors on gold for impedimetric anion sensing.

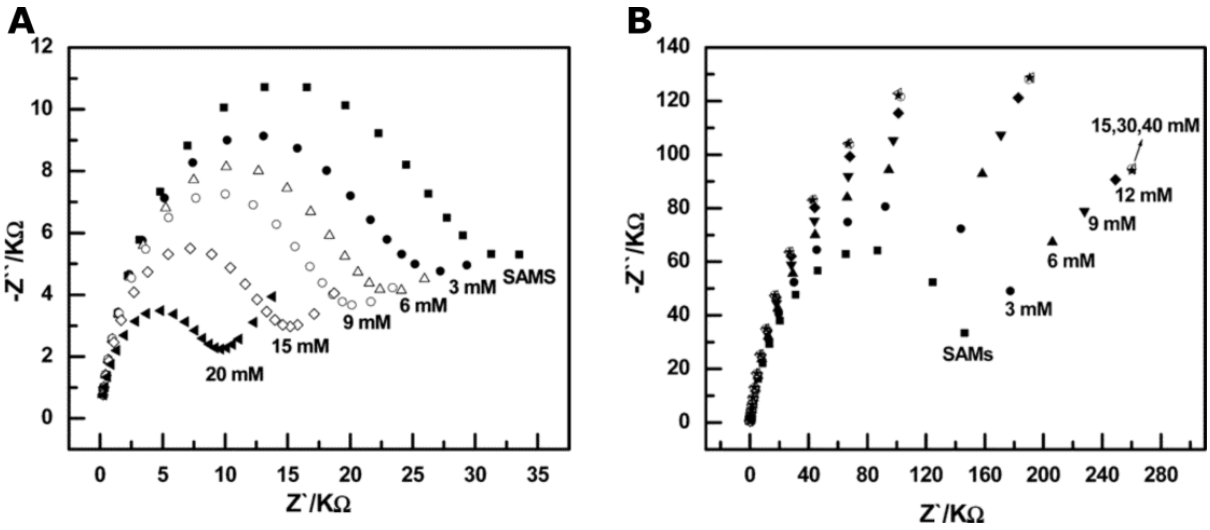


Figure 1.24. Impedimetric Nyquist plots of **1.47**$_{SAM}$ in the presence of increasing $[OAc^-]$ utilising $[Ru(NH_3)_6]^{2+/3+}$ (A) or $[Fe(CN)_6]^{3-/4-}$ (B) as redox probes. In both plots the change of the impedance (charge-transfer resistance) can be seen, which arises from electrostatic attraction and repulsion between the bound anion and the redox probe, respectively. Reprinted with permission from ref.[238] Copyright 2005 American Chemical Society.

The impedimetric sensing of $H_2PO_4^-$ was also achieved at SAMs of free-base porphyrin with good selectivity over other anions such as NO_2^-, Br^-, NO_3^- and Cl^-.[240] Interestingly, the R_{ct} of this interface decreased upon addition of $H_2PO_4^-$ (in the presence of $[Fe(CN)_6]^{3-/4-}$). This was rationalised by double-protonation of the porphyrin-core in the presence of the anion, resulting in an overall positively charged SAM with an enhanced electron transfer by virtue of the electrostatic attraction of the solution redox probe. Similarly, the highly toxic $HCrO_4^-$ was detected at azacrown ether modified interfaces where the chromate is supposedly sandwiched between azacrown ethers complexed with K^+/H^+.[241] Sensing of the analyte in aqueous KCl (pH 5.0) in the presence of $[Fe(CN)_6]^{3-/4-}$ was achieved with an exceptionally low limit of detection (LOD) of 78 pM. Impedimetric anion sensing has also been carried out at non-SAM interfaces such as a recently reported acridine-modified electrode for the impedimetric sensing of SeO_3^{2-}.[242]

Only a few reports exist of impedimetric anion sensing that do not rely on specific, supramolecular anion-receptor interactions. This includes a CN^- selective sensor,[243] a phosphate sensor based on Zr^{4+}-modified SAMs[244] as well as an ascorbate sensor exploiting its ability to catalyse click reactions.[245]

Further details and discussion about impedimetric anion sensing can also be found in Section 3.1.

1.2.4 Other Anion Sensors

Apart from the electrochemical anion sensors described above a variety of other techniques have been explored to detect anions. This includes, for example, field-effect transistors (FETs),[246-248] such as a recently developed organic FET (OFET) based on a SAM of a phenylboronic acid derivative for sensing of F^- in water.[249] It should be noted that FETs are similar to potentiometric devices such as ISEs and are often operated in configurations in which selectivity is imparted through ionophore-doped membranes. Similarly, anion sensing in a chemiresistor format, where conducting carbon nanotubes were modified with squaramide anion receptors, was recently reported.[250]

The second major class of anion sensors are those based on optical transducers, including colorimetric and luminescent sensors. In comparison to electrochemical anion sensors these formats are often more sensitive and can be operated under more dilute conditions. Disadvantageously, they usually rely on more sophisticated/expensive instrumentation. This can sometimes be circumvented if naked-eye detection can be achieved; however this only offers qualitative information about analyte presence.

Based on perhaps the most straightforward transduction approach, colorimetric sensors have, for decades, received large attention as ion sensors. The simple modulation of the hosts´ absorbance upon ion binding is easy to measure and interpret. Furthermore, an enormous variety of optical reporter groups can easily be incorporated into almost any host framework, including acyclic,[251] macrocyclic[252,253] and interlocked structures.[254,255] Advantageously, many of these sensors provide a concomitant fluorescent readout, which is often responsive to anion binding as well.

Recent examples of fluorescent anion sensors include an aryl-triazole foldamer (**1.49**, Figure 1.25) with napthalimide appendages.[256] The free host displays a fluorescent signature that can be ascribed to monomer emission of the naphthalimide moiety. In the presence of halide anions in THF the receptor folds inducing excimer formation and an associated change in fluorescence. The change of conformation upon anion binding and associated changes in fluorescence were also exploited in a series of chiral HB, XB and ChB triazole-appended BINOL-receptors (**1.50XB/HB/ChB**, Figure 1.25).[257] Interestingly, the response (and binding selectivity) of these systems towards stereo- and geometric isomers of dicarboxylates was significantly different; some displayed a decreased fluorescence intensity upon binding while others showed an enhanced fluorescence. Additionally the emission maximum shifted to lower or higher wavelength depending on the receptor and anion. These complex observations were attributed to unique changes in the torsion angle of the BINOL-core upon anion binding. Other examples of fluorescent anion sensors based on XB receptors include a heteroleptic Ru(II) complex reported by Ghosh and co-workers[258] as well as a variety of interlocked hosts by Beer and co-workers.[259-261]

Chemodosimeters are another noteworthy, commonly employed class of anion sensors, which rely on a chemical reaction to induce a change in response (most commonly this response is optical).[262,263] While often highly selective, their utility is significantly impeded by their irreversible nature; stoichiometric amounts of sensor are required.

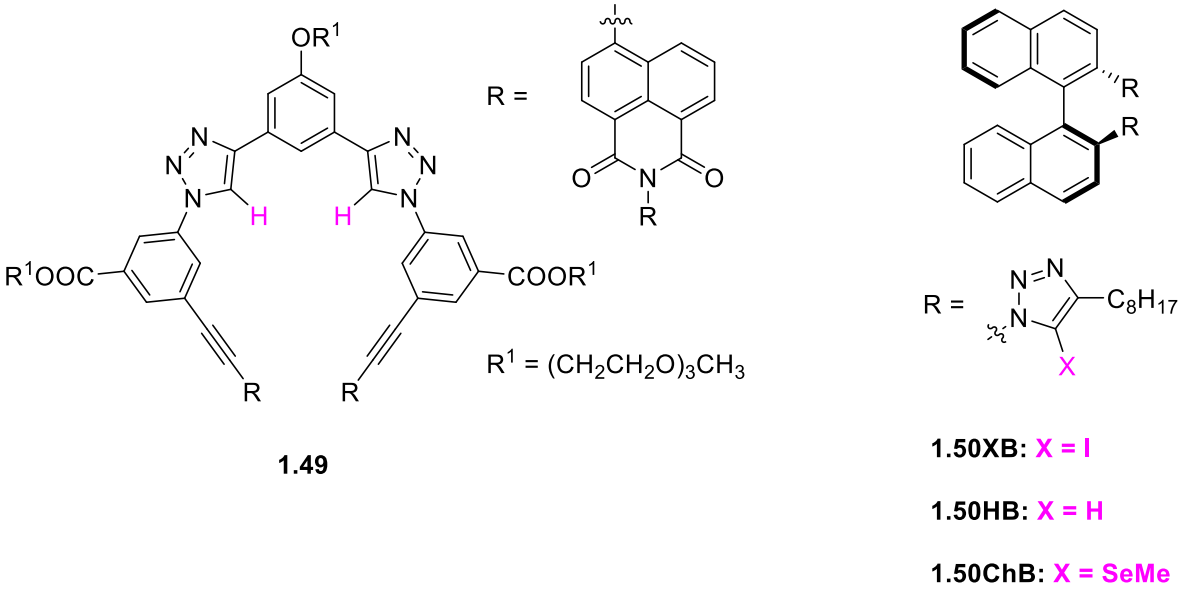


Figure 1.25. Chemical structures of fluorescent anion sensors based on naphalimide appended aryl-triazole foldamer **1.49** and XB, HB and ChB BINOL receptors **1.50XB/HB/ChB**.

1.3 Thesis Aims

This thesis is concerned with the design, synthesis and application of supramolecular, electrochemical anion sensors. This includes in-depth binding studies in solution and at receptive interfaces using voltammetric and impedimetric/capacitive methodologies. Special attention is given to elucidating the operational electrochemical sensing principles that govern the transduction of anion binding to novel synthetic hosts. Halogen bonding and hydrogen bonding binding sites, mainly integrated into the 1,2,3-triazole heterocyclic motif, are utilised to drive anion recognition, and the novel hosts' binding strengths and selectivities are discussed in detail. The specific aims as well as further considerations that are pertinent to the individual projects are detailed in the introductory sections of each chapter.

Chapter 2

Voltammetric Anion Sensing in Solution and at Receptive SAMs

Chapter 2: Voltammetric Anion Sensing in Solution and at Receptive SAMs

2.1 Introduction and Chapter Aims

As highlighted in Chapter 1, the voltammetric sensing of anions using synthetic redox-active receptors, both in solution and immobilised onto conducting (electrode) surfaces has received considerable attention over the past decades. However, in spite of continuous advances, numerous challenges remain, which include:

1) Developing a better understanding of the mechanisms that govern the sensory performance of the redox-active systems. In particular, the often observed enhanced anion sensing response at receptive interfaces is poorly understood and rarely studied in detail (see Section 1.2.2.3).

2) An exploration of novel redox transducers and receptor designs that include the application of underexploited non-covalent interactions, *e.g.* sigma-hole interactions, to drive anion recognition.

Building on the concepts introduced in Chapter 1, Section 1.2.2, the remaining introductory part of this chapter discusses experimental and theoretical considerations that are pertinent to voltammetric anion sensors investigated in this thesis. The most relevant consideration briefly reiterated here, is the magnitude of the voltammetric perturbation ΔE of a redox-active host $[H]$ upon anion binding is given by two equations, where eqn. 2.2 can be considered a special case of eqn. 2.1, and applies if $[A^-] >> [H]$ and if fast-exchange conditions are satisfied.[81]

$$\Delta E = -\frac{RT}{nF} * \ln\left(\frac{K_{Ox}}{K_{Red}}\right) \qquad \text{eqn. 2.1}$$

$$\Delta E = -\frac{RT}{nF} * \ln\left(\frac{1+K_{Ox}*[A^-]}{1+K_{Red}*[A^-]}\right) \qquad \text{eqn. 2.2}$$

From both equations it is apparent that the voltammetric response is enhanced if the ratio of K_{Ox} and K_{Red} is large, *i.e.* if binding of the anion is strongly affected by the change in oxidation state. This is illustrated in Figure 2.1, where it can be observed that the binding enhancement factor (BEF = K_{Ox}/K_{Red}) is a much more important determinant of signal response than the magnitude of either of the binding constants.

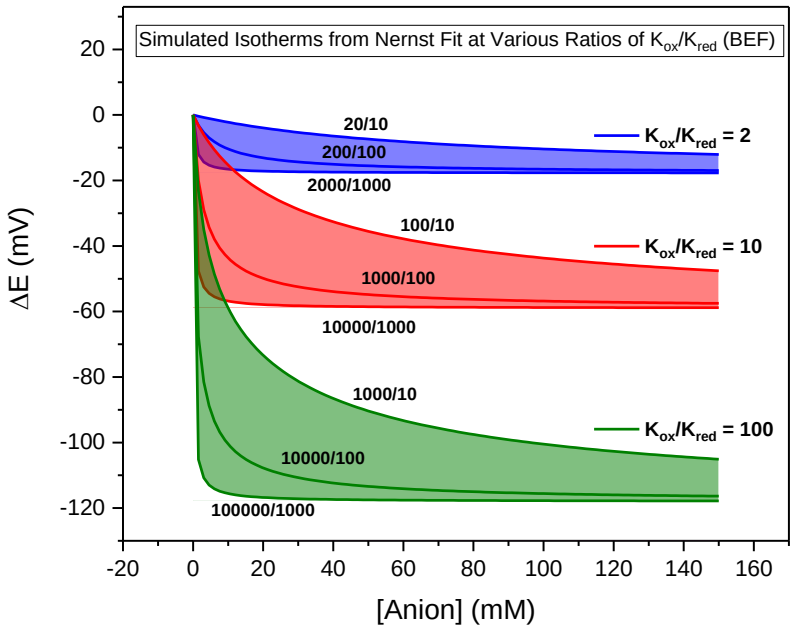


Figure 2.1. Simulated binding isotherms according to eqn. 2.2 at various ratios of K_{Ox}/K_{Red} (BEF, binding enhancement factor). The magnitude of the cathodic shift upon anion binding to a redox-active host, according to this model with $[A^-] >> [H]$ (and fast exchange), is thus mainly determined by the ratio of the binding constants rather than their magnitude.

In turn, the magnitude of the voltammetric shift thus directly reports on the BEF, which can be determined by eqn. 2.1 at ΔE_{max}, or by fitting of the binding isotherms according to

eqn. 2.2. The latter also affords the absolute values of K_{Ox} and K_{Red}, but is only applicable in a fast-exchange regime (*i.e.* if the response is a continuous shift and not a "two-wave" behaviour). Saliently, this is the case in many voltammetric anion sensors and for all receptors discussed in this chapter.

An analysis of voltammetric binding isotherms can thus provide detailed insights into the sensory and binding properties of electrochemically active (an)ion receptors, but is rarely carried out. In pioneering work, Schöllhorn and co-workers applied such analyses on iodo-TTF XB donors,[81,161] however more systematic studies of other redox transducers, receptor designs or sensing configurations (*i.e.* surface-confined voltammetric anion sensors) remain underdeveloped.[219,264,265] This is somewhat surprising considering that these voltammetric experiments are relatively straightforward and can, simultaneously, provide (an)ion binding constants to a receptor in multiple oxidation states, an analysis that is often impractical or impossible based on "established" techniques such as NMR or UV-vis/fluorescence spectroscopy (*e.g.* because one of the oxidation states is difficult to isolate chemically and/or paramagnetic).

In any idealised voltammetric analysis, the reporting signal transduces the specific anion binding event only; in reality a number of dielectric and ion pairing effects can contribute in a manner that is highly dependent on the electrolyte(s) used. In order to minimise errors associated with solution-phase resistance (*i.e.* ohmic drop) to voltammetric peak positions a large excess (≥100 mM) of a supporting electrolyte is usually employed. It is imperative that this electrolyte does not interfere with the anion binding event. Hence, large non-coordinating anions (like perchlorate (ClO_4^-) or hexafluorophosphate (PF_6^-) as tetrabutylammonium (TBA) salts) are most commonly used. Another important, yet often

overlooked, consideration is the inherent electrostatic (de)stabilisation[266] of the (charged) redox states in the presence/absence of the supporting electrolyte and solvent. For example, the half-wave potential of the simple ferrocene/ferrocenium (Fc/Fc^+) couple is strongly dependent on the concentration (and nature) of the supporting electrolyte as well as the solvent.[267] At higher salt concentrations and/or in more polar solvents the charged ferrocenium is more strongly stabilised through charge screening. This effect is particularly dramatic in non-polar solvents such as DCM, where the half-wave potential of Fc/Fc^+ is strongly dependent on the electrolyte concentration up to 500 mM. While this effect has not been investigated in depth for different solvents, electrolytes and redox transducers[268] it is most likely a general observation that should be taken into account, especially in non-polar solvents. In order to avoid any non-specific effects related to a change in the electrolyte concentration it is preferable to carry out all experiments at constant ionic strength and/or conduct control experiments with a non-receptive model compound.

Another experimentally relevant consideration is the electrochemical reversibility of the integrated redox reporter. Most of the parent redox transducers (for examples and their general characteristics see Section 1.2.2.2) display fully or quasi-reversible electrochemical behaviour, however this is often not the case for the modified (receptive) transducers, particularly in the presence of nucleophilic anions and in non-competitive solvents. For example, while the Fc/Fc^+ couple is fully reversible in organic solvents, the presence of certain anions (*e.g.* phosphates) almost always induces a certain degree of irreversibility. The reversibility of a diffusive electrochemical system can most easily be assessed by cyclic voltammetry where in an ideal (fully reversible) system the peak separation between anodic and cathodic peaks is 59 mV/n, where n is the number of electrons transferred. Furthermore, the ratio of anodic and cathodic peak currents i_{pa}/i_{pc} should be close to unity

(all electrochemically generated species being fully transformed back during the reverse scan) and the peak current should be linearly dependent on the square-root of the scan rate (see Randles-Sevcik equation). Under real measuring conditions, almost all systems display quasi-reversible behaviour (with small deviations from these idealities). For solution-phase voltammetric anion sensing (quasi-)reversibility is not an absolute requirement and irreversible transducers can theoretically be used. However, this significantly complicates data analysis and applicability as useful sensors, where reusability is often envisioned.

In contrast to solution-phase (*i.e.* diffusive) voltammetry the redox behaviour (and reversibility) of surface-confined redox-active receptors cannot be described by the Randles-Sevcik equation, instead the peak currents of electroactive films are directly proportional to the scan rate. Furthermore, under ideal conditions, the peak separation $E_{pa} - E_{pc}$ should be 0 (at low scan rates) and the full width at half maximum height (FWHM) is 90 mV.[269] Of further note is the electrochemical reversibility requirements are more stringent for such interfacial sensors as discussed in more detail in Section 2.2.3.2.

As highlighted in Section 1.2.2.3, the use of surface-immobilised redox-active receptors as sensors is of particular interest in real-life applications, allowing sensor re-use, sensing under flow and utilises significantly smaller quantities of receptor. Additionally, an often enhanced sensory performance is observed upon surface-confinement of the redox-active hosts.[208,270] In spite of these advantages, our understanding of anion sensing at redox-active interfaces remains underdeveloped, in particular the quantitative investigation of their binding/sensing performance.[219,271] The use of XB to mediate anion binding at a surface is also underdeveloped and was only reported recently for the first time, where a bis(iodo)TTF receptor was employed to sense Cl^- and Br^- in ACN (**1.46$_{SAM}$**, Figure 1.22).[219]

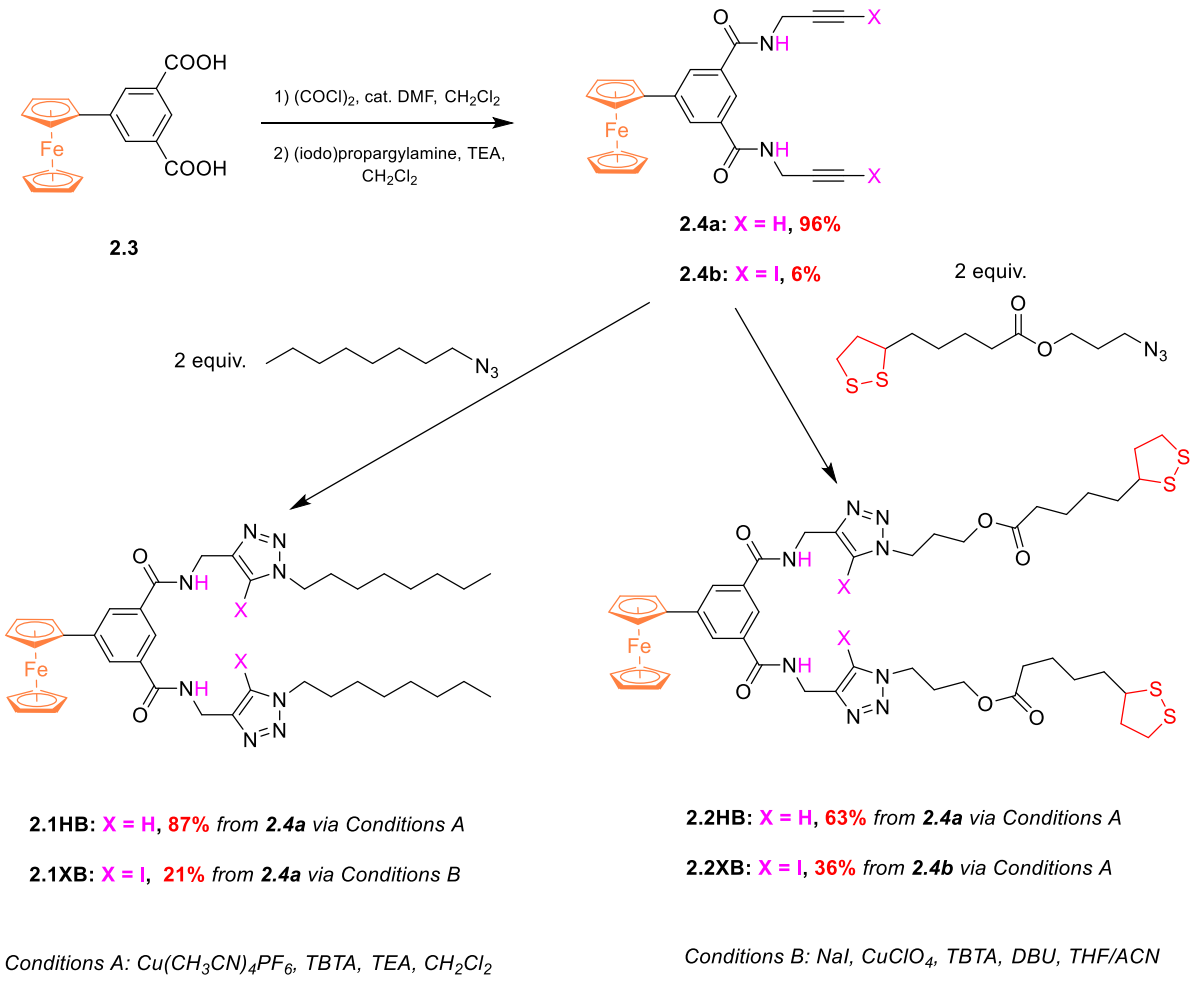
This thesis chapter aims to address these challenges by synthesising and systematically investigating a range of novel redox-active HB and XB anion receptors. This analysis will specifically focus on the elucidation of the fundamental properties that govern the sensory properties of these systems and will be carried out by voltammetry and supplemented by other techniques (*e.g.* ^{1}H NMR titrations), where applicable. Furthermore, the differences between HB and XB receptors as well as their performance in both diffusive and surface-confined configurations will be scrutinised. In all cases special attention will be given to the considerations outlined above, including voltammetric properties (*e.g.* reversibility), redox-induced binding modulation as well as solvent effects. Firstly, a detailed study of the sensory behaviour of new Fc-containing isophthalamide-triazole anion receptors both in solution and in SAM-based architectures is presented (Section 2.2). The voltammetric sensing of anions in more competitive aqueous solvent systems will then be demonstrated in Section 2.3 where a rarely utilised osmium(II)-bipyridyl electro- and photoactive transducer is integrated into acyclic water-soluble anion receptors. Lastly a brief discussion of preliminary results and on-going investigations into redox-active anion sensors is provided (Section 2.4.2).

2.2 Electrochemical Anion Sensing at Ferrocenyl Hydrogen and Halogen Bonding SAMs

2.2.1 Receptor Design and Synthesis

Based on a previously utilised 5-ferrocenylisophthalamide motif,[272] the novel redox-active amide- and triazole-containing receptors **2.1XB/HB** and **2.2XB/HB** were synthesised as

depicted in Scheme 2.1. Containing a single Fc reporter group as well as two HB amides and two triazole XB/HB bond donors, this scaffold was envisioned as a potent as well as versatile platform for the voltammetric sensing of anions.



Scheme 2.1. Synthetic route towards halogen and hydrogen bonding redox-active receptors **2.1XB/HB** and **2.2XB/HB**.

The synthesis of the receptors can be broken down into two main steps: an amide condensation of 5-ferrocenylisophthalic acid and a propargyl amine-based component as well as a click reaction between propargyl amine and a (functional) azide. The Fc-appended bis acid building block is readily available in a two-step procedure *via* diazotisation of commercially available dimethyl 5-aminoisophthalate followed by reaction with

ferrocene.[272] This affords 5-ferrocenyl dimethylisophthalate which can be hydrolysed to the free bis acid **2.3**. Generation of the corresponding bis(acid chloride) *via* reaction with oxalyl chloride followed by condensation with two equivalents of propargylamine afforded the bis alkyne **2.4a** in excellent yield (96%). Conversion to the octyl- or disulfide-appended receptors **2.1HB** and **2.2HB** was achieved *via* copper(I)-catalyzed azide-alkyne cycloaddition (CuAAC) with respectively two equivalents octyl azide (obtained in one step from 1-bromooctane)[273] or disulfide-azide (obtained in two steps from lipoic acid and 3-bromo-1-propanol) (Conditions A).[274] The synthesis of the corresponding XB receptors **2.1XB** and **2.2XB** was significantly more challenging. The two most common synthetic methodologies that afford 5-iodo-1,2,3-triazoles were found to be problematic: the formation of the bis(iodo)alkyne **2.4b** followed by click reaction with the azide under standard CuAAC conditions did afford **2.2XB**, albeit in very poor overall yield. This may be attributed to the poor stability of iodopropargylamine (obtained in one step and used immediately)[275] and the corresponding bis(iodoalkyne) **2.4b**. Alternatively, the iodotriazole moiety can be prepared in one step by reaction of a protoalkyne with the azide in the presence of *in situ* generated electrophilic triiodide (conditions B).[276] This also proved problematic, presumably as a result of deprotonation of the isophthalamide protons under the basic reaction conditions. Nevertheless, reaction of two equivalents of disulfide-azide with **2.4a** under these conditions afforded the desired receptor **2.1XB**, however in only after difficult purification by preparative TLC and with low yield (21%). All compounds were characterised by ^{1}H NMR, ^{13}C NMR and high-resolution mass spectrometry (see Chapter 7 for further details).

2.2.2 Solution-Phase Binding Studies

2.2.2.1 ^{1}H NMR Titrations

The solution-phase binding performance of **2.1XB/HB** was initially investigated by ^{1}H NMR titrations in CD_3CN. Addition of TBA salts of various anions induced significant downfield perturbations of the internal aromatic proton H_a, isophthalamide proton H_d and triazole proton H_c of receptor **2.1HB** (Figure 2.2).

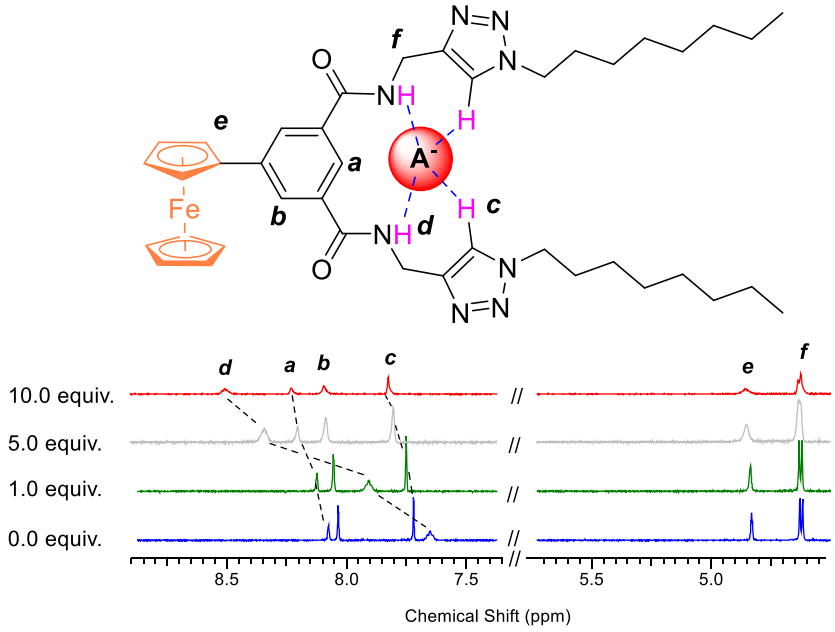


Figure 2.2. Partial ^{1}H NMR spectra of receptor **2.1HB** in CD_3CN in the presence of 0.0, 1.0, 5.0 and 10.0 equivalents of $TBAHSO_4$. As only protons a, c and d display significant perturbations, anion binding in the central cavity *via* multiple convergent HB´s (blue dashed lines) can be inferred as schematically depicted.

This is indicative of anion binding within the cavity of the receptor *via* multiple, convergent HB interactions from the isophthalamide as well as the proto-triazole groups as schematically shown in **Figure 2.2**. This binding mode is further evidenced by negligible perturbations of the protons that are further removed (H_b and H_e) or pointing away from the binding site (H_f). Addition of Cl^-, Br^-, $H_2PO_4^-$ and BzO^- induced similar shift patterns

(Figures A2.1-A2.8) while the presence of ClO_4^-, ReO_4^- and NO_3^- caused minimal perturbations indicating, as expected, negligible binding as a result of their low charge-density. Similar perturbations were observed for the titration of **2.1XB** with this range of anions, suggesting a similar binding mode.

Titrations with increasing concentrations of various anions afforded well-defined binding isotherms (Figure 2.3) that were analysed by a 1:1 stoichiometric host–guest binding model as described in Chapter 7, Section 7.1.2.

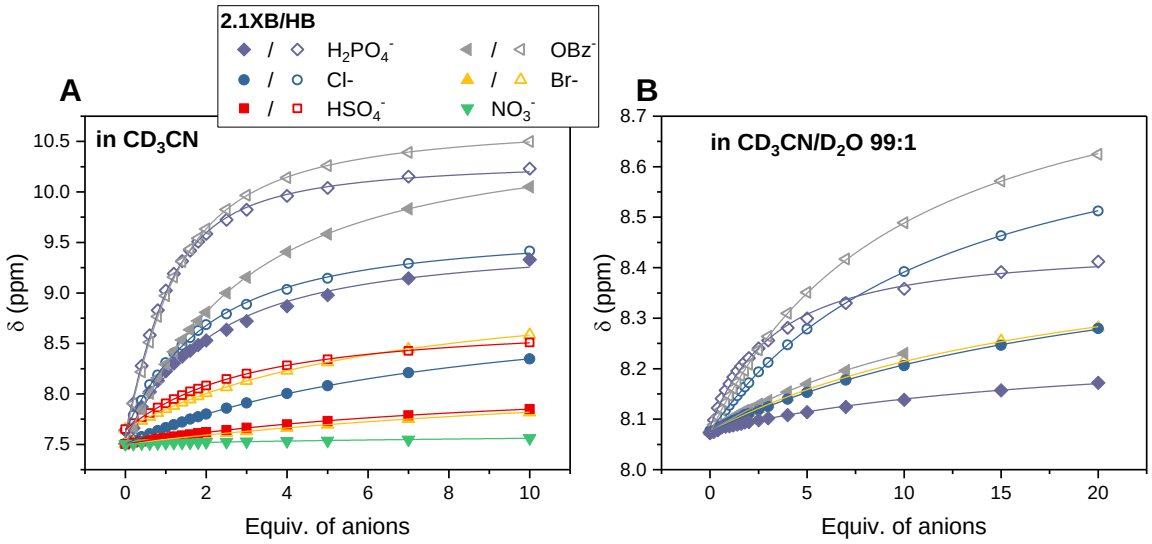


Figure 2.3. Chemical shifts of A) The amide proton H_d of receptor **2.1XB/HB** in CD_3CN and B) The internal isophthalamide proton H_a of receptor **2.1XB/HB** in CD_3CN/D_2O (99:1 *v*/*v*) as function of the concentrations of various anions. Filled symbols represent **2.1XB**, empty symbols represent **2.1HB**. Solid lines represent fits according to a 1:1 stoichiometric host-guest model.

The binding constants K (M^{-1}) obtained from this quantitative analysis are shown in Table 2.1. In CD_3CN receptor **2.1HB** displays a markedly higher affinity for the more basic anions $H_2PO_4^-$ and OBz^- in comparison to the halides, HSO_4^- or NO_3^-. Of note is a modest preference for the tetrahedral $H_2PO_4^-$ over the trigonal planar OBz^-. Surprisingly, the anion binding affinity is significantly diminished for **2.1XB** in all cases, apart from nitrate, which

weakly binds to this receptor, but does not interact with **2.1HB.** This trend is in marked contrast to many previously reported systems in which stronger binding to the XB receptor is normally observed.[15,16] This behaviour may arise from geometric constraints imposed by the more bulky C–I XB donor groups in **2.1XB**, sterically impeding convergent binding from all donor groups within the receptor cavity.

The introduction of 1% D_2O to the solvent system greatly reduces the anion binding affinities of both hosts, especially for $H_2PO_4^-$, HSO_4^- and OBz^-, as a result of the more competitive nature of the solvent medium. In fact, HSO_4^- and NO_3^- binding is completely supressed, while binding of $H_2PO_4^-$ and OBz^- is diminished by approximately one order of magnitude for both **2.1XB/HB** (Table 2.1).

Table 2.1. Solution-phase anion binding constants K (M^{-1}) of **2.1XB/HB** as determined by ^1H NMR titrations experiments. All isotherms were fitted to a 1:1 stoichiometric host-guest model (Figure 2.3). n. b. – No binding. / – Not conducted. Standard errors from fitting are <10% unless indicated otherwise.

	CD_3CN		**CD_3CN/D_2O 99:1**	
	2.1XB	**2.1HB**	**2.1XB**	**2.1HB**
Cl^-	110	340	26	65
Br^-	38	75	n. b.	33
HSO_4^-	91	196	n. b.	n. b.
$H_2PO_4^-$	638[a]	2110	37[a]	341
OBz^-	422	1380	47	89
NO_3^-	16[b]	n. b.	n. b.	/
ClO_4^-	n. b.	n. b.	/	/
ReO_4^-	n. b.	n. b.	/	/

a – Standard errors from fitting ≤16%. b – 24%.

Apart from Br^- binding to **2.1XB**, which is negligible in CD_3CN/D_2O, the binding of halides is attenuated by the introduction of D_2O, however not as strongly as that of the oxoanions. These observations are in good agreement with a stronger hydration of $H_2PO_4^-$ and OBz^- over the halides (Hofmeister series, Section 1.1.2.1).

2.2.2.2 Voltammetric Studies

2.2.2.2.1 Redox Properties of 2.1XB/HB and Response Towards Anions

The electrochemical properties of **2.1XB/HB** were studied in the same solvent systems as the NMR titration experiments (ACN and ACN/H_2O 99:1) in the presence of 100 mM $TBAClO_4$ as supporting electrolyte. In all cases a well-defined one-electron redox wave at moderate potentials, corresponding to the Fc/Fc^+ couple, was observed. The CVs at varying scan rates (Figure 2.4 and Figure A2.9) revealed that this couple was quasi-reversible (with the ratio of anodic and cathodic peak currents close to unity) and that the redox process was diffusion controlled, indicating minimal adsorption of the receptors onto the glassy carbon working electrode. The half-wave potential for **2.1XB** was observed at a slightly more anodic potential of 184 mV in comparison to **2.1HB** which exhibited an $E_{1/2}$ of 178 mV (in ACN, *vs.* $Ag|AgNO_3$).

This observation is in good agreement with previous reports[158,159] and is a result of the more electron withdrawing nature of the iodotriazole groups in **2.1XB**, rendering this receptors' Fc substituent more electron deficient.

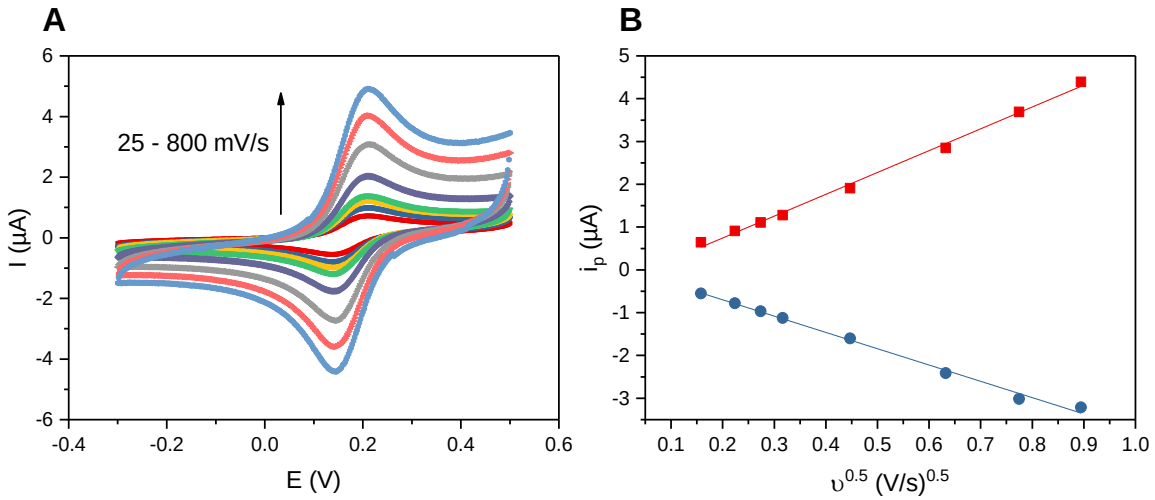


Figure 2.4. A) CVs at varying scan rate of 0.1 mM **2.1HB** in ACN, 100 mM $TBAClO_4$. B) The associated anodic and cathodic peak currents as a function of the square-root of the scan rate including linear fits.

The solution-phase voltammetric sensing properties of **2.1XB/HB** in both solvent systems (ACN and ACN/H_2O 99:1; containing 100 mM $TBAClO_4$ as electrolyte) were investigated by titration with various anions (at constant salt concentration to minimise any voltammetric perturbations arising from altered electrostatic interactions at different ionic strength). Specifically, the $E_{1/2}$ of the receptors in the presence of increasing anion concentrations was assessed by SWV, as representatively shown for the titration of **2.1XB** with HSO_4^- in ACN (Figure 2.5; for further experimental details see Section 7.2).

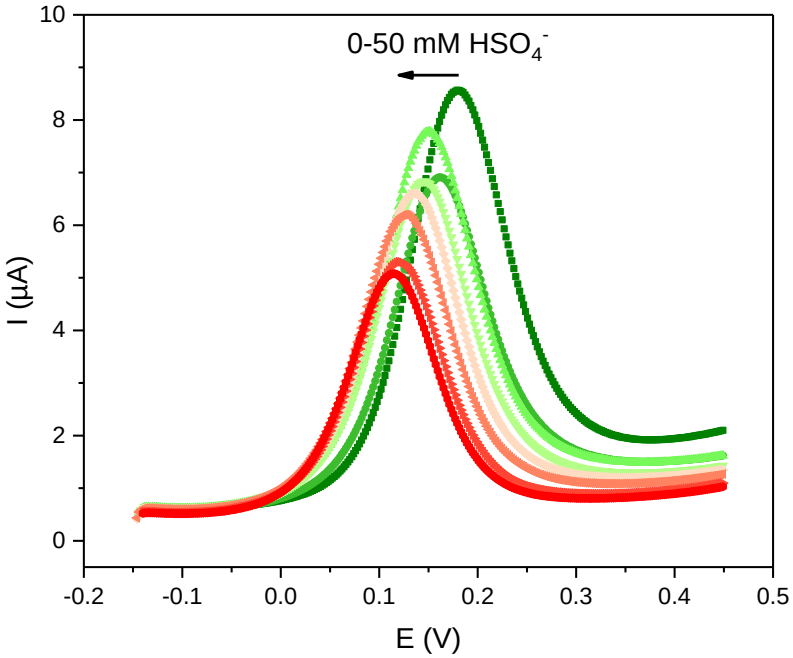


Figure 2.5. SWVs of 0.1 mM **2.1XB** in ACN, 100 mM $TBAClO_4$ upon titration with HSO_4^-.

As can be seen in Figure 2.6, significant cathodic perturbations of the Fc/Fc^+ couple can be observed in ACN for both receptors upon titration with HSO_4^-, Cl^-, Br^-, $H_2PO_4^-$ and OBz^-, while NO_3^- only induced a response for **2.1XB**. For both receptors the overall binding trends are similar where $H_2PO_4^-$, induces the largest magnitude response of up to −170 mV for **2.1XB** and −110 mV for **2.1HB**. In both cases the second largest response was observed for OBz^-, while, in comparison, the halides induced larger cathodic perturbations with **2.1XB.** In summary, Table 2.2 shows the overall anion response trends, for **2.1XB:** $H_2PO_4^-$ > OBz^- > Cl^- > HSO_4^- ≈ Br^- > NO_3^-; **2.1HB:** $H_2PO_4^-$ > OBz^- > HSO_4^- > Cl^- ≈ Br^-, with no response towards NO_3^-.

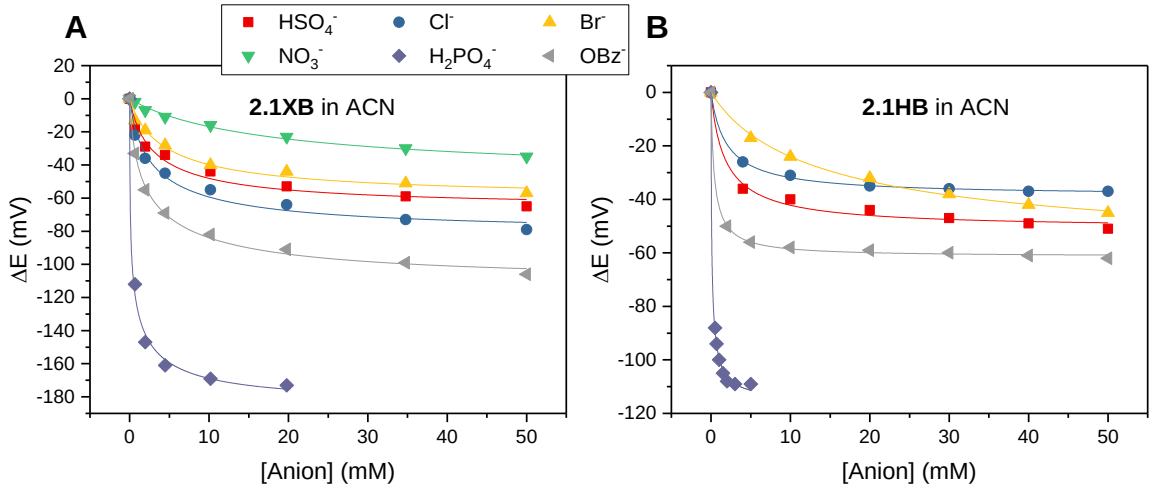


Figure 2.6. Cathodic voltammetric shifts of **2.1XB** (A) and **2.1HB** (B) in ACN, 100 mM $TBAClO_4$ upon titration with various anions. **[2.1XB/HB]** = 0.1 mM. Solid lines represent fits to the 1:1 host-guest Nernst model (eqn. 2.2). Note the different y-axis scaling for both graphs.

In the presence of 1% H_2O the response towards all anions was diminished for both receptors as can be seen in Figure 2.7 and Table 2.2 (a direct comparison for each anion is also shown in Figures A2.10-A2.15).

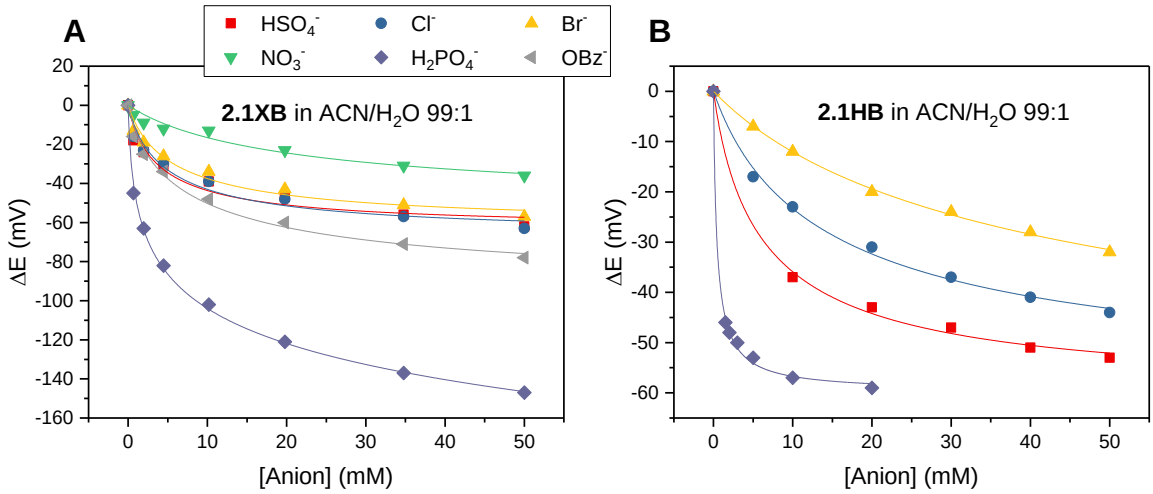


Figure 2.7. Cathodic voltammetric shifts of **2.1XB** (A) and **2.1HB** (B) in ACN/H_2O 99:1 upon titration with various anions. **[2.1XB/HB]** = 0.1 mM with 100 mM $TBAClO_4$ supporting electrolyte. Solid lines represent fits to the 1:1 host-guest Nernst model (eqn. 2.2). Note the different y-axis scaling for both graphs.

In this solvent system **2.1XB** still responded to all aforementioned anions with a similar trend as in ACN: $H_2PO_4^-$ > OBz^- > Cl^- ≈ HSO_4^- ≈ Br^- > NO_3^-. Interestingly, the trend of the response of **2.1HB** changed more significantly: $H_2PO_4^-$ > HSO_4^- > Cl^- > Br^-, with a notable lack of response towards OBz^-.

Of particular importance is the observation that the magnitude of cathodic perturbation in the presence of the tested anions in both solvent systems is larger for **2.1XB** over **2.1HB** in all cases (Figures A10-15). This is perhaps somewhat surprising considering that the anion binding strength to the native receptors, as elucidated by ^{1}H NMR titrations (discussed above), is larger for **2.1HB** in almost all cases. However, this importantly illustrates the performance of the sensor (*i.e.* the magnitude of the shift) is not simply governed by anion binding strength to the neutral receptor, as discussed in Section 2.1.

Furthermore, the ^{1}H NMR anion binding strength of the native receptor does also not directly correlate with the observed response. While $H_2PO_4^-$ elicited the largest voltammetric response and also displayed the strongest binding in all cases, this correlation is poor for other anions, in particular in the more competitive solvent system. For example, in the ^{1}H NMR titration experiment CD_3CN/D_2O 99:1, HSO_4^- did not elicit any binding to either **2.1XB/HB**, however both receptors displayed a significant voltammetric response towards this anion. In contrast, in the same solvent system OBz^- was bound comparatively strongly by both native receptors, however did not induce any perturbation of the Fc/Fc^+ couple of **2.1HB**. In CD_3CN the ^{1}H NMR anion binding strength correlates somewhat better with the magnitude of the cathodic perturbations, however both trends are not fully identical.

Table 2.2. ΔE (mV) of **2.1XB/HB** in ACN or ACN/H_2O 99:1 in the presence of 50 mM of various anions. n.r. – No response.

	ACN		ACN/H_2O 99:1	
	2.1XB	**2.1HB**	**2.1XB**	**2.1HB**
Cl^-	−79	−37	−63	−44
Br^-	−57	−45	−57	−32
HSO_4^-	−65	−51	−62	−53
$H_2PO_4^-$	−173	−109	−147	−59
OBz^-	−106	−62	−78	n.r.
NO_3^-	−35	n.r.	−36	n.r.

2.2.2.2.2 Quantitative Analysis of Binding Isotherms and the BEF

In order to further elucidate the principles that underpin these observations the voltammetric binding isotherms were fitted to a 1:1 host-guest stoichiometric Nernst binding model (eqn. 2.2), allowing the extraction of not only the absolute anion binding constant to the neutral (reduced) receptor (K_{Red}) but also to the oxidised receptor (K_{Ox}). This analysis then also affords the binding enhancement factor (BEF = K_{Ox}/K_{Red}).

This model accurately describes the obtained binding isotherms in all cases, with only slight deviations from ideality in a few cases. The binding constants obtained from this analysis are shown in Table 2.3, where it can be seen that in all cases K_{Ox} is, as expected, significantly larger than K_{Red}. The anion binding constants of the neutral receptors are of similar magnitude as those obtained by ^{1}H NMR titrations, and slight deviations can most likely be attributed to 1) a different signal transduction and 2) a slightly different solvent system where in the electrochemical titrations non-deuterated solvents are utilised and excess of supporting electrolyte is present. While the supporting electrolyte is not expected

to bind to the receptor (and thus compete with anion binding) it has to be noted that the presence of large concentrations of ions certainly affects the dielectric constant of the medium, in turn potentially affecting anion binding.

Table 2.3. Solution-phase binding constants K_{Ox} and K_{Red} (M^{-1}) of various anions to **2.1XB/HB** as determined by diffusive electrochemical titrations. All isotherms were fit to eqn. 2.2 to obtain absolute binding constants. n. r. – No response. / – Not conducted. Mathematical errors from the fitting are generally <20%, but can be larger for all binding constants close to 0 (see Section 7.4 for further details).

	2.1XB in ACN		**2.1XB in ACN/H_2O 99:1**		**2.1HB in ACN**		**2.1HB in ACN/H_2O 99:1**	
	K_{Ox}	**K_{Red}**	**K_{Ox}**	**K_{Red}**	**K_{Ox}**	**K_{Red}**	**K_{Ox}**	**K_{Red}**
Cl^-	1600	68	724	54	1030	222	201	21
Br^-	683	66	547	50	208	20	70	4
HSO_4^-	1110	85	847	73	1460	201	503	57
$H_2PO_4^-$	161000	121	5590	-2[a]	99200	1090	7360	715
OBz^-	3930	52	753	20	8200	746	n. r.	n. r.
NO_3^-	132	20	122	16	n. r.	n. r.	/	/
ReO_4^-	/	/	/	/	n. r.	n. r.	/	/

a – See Section 7.4.

From this quantitative analysis it can be seen that, as expected, anion binding to both oxidation states is diminished in the more competitive, organic/aqueous solvent system for all anions.

Of note are the particularly large binding constants towards $H_2PO_4^-$ in the oxidised state, with K_{Ox} of up to 161000 for **2.1XB** in ACN. Although K_{Ox} is not always larger for **2.1XB** in comparison to **2.1HB**, the BEF, *i.e.* the binding switch-on upon oxidation, is larger for **2.1XB**

in all cases apart from Br^- in ACN/H_2O 99:1 (Table 2.4). This is in excellent agreement with the qualitative observations of the voltammetric response discussed above, where **2.1XB** always outperforms **2.1HB**, confirming that the magnitude of the voltammetric shift is primarily dependent on the BEF as discussed in Section 2.1.

Table 2.4. Binding enhancement factors (BEF = K_{Ox}/K_{Red}) for diffusive binding studies of **2.1XB/HB** in ACN or ACN/H_2O 99:1. K_{Ox} and K_{Red} were obtained from fitting to the 1:1 host-guest Nernst model (eqn. 2.2); Table 2.3. / – Not applicable.

	ACN			ACN/H_2O 99:1		
	2.1XB	**2.1HB**	**Ratio XB/HB**	**2.1XB**	**2.1HB**	**Ratio XB/HB**
Cl^-	23.5	4.64	5.07	13.4	9.57	1.40
Br^-	10.4	10.4	1.00	10.9	17.5	0.63
HSO_4^-	13.1	7.26	1.80	11.6	8.83	1.32
$H_2PO_4^-$	1330	91.0	14.6	[a]	10.3	[a]
OBz^-	75.6	11.0	6.88	37.7	/	/
NO_3^-	6.6	/	/	7.63	/	/
ReO_4^-	/	/	/	/	/	/

a – Errors too large for accurate comparison.

Another important conclusion that can be drawn from these results is that halogen bonding appears to be an innately superior non-covalent interaction for voltammetric solution-phase anion sensing, as similarly observed in other examples (see Chapter 1, Section 1.2.2.2.3).[158,159,162,277] As qualitatively discussed above, the cathodic perturbations of **2.1XB** are larger in all cases than those of **2.1HB**; in most cases significantly so, but the difference in response is not constant across the range of anions tested. For example, in both solvent systems the difference in response of both receptors towards HSO_4^- is significantly smaller

than that towards $H_2PO_4^-$. Attributing this observation to specific anion (or host-guest) properties is difficult, but is overall indicative of fundamentally different energetic contribution towards the binding of different anions. Specifically, based on simple electrostatic considerations, the binding enhancement upon oxidation should affect all the monovalent anions equally (*i.e.* the relative change in binding should be equal resulting in an equal BEF and thus response). As this is not the case, this suggests that the non-covalent XB/HB interactions that drive anion recognition in these receptors are not purely electrostatically driven and/or that other factors (such as receptor/anion solvation) play a crucial role in these systems.

In order to further elucidate the difference in response of **2.1XB/HB** a quantitative comparison of the BEF between both systems was carried out. Specifically, the ratio of the BEFs, *i.e.* a sort of XB enhancement factor that is given by BEF_{XB}/BEF_{HB}, as shown in Table 2.4, was calculated. In both solvent systems the largest XB enhancement is observed for $H_2PO_4^-$, in agreement with the qualitative observation that there is a notable difference in shift magnitude between both receptors. Specifically, in ACN a XB enhancement factor of 14.6 is obtained for this anion; *i.e.* while the binding-switch on upon oxidation is already large for **2.1HB** (91) the BEF for **2.1XB** is significantly larger (1330). This almost 15-fold difference indicates that anion binding at the XB receptor is 15-times more sensitive to the voltammetric generation of a positive charge than the HB analogue. This significant difference is even more astounding considering the triazole binding sites are spatially quite far removed from the Fc transducer. However, as highlighted above, this XB enhancement is non-uniform across the range of different anions being much smaller for Cl^- and HSO_4^- and negligible for Br^-.

The higher sensitivity of the XB interaction towards modulation of the receptors´ oxidation state is potentially reflective of an increased covalent character of the XB interaction,[278] where any modulation of the charge more effectively influences anion binding. Related discussions on the electrostatic interactions within these receptors can be found in Section 2.2.4.

2.2.2.2.3 Summary of Diffusive Voltammetric Sensory Performance

To sum up thus far, both novel Fc-isophthalamide-triazole receptors **2.1XB/HB** display a well-defined electrochemical response towards a wide range of halides and oxoanions in both pure organic solvent (ACN) as well as in an organic/aqueous mixture (ACN/H_2O 99:1). Interestingly, significant differences between both receptors were observed, in spite of their structural similarity, as qualitatively summarised in Table 2.5. ^{1}H NMR titrations afforded binding constants to the native receptor that were, unexpectedly, larger for **2.1HB** in almost all cases. In contrast, **2.1XB** displayed larger cathodic perturbations towards all tested anions, which can largely be attributed to an enhanced BEF as quantified by fitting of the voltammetric binding isotherms to a 1:1 host-guest Nernst model. These significant deviations between the XB and HB sensors directly report on fundamental differences in the nature of these non-covalent interactions.

Table 2.5. Qualitative comparison of **2.1XB** and **2.1HB** for the solution-phase recognition and sensing of anions in ACN and ACN/H_2O 99:1. If **2.1HB** outperforms **2.1XB** the entries are coloured in red while they are coloured in green for XB > HB. In all cases data analysis was performed according to the 1:1 host-guest Nernst fit (eqn. 2.2; Table 2.3). / – Not applicable.

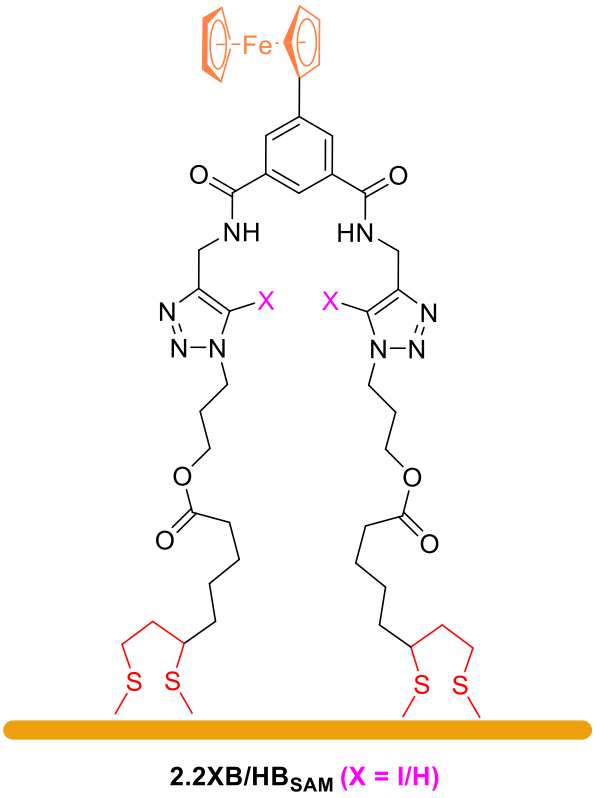
Solvent	Anion	K (NMR)	K_{Red}	K_{Ox}	BEF	ΔE
ACN	Cl^-	HB > XB	HB > XB	XB > HB	XB > HB	XB > HB
	Br^-	HB > XB	XB > HB	XB > HB	XB = HB	XB > HB
	HSO_4^-	HB > XB	HB > XB	HB > XB	XB > HB	XB > HB
	$H_2PO_4^-$	HB > XB	HB > XB	XB > HB	XB > HB	XB > HB
	OBz^-	HB > XB	HB > XB	HB > XB	XB > HB	XB > HB
	NO_3^-	XB > HB	XB > HB	XB > HB	/	XB > HB
ACN/H_2O 99:1	Cl^-	HB > XB	XB > HB	XB > HB	XB > HB	XB > HB
	Br^-	HB > XB	XB > HB	XB > HB	HB > XB	XB > HB
	HSO_4^-	/	XB > HB	XB > HB	XB > HB	XB > HB
	$H_2PO_4^-$	HB > XB	HB > XB	HB > XB	XB > HB	XB > HB
	OBz^-	HB > XB	XB > HB	XB > HB	/	XB > HB
	NO_3^-	/	XB > HB	XB > HB	/	XB > HB

2.2.3 Voltammetric Anion Sensing at Redox-Active SAMs

The promising solution-phase voltammetric sensing studies prompted the investigation of analogous surface-confined receptors. Specifically, the introduction of lipoic acid appendages into the receptor scaffold afforded **2.2XB/HB** (see Section 2.2.1), which enables facile formation of SAMs.

2.2.3.1 SAM Formation and Characterisation

The immobilisation of the receptors onto gold electrodes was achieved by overnight immersion of clean gold electrodes into a solution of **2.2XB/HB** (0.25 mM in ACN) affording **2.2XB/HB$_{SAM}$** (Figure 2.8). Water contact angle measurements indicate a moderate hydrophobicity which is somewhat larger for **2.2XB$_{SAM}$** (65°) than for **2.2HB$_{SAM}$** (59°), in agreement with the more hydrophobic character of the iodotriazole moiety (Table 2.8).



2.2XB/HB$_{SAM}$ (X = I/H)

Figure 2.8. Schematic representation of **2.2XB/HB$_{SAM}$** on a gold electrode.

2.2.3.1.1 X-ray Photoelectron Spectroscopy (XPS)

From XPS the elemental composition of **2.2HB$_{SAM}$** was determined, revealing, only the presence of C, N, O, S and Fe in the film (Figure 2.9).

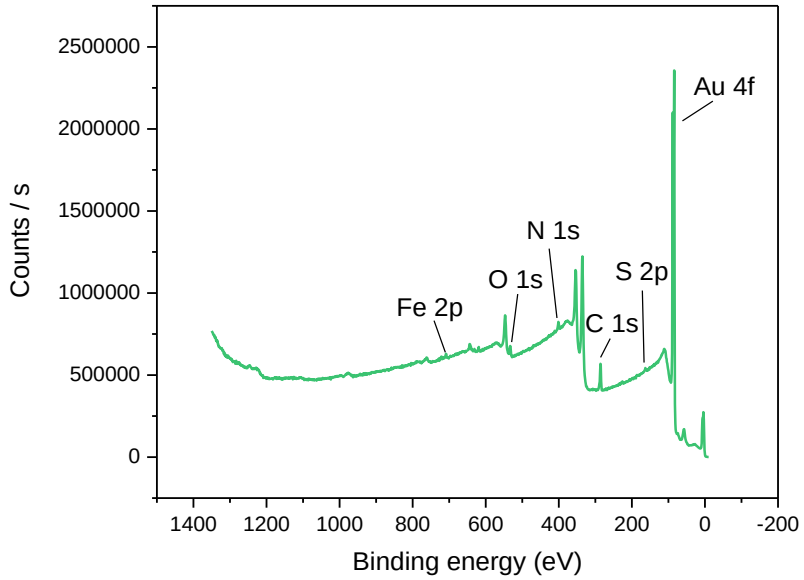


Figure 2.9. Low resolution survey XPS spectrum of **2.2HB$_{SAM}$**. All unassigned peaks arise from other orbitals of the same elements.

Importantly, the atomic ratios obtained from this analysis are in good agreement with the expected values based on the chemical formula of **2.2HB** (Table 2.6).

Table 2.6. Experimental and theoretical elemental composition of **2.2HB$_{SAM}$** determined by XPS. Values were normalised to Fe = 1. Errors represent one standard deviation of triplicate measurements.

	Experimental	**Theoretical**
C	44.61 ± 1.21	46
N	7.10 ± 0.71	8
O	6.94 ± 0.72	8
S	3.33 ± 0.545	4
Fe	1 ± 0.15	1

From peak fitting of the high resolution C, N and O spectra further information about the specific chemical environments of the receptors can be extracted (Figure 2.10). In the C 1s high resolution spectrum three distinct chemical environments can be observed and assigned to C–C, C–X (X = N, O, S) as well as C=O groups.[279-281] The ratio of these peaks roughly reflects the theoretical ratio (Table 2.7). In the N 1s high resolution spectrum two environments can be observed, one arising from N=N and N–H moieties as well as one arising from N–N. These peaks can be assigned based on previous reports of triazole[280] and amide-containing[281] films and their ratio is approximately in line with the expected values.

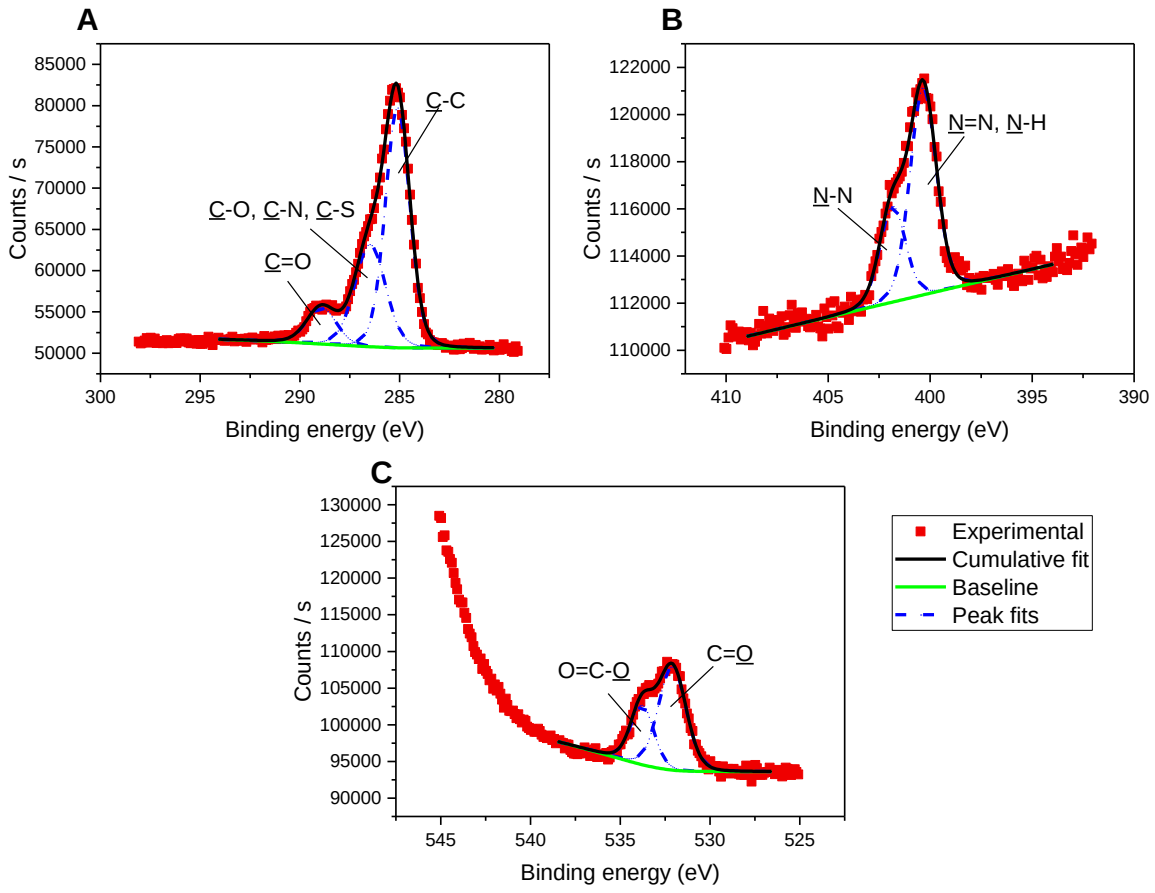


Figure 2.10. High resolution XPS spectra including peak fits of **2.2HB$_{SAM}$**. A) C 1s. B) N 1s C) O 1s.

An excellent agreement with the theoretically predicted peak ratios can be observed for the O 1s peaks assignable to a higher energy O=C−O contribution as well as the carbonyl oxygens.[279]

It should be noted that the different peaks in the S 2p and Fe 2p XPS spectra of **2.2HB$_{SAM}$** (Figure 2.11) are not reflective of different chemical environments around these atoms but arise from spin-orbit coupling. In both cases only one environment is present.

In the high resolution S 2p spectrum two peaks (arising from spin orbit coupling) can be fitted. The binding energies of these peaks of 162.0 eV and 163.5 eV (with a peak separation of 1.5 eV) are in line with previous reports.[282,283] These results are furthermore indicative of the formation of Au−S interactions (and thus a chemisorbed SAM). For a physisorbed thiol/disulfide a higher binding energy of the S 2p peaks of approx. 165 eV would be observed.[282,283]

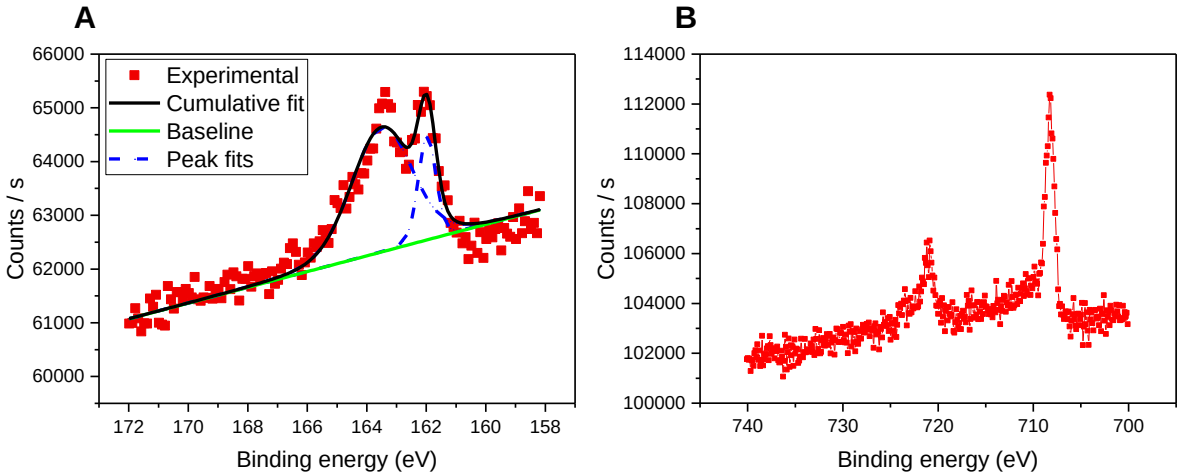


Figure 2.11. High resolution XPS spectra of **2.2HB$_{SAM}$**. A) S 2p. B) Fe 2p. The peaks in both spectra arise from spin orbit coupling and not from chemically different environments.

In summary, XPS confirms the formation of disulfide-tethered SAM, with a chemical composition of functional groups that is consistent with the chemical composition of the receptor.

Table 2.7. Peak binding energies and experimental and theoretical ratios for different chemical environments of C, N and O of **2.2HB$_{SAM}$**. The ratios shown here are obtained by peak fitting of the individual high resolution spectra and do not report on the overall ratio of the elements (see Table 2.6). Errors represent one standard deviation of triplicate measurements.

		Peak BE (eV)	Exp.	Theor.
C	C–C	285.07 ± 0.05	20.57 ± 1.21	28
	C–O, C–N, C–S	286.46 ± 0.05	10.75 ± 1.46	14
	C=O	288.86 ± 0.05	4	4
N	N=N, N–H	400.29 ± 0.11	4.38 ± 1.50	6
	N–N	401.77 ± 0.16	2	2
O	C=O	532.11 ± 0.02	4.17 ± 0.53	4
	(O=C) –O	533.80 ± 0.02	2	2

2.2.3.1.2 ATR-FTIR Spectroscopy

The SAMs were further analysed by attenuated total reflectance Fourier transform infrared spectroscopy (ATR-FTIR, Figure 2.12, Section 7.3.2). Both **2.2XB/HB$_{SAM}$** produced matching spectra, confirming the formation of chemically identical films. A number of functional groups can be observed, including asymmetric and symmetric methylene stretches at 2929 and 2857 cm^{-1}, respectively, in good agreement with previous reports of alkylthiol-based SAMs.[284,285] Broad peaks at 1740 and 1652 cm^{-1}, most likely arise from ester and amide functional groups, respectively. Another broad signal at 1465 cm^{-1} presumably arises from the triazole moieties.[286] Of note is the prominent peak at 2350 does not arise from the sample but can be assigned to atmospheric CO_2. As there are no significant differences

between both SAMs it can be concluded that bands arising from the C–I bonds in **2.2XB$_{SAM}$** fall, as expected for a carbon-halogen single bond, within the fingerprint region.

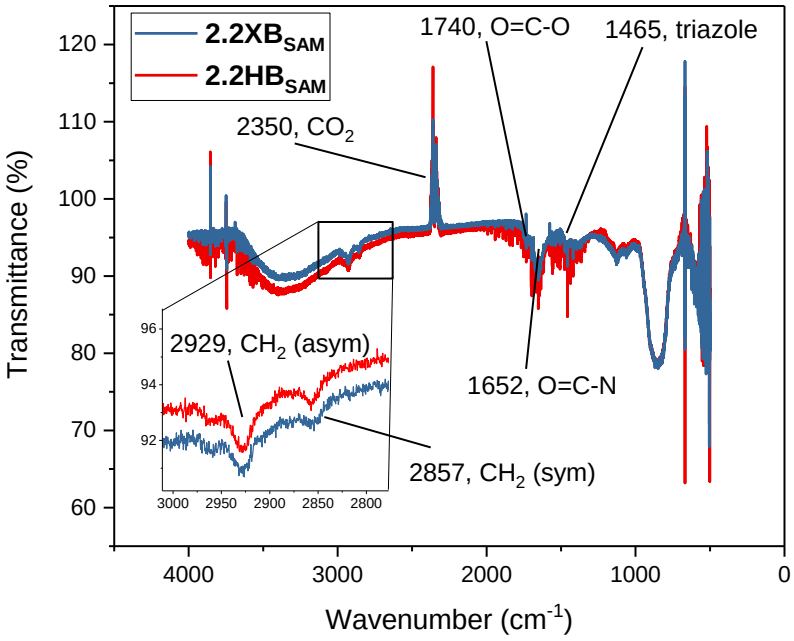


Figure 2.12. ATR-FTIR spectra of **2.2XB/HB$_{SAM}$** on gold.

2.2.3.1.3 Electrochemical Characterisation of the Receptive SAMs

Electrochemical experiments were carried out in the same solvent systems as used for diffusive studies. In all solvents both SAMs displayed a well-defined, quasi-reversible redox couple at potentials ≈10 mV more anodic than of the free monomers in solution (Figure 2.13A, Figure A2.16 and Table 2.8). This enhanced difficulty of oxidation presumably arises from slightly lowered solvent/electrolyte access which would stabilise the Fc^+ oxidation state. As can be seen in Figure 2.13B, the linear dependence of the peak currents on the scan rate as well as the low peak separation of ≈35 mV are indicative of a surface-bound redox-centre.

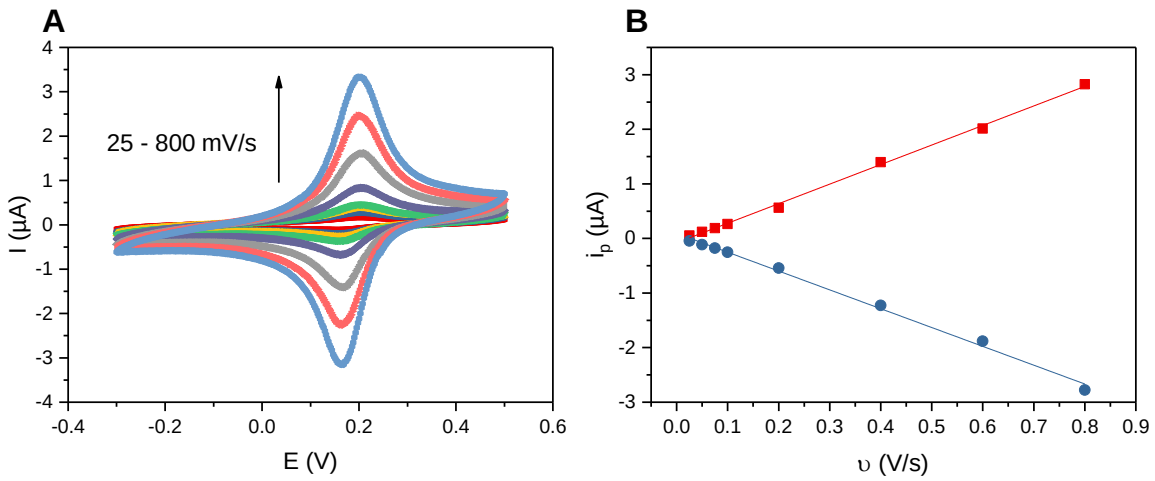


Figure 2.13. A) CVs at varying scan rate of **2.2HB$_{SAM}$** in ACN, 100 mM $TBAClO_4$. B) The associated anodic and cathodic peak currents as a function of the scan rate including linear fits.

The molecular surface coverage Γ was obtained by charge integration of the Fc transducer, affording a practically value of ≈10^{-10} mol/cm^2 for both films (Table 2.8), corresponding to a molecular footprint of 1.66 nm^2. This is in excellent agreement with the size of the receptors and indicative of a densely packed SAM where the molecules adopt an upright conformation as depicted in Figure 2.8.

Table 2.8. Surface characterisation of **2.2XB/HB$_{SAM}$**. Electrochemical measurements were carried out in ACN/H_2O 99:1 containing 100 mM $TBAClO_4$ as electrolyte.

	Water contact angle (°)[a]	**Γ (10^{-10} mol/cm^2)[b]**	**$E_{1/2}$ (mV) *vs.* Ag|AgNO$_3$**
2.2XB$_{SAM}$	68.4 ± 1.7	1.01 ± 0.18	193 ± 1
2.2HB$_{SAM}$	59.1 ± 1.1	1.15 ± 0.22	183 ± 2

a – Errors represent one standard deviation of 5 repeat measurements. b – Obtained from charge integration of the ferrocene peaks. Errors represent one standard deviation of independent experiments on three electrodes.

Upon repeated cycling of these films in various organic and aqueous solvent systems a gradual loss of redox-activity was observed, a well-known problem arising from a non-ideal

redox reversibility of the transducer. When using Fc-based redox-active systems this degradation arises from the reaction of ferrocenium (Fc^+) with (adventitious) nucleophiles or electrolyte anions and has been shown to be impeded by using aqueous electrolytes of low pH (*e.g.* 1 M aq. $HClO_4$), where basic nucleophiles are protonated and thus scavenged.[287-290] To date no reports have investigated if such conditions could improve the sensory performance (*i.e.* redox stability) of anion-receptive interfaces, most of which are probed in organic solvent media. However, high voltammetric stability is crucial for many applications where high baseline stability is often sought, especially if the continuous or repeat use of a sensor is envisioned. In Fc-containing redox-active sensors these reversibility requirements are usually only relevant in film-based sensors, where any non-ideal redox reversibility is amplified as degraded surface-tethered molecules cannot be diffusively replenished. In contrast, if the redox-active molecule is probed under homogeneous, diffusive conditions, these considerations are usually irrelevant; even if some degree of degradation occurs, fresh (unreacted) molecules can diffuse to the electrode surface. For example, no significant voltammetric loss was observed for **2.1XB/HB** under diffusive conditions. Only in the presence of high concentrations of basic anions, such as phosphate or benzoate is some degree of irreversibility observed in solution.

As shown in Figure 2.14, **2.2HB$_{SAM}$** displayed a decline in peak currents of 46% after 50 scans (as assessed by SWV in ACN/H_2O 99:1, 100 mM $TBAClO_4$, see Section 7.2.3). In ACN this degradation was even more significant (not shown), prompting only the use of the aqueous-organic solvent mixture for all further studies. It was speculated, as discussed above, that this degradation largely arises from the reaction of Fc^+ with nucleophiles, such as OH^-, and that the addition of acid would disfavour this reaction (by scavenging the nucleophiles). To

test this hypothesis, the redox-stability of the film in the same solvent system in the presence of additional $HClO_4$ (100 µM, 1 mM and 10 mM) was investigated. Interestingly, even small amounts of acid (100 µM H^+) can notably enhance the cycling stability of the films (with a current retention of 95% after 50 cycles and 55% after 500 cycles, Figure 2.14). The addition of higher concentrations of acid can further enhance the voltammetric stability of the films, where most notably 91% of redox-activity is retained after 500 cycles in the presence of 10 mM acid.

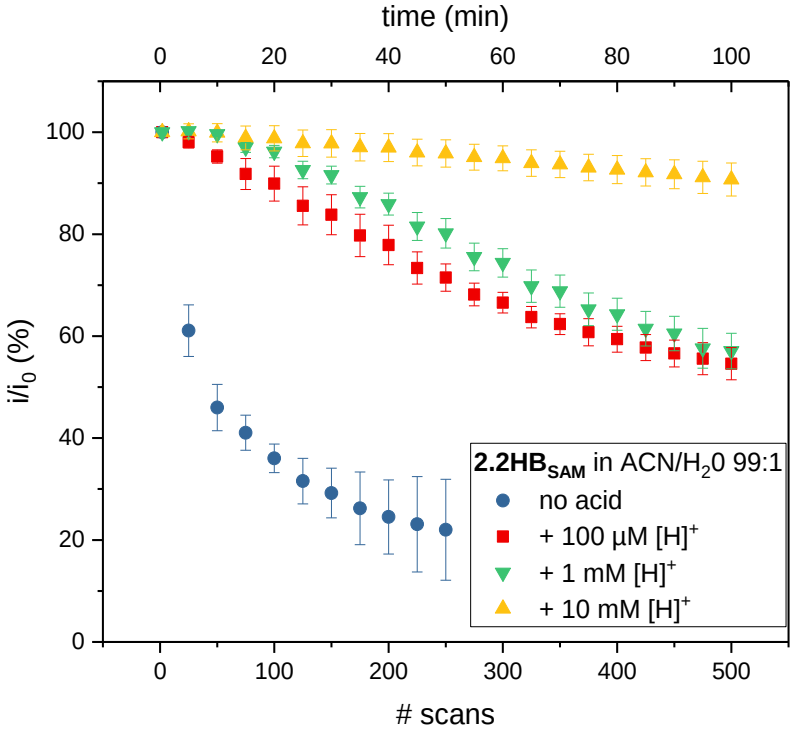


Figure 2.14. Redox stability, as assessed by the relative decrease in peak currents (i/i_0), of **2.2HB$_{SAM}$** upon repeated cycling in ACN/H_2O 99:1, 100 mM $TBAClO_4$ in the presence of various concentrations of $HClO_4$. The measurements in the absence of acid (blue circles) were stopped after 250 scans.

It is important to note that the addition of acid increases the ionic strength of the medium, which, as reported previously,[267] is an important factor that affects the stabilisation of the Fc^+ redox state, and thus influences the $E_{1/2}$. However, it can be ruled out that the

enhanced voltammetric stability in the presence of H^+ arises from a direct interaction of the acid with Fc/Fc^+. Firstly, the increase in ionic strength upon addition of acid is small (0.1−10%) and secondly, the half-wave potential of the couple remains unaffected by the addition of acid (even of 10 mM H^+), indicating that the small change in the ionic strength of the electrolyte does not lead to an enhanced stabilisation of the Fc^+ redox state. Hence, the enhanced voltammetric stability in the presence of acid has to arise from a change in the chemical composition of the electrolyte medium, in excellent agreement with the "scavenging" hypothesis. The significant improvement of the voltammetric stability even in the presence of small concentrations of acid is also in agreement with this hypothesis. Specifically, the concentration of OH^- (or any other adventitious nucleophile) is expected to be very small, such that even small acid concentrations will neutralise them effectively. Of course these effects are highly dependent on the specific solution-phase composition, pH and pK_a of all species involved (see Section 2.2.3.2.3).

2.2.3.2 Interfacial Anion Sensing

The significantly improved voltammetric stability of the SAMs prompted the investigation of their anion sensory properties in the presence of various concentrations of acid (initially in 100 µM and then also 1 mM and 10 mM, see below). Analogous to diffusive studies, the shift of the $E_{1/2}$ of the SAMs was assessed by SWV as representatively shown for titration of **2.2XB$_{SAM}$** in ACN/H_2O 99:1 + 100 µM H^+, 100 mM $TBAClO_4$ with HSO_4^- (Figure 2.15).

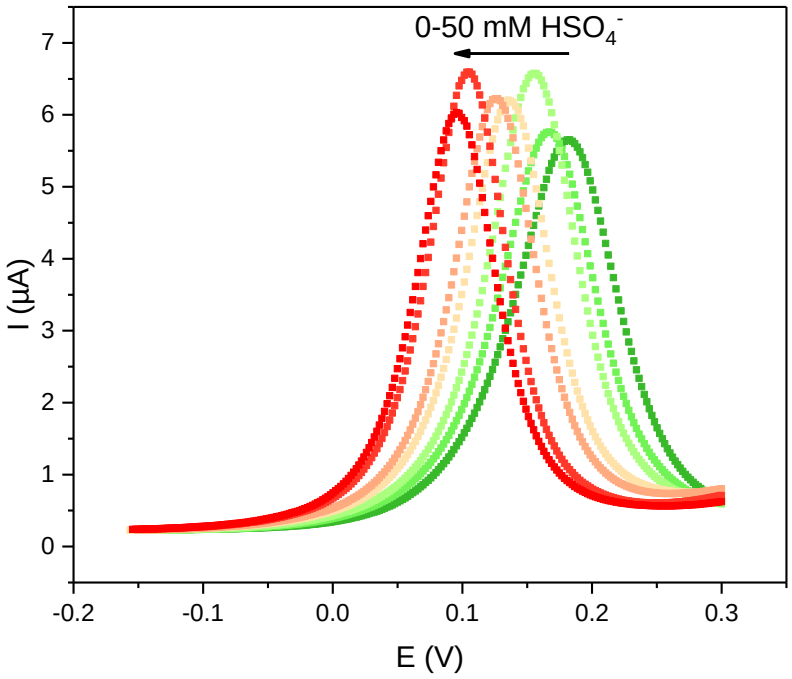


Figure 2.15. SWVs of **2.2XB$_{SAM}$** in ACN/H_2O 99:1 + 100 µM H^+ in the presence of increasing concentrations of HSO_4^-.

In the presence of this concentration of acid (100 µM) both SAMs respond to all tested anions where no large deviations from the expected binding isotherms are observed, indicating that this low acid concentration does, as expected, not significantly affect anion binding (Figure 2.16).

This was also confirmed by titration of **2.2HB$_{SAM}$** with HSO_4^- in the absence of any acid, where a very similar response as in the presence of 100 µM H^+ was observed. In general the reproducibility of the response across different repeats/electrodes is good. In contrast to solution-phase studies, no systematic anion binding studies were carried with OBz^-, largely as a result of compromised voltammetric stability at higher anion concentrations. Of note is also that the sensing of Br^- is restricted to low concentrations (typically <5 mM) as at higher concentrations the oxidation of Br^- notably overlaps with the Faradaic activity of the Fc-transducer, preventing accurate determination of the peak potentials.

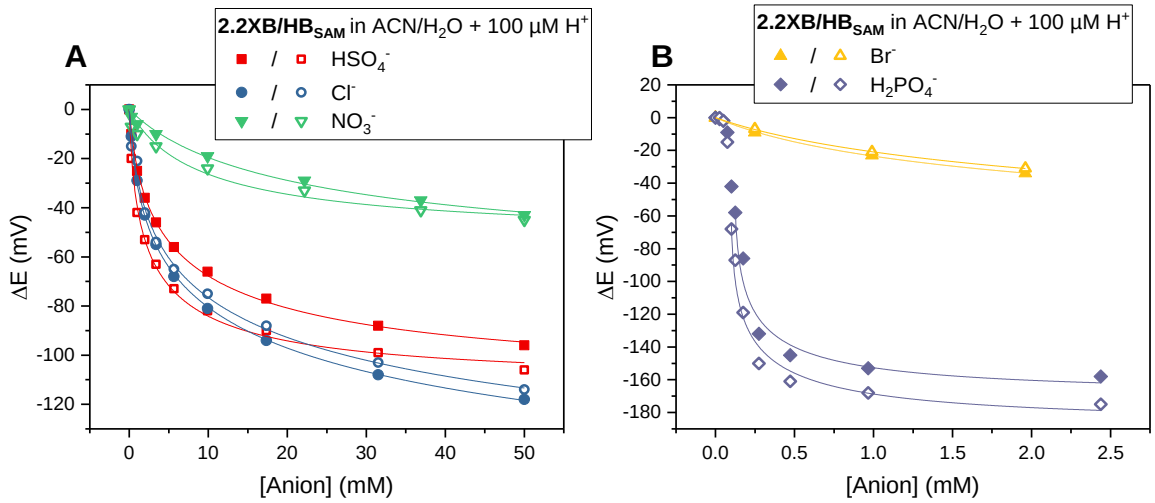


Figure 2.16. Cathodic voltammetric shifts of **2.2XB/HB$_{SAM}$** in ACN/H_2O 99:1 + 100 µM H^+ upon titration with various anions. Solid lines represent fits to the 1:1 host-guest Nernst model (eqn. 2.2 or eqn. 2.3 for $H_2PO_4^-$). Note the different y- and x-axis scaling for both graphs.

At both SAMs the largest response was observed for $H_2PO_4^-$, with smaller, but significant, cathodic shifts in the presence of HSO_4^-, Cl^- and Br^- (Table 2.9). The overall response trends of both interfaces were almost identical; $H_2PO_4^- > Cl^- > Br^- \approx HSO_4^- > NO_3^-$ for **2.2XB$_{SAM}$** and $H_2PO_4^- > Cl^- \approx Br^- \approx HSO_4^- > NO_3^-$ for **2.2HB$_{SAM}$**. These trends are similar to those observed for diffusive binding studies of **2.1XB/HB** in the same solvent with the notable exception that **2.2HB$_{SAM}$** elicited a response to NO_3^- while no perturbations were observed under diffusive conditions.

The sensory performance of **2.2XB/HB$_{SAM}$** was also investigated in the presence of higher concentrations of acid (1 mM and 10 mM). In contrast to the low acid concentration of 100 µM, the presence of these higher concentrations of acid does influence the sensor performance as shown for **2.2XB$_{SAM}$** in Figures 2.17−2.18 (the same data is shown for **2.2HB$_{SAM}$** in Figures A2.17−A2.18).

Table 2.9. ΔE (mV) of **2.2XB/HB$_{SAM}$** in ACN/H_2O 99:1 (+100 µM H^+) in the presence of the highest measured anion concentration (50 mM for Cl^-, NO_3^- and HSO_4^- and ≈2 mM for Br^- and $H_2PO_4^-$; see Figure 2.16). Shown are also K_{Ox} and K_{Red} (M^{-1}) as obtained from fitting of the data fits to the 1:1 host-guest Nernst model (eqn. 2.2 or eqn. 2.3 for $H_2PO_4^-$).

	2.2XB$_{SAM}$			**2.2HB$_{SAM}$**		
	ΔE	**K_{Ox}**	**K_{Red}**	**ΔE**	**K_{Ox}**	**K_{Red}**
Cl^-	−118	2280	3	−114	1957	4
Br^-	−34	1710	82	−31	53	53
HSO_4^-	−96	1590	20	−106	3920	51
$H_2PO_4^-$	−158	≈0.9×10^6	≈1000	−175	≈1.5×10^6	≈1000
NO_3^-	−43	138	11	−45	281	36

In particular the more basic anions are, expectedly, protonated to a significant extent when $[A^-] < [H^+]$, thus switching off binding (and any associated response) as observed particularly strongly for $H_2PO_4^-$ and NO_3^-. The specific degree of protonation of these anions is very difficult to assess; the well-known acidity trends in water ($HClO_4$ > HBr > HCl > H_2SO_4 > HNO_3 > H_3PO_4) do not directly translate to a (mixed) organic/aqueous solvent system. For example, in pure ACN the following trend would be expected: $HClO_4$ > HBr > H_2SO_4 > HNO_3 > HCl.[291] In this mixed electrolyte used herein it can be assumed that the added $HClO_4$ is the strongest acid, capable of almost complete protonation of $H_2PO_4^-$ and NO_3^- where only a small/negligible response at concentrations $[A^-] < [H^+]$ is observed. In contrast, the less basic Cl^-, Br^- and HSO_4^- remain deprotonated to a more significant degree with a smaller, yet still significant response at $[A^-] < [H^+]$. In the presence of multiple anions of significantly different basicity this can potentially be utilised to tune the selectivity of the sensor. For example, in a mixture of HSO_4^- and $H_2PO_4^-$ the overall response is presumably dominated by $H_2PO_4^-$ as this anion displays stronger binding as well as a larger cathodic

perturbation. In the presence of acid however, the more basic $H_2PO_4^-$ would be preferentially protonated and would not bind to the SAM while the more acidic HSO_4^- would bind and elicit a response. These selectivity considerations are of course unrelated to the SAM itself and are most likely not relevant for any real-life applications as high acid concentrations would not be encountered/compatible with analytically relevant samples.

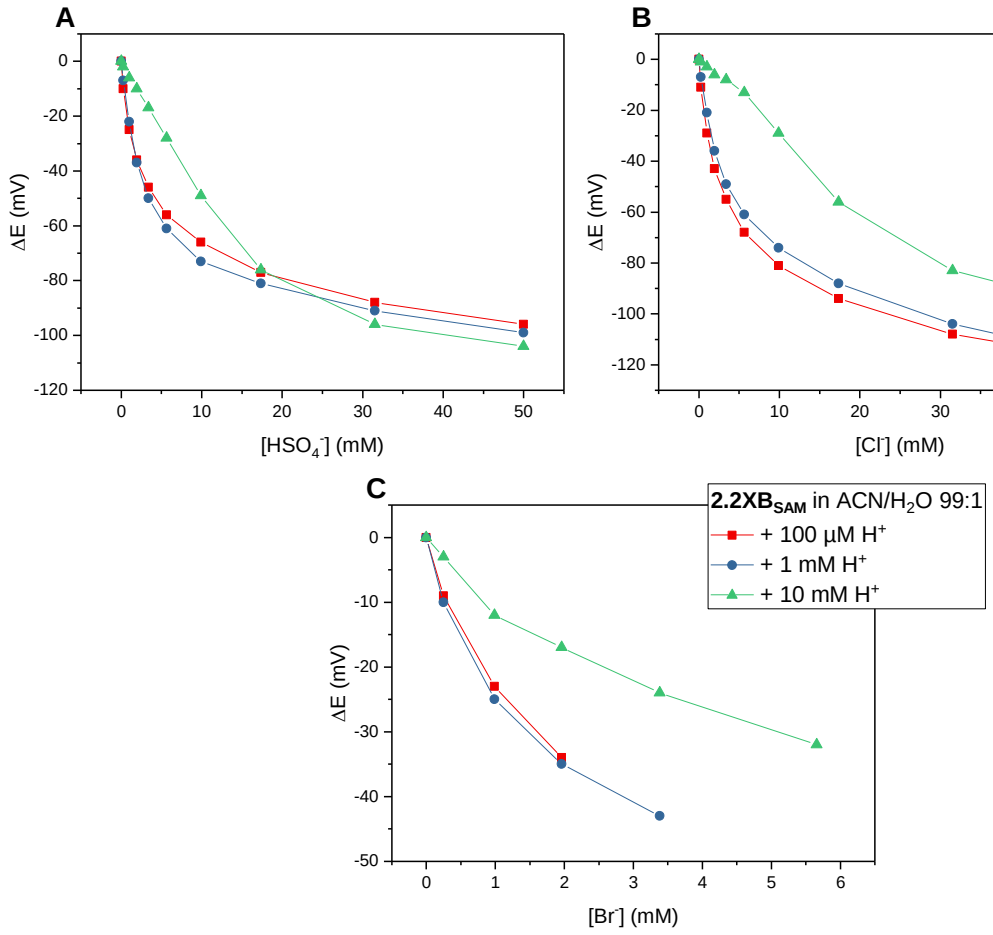


Figure 2.17. Cathodic voltammetric shifts **of 2.2XB$_{SAM}$** upon titration with HSO_4^-, Cl^- and Br^- in ACN/H_2O 99:1 and various concentrations of acid. Solid lines do not represent any fits and are only meant to guide the eye.

As the response patterns of both **2.2XB/HB$_{SAM}$** in the presence of various acid concentrations are identical it can be concluded that, the acid only influences the solution-

phase composition and does not influence the binding/response behaviour of the films directly.

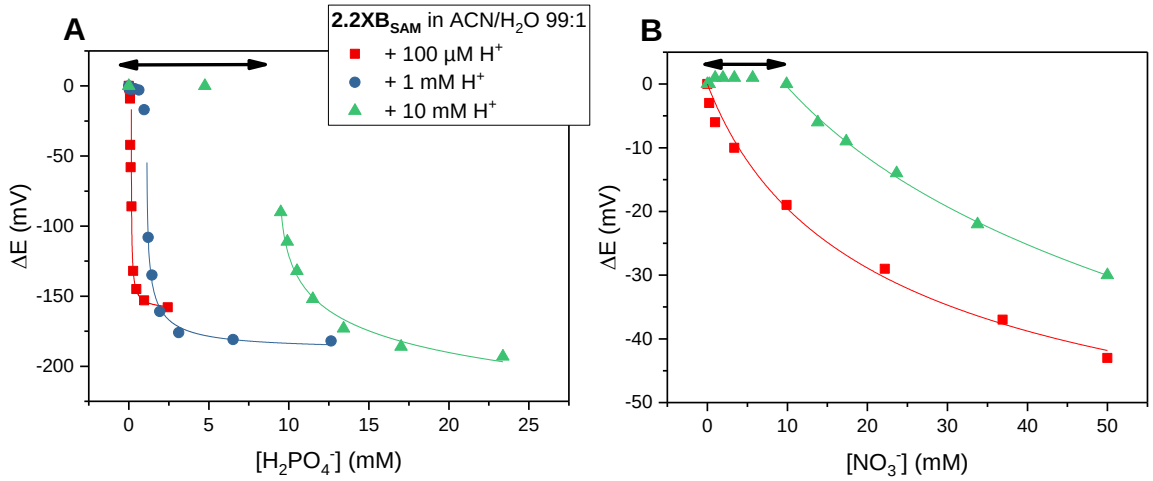


Figure 2.18. Cathodic voltammetric shifts of **2.2XB$_{SAM}$** upon titration with the basic anions $H_2PO_4^-$ and NO_3^- in ACN/H_2O 99:1 and various concentrations of acid. Solid lines represent fits according to the 1:1 Nernst model with an offset (eqn. 2.3). The offset (*i.e.* "delayed" response) of the binding isotherm in the presence of 10 mM acid is shown by the black arrows.

As shown above, in the presence of the smallest concentration of acid (100 µM), no significant derivations from an ideal, continuous binding isotherm were observed, apart from the most basic $H_2PO_4^-$ anion, where at very low concentration (<100 µM) no response is observed (Figure 2.16). In all other cases the response can still be accurately fitted to the standard 1:1 host-guest Nernst model (eqn. 2.2), which is used for all following quantitative analyses/discussions. In the case of $H_2PO_4^-$ and for the other anions in the presence of higher concentrations of acid, this model cannot be used anymore as the response at concentrations $[A^-] < [H^+]$ significantly deviates from the expected binding isotherm (Figures 2.17–2.18). Quantitative analysis of these isotherms based on established models is impossible; only a combined consideration of acid-base equilibria and the Nernst model

would be capable of modelling the response. If such a model could be devised the pK_a of the anion in the given solvent system could be obtained.

In the case of anions whose conjugate acid pK_a is significantly higher than that of $HClO_4$, *e.g.* $H_2PO_4^-$, it can be assumed that full protonation occurs until $[A^-] = [H^+]$ such that at concentration of $[A^-] > [H^+]$ no acid is present and the response thereafter strictly follows the Nernst model. In this case the binding isotherm is largely identical to that obtained in the absence of acid but is shifted (*i.e.* offset) by $\approx [H^+]$ (Figure 2.18).

This allows fitting of the $H_2PO_4^-$ binding isotherms by including an offset factor Z and disregarding the data points at low concentration such that:

$$\Delta E = -\frac{RT}{nF} * \ln\left(\frac{1+K_{Ox}*([A^-]+Z)}{1+K_{Red}*([A^-]+Z)}\right) \qquad \text{eqn. 2.3}$$

Eqn. 2.3 was used to obtain semi-quantitative binding data for $H_2PO_4^-$ in the presence of 100 µM H^+. In an ideal case this offset factor Z should be equivalent to the acid concentration, but only if 1) full protonation of the anion occurs and 2) there are no other basic species that are protonated, thereby lowering the free acid concentration. Hence, in reality the $H_2PO_4^-$ isotherms have to be fit according to eqn. 2.3 without fixing the offset factor Z at a specific value (concentration).

Saliently, the significantly improved voltammetric stability in the presence of acid does not only allow the repeat use of the sensory interface with high signal integrity (Figure 2.19), but can potentially enable the unprecedented sensing of anions based on redox capacitive methodologies where a high voltammetric stability is crucial (see Section 2.4.2.2).

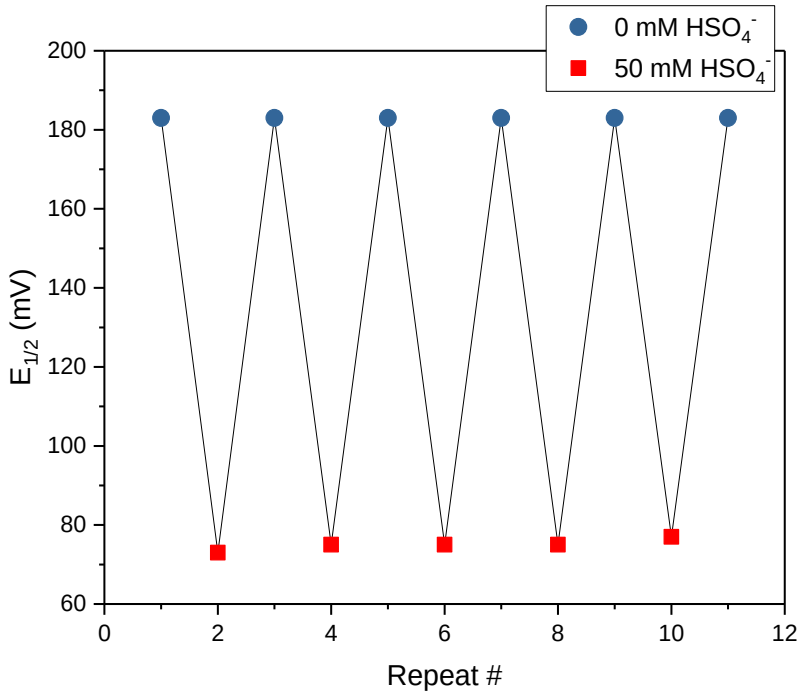


Figure 2.19. Potential response of **2.2HB$_{SAM}$** in ACN/H_2O 99:1 containing 10 mM $HClO_4$ in the alternating absence or presence of 0 or 50 mM HSO_4^-.

2.2.3.2.1 Analysis of Binding Isotherms by Langmuir Fitting

Analysis of the binding isotherms at the SAMs can also be carried out by fitting to a simple Langmuir adsorption model (eqn. 2.4) where θ is the fractional occupancy of receptive sites by the anion.

$$\theta = \frac{K[A^-]}{1+K[A^-]} \qquad \text{eqn. 2.4}$$

This model assumes 1:1 stoichiometric binding with no interactions between adjacent binding sites (*i.e.* no cooperative binding), conditions that are most likely satisfied here. In all cases a good fit of the experimental data to this model is obtained (Figure 2.20 and Table 2.10) from which the maximum response (*i.e.* max. cathodic shift ΔE_{max}) can be obtained. It is important to note that the binding constant in this case represents neither K_{Ox} nor K_{Red} but an apparent binding constant (K_{app}) that falls between both. This is

because the isotherm represents the following equilibrium during the voltammetric experiment: $H + A^- \rightleftharpoons H^+A^-$ (with K_{app}) and not the "standard" binding equilibria as depicted in the square scheme in Section 1.2.2 (Figure 1.10) with $H^+ + A^- \rightleftharpoons H^+A^-$ (K_{Ox}) and $H + A^- \rightleftharpoons HA^-$ (K_{Red}).

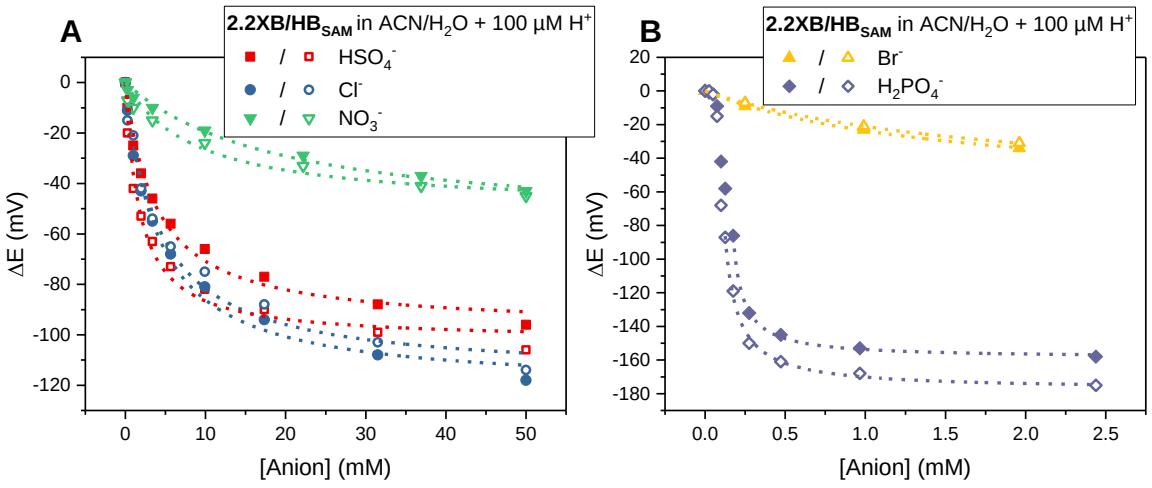


Figure 2.20. Cathodic voltammetric shifts of **2.2XB/HB$_{SAM}$** in ACN/H_2O 99:1 + 100 µM H^+ upon titration with various anions. Dotted lines represent fits to the Langmuir model (eqn. 2.4).

The apparent binding constants obtained from this analysis (Table 2.10) are similar for **2.2XB/HB$_{SAM}$**, in agreement with their near identical response and BEF values. The overall magnitude of K_{app} also correlates reasonably well with the qualitative and quantitative response and binding trends as discussed above. Specifically, the strength of "binding" of $H_2PO_4^-$ is significantly larger than that of the other anions, with NO_3^- binding weakest.

While the trends of K_{app} are similar to the response/BEF trends, the magnitude of K_{app} is significantly larger than the BEF in all cases. Furthermore, K_{app} does not represent the arithmetic mean of K_{Ox} and K_{Red} either. This indicates that the binding constant obtained from such "standard" binding isotherm analyses (here the Langmuir fitting) can potentially

report on overall binding/response trends but does not provide useful quantitative insights into relevant binding parameters (*i.e.* K_{Ox}, K_{Red}, BEF).

Table 2.10. Apparent binding constants K_{app} (M^{-1}) and maximum cathodic shift ΔE_{max} (mV) for binding of various anions to **2.2XB/HB$_{SAM}$** in ACN/H_2O 99:1 + 100 µM H^+ as obtained from fitting to the Langmuir model (eqn. 2.4).

	2.2XB$_{SAM}$			**2.2HB$_{SAM}$**		
	K_{App}	**ΔE_{max}**	**R^2**	**K_{App}**	**ΔE_{max}**	**R^2**
Cl^-	246	−121	0.9904	236	−116	0.9829
Br^-	644	−61	0.9990	526	−61	0.9999
HSO_4^-	263	−98	0.9883	551	−102	0.9803
$H_2PO_4^-$	35800[a]	−159	0.9987	25000[a]	−178	0.9954
NO_3^-	51	−58	0.9874	112	−50	0.9594

a – Large errors due to deviations from ideality at low concentrations (due to anion protonation).

2.2.3.2.2 Comparison of 2.2XB/HB$_{SAM}$

While, under diffusive conditions, the response of **2.1XB** towards all anions was much greater than that of **2.1HB** (as discussed in Section 2.2.2.2), this trend is interestingly not observed when comparing **2.2XB$_{SAM}$** and **2.2HB$_{SAM}$**. Specifically, the response towards all oxoanions was somewhat larger at **2.2HB$_{SAM}$** while **2.2XB$_{SAM}$** displayed a small preferential response towards the halides. However, in all cases the difference in response of the surface-confined receptors was relatively small, especially in comparison to that observed in solution (Figure 2.21).

Table 2.11. Binding enhancement factors (BEF; K_{Ox}/K_{Red}) of **2.2XB/HB$_{SAM}$** in ACN/H_2O 99:1 + 100 µM H^+. K_{Ox} and K_{Red} were obtained from fitting to the 1:1 host-guest Nernst model (eqn. 2.2 or eqn. 2.3; Table 2.9).

	ACN/H_2O 99:1 + 100 µM H^+		
	2.2XB$_{SAM}$	**2.2HB$_{SAM}$**	**Ratio XB/HB**
Cl^-	760	489	1.55
Br^-	20.9	26.0	0.80
HSO_4^-	79.5	76.9	1.03
$H_2PO_4^-$	≈900	≈1500	≈0.6
	476[a]	925[a]	0.52[a]
NO_3^-	12.5	7.81	1.60

a – Due to poor fitting of the isotherm according to eqn. 2.2/2.3 (as a result of $H_2PO_4^-$ protonation at low concentrations) the BEF was also obtained directly from the ΔE at the highest $H_2PO_4^-$ concentration (plateauing response) according to eqn. 2.1.

One might try to rationalise this unexpected (relatively) inferior performance of **2.2XB$_{SAM}$** based on the increased steric bulk of the iodotriazole groups, impairing anion binding, especially in a confined SAM environment. However, this explanation can only account for a diminished binding strength (in both reduced and oxidised states), but does not justify how this impacts the BEF, *i.e.* why binding switch-on is affected. Specifically, in stark contrast to diffusive studies, the BEFs for both SAMs across various anions is very similar as can be seen in Table 2.11. No clear differences/trends can be resolved where in most cases the ratio of BEFs for XB/HB SAMs (*i.e.* the XB enhancement factor) is ≈1, in good agreement with the near-identical response towards anions.

Such an observation is unprecedented, but indicates that immobilisation of the receptors either disproportionately improves the performance of the HB receptor or impairs that of the XB receptor (in relative terms). This may be due to (de)solvation effects which might

affect the diffusive/surface-bound XB and HB receptors differently. An alternative explanation is based on dielectric considerations as discussed in more detail in the following section.

2.2.4 Comparison of Diffusive and Surface-Confined Sensor Response

In all cases the response of the surface-confined receptors is significantly larger than under diffusive conditions (Figure 2.21), in good agreement with previous studies (see Chapter 1, Section 1.2.2.3).[210,212,221] Often the enhanced response of an interfacial (electrochemical) sensor is utilised to infer an enhanced binding strength which in turn is attributed to surface confined receptor preorganisation and/or cooperative/chelate binding.[210,212,219]

The former certainly plays a role in almost all surface-bound receptors and is expected to be relevant here as well. Specifically, immobilisation of the receptors *via* both disulfide appendages affords surface-anchored macrocyclic receptors where entropic penalties related to receptor conformations are certainly reduced. However, a large variety of other factors, including receptor and anion dehydration, which are altered at an interface, also play a role in determining the overall energetics of binding. Attributing an increased binding strength solely to preorganisation (or related considerations) is thus insufficient. More importantly, as highlighted throughout, the magnitude of the voltammetric response is determined by the BEF and not the magnitude of the binding. While cooperative effects or receptor preorganisation can rationalise enhanced/altered binding strength (in both oxidation states) they cannot explain why the relative change in binding constants upon oxidation (BEF) at an interfacial receptor would be larger.

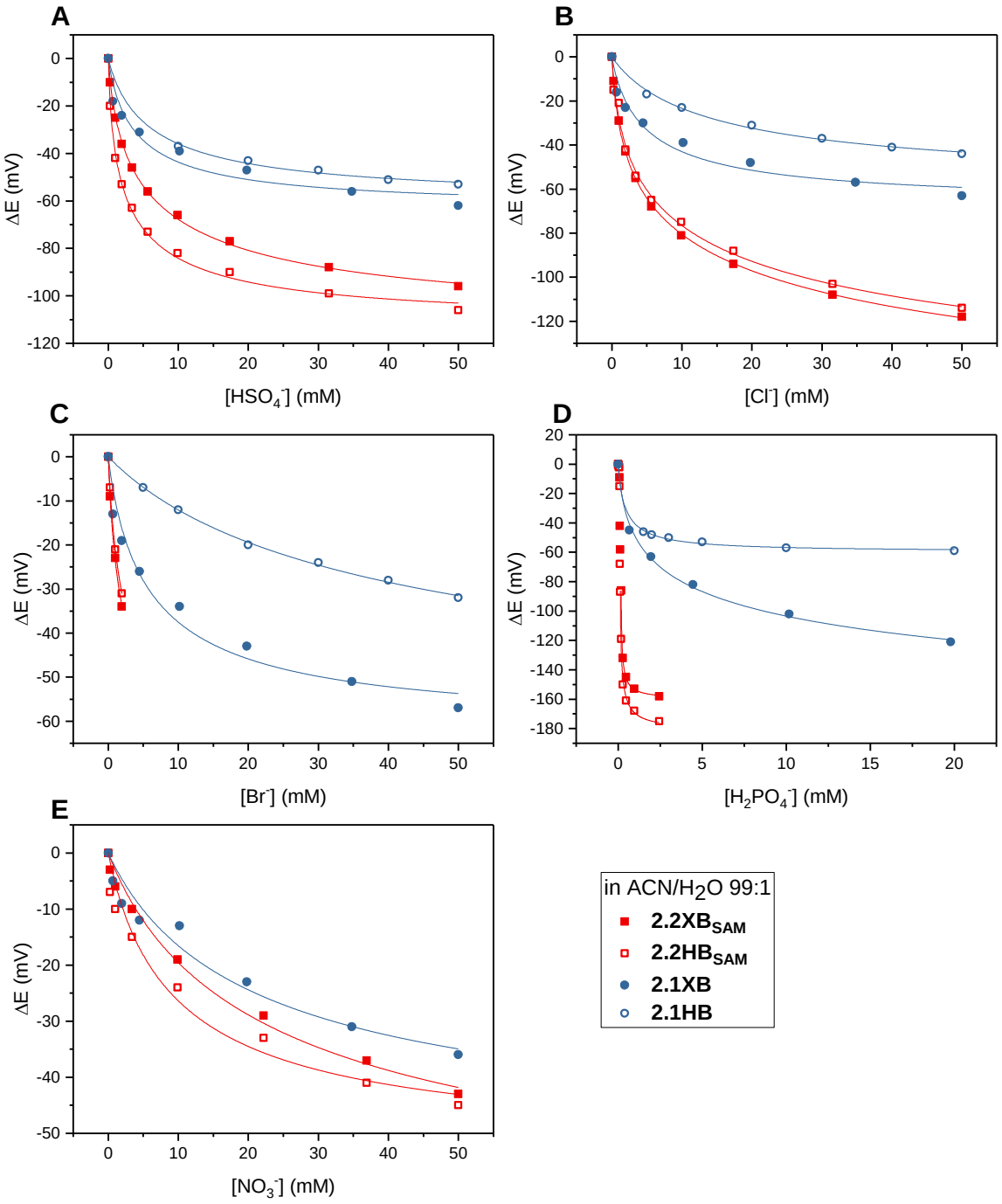


Figure 2.21. Comparison of cathodic voltammetric shifts under diffusive conditions (**2.1XB/HB** (blue circles)) and on the surface (**2.2XB/HB$_{SAM}$** (red squares)) in ACN/H_2O 99:1 (+ 100 µM H^+ for SAM titrations) upon titration with various anions: A) HSO_4^-, B) Cl^-, C) Br^-, D) $H_2PO_4^-$ and E) NO_3^-. Filled symbol represent the XB receptors while empty symbols represent the HB receptors. Solid lines represent fits to the 1:1 host-guest Nernst model (eqn. 2.2). Note the different y-axis scaling for the graphs.

An alternative model is proposed here, that justifies an enhanced BEF (and thus response) physicochemically, without explicit considerations of the magnitude of binding. Specifically, BEF is proposed to be enhanced as a result of diminished charge-screening (*i.e.* a diminished dielectric constant) within the hydrophobic SAMs. Pure alkanethiol SAMs have been shown to possess dielectric constants ε of ≈2–3,[285] and while **2.2XB/HB$_{SAM}$** are certainly of higher polarity than such alkanethiol SAMs, their dielectric constants are significantly smaller than that of the solvent. The ε of pure ACN is 37.5, already quite large; in the additional presence of 1% H_2O, as well as significant quantities of electrolyte, the solvent system employed will thus have an even larger ε. Voltammetrically generated Fc^+ is thus much less screened in the SAM environment than within the bulk solvent which will translate to significantly enhanced anion binding in the cationic state and hence a more significant binding switch-on (Figure 2.22).

As discussed in Section 2.2.3.2.2, the comparatively diminished performance of **2.2XB$_{SAM}$** with respect to its HB analogue **2.2HB$_{SAM}$**, is an unexpected observation considering **2.1XB** clearly outperformed **2.1HB** under diffusive conditions. This screening model can also account for this phenomenon by considering specific binding contributions that govern an enhanced anion binding to the oxidised receptor. Specifically, the oxidation of Fc to Fc^+ is expected to affect anion binding *via* two main pathways: 1) through-space (TS) electrostatic (*i.e.* coulombic) interactions between Fc^+ and the anion, and 2) through-bond (TB) enhancement of the XB/HB donor strength *via* an increased electron-withdrawing effect of the electron-deficient Fc^+.[78,79] Importantly, the contribution of each of these towards the overall binding strength is most likely not the same in a bulk solvent of high dielectric in comparison to the non-polar SAM environment. Specifically, the absolute TB contribution is presumably identical in both cases; bond polarisation strength should only be dependent on

the change in electron-density at the Fc transducer and not/much less on the dielectric of the environment. Importantly, the electron-density at the Fc is similar in solution as well as in the SAM as the half-wave potentials of both **2.2XB$_{SAM}$/2.1XB** and **2.2HB$_{SAM}$/2.1HB** only differ by ≈10 mV, *i.e.* the magnitude of screening of the Fc^+ by the electrolyte is similar in all cases (presumably because the Fc^+ transducer is well exposed to the solution even when-surface confined).

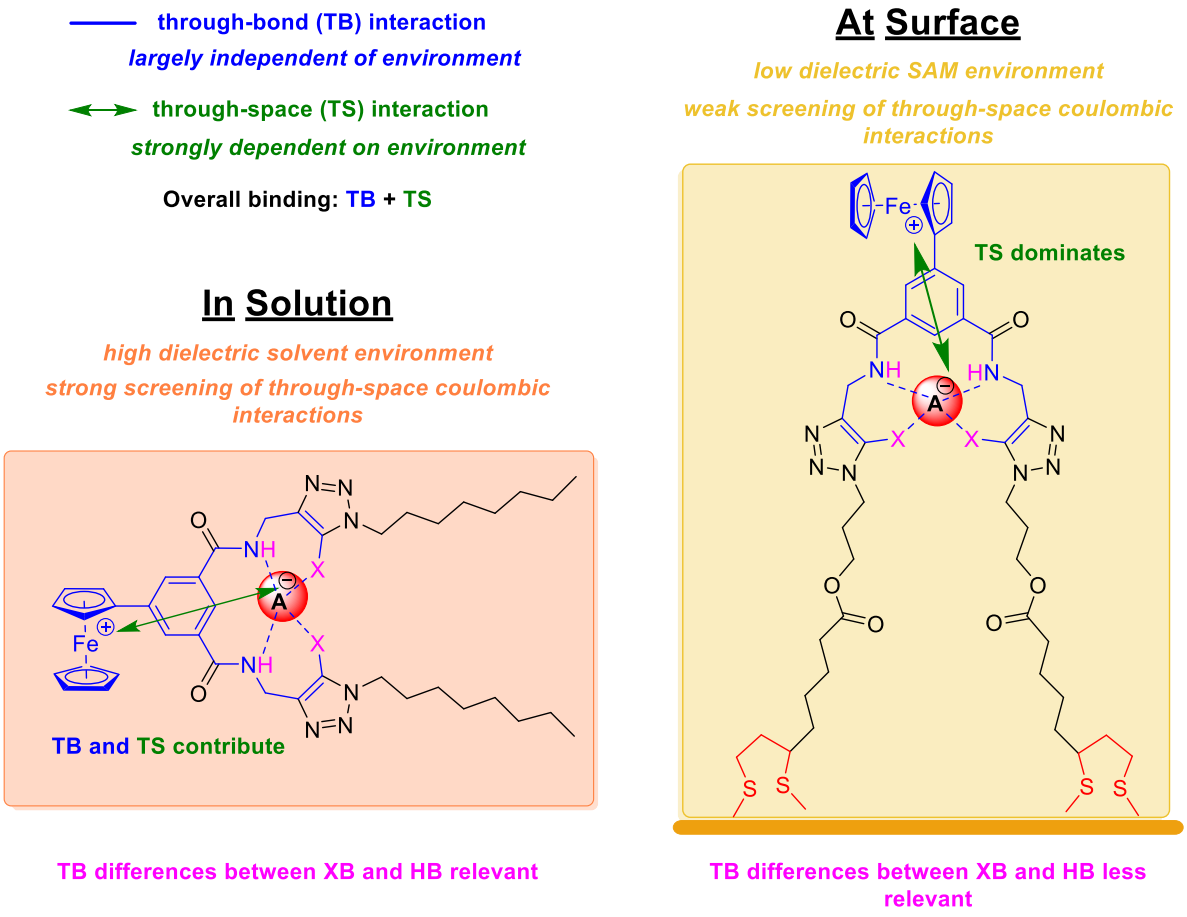


Figure 2.22. Schematic representation of through-bond (TB) and through space (TS) electrostatic interactions that drive anion recognition in the cationic state of **2.1XB/HB** in solution and at **2.2XB/HB$_{SAM}$**. In the more polar solvent environment of high dielectric the TS contribution is diminished and TB contributions, which differ between XB and HB receptors are relevant. In this case differences in the binding switch-on upon oxidation of the receptors can be resolved. In the SAM environment of lower dielectric TS contributions are strongly enhanced while TB effects are expected to be constant. The overall binding in the cationic state is thus switched-on more strongly inducing a larger response of the interfacial sensor. As the overall binding is now dominated by TS coulombic interactions any TB differences between XB and HB are less significant and the response of XB and HB sensors is more similar.

The screening of the TS interaction between the Fc^+ and the anion, which is bound within the film, is however strongly diminished such that the coulombic interaction is significantly enhanced and thus contributes more towards overall binding. Interfacial binding enhancement is thus driven largely by coulombic TS effects which dominate over any TB differences between XB/HB interactions. In contrast, in the bulk solvent coulombic interactions are attenuated such that differences in TB XB/HB anion interactions are more apparent.

As shown in Table 2.12 the BEF on the surface is significantly larger in all cases than in solution (Table 2.4). For example, BEF enhancement upon immobilisation is greatest for Cl^- with ≈50, the most charge-dense anion. This indirectly supports the proposed screening model, where surface response enhancement is largely driven by coulombic contribution to binding, which will be significantly affected the most by charge-dense anions.

Table 2.12. Ratio of BEF, K_{Ox} and K_{Red} of surface bound (**2.2XB/HB$_{SAM}$**) and diffusive receptors (**2.1XB/HB**) in ACN/H_2O 99:1 (+ 100 µM H^+ for measurement on SAMs).

	Ratio Surface/Solution					
	BEF		**K_{Ox}**		**K_{Red}**	
	XB	**HB**	**XB**	**HB**	**XB**	**HB**
Cl^-	56.7	51.1	3.15	9.74	0.06	0.19
Br^-	1.92	1.49	3.13	19.7	1.64	13.25
HSO_4^-	6.85	8.71	1.88	7.79	0.27	0.90
$H_2PO_4^-$	[a]	[a]	[a]	[a]	[a]	[a]
NO_3^-	1.64	/	1.13	/	0.69	/

a – Errors too large for accurate comparison.

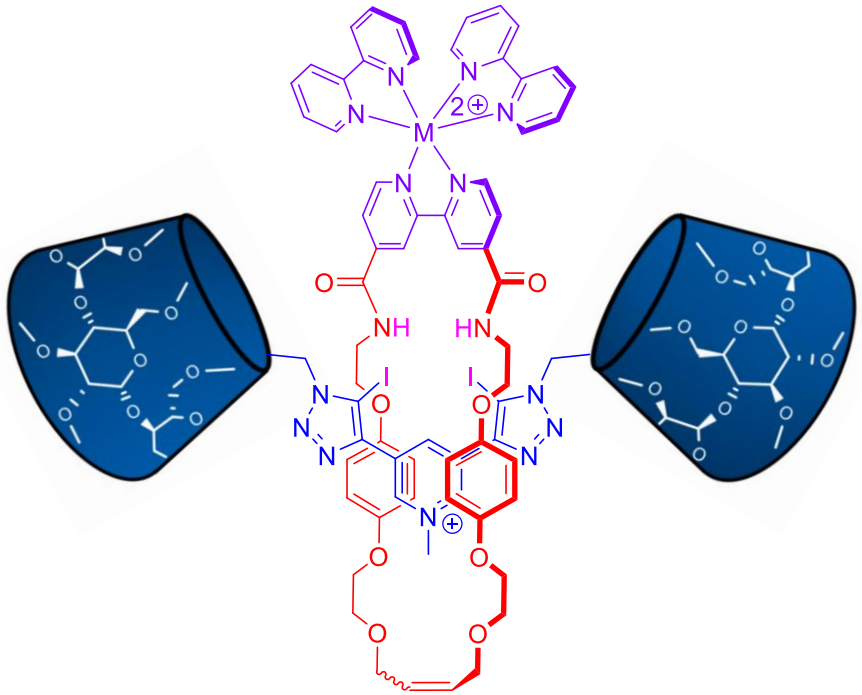
In further support of this dielectric model, the BEF enhancement indeed arises from an increased K_{Ox} at the interface (larger in all cases), while K_{Red} is similar (or even smaller) in comparison to diffusive conditions (Table 2.12). The similar or diminished interfacial anion binding strength in the neutral state also directly contradicts the "standard" models (cooperativity/preorganisation) which would predict enhanced binding in both oxidation states.

Notably, consideration of these screening effects not only provides an in-depth rationalisation for an enhanced interfacial response in voltammetric ion sensors, but can also explain differences in selectivity/response patterns across different XB/HB receptors. These results highlight the attention that needs to be paid to the dielectric properties of the solvent environment and the interface.

2.3 Acyclic Osmium(II) Bipyridyl-Containing Receptors

2.3.1 Previous Work

The sensing of anions in pure water is particularly challenging yet of great interest for most envisioned sensing applications. In working towards this goal two main requirements have to be met: 1) anion binding needs to be strong in order to overcome the significant energetic penalty of anion dehydration and 2) if sensing in solution is envisioned the receptor must be water-soluble. The former is often achieved by the use of highly cationic receptors or more advanced architectures such as mechanically interlocked receptors.[292,293] The latter is usually accomplished by the incorporation of polar, hydrophilic solubilising groups, such as poly(ethylene glycol) or charged functional groups. Recently, halogen bonding has been shown to be a potent driving force for anion recognition in pure water and has been exploited in a range of acyclic,[294,295] foldamer[296] and interlocked receptors.[259,297] Anion sensing in pure water based on XB receptors remains rare and is currently limited to optical sensors.[259,294] For example, the permethylated beta-cyclodextrin-stoppered Ru(II)(bipy)$_3$-containing XB rotaxane **2.5** (Figure 2.23) was used for the sensing of Br^-, I^- and SO_4^{2-}, however in all cases the MLCT emission luminescence response was modest.



2.5: M = Ru(II)

2.6: M = Os(II)

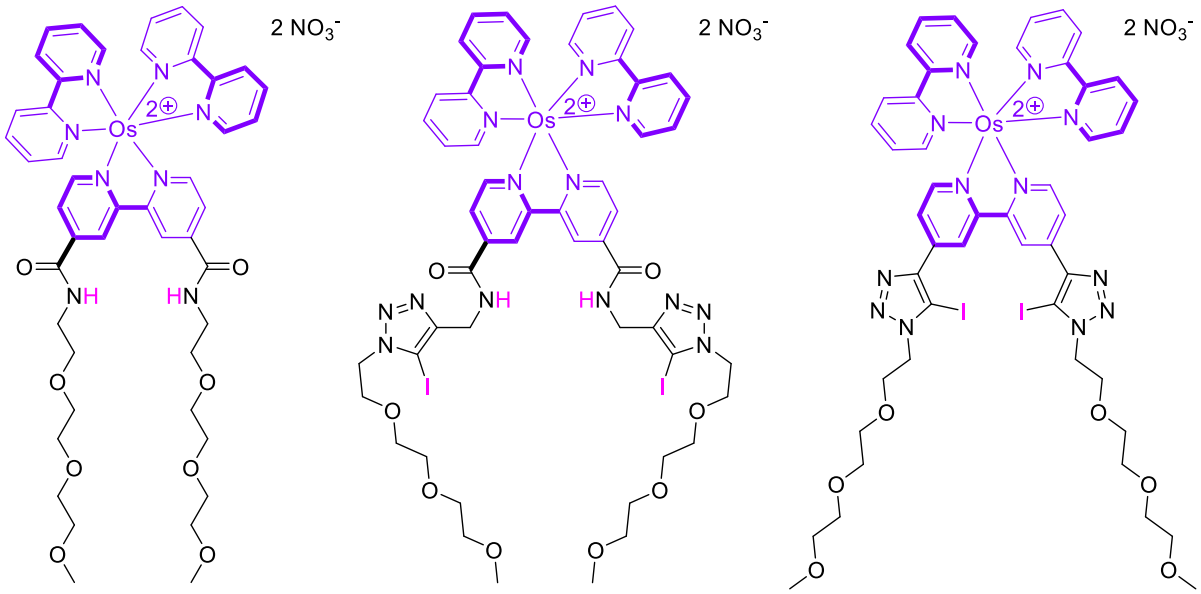
Figure 2.23. Cyclodextrin-stoppered water-soluble XB rotaxanes containing Ru/Os(bipy)$_3$ for luminescent anion sensing.

As highlighted in Section 1.2.2, such metal complexes can also be utilised for the voltammetric sensing of anions, including those based on copper,[149] iron[175] and in particular osmium.[133-137] The latter was also recently incorporated into the above-mentioned rotaxane scaffold to afford **2.6** (Figure 2.23).[298] This receptor proved capable of halide recognition in pure water, however luminescence sensing studies were hampered by strong quenching of the MLCT emission in this medium. This prompted the investigation of its voltammetric behaviour, interestingly revealing a very complex and irreversible redox signature, a behaviour that was briefly alluded to previously in a similar interlocked Os(bipy)$_3$-containing receptor.[137]

Building on this prior work, a range of structurally related, but simpler, acyclic Os(II)(bipy)$_3$ anion receptors were designed in collaboration with Thanthapatra Bunchuay, who synthesised the novel receptors **2.7** and **2.8** (Figure 2.24).[298]

2.3.2 Receptor Design and Synthesis

These receptors contain the same Os(II)(bipy)$_3$ transducer and bis-amide anion binding site as the macrocycle in **2.5** and **2.6**. Tri(ethylene glycol) groups were introduced to endow high (water) solubility and receptor **2.8** was also equipped with additional iodotriazole binding sites. The arrangement of the HB and XB donors in **2.8** is identical to that of **2.1XB** with the notable difference that both amide-iodotriazole binding arms are spaced further apart in **2.8**, thereby alleviating steric constraints, especially for the binding of larger anions.



2.7 **2.8** **2.9**

not synthetically accessible

Figure 2.24. Chemical structures of novel Osmium-containing acyclic anion receptors.

We also envisioned the synthesis of the related **2.9** where the (iodo)triazole binding sites are directly tethered to the Os(bipy)-transducer, however this endeavour was unsuccessful as metallation of the free bipy ligand with Os(II) proved impossible, presumably as a result of its low electron-density and thus poor coordinating ability.

Both **2.7** and **2.8** were isolated as nitrate salts, as this counter anion is not expected to bind to the receptor while endowing good solubility, especially in aqueous media. Binding and sensing studies of both receptors were carried out by MLCT luminescence titrations. As found with rotaxane host **2.6,** in water quenching of the MLCT emission band was observed for both **2.7** and **2.8**, prompting further luminescence binding studies in pure ACN. Addition of I^- did not induce any response for either receptor while Cl^-, Br^- and SO_4^{2-} induced notable MLCT emission enhancements as well as small hypsochromic shifts (Figure 2.25).

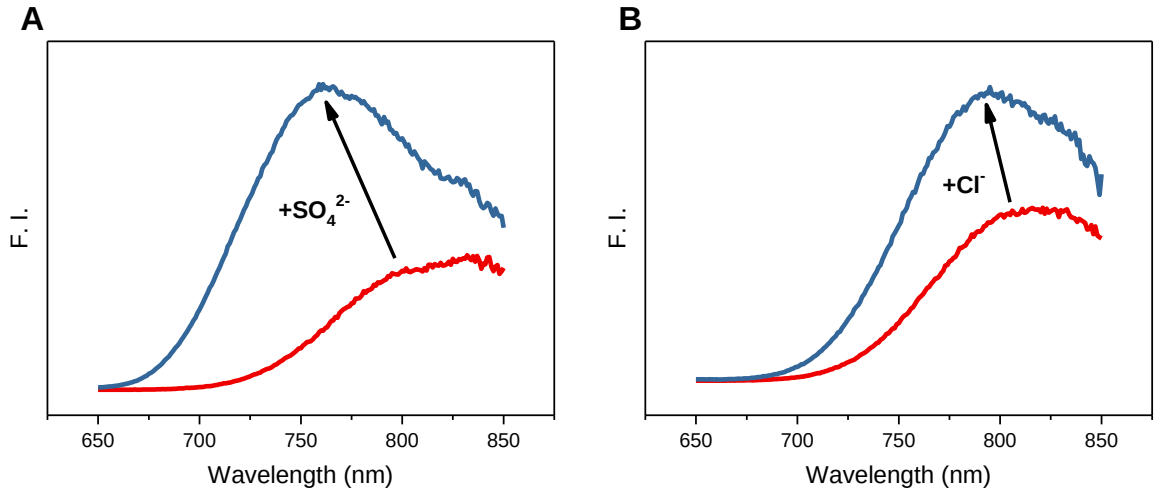


Figure 2.25. Fluorescence emission spectra of 50 µM **2.8** in ACN upon addition of 50 equiv. SO_4^{2-} (A) or Cl^- (B).

The magnitude of this enhanced intensity followed the same trend for both receptors with SO_4^{2-} > Cl^- > Br^- (at saturation), where the response towards SO_4^{2-} was significantly larger than that of the other anions with an increase of 152% and 213% for both **2.7** and **2.8**,

respectively (Table A2.1).[298] An increased response of **2.8** in comparison to **2.7** was also observed for the two halides, highlighting the incorporation of additional XB iodotriazole binding sites is beneficial to anion sensing/binding.

2.3.3 Electrochemical Properties of 2.7 and 2.8

The electrochemical behaviour of both receptors was first investigated in ACN. Under anhydrous and oxygen-free conditions four redox couples were observed for both receptors as shown in Figure 2.26 and Figure 2.28.

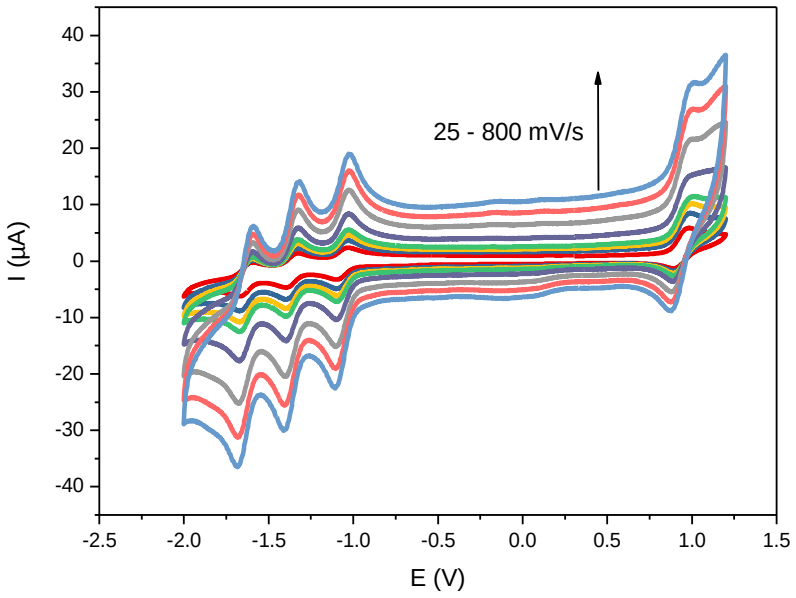


Figure 2.26. CVs of 0.3 mM **2.7** in dry, degassed ACN, 100 mM $TBAPF_6$ at varying scan rates. Potentials are reported with respect to the Ag|AgCl reference electrode.

The redox process at high potential can be ascribed to the metal-centred $Os^{2+/3+}$ couple while the three couples at low potential correspond to the stepwise one-electron reduction of each of the bipy ligands.[137] The most anodic of these can be assigned to the receptive

bipy ligand as it is rendered most electron-deficient and thus prone to reduction as a result of the electron-withdrawing amide(-triazole) functional groups. Reversibility studies for **2.7** revealed quasi-reversible redox couples with the ratio of anodic and cathodic peak currents i_{pa}/i_{pc} close to unity as well as excellent linear dependence of peak currents on the square-root of the scan rate for all couples (Figure 2.27).

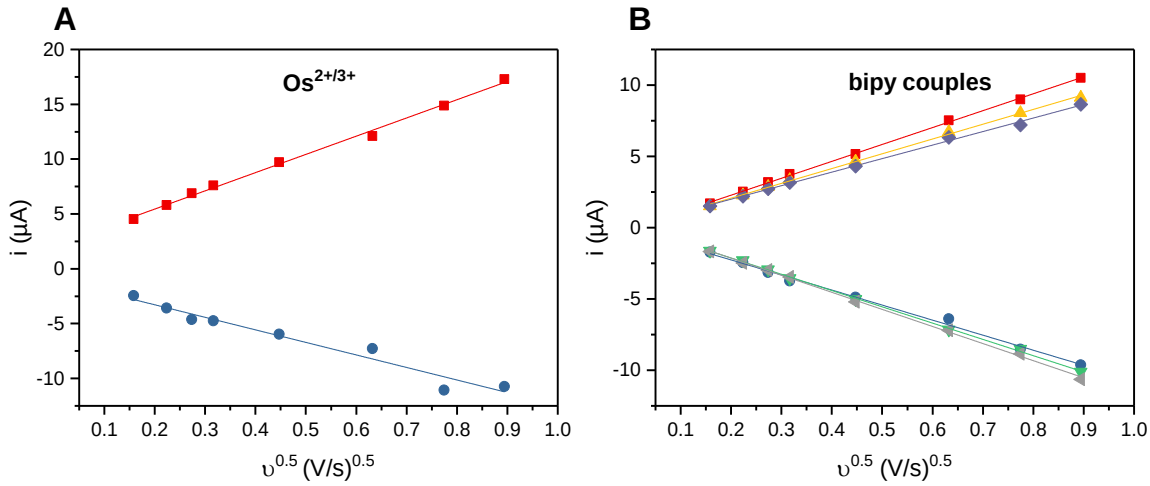


Figure 2.27. Anodic and cathodic peak currents of 0.3 mM **2.7** in dry, degassed ACN, 100 mM $TBAPF_6$ at varying scan rates of $Os^{2+/3+}$ (A) and bipy couples (B).

The behaviour of **2.8** was somewhat less ideal (Figure 2.28A). Specifically, the bipy couples are slightly less well-resolved and an additional redox couple around 0.3 V is observed, in particular at high scan rates. This additional couple was also resolved by SWV as shown in Figure 2.28B. It is not clear which redox process is responsible for this additional wave, but as this behaviour was observed for two independently prepared samples it is unlikely to arise from an impurity. This couple may instead arise as a result of receptor degradation *via* an EC mechanism induced by the presence of the iodotriazole groups.

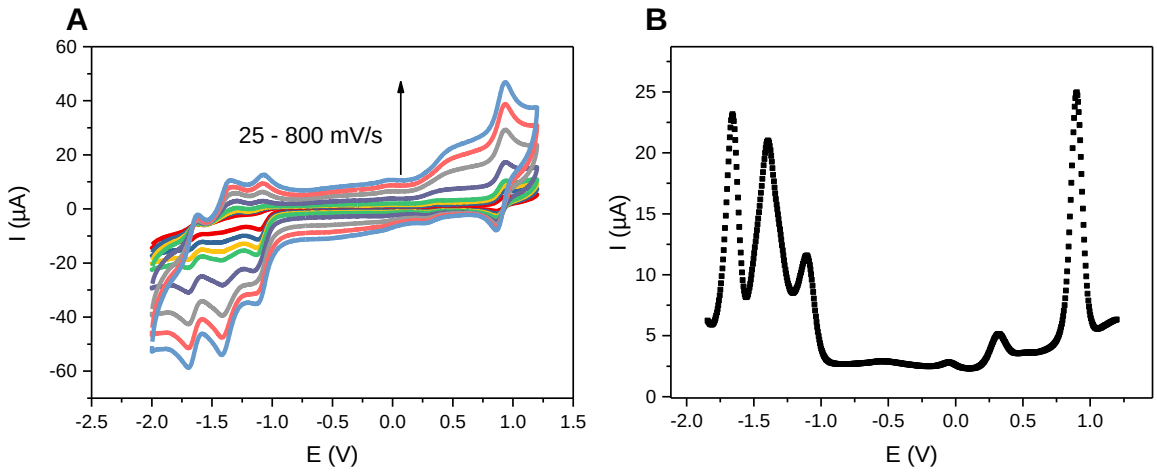


Figure 2.28. A) CVs at varying scan rates and B) SWV of 0.3 mM **2.8** in dry, degassed ACN, 100 mM $TBAPF_6$.

The voltammetric behaviour of both receptors was also studied in MeOH (containing 50 mM $TBAPF_6$ as electrolyte; lower concentration for solubility reasons) and water (containing 100 mM $NaNO_3$ as electrolyte). In these protic solvents voltammetric analysis is restricted to the $Os^{2+/3+}$ couple as the bipy couples are not accessible because of solvent reduction significantly overlapping with these cathodic waves. As can be seen in Figures A2.19–A2.22 the $Os^{2+/3+}$ couple is well resolved and displays a high reversibility in all cases. Only for **2.8** in MeOH are slight distortions observed in the CVs. The half-wave potentials of all couples in the three solvents are displayed in Table 2.13. In all cases the $E_{1/2}$ of the $Os^{2+/3+}$ couple (and also for almost all bipy couples) is ≈10 mV more anodic for **2.8** than **2.7**, in good agreement with observations for **2.1XB/HB**, attributable to the electron-withdrawing nature of the iodo-triazole moiety.

Table 2.13. $E_{1/2}$ (V) of **2.7** and **2.8** in various solvent systems as determined by SWV. Unless otherwise noted all potentials are reported *vs.* Ag|AgCl. $TBAPF_6$ was used as electrolyte in ACN (100 mM) and MeOH (50 mM). 100 mM $NaNO_3$ were used as electrolyte in H_2O. n.a. – Not accessible.

	OsAmidePEG		**OsTzPEG**	
	$Os^{2+/3+}$	**Bipy couples**	**$Os^{2+/3+}$**	**Bipy couples**
ACN	0.919 0.523[a]	− 1.652, −1.380, −1.080 −2.048[a], −1.776[a], −1.476[a]	0.927 0.531[a]	−1.630, −1.367, −1.080 −2.026[a], −1.763[a], −1.476[a]
MeOH	0.927	n.a.	0.941	n.a.
H_2O	0.758	n.a.	0.767	n.a.

a – *vs.* $Fc|Fc^+$ as internal reference.

As expected, the $Os^{2+/3+}$ oxidation occurs at a significantly less anodic potential in water, undoubtedly as a result of the significantly better electrostatic stabilisation of the highly cationic redox transducer by this polar solvent. This effect would also be expected for MeOH over ACN, however this is not observed as the half-wave potentials in MeOH are actually slightly higher than in ACN. This is most likely a consequence of the lower electrolyte concentration of 50 mM $TBAPF_6$ in MeOH in comparison to 100 mM $TBAPF_6$ in ACN.

2.3.4 Voltammetric Anion Binding Studies

As highlighted above, the $Os^{2+/3+}$ redox couple of both receptors is well resolved in all solvents and was utilised as the transducer for anion binding studies. The bipy couples are also responsive to anion binding, as noted previously.[137] However they can only be used for sensing in dry, deoxygenated solvents. Furthermore, they are binding switch-off transducers as reduction deactivates anion binding with respect to the native receptor. In contrast,

$Os^{2+/3+}$ is a switch-on transducer, akin to Fc, albeit with a significantly higher half-wave potential. This unfortunately precludes the study of multiple anions that are electroactive at these high potentials, including Br^- (as well as I^-, which can also not be investigated with Fc transducers). Voltammetric anion sensing studies were thus carried out with Cl^-, ReO_4^- as well as the divalent SO_4^{2-} and oxalate $(CO_2)^{2-}$. The latter anions were chosen as SO_4^{2-} elicited the largest response in luminescence studies as discussed in Section 2.3.1.

Quantitative voltammetric titrations with these four anions were undertaken at constant ionic strength in the competitive solvent mixture of ACN/H_2O 9:1 (containing 100 mM $TBAPF_6$). As can be seen in Figure 2.29, titration of both receptors with monovalent anions induces only small cathodic shifts, while addition of the divalent anions induces large voltammetric shifts of up to −100 mV.

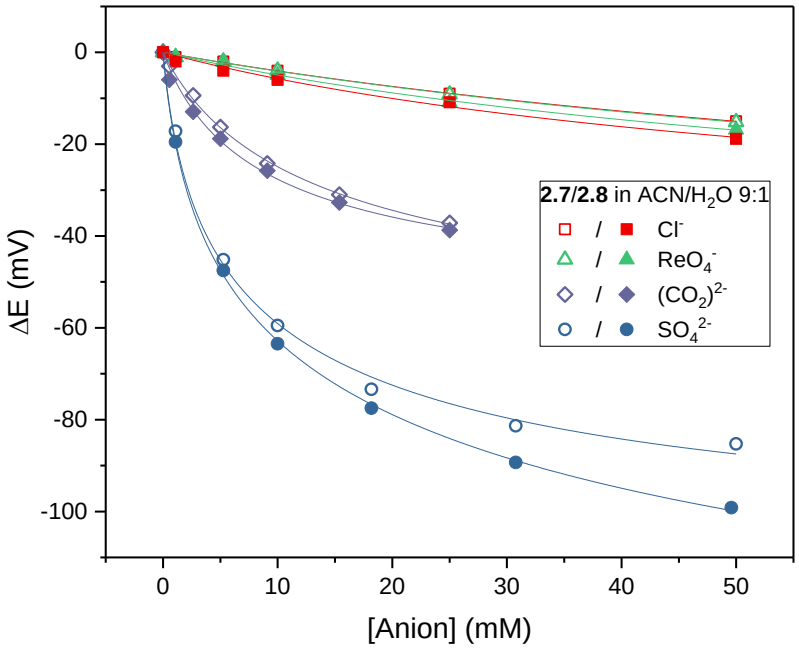


Figure 2.29. Shift of half-wave potential of $Os^{2+/3+}$ redox couple of **2.7** (empty symbols) and **2.8** (filled symbols) in the presence of various anions in ACN/H_2O 9:1. Isotherms were fitted according to eqn. 2.2.

In all cases **2.8** displays a larger magnitude of response in comparison to **2.7,** albeit the difference is modest, especially for the monovalent anions. Additionally, the response towards both Cl^- and ReO_4^- is largely identical, even though both anions would be expected to bind differently to both receptors. The response towards the divalent anions is more distinctive, especially for SO_4^{2-}. This observation suggests the additional iodotriazole groups in **2.8** play a significant role in the binding of this anion. These results also confirm that the response of these sensors is at least partially dictated by anion binding at the engineered XB/HB binding sites and not purely driven electrostatically.

Quantitative analysis of the binding isotherms according to eqn. 2.2 was again carried out to gain further insights into the response/binding phenomena. In all cases excellent fits were obtained, revealing negligible binding of all anions to **2.7** in the native state (K_{Red} < 19 M^{-1}; Table 2.14). K_{Red} for **2.8** was slightly larger in most cases, however an accurate comparison of these near-zero values is meaningless, especially since the (absolute) fitting errors of K_{Red} are comparatively large (see Section 7.4). Anion binding strength in the oxidised state was larger for **2.8** in comparison to **2.7** for all anions with the largest value of K_{Ox} = 1089 M^{-1} for SO_4^{2-}, indicating that the XB iodotriazole groups, as expected, enhance anion binding strength.

While the magnitude of the BEF correlated very well with the response of **2.1XB/HB** and **2.2XB/HB$_{SAM}$,** as discussed in Section 2.2, this is not the case here. Both receptors show the largest BEF and response towards SO_4^{2-}, however, there are no clear trends that otherwise correlate with the response towards the other anions. This is herein most likely a reflection of the large errors of the BEF, as the values of K_{Red} are close to zero and even small absolute errors of K_{Red} induce large errors in the ratio of K_{Ox}/K_{Red} (BEF). Nevertheless, it is

apparent that the BEF and response of both receptors to SO_4^{2-} is significant and also larger than the response of **2.1XB/HB** towards most anions. This is even more impressive considering that **2.7** and **2.8** were investigated in a much more competitive organic/aqueous solvent system with a water content that is 10x higher than that employed for studies of **2.1XB/HB**. However, a direct comparison of the performance is difficult as different anions were used in both studies. As stated in Section 1.1.2, some of the anions tested (most notably HSO_4^-/SO_4^{2-} and $H_2PO_4^-$) will, depending on pH, dissociate into multiple coexisting species of different charge. Theoretically, titrations with either HSO_4^- or SO_4^{2-} should afford similar results as both will form the same species in solution. Hence, the response of **2.7/2.8** and **2.1XB/HB** towards sulfate can be compared, with the caveat that altered electrolyte compositions might influence the (de)protonation equilibria somewhat.

Table 2.14. Binding constants K_{Ox}/K_{Red} (M^{-1}) and BEF of **2.7** and **2.8** from fitting of binding titrations with various anions in ACN/H_2O 9:1 according to eqn. 2.2.

	2.7			**2.8**		
	K_{Ox}	**K_{Red}**	**BEF[a]**	**K_{Ox}**	**K_{Red}**	**BEF**
Cl^-	19	2	10.5	25	3	7.4
ReO_4^-	19	2	11.5	31	5	6.4
$(CO_2)^{2-}$	216	19	11.1	303	37	8.2
SO_4^{2-}	1058	15	69.7	1089	2	454

a – Calculated from unrounded values of K_{Ox} and K_{Red}, errors large where K_{Red} ≈0.

The sensing capabilities of **2.8** towards sulfate were further investigated in more competitive solvent systems, where even in ACN/H_2O 4:1 and ACN/H_2O 7:3 pronounced voltammetric shifts arise (Figure 2.30).

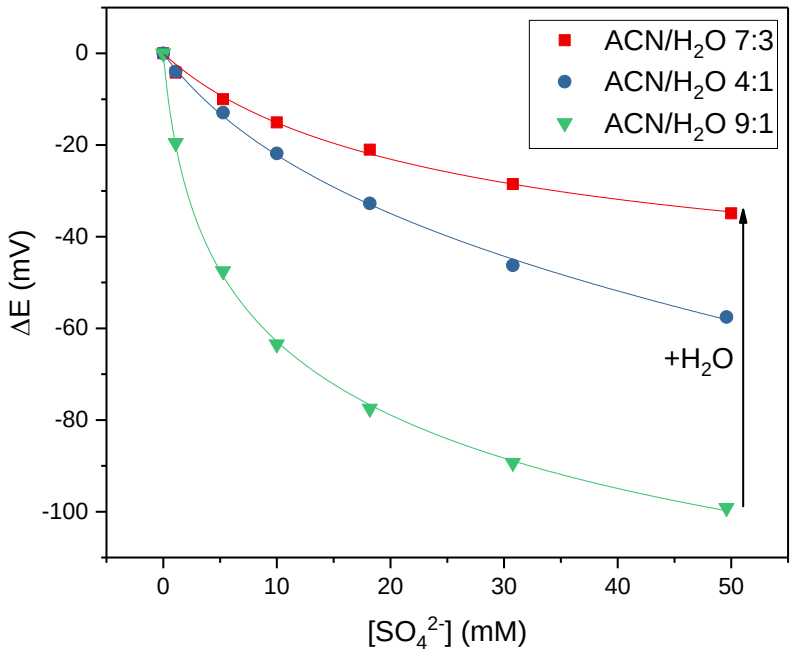


Figure 2.30. Shift of half-wave potential of $Os^{2+/3+}$ redox couple of **2.8** as a function of SO_4^{2-} concentration in ACN/H_2O 9:1, ACN/H_2O 4:1 and ACN/H_2O 7:3. Isotherms were fitted according to eqn. 2.2.

As can be seen in Table 2.15, the diminished response in the more competitive media arises from significantly weaker binding of SO_4^{2-} by the oxidised receptor where in ACN/H_2O 4:1 K_{Ox} drops by almost a factor of 10 to 126 M^{-1} and further to 101 M^{-1} in ACN/H_2O 7:3. It is of course expected that a relatively smaller K_{Ox} value in the more competitive solvent medium is the cause of the lower response as K_{Red} is already negligible in the least competitive solvent and cannot decrease further.

Table 2.15. Binding constants K_{Ox}/K_{Red} (M^{-1}) of sulfate to **2.8** from fitting of binding titrations in various ACN/H_2O mixtures according to eqn. 2.2.

	K_{Ox}	K_{Red}
ACN/H_2O 9:1	1089	4
ACN/H_2O 4:1	126	-5[a]
ACN/H_2O 7:3	101	11

a – See Section 7.4 for clarification.

As expected in highly competitive solvents MeOH and pure water, no response towards various anions was observed. However, these results present an important step towards the development of voltammetric anion sensors that can operate in pure water and highlight the potency of XB interactions in achieving this goal.

2.4 Conclusions and Future Work

2.4.1 Conclusions

Detailed anion binding studies of novel XB and HB ferrocene-isophthalamide-triazole receptors were carried out by ^{1}H NMR and electrochemical experiments. Interestingly, the native, neutral HB receptor largely outperformed the analogous XB receptor in terms of anion binding strength as assessed by ^{1}H NMR titrations. However, in a diffusive voltammetric format the XB system displayed larger cathodic responses for all anions. This can be attributed to an enhanced binding switch-on upon oxidation of the XB receptor as quantified by fitting of the electrochemical binding isotherms. The surface-immobilisation of these receptors *via* formation of well-defined SAMs enabled anion sensing with a significantly enhanced response in all cases and interesting selectivity patterns where the response for halides is larger at the XB films while oxoanions are more sensitively detected at HB SAMs. Detailed analysis of the binding isotherms afforded unprecedented insights into the transduction principles that govern an enhanced interfacial response to anions. Specifically, it is proposed that the commonly invoked cooperativity or preorganisation arguments fail to explain a greater anion binding enhancement upon oxidation which ultimately determines the magnitude of the response. Rather, a new model based on dielectric considerations was proposed where the improved interfacial sensory performance

can be rationalised by the less polar film environment in which anion binding enhancement upon oxidation is more pronounced as a result of stronger electrostatic interactions.

This work not only provides the first detailed comparison of redox-active XB and HB anion receptors in diffusive and interfacial formats but also pioneers the use of quantitative Nernst binding isotherm analysis of surface-confined voltammetric anion sensors. Furthermore, the influence of electrolyte acidity on the voltammetric stability and anion sensing performance of anion receptive redox-active films was investigated for the first time. Specifically, the addition of even small amounts of acid can significantly improve the redox reversibility of the surface-bound receptors, a crucial requirement for any envisioned real-life sensor and potentially enabling the utilisation of other electrochemical methodologies (see Section 2.4.2.2). In addition, altering the electrolyte acidity has been shown to affect the sensory response, as a result of acid-base equilibria, which can potentially enable the tuning of the sensors' selectivity.

In addition, the rarely utilised Os(II)$(bipy)_3$ luminescent redox transducer was incorporated into two novel amide and amide-iodotriazole acyclic anion receptors and studied in a variety of solvents. The doubly cationic motif enabled sensing of SO_4^{2-} in ACN/H_2O mixtures containing up to 30% water and highlights the potential of this transducer in protic polar solvents, in particular if combined with the potent XB iodotriazole motif.

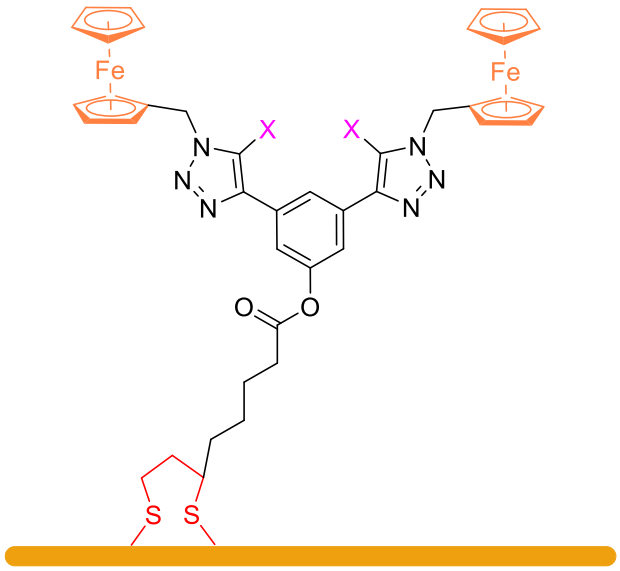
2.4.2 Future work

2.4.2.1 Further Exploration of Signal Transduction Principles at Redox-Active Interfaces

A more detailed investigation of anion receptive interfaces can further improve our understanding of their underlying working principles. As discussed above, the origin of an

enhanced voltammetric sensing performance is poorly understood. A novel dielectric model was proposed that can account for an enhanced interfacial performance based on principles of diminished electrostatic screening within films of lower dielectric than the bulk solvent environment. In order to further validate this model, detailed comparative voltammetric anion sensing studies should be carried out in which the respective solvent and film environments are systematically altered. This can be achieved in two ways: 1) investigation of a range of different solvents (*e.g.* aqueous/organic mixtures of different composition) thereby allowing a systematic modulation of the solvent while the film environment is largely unaltered; 2) the modulation of the film environment by, for example, formation of mixed SAMs containing receptors as well as other components that can modulate the dielectric properties of the film (*e.g.* the use of perfluoroalkane thiols to further diminish ε of the film).

To address some of these challenges the anion sensory properties of XB/HB SAMs containing two Fc appendages (**2.10XB/HB$_{SAM}$**, Figure 2.31) are currently being investigated in a wide range of aqueous/organic solvent systems. This design allows for an additional modulation of anion binding by generation of a dicationic receptor upon oxidation. Also the close proximity between the XB/HB triazole binding site and the Fc transducers is expected to enable an efficient binding switch-on and thus signal transduction.



2.10XB/HB$_{SAM}$ (X = I/H)

Figure 2.31. Schematic representation of **2.10XB/HB$_{SAM}$** for further voltammetric anion sensing studies.

2.4.2.2 Redox Capacitive Anion Sensing

As highlighted in Section 2.2.3.2, a high voltammetric stability of redox-active ion receptive interfaces is not only relevant for continuous or repeat sensor operation but can enable the sensing *via* other methodologies. One of those is redox capacitive sensing, an impedance-based technique that utilises a capacitance arising from a surface-immobilised redox transducer to report on interfacial events, most commonly binding of large biomolecules.[299,300] The principles of this methodology will not be discussed in detail here, but many considerations are similar to other impedance-based methodologies as discussed in Section 1.2.3 and Chapter 3. Specifically, redox-capacitive sensors have been shown to be highly sensitive and can operate without the use of any solution-phase redox amplifiers.[301,302] In spite of these advantages the redox capacitive sensing of ions is significantly underdeveloped; it has been preliminarily investigated for the sensing of cations at crown ether films,[303] but the redox capacitive detection of anions is unprecedented.

A crucial requirement in redox capacitive sensors is the baseline stability, which is inherently related to the voltammetric stability of the redox-active film as the redox capacitance C_r at a given potential is directly proportional to the number of redox states at that potential.[304] As demonstrated above, in the presence of acid the baseline instabilities of **2.2XB/HB$_{SAM}$** are largely supressed prompting the preliminary investigation of their potential as redox capacitive anion sensors.

The same electrolyte system as described above (ACN/H_2O 99:1) containing 10 mM H^+ was utilised for these initial studies. Specifically, the redox capacitance C_r as a function of potential was determined (representing the redox density of states) as described in the Experimental Section (Section 7.2.4). This affords plots as depicted in Figure 2.32A, where the redox capacitance is, as expected, dependent on the voltammetric signature of the film. Specifically, the largest C_r is obtained at the half-wave potential and the peak shape is almost identical to that obtained by SWV. Hence, this capacitive methodology affords plots that contain the same voltammetric information content as SWV/DPV (*i.e.* they accurately report on the $E_{1/2}$ of the system) while additionally reporting on the (redox) capacitive signatures of the interface, thus enabling the simultaneous study of voltammetric and redox capacitive changes to anion binding. The latter is expected to be dependent on anion binding by an overall shift of the redox density of states distribution to a lower potential (analogous to a voltammetric shift as resolved by SWV), with no significant changes to the height of the distribution (*i.e.* no changes to the maximum C_r). As can be seen in Figure 2.32A, a shift in the peak potential is observed, which exactly mirrors that obtained by standard voltammetric analysis. There is still some notable loss in signal (*i.e.* decrease of C_r), however this baseline drift can be corrected for.

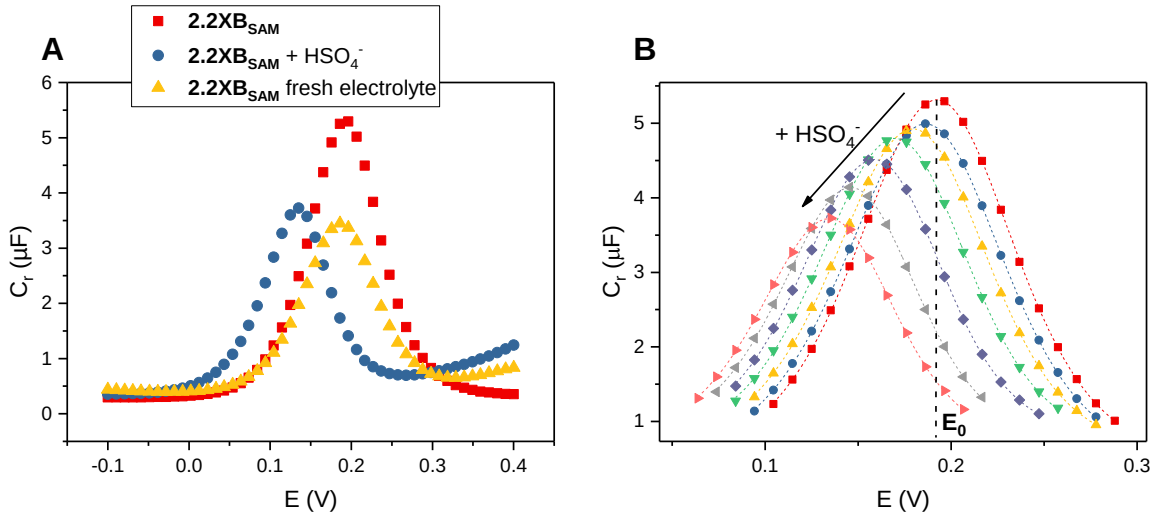


Figure 2.32. Redox capacitive response of **2.2XB$_{SAM}$** towards HSO_4^- in ACN/H_2O 99:1, containing 10 mM H^+. A) Redox capacitive signature of the interface after exposure to HSO_4^- and washing + reimmersion into the original electrolyte as tracked by a redox density of states analysis (capacitance measurement as a function of potential at one frequency). B) The same measurement as in A) at multiple HSO_4^- concentrations. The dotted lines represent fits to an asymmetric double sigmoidal peak function utilised for baseline correction and the accurate determination of peak potentials. The black dotted line represents the initial peak potential of the sensor at which C_r was tracked as a function of anion concentration (see Figure 2.33).

From these drift-corrected distributions the change of C_r at the initial peak potential ($E_{0,}$ in the absence of anion; black dashed line in Figure 2.32B) as a function of anion concentration can be obtained as shown in Figure 2.33.

As expected, this response is characterised by a decrease in C_r at the initial potential because the redox density of states distribution shifts to more cathodic potentials and thus C_r at the initial potential now lies within the tail of the distribution and is smaller. Importantly, the response of this parameter matches the response of the standard voltammetric analysis very well, indicating that anion binding can indeed be followed by this analysis. This is of interest for two main reasons: 1) The sensitivity of this redox capacitive signal might be larger than that of the half-wave potential. This is difficult to assess without further studies as ΔE and ΔC_r cannot be directly compared (the former can only be

expressed as an absolute response while the latter would usually be expressed as a relative response). 2) This capacitive analysis can theoretically be carried out at (any) fixed potential in a one-frequency EIS measurement.

This would most likely allow for very rapid measurements under flow, reporting on kinetic parameters of anion binding at interfaces. Furthermore, it could allow for the investigation of anion binding at equilibrium at a chosen potential where anion binding might be tuneable *via* specific surface polarisation.

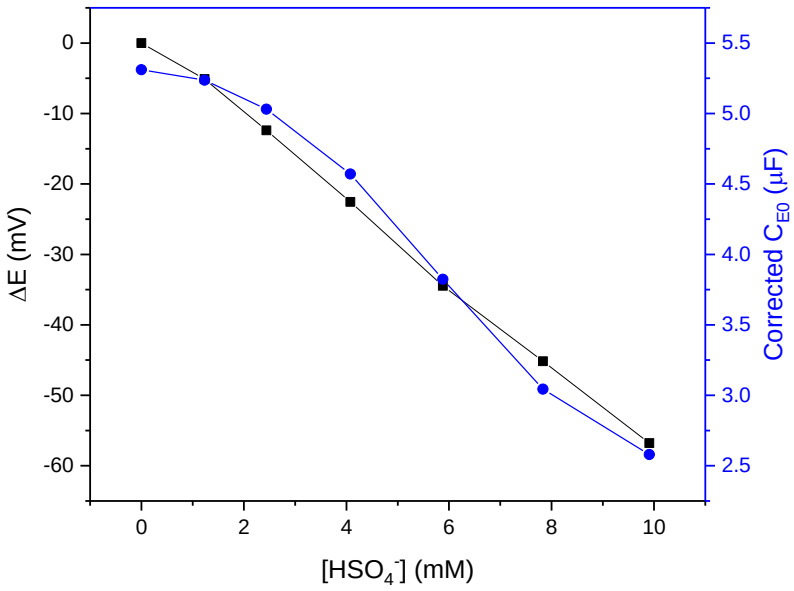


Figure 2.33. Response of **2.2XB$_{SAM}$** towards HSO_4^- in ACN/H_2O 99:1, containing 10 mM H^+ as assessed by standard voltammetric analysis (SWV; black squares) or redox capacitive analysis (blue circles). The redox capacitance was tracked at the initial $E_{1/2}$ of the SAM and was baseline corrected for drifts induced by voltammetric degradation.

Chapter 3

Non-Faradaic Capacitive Anion Sensing at Foldamer SAMs

Chapter 3: Non-Faradaic Capacitive Anion Sensing at Foldamer SAMs

3.1 Introduction and Chapter Aims

Electrochemical impedance spectroscopy (EIS) is a particularly powerful electroanalytical technique to study interfacial properties and events thereat, including, binding/adsorption phenomena as well as (redox) reactions. In applying an AC perturbation of small amplitude (at a fixed bias potential and over a wide range of AC frequencies) a number of interfacial parameters (*e.g.* resistance and capacitance) can be obtained. Importantly, these minor perturbations allow for the study of systems at equilibrium. In addition to providing a high information density, EIS is particularly sensitive (to interfacial changes), and this has been exploited in numerous sensory applications, most notably with a large range of biosensors.[233,305] In its most common format, a change in the charge-transfer resistance (R_{ct}) between a (receptor-modified) electrode and a solution-phase redox probe is utilised to transduce a specific binding event (Faradaic EIS). For example, the R_{ct} of an antibody-modified interface will typically increase when an antigen binds. This is, primarily, the result of the increased crowding of the interface upon binding of the (large) target biomolecule, sterically hampering electron transfer from the solution-phase redox probe to the electrode. The R_{ct} can also be modulated by electrostatic interactions; the typically used redox probes $[Ru(NH_3)_6]^{2+/3+}$ and $[Fe(CN)_6]^{3-/4-}$ are highly charged and will, if a charge is introduced onto the interface, be either repelled or attracted, leading to an increase or decrease of the R_{ct}, respectively. This has also been utilised for the impedimetric detection of cations at, for example, crown-ether modified electrodes.[235,306,307] The analogous

detection of anions is much less developed, as discussed Section 1.2.3). This is somewhat surprising considering that promising initial work was reported by Echegoyen´s group in 2005/2006.[238,239] Since then only a small number of impedimetric anion sensors based on receptive interfaces have been reported.[240-242] This can mainly be attributed to the need for a redox probe which imposes multiple restrictions on sensor design and performance: Specifically:

1) Faradaic EIS is almost exclusively performed in aqueous electrolyte media due to lack of suitable (charged) redox probes compatible with organic solvents (poor solubility and/or unfavourable charge-transfer characteristics). This requires the synthesis of anion receptors that not only contain anchor groups for surface-immobilisation, but that are also capable of anion recognition in pure water.
2) The DC bias potential during the measurement is fixed to the half-wave potential of the redox probe prohibiting detection of anions that are electroactive close to these potentials.
3) Interactions of the redox probe with the interface might lead to baseline instabilities and/or compete with binding.

The omission of a redox probe can potentially circumvent these disadvantages and enable sensitive ion sensing in the absence of any redox transducer. This has been preliminarily investigated for the sensing of alkali metal cations at crown-ether modified electrodes.[236,237] Specifically, the increase in the interfacial capacitance upon cation binding has been utilised as a signal transducer, whereby the change in capacitance was attributed to an increased dielectric constant of the film. In spite of these promising reports, a detailed analysis of the

capacitive methodology as well as its application for the sensing of anions is hitherto unprecedented. The aim of this thesis chapter is to investigate the feasibility of impedance-based capacitance spectroscopy for the sensing of anions at a designed foldamer molecular film and the in depth characterisation of its sensing properties.

For the design of the receptive film the following criteria were considered:

1) The receptor should be capable of binding anions in pure water.
2) A soluble solution-phase analogue of the receptor should be available to compare solution-phase and interfacial binding properties.
3) The immobilisation of the receptor should be facile and yield molecularly well-defined films.

3.2 Molecular Design and Synthesis

Based on the criteria outlined above, the halogen and hydrogen bonding receptors **3.1XB/HB** were designed based on a recently developed tetra(iodo)triazole foldamer scaffold (Figure 3.1).[296,308]

Foldamers, acyclic oligomers that can fold into specific, well-defined conformations, such as helices, have recently gained attention as anion receptors.[296,308,309] More flexible than macrocyclic receptors, they can adopt conformations that are highly conducive to anion binding where favourable interactions between the foldamer subunits compensate for entropic losses upon these conformational changes. Borissov *et al.* recently developed a range of neutral tetra(iodo)triazole foldamers as potent XB and HB receptors for a variety of

anions in organic solvent ($CHCl_3$/acetone 1:1).[308] This design was improved upon by the integration of additional amide-PEG groups which not only endow water solubility but also preorganise the (iodo)triazole groups (**3.2XB/HB**, Figure 3.1). Specifically, the amide-PEG appendages prevent rotation around the triazole-benzene bonds such that the XB/HB donors are forced to converge. This is assisted by hydrophobic interactions; the aromatics fold onto each other forming a hydrophobic core while the peripheral PEG groups are exposed to the solution.

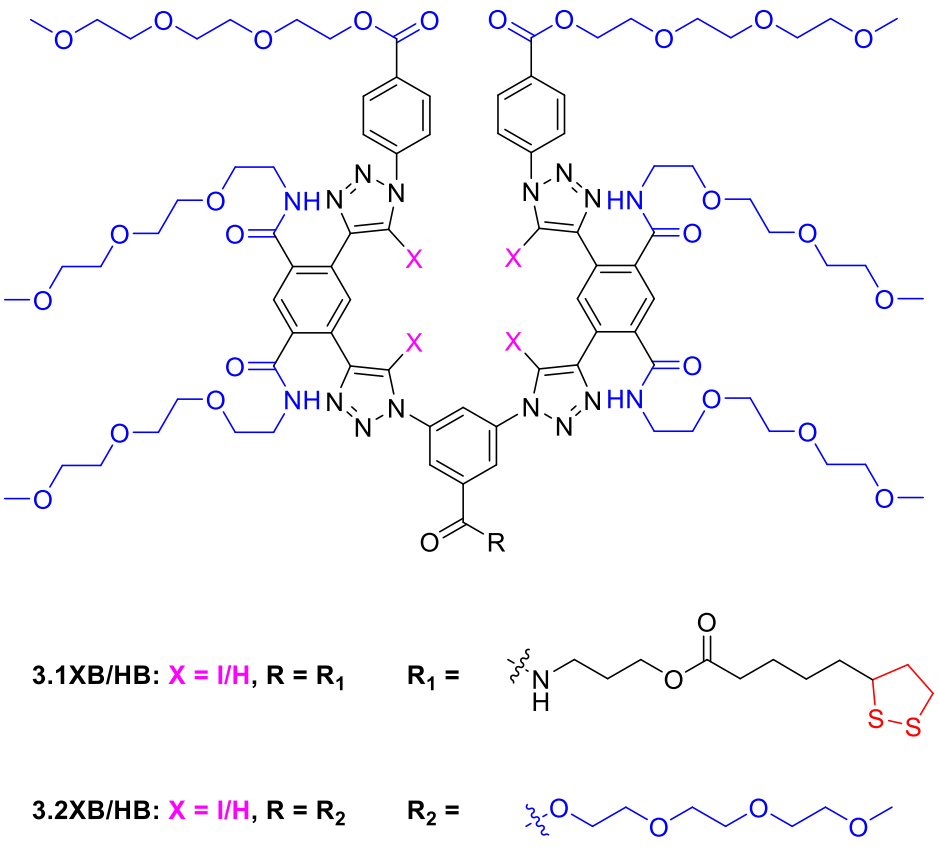


Figure 3.1. Chemical structures of foldamer receptors **3.1XB/HB** and **3.2XB/HB**.

These second-generation triazole foldamer receptors were shown to be capable of strong solution-phase anion binding in pure water *via* formation of 2:1 stoichiometric host-guest complexes as shown for the binding of I^- by **3.2XB** (Figure 3.2).[296]

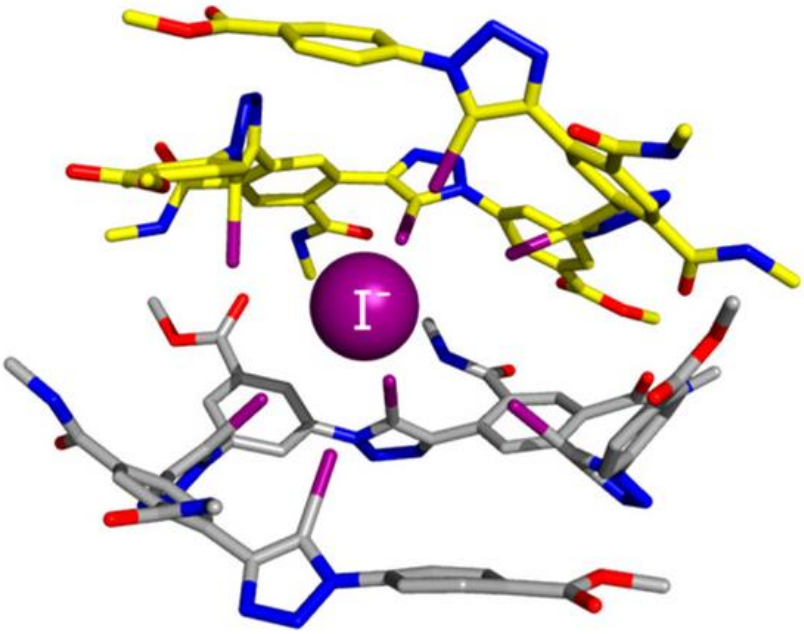
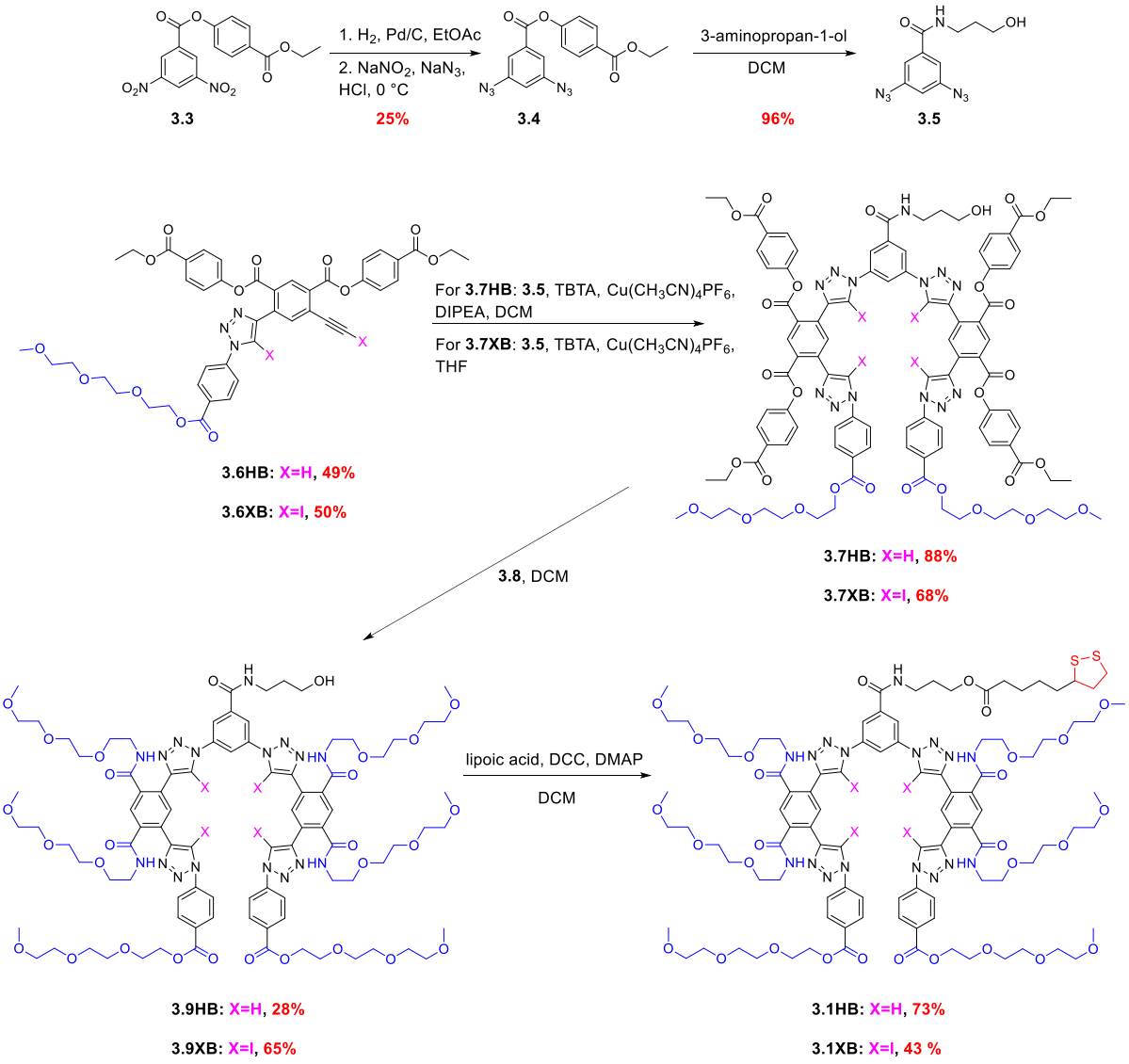


Figure 3.2. Model of **(3.2XB)$_2$●I$^-$** complex as obtained by MD simulations in water. For simplicity the solubilising PEG sidechains are omitted. Reproduced with permission from ref.[296] Copyright 2019 American Chemical Society.

3.2XB displayed very strong binding to various anions (Br^-, I^-, SCN^-, ReO_4^- and ClO_4^-) in pure and buffered water with $\beta = K_1 * K_2$ up to 10^{11} (M^{-2}) for I^- (Table A3.1 and A3.2). Anion binding towards **3.2HB** was notably weaker with no binding of Br^- or ReO_4^-. Furthermore, **3.2HB** bound all anions in a 1:1 stoichiometry, while **3.2XB** displayed 2:1 binding in all cases, as shown above. This was attributed to differences in the steric bulk of XB and HB donor atoms and the higher hydrophobicity of the iodotriazole binding sites inducing a "hydrophobic collapse" resulting in the formation of a dimeric, folded binding capsule with a hydrophobic, shielded interior.

As a result of strong anion binding, charge-neutrality and water solubility (allowing comparison between solution-phase and interfacial binding performance) these second generation foldamers **3.2XB/HB** were chosen as the scaffold for an interfacial receptor/sensor. To enable surface-immobilisation, the receptor was endowed with a disulfide anchor group affording **3.1XB/HB**, as outlined in Scheme 3.1 (all steps apart from the final esterification were carried out by Arseni Borissov).



Scheme 3.1. Synthetic route towards **3.1XB/HB**. The syntheses of **3.6XB/HB** and **3.8** are shown in Scheme A3.1 and Scheme A3.2.

The synthesis of these receptors is largely analogous to that of the parent receptors **3.2XB/HB** with the notable difference that a novel alcohol-appended bis-azide **3.5** was employed as the central building block of the foldamer. A series of CuAAC reactions afforded first the (iodo)triazole-(iodo)alkyne synthons **3.6XB/HB** and then the alcohol-appended foldamer **3.9XB/HB**. Upon esterification of **3.9XB/HB** with lipoic acid in the presence of DCC/DMAP the desired receptors **3.1XB/HB** were obtained. Interestingly, the yield of this reaction was significantly lower for the XB foldamer (43% *vs.* 73% for HB). This outcome was reproducible and may indicate a lowered reactivity arising from a XB interaction between the alcohol appendage and the central binding site in the nonpolar solvent DCM.

3.3 Film Formation and Characterisation

Formation of SAMs of the receptors was carried out by exposure of clean gold substrates to **3.1XB/HB** (0.25 mM in ACN/H_2O 1:1) overnight yielding **3.1XB/HB$_{SAM}$**. The generated films were then characterised by a variety of surface analytical techniques. The ellipsometrically determined film thicknesses of 3.22 ± 0.21 nm and 3.51 ± 0.40 nm for **3.1XB/HB$_{SAM}$**, respectively, are in good agreement with the formation of monolayers and an upright conformation of the receptors as schematically depicted in Figure 3.3. This upright conformation was further confirmed by reductive thiol stripping, revealing a molecular surface coverage Γ of (8.85 ± 1.70) × 10^{-11} mol/cm^2 and (6.40 ± 1.60) × 10^{-11} mol/cm^2 for **3.1XB/HB$_{SAM}$**, respectively. The corresponding molecular footprints of approx. 2 nm^2 are in good agreement with the size of the monomeric receptor and are indicative of a high packing.

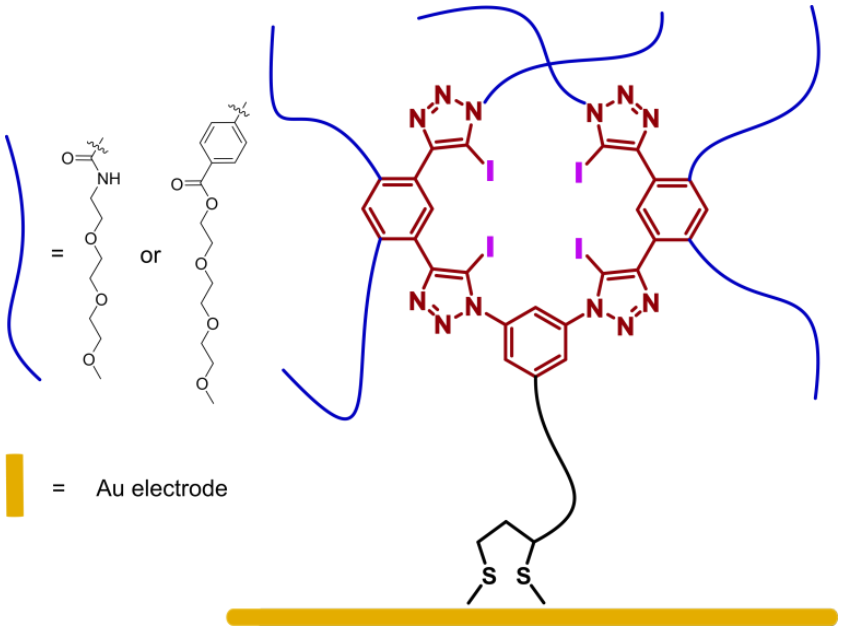


Figure 3.3. Schematic depiction of the foldamer receptor **3.1XB** on a gold electrode (**3.1XB$_{SAM}$**).

Water contact angle measurements indicated a relatively high hydrophilicity of the films with contact angles of 60° and 55°, for **3.1XB/HB$_{SAM}$**, respectively, in good agreement with similar reports of PEG-based SAMs.[310] The somewhat larger water contact angle for **3.1XB$_{SAM}$** potentially reports on the higher hydrophobicity of the iodo-triazole core of the receptor, as similarly observed for **2.2XB/HB$_{SAM}$**.

3.3.1 X-ray Photoelectron Spectroscopy (XPS)

A more detailed compositional analysis of the SAMs was again carried out by X-ray photoelectron spectroscopy (XPS). The low resolution survey XPS spectra of both films revealed the presence of C, O, N and S in both films, with iodine, as expected, only present in **3.1XB$_{SAM}$** (Figure 3.4 and Tables A3.3 and A3.4). Importantly, the elemental composition of the SAMs was in excellent agreement with the theoretical atomic ratios of the receptors

(Table 3.1). This confirms the expected formation of pure films that contain only the desired receptor and negligible contamination.

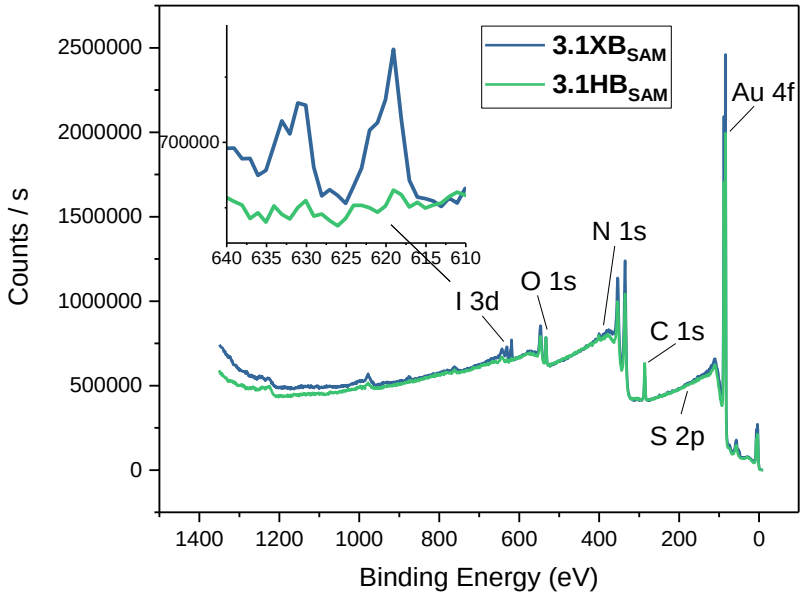


Figure 3.4. Low resolution survey XPS spectra of **3.1XB/HB$_{SAM}$** indicating identical composition of both films apart from presence of iodine for **3.1XB$_{SAM}$**. All unassigned peaks arise from other orbitals of the same elements. Inset: Magnification of I 3d region.

Table 3.1. Experimental and theoretical elemental composition of **3.1XB/HB$_{SAM}$** determined by XPS. Apart from these elements as well as Au, no significant other peaks were observed. Values were normalised to S = 2. Errors represent one standard deviation of triplicate measurements.

	3.1XB$_{SAM}$		**3.1HB$_{SAM}$**	
Element	**Experimental**	**Theoretical**	**Experimental**	**Theoretical**
C	93.92 ± 8.69	98	101.86 ± 5.17	98
N	16.65 ± 3.42	17	16.68 ± 1.25	17
O	25.47 ± 2.48	29	28.33 ± 1.02	29
S	2 ± 0.46	2	2 ± 0.39	2
I	3.54 ± 0.24	4	-	-

A further subdivision of these peaks can, through peak fitting, reveal specific chemical environments within the film which confirm the presence of the expected functional groups as representatively shown for **3.1XB$_{SAM}$** (Figure 3.5). These high-resolution scans are identical for both films as shown in Figures A3.1-3.3.

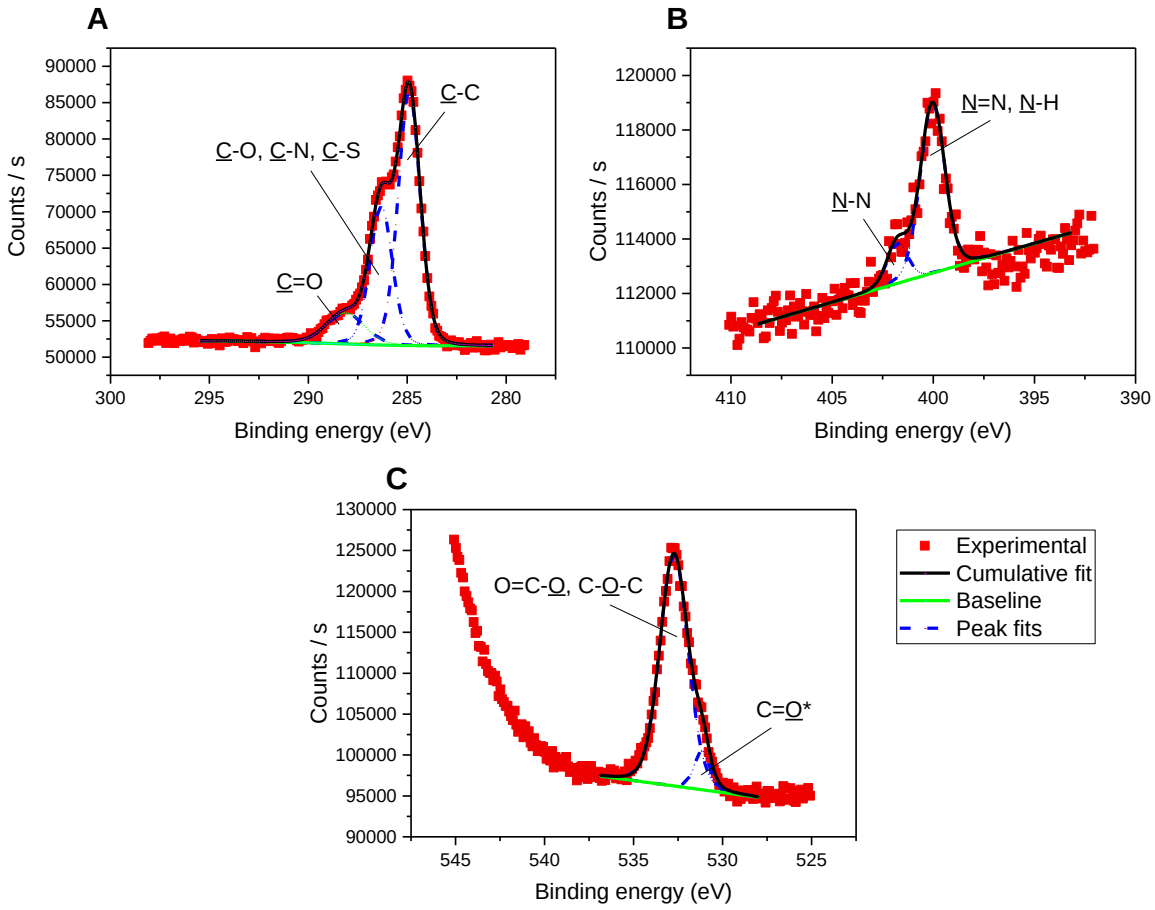


Figure 3.5. High resolution XPS spectra including peak fits of **3.1XB$_{SAM}$**. A) C 1s. B) N 1s C) O 1s. *Tentative assignment, for further information see main text.

As observed for **2.2HB$_{SAM}$** (Section 2.2.3.1.1), three peaks can be fitted to the high resolution C 1s spectra, presumably arising from the afore-discussed C–C, C–X (X = N, O, S) as well as C=O environments, respectively.[279-281] For both **3.1XB$_{SAM}$** and **3.1HB$_{SAM}$** the ratio of these peaks is not directly reflective of those expected based on the theoretical

assignments, indicating that in these chemically complex films some bonding environments possess different binding energies than predicted. This problem is even more apparent in the O 1s high resolution spectra where two distinct environments can be observed. The component of higher binding energy can be, as discussed in Section 2.2.3.1.1, assigned to O=C−O and additionally contain the C−O−C groups.[279,280] The peak at lower binding energy was ascribed to (ester) carbonyl oxygens in the previous chapter, however, this turns out to be rather problematic in this context as the experimentally obtained O 1s peak ratio for both films significantly deviates from the theoretical ones. Specifically, if the lower energy component arises from C=O groups then a theoretical peak ratio of 8:21 (5 amide + 3 ester C=O; 18 ether + 3 ester O=C−O) would be expected, widely differing from the experimental values (Tables 3.2-3.3). The peak at lower binding energy potentially arises only from amide carbonyl groups while the ester carbonyl groups fall within the higher energy component. In line with this assumption, such an O 1s peak difference between amide and ester carbonyl has been reported.[311] In this case a theoretical ratio of 5:24 would be expected, in better agreement with the experimental values, especially for **3.1HB$_{SAM}$**. It should however be noted that the peak fitting was carried out without any restrictions on the FWHM or peak positions. The errors associated with these fits are potentially large, in particular when the relative ratio of different chemical environments is large (as is the case here for O 1s) and the smaller peak "disappears" within the larger peak or the baseline (see Figure 3.5C and further discussions in Section 7.3.3). A clearer picture can only be developed when further information about the specific number and peak nature of different components can be obtained, for example with control experiments/compounds.

A much better agreement of experimental data with theoretical predictions was observed for the peak fitting of the high resolution N 1s spectra where the assignment of the peaks

(low energy component: N=N + N−H; higher energy component: N−N)[280,281] is analogous to that for **2.2HB$_{SAM}$**.

Table 3.2. Peak binding energies and experimental and theoretical ratios for different chemical environments of C, N and O of **3.1XB$_{SAM}$**. The ratios shown here are obtained by peak fitting of the individual high resolution spectra and do not report on the overall ratio of the elements (see Table 3.1).

		Peak BE (eV)	Exp.	Theor.
C	C−C	284.91 ± 0.06	36.29 ± 3.67	32
	C−O, C−N, C−S	286.32 ± 0.07	22.83 ± 1.65	58
	C=O	288.21 ± 0.16	8	8
N	N=N, N−H	400.01 ± 0.07	17.44 ± 3.43	13
	N−N	401.44 ± 0.72	4	4
O	(NH) −C=O	531.09 ± 0.14	5	5
	(O=C)−O, C−O−C, (O=C)−O	532.72 ± 0.06	80.87 ± 33.56	24

Table 3.3. Peak binding energies and experimental and theoretical ratios for different chemical environments of C, N and O of **3.1HB$_{SAM}$**. The ratios shown here are obtained by peak fitting of the individual high resolution spectra and do not report on the overall ratio of the elements (see Table 3.1).

		Peak BE (eV)	Exp.	Theor.
C	C−C	284.23 ± 0.05	34.95 ± 11.59	32
	C−O, C−N, C−S	286.71 ± 0.06	20.61 ± 2.62	58
	C=O	288.44 ± 0.08	8	8
N	N=N, N−H	400.29 ± 0.03	10.20 ± 1.94	13
	N−N	402.06 ± 0.08	4	4
O	(NH) −C=O	531.58 ± 0.02	5	5
	(O=C)−O, C−O−C, (O=C)−O	533.12 ± 0.02	28.63 ± 6.68	24

As highlighted above, the presence of iodine in the survey scan was only detected for **3.1XB$_{SAM}$**. In the high resolution scan 4 peaks are observable, indicative of two different iodine species, where due to spin-orbit coupling two peaks with a separation of 11.5 eV can be seen for each species (Figure 3.6A). This is unexpected as all four iodine atoms from the

iodotriazole donors should be chemically identical. In fact, the peaks highlighted with an asterisk almost certainly do not arise from **3.1XB$_{SAM}$**, but rather some (*in situ* generated) modification. From the aforementioned peak separation and the binding energies it can be safely assumed that this contamination is an iodine species. This is potentially a metal iodide (*e.g.* gold iodide)[312] and is most likely generated under the measurement conditions, where presumably some of the iodotriazole groups are degraded by the high energy X-ray radiation and/or the high vacuum conditions. This hypothesis is further supported by the fact that samples containing no iodine in the SAMs also display these peaks when measured in the same chamber (see Section 4.2.2.2).

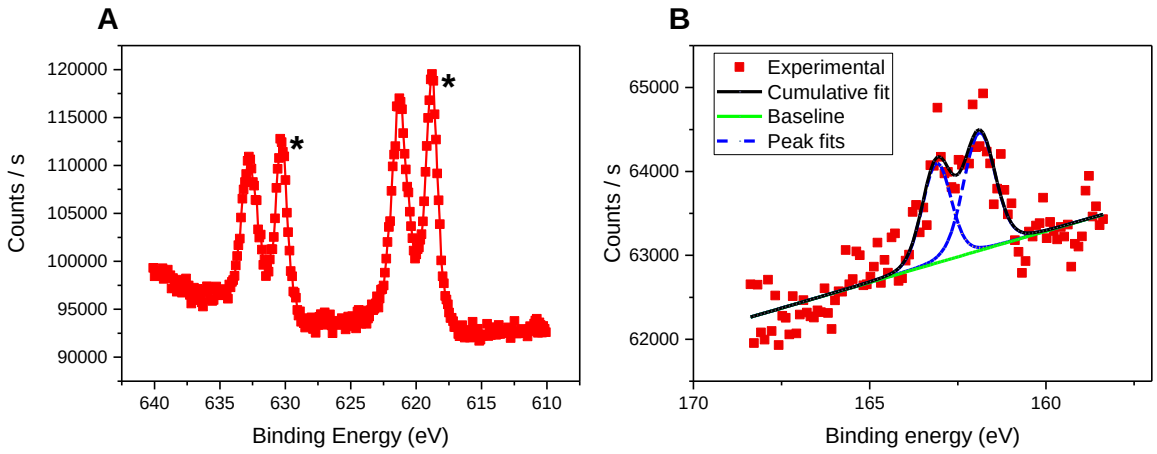


Figure 3.6. High resolution XPS spectra of **3.1XB$_{SAM}$**. A) I 3d. The peaks denoted with an asterisk presumably arise from an iodine species that is generated under the measurement conditions and does not arise from the SAM. B) S 2p. The two peaks fitted in this spectrum as well as the doublets in the I 3d spectrum arise from spin orbit coupling and not from chemically different environments.

Fitting of the high resolution S 2p spectra affords, as expected, two peaks (arising from spin orbit coupling) with binding energies of 161.9 eV and 163.1 eV, where both the peak positions and the peak separation (1.2 eV) are in excellent agreement with previous reports.

As highlighted before, these binding energies are consistent with SAM formation *via* the disulfide anchor group; for a non-adsorbed thiol/disulfide a higher binding energy of around 165 eV would be expected.[282,283]

Overall these XPS experiments confirm the formation of pure, disulfide-tethered SAMs, where the expected functional groups within the receptors can be observed. Importantly, XPS and other surface characterisation confirm that films of both receptors are structurally and chemically identical, apart from their central binding site, which is characterised by the presence of the iodine-based XB donors in **3.1XB$_{SAM}$**.

3.4 Anion Sensing *via* Non-Faradaic Capacitance Spectroscopy

3.4.1 Voltammetric and Impedimetric Investigation of the SAMs

The electrochemical investigation of the films was carried out in pure water containing 100 mM NaCl supporting electrolyte. This salt was chosen as it is not expected to interact with the foldamer films since Cl^- exhibits no binding to the parent foldamer receptors in solution[296] and due to its abundance in relevant real-life media. As expected, CV reveals no Faradaic processes in the absence of a solution-phase redox probe (Figure 3.7).

Even in the presence of high concentrations of $[Fe(CN)_6]^{3-/4-}$ no clear redox-activity can be observed indicating the formation of dense, blocking films, as already indicated by the measurements detailed in Section 3.3.

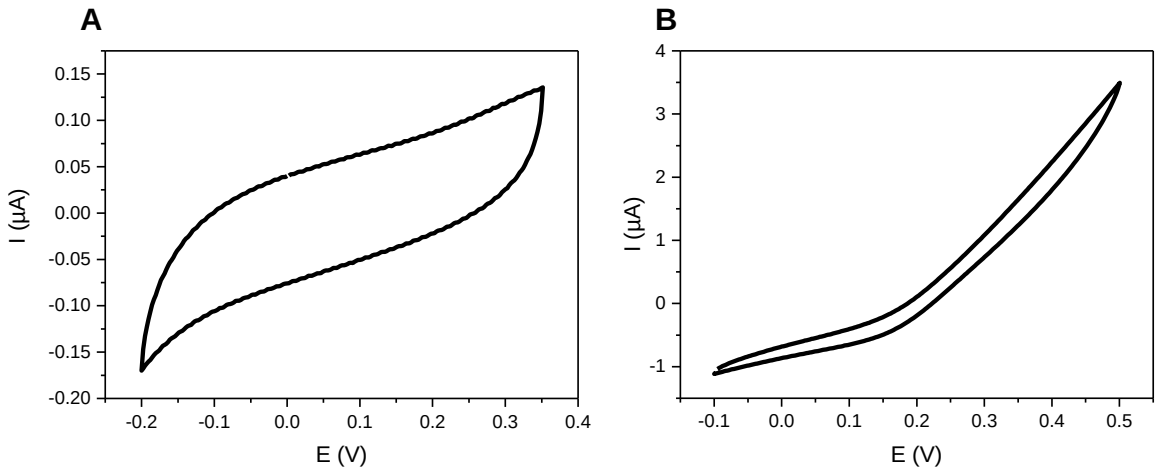


Figure 3.7. CVs of **3.1XB$_{SAM}$** in A) 100 mM NaCl and B) 10 mM $[Fe(CN)_6]^{3-/4-}$ and 100 mM NaCl.

This is further corroborated by Faradaic EIS in the presence of 10 mM $[Fe(CN)_6]^{3-/4-}$ where even at low frequencies (0.1 Hz) no full semicircle can be resolved in the impedimetric Nyquist plots (Figure 3.8). Of further note is the high R_{ct} (> 200 kΩ) which is not particularly well-resolved. The addition of ReO_4^-, an anion that is expected to bind to the film, as also confirmed by capacitive measurements (*vide infra*), did not induce any significant impedimetric perturbations. This lack of response can potentially be attributed to the high baseline impedance which might not respond to any additional events that would further affect (*i.e.* block) electron transfer.

These observations again highlight the value of an impedance-based methodology that does not rely on the use of a signal-amplifying redox probe, thereby potentially circumventing the poorly resolved impedimetric signature/response of the film.

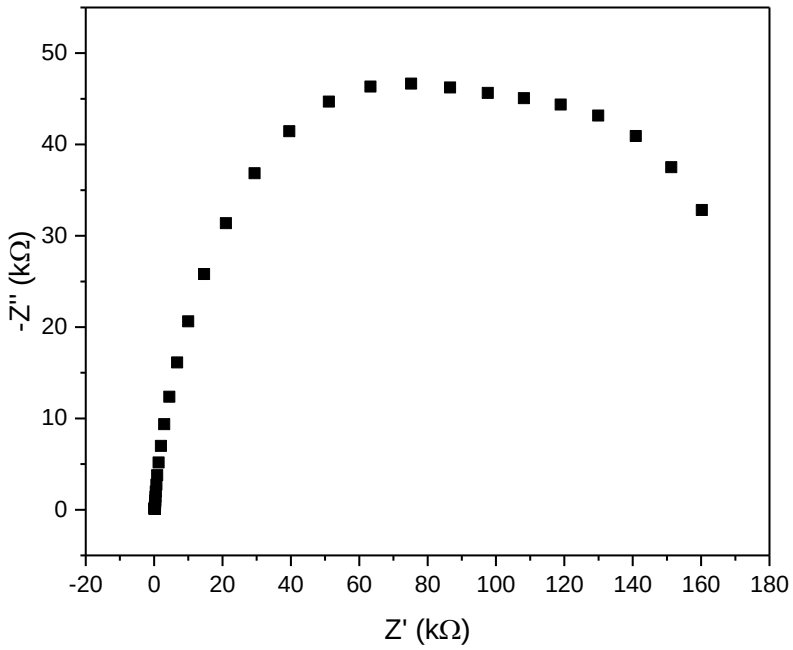


Figure 3.8. Impedimetric Nyquist plot of **3.1XB$_{SAM}$** in 10 mM $[Fe(CN)_6]^{3-/4-}$ and 100 mM NaCl at a DC bias potential of 0.21 V in the AC frequency range of 100 kHz – 0.1 Hz.

3.4.2 Capacitive Investigation of the SAMs and Anion Sensing

In order to test the viability of a non-Faradaic approach, EIS in the absence of any redox probe was carried out at the open circuit potential (OCP, ≈0 V) in the same aqueous electrolyte (100 mM NaCl). As a result of the lack of a redox transducer in solution or within the SAM, the impedimetric signatures of the films are now devoid of any semi-circular charge-transfer features (Figure 3.9A). The impedimetric data was transformed into its capacitive components *via* $C''(\omega) = Z'/\omega|Z|^2$ and $C'(\omega) = Z''/\omega|Z|^2$, where ω is the angular frequency, and C'/Z' and C''/Z'' are the real and imaginary capacitance and impedance, respectively and $|Z|$ the impedance modulus. This data is then represented in a capacitive Nyquist plot, where the well-defined semi-circular region reports on the interfacial capacitance (Figure 3.9B).

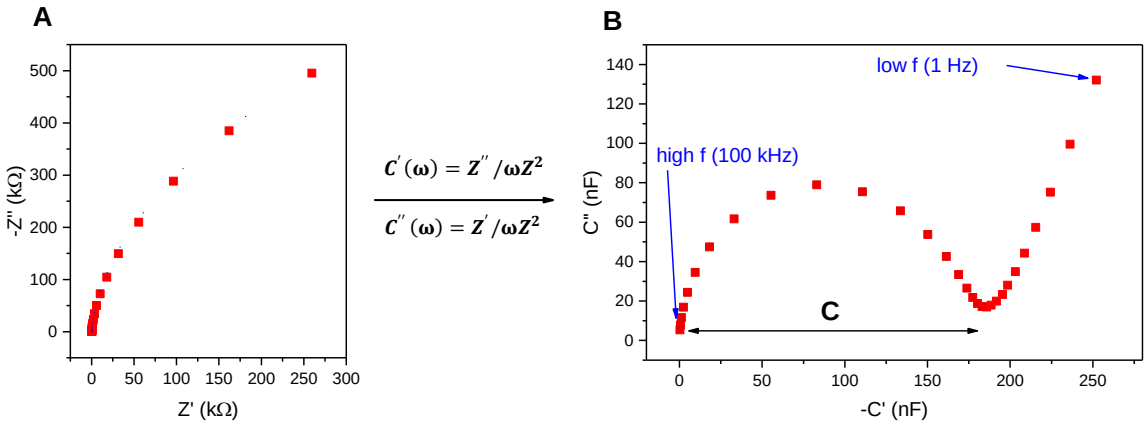


Figure 3.9. Impedimetric and capacitive signature of **3.1XB$_{SAM}$** in 100 mM NaCl. A) Impedimetric Nyquist plot and B) Capacitive Nyquist plot obtained from the impedimetric data *via* the given equations.

The capacitance of the film C, can be obtained graphically as the semicircle diameter of the capacitive Nyquist plot *via*, for example, fitting to a semicircle or ellipse function, or can be approximated as the C' at the inflection point. Alternatively, the capacitance can also be obtained from fitting to an equivalent circuit, however this relies on certain assumptions about the interface. Herein, both approaches afford almost identical values, the former is however more straightforward and avoids complications arising from circuit fitting and the necessity for appropriate equivalent circuit models (see Section 3.5.1).

The capacitance of the receptive films was determined as 4.85 ± 0.36 µF/cm^2 and 4.83 ± 0.72 µF/cm^2 for **3.1XB/HB$_{SAM}$**, respectively. This capacitance is largely independent of the concentration of the NaCl electrolyte between 10 mM and 1 M with a minimal increase of <10% over a 2-order of magnitude increase in the ionic strength.

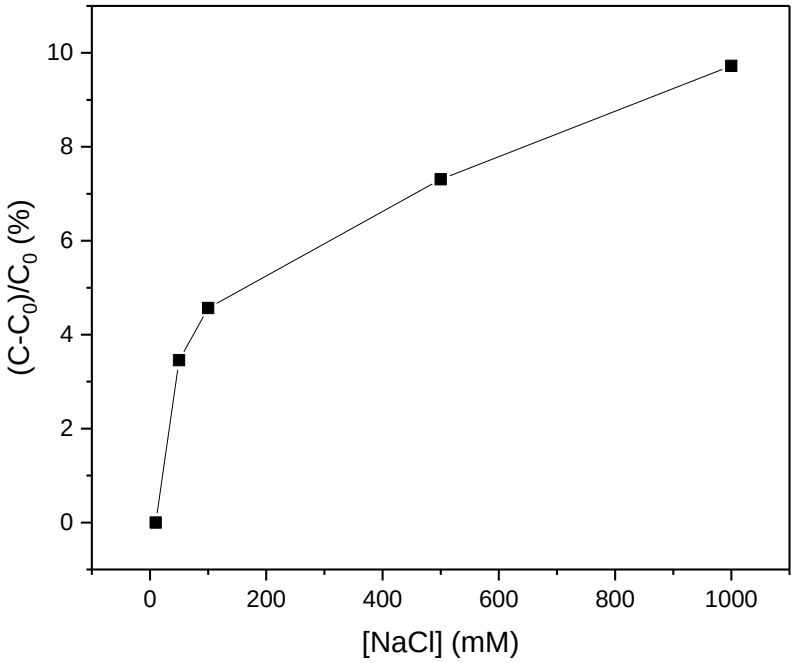


Figure 3.10. Normalised capacitance increase of **3.1XB$_{SAM}$** in the presence of various concentrations of NaCl as electrolyte. All values were normalised to the capacitance at 10 mM NaCl.

This change is significantly lower than that arising from a specific ion binding event (*vide infra*) and indicates that there is a minimal interaction between the electrolyte and the film (Figure 3.10). Another crucial observation is that the baseline stability in this non-Faradaic format is excellent, with minimal changes upon repeat measurements.

Importantly, the film capacitance is sensitive to the presence of specifically binding anions as can be seen in Figure 3.11B, where a large increase in C is observed in the presence of 50 mM ReO_4^- while in the corresponding impedimetric Nyquist plots (Figure 3.11A) no clear changes are observed.

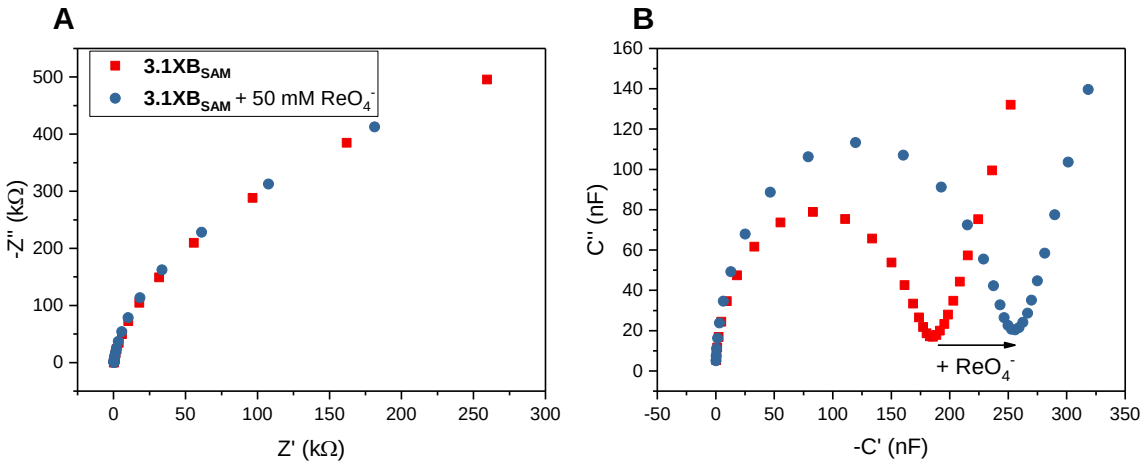


Figure 3.11. EIS/ECS response of **3.1XB$_{SAM}$** in 100 mM NaCl at OCP in the presence (blue circles) and absence (red squares) of 50 mM ReO_4^-. A) Impedimetric and B) Capacitive Nyquist plot.

This behaviour is also resolved in the Bode plots (Figures 3.12 and 3.13), where no significant changes in $|Z|$ or the phase are evident while both C' and C'' are clearly responsive to the presence of ReO_4^-. The high phase angle of ≈85° that can be observed in Figure 3.12 is additional evidence for the formation of densely packed SAMs with almost ideal capacitive behaviour (an ideal capacitor would induce a phase shift of 90°).

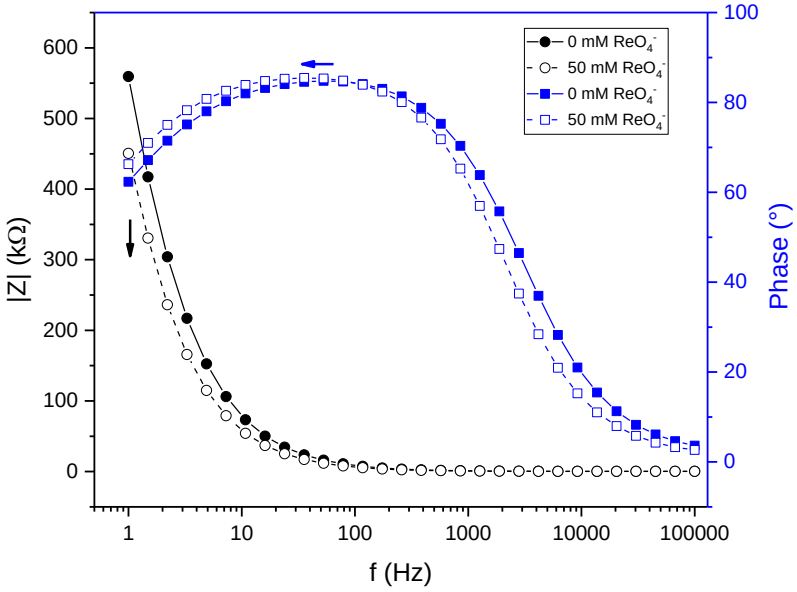


Figure 3.12. Bode plots of impedance modulus (black, circles) and phase (blue, squares) of **3.1XB$_{SAM}$** in the presence (empty symbols) and absence (filled symbols) of 50 mM ReO_4^-.

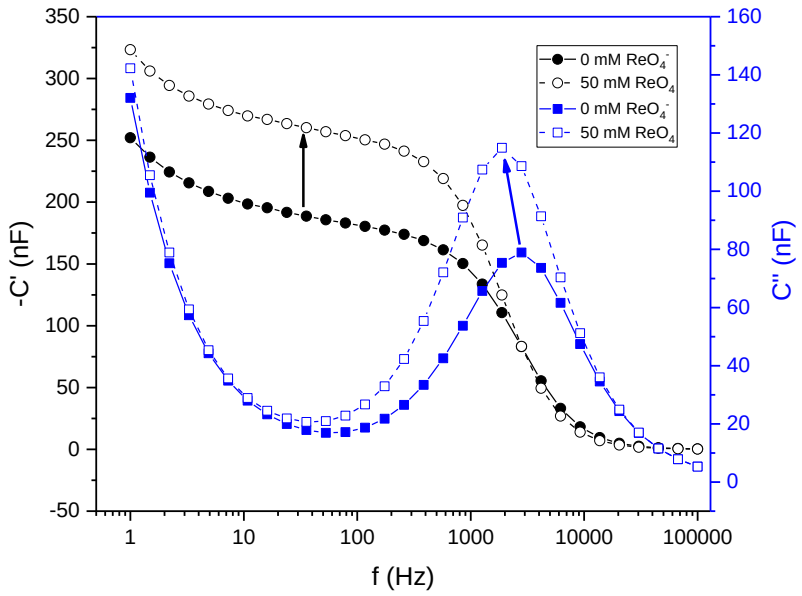


Figure 3.13. Bode plots of real (blue, circles) and imaginary (blue, squares) capacitance of **3.1XB$_{SAM}$** in the presence (empty symbols) and absence (filled symbols) of 50 mM ReO_4^-.

More detailed anion binding studies were then carried out by titration of the receptive interfaces with increasing concentrations of anions. All these experiments were carried out at constant ionic strength (*i.e.* in the presence of 100 mM salt) where the original electrolyte solution containing 100 mM NaCl was titrated with an aqueous solution of the sodium salt of the anion (100 mM) such that: x NaCl + y NaA, x + y = 100 mM. This was done in order to eliminate any influence of the overall concentration of electrolyte ions on the capacitive response of the interface.

Both films elicited a significant increase in their capacitance upon exposure to ReO_4^-, I^- and SCN^-. These results are in good agreement with the solution-phase binding preference of these receptors as discussed above. In solution a strong 2:1 host-guest complex formation is not only observed with the three aforementioned anions, but also with bromide and perchlorate (for **3.2XB**). Interestingly, **3.1XB/HB$_{SAM}$** did not significantly respond to these latter anions nor nitrate (change in C of <2% at $[A^-]$ > 10 mM). The surface-confined

receptors thus display a higher selectivity than in solution being able to differentiate the very similar ReO_4^- and ClO_4^- as well as I^- and Br^- (see Section 3.2). As depicted in Figure 3.14, the response of both films to the three binding anions ReO_4^-, I^- and SCN^- can be accurately described by the Langmuir adsorption isotherm:

$$\theta = \frac{K*[A^-]}{1+K*[A^-]} \qquad \text{eqn. 3.1}$$

where θ is the fractional occupancy of the receptive sites and K the binding constant of the anion to the receptor (this eqn. is equivalent to eqn. 2.4). As discussed in Section 2.2.3.2.1, this simple model assumes the formation of 1:1 stoichiometric host-guest complexes as well as negligible interactions between adsorbed (bound) anions. It is not possible to ascertain the binding stoichiometry in the receptive film but the formation of a 2:1 stoichiometric host-guest complex, as observed for **3.2XB** in solution (Figure 3.2), seems unlikely as a result of steric/geometric constraints. These assumptions are indirectly validated by the good agreement of the experimentally obtained data with this model (eqn. 3.1, with $R^2 > 0.967$ in all cases, Table 3.4).

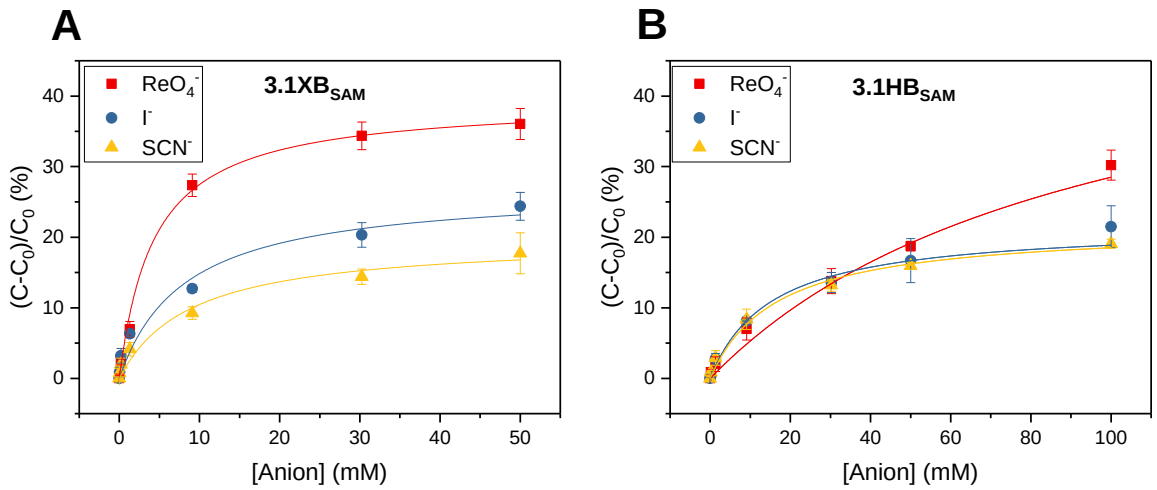


Figure 3.14. Normalised capacitance increase of **3.1XB$_{SAM}$** (A) and **3.1HB$_{SAM}$** (B) at OCP in the presence of increasing amounts of ReO_4^- (red squares), I^- (blue circles) and SCN^- (yellow triangles). Fits were obtained according to the Langmuir adsorption model (eqn. 3.1). Error bars represent one standard deviation across three separate electrodes. Note the different concentration ranges for both graphs.

From this data fitting binding constants of 231, 123 and 112 M^{-1} for ReO_4^-, I^- and SCN^- at **3.1XB$_{SAM}$** can be obtained, respectively (Table 3.4). The binding of these anions to the corresponding HB SAM is significantly weaker in all cases with 11, 66 and 61 M^{-1} for ReO_4^-, I^- and SCN^-, respectively. These results are in good agreement with solution-phase binding studies where enhanced binding constants for the XB receptor are observed, as has been the norm for XB anion receptors capable of functioning under competitive aqueous conditions (see Chapter 1).[15,16]

An interesting observation is the significant difference in the maximum response that can be observed for the three different anions, highlighting that the response is most likely not simply dictated by the introduction of a negative charge into the SAM, but some more complex phenomena that affect the interfacial capacitance. This behaviour will be discussed in more detail in Section 3.5.

It is important to note that the binding isotherm for I^- slightly deviates from an ideal Langmuir-type behaviour, especially at **3.1XB$_{SAM}$**. Specifically, if an error-weighted fit is performed, the data points at higher concentration deviate significantly from the Langmuir isotherm which plateaus at a lower relative increase in C (18.3%) with a much larger binding constant of 362 M^{-1}. This is because the (cumulative) error after the first additions of analyte is lower, forcing a better fit through the first data points. There is however no inherent reason why the actual error should significantly differ for different data points. The values in Table 3.4 and the isotherms in Figure 3.14 were thus obtained from fitting of a non-weighted average of the data points. Only in the previously discussed case does this return a different K and ΔC_{max} in comparison to an error-weighted fit. It should be noted that while the oxidation potential of iodide is around 0.5 V and the OCP of the system,

which was chosen as the DC bias potential, is around 0 V, that the onset of the I^- oxidation can be at significantly lower potentials, in particular at higher concentrations. This might explain slight deviations from ideality in the sensing of I^-. During the course of the titration the OCP of the system does not change significantly (< 50 mV) This small change is also not monotonically dependent on the concentration of the target analyte and is thus most likely not caused by the presence of the anion (but rather some general drifts) and is therefore not analytically useful.

Table 3.4. K (M^{-1}), LOD, R^2 and ΔC_{max} for binding of various anions to **3.1XB/HB$_{SAM}$** according to the Langmuir model (eqn. 3.1). ΔC_{max} – maximum capacitance increase at [Anion] = ∞. / – No binding/response (negligible increase of C). Estimated errors for K and LOD: <20%.

	3.1XB$_{SAM}$				**3.1HB$_{SAM}$**			
	K	**LOD (µM)**	**R^2**	**ΔC_{max} (%)**	**K**	**LOD (µM)**	**R^2**	**ΔC_{max} (%)**
ReO_4^-	231	28	0.9965	39.3	11	80	0.9910	55.6
I^-	123	14	0.9678	26.9	66	47	0.9993	21.7
SCN^-	112	42	0.9747	16.8	61	113	0.9955	21.5
ClO_4^-	/	/	/	/	/	/	/	/
Br^-	/	/	/	/	/	/	/	/
NO_3^-	/	/	/	/	/	/	/	/

The limit of detection (LOD) of the sensors was then determined *via* $LOD = \frac{3*\sigma_{C_0}}{s}$ where σ_{C_0} is the standard deviation of the blank (interface in absence of target anion; baseline) and s the slope of the linear region of the calibration curve. This slope was determined in the range between 0 and 9 mM of anion, where the response is almost linear. The LODs as reported in Table 3.4 can be considered conservative estimates, where the real LODs are presumably somewhat lower (see Section 7.4). It should also be noted that the standard deviation of the blank was obtained for every sensor/titration separately where the initial

baseline stability was assessed by multiple repeat measurements (8 repeats) before exposure to the anions. The difference in LODs for different anions thus not only reflects the difference in their slope of their calibration curve but is also influenced by differing baseline stabilities between experiments.

With LODs of 28, 14, and 42 μM for ReO_4^-, I^- and SCN^-, respectively, **3.1XB$_{SAM}$** was markedly more sensitive than **3.1HB$_{SAM}$**, which possessed LODs of 80, 47 and 113 μM for the same anions. These observations are generally reflective of the increased binding affinity of **3.1XB$_{SAM}$** and highlight the superiority of XB-driven anion binding not only in solution but also at a receptive interface. To the best of our knowledge this is the first report of interfacial anion sensing mediated by XB in water.

In addition, this sensor (in particular **3.1XB$_{SAM}$**) could theoretically be used for the real-life sensing of the biologically and environmentally relevant ReO_4^-, I^- and SCN^-.[4,313] This is enabled by an excellent selectivity over all other tested anions (Table 3.4) and the fact that the three binding anions are not expected to coexist in any analytical sample. The LOD for ReO_4^- (28 μM), a surrogate for TcO_4^-, is low enough that TcO_4^- sensing in nuclear waste water samples could be conducted, where pertechnetate levels are expected to fall in the 10−100 μM range.[314]

As an initial test of the sensors' viability in a more complex fluid, the capacitive response of **3.1XB$_{SAM}$** towards ReO_4^- was assessed in the presence of 1 mg/mL of bovine serum albumin (BSA), the most abundant serum protein. Over 18 repeat measurements (≈30 min) the initial capacitance of the interface continually decreased by −2.4% (in the absence of any target anion), attributable to some degree of physisorption of BSA onto the interface. Subsequent addition of 25 mM ReO_4^- (in the presence of BSA) induced an increase in the capacitance of

9%, indicating that operation of the sensor is still possible, albeit with a smaller response than what can be attained under the same conditions in the absence of BSA (≈30% increase in C, see Figure 3.14A). This importantly highlights the general viability of this sensor for sensing in real-life relevant media, in particular when deleterious effects from fouling can be mitigated, for example, *via* the additional integration of antifouling chemistries into the interface.[315]

The reversibility of the non-covalent binding of the anion to the receptive films enables sensor re-use as shown in Figure 3.15, where after rinsing with water the initial capacitance can be almost fully recovered. Upon subsequent repeated exposure and washing steps (including sonication in water), some attenuation, both in baseline capacitance and magnitude of response, was observed. This can potentially be attributed to some degree of film rearrangement or degradation during washing or the physical entrapment of some anions within the film. Nevertheless, it is expected that under more controlled conditions these films can retain a high degree of reversibility/reusability and could be utilised for the continuous, real-time monitoring of ReO_4^-, I^- and SCN^- under flow.

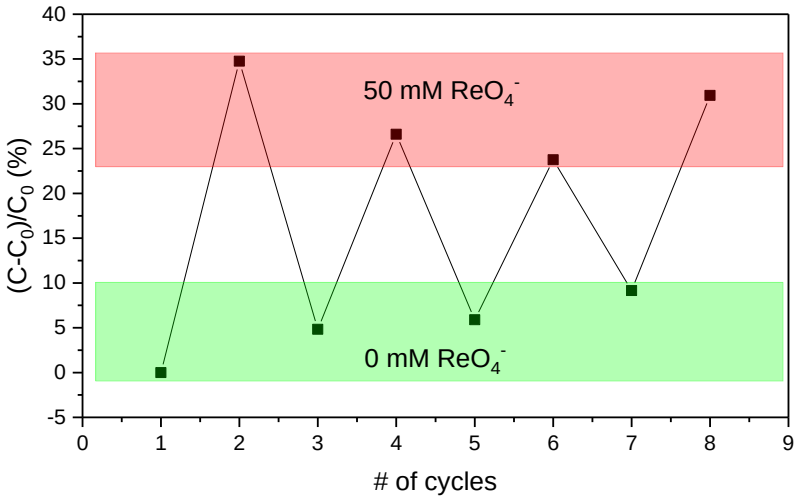


Figure 3.15. Normalised capacitance change of **3.1XB$_{SAM}$** in alternating presence and absence of 50 mM ReO_4^-.

A crucial observation in all of these studies is that for all tested anions the response is substantially different between both SAMs. As highlighted in Section 3.3, all surface analyses indicate that both SAMs are structurally identical. Any observed sensory difference thus has to arise from the differing binding sites, crucially confirming that the measured change in the capacitance can be attributed to a specific binding event at the central tetra-(iodo)triazole binding site rather than any other association/interaction with the interface. This is further confirmed by control experiments with non-receptive SAMs (here undecanethiol-SAMs) where negligible changes in the capacitance are observed upon exposure to high concentrations of ReO_4^- under assaying conditions (<2%).

However, that the response arises from a specific binding event does not provide any insights into the specific transduction principles of the sensor. Specifically, the origin of the capacitive change has not been elucidated yet and will be discussed in more detail in Section 3.5.

Importantly, it should also be noted that the relative binding trends of **3.1XB$_{SAM}$** and **3.1HB$_{SAM}$** differ for the tested anions. This shows that anion binding is indeed dependent on the specifically engineered tetra-proto/iodo triazole binding site and not purely dominated by the desolvation (hydrophobicity) of the anions (*i.e.* Hofmeister bias). Thus, sensing of any desired anion should be achievable *via* this novel methodology, if the appropriately designed receptor is employed.

3.4.3 Capacitive Measurements at Different Potentials

In contrast to standard Faradaic EIS where the electrode potential is restricted to the formal potential and solution-phase conditions (solubility) suitable for the redox probe (*e.g.*

$[Fe(CN)_6]^{3-/4-}$, see Section 1.2.3 and Section 3.1) the herein described capacitive method can be carried out at any DC electrode potential and, in theory, in any solvent. The former is relevant for sensing of analytes such as iodide (achieved herein) whose moderate oxidation potential would overlap with the most commonly used $[Fe(CN)_6]^{3-/4-}$ in Faradaic EIS. Not only does the free choice of electrode potential allow measurement conditions that are more compatible with the analyte or interface of choice, it may enable modulation of (an)ion binding strength and selectivity through specific surface polarisation. It was speculated that the polarisation of the electrode might additionally drive (positive potentials) or impede (negative potentials) anion binding, which could potentially be used for tuning selectivity. To this end the capacitance of the films was measured at four different concentrations of ReO_4^- over a wide potential range (−0.1 to 0.5 V). The repeat measurement of full Nyquist plots over a wide range of frequencies would be prohibitively time consuming at different potentials. An adapted protocol was thus employed where first a full capacitive Nyquist plot was measured at OCP from which the frequency at which the real part of the capacitance (C') corresponds to the film capacitance C (*i.e.* the frequency of the inflection point) was determined. All subsequent measurements were carried out at this one frequency, starting from a DC potential of −0.1 V which was increased in 50 mV steps up to 0.5 V (corresponding to 13 different DC potentials). At each potential the electrode was equilibrated for 30 s prior to the measurement (see Section 7.2.7).

As can be seen in Figure 3.16 the capacitance of both SAMs is dependent on the potential, with larger capacitances at higher potential. A simple Helmholtz model (ideal system; plate capacitor) would predict that the capacitance is independent of the applied potential. The deviation from this ideality indicates that a more elaborate model, such as the Gouy-Chapman or the Stern model might be more appropriate in describing the observations.

These models predict an enhanced capacitance at potentials more positive or negative than the point of zero charge (pzc), in agreement with the recorded data. This indicates that there is some detectable double layer contribution to the capacitive response, but it should also be considered that ion binding might be potential dependent, significantly complicating the capacitive behaviour of the films (see also Section 3.5). Another factor that can contribute to an increased capacitance upon changing the potential are rearrangements within the film, which could, for example, alter its ionic permeability, as previously reported for alkanethiol SAMs.[316,317]

As detailed in Section 3.5.1, multiple capacitive components are present within the film, including a double layer type capacitance as well as capacitance(s) arising from ionic ingress within the film (denoted C_t and C_{μ_i} in the following), where the latter are presumably more sensitive to changes in the electrode polarisation.

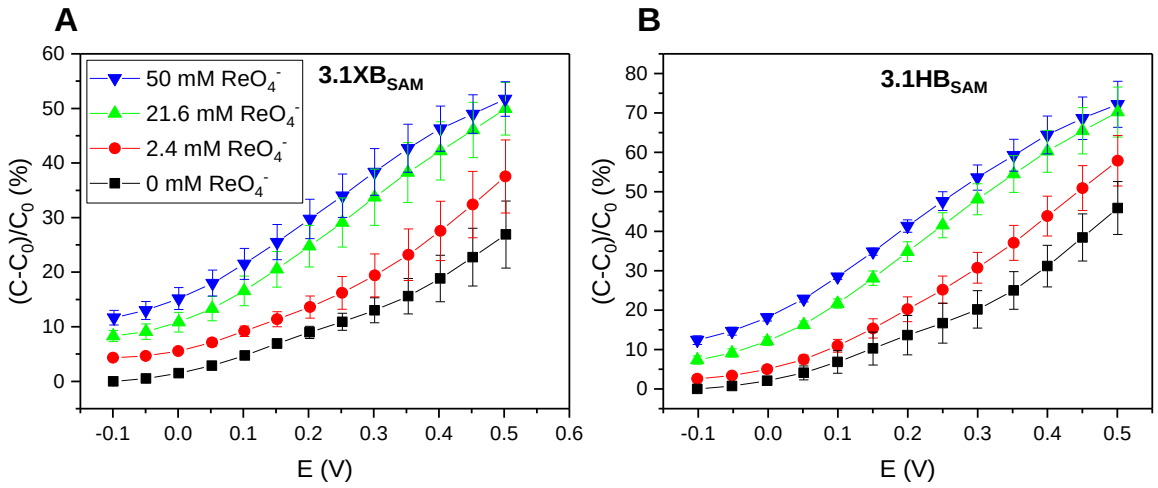


Figure 3.16. Overall change in capacitance of **3.1XB$_{SAM}$** (A) and **3.1HB$_{SAM}$** (B) at different concentrations of ReO_4^- at varying DC bias potentials. All values are normalised to the initial capacitance at −0.1 V in the absence of target analyte (*i.e.* in pure 100 mM NaCl). The normalised response at an individual potential is depicted in Figure 3.17. Error bars represent one standard deviation of measurements on three independent electrodes.

Importantly, the data as depicted in Figure 3.16 reports on the overall increased capacitance at higher potentials, but not directly on how sensitive this increased (baseline) capacitance is towards binding of ReO_4^-. To this end the data was additionally normalised at each potential (*i.e.* to the black trace in Figure 3.16), where the resulting plots as shown in Figure 3.17 now depict the relative capacitance change upon anion binding at each potential.

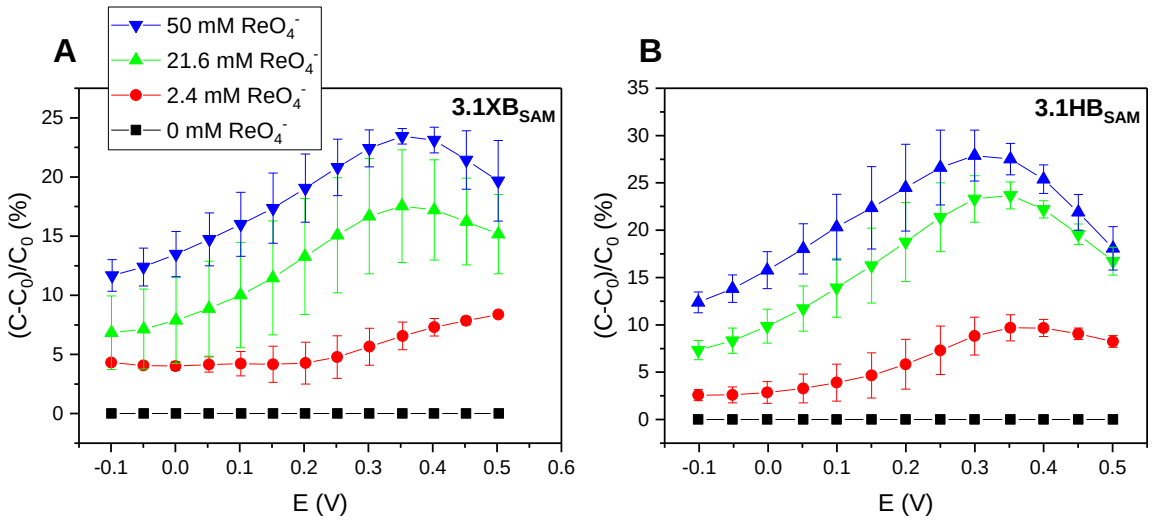


Figure 3.17. Relative change in capacitance of **3.1XB$_{SAM}$** (A) and **3.1HB$_{SAM}$** (B) upon exposure to three concentrations of ReO_4^- at varying DC bias potentials. All values are normalised to the initial capacitance at each potential in the absence of target analyte (*i.e.* in pure 100 mM NaCl). These plots thus represent the overall capacitive response that can be observed at a chosen DC bias potential. Error bars represent one standard deviation of measurements on three independent electrodes.

It appears that for both films there is some small enhancement in response at higher potentials (0.3 − 0.4 V) however, it has to be noted that the errors associated with these experiments are very large. For example, these measurements at **3.1XB$_{SAM}$** were repeated at least three times (with three electrodes each) with very poor reproducibility. Furthermore, the magnitude of the response at higher [ReO_4^-] is much lower than expected (in comparison to assays at OCP were full capacitive Nyquist plots are recorded). This could be due to a defective SAM, SAM/foldamer decomposition or deterioration of the

electrodes. It should also be noted that large errors are probably introduced because the measurements are performed without long pre-equilibration at each potential (equilibration time = 30 s). When performing measurements at potentials far away from OCP the capacitive stabilisation usually takes a lot of time (sometimes hours, depending on film). This might be due to (slow) ionic ingress or SAM rearrangement, but is difficult to assess and control.

3.5 Elucidation of the Signal Transduction Mechanism

The general observation of a capacitance change (here an increase) is generally sufficient to provide a useful sensory signal, as demonstrated above. However, a detailed understanding of the origins of this capacitive response can potentially elucidate interesting interfacial (binding) phenomena and guide the design of improved sensory interfaces. To this end a detailed analysis of the capacitive data was carried out and two different models proposed, as discussed in Section 3.5.2 and 3.5.3.

We should first consider the general meaning of a capacitance, which is defined as the ability of a system to store charge (q) as function of an applied potential (V), as shown by the following equation:

$$C = \frac{q}{V} \qquad \text{eqn. 3.2}$$

From this simple equation, it can already be qualitatively inferred that an accumulation of charge (in the form of a bound anion) at a receptive SAM would result in an enhanced capacitance. However, this simple model does not accurately describe the capacitance signatures of the interface.

It should be noted that at the working electrode interface multiple resistive and capacitive components can be present and can respond differently to the target analyte. This can be elucidated by an equivalent circuit analysis as detailed in the following section.

3.5.1 Equivalent Circuit Analysis

Certain circuit elements will always be present/develop upon immersion of a conducting electrode into an electrolyte solution, including a solution resistance R_s as well as a capacitance, which in the case of a simple, unmodified electrode is the double layer capacitance C_{dl}.

The capacitive signature of a thiol SAM on gold, as sampled in a non-Faradaic format, can be theoretically described by an $R_s(C_m[R_tC_t])$ equivalent circuit, as described previously (Figure 3.18).[284] Here C_m describes a native capacitance arising from the film itself (and the associated double layer above). It is comprised of two series capacitors C_b, the SAM capacitance in the absence of any ions within the film, and C_{dl}, the double layer capacitance, such that: $\frac{1}{C_m} = \frac{1}{C_b} + \frac{1}{C_{dl}}$. This capacitance is usually very small for thick/dense SAMs and can be resolved in the capacitive Nyquist or Bode plots at high frequency and is furthermore expected to be constant in our case (constant ionic strength). At intermediate frequencies a capacitance, as represented by the semicircle in a capacitive Nyquist plot, can be resolved, arising from the RC branch (composed of the R_t and C_t elements). This capacitance has been attributed to non-specific ionic ingress into the SAM (*i.e.* ingress of electrolyte ions or other adventitious ions).[284,318] This capacitance (C_t), as well as a capacitance that is introduced upon anion binding, called herein ion binding capacitance

C_{μ_i}, are the only capacitive components that are of relevance for the following discussions. As examined in Section 3.5.3, C_{μ_i} could be considered a special case of/contribution to C_t and both capacitances can be represented as parallel elements as shown in the yellow box in Figure 3.18. Of note is also that these capacitances each contain additional (serial) electrostatic (C_{e_i}) and quantic contributions (C_{q_i}) which are not relevant for the subsequent discussions and can also not be delineated.

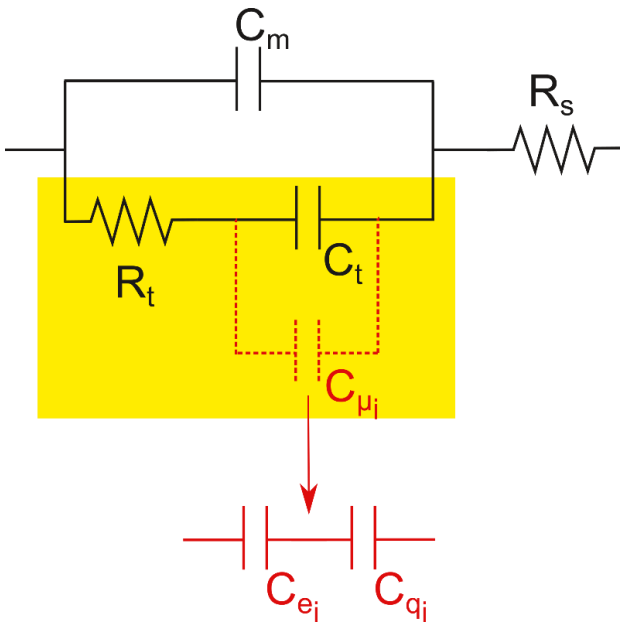


Figure 3.18. Proposed equivalent circuit diagram that describes the ion-receptive SAMs. The black elements describe a generic (non-receptive) SAM, where the C_m term contains "classical" double layer as well as film dielectric contributions. Of interest for the discussion herein, and dominating the capacitive signature of the receptive SAMs, are only the elements highlighted in yellow where C_t arises from non-specific ionic ingress. In the presence of a specifically bound (an)ion an additional ionic capacitance C_{μ_i} is introduced (red elements; comprised of classical electrostatic (C_{e_i}) and quantic contributions (C_{q_i})). The overall measured electrochemical capacitance is then given by $C_{\bar{\mu}} = C_t + C_{\mu_i}$.

In the subsequent discussion the following is defined: $C_{\bar{\mu}} = C_t + C_{\mu_i}$, where $C_{\bar{\mu}}$ denotes the overall measured electrochemical capacitance (in the preceding sections denoted only as C; Figure 3.19). The baseline level of this capacitance (in the absence of specifically bound anion) is a direct reflection of C_t, *i.e.* $C_{\bar{\mu}_0} = C_t$. The specific ionic capacitance of binding (at a

given anion concentration) can then be obtained by subtracting the baseline capacitance from the total capacitance: $C_{\mu_i}[A^-] = C_{\bar{\mu}}[A^-] - C_t = C_{\bar{\mu}}[A^-] - C_{\bar{\mu}_0}$. For simplicity, the dependence of C_{μ_i} on the anion concentration will be omitted in the following, *i.e.* $C_{\mu_i}[A^-]$ will be abbreviated as C_{μ_i}, which is however always dependent on the concentration of the target anion.

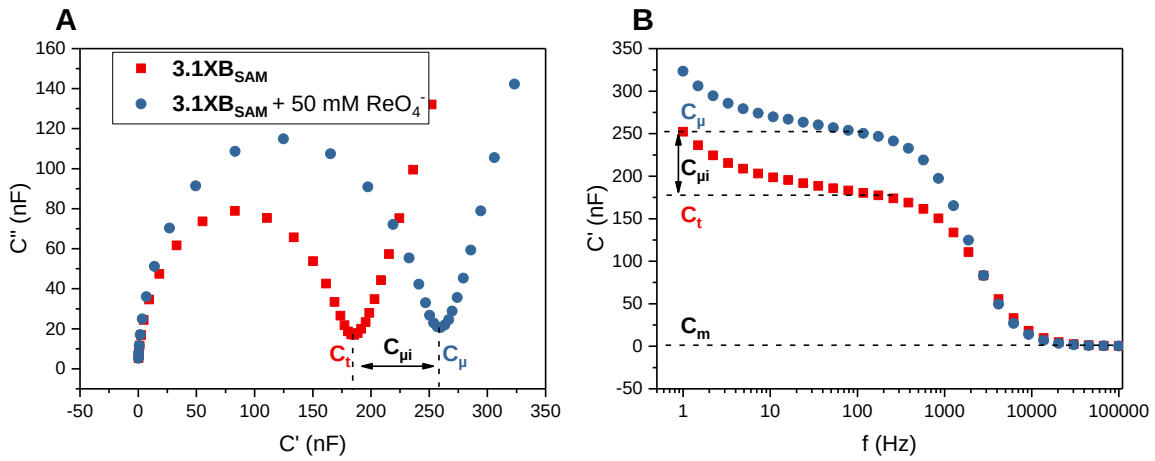


Figure 3.19. Capacitive Nyquist (A) and Bode plots (B) of **3.1XB$_{SAM}$** in the presence (red squares) and absence (blue circles) of 50 mM ReO_4^-. Explicitly shown are the baseline capacitance C_t, the overall electrochemical capacitance $C_{\bar{\mu}}$ as well as the specific ionic capacitance $C_{\mu_i} = C_{\bar{\mu}} - C_t$.

Data fitting according to the model shown in Figure 3.18 can theoretically be carried out using the circuit fitting option in different software packages. This is often very difficult and unsuccessful as a result of various factors, including: 1) Outliers or noise at high or low frequency. 2) The algorithm getting stuck in local minima, requiring careful parameter initialisation (potentially biased). 3) The non-ideal behaviour of the circuit elements.

The latter point is of importance where it has to be noted that no SAM behaves like an ideal capacitor, but is in reality more accurately modelled by a constant phase element (Q;

"leaky" capacitor). The application of the proposed equivalent circuit with ideal elements thus not completely reflects the experimental data.

Many circuit parameters can be directly extracted from the raw data circumventing explicit circuit fitting. This was carried out to extract R_s, R_t and the overall $C_{\bar{\mu}}$ to evaluate their dependence on the anion concentration. The solution resistance R_s was simply obtained as Z' at the highest measured frequency while $C_{\bar{\mu}}$ was obtained by graphical analysis of the semicircle diameter in the capacitive Nyquist plots, specifically by fitting to an ellipse function (the data is more accurately described by an ellipse than the theoretical semicircle shape).

It is important to note that changes in R_s during the course of the titrations are very small, as both assessed by the impedimetric Nyquist plots as well as conductometric measurements of the electrolyte solution. As shown in Figure A3.4, the conductivity of the solution decreases upon exchange of Cl^- for ReO_4^-, in good agreement with a lowered ionic conductivity of the larger perrhenate. Overall the change of conductivity under assay conditions is however much lower (6%) than the change in capacitive response (35%), independently proving that the change in R_s is not an important factor.

R_t can be obtained with the help of the relaxation time constant τ_t which is related to the frequency of the peak maximum in the imaginary bode plot of the capacitance (Figure 3.20):

$$\tau_t = R * C_{\bar{\mu}} = \frac{1}{f_t} \qquad \text{eqn. 3.3}$$

Whereby:

$$R = R_s + R_t \qquad \text{eqn. 3.4}$$

Thus:

$$R_t = \frac{\tau_t}{C_{\bar{\mu}}} - R_s = \frac{1}{C_{\bar{\mu}} * f_t} - R_s \qquad \text{eqn. 3.5}$$

The frequency of the peak does not always fall onto one of the measured frequencies as can be seen in Figure 3.20. In order to obtain the most accurate f_t the C'' bode plots were fitted to a 9th order polynomial, which very accurately describes the peak shape (R^2 >0.9999 in all cases). f_t was then obtained as the frequency value of the fit that was closest to zero after the first derivative of the polynomial function was calculated.

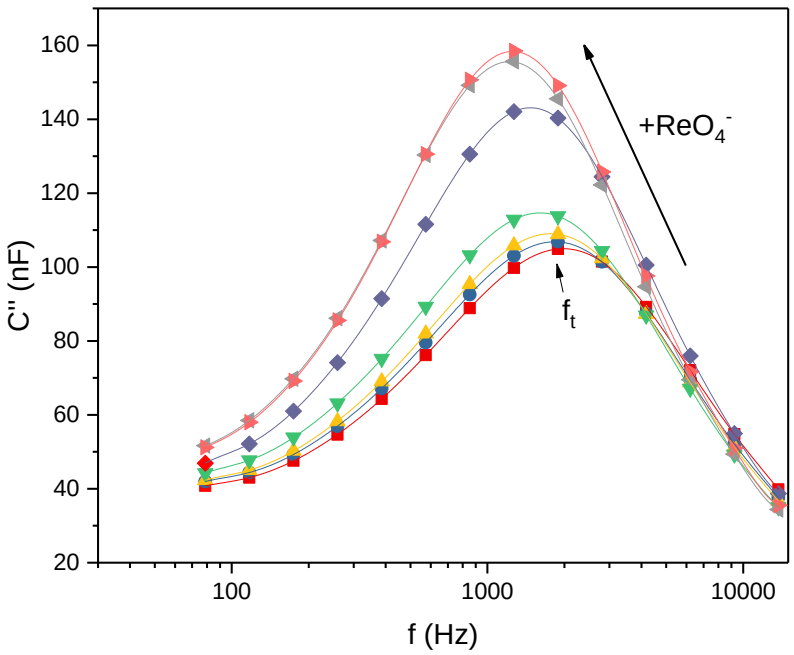


Figure 3.20. Bode plot of imaginary capacitance of **3.1XB$_{SAM}$** upon titration with ReO_4^- (limited frequency range shown, for full plot across the full frequency range see Figure 3.13). The peak frequency f_t is the inverse of the relaxation time constant $\tau_t = R * C_{\bar{\mu}}$. Solid lines represent fits to a 9th order polynomial.

As can be seen in Figure 3.21A the relaxation frequency f_t decreases significantly upon binding of ReO_4^- to **3.1XB$_{SAM}$** (also for the other anions, see Figures A3.5-A3.6), in good agreement with an increased relaxation time constant τ_t. The initial value of f_t is hereby

quite dependent on the specific electrode (see large error bars in Figure 3.21A) and the relative change of f_t (Figure 3.21B) was with approximately 35% of a similar magnitude as the change in C (see Figure 3.14A). This reveals, as detailed below, that the response of the interface is purely capacitive as $\tau_t \sim C_{\bar{\mu}}$**.** The response of f_t towards the anions can also be fitted according to the Langmuir isotherm (Figure 3.21B and Figures A3.5-A3.6), affording $K = 188\ M^{-1}$ for ReO_4^- at **3.1XB$_{SAM}$**, a similar value as obtained from fitting of the capacitance response (see Table 3.4).

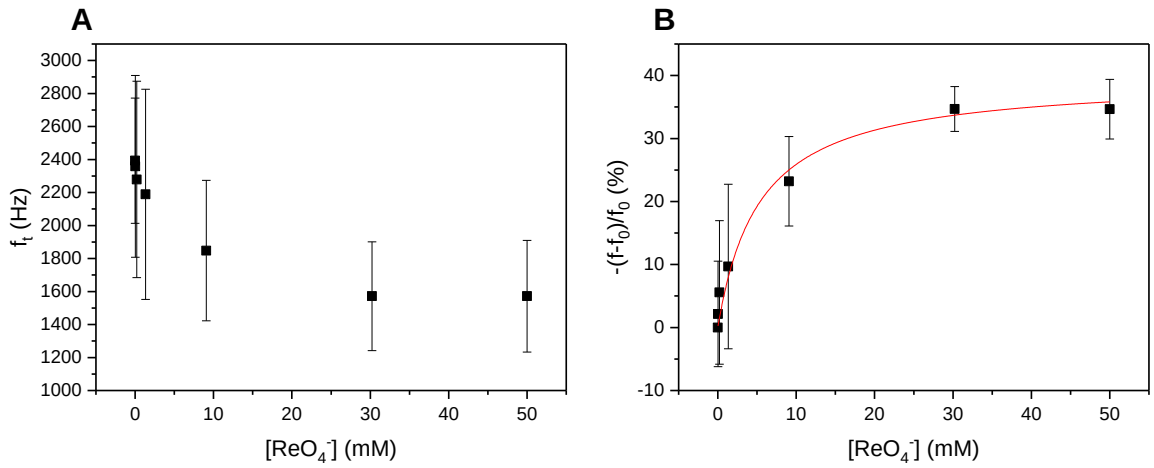


Figure 3.21. A) Absolute and B) normalised change of f_t of **3.1XB$_{SAM}$** in the presence of increasing concentrations of ReO_4^-. The solid line represents a fit to the Langmuir isotherm (eqn. 3.1). Error bars represent one standard deviation of three independent measurements.

R_t can now be calculated from f_t , $C_{\bar{\mu}}$ and R_s *via* eqn. 3.5. Importantly, no significant changes (or trends) of R_t are observed as a function of $[ReO_4^-]$ in all cases (Figure A3.7), as representatively shown in Figure 3.22. This observation highlights that the experimentally resolved changes in the capacitive Nyquist plots only reflect a change in the capacitance.

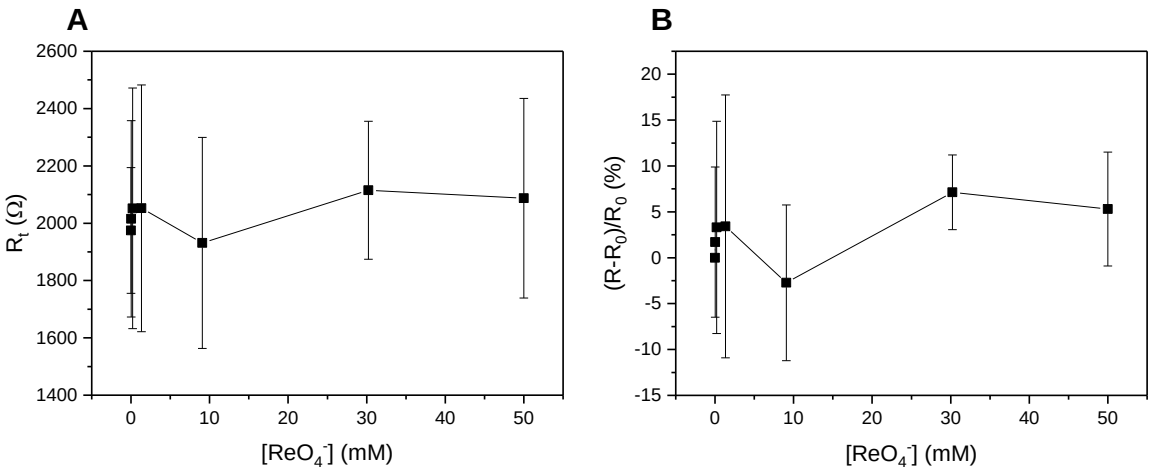


Figure 3.22. A) Absolute and B) normalised change of R_t of **3.1XB$_{SAM}$** in the presence of increasing concentrations of ReO_4^-. Error bars represent one standard deviation of three independent measurements. Solid lines are meant to guide the eye only and do not represent any fits.

The proposed $R_s(C_m[R_tC_{\overline{\mu}}])$ equivalent circuit can indeed quite accurately describe the observed capacitive signatures as shown in Figure 3.23. Here, the simulated plots were obtained according to this theoretical equivalent circuit using the manually obtained values for the individual parameters as described above. Importantly, the main feature of the plots (*i.e.* the semicircle diameter) is accurately reproduced and, again, confirms that the graphical analysis does indeed reflect the capacitance of interest. As highlighted above, minor deviations from the ideal behaviour (slight depression of the semicircle and diffusional tail) arise from the non-ideal behaviour of the circuit elements, specifically the capacitive elements, which behave more like constant phase elements with the n-value close to unity (minor deviations from an ideal capacitor).

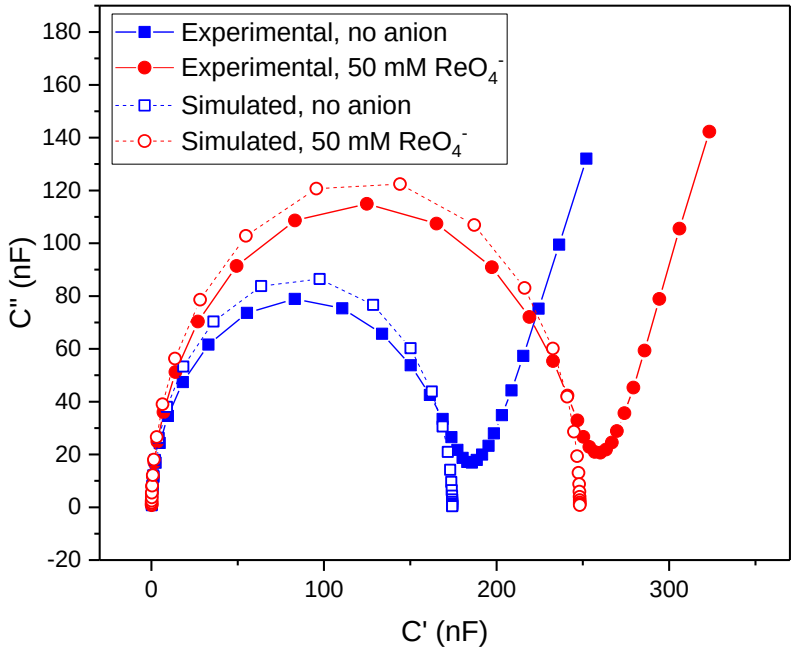


Figure 3.23. Experimental (filled symbols) and simulated (empty symbols) capacitive Nyquist plots of **3.1XB$_{SAM}$** in the presence and absence of 50 mM ReO_4^-. Simulations were carried out according to the proposed $R_s(C_m[R_tC_{\bar{\mu}}])$ equivalent circuit. The values for the individual circuit elements were obtained without explicit circuit fitting as described in the text.

3.5.2 Dielectric Model

The conclusion that the observed changes are truly reflective of an altered interfacial capacitance is important; however, it still does not provide any mechanistic detail. The simplest model that can justify an increased capacitance upon ion binding to the receptive film, as reported previously,[10,11] is based on the assumption that the SAM behaves like a simple plate capacitor (Helmholtz model), whose capacitance can be described by:

$$C = C_{\bar{\mu}} = \frac{\varepsilon_0 * \varepsilon_r * A}{d} \qquad \text{eqn. 3.6}$$

where ε_0 is the vacuum permittivity, ε_r the dielectric constant, d the thickness of the film and A the electrode area. As ε_0, d and A are constant upon anion binding (assuming no

significant film rearrangements), C is directly proportional to the dielectric constant of the SAM.

Using the ellipsometrically determined film thickness (which is expected to be constant upon anion binding), the dielectric constant ε_r of **3.1XB/HB$_{SAM}$** in the absence of specifically bound anion can be calculated *via* eqn. 3.6 as 17.6 and 19.2, respectively. These dielectric constants are significantly larger than for a simple alkyl-thiol SAMs and similar to that of acetone ($\varepsilon_r = 21$), in good agreement with a high polarity as a result of the amide-PEG appendages. The slightly lower ε_r for the XB film is most likely a reflection of the larger hydrophobicity of the iodo-triazole groups (as similarly resolved by water contact angle measurements, *vide supra*), or could indicate a diminished hydration of the central anion binding site.

Upon anion binding, the dielectric constant of the films increases, consistent with the introduction of a charged guest species and most likely a concomitant hydration of the hydrophobic core (*i.e.* binding site) of the SAM. For example, ε_r increases to 23.8 for **3.1XB$_{SAM}$** in the presence of 50 mM ReO_4^- (35%). Interestingly, these changes are much smaller for iodide and thiocyanate (≈15%), an observation that cannot be easily justified based on electrostatic/dielectric considerations. Small discrepancies might arise from a different hydration of the anion-receptor complex, but the large differences in response are more likely a reflection of the limitations of this dielectric model. This then necessitates a more fundamental consideration of the transduction mechanisms as discussed in the next section.

3.5.3 Mesoscopic Model

As highlighted above, capacitive phenomena at sensory interfaces are usually interpreted based on classical double layer effects.[319] These effects are significantly attenuated in the presence of dense SAMs and the measured capacitance is dominated by the Debye "electrostatics" of the SAM itself, largely arising from non-specific ionic ingress (C_t).[284,318] This capacitance is the baseline capacitance of the SAMs and ion binding induces an additional capacitance C_{μ_i} that acts as a parallel capacitor such that the overall electrochemical capacitance $C_{\overline{\mu}} = C_t + C_{\mu_i}$ (see also the corresponding equivalent circuit in Figure 3.18). This ion binding capacitance C_{μ_i} can be considered a special case of C_t, however it manifests itself somewhat differently as would be expected based on previous studies on C_t.[284] Specifically, the significantly different C_{μ_i} induced by different anions cannot be accounted for based on the commonly invoked Debye models, which would predicting an identical maximum response based on simple electrostatic effects.

An important consideration in deriving a more precise model that can accurately describe the response of the capacitive (an)ion receptive interfaces, is that these films are mesoscopic system. Macroscopic in two dimensions (*i.e.* along the electrode dimension) and nanoscopic in the third dimension (*i.e.* the thickness of the SAM), such mesoscopic interfaces possess properties that lie between classical and quantum mechanical features.[301,320] The energy of such systems can be described using Density Functional Theory (DFT) and solving an appropriate Hamiltonian[320] wherein the overall ion occupancy of the SAMs is dictated by statistical mechanics.

Let us first consider a single foldamer receptor within the SAM, which in the following will be referred to as a mesoscopic receptor-electrode interfacial (MREI) site. Specifically, each

MREI site comprises a mesoscopic element at which the "electrostatic" perturbation within the film associated with an incoming ionic binding event is screened by a counter electron redistribution in the underlying surface (Figure 3.24).

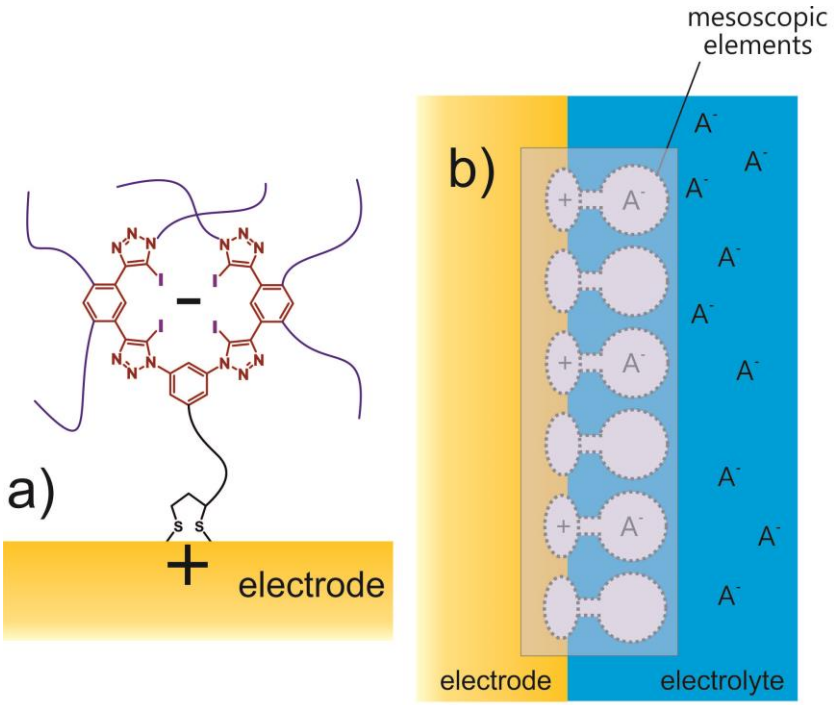


Figure 3.24. A) Schematic depiction of an occupied **3.1XB$_{SAM}$** foldamer receptor (MREI site), where the minus sign depicts a generic, bound anion. The positive sign denotes an induced mirror charge in the electrode. B) Schematic depiction of the electrode-electrolyte interface including the anion receptive mesoscopic binding sites.

At low MREI site occupancy (*i.e.* low anion concentration), this screening is primarily "classic" and Debye in origin (where the localised perturbations are exactly equivalent to classic "space charge effects" and in agreement with the previously described models (solid lines in Figure 3.25; at concentrations <≈2 mM)). However, as noted above, this classical interpretation fails to explain the very clear differences in capacitance magnitude across the different anions. Using a combined statistical mechanics and conceptual DFT[301,320] approach the magnitude of C_{μ_i} can be directly correlated to the free-energy change upon binding and

the energy used in generating the screening electron redistribution at the MREI site. Specifically, $\theta = \langle \mathcal{N}_i \rangle / N_a = (1 + e^{-\beta \Delta \mu_i})^{-1}$, where N_a is the maximum number of available MREI sites. $\langle \mathcal{N}_i \rangle$ is the average number of occupied sites as a function of $[A^-]$ and $\beta = 1/k_B T$, where k_B is the Boltzmann constant and T is the absolute temperature. $\Delta \mu_i = \mu_i - E_i$ is the variation of chemical potential of MREI sites μ_i with respect to the association energy E_i of the ions into unoccupied MREI sites within the film. The C_{μ_i} response can then be related to θ through:

$$C_{\mu_i}(\theta) = C_{\overline{\mu}}(\theta) - C_t = \beta N_a e^2 \theta \qquad \text{eqn. 3.7}$$

where e is the elementary charge. This can be rewritten as:

$$\beta N_a \left(\frac{e^2}{C_{\mu_i}} \right) = \theta^{-1} \qquad \text{eqn. 3.8}$$

The experimentally measured isotherms for **3.1XB$_{SAM}$** comply with this model where at low occupancy θ^{-1} equates to $e^{-\beta \Delta \mu_i}$ and Boltzmann statistics (and Debye screening) apply. At higher levels of site occupancy, the response of the film to incoming targets can only be described by considering a perturbation of the mesoscopic site Hamiltonian. Specifically, at higher anion concentrations Fermi-Dirac statistics apply (which are associated to Thomas-Fermi screening). These effects are specifically dependent on the MREI electron-density and thus the nature of the anion and the anion-receptor interaction.

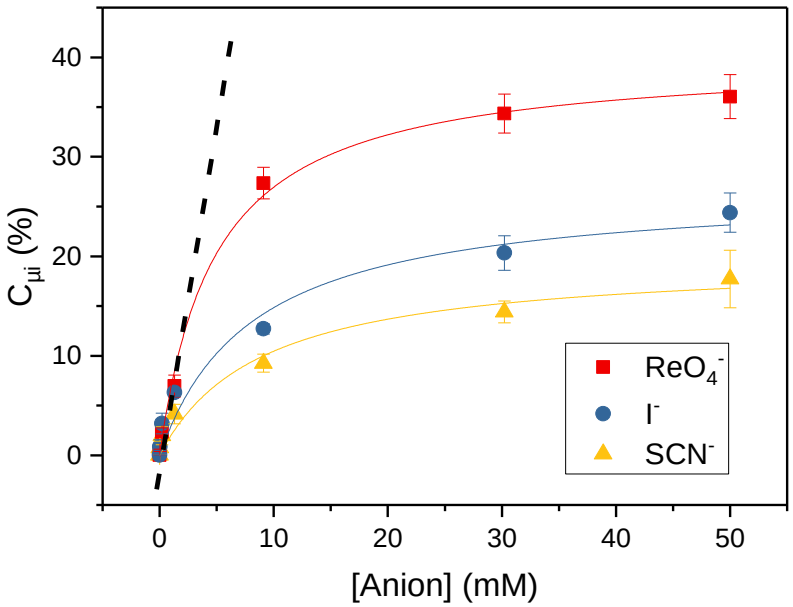


Figure 3.25. Normalised increase of $C_{\mu_i}(\%) = (C_{\bar{\mu}} - C_t)/C_t$ of **3.1XB$_{SAM}$** in the presence of increasing concentrations of ReO_4^-, I^- or SCN^-. The black dashed line represents the Debye electrostatic regime where all anions induce the same response.

Accordingly, in dilute anion solutions the anions binding at MREI sites are indistinguishable (there is no specificity and resolved C_{μ_i} values are ion independent, as Debye screening is not dependent on the electronic structure of the MREI site). Detectable target specificity is only possible at higher concentrations wherein binding induced differences in film electronic structure become notable and occupation follows $\theta = (1 + e^{-\beta\Delta\mu_i})^{-1}$ (Thomas-Fermi regime) (note that Debye effects represent an approximation of Thomas-Fermi screening at the low ionic occupancy limit).

These results not only demonstrate that anion sensing *via* non-Faradaic capacitance spectroscopy can be accurately described by the equations derived above, but also aid in designing sensors based on this novel methodology. According to the general principles of field screening, a large response would be expected when the distance between the electrode and the binding site is small and if this path is of low dielectric (in the Debye

regime). In this regime, however, all binding anions evoke the same response; differentiation is only possible in the Thomas-Fermi regime where difference between binding targets occurs through the relative degree to which they perturb the electronic structure of the MREI site. The response at higher ionic occupancy of the film is associated specifically with variations in the electronic structure of the foldamer. A Debye screening model makes no consideration of these effects and is concerned only with discrete charge (electrostatics) accumulation at the interface.

In addition, from eqn. 3.8 the actual occupancy fraction of the MREI sites can be calculated with the help of the known constants β, N_a and e^2 *via* $\theta = C_{\mu_i}/(\beta N_a e^2)$ (at low overall occupancy; a valid assumption, as can be seen below). With the help of N_a, obtained from thiol stripping, as well as C_{μ_i} at $[A^-]$ = 50 mM, θ at this concentration can be calculated as 0.053%, 0.026% and 0.036% for ReO_4^-, SCN^- and I^-, respectively. This corresponds to a receptor-to-ion ratio of 1910, 3880 and 2820, respectively, indicating that the vast majority of MREI sites remain unoccupied, even at high $[A^-]$. This confirms that the bound anions do not interact with each other and each anion binding event is independent. Furthermore, this indicates that a significantly higher response could be expected if more MREI sites could be occupied. This could be achieved, for example, by raising the potential of the ionic (electrolyte) reservoir or increasing the binding energy E_i (by designing more effective receptors).

Of note is that this model and the derived physical parameters, *i.e.* the low physical occupation of the films by anions, do not contradict the Langmuir analyses as discussed in Section 3.4.2. However, this mesoscopic model relies on the assumption that the response

can be described based on the mirror-charge considerations as discussed above. The counterintuitive observation that the vast majority of receptive sites within the film remain unoccupied, even at high anion concentration and a plateauing response, is however consistent with the fact that there is an energy penalty associated with the generation of the mirror charge that is subsequently "sensed" by the electrode. This observation can potentially explain why the binding constants at the interface are multiple orders of magnitude lower than under diffusive conditions, albeit altered enthalpic and entropic binding contributions could also play major roles in this diminished binding strength. Furthermore, this model does not account for anions that are bound within the film but whose presence is screened by, for example, counter cations from the solution or within the film and thus do not generate a "mirror charge". Considering that in pure aqueous solution the employed sodium salts should be fully dissociated and that there should be little interaction between the sodium ions and the films, this screening contribution is presumably small, but cannot be ruled out.

The equations and models described in this thesis Section (3.5.3) were largely developed by Prof. Paulo R. Bueno and are described in more detail elsewhere (including full derivations).[321]

3.6 Conclusions and Future Work

3.6.1 Conclusions

In summary, this work reports on the preparation and characterisation of novel, well defined SAMs of XB and HB foldamers for the sensing of the environmentally and biologically relevant anions ReO_4^-, I^- and SCN^-. This was achieved based on the

unprecedented use of reagentless and unamplified non-Faradaic capacitance spectroscopy for the sensing of anions. Furthermore this work presents one of the first examples of a XB receptive interface as well as the first report of the detection of the three aforementioned anions *via* any EIS-based methodology at receptive interfaces. The capacitive approach enabled not only selective and sensitive sensing of the three anions with µM LODs in pure water but is also operationally simple and circumvents the use of an integrated or doped redox transducer. This has multiple advantages, including a higher baseline stability as well as the free choice of DC bias potential, enabling sensing of redox-active species such as iodide and potentially allowing tuning of the response/binding properties *via* surface-polarisation. Through detailed analyses of the capacitive properties of the system it was shown that the response of the sensor towards interfacial anion binding is a result of an enhanced interfacial capacitance. Importantly, the physical characterisation of the interface *via* a multitude of techniques such as ellipsometry, XPS and thiol stripping showed that the both XB and HB receptive interfaces possess the same SAM structure and only differ in their central anion binding site. This, together with control experiments at non-receptive SAMs conclusively proves that the capacitive response arises from specific anion binding at the designed binding sites. Further (theoretical) analyses indicate that the description of the capacitive response *via* a standard dielectric model can only qualitatively describe the sensory behaviour but fails to account for unique signatures of the different anions. These phenomena are more accurately described by a novel DFT-derived model taking into account the mesoscopic nature of the interface. This revealed Debye type of screening at low ionic concentration (*i.e.* a classical electrostatic “mirror charge” effect), while at higher receptor occupancy Thomas-Fermi screening, which is dependent on the electronic structure of the host-guest ensemble, dominates. From this model important parameters,

such as the receptor occupancy, was shown to be very low at around 0.05%. As a result of these considerations design principles for improved capacitive ion sensors were derived, highlighting the importance of (an)ion binding strength as well as the coupling of the receptor to the underlying electrode (including dielectric as well as spatial considerations).

This capacitive methodology not only enables facile and sensitive sensing of anions, but also is, as a result of its high information density, a useful tool to investigate fundamental properties of anion-receptor interactions at interfaces, thus combining the advantages of both voltammetric and potentiometric techniques. As a flexible approach, without the need for any specific transducer, it should be extendable to the sensing of any ionic species if the appropriate anion receptor is employed. Furthermore, it is expected that this methodology can be utilised in different solvents and in sensors based on other architectures, including different electrode configurations or polymeric films.

3.6.2 Future work

3.6.2.1 Exploring Other Anion Receptive Interfaces

As speculated above, the presented methodology should be applicable in a wide range of interfacial sensors. An important step towards more real-life relevant sensors would be the investigation of receptive interfaces based on simpler receptors. For example, SAMs based on simpler analogues of **3.1XB/HB** could be envisaged where the amide-PEG appendages are removed. The omission of these water-solubilising appendages however would not allow comparative solution-phase binding studies, but would significantly simplify receptor synthesis and allow further investigation of the effect of the hydration/dielectric properties of the SAM on anion binding and signal transduction.

Another such investigation that would significantly improve our understanding of these capacitive (an)ion sensors would be a systematic study of the effect of the film structure (*e.g.* thickness, surface coverage, electrode roughness) on the capacitance response. Similarly, a detailed investigation of the effect of the distance between the electrode and the (an)ion binding site would be of interest.

3.6.2.2 Further Investigations of the Capacitive Transduction Principles

Based on the derived theoretical models a further analysis of interfacial and ion binding properties is envisaged. Specifically, it was recently demonstrated that the chemical hardness η of mesoscopic interfaces can be assessed by capacitance spectroscopy, an approach that might be extendable to the systems described herein.[322] From this a more detailed understanding of the host guest complex, for example the specific nature of the interaction and/or the softness of the (an)ions might be assessable.

Of further interest would also be a detailed analysis of capacitive ion sensing platforms in non-aqueous solvents. While for most applications sensing in pure water is sought, the investigation of host-guest interactions in other solvents is of significant fundamental interest and could provide important insights into binding phenomena at interfaces as well as more details about transduction mechanisms in capacitive sensors. Such an investigation in non-aqueous solvents is unprecedented using impedance based techniques, because standard Faradaic impedance is heavily reliant on redox probes with suitable charge transfer characteristics (such as $[Fe(CN)_6]^{3-/4-}$), which are not soluble in organic solvents.

Chapter 4

Non-Faradaic Capacitive Enantioselective Anion Sensing at Chiral SAMs

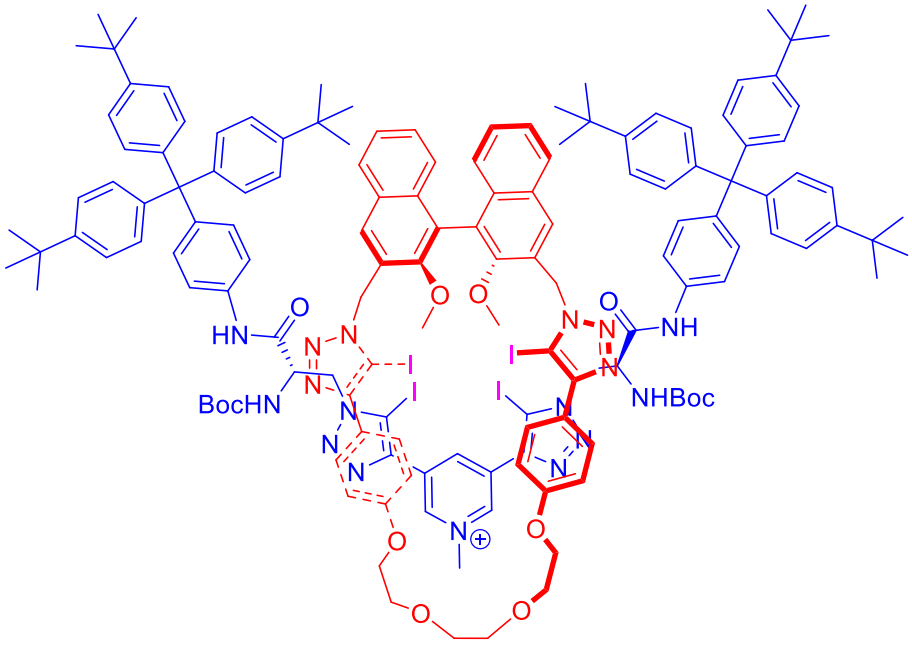
Chapter 4: Non-Faradaic Capacitive Enantioselective Anion Sensing at Chiral SAMs

4.1 Introduction and Chapter Aims

Pivotal to many biological and chemical processes, the discrimination of chiral molecules continues to receive enormous attention in various fields, from catalysis to medicine.[323-325] As such they are important analytical targets, prompting the development of sensors capable of discriminating different enantiomers/diastereomers.[326,327] Ionic chiral analytes are of particular importance, the most prominent ones being amino acids and their derivatives. Suitably designed, comparably simple synthetic receptors and sensors can serve as powerful tools to both detect these species and to elucidate the fundamental processes that govern their chiral influence. This has led to the development of a variety of synthetic chiral receptors, including anion receptors based on HB, and more recently, XB interactions.[257,277,328-331] The latter is particularly promising, not only due to often improved binding performance over analogous HB receptors (as highlighted in Chapters 1–3), but also because of enhanced enantiodiscrimination, most likely as a result of the more stringent geometric binding preferences of XB donors (*i.e.* linear binding modes are strongly preferred). For example, a chiral (*S*)-BINOL-containing XB [3]rotaxane was recently developed for the recognition and fluorescence sensing of dicarboxylates.[330] This system was capable of differentiating the geometric isomers fumarate and maleate as well as the stereoisomers (*R/S*)-*N*-Boc-glutamate with $K_S/K_R = 5.66$. Notably, the axle component alone, despite being the sole chiral component, did not show significant enantiodiscriminative binding ($K_S/K_R = 0.96$).

Another systematic study of a series of chiral XB [2]rotaxanes investigated the influence of location of the chiral component (axle, macrocycle or both) on the enantioselective binding of a range of chiral anions (*N*-Boc-leucine, *N*-Boc-tryptophan, *N*-Boc-proline and BINOL-PO_4^-).[332] While each chiral component on its own was capable of inducing some degree of enantioselectivity for all anions, the most significant binding discrimination was observed for the chiral axle + chiral macrocycle rotaxane **4.1** (Figure 4.1) as well as the rotaxane containing a chiral macrocycle and an achiral axle.

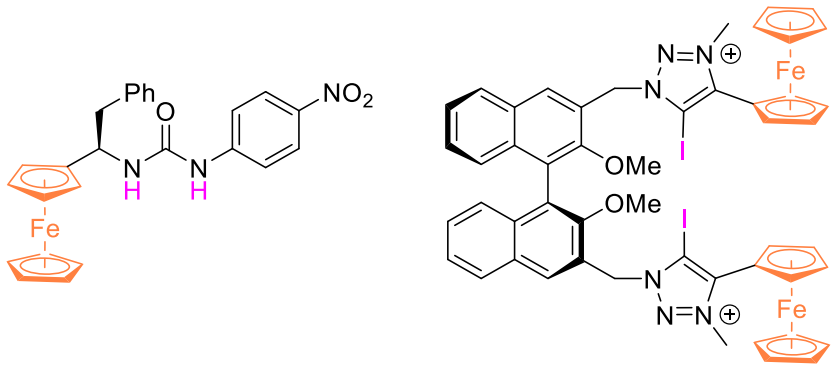
These observations highlight that a well-expressed three-dimensional chiral space around the binding site is crucial in attaining significant enantiodiscrimination. This is related to the three-point model between the receptor and analyte stipulating that at least three simultaneous attractive or repulsive (*e.g. via* steric exclusion) interactions are required to promote efficient chiral differentiation.[333]



4.1

Figure 4.1. Chemical structure of chiral XB rotaxane **4.1** containing a chiral (*S*)-BINOL macrocycle and a chiral bis((*S*)-serine iodotriazole) axle.

While these receptors are capable of chiral recognition, concomitant anion sensing remains rare, in particular *via* electrochemical methodologies. In working towards this goal the groups of Tucker and Moody attempted to prepare a Fc-based voltammetric chiral anion sensor in the early 2000s.[334] While this system was able to bind and respond to chiral carboxylates, no enantiodiscrimination was observed. The same groups later revisited and improved on their initial receptor design and investigated a range of similar chiral receptors based on Fc-urea derivatives.[335] Receptor **4.2** (Figure 4.2) was found to be able to electrochemically differentiate between the enantiomers of *N*-benzenesulfonyl proline, albeit with very small difference in response in ACN (cathodic shifts of −83 mV for the *S* enantiomer *vs.* −78 mV for *R*). An enhanced voltammetric enantioselective response was achieved more recently utilising the (*S*)-BINOL-based XB receptor **4.3**.[277] This system displayed significantly different cathodic perturbation for the enantiomers of *N*-Boc-Alanine (−57 mV *(S)*, −63 mV *(R)*), *N*-Boc-Leucine (−55 mV *(S)*, −77 mV *(R)*) and BINOL-phosphate (−55 mV *(S)*, −38 mV *(R)*) in ACN.



4.2 **4.3**

Figure 4.2. Fc-containing receptors for the enantioselective voltammetric sensing of chiral anions.

A variety of other electrochemical chiral (anion) sensors have been developed, however most rely on redox-transducers or the inherent electroactivity of the analyte.[336-340]

An exploration of non-Faradaic chiral anion sensing at synthetic XB and HB hosts, for example based on the capacitive approach introduced in Chapter 3, would be unprecedented and will be the main focus of this thesis chapter. To this end novel XB and HB chiral SAMs were designed as described below. As mentioned in previous chapters, the use of such interfaces is particularly promising for real-life applications. The non-Faradaic methodology introduced in Chapter 3 is expected to be readily extendable to various analytes, including other small, inorganic (an)ions, but also small ionic organic molecules. Enantioselective binding of chiral anions at SAMs is potentially amplified as a result of the more spatially defined 2-dimensional nanospace, and should also be reflected in a distinct sensor response towards different enantiomers. Specifically, at a given anion concentration the enantiomer which displays stronger binding should elicit a larger response. In addition, as briefly discussed in Section 3.5.3, the response magnitude of the sensor in a non-Faradaic capacitive format may also be overall dependent on anion binding strength, such that even at saturation a larger response for the stronger-binding enantiomer may be observed.

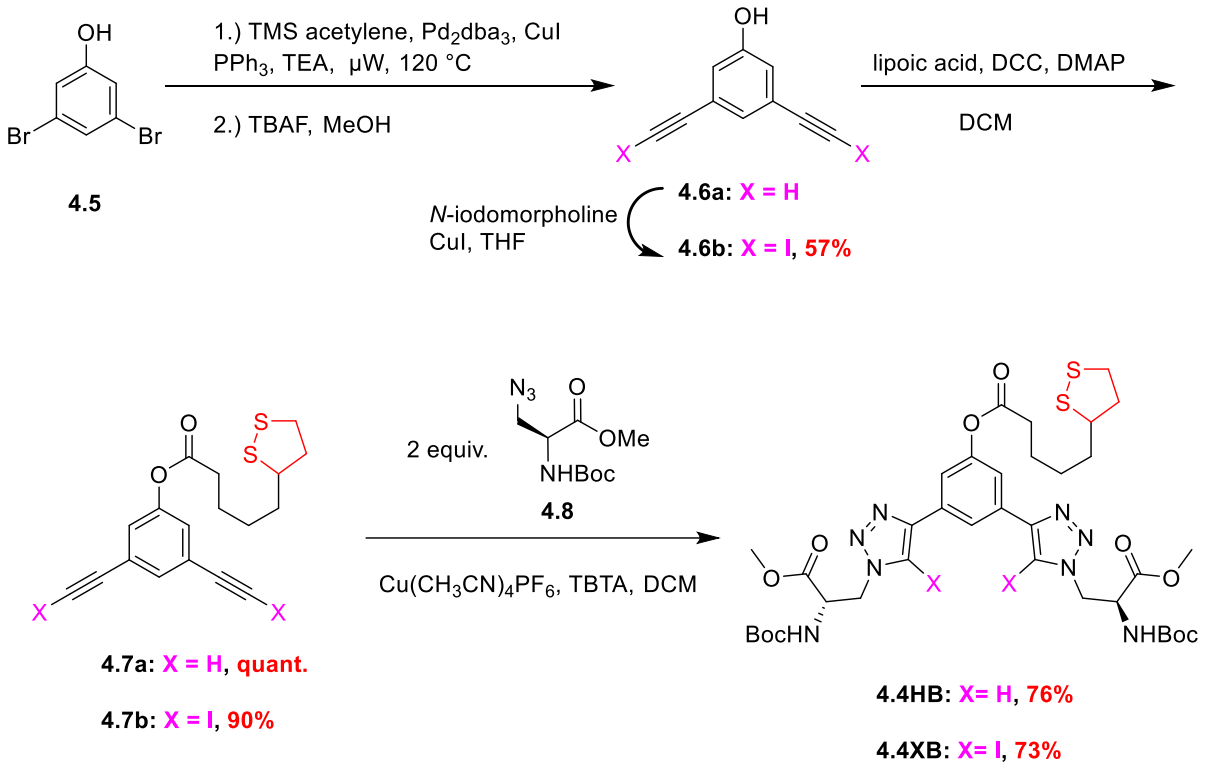
4.2 Anion Sensing at Chiral SAMs

4.2.1 Receptor Design and Synthesis

As highlighted in Section 4.1.1, interlocked chiral receptors have been shown to be capable of enantioselective binding. However, the incorporation of anchor groups to allow surface-confinement of such higher-order structures is synthetically challenging, prompting the design of simpler, acyclic chiral receptors **4.4XB/HB** (Scheme 4.1). This design incorporates a well-established 1,3-bis(iodo)triazole benzene core as well as chiral appendages derived from *N*-Boc-*L*-serine methyl ester. This chiral receptive scaffold is structurally similar to the XB axle component of the chiral rotaxane **4.1** which was shown by NMR to be capable of enantioselective anion binding (*N*-Boc-leucine, *N*-Boc-tryptophan, *N*-Boc-proline and BINOL-PO_4^-) in d_6-acetone/D_2O 98:2, with K_S/K_R of 1.30, 1.41, 1.22 and 0.82, respectively (acyclic axle alone).[332]

As an anchor group for receptor immobilisation, lipoic acid was again chosen and incorporated into the receptor architecture *via* esterification with 3,5-bis(iodo)ethynylphenol **4.6a/b** to afford the versatile synthons **4.7a/b** in good yields (quant. and 90%, respectively).

The former was obtained *via* Sonogashira coupling of commercially available 3,5-dibromo phenol **4.5**, affording **4.6a**, which was subsequently iodinated to form **4.5b**.



Scheme 4.1. Synthetic route towards chiral XB and HB anion receptors **4.4XB/HB**.

In the final step receptors **4.4XB/HB** were obtained by CuAAC reaction between the disulfide-appended bis(iodo)alkyne **4.7a/b** and the chiral azide **4.8**, which was obtained from *N*-Boc-*L*-serine methyl ester *via* mesylation and subsequent azidation.[341] This chiral group was chosen as it is charge-neutral and contains two additional N−H HB donors, which can potentially assist in anion binding. In addition, the bulky Boc-groups are expected to assist in the formation of a distinct chiral binding space and hence in the enantiodiscrimination of chiral anions. Detailed synthetic procedures as well as full characterisation of all compounds can be found in Chapter 7. The design of these receptors was carried out in collaboration with Andrew Docker who synthesised all compounds.

No solution-phase ^{1}H NMR binding studies were carried out, as these receptors are only soluble in nonpolar solvents and not in the aqueous media employed in sensing studies at the chiral SAMs (Section 4.2.3),

4.2.2 SAM Formation and Characterisation

Formation of **4.4XB/HB$_{SAM}$** (Figure 4.3) was initially carried out under identical conditions used for the immobilisation of **3.1XB/HB$_{SAM}$** (0.25 mM in ACN/H_2O 1:1, overnight immersion; see Chapter 7, Section 7.3.1). However, this protocol afforded SAMs of low molecular density as assessed by reductive thiol stripping. Specifically, the surface coverage of both **4.4XB/HB$_{SAM}$** formed under these conditions of (3.79 ± 0.38) and (2.70 ± 0.72) x 10^{-11} mol/cm^2, respectively, is low (Table 4.1, entry 1); significantly lower than that of either **2.2XB/HB$_{SAM}$** (≈10^{-10} mol/cm^2) or **3.1XB/HB$_{SAM}$** (≈8 x 10^{-11} mol/cm^2), even though the latter receptor is larger. This is problematic as it potentially allows for interactions of the analyte with the underlying gold substrate (if the film is not densely packed) or indicates that the receptors are lying flat on the surface, rather than adopting an upright conformation with an accessible binding site. The latter hypothesis was indirectly confirmed by ellipsometric measurements, revealing low film thicknesses of <1.15 nm, in agreement with a “lying down” receptor conformation.

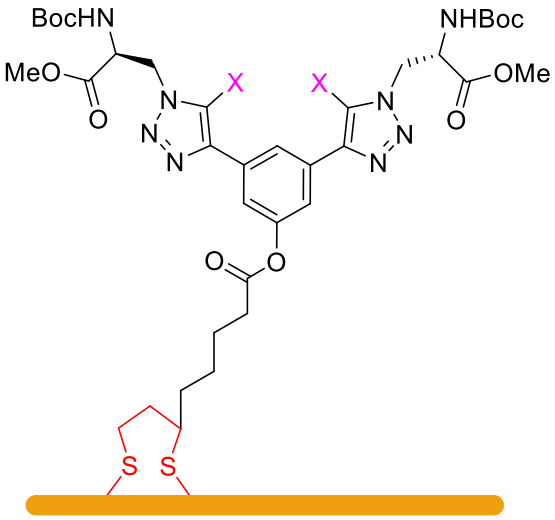


Figure 4.3. Schematic representation of **4.4XB/HB$_{SAM}$**.

In order to circumvent problems arising from this "lying down" conformation, alternative SAM formation conditions were tested, specifically different solvents as well as higher receptor concentrations. Longer immersion times were not tested, as it is both experimentally impractical and significant evaporation of volatile solvents is commonly observed, which not only changes the concentration overtime, but is also often irreproducible.

As can be seen in Table 4.1, denser films were obtained when lower polarity solvents were used. For example, in EtOH (entry 2) no significant improvement was observed, however in DCM or $CHCl_3$, an almost 10-fold increase in surface coverage of **4.4XB$_{SAM}$** was achieved (entries 3 and 4). An increase of receptor concentration to 1 mM did result in a higher surface coverage as can be seen in entries 5 and 6, however a significant improvement is only observed in DCM.

Table 4.1. Molecular surface coverages Γ and film thicknesses d of **4.4XB/HB$_{SAM}$** under different conditions of SAM formation. All errors represent on standard deviation of triplicate measurements on independent electrodes.

	Conditions for SAM formation	Γ (mol/cm^2) x 10^{-11}		d (nm)	
		4.4XB$_{SAM}$	**4.4HB$_{SAM}$**	**4.4XB$_{SAM}$**	**4.4HB$_{SAM}$**
1	0.25 mM in ACN/H_2O 1:1	3.79 ± 0.38	2.70 ± 0.72	0.47	1.15
2	0.25 mM in EtOH	2.31 ± 0.41	/	/	/
3	0.25 mM in DCM	27.8 ± 8.29	/	/	/
4	0.25 mM in $CHCl_3$	29.0 ± 11.1	/	/	/
5	1 mM in ACN	5.59 ± 1.53	/	/	/
6	1 mM in DCM	44.1 ± 5.03	34.8 ± 2.42	1.84	[a]

/ – Not conducted. a – Data quality too poor for reliable quantification.

Under these conditions (1 mM in DCM), which were subsequently used as the standard conditions, densely packed films (≈40 x 10^{-10} mol/cm^2) were obtained, with a molecular footprint of approx. 0.4 nm^2. This was also confirmed by ellipsometry where a much higher thickness of 1.84 nm for **4.4XB$_{SAM}$** was observed, indicative of the desired upright receptor conformation.

The significant improvement in the surface coverage when using less polar solvents most likely arises from diminished solvophobic effects, which in the case of the more polar solvents enhances physisorption of the hydrophobic receptors onto the bare (hydrophobic) gold electrode.

A high hydrophobicity of the receptor is not only evidenced by its poor solubility in polar solvents, but also indirectly by water contact angle measurements which confirm poorly hydrated films with contact angles of 81.8 ± 2.8° and 75.5 ± 1.2° for **4.4XB/HB$_{SAM}$**, respectively. These values are ≈15° larger than those of **2.2XB/HB$_{SAM}$**, perhaps as a result of the exposed Boc groups. In excellent agreement with observations at both **2.2XB/HB$_{SAM}$** as

well as **3.1XB/HB$_{SAM}$** is a ≈5° larger contact angle for the XB SAM in comparison to the HB film.

4.2.2.1 ATR-FTIR Spectroscopy

ATR-FTIR spectroscopy was carried out on both films **4.4XB/HB$_{SAM}$** as well as solid samples of the receptors **4.4XB/HB**, as shown in Figure 4.4. As expected, all spectra are largely identical with most of the prominent peaks observed for **4.4XB/HB** also visible in **4.4XB/HB$_{SAM}$**.

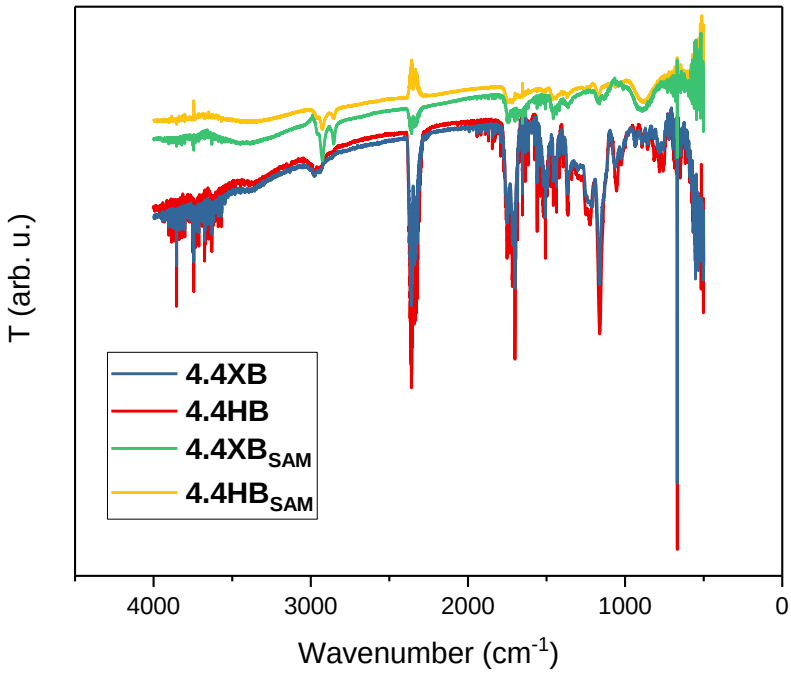


Figure 4.4. ATR-FTIR spectra of **4.4XB/HB** and **4.4XB/HB$_{SAM}$**.

Figure 4.5 depicts magnifications of relevant regions within the IR spectra, where in Figure 4.5A three peaks are observed at 2959, 2926 and 2854 cm^{-1} (centred on the film peaks). The latter two peaks can be assigned to the asymmetric and symmetric methylene

stretches, as similarly resolved in IR spectra of **2.2XB/HB$_{SAM}$**. The additional higher energy peak at 2959 cm^{-1} arises from the asymmetric stretching mode of the CH_3 groups.[285] Also of note is all three peaks are observed at slightly higher energies in the non-immobilised samples **4.4XB/HB**, as seen previously in alkane thiol SAMs.[285]

As shown in Figure 4.5B, another five peaks at 1749, 1457, 1439, 1366 and 1161 cm^{-1} are clearly resolved in the four spectra, with a variety of other peaks only prominently visible in the solid samples of **4.4XB/HB**, most notably peaks at 1713 and 1511 cm^{-1}. The peaks at 1749 and 1713 cm^{-1} are expected to arise from ester and amide functional groups, respectively.

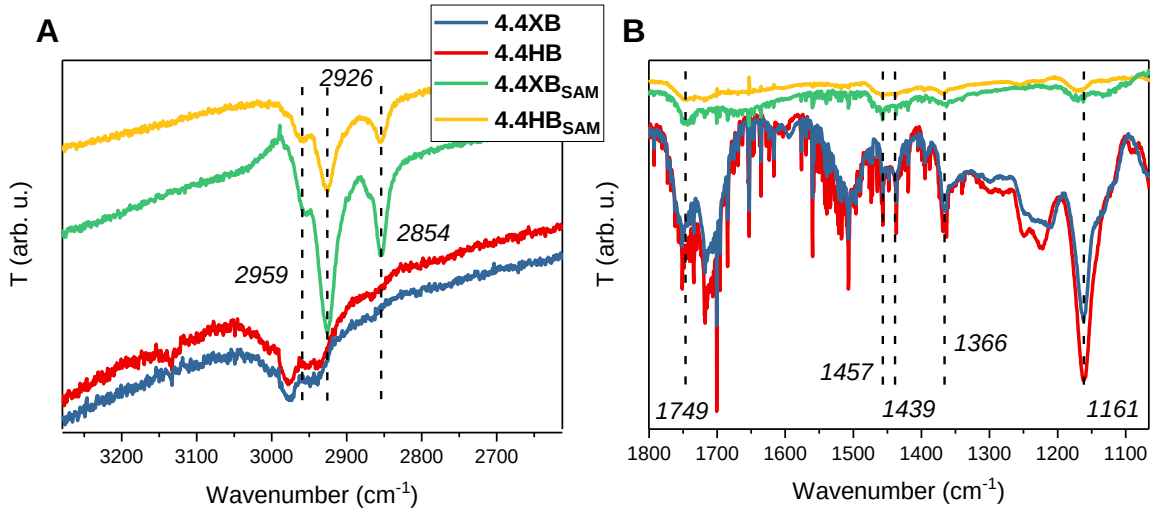


Figure 4.5. Magnification of ATR-FTIR spectra of **4.4XB/HB** and **4.4XB/HB$_{SAM}$** between 3200–2700 cm^{-1} (A) and 1600–1100 cm^{-1} (B). The dotted lines indicate peaks that can be observed in all 4 samples and are centred around the most prominent peaks (**4.4XB/HB$_{SAM}$** in A and **4.4XB/HB** in B).

4.2.2.2 X-ray Photoelectron Spectroscopy (XPS)

XPS confirms, in analogy to XPS analysis discussed in Chapters 2 and 3, the presence of C, O, N and S in both films (Figure 4.6). Only for **4.4XB$_{SAM}$** is the presence of I observed. The relative elemental composition of both films is in good agreement with the expected

composition based on the molecular formulae of the receptors (Table 4.2 and Tables A4.1−4.2).

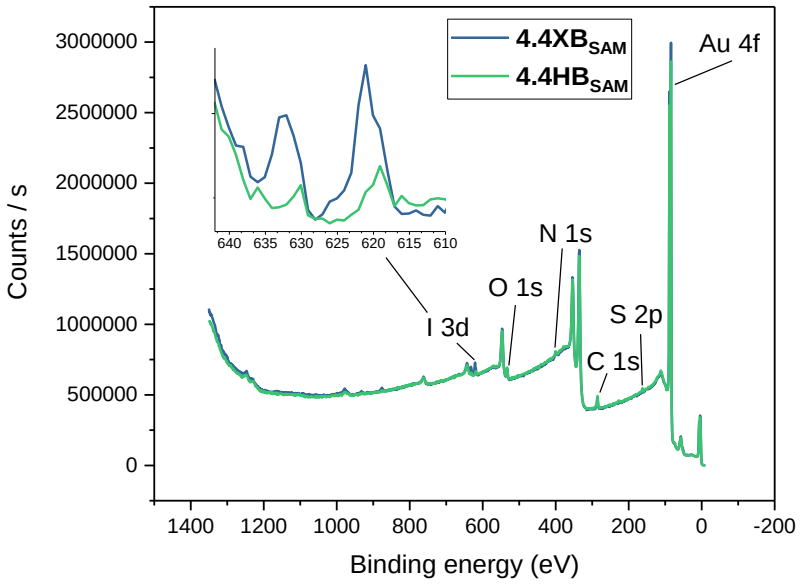


Figure 4.6. Low resolution survey XPS spectra of **4.4XB/HB$_{SAM}$** indicating identical composition of both films apart from presence of iodine for **4.4XB$_{SAM}$**. All unassigned peaks arise from other orbitals of the same elements. Inset: Magnification of I 3d region.

The high resolution scans of both films are, as expected, largely identical (Figures A4.1-A4.4) and were further analysed by peak fitting as shown for **4.4XB$_{SAM}$** in Figure 4.7.

Table 4.2. Experimental and theoretical elemental composition of **4.4XB/HB$_{SAM}$** determined by XPS. Values were normalised to I = 2 for **4.4XB$_{SAM}$** and O = 10 for **4.4HB$_{SAM}$**. Errors represent one standard deviation of triplicate measurements.

	4.4XB$_{SAM}$		**4.4HB$_{SAM}$**	
Element	**Experimental**	**Theoretical**	**Experimental**	**Theoretical**
C	44.12 ± 5.33	36	37.60 ± 0.19	36
N	11.35 ± 2.28	8	7.29 ± 0.21	8
O	9.38 ± 0.37	10	10.00 ± 0.50	10
S	1.71 ± 0.58	2	3.53 ± 0.15	2
I	2.00 ± 0.20	2	-	-

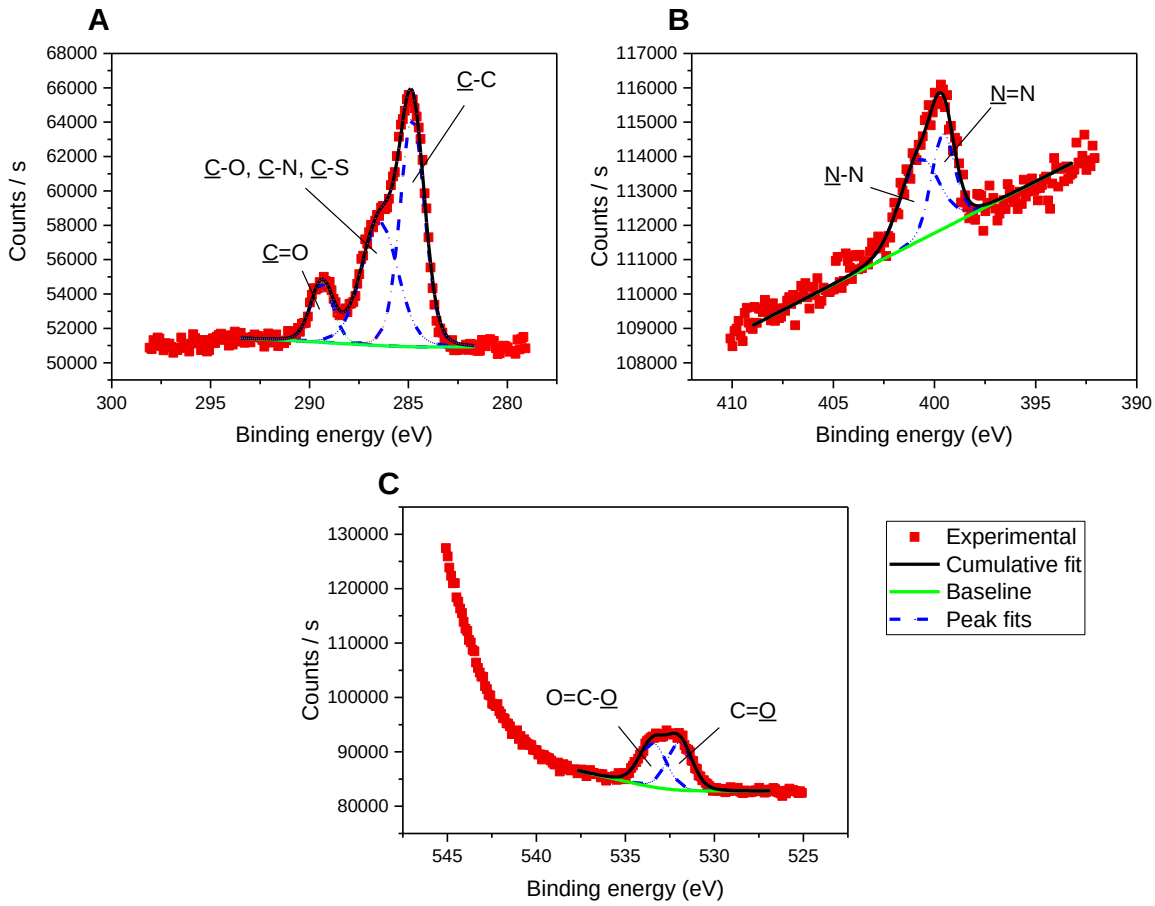


Figure 4.7. High resolution XPS spectra including peak fits of **4.4XB$_{SAM}$**. A) C 1s. B) N 1s C) O 1s.

The assignment of these peaks to specific functional groups is analogous to that of **2.2HB$_{SAM}$** (Section 2.2.3.1.1) and **3.1XB/HB$_{SAM}$** (Section 3.3.1) and will not be reiterated here. The ratio of these chemical environments is close to the theoretical expectations for the C components (Tables 4.3-4.4) for both films, however for N and O larger discrepancies are observed, presumably as a result of larger errors between repeat measurements.

Table 4.3. Peak binding energies and experimental and theoretical ratios for different chemical environments of C, N and O of **4.4XB$_{SAM}$**. Errors represent one standard deviation of triplicate measurements.

		Peak BE (eV)	Exp.	Theor.
C	C−C	284.63 ± 0.05	21.17 ± 2.43	16
	C−O, C−N, C−S	286.2 ± 0.07	15.98 ± 2.00	15
	C=O	289.11 ± 0.04	5	5
N	N=N, N−H	399.65 ± 0.10	1.00 ± 0.07	6
	N−N	400.66 ± 0.08	2	2
O	(O=C)−O	531.92 ± 0.10	5	5
	(O=C)−O	533.22 ± 0.24	16.86 ± 14.20	5

Table 4.4. Peak binding energies and experimental and theoretical ratios for different chemical environments of C, N and O of **4.4HB$_{SAM}$**. Errors represent one standard deviation of triplicate measurements.

		Peak BE (eV)	Exp.	Theor.
C	C−C	284.80 ± 0.01	18.80 ± 1.47	16
	C−O, C−N, C−S	286.43 ± 0.05	15.47 ± 0.61	15
	C=O	289.38 ± 0.01	5	5
N	N=N, N−H	399.96 ± 0.01	1.45 ± 0.85	6
	N−N	401.12 ± 0.19	2	2
O	(O=C)−O	532.12 ± 0.18	5	5
	(O=C)−O	533.51 ± 0.31	14.78 ± 18.2	5

As can be seen in Figure 4.8A, the I 3d high resolution spectrum of **4.4XB$_{SAM}$** displays two sets of doublets identical to that of **3.1XB$_{SAM}$**. As previously speculated, the lower energy peaks, denoted with an asterisk, are not expected to arise from the SAM itself but rather from an in situ generated iodine species. This is indirectly confirmed by observations at **4.4HB$_{SAM}$**, where this set of peaks is also clearly visible (albeit with smaller intensity), most likely because the irradiation of the **4.4XB$_{SAM}$** sample under high vacuum conditions generates a volatile iodine species that contaminates all samples in the chamber. A similar behaviour was reported for other iodine compounds.[342] Importantly, this confirms that the

iodotriazole moieties in both **4.4XB$_{SAM}$** as well as **3.1XB$_{SAM}$** are in identical environments, as expected based on the receptor geometries. The S 2p spectra of **4.4XB/HB$_{SAM}$** are also largely identical to those of **3.1XB/HB$_{SAM}$** and **2.2HB$_{SAM}$** (Figure 4.8B) and are, as discussed in Section 2.2.3.1.1 and Section 3.3.1, indicative of SAM formation.

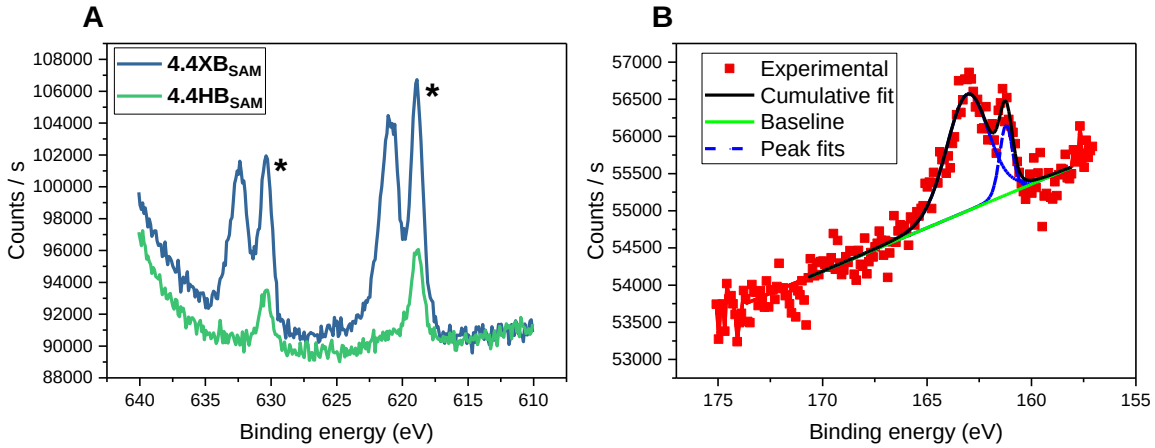


Figure 4.8. High resolution XPS spectra of **4.4XB/HB$_{SAM}$**. A) I 3d. The peaks denoted with an asterisk presumably arise from an iodine species that is generated under the measurement conditions and does not arise from the SAM. B) S 2p spectrum of **4.4XB$_{SAM}$**. The two peaks fitted in this spectrum as well as the doublets in the I 3d arise from spin orbit coupling and not from chemically different environments.

As highlighted in previous chapters, these combined surface analyses confirm the formation of chemically well-defined, densely-packed molecular films **4.4XB/HB$_{SAM}$** with a high surface coverage and an identical composition (apart from the XB/HB binding sites).

4.2.3 Chiral Anion Sensing

4.2.3.1 Capacitive Properties of 4.4XB$_{SAM}$

In analogy to studies described in Chapter 3, capacitance measurements were carried out at OCP and (initially) in the presence of NaCl as supporting electrolyte (90 mM). Due to limited

solubility of the chiral analytes in pure water, sensing studies were carried out in the presence of H_2O/ACN 9:1.

Initial chiral sensing studies were first undertaken using **4.4XB$_{SAM}$**, as this interface was expected to display both stronger binding as well as enhanced enantioselectivity (see Section 4.1.1). As can be seen in Figure 4.9 (blue circles), the capacitive signature of this film is similar to that of **3.1XB/HB$_{SAM}$**, with a well-defined semi-circular region whose diameter reports on the interfacial capacitance C.

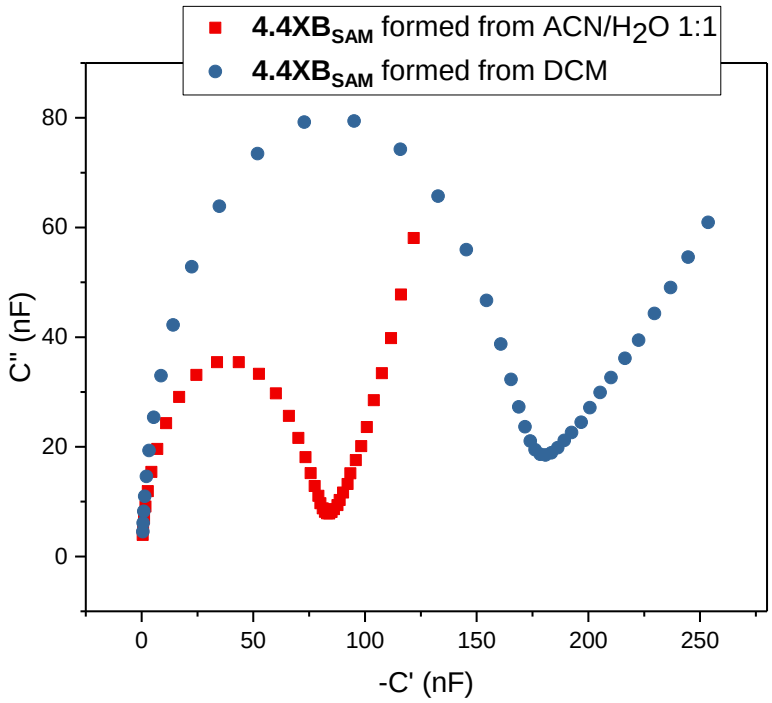


Figure 4.9. Capacitive Nyquist plots of **4.4XB$_{SAM}$** formed from DCM or ACN/H_2O measured at OCP in H_2O/ACN 9:1 containing 90 mM NaCl.

This capacitance is with 5.81 ± 0.62 µF/cm^2 slightly larger than that of **3.1XB/HB$_{SAM}$**, most likely as a result of its lower thickness. From this value and the film thickness (1.84 nm), the dielectric constant of the film can be resolved as 11.9 *via* eqn. 3.6 (Helmholtz model).

Unsurprisingly, this dielectric constant is significantly lower than that of **3.1XB/HB$_{SAM}$**, reflective of the lower polarity of the receptive film as similarly resolved by water contact angle measurements. It should however be noted that the accuracy of this value is dependent on the accuracy of the film thickness, which is here based on a single ellipsometric measurement. The film thickness of the structurally related films **5.5XB/HB$_{SAM}$** is with ≈3.5 nm significantly larger (see Section 5.2.2), indicating that the thickness of **4.4XB/HB$_{SAM}$** might actually also be somewhat larger.

In Figure 4.9 the capacitive signature of **4.4XB$_{SAM}$** formed from ACN/H_2O 1:1 (250 µM, entry 1, Table 4.1) is also shown (red squares). This capacitance is significantly lower (2.82 ± 0.26 µF/cm^2), confirming that, as speculated in Section 4.2.1, under these conditions a SAM of a different structure is formed (*i.e.* a receptor "lying down" conformation).

In the phase Bode plots (Figure 4.10) it can be seen that for all films, regardless of measurement or SAM formation conditions, a high peak phase angle of >80° is observed, indicative of near-ideal capacitive behaviour and the formation of densely packed SAMs.

As discussed in Section 4.2.1, for all subsequent sensing studies SAMs formed from DCM were used. It should be noted that, in contrast to capacitive measurements of **3.1XB/HB$_{SAM}$**, some small baseline drifts were initially observed at **4.4XB$_{SAM}$**, which were eliminated by conditioning the film in the measurement electrolyte solution for 24 h.

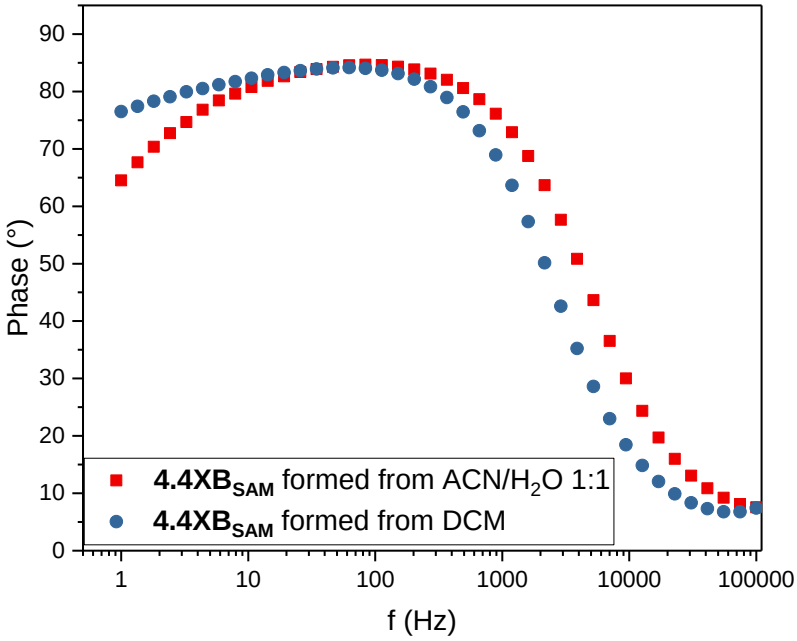
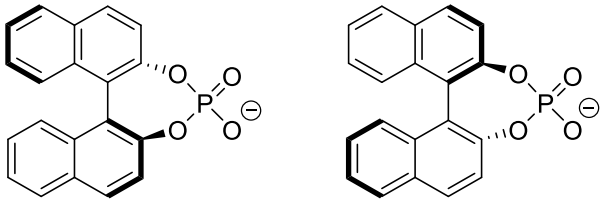


Figure 4.10. Bode plots of the phase of **4.4XB$_{SAM}$** formed from DCM or ACN/H_2O measured at OCP in H_2O/ACN 9:1 containing 90 mM NaCl.

4.2.3.2 Non-Faradaic Capacitive BINOL-PO_4^- Sensing

For initial sensing studies, (*R*)- and (*S*)-BINOL-phosphate (Figure 4.11) were chosen as chiral analytes, as enantioselective recognition of this chiral anion has been previously demonstrated at similar receptors (see Section 4.1.1). In addition, both enantiomers are often used as building blocks in enantioselective catalysis and are commercially available as BINOL-phosphoric acid from which the sodium salts of both enantiomers were prepared *via* reaction with 1 equiv. NaOH in MeOH/H_2O (Section 7.5.4).



(*S*)-BINOL-PO_4^- (*R*)-BINOL-PO_4^-

Figure 4.11. Chiral anions used herein (as sodium salts).

The addition of BINOL-PO_4^- to **4.4XB$_{SAM}$** in H_2O/ACN 9:1, 90 mM NaCl induced marked changes in the capacitance of the interface as shown in Figure 4.12. In all cases quantitative sensing studies were carried out at constant ionic strength (90 mM salt) with a maximum analyte concentration of 45 mM.

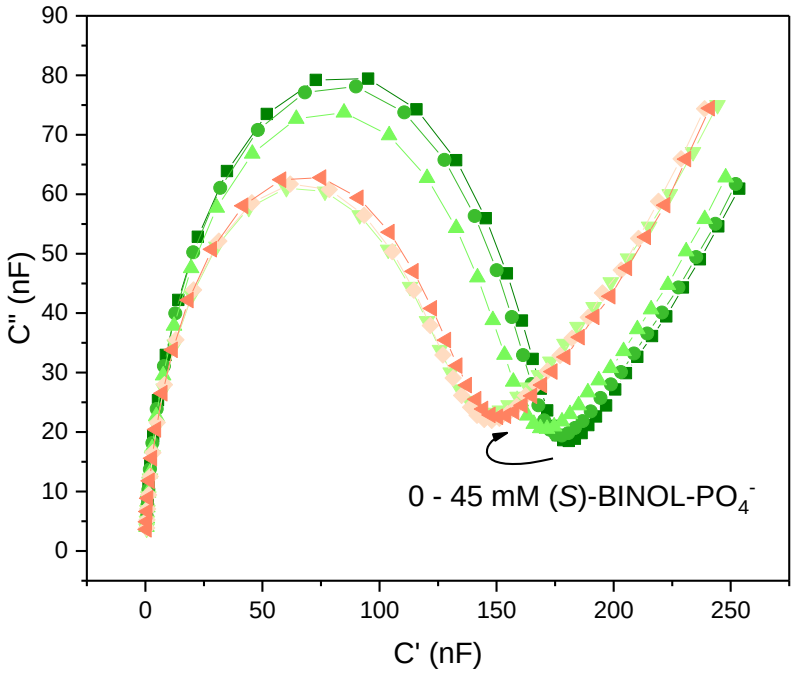


Figure 4.12. Capacitive Nyquist plots of **4.4XB$_{SAM}$** in H_2O/ACN 9:1, 90 mM NaCl in the presence of increasing concentrations of (*S*)-BINOL-PO_4^-. The response is not monotonic; at concentrations above ≈5 mM (*S*)-BINOL-PO_4^- the capacitance slightly increases again as indicated by the curly arrow.

Interestingly, these capacitive changes are significantly different to those observed at **3.1XB/HB$_{SAM}$**. Specifically, binding of either enantiomer of BINOL-PO_4^- induces a decrease in the capacitance rather than the expected increase. From a dielectric point-of-view this observation can be justified by the large non-polar BINOL backbone which will overall lower the dielectric of the film and overcompensates any dielectric increase induced by the anionic phosphate group. As the binding site is projected into the solution, BINOL-PO_4^- binding will not only displace a significant amount of water from/above the binding site

(thereby indirectly lowering the dielectric of the SAM), but will also result in an overall thicker SAM (see Helmholtz model, eqn. 3.6).

Another unexpected observation is that the response of **4.4XB$_{SAM}$** in H_2O/ACN 9:1 (90 mM NaCl) towards both enantiomers of BINOL-PO_4^- is non-monotonic, as can be seen in Figure 4.13. An initial maximum response of ≈−20% is attained at an analyte concentration of approx. 5 mM, whereafter a small, but significant and reproducible decrease of the response (*i.e.* a shift back towards a higher capacitance) is observed.

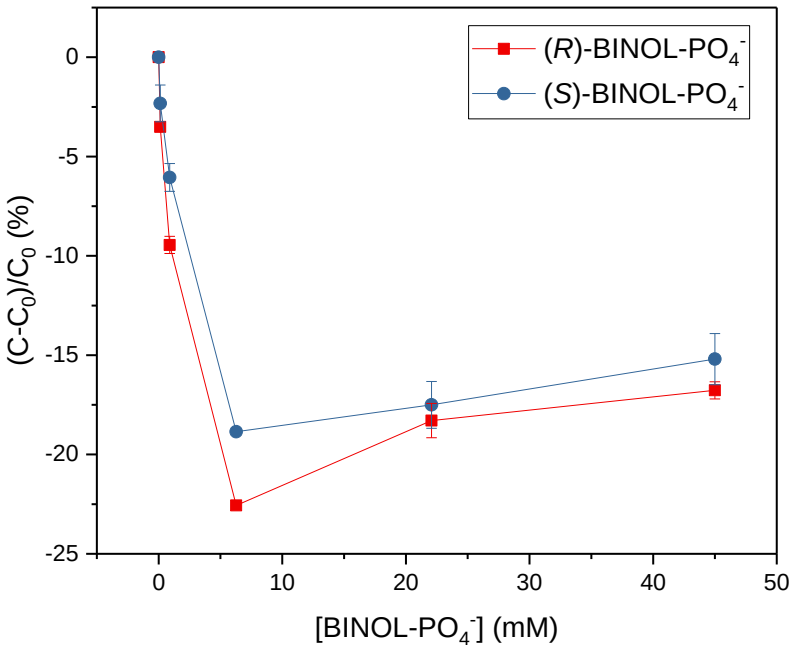


Figure 4.13. Normalised capacitance change of **4.4XB$_{SAM}$** in H_2O/ACN 9:1, 90 mM NaCl in the presence of increasing concentrations of (*R*/*S*)-BINOL-PO_4^-. Error bars represent one standard deviation of two independent measurements. Solid lines do not represent fits and are meant to guide the eye only.

This indicates that at higher concentrations non-specific effects can induce changes in the response, which may be related to, for example, film rearrangement or a significant change in the nature of the electrolyte at higher concentrations of BINOL-PO_4^-. This could be related to the significantly larger size and/or hydrophobicity of the BINOL-PO_4^- anion in

comparison to Cl^-. As mentioned above, this analyte possesses limited solubility and may, as a result of its amphiphilic nature, form micelles in water.

In order to investigate whether the electrolyte plays a role in the non-monotonic sensor response a different electrolyte, $NaPF_6$, was tested in the same solvent system. The baseline capacitance of **4.4XB$_{SAM}$** in this electrolyte is somewhat larger (6.83 ± 0.82 µF/cm^2), however not significantly more so than in 90 mM NaCl (see also Figure 4.17).

As shown in Figure 4.14, the response of the sensor towards BINOL-PO_4^- in this electrolyte is largely identical to that in the presence of Cl^- as electrolyte. Again a response of up to ≈−20% was observed, with the notable difference that the response is overall monotonic. This indicates that the non-idealities observed in the presence of NaCl arise from the Cl^- counter anion, presumably not as a result of any specific interaction with the receptive SAM, but rather as during the course of the titration this hydrophilic anion is replaced with the significantly more hydrophobic BINOL-PO_4^-. This significant change in the nature of the electrolyte (*e.g.* its overall solvent structure) could, for example, induce minor changes in the structure of the SAM and its capacitance.

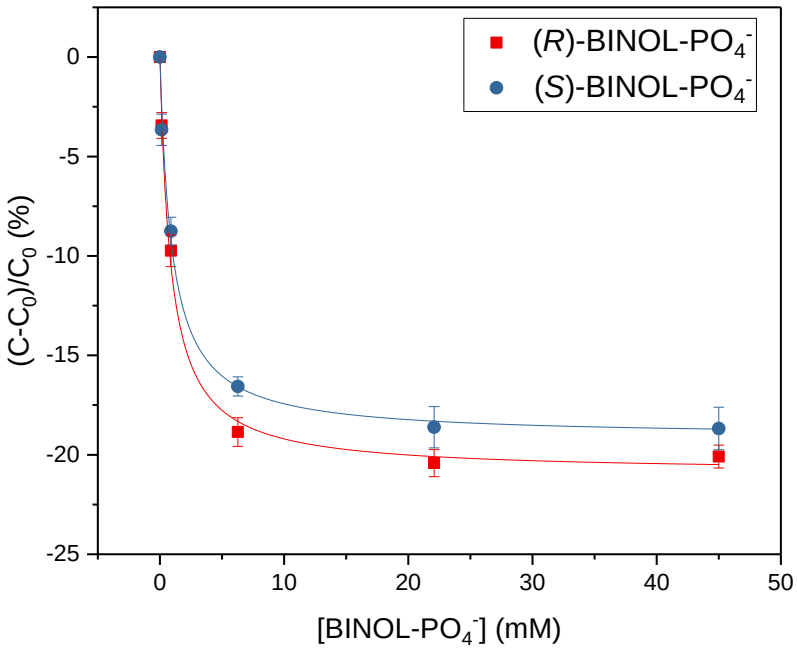


Figure 4.14. Normalised capacitance change of **4.4XB$_{SAM}$** in H_2O/ACN 9:1, 90 mM $NaPF_6$ in the presence of increasing concentrations of (*R*/*S*)-BINOL-PO_4^-. Error bars represent one standard deviation of four independent measurements. Solid lines represent fits according to the Langmuir model (eqn. 3.1).

As the response in the presence of the $NaPF_6$ electrolyte is monotonic the isotherms can be fitted according to the Langmuir model as also applied in Chapters 2 and 3 (eqn. 3.1), affording binding constants and theoretical maximum responses (ΔC_{max}) as shown in Table 4.5.

Table 4.5. Binding constants and maximum capacitive response ΔC_{max} of **4.4XB$_{SAM}$** upon exposure to (*R*/*S*)-BINOL-PO_4^- in H_2O/ACN 9:1, 90 mM $NaPF_6$. The data was obtained by isotherm fitting (averaged response of four independent measurements, Figure 4.14) according to the Langmuir adsorption model (eqn. 3.1, with error weighting). Errors represent standard errors from fitting.

	K (M^{-1})	**ΔC_{max} (%)**	**R^2**
(*R*)-BINOL-PO_4^-	1135 ± 147	-20.9 ± 0.4	0.9924
(*S*)-BINOL-PO_4^-	1044 ± 155	-19.1 ± 0.6	0.9860

From this quantitative analysis, as well as the qualitative analysis of the binding isotherms in both electrolyte media, a modest binding and response preference for the *R*-enantiomer of BINOL-PO_4^- is observed. The enantioselectivity of K_R/K_S as well as $\Delta C_{max,\ R}/\ \Delta C_{max,\ S}$ are with 1.087 and 1.094 almost identical and show the same preference for the *R*-enantiomer as seen previously at a similar receptor, which however displayed a slightly larger enantiodiscrimination ($K_R/K_S = 1.22$ see Section 4.2.1).[332] This preference can also be tentatively inferred from a simple schematic analysis of a proposed binding mode between the receptive SAM and the BINOL-PO_4^- anion, shown in Figure 4.15. Specifically, the steric clash highlighted between the *S*-enantiomeric BINOL anion and the receptor may decrease the binding strength. However, this is a very simplistic analysis that is not necessarily reflective of the true binding geometries.

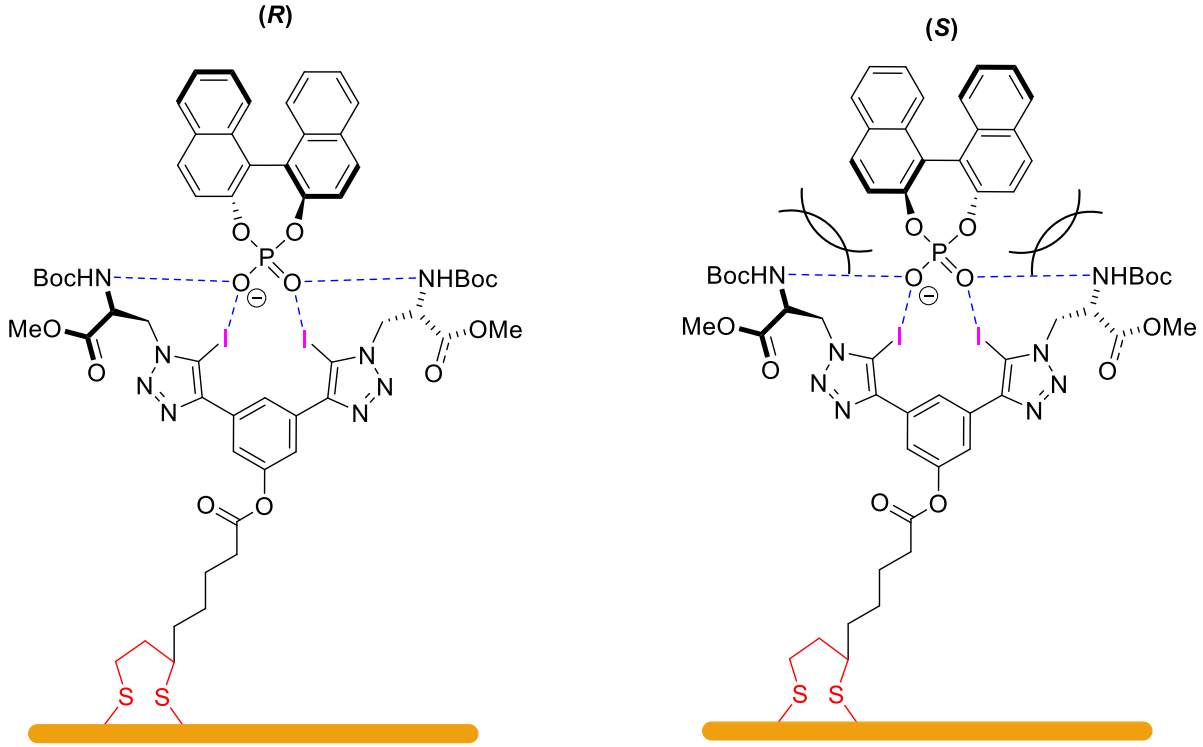


Figure 4.15. Schematic representation of binding of (*R*)-BINOL-PO_4^- (left) and (*S*)-BINOL-PO_4^- to **4.4XB$_{SAM}$**. From this simplistic depiction a binding preference for the *R*-enantiomer may be inferred. The blue dashed lines represent possible XB and HB interactions between the receptor and the anion.

Another crucial consideration is that the small enantiodiscrimination, albeit reproducible across independent experiments, is most likely not statistically significant (as there a multitude of experimental errors that could affect the results) or could arise from various non-specific effects.

Importantly, the interaction of BINOL-PO_4^- with the SAM is reversible, as the initial capacitance can be almost fully recovered upon washing of the interface. However, this does not directly prove that anion binding (exclusively) occurs *via* specific XB/HB interactions as depicted in Figure 4.15. For example, hydrophobic interactions between the analyte and the poorly hydrated interface certainly play a role in this system as indicated by preliminary experiments in less competitive, less polar aqueous/organic solvent mixtures.

Specifically, quantitative binding studies of (*R*)-BINOL-PO_4^- were carried out in H_2O/ACN 7:3 and H_2O/ACN 1:1 (containing 90 mM $NaPF_6$), as shown in Figure 4.16. In both cases the response is with ≈5% (at 45 mM analyte) ≈4x lower than that under standard conditions (*i.e.* in H_2O/ACN 9:1). Additionally, binding strength is with 137 and 19 M^{-1}, respectively, significantly smaller than in H_2O/ACN 9:1. This counter-intuitive observation indicates that binding of the phosphate headgroup *via* XB/HB interactions is not the main driving force for BINOL-PO_4^- binding, as this interaction would be expected to be amplified in less competitive aqueous mixtures. Rather, in these solvents the hydrophobic effect is reduced, indicating that physisorption is an important driving force.

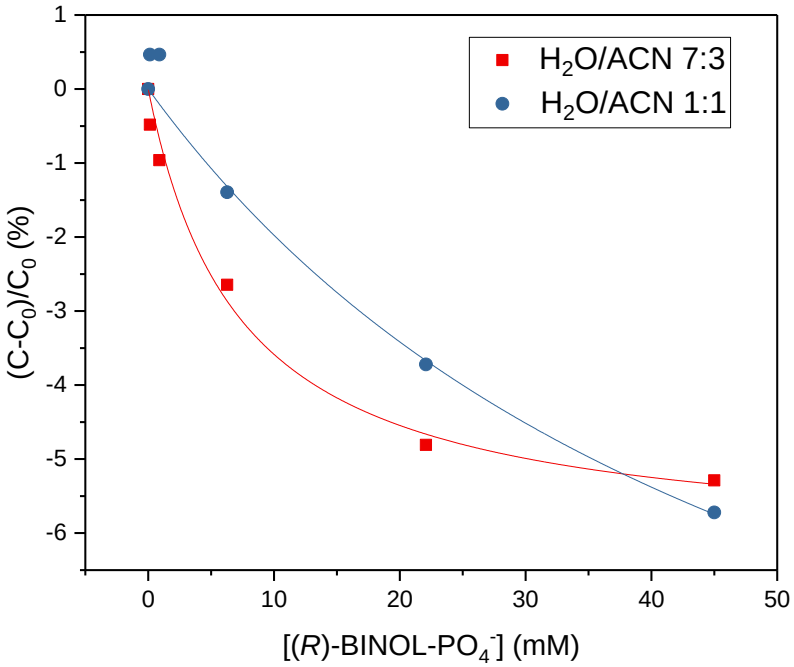


Figure 4.16. Capacitive response of **4.4XB$_{SAM}$** upon titration with (*R*)-BINOL-PO$_4^-$ in H$_2$O/ACN 7:3 (red squares) or H$_2$O/ACN 1:1 (blue circles), containing 90 mM NaPF$_6$. Solid lines represent fits according to the Langmuir model (eqn. 3.1).

The response of **4.4XB$_{SAM}$** towards BINOL-PO$_4^-$ can also be analysed by monitoring the relative change of the real or imaginary capacitance C'/C'' at other frequencies, rather than only considering the film capacitance (*i.e.* semicircle diameter). For example, herein the relative change of the apex of the semicircular region of the capacitive Nyquist plot (C''_{apex}) is larger than that of C (Figure 4.17 and 4.18). This is to say the overall shape of the capacitive Nyquist plot changes upon BINOL-PO$_4^-$ binding such that there is a disproportionately larger response of C''_{apex}, which corresponds to a "flattening" of the semicircular region. Monitoring the change of C''_{apex} is thus somewhat more sensitive towards BINOL-PO$_4^-$ than the standard analysis of C.

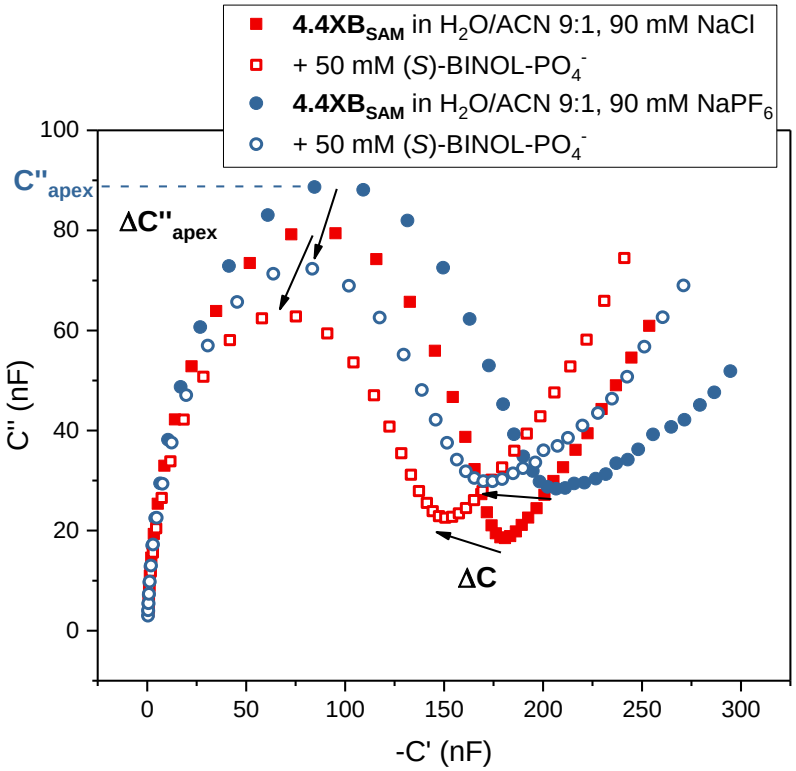


Figure 4.17. Capacitive Nyquist plots of **4.4XB$_{SAM}$** in H_2O/ACN 9:1, 90 mM $NaPF_6$ (blue circles) or 90 mM NaCl (red squares) in the presence (empty symbols) and absence (filled symbols) of 45 mM (*S*)-BINOL-PO_4^-. Black arrows indicate the changes in semicircle diameter (ΔC) and semicircle height ($\Delta C''_{apex}$) upon anion binding, whereby the latter is slightly larger in both electrolytes.

As shown in Figure 4.17, this behaviour is most significant in the presence of NaCl electrolyte, however it is also observed in the presence of $NaPF_6$. In the presence of the latter, the maximum normalised response is with $\Delta C''_{apex,\ max} = -22.5\%$ and −21.1% (for the *R*- and *S*-enantiomers, respectively), ≈10% larger in comparison to ΔC_{max} (Table 4.6).

Interestingly, the enantiodiscrimination of the binding strength is $K_R/K_S = 1.18$ which is slightly larger in this analysis of C''_{apex}. However, taking into account the large errors, this observation is most likely not statistically significant. This behaviour, where $\Delta C''_{apex}$ is larger than ΔC is only observed here and not at **3.1XB/HB$_{SAM}$**, indicating that the capacitive transduction principles at **4.4XB$_{SAM}$** are different than those established in Chapter 3,

Section 3.5). This is also supported by the analysis of the capacitive Bode plots as discussed in more detail in the appendix (Figure A4.5).

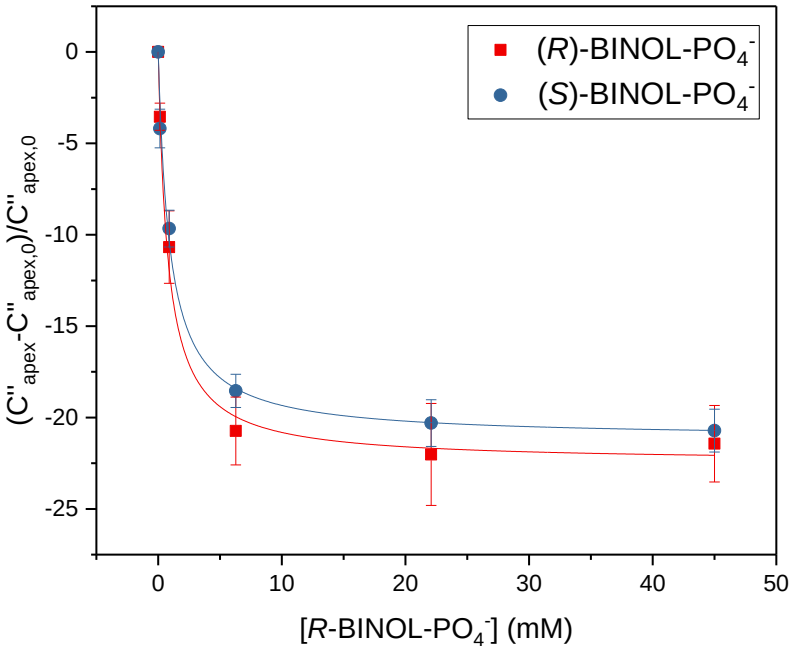


Figure 4.18. Normalised change of C''_{apex} of **4.4XB$_{SAM}$** in H_2O/ACN 9:1, 90 mM $NaPF_6$ in the presence of increasing concentrations of (*R*/*S*)-BINOL-PO_4^-. Error bars represent one standard deviation of four independent measurements. Solid lines represent fits according to the Langmuir model (eqn. 3.1).

Table 4.6. Binding constants and maximum value of C''_{apex} response ($\Delta C''_{apex,\ max}$) of **4.4XB$_{SAM}$** upon exposure to (*R*/*S*)-BINOL-PO_4^- in H_2O/ACN 9:1, 90 mM $NaPF_6$. The data was obtained by isotherm fitting (averaged response of four independent measurements, Figure 4.18) according to the Langmuir adsorption isotherm (eqn. 3.1, with error weighting). Errors represent standard errors from fitting.

	K (M^{-1})	**$\Delta C''_{apex,\ max}$ (%)**	**R^2**
(*R*)-BINOL-PO_4^-	1273 ± 141	-22.5 ± 0.7	0.9933
(*S*)-BINOL-PO_4^-	1076 ± 173	-21.1 ± 0.7	0.9831

4.2.3.3 Faradaic Impedimetric BINOL-PO_4^- Sensing

In order to gain further insights into the BINOL-PO_4^- binding and sensing properties of **4.4XB$_{SAM}$**, Faradaic impedimetric studies were carried out in the presence of 9 mM ferri/ferrocyanide ($[Fe(CN)_6]^{3-/4-}$, in H_2O/ACN 9:1, 90 mM NaCl at OCP). The impedimetric properties of the film in the presence of this solution-phase redox amplifier are shown in Figure 4.19 (red squares), where a high charge-transfer resistance (R_{ct}) of >400 kΩ is observed. This is in excellent agreement with a blocking, densely packed film and also confirmed by negligible Faradaic activity in CV (Figure A4.6).

The addition of BINOL-PO_4^- induces significant changes in the impedimetric signature of the film as shown in Figure 4.19. Specifically, analyte binding induces additional impediments to charge-transfer as expected from both steric and electrostatic repulsion of the negatively charged redox probe upon interfacial anion binding. The change in impedance upon addition of BINOL-PO_4^- is very significant, much more so than the capacitive response.

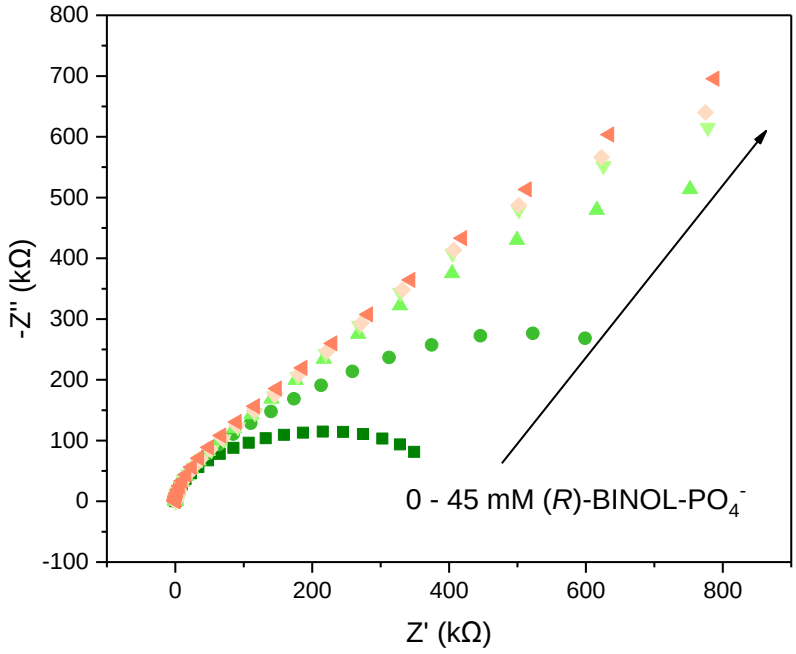


Figure 4.19. Impedimetric Nyquist plots of **4.4XB$_{SAM}$** in H_2O/ACN 9:1, 9 mM $[Fe(CN)_6]^{3-/4-}$, 90 mM NaCl in the presence of increasing concentrations of (*R*)-BINOL-PO_4^-. Measurements were conducted at OCP over a frequency range of 100 kHz – 0.1 Hz.

As discussed in Section 3.1, the R_{ct} of the interface is most commonly used as the transducer for an interfacial binding event and is assessed by either equivalent circuit fitting or by graphical analysis of the semicircle diameter in the impedimetric Nyquist plot. The former is for various reasons not viable here (as discussed in more detail in Section 3.5.1). The latter is also difficult as even the initial impedimetric signature of the film is only pseudo-semicircular and anion binding induces further distortions that cannot be analysed graphically.

Hence, in these preliminary studies the modulus of the impedance $|Z|$ at the lowest measured frequency (0.1 Hz) was utilised to investigate anion binding (Figure 4.20).

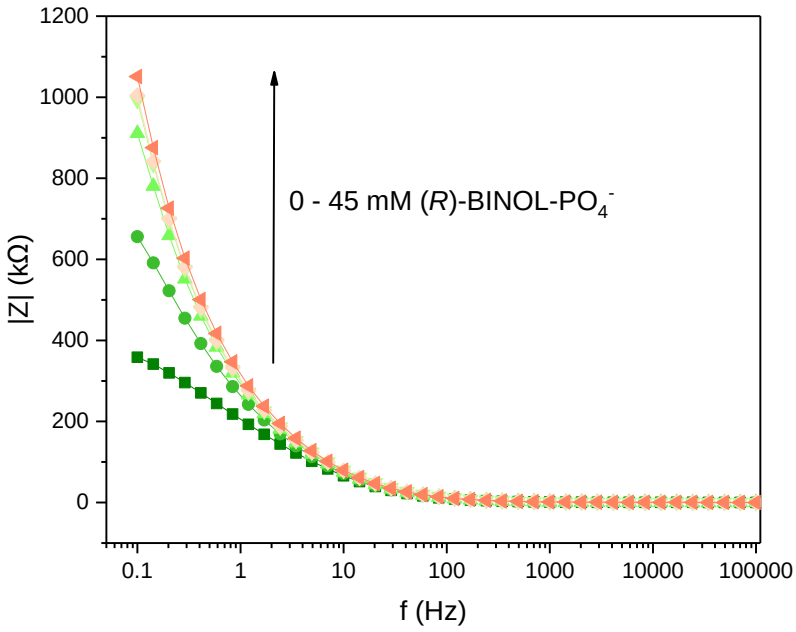


Figure 4.20. Bode plots of the impedance modulus $|Z|$ of **4.4XB$_{SAM}$** in H_2O/ACN 9:1, 9 mM $[Fe(CN)_6]^{3-/4-}$, 90 mM NaCl in the presence of increasing concentrations of (*R*)-BINOL-PO_4^-.

From this analysis binding isotherms for (*R*/*S*)-BINOL-PO_4^- to two independent films each were obtained and fitted as shown in Figure 4.21. Notably, the overall magnitude of the

response ($\Delta|Z|$) is significantly different for all electrodes, with no clear preference for either enantiomer (*R*-preference at electrode 1 and *S*-preference at electrode 2).

However, a more in depth analysis of the parameters obtained from fitting to the Langmuir model reveals that in all cases the *R*-enantiomer displays stronger binding (27% larger at electrode 1 and 356% larger at electrode 2; Table 4.7), even if the magnitude of the response is not always larger.

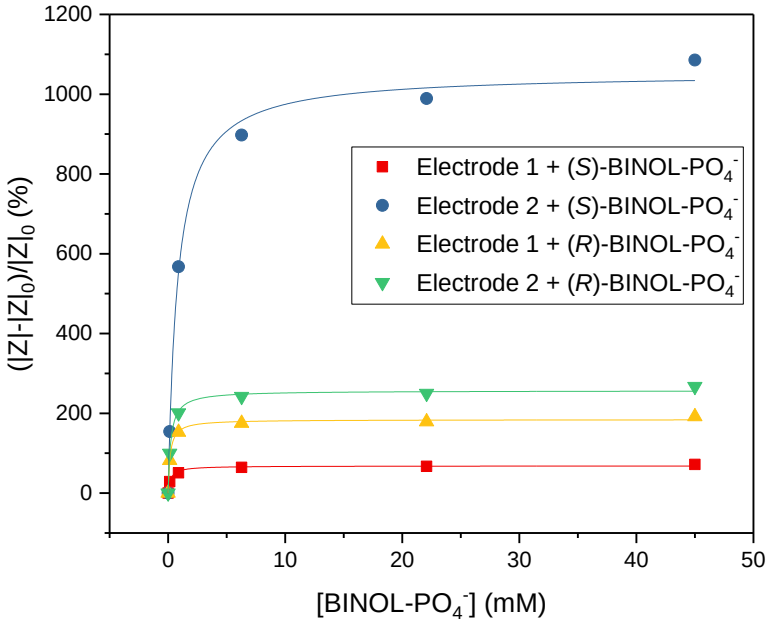


Figure 4.21. Normalised response of impedance modulus $|Z|$ of **4.4XB$_{SAM}$** (on two independent electrodes) in H_2O/ACN 9:1, 9 mM $[Fe(CN)_6]^{3-/4-}$, 90 mM NaCl in the presence of increasing concentrations of (*R/S*)-BINOL-PO_4^-. Solid lines represent fits according to the Langmuir model (eqn. 3.1).

This is of course insufficient proof for clear enantiodiscrimination, but supports the picture that was developed from the capacitive analysis discussed in Section 4.2.3.2, specifically, all analyses point towards a stronger binding of the *R*-enantiomer with a concomitant larger response (in almost all cases). Additionally, as a result of a significantly larger relative

response in the impedimetric format (*i.e.* $\Delta|Z| > \Delta C$) a higher sensitivity may be attained (if baseline stability is comparable).

Table 4.7. Binding constants and maximum impedimetric response $\Delta|Z|_{max}$ of **4.4XB$_{SAM}$** upon exposure to (*R/S*)-BINOL-PO_4^- in H_2O/ACN 9:1, 9 mM $[Fe(CN)_6]^{3-/4-}$, 90 mM NaCl. The data was obtained by data fitting (Figure 4.21) according to the Langmuir model (eqn. 3.1).

		K (M^{-1})	$\Delta\|Z\|_{max}$ (%)	R^2
Electrode 1	**(*R*)-BINOL-PO_4^-**	5820	184	0.9954
	(*S*)-BINOL-PO_4^-	4580	68.2	0.9875
Electrode 2	**(*R*)-BINOL-PO_4^-**	4450	257	0.9951
	(*S*)-BINOL-PO_4^-	1250	1050	0.9942

It is also noteworthy that the response in the impedimetric format displays a strictly monotonic, Langmuir behaviour, despite these experiments being conducted in NaCl electrolyte, where in the non-Faradaic capacitive formats deviations were observed (Figure 4.13). This provides clear evidence for the hypothesis that the capacitive behaviour at high analyte concentrations is indeed related to electrolyte effects and not to binding phenomena.

Interestingly, even in the Faradaic impedimetric format, capacitive Nyquist plots (Figure A4.7) are responsive to BINOL-PO_4^- binding, with an overall response that is qualitatively (non-monotonic behaviour) and quantitatively (response of ≈−20%) very similar to that obtained in the absence of the redox probe (Figure 4.22). Importantly, this indicates that simultaneous analysis of impedimetric and capacitive properties is feasible, as long as the redox probe does not interfere with the binding or otherwise restricts the analysis (as is the case here).

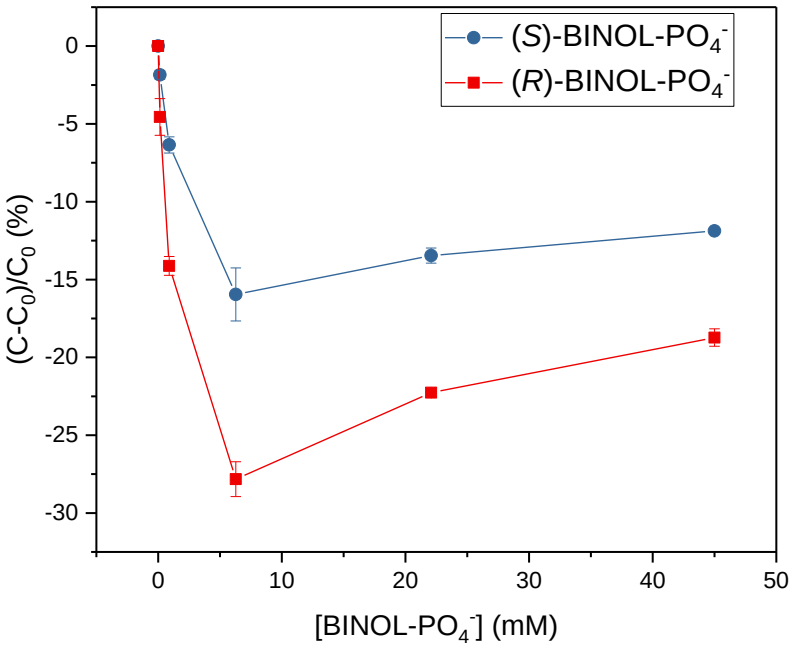


Figure 4.22. Normalised capacitance change of **4.4XB$_{SAM}$** in H_2O/ACN 9:1, 9 mM $[Fe(CN)_6]^{3-/4-}$, 90 mM NaCl in the presence of increasing concentrations of (*R*/*S*)-BINOL-PO_4^-. Error bars represent one standard deviation of two independent measurements. Solid lines do not represent fits and are meant to guide the eye only.

In the presence of the redox probe the capacitive enantiodiscrimination seems to be significantly larger than in previous capacitive analyses, however this data is only an average of two independent measurements.

4.3 Conclusions and Future Work

4.3.1 Conclusions

In this proof-of-concept work, chiral anion sensing at XB and HB anion receptive SAMs was investigated. In an optimised protocol, the immobilisation of novel chiral disulfide functionalised bis(amide-(iodo)triazole) receptors **4.4XB/HB** afforded densely packed SAMs of well-defined molecular composition as investigated by XPS, ATR-IR and water contact

angle measurements. Preliminary chiral sensing studies at **4.4XB$_{SAM}$** were carried out with (*R/S*)-BINOL-PO_4^- in various aqueous electrolyte systems using both non-Faradaic capacitive as well as Faradaic impedimetric methodologies. In the former an interesting, yet unusual sensor response, characterised by a decrease in the interfacial capacitance, was observed, which was also shown to be dependent on the nature of the electrolyte, most likely as a result of non-specific electrolyte effects. The latter was carried out in the presence of ferri/ferrocyanide as a solution-phase redox probe, enabling sensitive BINOL-PO_4^- sensing *via* monitoring of the impedance of the interface.

In all cases a modest binding/response preference for the *R*-enantiomer was observed (typically ≈10%), in good agreement with expectations based on simplistic steric considerations as well as previous reports. However, this relatively small degree of enantiodiscrimination is close to experimental errors and cannot be unequivocally assigned to arise from a specific enantioselective XB/HB binding interaction, yet.

In order to unambiguously prove that the chiral interfaces are indeed capable of enantioselective binding and sensing of chiral anions further studies need to be carried out as discussed in the following section.

4.3.2 Future work

4.3.2.1 Further Exploration of Impedimetric/Capacitive Chiral Anion Sensing

Pivotal to gaining a more detailed understanding of binding processes at the chiral SAM interfaces is the compilation of larger/repeat data sets, both by repetition of experiments described above as well as a further exploration of solvent/electrolyte conditions on chiral anion binding and sensing. This also includes the investigation of a larger range of chiral

analytes, such as those depicted in Figure 4.23, in particular biologically relevant anionic amino acids (or derivatives thereof), and other chiral organic anions such as mandelate or 10-camphorsulfonate.

Preliminary investigations with *L*-Boc-phenylalanine indicate a response with **4.4XB$_{SAM}$**, highlighting, as expected, the capability to extend this methodology to the sensing of a range of (chiral) analytes.

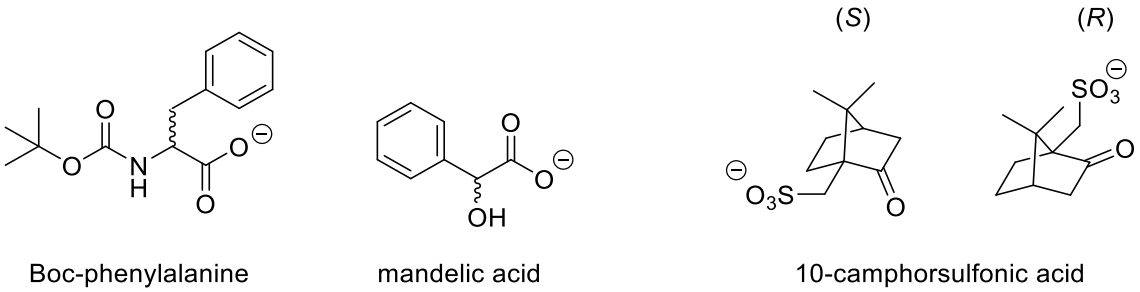


Figure 4.23. Chemical structures of chiral anions for further chiral sensing studies.

Also important are equivalent sensing experiments at the HB film, as any resolved differences in response and/or enantiodiscrimination between **4.4XB$_{SAM}$** and **4.4HB$_{SAM}$** would directly confirm the influence of the XB/HB triazole binding sites on anion binding and thus serve as important control experiments (see Section 3.4.2).

4.3.2.2 Anion Sensing at Dicationic Chiral SAMs

The cleavage of the Boc protecting groups of **4.4XB/HB$_{SAM}$** can be used to generate amine containing receptors, which, depending on pH, can exist in a doubly protonated, dicationic state in which anion recognition should be enhanced through additional electrostatic and HB interactions. In particular the binding and sensing of divalent anions such as sulfate or

phosphate(s) might be enabled. As the lipoic acid appendages of the free **4.4XB/HB** readily polymerise in the presence of acid, solution-phase Boc deprotection and subsequent immobilisation of the deprotected receptors is not feasible. However, Boc protection of **4.4XB/HB$_{SAM}$** under acidic conditions should be viable thereby forming **4.9XB/HB$_{SAM}$** as shown in Figure 4.24. This *in situ* generated interface can then be used for further anion sensing studies.

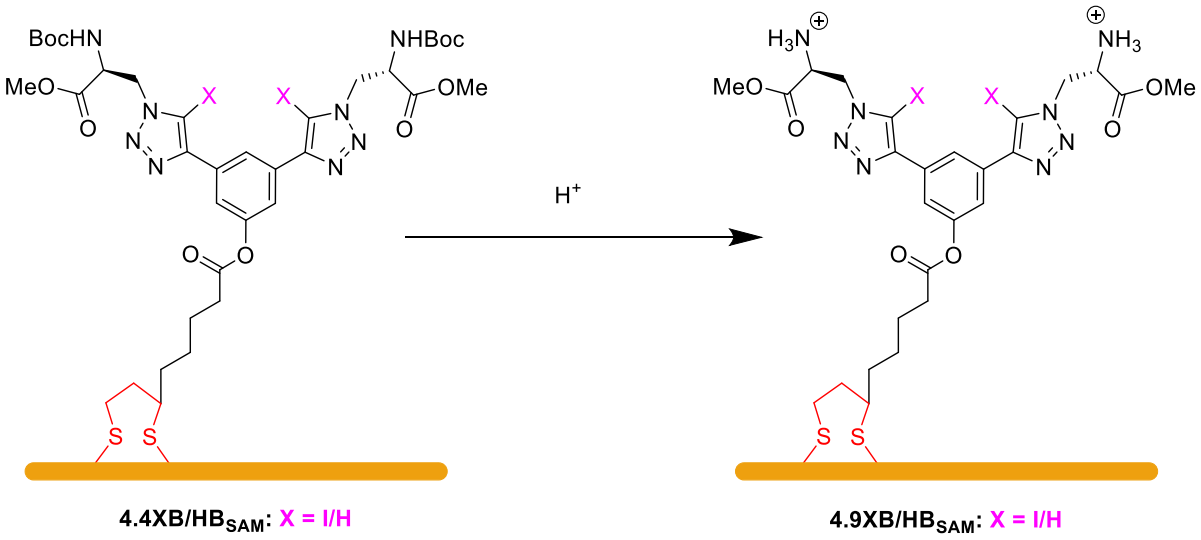
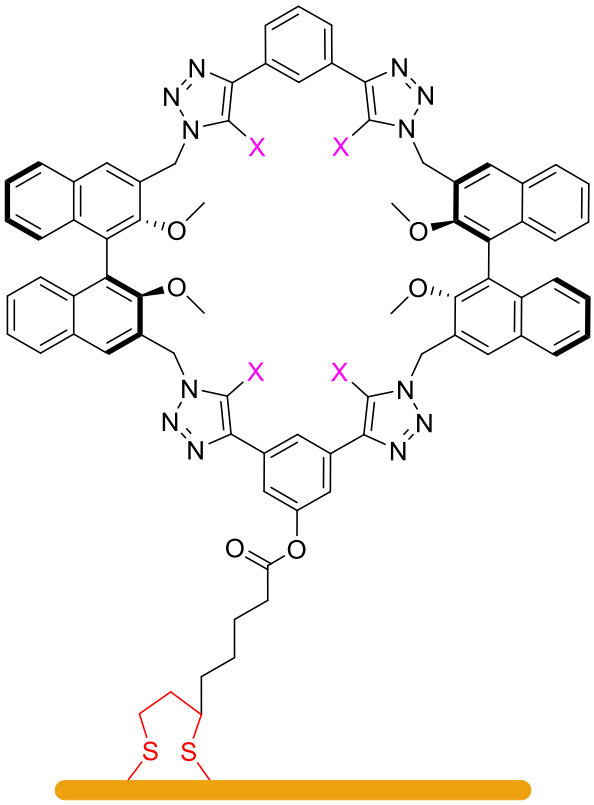


Figure 4.24. Formation of a dicationic chiral anion receptive interface *via* Boc deprotection.

4.3.2.3 More Advanced Chiral Receptors

The design of the **4.4XB/HB** scaffold allows for simple alteration of the receptor. For example, a wide range of chiral azides may be reacted with **4.7a/b** to afford similar disulfide-appended receptors with varying chiral groups, such as those based on sugars or BINOL. Similarly, this platform can also be extended to macrocyclic or perhaps even mechanically interlocked receptors. An example of a synthetically accessible chiral

macrocyclic receptor, **4.10XB/HB$_{SAM}$** (Figure 4.25), may be assembled *via* CuAAC reaction of (*S*)-BINOL-bisazide with suitable bis(iodo)alkynes.



4.10XB/HB$_{SAM}$: X = I/H

Figure 4.25. Macrocyclic (*S*)-BINOL-based chiral receptive interface.

Chapter 5

Non-Faradaic Capacitive Ion-Pair Sensing at Heteroditopic SAMs

Chapter 5: Non-Faradaic Capacitive Ion-Pair Sensing at Heteroditopic SAMs

5.1 Introduction

5.1.1 Ion-Pair Recognition

The simultaneous recognition of both a cation and an anion as an ion-pair has gained increasing attention in supramolecular chemistry with potential applications across a wide range of fields including, salt extraction and solubilisation,[343] membrane transport[344] as well as sensing.[345-347] This has led to the development of a range of acyclic, macrocyclic and interlocked heteroditopic receptors containing both discrete anion and cation binding sites most commonly, crown ethers (or derivatives thereof) and N−H HB donors such as amines, amides and ureas, respectively.[345-347] Saliently, the dual recognition of oppositely charged ions often benefits from enhanced binding strength and/or selectivities in comparison to simple monotopic receptors for either ion alone. This is often attributed to cooperative and/or allosteric effects which can be controlled by a careful consideration of the spatial arrangement of both cation and anion binding sites within suitable receptor scaffolds. For example, if both binding sites are in close proximity, a salt is typically bound as a contact ion-pair, while a larger distance between the receptive units induces formation of receptor-bound solvent-separated ion-pairs. In both cases binding of either ion is typically enhanced when its corresponding counter ion is bound to the receptor, both as a result of direct electrostatic binding enhancement as well as reduced energetic penalties of the separation of the ion-pair which can significantly impede ion binding at simple anion or cation

receptors. All of these effects are strongly dependent on the distance between the binding sites, their geometry as well as the solvent in which the recognition takes place.

In spite of these advantages the use of ion-pair receptors is comparatively underdeveloped, undoubtedly as a result of their more challenging syntheses but in particular because ion-pair binding studies are inherently more complex. For example, a significant impediment in the study of ion-pair binding processes is the presence of various (competing) equilibria as depicted in Figure 5.1. Not only are all binding equilibria of importance (cation, anion and ion-pair binding, each associated with distinct equilibrium constants), but also the competing salt recombination. The latter often experimentally manifests as the precipitation of the salt, especially in non-polar solvent media.[346]

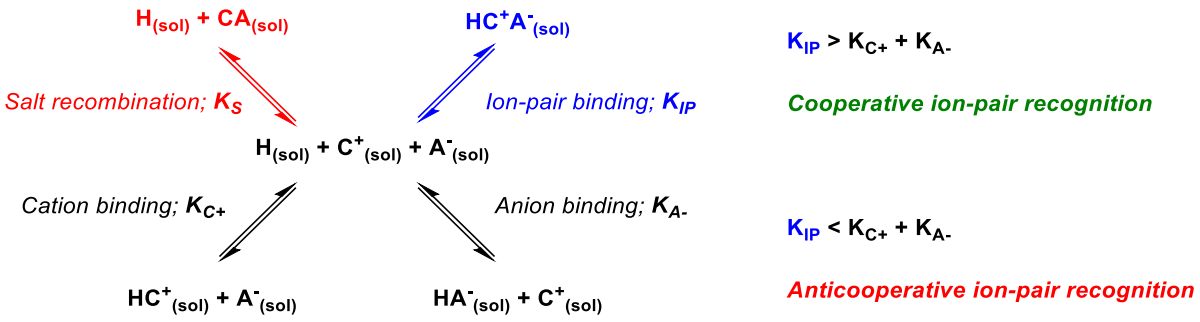
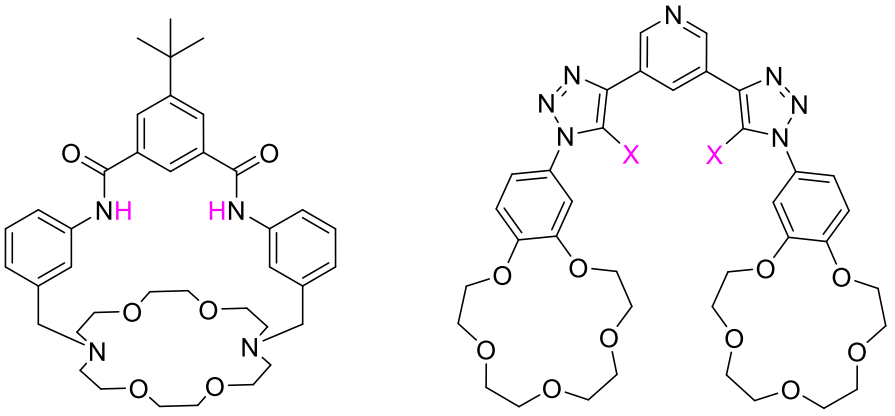


Figure 5.1. Schematic depiction of important equilibria in ion-pair recognition at a heteroditopic host (H). Highlighted in blue is the desired ion-pair binding equilibrium while the competing, undesired salt recombination is shown in red. The "(sol)" subscript refers to solvation of the depicted species.

Nevertheless, a range of potent ion-pair receptors have been developed, where in many cases cooperative binding is observed and desired. An early example is cryptand **5.1**, reported by Smith and co-workers in 2001, combining isophthalamide anion binding sites with a diazacrown ether cation binding site (Figure 5.2).[348] This receptor displayed significant cooperative effects in the binding of NaCl and in particular KCl as a contact ion-

pair in DMSO. For example, Cl^- binding to **5.1●K^+** is enhanced ≈40 fold in comparison to the free **5.1**, while K^+ binding to **5.1●Cl^-** is enhanced ≈10 fold. In less polar solvent mixtures this enhancement was even more pronounced, highlighting the role of electrostatic interactions in the cooperative binding behaviour of this ditopic receptor.



5.1

5.2HB: X = H

5.2XB: X = I

5.2ChB: X = TeMe

Figure 5.2. Examples of heteroditopic ion-pair receptors based on crown-ether and amide or triazole motifs.

More recently ion-pair receptors based on XB and ChB bond donors have gained attention.[349-352] In a particularly noteworthy study, a range of HB, XB and ChB bis(triazole-benzo-15-crown-5) receptors **5.2XB/HB/ChB** were investigated for ion-pair recognition.[350] ^{1}H NMR binding studies in $CDCl_3/d_6$-DMSO 9:1 revealed a large enhancement of halide binding in the presence of sodium cations. Interestingly, the cooperativity $\alpha = K_{Na^+}/K_{free}$, where K_{Na^+} is the anion binding constant to the sodium-precomplexed receptor and K_{free} is the binding constant to the native receptor, was significantly different for the three receptors. With **5.2HB**, the cooperativity factors of $\alpha = 21$ and 32 for Br^- and I^- were relatively modest. However, the XB and ChB analogues demonstrated considerably larger

cooperativity factors of $\alpha = 127$ and 162 for **5.2XB**, and in particular of $\alpha = 280$ and 216 for **5.2ChB**, for Br^- and I^-, respectively. This was attributed to the greater polarisation of the XB/ChB bond donors upon sodium cation binding, importantly highlighting the potential of XB and ChB interactions in ion-pair receptors.

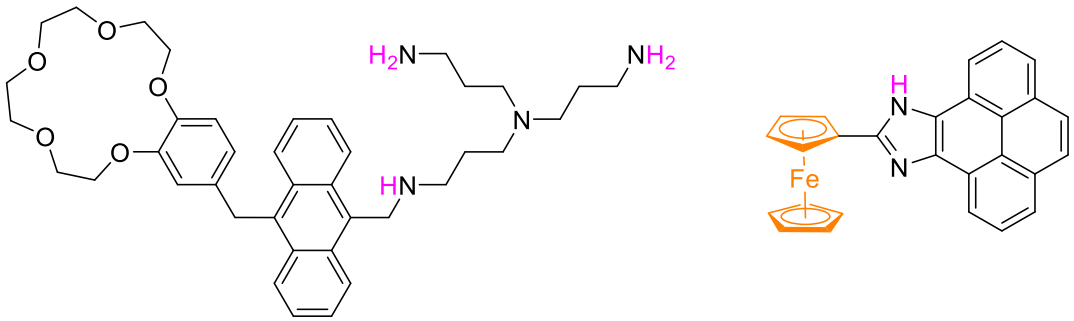
5.1.2 Ion-Pair Sensing

The sensing of ion-pairs is particularly challenging, as reflected by the sparse literature on the topic. This can mainly be attributed to two major factors:

1) The incorporation of an electrochemical or optical transducer into the heteroditopic scaffold is synthetically challenging as an efficient transduction of cation and anion presence typically requires intimate spatial/electronic coupling to both binding sites, without interruption of the binding of either ion.
2) For *true* ion-pair sensing, the transducer has to be responsive to both ions. For example, if a specific signal output is generated in the presence of only one of the ions, then this sensor cannot inherently distinguish between the binding of only this ion and the simultaneous binding of the ion-pair. In the latter case binding of the signal-generating ion might be enhanced such that a higher sensitivity is attained, however the maximum sensor response is not altered as the response at saturation is identical. Relatedly, the signal output of the transducer also has to be additive, such that both cation and anion binding induce a response that is overall larger than binding of either ion alone. This is highly problematic in transducer formats that rely on electrostatic interactions (*i.e.* most electrochemical methodologies) as the two

ions typically have opposing effects on the transducer (for example in voltammetric sensors as discussed below).

In spite of these challenges a range of ion-pair sensors have been developed, most commonly based on optical readouts.[353,354] A landmark early example of such a sensor was reported by de Silva and co-workers in 2003, combining a fluorescent anthracene transducer with benzo-15-crown-5 ether and a polyamine as cation and anion binding sites, respectively, to afford **5.3** (Figure 5.3).[354] Only in the presence of both Na^+ and phosphate (in 1:1 MeOH/H_2O, $pH = 8$) did the sensor display significant fluorescence, thus behaving as a molecular logic AND gate. This was attributed to binding-induced deactivation of photoinduced electron transfer (PET) from both of the uncomplexed binding sites. However, as a result of the significant distance between the ion binding sites no cooperative binding was observed.



5.3 **5.4**

Figure 5.3. Chemical structures of heteroditopic ion-pair sensors **5.3** and **5.4** based on fluorescent or voltammetric readouts.

Ion-pair sensing using redox-active heteroditopic receptors was reported for the first time in 1995.[355] Since then a variety of voltammetric ion-pair sensors have been prepared, most

commonly based on Fc transducers.[105,356-362] For example, the Fc-imidazopyrene **5.4** was developed as a dual redox and fluorescent ion-pair sensor.[363] The imidazole subunit enabled both cation (Zn^{2+}, Hg^{2+} or Pb^{2+}) and/or anion binding (OAc^- or $H_2PO_4^-$) which in a voltammetric format was transduced as anodic and cathodic shifts, respectively (separately, in ACN). In the presence of both Zn^{2+} and $H_2PO_4^-$ an overall response that lies between that of each ion individually was observed. This behaviour is, expectedly, observed in almost all voltammetric ion-pair sensors as the opposing response for the differently charged ions largely cancels. As discussed above, this precludes *true* ion-pair sensing and is expected to similarly hinder sensing in other formats, such as Faradaic EIS (unprecedented).

Of final note is that many ion-pair receptors and sensors have also been developed for covalently linked ion-pairs, most notably zwitterionic amino acids.[345-347]

5.1.3 Chapter Aims

As introduced in Chapter 3, the capacitive response of a receptive interface towards an inorganic anion is characterised by an increased capacitance. The same effect has been previously demonstrated for the capacitive sensing of cations.[236,307] Based on these observations, it was speculated that a surface-immobilised heteroditopic ion-pair receptor would enable ion-pair sensing *via* non-Faradaic capacitance spectroscopy. Specifically, the response should be characterised by an additive increase in the capacitance upon cation and anion binding.

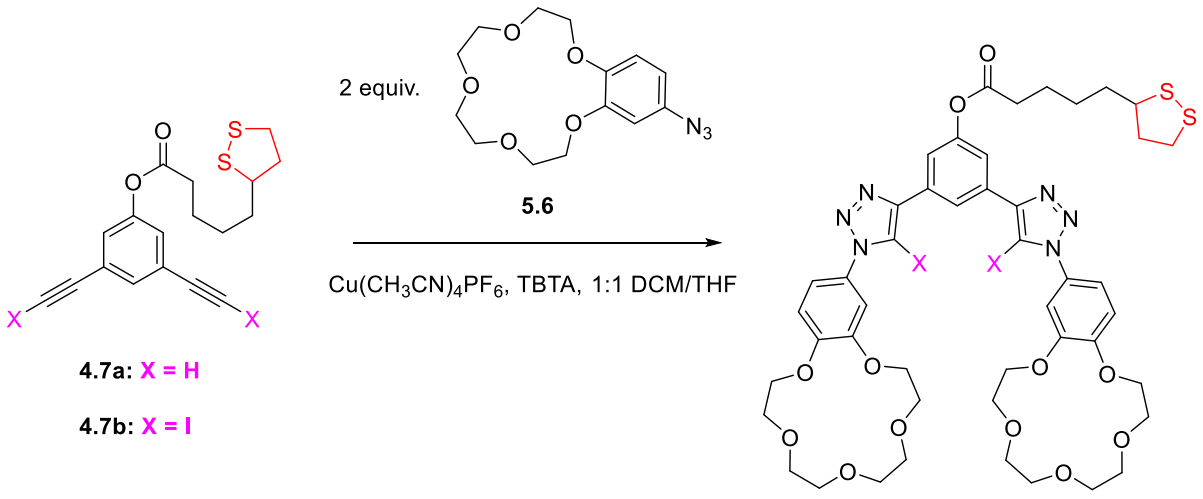
The goal of this thesis chapter is to report on an investigation of the feasibility of this approach at heteroditopic XB and HB SAMs. As highlighted above, this would be the first

electrochemical sensor for an inorganic ion-pair as well as the first investigation of XB-mediated ion-pair recognition at interfaces.

5.2 Ion-Pair Sensing at Heteroditopic SAMs

5.2.1 Receptor Design and Synthesis

Based on the impressive cooperative ion-pair recognition performance of the bis((iodo)triazole-benzo-15-crown-5) receptor **5.2**, this heteroditopic scaffold was adapted for surface-immobilisation. To this end the previously developed disulfide-appended bis(iodo)alkyne synthon **4.7a/b** was converted to receptors **5.5XB/HB** *via* CuAAC reaction with two equivalents of benzo-15-crown-5-azide **5.6** in moderate yields (Scheme 5.1).

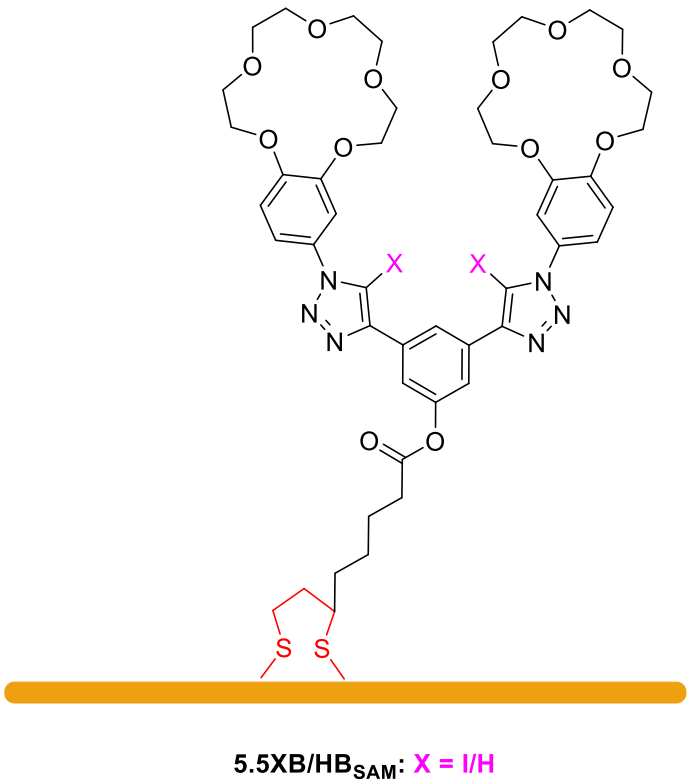


Scheme 5.1. Synthetic route towards disulfide-appended heteroditopic ion-pair receptors **5.5XB/HB**.

All synthetic procedures and compound characterisation are detailed in Chapter 7. The design of this receptor was undertaken in collaboration with Andrew Docker, who carried out all synthetic steps.

5.2.2 SAM Formation and Characterisation

The immobilisation of **5.5XB/HB** onto gold electrodes was carried out under the same conditions as described in Chapter 3, specifically *via* exposure of clean gold electrodes to 0.25 mM receptor in ACN/H_2O 1:1, affording **5.5XB/HB$_{SAM}$** (Figure 5.4).



5.5XB/HB$_{SAM}$: X = I/H

Figure 5.4. Schematic representation of **5.5XB/HB$_{SAM}$**.

SAM characterisation was carried out *via* analogous techniques as described in the previous chapters (see Section 2.2.3.1, 3.3, 4.2.2 and 7.3). The water contact angles of both films are, as a result of the exposed crown-ether groups, low (≈45°, Table 5.1). This indicates a high hydrophilicity, larger than that of any of the other films discussed in this thesis. Interestingly, and in contrast to all other XB/HB receptive SAMs, no difference between the films is observed.

The ellipsometrically determined film thickness of ≈3.5 nm of **5.5XB/HB$_{SAM}$** is significantly larger than that of the structurally related **4.4XB/HB$_{SAM}$** as alluded to in Section 4.2.2. This value is perhaps somewhat larger than expected and even slightly larger than that of **2.1XB/HB$_{SAM}$**, but still in good agreement with the formation of a monolayer and indicative of an upright receptor conformation, as schematically shown in Figure 5.4. This was also confirmed by a high surface coverage of >10^{-10} mol/cm^2 (Table 5.1).

Table 5.1. Water contact angle, thickness d and molecular surface coverage Γ of **5.5XB/HB$_{SAM}$**.

	Water contact angle (°)[a]	**d (nM)[b]**	**Γ (10^{-10} mol/cm^2)[c]**
5.5XB$_{SAM}$	45.0 ± 1.4	3.50 ± 0.12	1.24 ± 0.76
5.5HB$_{SAM}$	47.3 ± 2.1	3.42 ± 0.14	1.87 ± 0.86

a – Errors represent one standard deviation of 5 repeat measurements. b – Errors represent one standard deviation of at least 3 repeat measurements. c – Obtained from reductive thiol stripping. Errors represent one standard deviation of six independent experiments for **5.5XB$_{SAM}$** and three for **5.5HB$_{SAM}$**.

5.2.2.1 X-ray Photoelectron Spectroscopy (XPS)

XPS analysis of both films revealed the presence of all expected elements as shown in Figure 5.5.

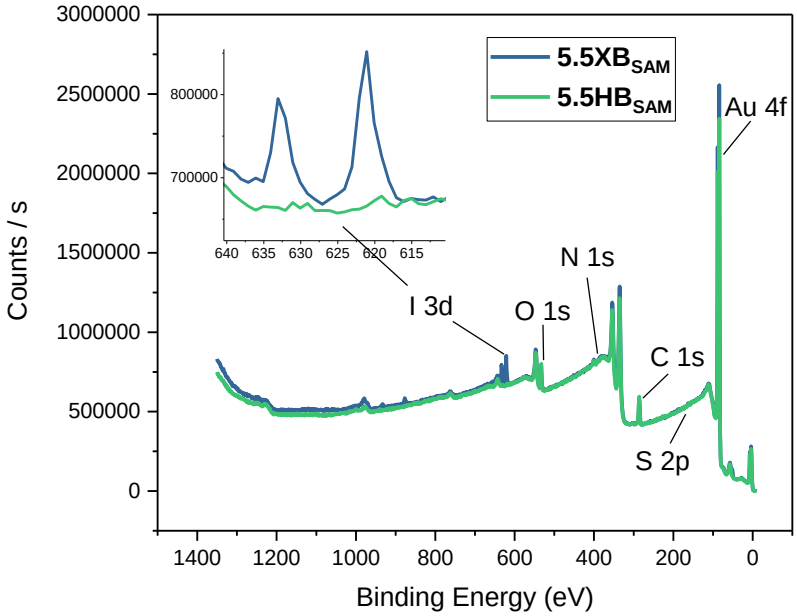


Figure 5.5. Low resolution survey XPS spectra of **5.5XB/HB$_{SAM}$**. Inset: I 3d region.

For both films the experimental and theoretical atomic ratios are in good agreement, confirming the formation of pure SAMs (Table 5.2 and A5.1-A5.2, Figures A5.1-A5.4).

Table 5.2. Experimental and theoretical elemental composition of **5.5XB/HB$_{SAM}$** determined by XPS. Values were normalised to I = 2 for **5.5XB$_{SAM}$** and O = 12 for **5.5HB$_{SAM}$**. Errors represent one standard deviation of triplicate measurements.

	5.5XB$_{SAM}$		**5.5HB$_{SAM}$**	
	Experimental	**Theoretical**	**Experimental**	**Theoretical**
C	51.0 ± 2.5	46	43.1 ± 1.7	46
N	7.0 ± 2.2	6	8.1 ± 2.4	6
O	12.3 ± 1.3	12	12.0 ± 1.0	12
S	1.42 ± 0.4	2	1.1 ± 0.3	2
I	2.0 ± 0.3	2	-	-

In the high resolution spectra of all elements the same peaks can be fitted as for the aforementioned films (Figure 5.6 and 5.7). However, the experimental to theoretical ratio of most subcomponents is quite poor, in particular for the oxygen environments (Tables 5.3−5.4).

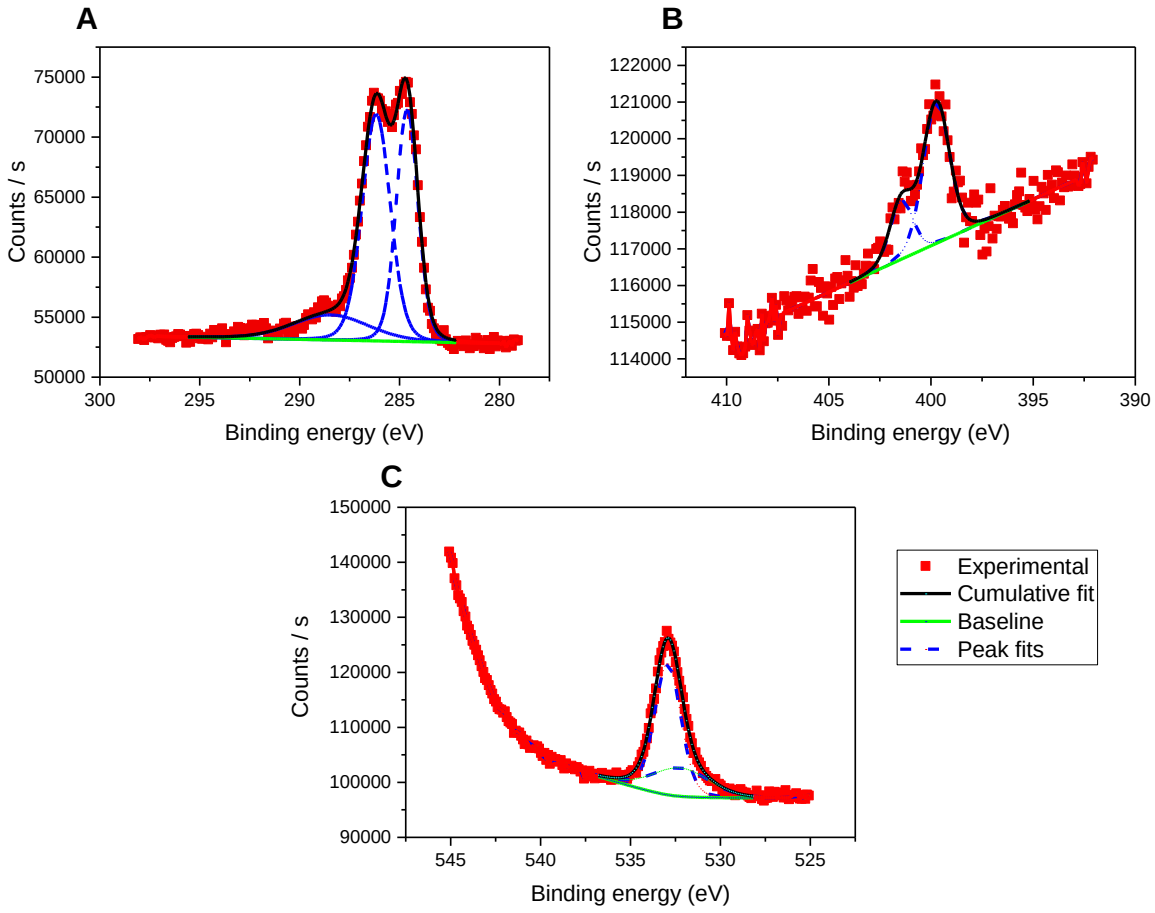


Figure 5.6. High resolution XPS spectra including peak fits of **5.5XB$_{SAM}$**. A) C 1s. B) N 1s. C) O 1s.

This is most likely a reflection of the large theoretical peak ratio of 1:11 for the C=O to ((O=C)−O + C−O−C)) components such that the former lower energy component cannot be fitted properly without explicit assumption about the peak shape/position (as seen by the

large peak width (Figure 5.6C), for further discussions see Section 7.3.3). For the same reason the peak integral of the higher energy C=O appears to be significantly overestimated.

Table 5.3. Peak binding energies and experimental and theoretical ratios for different chemical environments of C, N and O of **5.5XB$_{SAM}$**.

		Peak BE (eV)	Exp.	Theor.
C	C−C	284.62 ± 0.03	3.03 ± 0.68	16
	C−O, C−N, C−S	286.19 ± 0.01	3.86 ± 0.74	29
	C=O	288.50 ± 0.05	1	1
N	N=N	399.78 ± 0.06	6.48 ± 1.20	4
	N−N	401.49 ± 0.14	2	2
O	C=O	532.39 ± 0.17	1	1
	(O=C) −O, C−O−C	532.92 ± 0.02	1.82 ± 0.30	11

Table 5.4. Peak binding energies and experimental and theoretical ratios for different chemical environments of C, N and O of **5.5HB$_{SAM}$**.

		Peak BE (eV)	Exp.	Theor.
C	C−C	284.84 ± 0.07	4.50 ± 1.82	16
	C−O, C−N, C−S	286.39 ± 0.12	5.02 ± 1.41	29
	C=O	288.86 ± 0.29	1	1
N	N=N	399.91 ± 0.15	2.38 ± 1.26	4
	N−N	401.52 ± 0.36	2	2
O	C=O	530.83 ± 0.05	1	1
	(O=C) −O, C−O−C	533.04 ± 0.01	18.41 ± 6.32	11

The high resolution I 3d and S 2p spectra (Figure 5.7) of both films are analogous to those of the other SAMs, for further discussions see Sections 3.3.1 and 4.2.2.2.

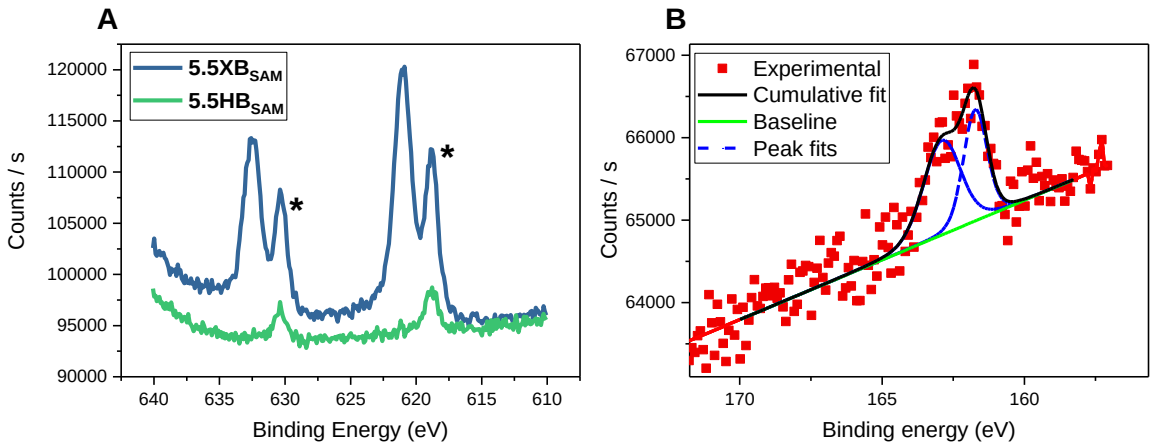


Figure 5.7. High resolution XPS spectra of **5.5XB/HB$_{SAM}$**. A) I 3d. The peaks denoted with an asterisk presumably arise from an iodine species that is generated under the measurement conditions and does not arise from the SAM. B) S 2p spectrum of **5.5XB$_{SAM}$**.The two peaks fitted in this spectrum as well as the doublets in the I 3d arise from spin orbit coupling and not from chemically different environments.

5.2.2.1.1 ATR-FTIR Spectroscopy

The ATR-FTIR spectra of both films, are as depicted in Figure 5.8, identical. This is an additional confirmation of the formation of chemically/structurally identical films, only differing in the XB/HB triazole binding site, which as discussed previously, is not expected to be resolvable by IR.

A more detailed analysis of the IR spectra reveals well-resolved asymmetric and symmetric methylene stretches at 2926 and 2854 cm^{-1}, respectively, in excellent agreement with observations at **2.2XB/HB$_{SAM}$**, **4.4XB/HB$_{SAM}$** and literature (Figure 5.9A).[285] A variety of other peaks at 1684, 1521, 1458, 1271 and 1142 cm^{-1} are prominently resolved in both films (Figure 5.9B). The former most likely arises from the ester functional groups, is however observed at somewhat lower energies than those of **2.2XB/HB$_{SAM}$** or **4.4XB/HB$_{SAM}$** (this discrepancy likely arises as the exact peak position is difficult to determine due to significant peak broadening). Another peak, around ≈1460 cm^{-1}, can be resolved in all three SAMs, supporting its assignment as a triazole signal, as speculated in Section 2.2.3.1.2.[286]

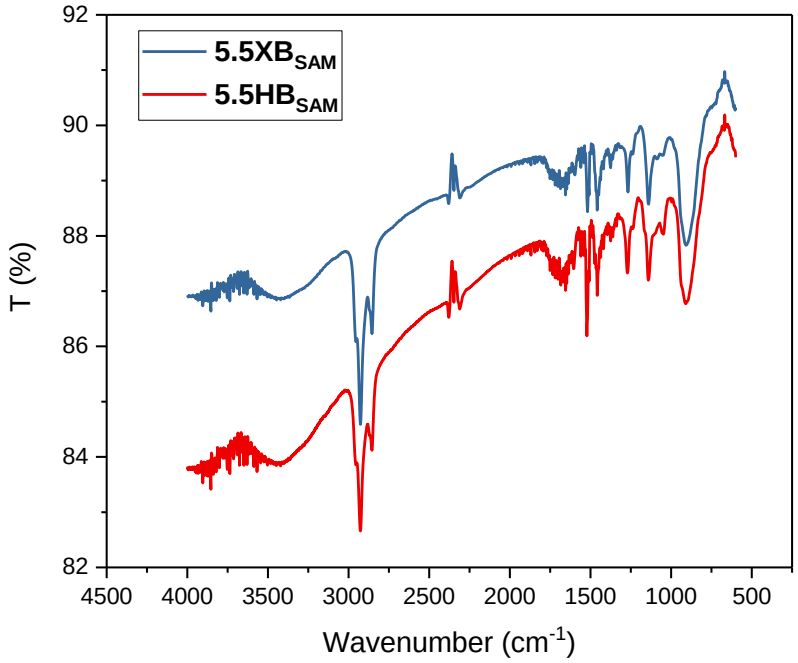


Figure 5.8. ATR-FTIR spectra of **5.5XB/HB$_{SAM}$**.

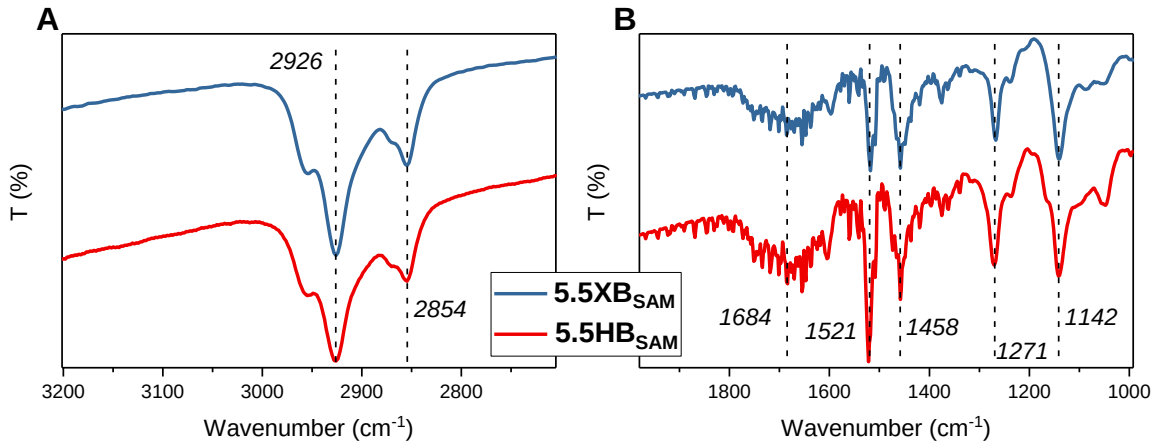


Figure 5.9. Magnification of ATR-FTIR spectra of **5.5XB/HB$_{SAM}$** between 3200−2700 cm^{-1} (A) and 1900−1000 cm^{-1} (B). The dotted lines indicate prominent peaks that can be observed in both SAMs.

5.2.2.2 Atomic Force Microscopy (AFM)

The formation of a homogeneous SAM of **5.5XB$_{SAM}$** was also confirmed by atomic force microscopy (AFM, in tapping mode). A low resolution scan over a large surface area (10 x 9 µm) showed, as expected, the absence of any large scale features (Figure A5.5). The isolated

spikes can probably be attributed to contaminations of the underlying surface or dust and are notably more than two orders of magnitude smaller than the sampled area.

A higher resolution analysis of a smaller area (1 x 1 µM) shows excellent homogeneity (RMS roughness = 0.858 nm) as expected for a monolayer film (Figure 5.10). Importantly, the height fluctuations are within a very narrow range (Figure 5.11) around a mean height of ≈4.2 nm. Under the assumption that the lowest measured point (0 nm) is the underlying gold substrate, this indicates monolayer coverage with film thickness in good agreement with ellipsometry (3.5 nm).

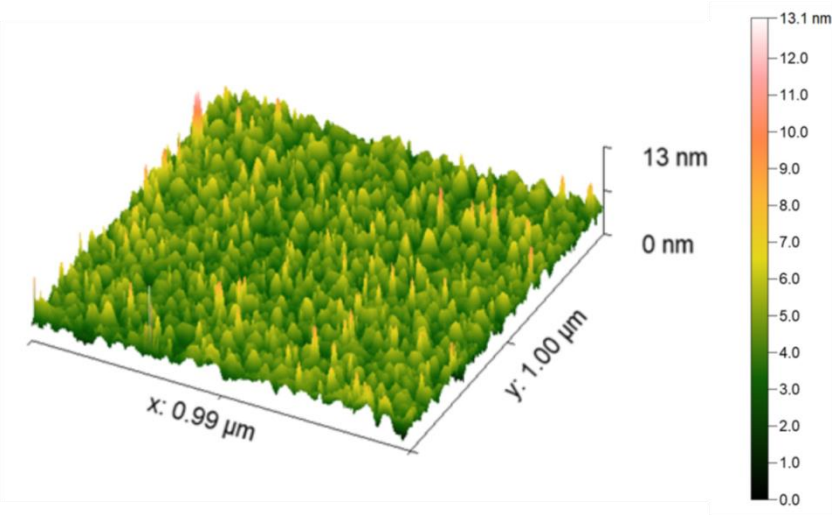


Figure 5.10. High resolution AFM image of **5.5XB$_{SAM}$**.

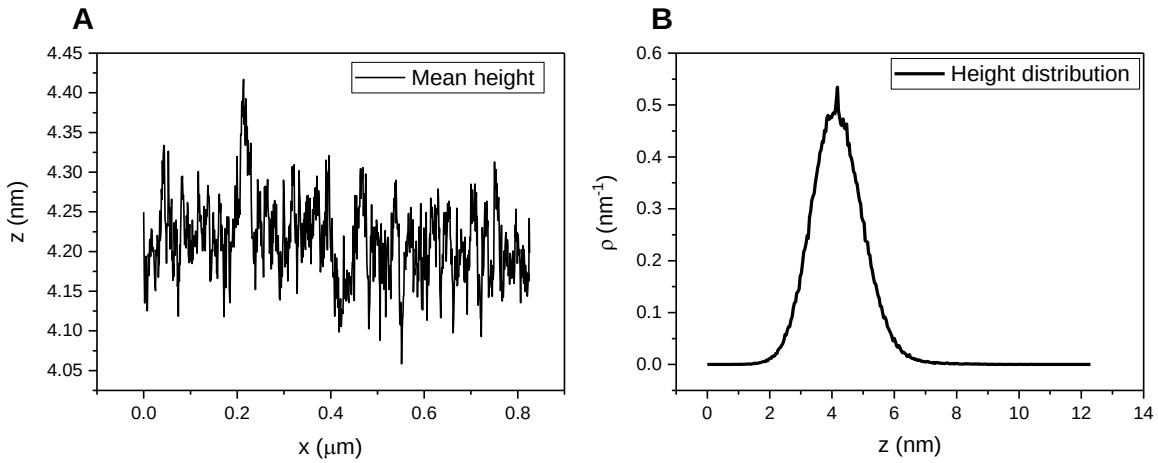


Figure 5.11. Mean height (averaged along y-axis) (A) and height distribution (B) of **5.5XB$_{SAM}$** as measured by AFM. Measured area: 1 x 1 μm (high resolution, Figure 5.10).

5.2.3 Ion-Pair Sensing

5.2.3.1 General Considerations and Capacitive Properties of 5.5XB$_{SAM}$

A crucial consideration for ion-pair investigations is the choice of the electrolyte. Specifically, for cation binding studies an electrolyte salt that does not interact with the crown-ether binding sites has to be employed. This limits the electrolyte choice to TBA-salts, as the TBA cation is one of the few commonly employed/available cations that does not interact with crown ethers. Similarly, anion binding studies need to be carried out in the presence of a non-competing electrolyte counter anion (*e.g.* PF_6^-, ClO_4^- or Cl^- as utilised in Chapters 2–4). This significantly restricts the electrolyte that can be used for ion-pair binding studies. While $TBAClO_4$ or $TBAPF_6$ would be ideal, they are poorly soluble in aqueous media, in particular at "electrolyte concentrations" (*e.g.* ≈100 mM). Similarly, the use of TBACl as electrolyte may be problematic, as sensing studies at **4.4XB$_{SAM}$** (which is structurally related to **5.5XB$_{SAM}$**) revealed a complex capacitive response in the presence of Cl^- (see Section 4.2.3.2). Additionally, while Cl^- is not expected to bind to the native **5.5XB/HB$_{SAM}$**, in ion-pair binding studies, *i.e.* when cations are bound at the interface, the

anion binding properties of the cationic SAM are expected to be different. Specifically, significant additional electrostatic contributions to anion binding might favour the recognition of the charge-dense Cl^-, thereby potentially competing with binding of the analyte anion.

For these reasons the water-soluble $TBANO_3$ was employed as an electrolyte in all binding studies in predominantly aqueous media, as the NO_3^- counter anion is both relatively hydrophilic and is not expected to significantly bind to either the neutral or cationic SAM interface. In predominantly organic media $TBAPF_6$ was used.

Initial studies were carried out at **5.5XB$_{SAM}$**, as this interface is expected to display enhanced anion binding. All capacitance measurements were carried out at OCP at constant ionic strength. In all aqueous electrolyte media the film displayed excellent capacitive baseline stability. The capacitance of **5.5XB$_{SAM}$** in H_2O, 100 mM $TBANO_3$ is 3.78 ± 0.84 μF/cm^2, which, considering a thickness of 3.50 nm, corresponds to a dielectric constant of 15.0 (*via* eqn. 3.6). Gratifyingly, this value lies in between that of the more polar **3.1XB/HB$_{SAM}$** (≈19) and the less polar **4.4XB/HB$_{SAM}$** (≈12).

The high phase angle of ≈85° resolved in the phase Bode plot (Figure A5.6) is also indicative of the formation of densely packed SAMs with near-ideal capacitive properties. The formation of a dense, blocking film was further confirmed by CV in the presence of $[Fe(CN)_6]^{3-/4-}$, where in analogy to **3.1XB/HB$_{SAM}$** and **4.4XB/HB$_{SAM}$** no Faradaic activity was resolved (corresponding to a high impedance; Figure 5.12).

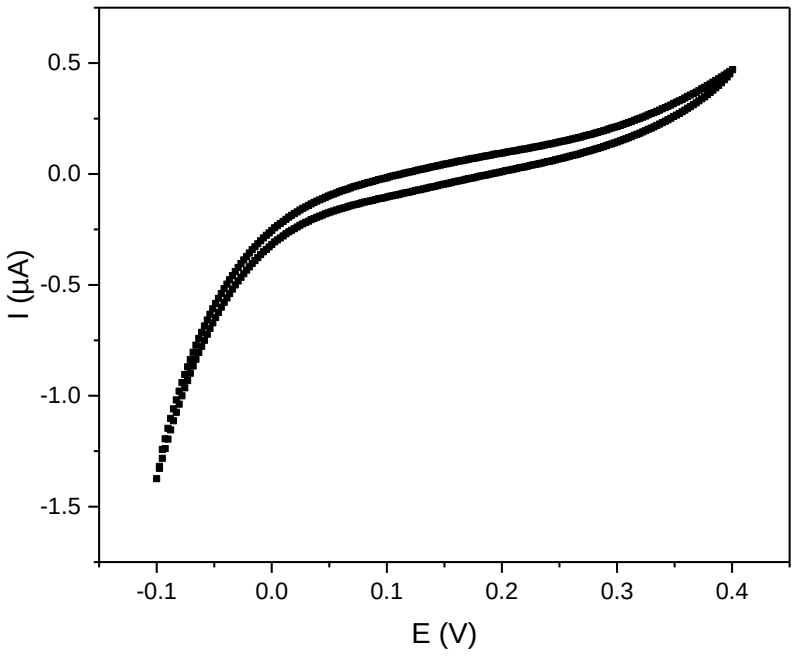


Figure 5.12. CV of **5.5XB$_{SAM}$** in H_2O 100 mM $TBANO_3$ and ≈2 mM $[Fe(CN)_6]^{3-/4-}$.

Before carrying out ion-pair sensing studies, the cation and anion binding properties were investigated separately.

5.2.3.2 Capacitive Cation Sensing

Initial cation binding studies were carried out by non-Faradaic capacitance in pure water containing 100 mM $TBANO_3$. The addition of Na^+ induced a small, but notable increase in the interfacial capacitance as shown in Figure 5.13 (as also resolved in the bode plots shown in Figure A5.7).

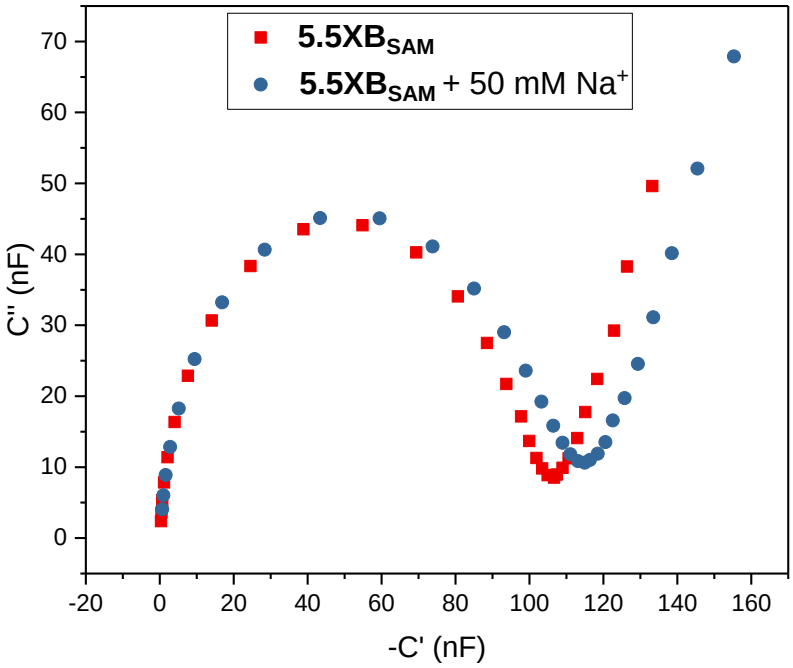


Figure 5.13. Capacitive Nyquist plots of **5.5XB$_{SAM}$** in the presence (blue circles) and absence (red squares) of 50 mM Na^+. Measurements were carried out at OCP in pure water containing 100 mM $TBANO_3$.

A quantitative investigation of the Na^+ sensing properties was then carried out by titration experiments as shown in Figure 5.14. In analogy to anion binding studies described in Chapter 3 and 4, the sensor response can be described by a Langmuir isotherm (eqn. 3.1). This analysis reveals significant binding ($K = 124$ M^{-1}), in spite of the small response (≈6% at 50 mM Na^+). This binding constant is in excellent agreement with prior observations at electrografted benzo-15-crown-5 films ($K = 120$ M^{-1})[307] and 15-crown-5 SAMs ($K = 60$ M^{-1}).[236]

Interestingly, no significant capacitive perturbations were observed in the presence of excess K^+, Mg^{2+} or Zn^{2+}. In particular the lack of response towards K^+ is unexpected, as (benzo-)15-crown-5 is well known to bind a range of alkali metal cations in solution and also in surface-confined architectures.[235,236,307,364] This may indicate that K^+ binding is very weak

or that it cannot be easily resolved as a result of a small response magnitude (*i.e.* poor signal-to-noise ratio).

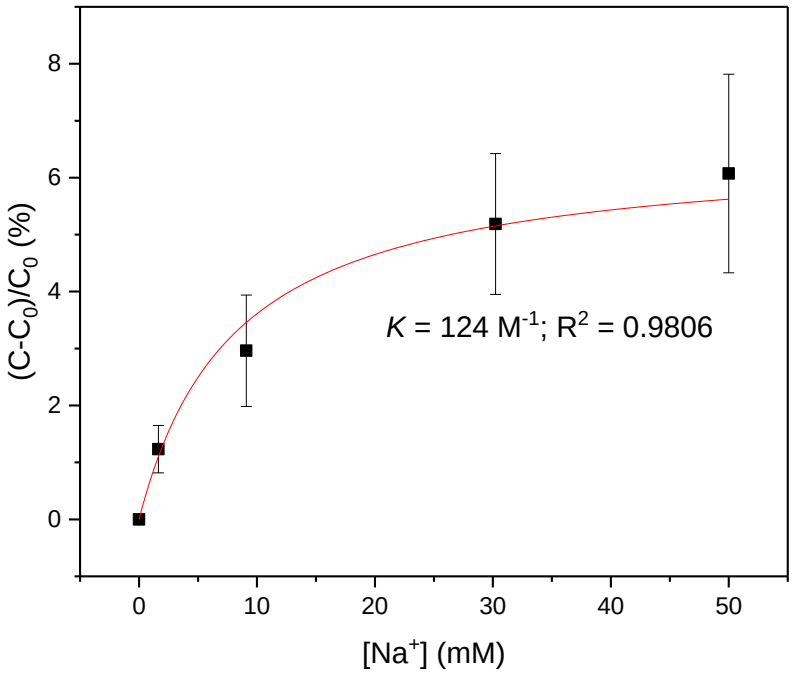


Figure 5.14. Normalised change in capacitance of **5.5XB$_{SAM}$** upon titration with Na^+ in H_2O, 100mM $TBANO_3$. Error bars represent one standard deviation of three independent measurements. The solid line represents a fit according to the Langmuir model (eqn. 3.1).

The modest response towards Na^+ is surprising, especially when compared to that of **3.1XB/HB$_{SAM}$** or **4.4XB$_{SAM}$**. This phenomenon may be related to the overall structure of the film and the distance between the crown ether cation binding sites and the electrode. In a previous study on the capacitive sensing of alkali metal cations at crown ether SAMs, Flink *et al.* noted a similar effect where the distance between the binding site and the electrode significantly affected the magnitude of the capacitance response.[236] Specifically, receptive SAMs with longer anchor groups displayed a significantly smaller capacitance increase in response to Na^+ or K^+ than SAMs composed of crown ethers with short anchor groups. The authors rationalised this behaviour by assuming that the overall SAM capacitance is

composed of two series contributions, the anchor capacitance as well as the binding site capacitance component (as schematically shown in Figure 5.15).

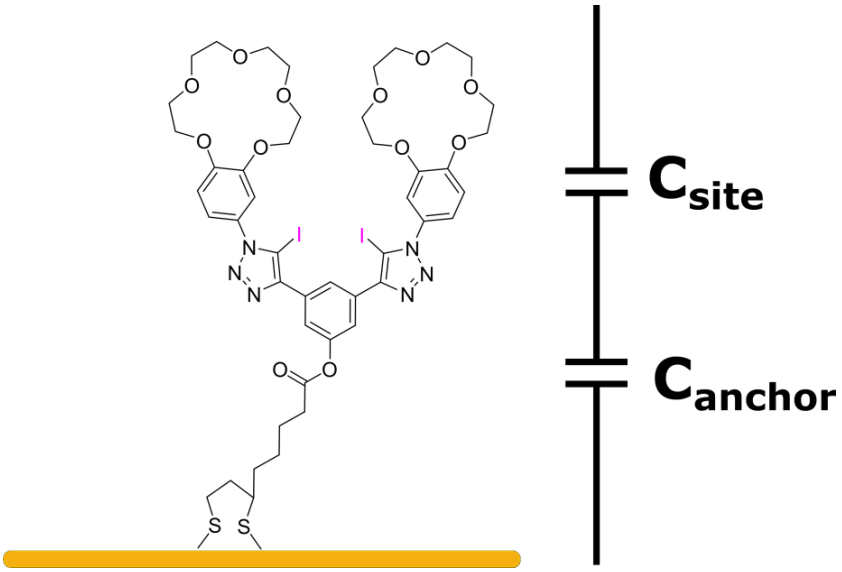


Figure 5.15. Schematic depiction of **5.5XB$_{SAM}$** including proposed capacitive subdivision into a capacitance of the anchor component as well as a capacitance of the binding site.

In this case the overall SAM capacitance C is given by:

$$\frac{1}{C} = \frac{1}{C_{anchor}} + \frac{1}{C_{site}}$$

According to this model the capacitance of a film without a substantial anchor group, where the binding site is in close proximity of the electrode, is only determined by C_{site}, which sensitively reports on a cation binding event. When a long anchor group is present the additional series C_{anchor} contribution towards the overall capacitance significantly "dilutes" the C_{site} contributions and thus the overall response. (Note that the overall capacitance is dictated by the smallest series capacitor, which will typically be C_{anchor}, both as a result of a low dielectric constant as well as a significant "thickness" of the (alkyl) anchor chains.)

One could invoke a similar explanation here, especially when considering that the crown-ether binding sites of **5.5XB$_{SAM}$** are indeed quite far removed from the electrode (most likely somewhat further than those of **3.1XB/HB$_{SAM}$** or **4.4XB$_{SAM}$**), as also highlighted by the significant SAM thickness of 3.5 nm.

It should also be noted that a similar argument based on dielectric considerations can be made, *i.e.* the long non-receptive portion of the film overall dominates the dielectric (and capacitive) properties of the film such that peripheral cation binding induces only small perturbations. Additionally, the polarity of the free, exposed crown ethers will, in a purely aqueous environment, be considerable (due to significant hydration) such that the binding of a cation will not influence (*i.e.* enhance) the polarity/dielectric to the same extent.

Further cation binding studies were also carried out in organic solvent. In ACN a clear increase in the capacitance can be observed in the presence of Na^+ (not quantified). Quantitative Na^+ binding studies were then carried out in ACN/H_2O 9:1 (100 mM $TBAPF_6$) as this solvent system and this cation were later utilised in initial ion-pair binding studies, see Section 5.2.3.4. In this solvent system the capacitance of **5.5XB$_{SAM}$** is 2.80 ± 0.52 µF/cm^2 which is ≈26% smaller than measured in H_2O, 100 mM $TBANO_3$. Assuming a constant film structure in both solvents (*i.e.* thickness), this indicates a lower dielectric (of 11.1; *cf.* 15.0 in water), suggesting that the film contains significant amounts of solvent which affect its polarity and capacitance. Here this can be easily justified considering that the Y-shaped receptor is “open” and the binding sites (in particular the exposed crown ethers) will significantly interact with the solvent (especially water).

In this aqueous-organic solvent a much more significant response of up to 20% is observed (Figure 5.16). Unsurprisingly, the binding constant of Na^+ in this less competitive system is

much larger (704 M^{-1}). Regardless of solvent however, the exact stoichiometry of Na^+ binding to the receptor cannot be ascertained.

As neither in this solvent, nor in water, any significant deviations from the Langmuir isotherm are observed it can be inferred that there is no significant electrostatic communication (*i.e.* repulsion of cations) between the two crown-ether binding sites and that two cations bind to one receptor (see also Figure 5.18).

It should be noted that the larger binding constant in the less competitive solvent also clearly correlates with a larger response, as alluded to in Section 3.5.3. However, it also has to be taken into account that these experiments were conducted in a different solvent/electrolyte system. As highlighted above, the initial baseline capacitance of the SAM in this less polar environment is smaller, most likely as a result of a lower film dielectric. Upon cation binding the dielectric of the less polar interface is thus more strongly increased (in relative terms) such that a larger relative capacitive response is observed.

5.2.3.3 Capacitive Anion Sensing

In H_2O 100 mM $TBANO_3$ the addition of anions (Cl^-, Br^- or I^-) did not induce any significant capacitive perturbations. This is perhaps expected, considering that the more elaborate tetra(iodotriazole) film **3.1XB$_{SAM}$** does not interact with Cl^- or Br^- either and only displays moderate binding to I^- (as well as SCN^- and ReO_4^-, not tested here).

More surprisingly, **5.5XB$_{SAM}$** did not display any significant capacitive response towards various anions in a range of relatively less competitive aprotic organic solvent systems. For example, in pure ACN no response to either Cl^- or Br^- was resolved. This behaviour was also

observed with Br^- in DCM. A variety of mixed solvent systems were also tested ($CHCl_3$/DMSO 9:1, ACN/$CHCl_3$ 1:1, ACN/H_2O 99:1). In all of these mixtures either complex behaviour with poor baseline stability (potentially due to decomposition, especially in the non-polar solvents) or no response was observed (anions tested: Cl^-, Br^- and $H_2PO_4^-$). This suggests that anion binding is either very weak or not transduced efficiently. However, anion binding is expected to be significantly enhanced in the presence of a bound cation. Hence a lack of anion binding by the native receptor is not necessarily detrimental to ion-pair sensing studies, as discussed below.

5.2.3.4 Capacitive Ion-Pair Sensing

Preliminary ion-pair sensing studies were carried out with sodium halide salts. In H_2O 100 mM $TBANO_3$ the capacitive response towards NaBr or NaI was not significantly different to that of Na^+ alone (*i.e.* $NaNO_3$), indicating that neither Br^- nor I^- were bound in addition to Na^+.

In contrast, the addition of Br^- to a solution of 50 mM Na^+ in ACN/H_2O 9:1 did induce a significant additional increase of the capacitance (at constant ionic strength and constant sodium concentration; Figure 5.16).

It should be noted that this increase seems to arise from the specific presence (binding) of bromide, not simply an increase in binding strength (and binding site occupancy) of Na^+ as the Na^+ response is at plateau already. This indicates that, as intended, the presence of both cation and anion induce a change (increase) in capacitance C.

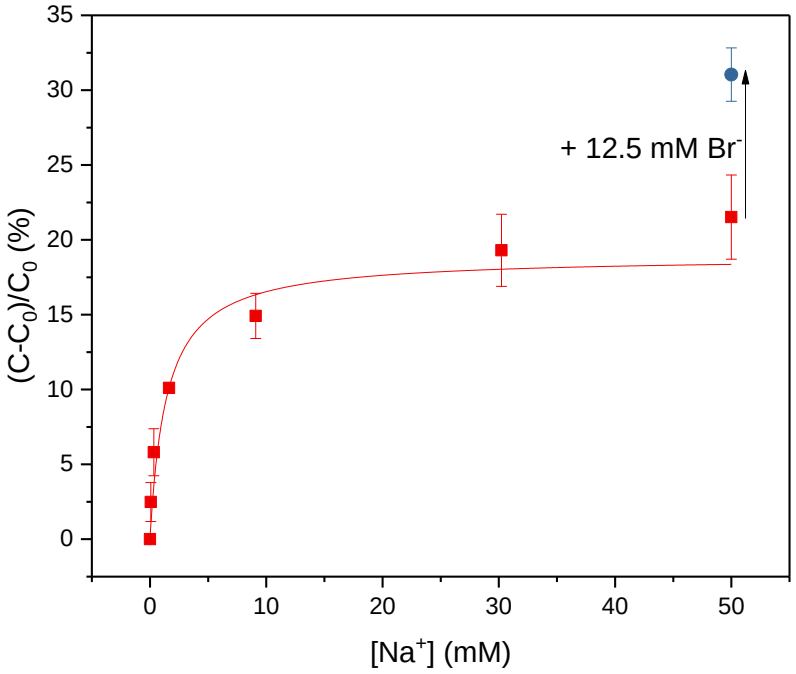


Figure 5.16. Normalised change in capacitance of **5.5XB$_{SAM}$** upon titration with Na^+ in ACN/H_2O 9:1, 100 mM $TBAPF_6$. Shown as the blue circle is the additional capacitance increase that is induced by addition of 12.5 mM Br^- (at 50 mM Na^+, see Section 5.2.3.4). Error bars represent one standard deviation of three independent measurements. The solid line represents a fit according to the Langmuir model (eqn. 3.1).

To further investigate this behaviour **5.5XB$_{SAM}$** was titrated with NaBr in the same solvent system revealing a much larger response than for Na^+ alone (Figure 5.17), as expected for true ion-pair sensing (capacitive Nyquist and Bode plots are shown in Figures A5.7-A5.8).

It should be noted that in this case data fitting to the simple Langmuir adsorption isotherm does not describe the sensor behaviour appropriately anymore. This is most likely due to the presence of much more complicated binding equilibria involving multiple different binding sites and ions.

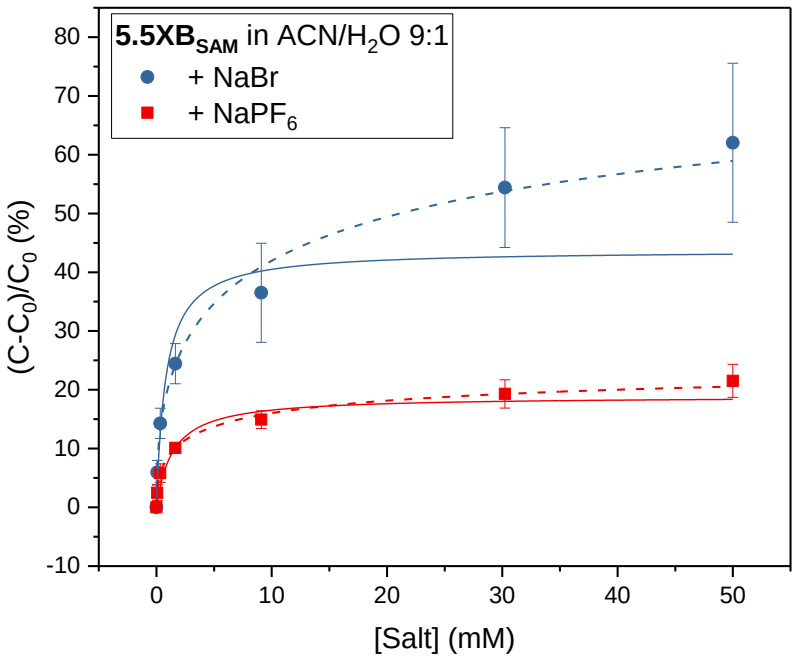


Figure 5.17. Normalised change in capacitance of **5.5XB$_{SAM}$** upon titration with $NaPF_6$ (blue cirlces) or NaBr (red squares) in ACN/H_2O 9:1, 100 mM $TBAPF_6$. Error bars represent one standard deviation of three independent measurements. The solid lines represent fits according to the Langmuir model (eqn. 3.1). The dashed lines represent fits according to the Langmuir-Freundlich model (eqn. 5.1).

Fitting to a Langmuir-Freundlich isotherm (eqn. 5.1) affords much better fits as shown by the dashed lines in Figure 5.17.

$$\theta = \frac{(K*[Salt])^{\mathrm{n}}}{1+(K*[Salt])^{\mathrm{n}}} \qquad \text{eqn. 5.1}$$

When $n = 1$ this model is equivalent to the Langmuir model. It should be noted that eqn. 5.1 is an empirical model, such that no physical meaning can be assigned to "n". Nevertheless, this parameter is usually interpreted as a heterogeneity factor, such that when $n \neq 1$ non-ideal Langmuir behaviour is observed.[365,366] This empirical model is, unsurprisingly, much better at describing the sensor response, but it is difficult to extract useful information from either "n" or K (Table 5.5 and Table A5.6). In reality a much more complex model that can take into consideration (cooperative) recognition events at both

binding sites needs to be employed for quantitative analysis of the binding isotherms (see Section 5.3.2.2).

Table 5.5. Binding constants, maximum capacitive response (ΔC_{max}) and n values of **5.5XB$_{SAM}$** upon exposure to $NaPF_6$ or NaBr in ACN/H_2O 9:1, 100 mM $TBAPF_6$. The data was obtained by isotherm fitting (Figure 5.17) according to the Langmuir ("LM", eqn. 3.1) or the Langmuir-Freundlich model ("LMF" eqn. 5.1).

	$NaPF_6$		**NaBr**	
	LM - eqn. 3.1	LMF - eqn. 5.1	LM - eqn. 3.1	LMF - eqn. 5.1
K (M^{-1})	704	229	1240	71
ΔC_{max} (%)	18.9	26.6	43.7	91.3
n	1	0.501	1	0.473
R^2	0.9992	0.9999	0.3233[a]	0.3666[a]

a – The low R^2 is a result of the large error bars of the data points at high concentration; a non-weighted fit returns similar values with high R^2.

Another important consideration is the question whether the additional response (which was preliminarily assigned to binding of an anion) occurs at the engineered XB/HB binding site (Figure 5.18) or simply arises from electrostatic ion-pairing without the involvement of noncovalent XB/HB interactions. This may be elucidated by control experiments with equivalent crown-ether-containing receptors without the XB/HB triazole anion binding sites (*e.g.* using non-receptive fluorotriazoles; synthetically challenging) or alternatively by a detailed comparison of the response of the XB and HB ditopic SAMs. If a different sensor response towards a salt is observed, then this difference has to arise from a specific interaction that involves the anion binding site (as long as the anion binding site does not indirectly affect cation recognition at the crown ethers).

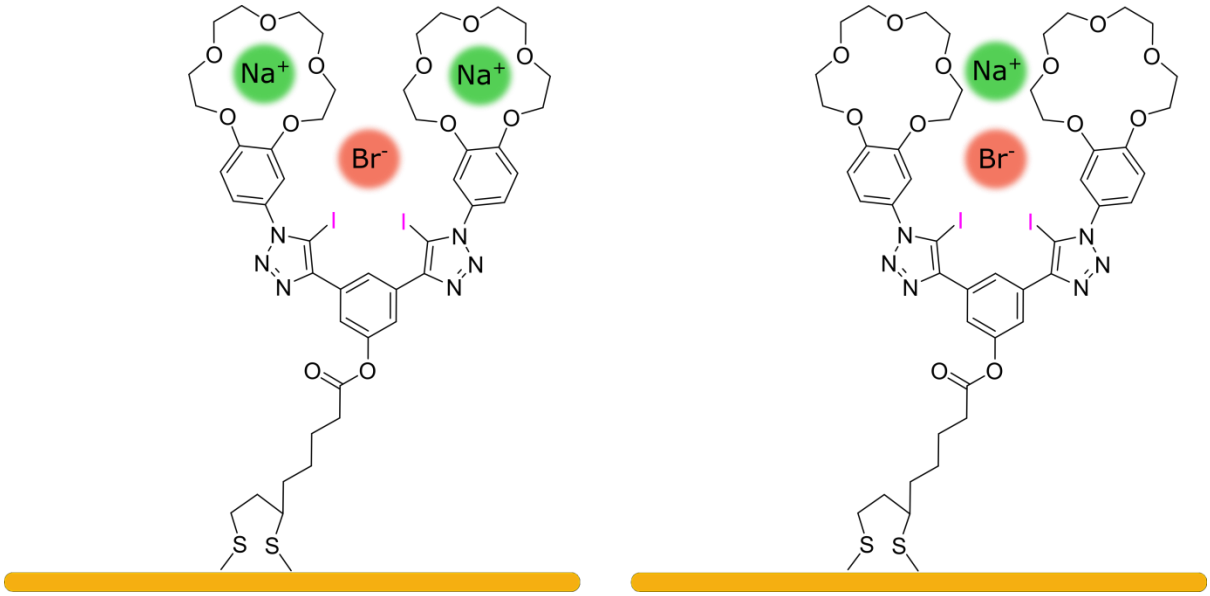


Figure 5.18. Schematic representation of possible binding modes of NaBr at **5.5XB$_{SAM}$**. Proposed herein is that binding occurs as shown on the left hand side with alkali metal cation binding occurring independently at each crown ether unit and halide binding at the XB triazole binding site.

In a preliminary investigation, binding studies of **5.5XB/HB$_{SAM}$** with NaBr in ACN/H_2O 4:1 were undertaken. (This more aqueous solvent system was employed as the solubility of NaBr in ACN/H_2O 9:1 is limited and temperature dependent, such that at a concentration of 100 mM phase separation of the titrant stock solution was observed in some instances.)

Gratifyingly, a small difference between both films is observed with an enhanced performance at **5.5XB$_{SAM}$** (Figure 5.19, Table A5.6), suggesting that the XB anion binding site does indeed play a role in ion-pair recognition. In order to conclusively prove this assertion further (repeat) studies and other control experiments, as detailed in Section 5.3.2, need to be carried out in the future.

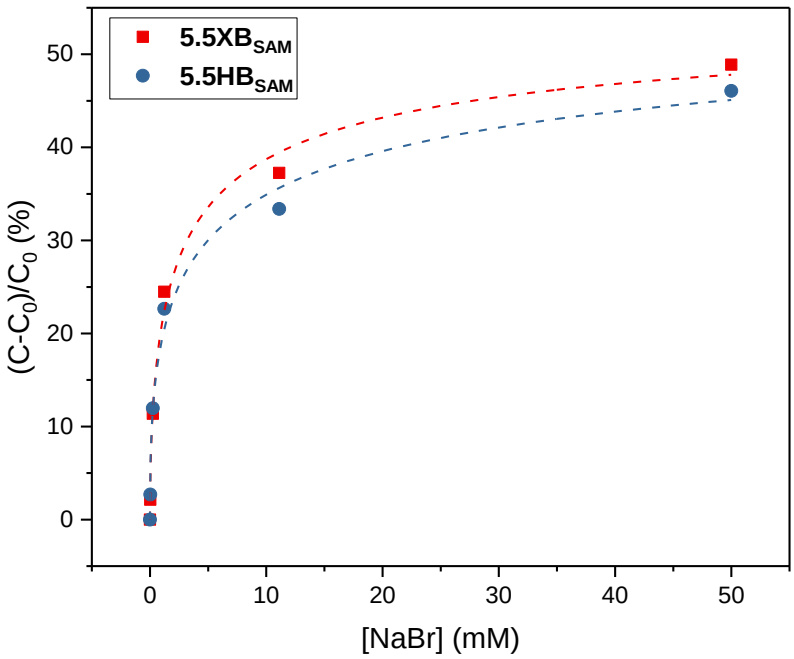


Figure 5.19. Normalised change in capacitance of **5.5XB/HB$_{SAM}$** upon titration with NaBr in ACN/H_2O 4:1 $TBAPF_6$. Dashed lines represent a fit according to the Langmuir-Freundlich model (eqn. 5.1).

5.3 Conclusions and Future Work

5.3.1 Conclusions

The surface-confinement of novel heteroditopic disulfide-appended bis(crown-ether-(iodo)triazole) ion-pair receptors afforded well-defined, densely packed SAMs as assessed by a range of surface analytical techniques (ellipsometry, XPS, ATR-IR, AFM). Non-Faradaic capacitance sensing studies were then carried out to independently investigate the cation, anion and ion-pair sensing properties of **5.5XB$_{SAM}$.** In agreement with literature, the film displayed a notable, but modest, response to Na^+ in pure water. Interestingly, no response to K^+ was observed in this solvent. In aqueous-organic mixtures (ACN/H_2O 9:1) a notably larger response and stronger binding to Na^+ was observed, a behaviour that was justified based on dielectric as well capacitive models.

Unfortunately, no significant/conclusive capacitive response towards a range of anions was observed in various aqueous or organic solvents, including non-competitive, non-polar solvents like DCM.

Although systematic ion-pair sensing studies were significantly hampered by various experimental difficulties (small response magnitudes, solvent/electrolyte conditions, solubility constraints and salt recombination), preliminary evidence for true ion-pair sensing was obtained. Specifically, the capacitive response towards NaBr (in ACN/H_2O 9:1 or 4:1) was significantly larger than that of $NaPF_6$ alone, indicative of simultaneous binding and sensing of both the cation and anion. Exploratory comparative studies of **5.5XB/HB$_{SAM}$** also provided some additional evidence that anion binding occurs at the XB/HB binding sites.

If these results can be conclusively attributed to *specific* ion-pair binding at the interface then this work presents, to the best of my knowledge, not only the first investigation of capacitive ion-pair sensing, ion-pair binding at interfacial XB/HB ditopic receptors, but importantly the first example of a *true* electrochemical ion-pair sensor that can respond to cation *and* anion presence by generating a useful (additive) signal.

In order to validate these findings, in future work a variety of important experiments are envisioned as described in the following sections.

5.3.2 Future work

5.3.2.1 Further Capacitive Ion-Pair Sensing Studies in Aqueous-Organic Media

Most importantly, the herein presented experimental results need to be repeated to obtain statistically significant data that can be further (quantitatively) analysed (see also Section 5.3.2.2). Envisioned are also a range of experiments at both **5.5XB/HB$_{SAM}$** with different salts (mainly alkali metal halides) and in different solvent systems (different ACN/H_2O mixtures, if the solubility of electrolyte and analyte ions is sufficient).

5.3.2.2 Development of Appropriate Models

As alluded to in Sections 5.1.1 and 5.2.3.5, the theoretical description of the binding equilibria and sensor response towards ion-pairs is very complex such that the standard Langmuir model is insufficient in describing the system. Almost any empirical Langmuir-type model with ≥3 parameters will afford good fits (mathematically), however the interpretation of these parameters is often very complex and not reflective of the actual physical binding phenomena. In order to develop more appropriate models, multiple important factors have to be taken into consideration. In the following a few such models are proposed. In all cases it is assumed that the overall sensor response (C) is an additive contribution of a capacitance change as a result of cation binding (C_{C^+}) and anion binding (C_{A^-}) such that $C = C_{C^+} + C_{A^-}$.

Firstly, the cation and anion binding sites are not equivalent and possess different binding affinities. This is taken into account in a dual-site Langmuir model, here represented in the form of the capacitance as a function of cation/anion concentration ($[C^+]/[A^-]$:[365,366]

$$C = C_{C^+,max}\frac{K_{C^+}[C^+]}{1+K_{C^+}[C^+]} + C_{A^-,max}\frac{K_{A^-}[A^-]}{1+K_{A^-}[A^-]} \quad \text{eqn. 5.2}$$

However, this model does not consider cooperative effects, but treats cation and anion binding as independent events.

The simplest cooperate adsorption model is the quadratic adsorption isotherm:[365,366]

$$C = C_{max}\frac{2K[X]+2K^2[X]^2\phi}{1+2K[X]+K^2[X]^2\phi} \quad \text{eqn. 5.3}$$

where ϕ is a cooperativity factor. However, eqn. 5.3 describes the general case for cooperative binding of one species "X" with one binding constant such that this model cannot account for multi-site binding of different species. A combination of both eqn. 5.2 and eqn. 5.3 is thus proposed as the most general model that can take into account both cooperative and dual-site binding:

$$C = C_{C^+,max}\frac{2K_{C^+}[C+]+2K_{C^+}{}^2[C^+]^2\phi}{1+2K_{C^+}[C+]+K_{C^+}{}^2[C^+]^2\phi} + C_{A^-,max}\frac{2K_{A^-}[A-]+2K_{A^-}{}^2[A^-]^2\phi}{1+2K_{A^-}[A-]+K_{A^-}{}^2[A^-]^2\phi} \quad \text{eqn. 5.4}$$

In our case $[C^+] = [A^-] = [Salt]$, such that five independent parameters remain ($C_{C^+,max}$, $C_{A^-,max}$, K_{C^+}, K_{A^-}, ϕ). As mentioned before, fitting of any isotherm according to a model with ≥3 parameters will almost always afford "good" fits, a proper validation of this dual-site cooperative model can thus only be achieved by careful analysis of larger data sets.

5.3.2.3 Capacitive Investigations at lower Ionic Strength

As discussed in Section 5.2.3.2 one may model the overall capacitive properties of the film by considering multiple series capacitive components. A slightly different interpretation within this context is not a subdivision into an anchor (C_{anchor}) and a binding site

component (C_{site}) as discussed above, but rather a subdivision into a "buried" and an "exposed" component. Specifically, one may consider that the capacitance of the exposed periphery of the SAM is not only dictated by the SAM itself (*i.e.* the crown ether binding sites) but also by solvent and ion "penetration"/association into/with the film. This is to say that for these peripherally "open" films significant "classical" double layer effects contribute towards $C_{exposed}$. These effects are of course strongly dependent on the nature of the electrolyte, specifically its concentration, such that at high ionic strength $C_{exposed}$ is large and overall contributes little towards C (as the $1/C_{exposed}$ term is small):

$$\frac{1}{C} = \frac{1}{C_{buried}} + \frac{1}{C_{exposed}}$$

A binding-induced increase in $C_{exposed}$ thus does not significantly influence C, which is largely determined by the $1/C_{buried}$ term.

It should be noted that these interpretations and the naming of the capacitive subcomponents is not inherently different to that presented in Section 5.3.2.3, but rather focuses on additional contributions towards (or a different interpretation of) this capacitance (*i.e.* electrolyte/double layer effects).

Additionally, a similar argument can be constructed based on purely dielectric considerations. At high electrolyte concentrations the environment around the crown ether binding sites already contain a high number of (electrolyte) ions, such that specific cation binding does not significantly affect the local ion concentration (and thus dielectric).

It was hypothesised that these problems can be circumvented by conducting the sensing studies in an electrolyte of lower ionic strength. This would significantly lower $C_{exposed}$ (and

the dielectric/ion concentration around the exposed binding sites) such that it contributes more towards the overall capacitance and more sensitively reports on ion binding.

Preliminary investigations appear to confirm this hypothesis; in H_2O 10 mM $TBANO_3$ the addition of 10 mM Na^+ induces a much more significant capacitance increase (≈15%), a value that far exceeds that attainable in the presence of 100 mM $TBANO_3$ electrolyte. Interestingly, the further addition of 5 mM I^- induces and additional increase in the capacitance (to ≈28%), indicative of ion-pair binding. However these observations need to be further validated and careful control experiments need to be carried out to ensure that this is a specific response that does not arise from a change in the electrolyte or other non-specific effects.

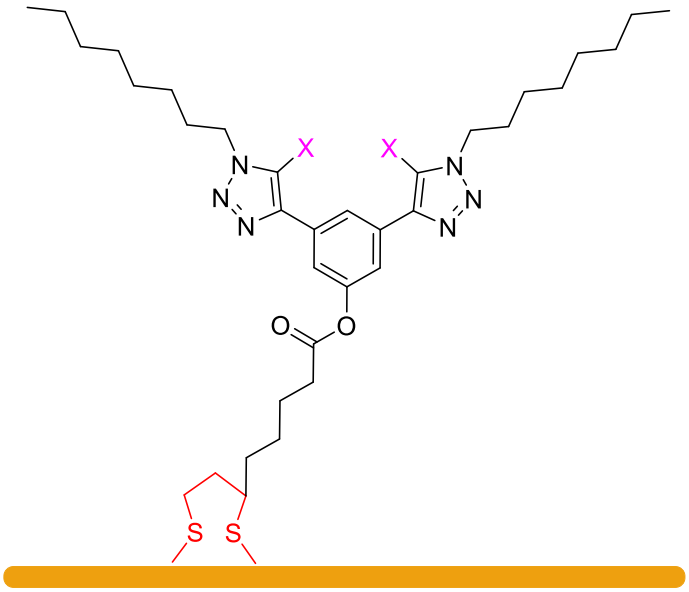
5.3.2.4 Amino Acid Sensing

As highlighted in Section 5.1 heteroditopic receptors are also often employed for the recognition and sensing of covalently linked ion-pairs, in particular zwitterionic amino acids. Preliminary investigations into the sensing properties of **5.5XB$_{SAM}$** towards glycine, phenylalanine and arginine were carried out in ACN, ACN/H_2O mixtures as well as pure water. Unfortunately, in all cases no significant changes in the capacitance were observed. This indicates that the heteroditopic binding site of the receptor is not conducive to binding of these ion-pairs, potentially as a result of geometric constraints, in particular within the crowded SAM environment. However, in the case of the amino acids it could also be argued that the presence of the aliphatic/aromatic backbones may induce a capacitive response that cancels that of the ionic ammonium and carboxylate groups (as observed in Section 4.2.3.2).

In this case amino acid sensing might be viable *via* Faradaic impedance. While the oppositely charged groups should overall induce a net-neutral interaction with the solution-phase redox probe, steric hindrance should induce an increase in the charge-transfer resistance. However, these investigations are experimentally difficult as the commonly utilised redox probes $[Ru(NH_3)_6]^{2+/3+}$ and $[Fe(CN)_6]^{3-/4-}$ are employed as their Cl^- and K^+/Na^+ salts, respectively (few other counter ions to these salts are known/available, presumably as a result of solubility constraints). These counter ions can potentially compete with binding and significantly complicate analyses. This has also largely prevented the impedimetric investigation of the binding properties of **5.5XB$_{SAM}$** towards inorganic metal cations and anions.

5.3.2.5 Control Experiments at Non-Receptive SAMs

As discussed above, a range of control experiments are required to conclusively assign the observations to specific binding events. Some evidence of this can arise from a detailed comparison of **5.5XB$_{SAM}$** and **5.5HB$_{SAM}$**. Additional control experiments are also envisioned at non-receptive SAM as well as receptor analogues **5.6XB/HB$_{SAM}$**, which do not contain crown ether cation binding sites (Figure 5.20).



5.6XB/HB$_{SAM}$: X = I/H

Figure 5.20. Schematic representation of **5.6XB/HB$_{SAM}$**.

5.3.2.6 Switching Surface Wettability

The hydrophilicity/hydrophobicity of a surface is one of its most important properties and plays a crucial role in its interaction with fluids and adsorbents. For example, a strong surface hydration is implicit in presenting a barrier to the non-specific adsorption (fouling) of (bio)molecules which is crucial in many biomedical devices and sensors.[315] The reversible switching of the surface hydration is thus of interest in smart, responsive interfaces, such as self-cleaning surfaces.

The generation of a more hydrophilic interface can be achieved by binding of ions or other polar molecules as demonstrated previously.[367-370] The heteroditopic interfaces **5.5XB/HB$_{SAM}$** may be particularly interesting for such applications as multiple host-guest complexes (with either anion or cation alone or as ion-pair) can be formed thereby giving additional control over the specific nature of the interface.

Chapter 6

Summary and Conclusions

Chapter 6: Summary and Conclusions

Presented in this thesis is a systematic investigation of the anion sensing capabilities of a range of novel XB and HB anion receptors in various electrochemical configurations. This includes redox-active anion receptors containing ferrocene or osmium (II) bipyridyl redox transducers enabling anion sensing *via* voltammetric techniques (Chapter 2). In all cases a well-defined cathodic perturbation of the redox couple was observed upon addition of specific anions in aqueous-organic solvent systems. Detailed analyses of the binding isotherms provided anion binding constants to both the native and oxidised receptors, revealing a pronounced binding enhancement (switch-on) upon receptor oxidation whose magnitude strongly correlates with the sensor response. For example, systematic studies of XB and HB Fc-((iodo)triazole-amide) receptors afforded unprecedented insights and detailed comparisons of voltammetric XB and HB sensors under diffusive as well as surface-confined conditions. In solution the XB receptor significantly outperformed its HB analogue for all anions tested, while upon surface-immobilisation a previously unobserved phenomenon was resolved. For both receptors the overall response was significantly amplified, however the difference between the XB and HB receptors diminished, with a modest preference for halides at the XB SAM and a preference for the oxoanions at the HB interface. All of these observations were analysed in detail and explained using a new dielectric model which explicitly considers how charge-screening affects the binding-switch on (and thus response) and how this differs for the XB and HB binding motifs.

Notably, detailed studies of the redox-active receptive films revealed the redox reversibility of the SAMs was significantly improved by the unprecedented use of an acidic aqueous-

organic electrolyte, even at low acid concentration. This circumvented problems arising from receptor degradation and enabled sensor re-use.

In Chapter 3 a label-free impedance-based capacitive approach for the sensing of anions was introduced. This methodology was previously applied to the sensing of cations but remained, hitherto, unexplored for the sensing of anions. Sensing of ReO_4^-, SCN^- and I^- was achieved at XB and HB foldamer SAMs which, upon anion binding in pure water, displayed an enhanced interfacial capacitance. Importantly, by omission of a redox probe this non-Faradaic impedance-based approach avoids problems that are typically associated with Faradaic EIS, such as poor baseline stability or the requirement for conditions that are compatible with the redox transducer. Additionally, the capacitive methodology can in principle be conducted at any potential and in any solvent.

The novel capacitive methodology was then also applied to the enantioselective sensing of anions at chiral SAMs as detailed in Chapter 4. These studies were conducted with (*R/S*)-BINOL-PO_4^- as model chiral anions, for which a small preference for the *R*-enantiomer was resolved, in agreement with both steric considerations and prior reports of similar chiral receptors. Interestingly, the capacitive response of this sensor was opposite to that observed towards small, inorganic anions, specifically, a decreased interfacial capacitance was observed upon BINOL-PO_4^- binding, attributed to the non-polar backbone of the analyte.

In further exploiting the non-Faradaic capacitance approach, Chapter 5 examined the feasibility of ion-pair recognition at heteroditopic SAMs. In pure water a small, but significant response towards Na^+ was observed with no significant capacitive perturbations in the presence of anions or ion-pairs. However, in mixed aqueous-organic solvent systems

the presence of NaBr induces an additive capacitance increase response that exceeds that obtainable by either ion alone. This is preliminary evidence for the unprecedented electrochemical sensing of inorganic ion-pairs *via* a useful, additive, readout. This is also the first demonstration of impedance-based ion sensing in a solvent that is not purely/predominantly aqueous (greatly increasing the applicability of this detection methodology). Hitherto the investigation of ion-binding phenomena at receptive interfaces *via* EIS-derived approaches was only demonstrated in pure water, thus requiring the use of potent receptors that are capable of ion binding in this highly competitive solvent, undoubtedly one of the main reasons for the limited use of EIS for (an)ion sensing applications.

The response of all capacitive sensors was, in analogy to voltammetric studies, interpreted by an analysis of changes in the film dielectric environment, highlighting that many observations, such as the magnitude of the sensor response, can be analysed without the derivation of specific (capacitive) models.

In summary, this thesis provides the first detailed investigation of XB anion receptors for the electrochemical sensing of anions and their detailed comparison with their HB analogues. In almost all cases the XB receptors display larger responses, highlighting the utility of the XB interaction not only for anion recognition but also for sensing applications. Only the surface bound redox-active XB receptor was outperformed by its HB analogue in a few cases but displayed an altered selectivity for halide anions over oxoanions.

The sensors reported herein are also the first examples of XB anion receptive interfaces, with only one other example reported to date,[219] and thus provide valuable insights into the characteristics of the XB interaction at molecular films. The understanding of these

interfacial processes is not only of fundamental interest, but also for many sensing applications as these interfacial sensors are of much higher real-life relevance. The latter was explicitly demonstrated by enhanced interfacial responses and/or selectivities, sensor re-use as well as sensing under otherwise inaccessible conditions (*i.e.* in aqueous solvents in which the receptors are typically not soluble). In addition, the in-depth investigation of these sensors provided unprecedented details into their transduction principles as well as binding phenomena at anion receptors. Importantly, the analyses and methodologies presented herein are expected to be readily translatable to a large variety of other electrochemical (ion) sensors and are thus important additions to the toolbox in the fields of supramolecular host-guest chemistry, electrochemical sensors and interfacial chemistry. For example, the analysis of voltammetric binding isotherms readily affords various important binding constants in an experimentally straight-forward manner, however this is rarely carried out. Similarly, capacitive approaches possess a high-information density and are expected to have greater real-life applicability as many inherent drawbacks of voltammetric sensors (such as voltammetric instabilities and a strong dependence on electrolyte conditions) are circumvented.

Chapter 7

Experimental

Chapter 7: Experimental

7.1 General Considerations

7.1.1 Chemicals and Solvents

Ultrapure water was drawn from a Milli-Q system (18.2 MΩ cm) and used in all aqueous solutions. All chemicals and solvents were obtained from commercial suppliers and used as received. All electrolyte salts were of analytical grade or of at least 99% purity. $TBAClO_4$ and $TBAPF_6$ were of electrochemical grade and obtained from Sigma Aldrich. Hygroscopic TBA-salts and $Cu(CH_3CN)_4PF_6$ were stored in a desiccator. For solvent mixtures, ratios are reported by volume (*v/v*). Anhydrous solvents were obtained from an MBraun MPSP-800 column. Triethylamine was distilled and stored over KOH.

All experiments were conducted at room temperature unless otherwise stated.

7.1.2 NMR and MS

NMR spectra were recorded on Bruker NMR spectrometers (AVIII HD 500 or AVIII HD 400) and referenced to the solvent residual signal. Chemical shifts δ are reported in parts per million relative to the residual solvent peak. Peak splittings are denoted as follows: singlet (s), doublet (d), triplet (t), quartet (quart.), quintet (quint.) and multiplet (m).

NMR titrations were carried out by titrating 500 µL of host solution (at a host concentration of 1 or 2 mM) with a high concentration of the anion (as TBA salt) in the same solvent. Typically 17 additions were carried out. Data fitting was performed with OriginPro 2017 utilising the established 1:1 host-guest binding model.[371] In all cases fast exchange was

observed. The majority of the NMR titrations (data acquisition) were carried out by Dr. Xiaoxiong Li.

Low resolution electrospray ionisation mass spectrometry (ESI-MS) was performed using a Waters Micromass LCT and was used for compounds which were previously reported. Novel compounds were characterised by high resolution ESI-MS recorded on a Bruker microTOF spectrometer.

7.2 Electrochemical Experiments

All electrochemical experiments were carried out with Autolab potentiostats (Metrohm; equipped with FRA32 and MUX modules) in a Faraday cage, using a three electrode setup. A platinum wire counter electrode was used in all experiments. Gold disc (1.6 mm diameter, BASi) or glassy carbon disc electrodes (3 mm diameter, BASi) were used as working electrodes. For all experiments described in Section 2.2 a non-aqueous reference electrode with a filling solution of 10 mM $AgNO_3$ and 100 mM $TBAClO_4$ in ACN was used. All other experiments were carried out with leak-free Ag|AgCl (3 M KCl) reference electrodes (Innovative Instruments or home-made with a Pt-wire frit). The Nova 1.11 software was used throughout. Unless explicitly stated, all electrochemical experiments were carried out in the presence of oxygen and in undried solvents. Please note that the nature and concentration of the supporting electrolyte is, for sake of simplicity, not stated in all figure or table captions, but is clearly indicated in the associated main text. $[Fe(CN)_6]^{3-/4-}$ was freshly prepared from an equimolar mixture of $K_3[Fe(CN)_6]$ and $K_4[Fe(CN)_6]\cdot 3H_2O$.

It should be noted that all sensing experiments were carried out with freshly prepared SAMs that were not previously subjected to extensive electrochemical analysis or had been in contact with any analyte solution, unless explicitly stated (*i.e.* for reusability experiments). Reductive thiol stripping experiments were also typically carried out on freshly prepared electrodes that were not previously subjected to any other electrochemical analysis or sensing studies.

7.2.1 Electrode Cleaning

Glassy carbon electrodes: Mechanical polishing was carried out with alumina slurry (particle size: 0.05 µm; Buehler). New or heavily contaminated electrodes were polished with coarser alumina abrasives (1 µm, 0.3 µm and then 0.05 µm). Afterwards, the electrodes were briefly sonicated in EtOH/H_2O and then dried under N_2.

Gold electrodes: Mechanical polishing was carried out as described above. Afterwards the electrodes were polished chemically by immersion in freshly prepared piranha acid (3:1 H_2SO_4/H_2O_2) for approx. 10 min. This was followed by electrochemical polishing in 0.5 M $KOH_{(aq)}$, between −0.7 and −1.7 V for approx. 1 h. Lastly the electrodes were electrochemically cleaned in 0.5 M $H_2SO_{4(aq)}$ between 0 and 1.5 V for at least 1 h. After rinsing with H_2O and EtOH the electrodes were dried under N_2 and used immediately. The electroactive surface area of the electrodes was determined from the CVs in 0.5 M $H_2SO_{4(aq)}$ (Figure 7.1) according to standard procedures, utilising 559 µC/cm^2 as the conversion factor.[372] The roughness factor (electroactive surface area/geometrical surface area) was typically between 1.5 and 2.1.

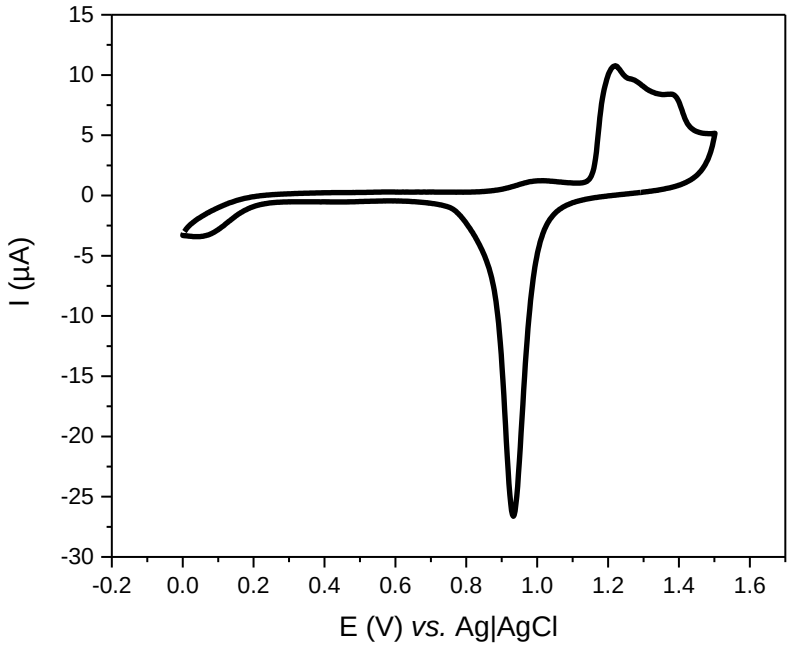


Figure 7.1. CV of bare Au disk electrode in 0.5 M $H_2SO_{4(aq)}$ (electrochemical polishing). The electroactive surface area of the electrode is determined from the peak area of the reductive peak at around 0.90 V.

7.2.2 Cyclic Voltammetry (CV)

Unless otherwise noted the following settings were used: 100 mV/s scan rate, 2.44 mV step potential. CVs at varying scan rates (for reversibility studies) were carried out at the following eight scan rates: 0.025, 0.05, 0.075, 0.1, 0.2, 0.4, 0.6 and 0.8 V/s.

7.2.3 Square Wave Voltammetry (SWV)

All experiments were carried out with an amplitude of 20 mV, a step size of 2 mV and a frequency of 25 Hz.

The redox stability of **2.2HB$_{SAM}$** shown in Figure 2.14 was assessed on three electrodes submerged in one cell. The electrodes were addressed sequentially *via* the use of a multiplexer module. SWV was measured as detailed above between −0.1 and 0.35 V

(*vs.* Ag|$AgNO_3$) for 50 scans. Afterwards, the electrode was polarised at the initial potential (−0.1 V) for 30 s to ensure full reduction of the film to its native state. The measurement was then carried out in the same fashion on the two other electrodes. This overall procedure (50 scans on three electrodes) was repeated 10 times, such that each electrode was subjected to 500 repeat SWV measurements. This corresponds to an overall measurement time of approx. 5 h (all three electrodes together, *i.e.* approx. 1.67 h per electrode). For the duration of the measurement the cell was not disturbed thereby ensuring that the distance between all electrodes was fixed throughout. The redox stability was assessed as the decrease in peak current. No significant changes in the $E_{1/2}$ were observed.

7.2.4 Electrochemical Impedance Spectroscopy (EIS)

EIS is one of the most sensitive electroanalytical techniques and has been established as a particularly useful tool to study conducting interfaces. Specifically, a small amplitude sinusoidal AC current is applied to the electrode at a fixed DC bias potential. Under these conditions the interface is not significantly perturbed and is thus probed at equilibrium. The sinusoidal current response that arises from the AC perturbation is recorded and directly reports on a variety of interfacial parameters (specifically the impedance, which is a complex number that is determined by the ratio of the applied voltage and the measured current and the phase shift between the two). This measurement is typically carried out over a wide-range of AC frequencies thereby reporting on a range of interfacial processes of different timescales with a high-information density (real and imaginary parts of impedance/capacitance/resistance/admittance and their response frequencies).

As highlighted in Chapter 1, this technique has been employed for sensing at receptive interfaces, in particular for the sensing of large biomolecules in the presence of a signal-amplifying redox probe (Faradaic EIS). For further information the interested reader is referred to literature reviews.[233,305,373,374]

EIS was recorded between 100 kHz and 1 Hz or 0.1 Hz for 30 or 40 frequencies (logarithmically stepped) using a 10 mV amplitude (root-mean square). The open-circuit potential (OCP) was typically chosen as the DC potential; in the presence of $[Fe(CN)_6]^{3-/4-}$ as redox probe the half-wave potential of the probe (≈0.21V, as determined by SWV) was sometimes used instead (as indicated; typically this value and the OCP were similar).

Capacitive Nyquist plots were calculated *via* $C''(\omega) = Z'/\omega|Z|^2$ and $C'(\omega) = Z''/\omega|Z|^2$, where ω is the angular frequency, C'/C'' the real and imaginary capacitance, Z'/Z'' the real and imaginary impedance and |Z| the modulus of the impedance. Electrochemical circuit fitting was carried out with Nova 1.11.

Capacitance measurements at different potentials were carried out by first measuring a full capacitive Nyquist plot at OCP (Chapter 3, Section 3.4.3) or the half-wave potential of the redox-active SAM (Chapter 2, Section 2.4.2.2). Subsequent measurements at different potentials were carried out at only one frequency, specifically the frequency that corresponds to the inflection point in the capacitive Nyquist plot. At this frequency the film capacitance C or the redox capacitance C_r was obtained as C'. For the different measurements described in different Chapters the following parameters were used:

Chapter 2, Section 2.4.2.2: 50 DC potentials between -0.1 and 0.4 V (*vs.* non-aqueous Ag|$AgNO_3$ reference electrode, corresponding to 10 mV steps; starting at the lower potential). Before each measurement the electrodes were polarised for 120 s at the first DC potential and then for 1 s at all other potentials.

Chapter 3, Section 3.4.3: 13 DC potentials between -0.1 and 0.5 V (*vs.* aqueous Ag|AgCl reference electrode, corresponding to 50 mV steps; starting at the lower potential). Before each measurement the electrodes were polarised for 120 s at the initial DC potential and then for 30 s at all other potentials.

All capacitive and impedimetric Nyquist and Bode plots that are shown are representative plots from one electrode that accurately reflect the general magnitude and "shape" of the response as observed for the large majority of measurements (*i.e.* in only very few cases were significant deviations from the behaviour as shown observed). All graphs that are shown within one plot were obtained on the same electrode such that they are directly comparable. The capacitance/impedance values shown in these plots were not normalised by the electrode area such that typically no direct comparison between the absolute values shown in different Nyquist/Bode plots can be made. For direct comparisons the reader is referred to the normalised values that are stated/tabulated within the text (averages of at least three independent measurements on different electrodes).

Unless explicitly stated, all analysis of capacitive and impedimetric Nyquist plots was carried out by graphical analysis.

7.2.5 Determination of Molecular Surface Coverage (Γ)

The molecular surface coverage (Γ) was calculated *via* $\Gamma = \frac{Q}{\mathrm{n}*F*A_e}$, where Q is the charge associated with the electrochemical process (reductive thiol stripping or peak integration of CVs of surface-confined redox probe), n the number of electrons transferred and A_e the electroactive surface area of the gold electrode.

7.2.6 Reductive Thiol Stripping

Reductive thiol stripping was carried out by CV (typically between 0 and −1.4 V) in deoxygenated 0.5 M $KOH_{(aq)}$ (Figure 7.2). The area under the peak was calculated with Nova 1.11 utilising an exponential baseline. n was assumed as two for each disulfide anchor group.

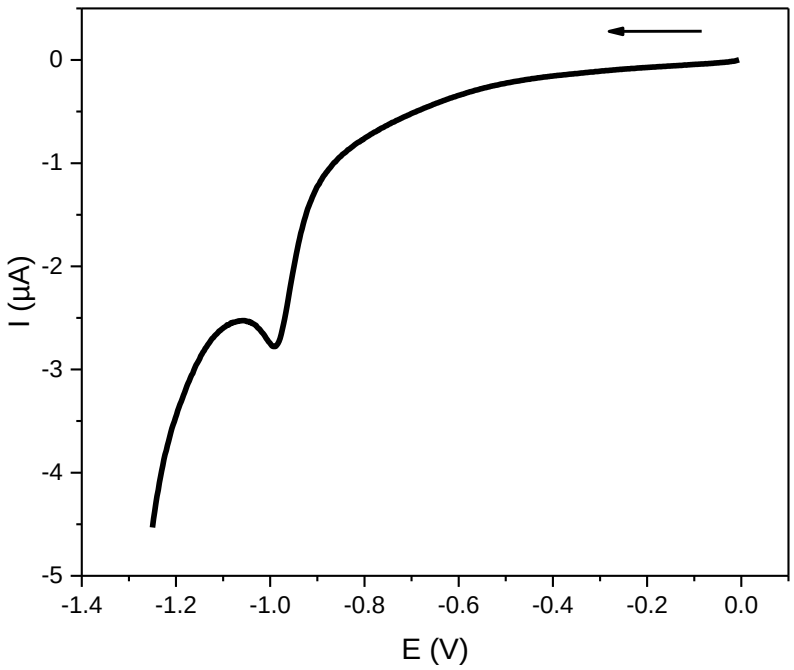


Figure 7.2. CV of reductive desorption of **3.1XB$_{SAM}$** in 0.5 M $KOH_{(aq)}$ (degassed) at a scan rate of 100 mV/s. Arrow indicates direction of scan.

7.2.7 Electrochemical Sensing Studies

7.2.7.1 General Considerations and Terminology

Throughout this thesis the term "response" refers to the change in signal arising in the presence of the target analyte. For all voltammetric sensors (Chapter 2), this refers to the absolute magnitude of change of the half-wave potential of the redox transducer (typically in mV). This response is a cathodic shift in all cases.

For all capacitive and impedimetric sensing studies (Chapters 3-5) the response is strictly discussed in relative terms, *i.e.* the normalised signal change:

$$RR\%[A] = \frac{R[A] - R_0}{R_0} * 100\%$$

where $RR\%$ refers to the relative response (in %; typically of the capacitance C), R_0 is the baseline signal and $R[A]$ is the signal as a function of the analyte (anion). Please note that in Chapters 3-5 all discussions are based on this normalised/relative response even if the "normalised"/"relative" qualifier is omitted for simplicity in some cases. The explicit dependence of the response on anion concentration is also omitted in most cases.

In the following a few commonly used symbols and terms are listed:

$\boldsymbol{\Delta E_{max}}$ – Maximum cathodic response at $[A^-]$ = ∞; obtained from fitting to the Langmuir model (absolute value; in mV).

$\boldsymbol{-C'/Z'}$ – Real capacitance/impedance.

$\boldsymbol{C''/-Z''}$ – Imaginary capacitance/impedance.

(The signs of these complex values is irrelevant for discussions herein and largely omitted.)

$\boldsymbol{C}$ – Capacitance of the SAM as resolved by the diameter of the semicircular region in capacitive Nyquist plots. This capacitance represents the overall electrochemical capacitance $C_{\overline{\mu}}$ as discussed in more detail in Chapter 3, Section 3.4 and 3.5.

$\boldsymbol{\Delta C}$ – Relative response of C. In Section 3.5.3 this value is equivalent to C_{μ_i}.

$\boldsymbol{\Delta C_{max}}$ – Maximum relative capacitive response at $[A^-]$ = ∞, obtained from fitting to the Langmuir model (relative value; in %).

$\boldsymbol{C''_{apex}}$ – "Apex" capacitance of the SAM as resolved by C'' at the apex of the semicircular region in capacitive Nyquist plots.

$\boldsymbol{\Delta C''_{apex}}$ – Relative response of C''_{apex} (relative value; in %).

$\boldsymbol{\Delta C''_{apex,\ max}}$ – Maximum relative response of C''_{apex} at $[A^-]$ = ∞; obtained from fitting to the Langmuir model (relative value; in %).

$\boldsymbol{|Z|}$ – Modulus of impedance, obtained as Z' at the lowest measured frequency (0.1 Hz).

$\boldsymbol{\Delta|Z|}$ – Relative response of $|Z|$ (relative value; in %).

$\boldsymbol{\Delta|Z|_{max}}$ – Maximum relative response of $|Z|$ at $[A^-]$ = ∞; obtained from fitting to the Langmuir model (relative value; in %).

$\boldsymbol{R_{ct}}$ – Charge-transfer resistance, resolved by the diameter of the semicircular region in impedimetric Nyquist plots.

7.2.7.2 Electrochemical Titrations

All electrochemical sensing studies presented herein (voltammetric, capacitive and impedimetric) were carried out at constant ionic strength (typically 100 mM); *i.e.* by titration of the initial electrolyte solution with a salt solution of the same concentration. The analyte solution was prepared from salts of the same counter cation as that of the initial electrolyte (*i.e.* TBA^+, or Na^+). Impedimetric and solution-phase voltammetric studies were carried out at a constant concentration of redox-active solution-phase species. All experiments were carried out in a cell with an initial electrolyte volume between 0.9 and 4 mL. After each addition of analyte the solution was thoroughly mixed by swirling. Unless absolutely required (*e.g.* for a re-assessment in analyte-free electrolyte) the working electrodes were not removed from the solution during the course of a titration.

Voltammetric binding studies were conducted by SWV. In all cases multiple scans were recorded to ensure reproducibility. Typically the second or third scan was used for analysis (always the same scan for one titration and never the first scan). After SWV scans at redox-active SAMs the electrode was briefly polarised at the initial (cathodic) potential to reduce the SAM to its native state. Solution-phase voltammetric binding studies were carried out at a constant receptor concentration of 0.1 mM. A bare, polished GC working electrode was used for all diffusive voltammetric studies and was re-polished between different sets of binding studies.

Capacitive and impedimetric binding studies were typically carried out by titration experiments on two or three electrodes in the same cell. Specifically, the electrodes were addressed sequentially *via* the use of a multiplexer module. The order in which the electrodes were measured was always the same. For all capacitive or impedimetric binding

studies at least five repeat measurements were performed to assess the initial baseline stability. After each addition of analyte, at least three repeats were recorded. The number of repeat measurements was kept constant in all cases where a direct comparison between the XB/HB performance or different anions was carried out. Similarly, wherever a direct comparison between experiments is presented, all experiments were carried out on the same set of electrodes (the specific electrodes and measurement parameters between the different projects are not always identical).

Voltammetric titrations of **2.1HB** in ACN were carried out by Dr. Xiaoxiong Li, who also carried out the voltammetric reversibility studies of **2.1HB** and **2.2HB$_{SAM}$**.

7.3 SAM Formation and Surface Characterisation

7.3.1 SAM Formation

SAMs were formed by immersion of the clean gold substrates into a solution of thiol/disulfide and were incubated overnight at room temperature in the dark. The nature of the solvent and concentration of the thiol/disulfide for the different receptors was as follows:

Chapter 2: 0.25 mM **2.2XB/HB** in ACN.

Chapter 3: 0.25 mM **3.1XB/HB** in ACN/H_2O 1:1. Control experiments were carried out on SAMs of 1-undecanethiol, which were formed from 2 mM thiol in EtOH.

Chapter 4: Various conditions for initial screening as detailed in Table 4.1. Standard conditions subsequently adopted: 1 mM **4.4XB/HB** in DCM.

Chapter 5: 0.25 mM **5.5XB/HB** in ACN/H_2O 1:1.

Subsequently, the substrates were thoroughly rinsed with the solvent that was used for SAM formation (organic solvent component only; *i.e.* ACN or DCM) and then further rinsed with EtOH. Electrodes or planar Au substrates for surface analysis *via* XPS, FT-ATR-IR, AFM or ellipsometry were then dried under a stream of N_2 and analysed as quickly as possible. Electrodes for electrochemical experiments were further rinsed with the electrolyte solvent, dried with N_2 and immediately subjected to electrochemical analysis.

For surface analysis *via* XPS, FT-ATR-IR, AFM and ellipsometry larger surface area substrates were required. To this end SPR gold sensor chips (Reichert) or gold on silicon (prepared in-house, Au thickness approx. 100 nm with a thin chromium adhesion layer) were used. These substrates were rinsed with copious amounts of solvent (DCM, EtOH and H_2O) and then dried. Subsequently they were cleaned by immersion into fresh piranha acid (3:1 H_2SO_4/H_2O_2) for at least 30 s followed by extensive rinsing with water and ethanol. SAM formation was then carried out as described above. Water contact angle measurements were typically carried out on the Au disk electrodes.

7.3.2 ATR-FTIR Spectroscopy

IR spectra were measured in transmission mode between 500 and 4000 cm^{-1} on an IRTracer-100 (Shimadzu). Typically, an average of 30 scans was recorded at a resolution of 0.5.

7.3.3 X-ray Photoelectron Spectroscopy (XPS)

Samples were analysed using a Thermo Scientific K-Alpha XPS instrument equipped with a microfocussed, monochromated Al X-ray source. The source was operated at 12 keV and a 400 micron spot size was utilised. The analyser was operated at a constant analyser energy (CAE) of 200 eV for survey scans and 50 eV for detailed scans. Charge neutralisation was applied using a combined low energy electron/ion flood source. The errors that are stated in this thesis were calculated based on measurements of three different spots on the same sample. Data acquisition was carried out by Dr. Philip Holdway.

All data analysis was carried out with CasaXPS (v2.3). Linear or Tougaard backgrounds were used in all cases. Peak fitting was carried out without any restrictions of the peak position, line shape, area or FWHM of the peak. In the case where the (theoretical) peak ratio of some subcomponents is large this can induce relatively large errors as the smaller peak does not sufficiently stand out from the spectrum and thus usually gets fitted as a very broad peak encompassing much of the baseline. This behaviour was most notably observed for fitting of the O 1s spectra (*e.g.* Figure 5.6C). This can be circumvented if the peak is restricted to a specific peak position/line shape and/or FWHM, this however requires prior knowledge/assumption of these values for the specific subcomponents.

7.3.4 Water Contact Angle Measurements

Static water contact-angle measurements were performed on a FTA1000B goniometer (First Ten Ångstroms) equipped with a manually operated microliter syringe. A sessile drop of deionised water (18.2 MΩ cm) was used as the wetting liquid. A point grey USB camera with

a Navitar lens was used to capture videos at 61 frames per second. Data analysis was carried out with the FTA32 software and all droplets were fitted to a spherical model.

7.3.5 Ellipsometry

Variable angle ellipsometric measurements were conducted on a Beaglehole Instruments Picometer Ellipsometer equipped with a 2 mW Helium-Neon laser (632.8 nm). The average dry thickness of SAMs was determined by fitting the data with a one-layer model, taking bare gold as the reference and 1.45 as the refractive index for the SAM layer. The IgorPro software (WaveMetrics) was used to analyse the data. The errors that are stated in this thesis were calculated based on measurements of different spots on the same sample. All measurements were carried out by Dr. Robert Jacobs or Dr. Candan Catli.

7.3.6 Atomic Force Microscopy (AFM)

AFM was recorded in ambient air in tapping mode on a JPK instrument. Tap300-G (BudgetSensors) tips with a radius of <10 nm and a resonance frequency of 300 kHz were used.

All data analysis was carried out using Gwyddion. The high-resolution data presented in Chapter 5, Section 5.2.2.3 was analysed using the following data treatment: data levelling by mean plane subtraction, correction of horizontal scars, alignment of rows as well as fixing the lowest point to zero.

7.4 Data Analysis and Fitting

Nova 1.11 was used for circuit fitting of all electrochemical data as well as all peak current/area measurements. All other data analysis and graphing was carried out with OriginPro 2017, unless otherwise noted. Fits were typically performed without weights.

All error bars represent one standard deviation, typically of three independent measurements.

All binding constants are rounded to three significant figures.

Eqns. 1.1 and 2.1, eqns 1.2 and 2.2 as well as eqns. 2.4 and 3.1 are equivalent and were only reiterated in different chapters due to their importance.

Specific Notes:

Chapter 2: BEFs from data fitting

As highlighted in both Chapters 1 and 2, the absolute determination of K_{Ox} and K_{Red} is only possible by fitting of the voltammetric binding isotherms according to eqn. 2.2. This equation is only valid under fast-exchange conditions (*i.e.* a progressive shift of the redox wave, rather than a "two-wave" behaviour, which is the case herein) and if the concentration of the anion is significantly larger than that of the redox-active receptor. The latter is also satisfied under diffusive conditions as $[H] = 0.1$ mM and titrations were generally performed until $[A^-] = 50$ mM. Importantly, this restriction needs to be satisfied in order for the equilibrium anion concentration $[A^-]_{eq}$ to be equal to the overall anion concentration $[A^-]_0$ (herein typically denoted as $[A^-]$ or $[G]$). This is to say, this restriction

does not arise from considerations of the host concentration $[H]$. This is important when applying eqn. 2.2 to a surface-confined voltammetric sensor, which, to the best of our knowledge, has not been previously carried out. Specifically, $[H]$ at an interface is not clearly defined (but may be assumed as unity, in analogy to the activity of a solid). This is however irrelevant here, as the overall amount of host is small, such that the overall equilibrium free anion concentration $[A^-]_{eq.}$ is still accurately described by the overall anion concentration $[A^-]_0$ in the cell. Based on these considerations eqn. 2.2 is expected to be a valid model to also describe the response of interfacial voltammetric (an)ion sensors, as also indirectly confirmed by the excellent fits obtained herein.

As also stated in the text, the conclusions that were drawn from the quantitative analyses presented in Chapter 2, which subsequently aided in the development of the dielectric model, do not explicitly rely on the specific values (K_{Ox} and K_{Red}) that were obtained from fitting to eqn. 2.2. Specifically, the same conclusions can be drawn when analysing the trends of ΔE_{max} at 50 mM anion which is, according to the most general case (eqn. 2.1), directly proportional to the BEF as well (and thus also reports on the ratio of K_{Ox}/K_{Red}).

It should be noted that all fits were carried out without any restriction of the parameters. In a few cases this affords a nonsensical, negative value for K_{Red} (*e.g.* Table 2.15, Chapter 2, Section 2.3.4). This is of course chemically impossible and purely arises from the fitting (*i.e.* this value afford the best mathematical fit to the Nernst model). If K_{Red} is restricted to 0 (the lowest chemically viable value) then an almost identical fit with slightly lower R^2 is obtained.

The standard errors from fitting are generally below 10%, are however significantly larger for all values <15 M^{-1}. This of course only the case for K_{Red}, in particular for sensing studies

of **2.7** and **2.8** (Table 2.14). The BEFs calculated from the fitted K_{Ox} and K_{Red} thus have large errors such that a comparison of the magnitude of the voltammetric shift is a more appropriate measure of the BEF in this case.

Chapter 3: LODs

As alluded to in Chapter 3, Section 3.4.2, the presented LODs can be considered a conservative estimate. This is because the Langmuir-type isotherm does not possess a true linear range. In order to calculate the LOD according to: $LOD = \frac{3*\sigma_{C_0}}{s}$, a pseudo-linear range between 0 and 9 mM $[A^-]$ was chosen and fitted to a linear regression. Importantly, this large range was chosen in order to encompass a reasonably large number of data points thereby minimising errors arising from outliers. However, when restricting the range to lower concentrations, or if only the slope at the origin is considered then higher slopes are obtained, corresponding to lower LODs.

7.5 Synthesis

All column chromatographic purification was carried out *via* silica gel column chromatography unless otherwise stated. Preparative TLC was carried out on 20 x 20 cm plates, with a silica layer thickness of 1 mm (Merck). Tris(benzyltriazolemethyl)amine (TBTA) was prepared according to literature procedures.[375] Aq. NH_4OH refers to a concentration of ≈17%.

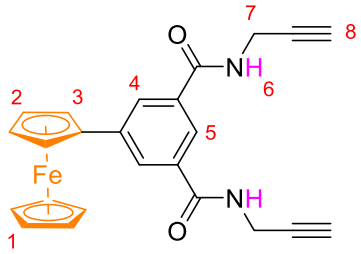
All following syntheses are reported in order of synthetic step towards the final receptor, not by compound number. For each compound it is separately indicated who carried out the synthesis using the following abbreviations: AB – Arseni Borissov; AD – Andrew Docker; RH – Robert Hein; XL – Xiaoxiong Li.

7.5.1 Synthesis for Chapter 2

The synthetic route towards **2.1XB/HB** and **2.2XB/HB** is shown in Scheme 2.1.

5-ferrocenyl isophthalic acid (**2.3**),[184] octyl azide[273] and disulfide-azide[274] were synthesised according to published procedures. Compound **2.1XB** was synthesised by Dr. Xiaoxiong Li.

Fc-isophthalamide-bis-alkyne 2.4a (RH)



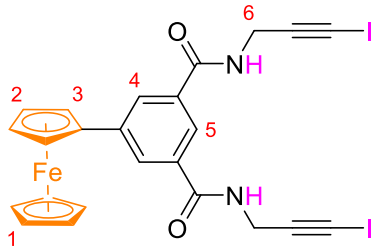
5-ferrocenyl isophthalic acid **2.3** (66 mg, 0.189 mmol) was suspended in 5 mL anhydrous DCM and cooled to 0 °C. A drop of DMF and $(COCl)_2$ (161 µL, 1.89 mmol) were then added. The mixture was stirred at rt for 4 h and then reduced *in vacuo*. The crude acid chloride was then redissolved in 3.5 mL anhydrous DCM and added dropwise to a solution of propargylamine (48 µL, 0.756 mmol) and TEA (66 µL, 0.473 mmol) in 5.5 mL anhydrous DCM under N_2. After 2 h the reaction was reduced *in vacuo* and **2.4a** isolated *via* silica gel column chromatography (2% MeOH/DCM) as an orange solid (77 mg, 0.181 mmol, 96%).

^{1}H NMR: (500 MHz, $CDCl_3$): δ 8.00 (2H, s, H^4), 7.96 (1H, s, H^5), 6.98 (2H, t, J = 5.0 Hz, H^6), 4.67 (2H, t, J = 1.6 Hz, H^3), 4.35 (2H, t, J = 1.6 Hz, H^2), 4.26 (4H, m, 4.26, H^7), 4.00 (5H, s, H^1), 2.30 (2H, t, J = 2.5 Hz, H^8).

^{13}C NMR: (126 MHz, $CDCl_3$): δ 166.7, 141.6, 134.2, 127.7, 122.3, 82.7, 79.3, 72.1, 69.8, 66.7, 29.9.

ESI-MS: m/z calcd. for $C_{24}H_{20}O_2N_2FeNa$ [M+Na$^+$] 447.07664, found: 447.07629.

Fc-isophthalamide-bis-iodoalkyne 2.4b (RH)



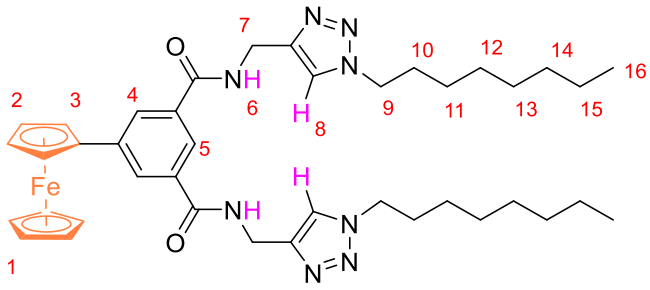
5-ferrocenyl isophthalic acid **2.3** (55 mg, 0.157 mmol) were converted to the corresponding acid chloride as described directly above (synthesis of **2.4a**). The crude acid chloride was dissolved in 5 mL anhydrous DCM and added dropwise to a solution of iodopropargylamine (86 mg, 0.471 mmol; freshly prepared according to literature procedure)[275] and TEA (0.3 mL, 2.15 mmol) in 10 mL anhydrous DCM under N_2. After 16 h the reaction mixtures was washed with H_2O twice and dried over $MgSO_4$. **2.4b** was then isolated *via* preparative TLC (1.5% MeOH/DCM) as an orange solid (6 mg, 8.9 µmol, 6%).

^{1}H NMR: (400 MHz, $CDCl_3$/MeOD 1:1): δ 8.09 (2H, d, *J* = 1.7 Hz, H^4), 8.02 (1H, t, *J* = 1.6 Hz, H^5), 4.79 (2H, t, *J* = 1.9 Hz, H^3), 4.37 (2H, t, *J* = 1.9 Hz, H^2), 4.33 (4H, s, H^6), 4.03 (5H, s, H^1).

^{13}C NMR: (126 MHz, $CDCl_3$/MeOD 1:1): δ 168.1, 142.0, 134.7, 128.4, 123.5, 89.6, 83.6, 70.2, 70.2, 67.2, 31.7.

ESI-MS: m/z calcd. for $C_{24}H_{18}O_2N_2FeI_2$ [M$^+$] 675.88106, found: 675.87975.

Fc-isophthalamide-bis-octyl-triazole 2.1HB (RH)



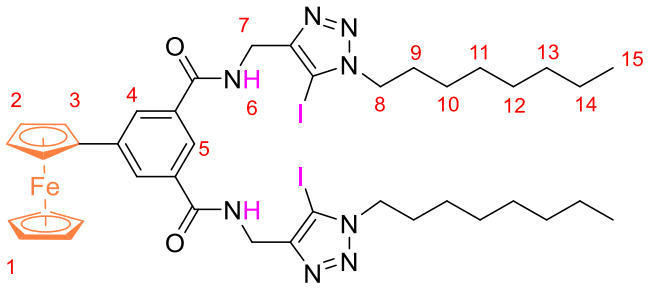
Fc-isophthalamide-bis-alkyne **2.4a** (73 mg, 0.172 mmol), octyl azide (59 mg, 0.3785 mmol), $Cu(CH_3CN)_4PF_6$ (13 mg, 0.0344 mmol), TBTA (9 mg, 0.0172 mmol) and TEA (35 mg, 0.344 mmol) were dissolved in 2 mL anhydrous DCM and reacted under N_2 for 47 h. The organic phase then washed with aq. NH_4OH twice, once with brine and dried over $MgSO_4$. **2.1HB** was then isolated by silica gel column chromatography (5% MeOH/DCM) as an orange solid (110 mg, 0.150 mmol, 87%).

^{1}H NMR: ($CDCl_3$, 500 MHz): δ 8.27 (2H, t, *J* = 5.3 Hz, H^6), 8.12 (2H, s, H^4), 8.09 (1H, s, H^5), 7.70 (2H, s, H^8), 4.68 (6H, m, H^3+ H^7), 4.34 (6H, H^2 + H^9), 3.98 (5H, s, H^1), 1.88 (4H, quint., *J* = 6.9 Hz, H^{10}), 1.34 – 1.26 (20H, m, $H^{11\text{-}15}$), 0.86 (6H, t, *J* = 7.2 Hz, H^{16}).

^{13}C NMR: ($CDCl_3$, 126 MHz): δ 165.9, 143.9, 140.2, 133.3, 127.0, 122.0, 121.1, 82.0, 68.7, 68.6, 65.7, 49.5, 34.4, 30.7, 29.2, 28.0, 27.9, 25.5, 21.6, 13.0.

ESI-MS: m/z calcd. for $C_{40}H_{55}O_2N_8Fe$ $[M+H^+]$ 735.37919, found: 735.37879.

Fc-isophthalamide-bis-octyl-iodotriazole 2.1XB (RH/XL)



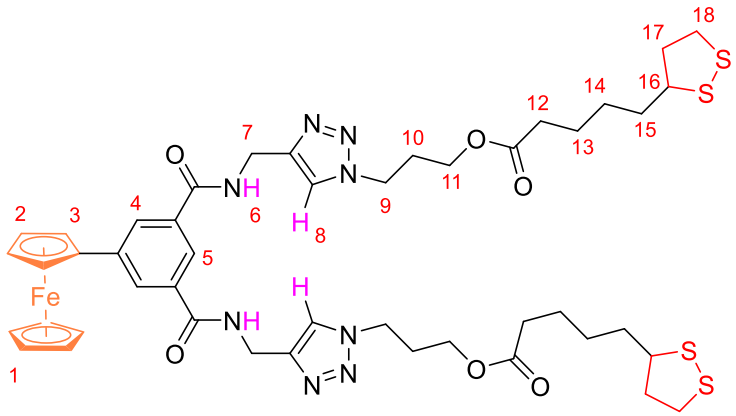
To a solution of octyl azide (74 mg, 0.48 mmol) in 2 mL THF was added $Cu(ClO_4)_2 \cdot 6H_2O$ (356 mg, 0.96 mmol) and NaI (288 mg, 1.92 mmol). The mixture was left to stir in the dark for 5 min before TBTA (13 mg, 0.025 mmol) was added. DBU (73 mg, 0.48 mmol) dissolved in 1 mL CH_3CN was added followed by addition of a solution of **2.4a** (101 mg, 0.24 mmol) in 1 mL CH_3CN. The reaction mixture was stirred at rt for 48 h. Subsequently, the mixture was washed with an EDTA solution (20 mL x 3), H_2O (3 x 30 mL) and then dried over $MgSO_4$. The solvent was removed *in vacuo* to afford a yellow solid. Purification of the compound was achieved by preparative TLC (3% MeOH/DCM) to afford **2.1XB** as a yellow solid (50 mg, 0.05 mmol, 21%).

^{1}H NMR: ($CDCl_3$, 500 MHz): δ 8.04 (2H, s, H^4), 8.01 (1H, s, H^5), 7.46 (2H, t, J = 5.5 Hz, H^6), 4.68 (6H, m, H^3 + H^7), 4.34 (6H, H^2 + H^8), 4.00 (5H, s, H^1), 1.89 (4H, quint., J = 7.3 Hz, H^9), 1.34 – 1.26 (20H, m, $H^{10\text{-}14}$), 0.88 (6H, t, J = 7.2 Hz, H^{15}).

^{13}C NMR: ($CDCl_3$, 126 MHz): δ 166.7, 148.0, 141.3, 134.4, 127.8, 122.3, 83.0, 78.7, 69.7, 66.8, 51.0, 36.1, 31.7, 29.9, 29.0, 29.0, 26.4, 22.6, 14.1.

ESI-MS: m/z calcd. for $C_{40}H_{52}O_2N_8FeI_2Na$ [M+Na$^+$] 1009.15442, found: 1009.15386.

Fc-isophthalamide-bis-disulfide-triazole 2.2HB (RH)



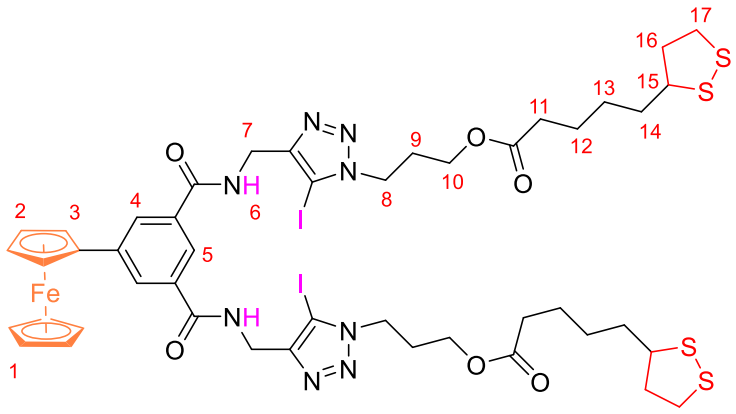
Fc-isophthalamide-bis-alkyne **2.4a** (50 mg, 0.118 mmol), disulfide-azide (75 mg, 0.259 mmol), $Cu(CH_3CN)_4PF_6$ (9 mg, 0.0236 mmol), TBTA (6 mg, 0.0118 mmol) and TEA (24 mg, 0.236 mmol) were dissolved in 3 mL anhydrous THF and reacted under N_2 in the dark for 16 h. DCM was then added and the organic phase was washed with aq. NH_4OH twice, once with brine and dried over $MgSO_4$. **2.2HB** was then isolated by silica gel column chromatography (6% MeOH/DCM) as an orange solid (75 mg, 0.0748 mmol, 63%).

^{1}H NMR: ($CDCl_3$, 500 MHz): δ 8.13 – 8.04 (4H, m, H^4 + H^6), 8.02 (1H, t, *J* = 1.7 Hz, H^5), 7.73 (2H, s, H^8), 4.72 – 4.62 (6H, m, H^3+ H^7), 4.45 (4H, t, *J* = 7.0 Hz, H^9), 4.32 (2H, t, *J* = 1.8 Hz, H^2), 4.08 (4H, t, J = 6.0 Hz, H^{11}), 3.98 (5H, s, H^1), 3.54 (2H, dq, *J* = 8.5, 6.3 Hz, H^{16}), 3.24 – 2.99 (4H, m, H^{18}), 2.43 (2H, tt, *J* = 12.5, 6.0 Hz, H^{17}), 2.31 (4H, t, *J* = 7.4 Hz, H^{12}), 2.24 (4H, q, *J* = 6.6 Hz, H^{10}), 1.88 (2H, dq, *J* = 13.6, 6.9 Hz, H^{17}), 1.77 – 1.55 (8H, m, H^{13} + H^{15}), 1.52 – 1.34 (4H, m, H^{14}).

^{13}C NMR: ($CDCl_3$, 126 MHz): δ 173.3, 167.0, 145.0, 141.3, 134.3, 127.9, 123.4, 122.2, 83.0, 69.7, 69.6, 66.7, 60.8, 56.3, 47.3, 40.3, 38.5, 35.4, 34.6, 33.9, 29.37, 28.7, 24.6.

ESI-MS: m/z calcd. for $C_{46}H_{58}O_6N_8FeS_4$ [M^+] 1002.27061, found: 1002.27081.

Fc-isophthalamide-bis-disulfide-iodotriazole 2.2XB (RH)



Fc-isophthalamide-bis-iodoalkyne **2.4b** (6 mg, 8.9 µmol), disulfide-azide (8 mg, 27.6 µmol), $Cu(CH_3CN)_4PF_6$ (13 mg, 0.0344 mmol), TBTA (cat.) and TEA (1 drop) were dissolved in 2 mL anhydrous DCM and reacted under N_2 in the dark for 24 h. The organic phase then washed with aq. NH_4OH twice, once with water and dried over $MgSO_4$. **2.2XB** was then isolated by preparative TLC (5% MeOH/DCM) as an orange solid (4 mg, 3.2 µmol, 36%).

^{1}H NMR: ($CDCl_3$, 500 MHz): δ 8.07 (2H, d, *J* = 1.6 Hz, H^4), 7.98 (1H, t, *J* = 1.6 Hz, H^5), 7.05 (2H, t, *J* = 5.2 Hz, H^6), 4.82 – 4.65 (6H, m, H^3+ H^7), 4.49 (4H, t, *J* = 7.1 Hz, H^8), 4.44 – 4.34 (2H, m, H^2), 4.14 (4H, t, *J* = 6.0 Hz, H^{10}), 4.04 (5H, s, H^1), 3.56 (2H, dd, *J* = 8.4, 6.1 Hz, H^{15}), 3.22 – 3.05 (4H, m, H^{17}), 2.46 (2H, m, H^{16}), 2.37 – 2.25 (8H, m, H^9+ H^{11}), 1.98 – 1.85 (2H, m, H^{16}), 1.75 – 1.62 (8H, m, H^{12} + H^{13}), 1.55 – 1.39 (4H, m, H^{13}).

^{13}C NMR: ($CDCl_3$, 126 MHz): δ 173.2, 166.5, 148.2, 141.6, 134.4, 127.8, 122.1, 82.9, 79.2, 69.8, 69.7, 66.81, 60.7, 56.4, 47.8, 42.3, 38.5, 36.1, 34.6, 34.0, 29.0, 28.8, 24.6.

ESI-MS: m/z calcd. for $C_{46}H_{56}O_6N_8S_4FeI_2Na$ [M+Na$^+$] 1275.05834, found: 1275.05200.

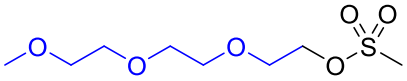
The synthesis of receptors **2.7** and **2.8** was carried out by Thanthapatra Bunchuay and is reported elsewhere.[298]

7.5.2 Synthesis for Chapter 3

The synthetic route towards **3.1XB/HB** is shown in Scheme 3.1 and Schemes A3.1-A3.2.

The synthesis and characterisation of all compounds was carried out by Arseni Borissov, apart from the final esterification to afford the title compounds **3.1XB/HB**.

Triethylene glycol mesylate 3.17 (AB)



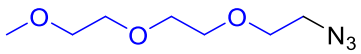
Triethylene glycol monomethyl ether (8 mL, 50 mmol) was added to DCM (125 mL) and combined with Et_3N (7.666 mL, 55 mmol). The mixture was cooled to 0 °C and methylsulfonyl chloride (4.257 mL, 55 mmol) was added. The mixture was stirred at 0 °C for 2 h and allowed to warm to rt. It was then washed with brine and concentrated *in vacuo*. The residue was partitioned in water and hexanes, the aqueous phase was separated, saturated with NaCl and extracted with DCM. The DCM extracts were dried with anhydrous Na_2SO_4 and concentrated *in vacuo* to provide 11.798 g (48.69 mmol, 97%) of **3.17** as a colourless oil.

^{1}H NMR: (400 MHz, $CDCl_3$): δ 4.39 – 4.33 (2H, m), 3.77 – 3.72 (2H, m), 3.68 – 3.58 (6H, m), 3.54 – 3.49 (2H, m), 3.35 (3H, s), 3.05 (3H, s).

^{13}C NMR: (101 MHz, $CDCl_3$): δ 71.94, 70.66, 70.58, 69.41, 69.06, 59.08, 37.75.

ESI-MS: m/z 265.0 $[M+H]^+$.

Triethylene glycol azide 3.18 (AB)



2-(2-(2-methoxyethoxy)ethoxy)ethyl methanesulfonate **3.17** (1.211 g, 5 mmol) was added to EtOH (10 mL). NaN_3 (390 mg, 6 mmol) was then added and the mixture was heated at reflux overnight. It was then evaporated, the residue redissolved in Et_2O, washed with brine, dried with anhydrous Na_2SO_4 and concentrated *in vacuo*. Crude material was purified by column chromatography (50% Et_2O/hexanes) to afford 683 mg (3.61 mmol, 72%) of **3.18** as a colourless oil.

^{1}H NMR: (400 MHz, $CDCl_3$): δ 3.69 – 3.63 (8H, m), 3.57 – 3.52 (2H, m), 3.41 – 3.34 (5H, m).

^{13}C NMR: (101 MHz, $CDCl_3$): δ 72.05, 70.83, 70.79, 70.74, 70.15, 59.15, 50.81.

ESI-MS: m/z 212.1 $[M+Na]^+$.

Triethylene glycol amine 3.8 (AB)



Compound **3.18** (517 mg, 2.73 mmol) was dissolved in dry Et_2O (6 mL). This solution was then slowly added to 2 M $LiAlH_4$ solution in THF (3 mL) and the mixture was stirred for 1 h at rt. It was then cooled to 0 °C and the excess $LiAlH_4$ was quenched with MeOH. The mixture was then partitioned in Et_2O and water containing Rochelle's salt and the aqueous phase

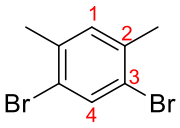
further extracted with DCM. The organic phases were dried with anhydrous Na_2SO_4, filtered and concentrated *in vacuo* to provide **3.8** (300 mg, 1.84 mmol, 67%) as a colourless oil.

^{1}H NMR: (400 MHz, $CDCl_3$): δ 3.69 – 3.58 (6H, m, CH_2), 3.54 (2H, m, CH_2), 3.49 (2H, t, *J* = 5.2 Hz, CH_2), 3.37 (3H, s, CH_3), 2.85 (2H, t, *J* = 5.2 Hz, NH_2).

^{13}C NMR: (101 MHz, $CDCl_3$): δ 73.61 (*C*H_2), 72.05 (*C*H_2), 70.72 (*C*H_2), 70.65 (*C*H_2), 70.39 (*C*H_2), 59.15 (*C*H_3), 41.92 (*C*H_2NH_2).

ESI-MS: m/z 164.1 $[M+H]^+$.

<u>1,5-dibromo-2,4-dimethylbenzene 3.10</u> (AB)



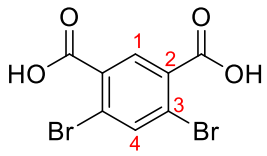
According to a literature procedure,[376] iodine (53 mg, 0.21 mmol) was added to *m*-xylene (3.68 mL, 30 mmol). The flask was covered with aluminium foil and bromine (4.15 mL, 81 mmol) was added dropwise over 2 h. The reaction was stirred at rt in darkness for 36 h and quenched by stirring with 20% KOH solution until the red colour disappeared. The resulting mixture was cooled to 0 °C and the aqueous solution was decanted from the precipitated white solid. The residue was dissolved in DCM, washed with brine, dried with anhydrous Na_2SO_4, filtered and concentrated. The product was purified by short path distillation (132 °C at 16 mbar) to give **3.10** as a white solid (4.500 g, 17.05 mmol, 57%).

^{1}H NMR: (400 MHz, $CDCl_3$): δ 7.68 (1H, s, H^4), 7.10 (1H, s, H^1), 2.31 (6H, s, CH_3).

^{13}C NMR: (101 MHz, $CDCl_3$): δ 137.01 (C^2), 135.05 (C^4), 132.73 (C^1), 122.15 (C^3), 22.39 (CH_3),

CI-MS: 264.9057 $[M+H]^+$.

4,6-dibromoisophthalic acid 3.11 (AB)



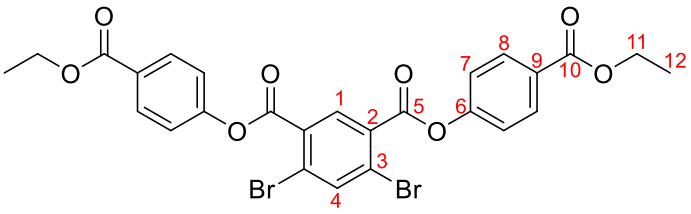
According to a literature procedure,[376] **3.10** (3.610 g, 13.68 mmol) was added to 1:1 ^{t}BuOH/H_2O (30 mL). $KMnO_4$ (4.755 g, 30.09 mmol) was added and the reaction was heated at reflux for 2 h. It was then brought to rt and another portion of $KMnO_4$ (4.755 g, 30.09 mmol) was added. The mixture was heated to reflux again for 20 h. It was then filtered through Celite and the filter washed with hot water. ^{t}BuOH was evaporated from the resulting clear solution, the resulting aqueous mixture was allowed to cool down to rt, washed with Et_2O and acidified with 1 M HCl. The resulting white precipitate was filtered off and recrystallised in water to afford **7** (2.630 g, 8.12 mmol, 59%) as a white solid.

^{1}H NMR: (400 MHz, $CDCl_3$ + 5% DMSO-d_6): δ 8.30 (1H, s, H^4), 7.88 (1H, s, H^1), 7.23 (2H, br s, COO*H*).

^{13}C NMR: (101 MHz, $CDCl_3$): δ 166.31 (*C*OOH), 139.32 (C^1), 134.25 (C^4), 131.49 (C^2), 125.11 (C^3).

ESI-MS: m/z 322.9 $[M-H]^-$.

Compound 3.12 (AB)



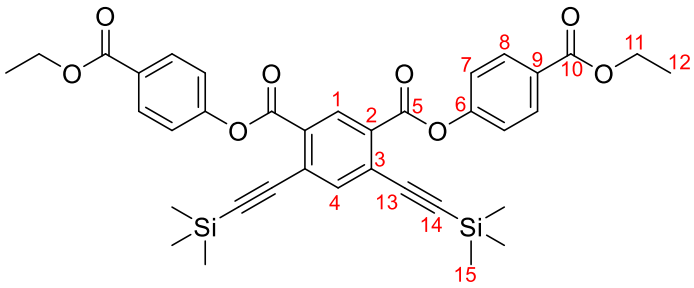
Dibromoisophthalic acid **3.11** (3.239 g, 10 mmol) was combined with $SOCl_2$ (20 mL) and a few drops of DMF. The mixture was heated at reflux for 5 h, concentrated and dried *in vacuo*. The resulting acyl chloride was combined with toluene (20 mL), ethyl p-hydroxybenzoate (3.656 g, 22 mmol) and DMAP (61 mg, 0.5 mmol). The reaction was heated under reflux overnight and concentrated *in vacuo*. The product was purified by column chromatography (0-2% MeOH/DCM) to provide **3.12** (5.710 g, 9.2 mmol, 92%) as a white solid.

^{1}H NMR: (400 MHz, $CDCl_3$): δ 8.60 (1H, s, H^1), 8.06 (1H, s, H^4), 8.05 – 8.01 (4H, m, H^8), 7.27 – 7.21 (4H, m, H^7), 4.29 (4H, q, J = 7.1 Hz, H^{11}), 1.30 (6H, t, J = 7.1 Hz, H^{12}).

^{13}C NMR: (101 MHz, $CDCl_3$): δ 165.59 (C^{10}), 162.19 (C^5), 153.73 (C^6), 140.61 (C^4), 134.92 (C^1), 131.28 (C^8), 129.90, 128.70 (C^9), 127.49, 121.48 (C^7), 61.23 (C^{11}), 14.36 (C^{12}).

CI-MS: m/z 620.9580 $[M+H]^+$.

Compound 3.13 (AB)



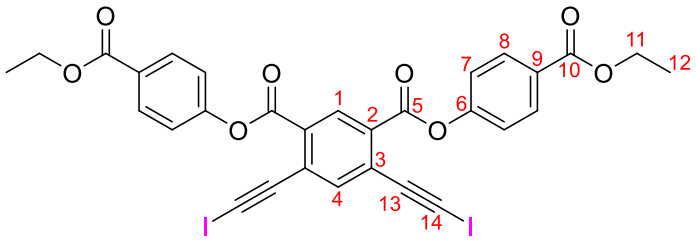
Compound **3.12** (3.950 g, 6.37 mmol) was added to dry, degassed THF (42 mL) under Ar. $Pd(PPh_3)_2Cl_2$ (223 mg, 0.318 mmol) was then added followed by Et_3N (5.326 mL, 38.21 mmol). The mixture was stirred at rt for 10 min and trimethylsilylacetylene (3.529 ml, 25.47 mmol) and CuI (61 mg, 0.318 mmol) were added. The reaction was stirred at rt for 4 h when it was determined to be complete by TLC. Reaction mixture was partially evaporated *in vacuo* and partitioned in Et_2O and dilute aqueous solution of citric acid. Organic phase was dried with anhydrous Na_2SO_4, decanted and evaporated. Crude product was dry loaded onto silica and purified by silica gel column chromatography (10-15% Et_2O/hexanes) to provide **3.13** (3.809 g, 5.82 mmol, 91%) as a white solid.

^{1}H NMR: (400 MHz, $CDCl_3$): δ 8.81 (1H, s, H^1), 8.20 – 8.10 (4H, m, H^8), 7.93 (1H, s, H^4), 7.40 – 7.30 (4H, m, H^7), 4.39 (4H, q, J = 7.1 Hz, H^{11}), 1.41 (6H, t, J = 7.1 Hz, H^{12}), 0.21 (18H, s, H^{15}).

^{13}C NMR: (101 MHz, $CDCl_3$): δ 165.91 (C^{10}), 162.87 (C^5), 154.19 (C^6), 141.13 (C^4), 133.88 (C^1), 131.35 (C^8), 130.26 (C^2), 128.52 (C^9), 128.06 (C^3), 121.69 (C^7), 106.10, 101.27, 61.29 (C^{11}), 14.48 (C^{12}), -0.22 (C^{15}).

ESI-MS: m/z calcd. for $C_{36}H_{39}O_8Si_2$ $[M+H]^+$ 655.21780, found: 655.21777.

Compound 3.14 (AB)



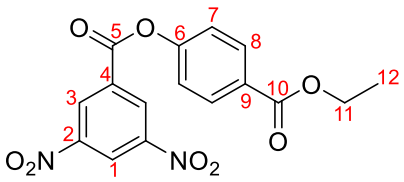
According to a modified literature procedure,[377] compound **3.13** (131 mg, 0.2 mmol) was dissolved in dry DMF (1.33 mL), combined with $AgNO_3$ (5 mg, 0.03 mmol) and cooled to 0 °C. NIS (94.5 mg, 0.42 mmol) was then added, the reaction was stirred in darkness at 0 °C for 10 min and at rt for 4 h. The reaction mixture was then combined with water (10 mL) and filtered. The collected solid was dissolved in DCM, the solution was washed with water, dried with anhydrous Na_2SO_4, filtered and evaporated, providing **3.14** (152 mg, 0.2 mmol, quant.) as an off-white solid.

^{1}H NMR: (400 MHz, $CDCl_3$/DMSO-d_6): δ 8.89 (1H, s, H^1), 8.19 – 8.09 (4H, m, H^8), 7.89 (1H, s, H^4), 7.41 – 7.32 (4H, m, H^7), 4.40 (4H, q, J = 7.1 Hz, H^{11}), 1.41 (6H, t, J = 7.1 Hz, H^{12}).

^{13}C NMR: (101 MHz, $CDCl_3$/DMSO-d_6): δ 165.41 (C^{10}), 162.21 (C^5), 153.85 (C^6), 141.97 (C^4), 133.48 (C^1), 130.98 (C^8), 130.05 (C^2), 128.41 (C^9), 128.19 (C^3), 121.51 (C^7), 90.06 (C^{13}), 60.95 (C^{11}), 14.17 (C^{12}).

ESI-MS: m/z calcd. for $C_{30}H_{21}I_2O_8$ $[M+H]^+$ 762.93203, found: 762.93197.

Compound 3.3 (AB)



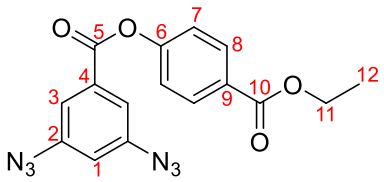
3,5-Dinitrobenzoic acid (1.060 g, 5 mmol) was combined with $SOCl_2$ (5 mL) and a few drops of DMF. The mixture was heated at reflux for 2 h, concentrated and dried *in vacuo*. The resulting acyl chloride was combined with toluene (8 mL), ethyl p-hydroxybenzoate (914 mg, 5.50 mmol) and DMAP (6 mg, 0.05 mmol). The reaction was heated under reflux overnight and concentrated *in vacuo*. The product was purified by column chromatography (DCM) to provide **3.3** (1.761 g, 4.89 mmol, 98%) as an off-white solid.

^{1}H NMR: (400 MHz, $CDCl_3$): δ 9.36 – 9.28 (3H, m, H^1 + H^3), 8.22 – 8.12 (2H, m, H^8), 7.42 – 7.31 (2H, m, H^7), 4.40 (2H, q, J = 7.1 Hz, H^{11}), 1.41 (3H, t, J = 7.1 Hz, H^{12}).

^{13}C NMR: (101 MHz, $CDCl_3$): δ 165.60 (C^{10}), 160.86 (C^5), 153.51 (C^6), 148.94 (C^2/C^4), 132.98 (C^2/C^4), 131.58 (C^8), 130.05 (C^3), 129.26 (C^9), 123.27 (C^1), 121.37 (C^7), 61.46 (C^{11}), 14.45 (C^{12}).

ESI-MS: m/z calcd. for $C_{16}H_{13}O_8N_2$ $[M+H]^+$: 361.06664, found: 361.06653.

Compound 3.4 (AB)



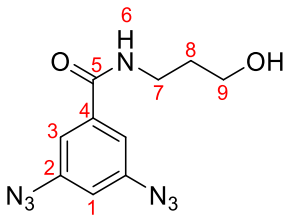
Compound **3.3** (1.735 g, 4.816 mmol) and 10% Pd/C (170 mg) were added to EtOAc (50 mL). The mixture was stirred in H_2 atmosphere until the reaction was complete. It was then filtered through Celite and concentrated *in vacuo*. The residue was dissolved in water (50 mL) with conc. HCl (4 mL) and the solution cooled to 0 °C. $NaNO_2$ (731 mg, 10.59 mmol) in small amount of water was then added slowly, followed after 15 min by NaN_3 (751 mg, 11.56 mmol) in small amount of water. The reaction was stirred for 15 min at 0 °C and for 1 h at rt. It was then extracted with EtOAc, the organic phase was washed with brine, dried with anhydrous Na_2SO_4, filtered and concentrated *in vacuo*. The residue was purified by silica gel column chromatography (15% Et_2O/hexanes) and the isolated product was recrystallised ($CHCl_3$/hexane) to provide **3.3** (426 mg, 1.209 mmol, 25%) as a white solid.

^{1}H NMR: (400 MHz, $CDCl_3$): δ 8.14 (2H, d, *J* = 8.7 Hz, H^8), 7.62 (2H, t, *J* = 1.6 Hz, H^3), 7.29 (2H, d, *J* = 8.9 Hz, H^7), 6.88 (1H, t, *J* = 2.0 Hz, H^1), 4.40 (2H, q, *J* = 7.1 Hz, H^{11}), 1.41 (3H, t, *J* = 7.1 Hz, H^{12}).

^{13}C NMR: (101 MHz, $CDCl_3$): δ 165.84 (C^{10}), 163.13 (C^5), 154.14 (C^7), 142.74 (C^2), 132.35 (C^4), 131.40 (C^8), 128.65 (C^9), 121.65 (C^7), 116.91 (C^3), 114.70 (C^1), 61.32 (C^{11}), 14.47 (C^{12}).

ESI-MS: m/z 375.0 $[M+Na]^+$.

Compound 3.5*, general procedure for amidation of reactive esters* (AB)



General procedure for amidation of reactive esters

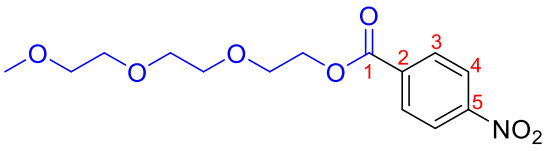
Compound **3.4** (70 mg, 0.200 mmol) and 3-aminopropan-1-ol (30 µL, 0.400 mmol) were combined in DCM (2 mL) and stirred at rt overnight. The product was purified by silica gel column chromatography (2-3% MeOH/DCM) to provide **3.5** (50 mg, 0.191 mmol, 96%) as a white solid.

^{1}H NMR: (400 MHz, $CDCl_3$/MeOD): δ 7.22 – 7.14 (2H, m, H^3), 6.70 – 6.62 (1H, m, H^1), 3.66 – 3.57 (2H, m, H^9), 3.51 – 3.41 (2H, m, H^7), 1.83 – 1.65 (2H, m, H^8).

^{13}C NMR: (101 MHz, $CDCl_3$/MeOD): δ 166.59 (C^5), 142.26 (C^2), 137.44 (C^4), 114.11 (C^3), 112.23 (C^1), 59.78 (C^9), 37.43 (C^7), 31.48 (C^8).

ESI-MS: m/z calcd. for $C_{10}H_{11}O_2N_7Na$ $[M+Na]^+$ 284.08664, found: 284.08673.

Triethyleneglycol 4-nitrobenzoate 3.15 (AB)



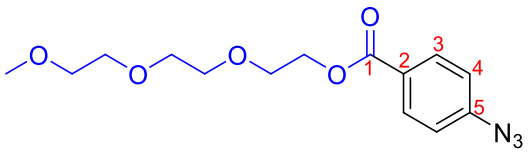
4-nitrobenzoic acid (1.671 g, 10 mmol) was added to $SOCl_2$ (20 mL). A few drops of DMF were then added and the mixture was heated at reflux for 2 h. It was then concentrated and dried *in vacuo*. The residue was dissolved in dry toluene (20 mL) and combined with tri(ethylene glycol) monomethyl ether (1.600 mL, 11 mmol) and DMAP (61 mg, 0.5 mmol). The reaction was heated at reflux overnight. The resulting mixture was concentrated *in vacuo* and separated by silica gel column chromatography (0.5-1.5% MeOH/DCM) to provide **3.15** (2.350 g, 7.50 mmol, 75%) as a brown oil.

^{1}H NMR: (400 MHz, $CDCl_3$): δ 8.31 – 8.26 (2H, m, H^4), 8.25 – 8.20 (2H, m, H^3), 4.56 – 4.49 (2H, m, TEG-CH_2), 3.88 – 3.83 (2H, m, TEG-CH_2), 3.75 – 3.69 (2H, m, TEG-CH_2), 3.69 – 3.62 (4H, m, TEG-CH_2), 3.56 – 3.51 (2H, m, TEG-CH_2), 3.37 (3H, s, TEG-CH_3).

^{13}C NMR: (101 MHz, $CDCl_3$) δ 164.82 (C^1), 150.68 (C^5), 135.63 (C^2), 130.98 (C^3), 123.65 (C^4), 72.05, 70.83, 70.79, 70.76, 69.12, 65.10, 59.21.

ESI-MS: m/z 336.1 $[M+Na]^+$.

Triethyleneglycol 4-azidobenzoate 3.16 (AB)



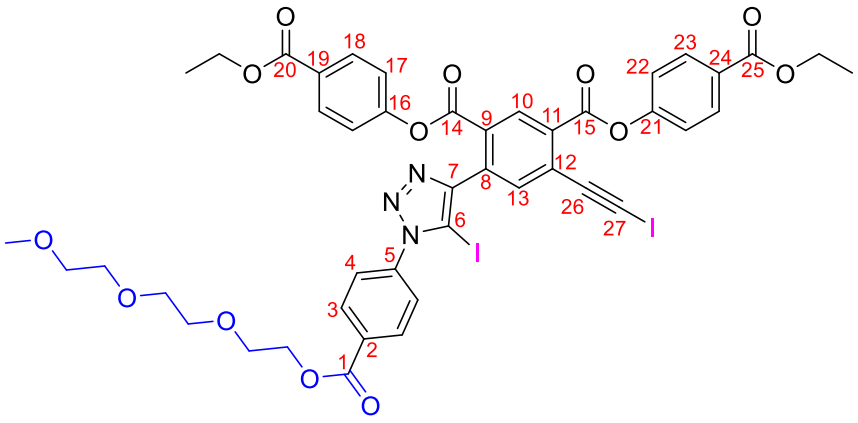
Compound **3.15** (2.350 g, 7.50 mmol) and 10% Pd/C (200 mg) were added to EtOAc (75 mL). The mixture was vigorously stirred under H_2 atmosphere for 24 h. It was then filtered through Celite and the filtrate concentrated *in vacuo*. The residue was dissolved in 1 M HCl and the solution was cooled to 0 °C. $NaNO_2$ (543 mg, 7.88 mmol) in small amount of water was then added slowly. The resulting yellow solution was stirred for 10 min at 0 °C and NaN_3 (536 mg, 8.25 mmol) in small amount of water was added slowly. The mixture was stirred for 10 min at 0 °C and for 30 min at rt. It was then neutralised with sat. aq. $NaHCO_3$ and extracted with Et_2O. Combined organic phases were dried with anhydrous Na_2SO_4, filtered and concentrated *in vacuo*. The product was purified by silica gel column chromatography (30-40% EtOAc/hexanes) to afford **3.16** (2.247 g, 7.26 mmol, 97%) as a yellow oil.

^{1}H NMR: (400 MHz, $CDCl_3$): δ 8.11 – 7.98 (2H, m, H^2), 7.12 – 6.99 (2H, m, H^3), 4.53 – 4.36 (2H, m, TEG-CH_2), 3.90 – 3.78 (2H, m, TEG-CH_2), 3.78 – 3.61 (6H, m, TEG-CH_2), 3.59 – 3.47 (2H, m, TEG-CH_2), 3.37 (3H, s, TEG-CH_3).

^{13}C NMR: (101 MHz, $CDCl_3$): δ 165.86 (C^1), 144.93 (C^2), 131.67 (C^3), 126.80 (C^5), 118.93 (C^4), 72.07 (TEG-CH$_2$), 70.84 (TEG-CH$_2$), 70.79 (TEG-CH$_2$), 70.74 (TEG-CH$_2$), 69.36 (TEG-CH$_2$), 64.34 (TEG-CH$_2$), 59.18.

ESI-MS: m/z calcd. for $C_{14}H_{19}O_5N_3Na$ $[M+Na]^+$: 332.12169, found: 332.12151.

Compound 3.6XB, *general procedure for azide-iodoalkyne cycloaddtion* (AB)



General procedure for azide-iodoalkyne cycloaddition

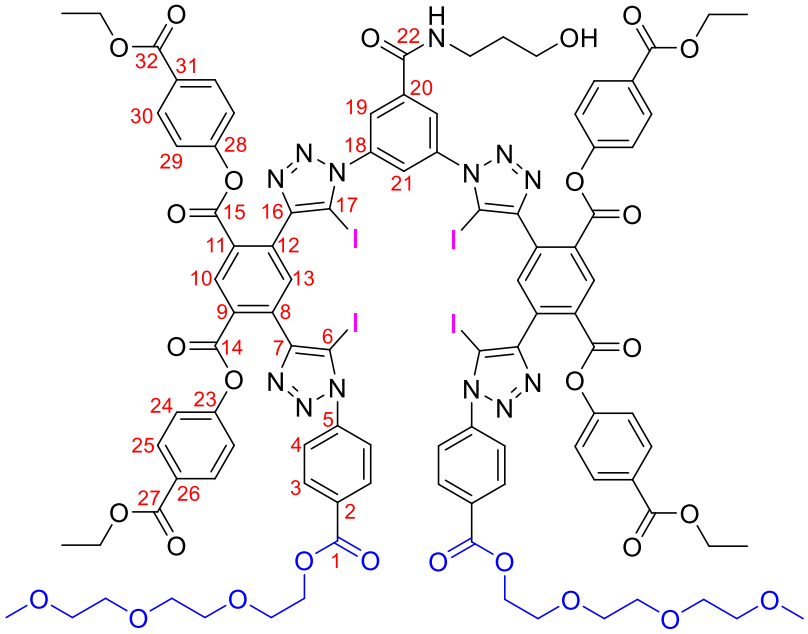
Compounds **3.16** (155 mg, 0.5 mmol) and **3.14** (457 mg, 0.6 mmol) were added to dry THF (5 mL) $Cu(CH_3CN)_4PF_6$ (19 mg, 0.05 mmol) and TBTA (27 mg, 0.05 mmol) were then added simultaneously. The reaction was then stirred overnight at rt under Ar atmosphere in darkness. The mixture was then partitioned between aqueous solution of Na_2EDTA and DCM. Organic fraction was dried with anhydrous Na_2SO_4, decanted and concentrated *in vacuo*. The residue was purified by silica gel column chromatography (1-1.5% MeOH/DCM) to provide **3.6XB** (270 mg, 0.252 mmol, 50%) as a yellow solid.

^{1}H NMR: (400 MHz, $CDCl_3$): δ 8.93 (1H, s, H^{10}), 8.28 – 8.21 (2H, m, H^3), 8.17 – 8.09 (2H, m, H^{18}/H^{23}), 8.09 – 8.03 (2H, m, H^{18}/H^{23}), 7.92 (1H, s, H^{13}), 7.68 – 7.60 (2H, m, H^4), 7.40 – 7.34 (2H, m, H^{17}/H^{22}), 7.25 – 7.19 (2H, m, H^{17}/H^{22}), 4.54 – 4.47 (2H, m, TEG-CH_2), 4.42 – 4.29 (4H, m, OCH_2CH$_3$), 3.88 – 3.81 (2H, m, TEG-CH_2), 3.73 – 3.68 (2H, m, TEG-CH_2), 3.68 – 3.59 (4H, m, TEG-CH_2), 3.55 – 3.47 (2H, m, TEG-CH_2), 3.33 (3H, s, TEG-CH_3), 1.41 – 1.32 (6H, m, OCH$_2$CH_3). **^{13}C NMR:** (101 MHz, $CDCl_3$): δ 165.70 (C^{20}/C^{25}), 165.62 (C^{20}/C^{25}), 165.17 (C^1), 163.40 (C^{14}/C^{15}), 162.48 (C^{14}/C^{15}), 154.07 (C^{16}/C^{21}), 153.92 (C^{16}/C^{21}), 149.93 (C^7), 139.93 (C^5), 138.69 (C^{13}), 134.94 (C^8), 133.71 (C^{10}), 131.99 (C^9/C^{11}), 131.86 (C^2), 131.30 (C^{18}/C^{23}), 131.22

(C^{18}/C^{23}), 130.96 (C^{3}), 129.80 (C^{9}/C^{11}), 128.52 (C^{19}/C^{24}), 128.50 (C^{19}/C^{24}), 128.41 (C^{12}), 125.96 (C^{4}), 121.63 (C^{17}/C^{22}), 121.38 (C^{17}/C^{22}), 91.31 (C^{26}), 80.40 (C^{6}), 71.92, 70.69, 70.65, 70.60, 69.08, 64.71, 61.19 (O*C*H_2CH$_3$), 61.16 (O*C*H_2CH$_3$), 59.05, 20.69 (C^{27}), 14.37 (OCH$_2$*C*H$_3$), 14.34 (OCH$_2$*C*H$_3$).

ESI-MS: m/z calcd. for $C_{44}H_{40}O_{13}N_3I_2$ $[M+H]^+$ 1072.06450, found: 1072.06392.

Compound 3.7XB (AB)



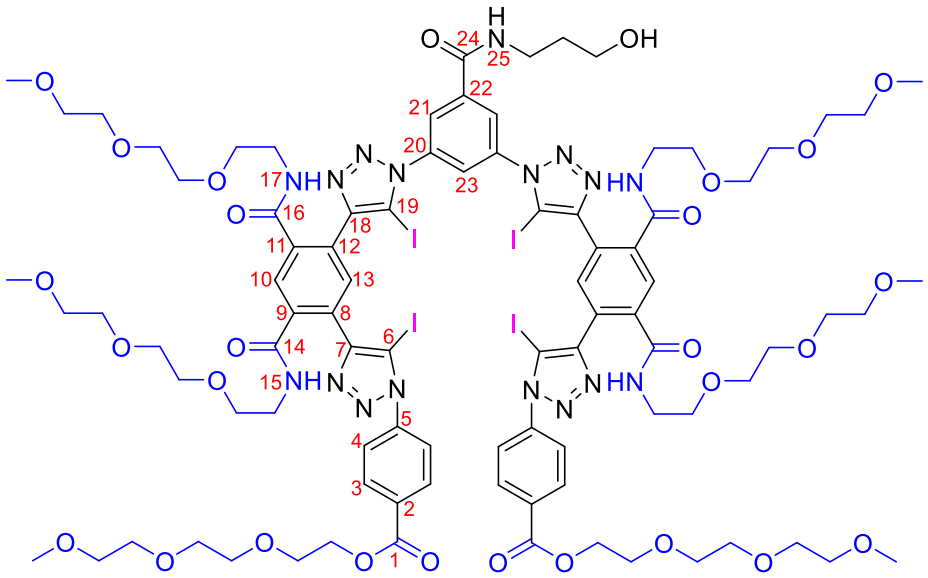
General procedure for azide-iodoalkyne cycloaddition was used to couple compound **3.6XB** (84 mg, 0.102 mmol) and **3.5** (17.5 mg, 0.0500 mmol). The product was purified by silica gel column chromatography (20-25% acetone/DCM) to provide **3.7XB** (68 mg, 0.0342 mmol, 68%) as a white solid.

^{1}H NMR: (500 MHz, $CDCl_3$): δ 8.94 – 8.78 (2H, m, H^{10}), 8.73 (2H, s), 8.61 (2H, s), 8.43 (4H, s), 8.07 (8H, t, *J* = 8.0 Hz, H^{3} + H^{25}/H^{30}), 7.99 (4H, d, *J* = 7.9 Hz, H^{25}/H^{30}), 7.81 (4H, d, *J* = 8.2 Hz, H^{4}), 7.37 – 7.27 (8H, m, H^{24} + H^{29}), 4.50 (6H, d, *J* = 39.8 Hz, TEG-CH_2), 4.37 (4H, q, *J* = 7.1 Hz, OCH_2CH$_3$), 4.30 (4H, q, *J* = 7.1 Hz, OCH_2CH$_3$), 3.91 – 3.75 (6H, m, TEG-CH_2), 3.65 (18H, ddt, *J* = 36.5, 19.9, 4.5 Hz, TEG-CH_2), 3.56 – 3.43 (6H, m, TEG-CH_2), 3.34 (6H, s, TEG-CH_3), 3.27 (3H, s, TEG-CH_3), 1.39 (6H, t, *J* = 7.1 Hz, OCH$_2$CH_3), 1.33 (6H, t, *J* = 7.1 Hz, OCH$_2$CH_3).

^{13}C NMR: (126 MHz, $CDCl_3$): δ 165.74 (C^{27}/C^{32}), 165.64 (C^{27}/C^{32}), 165.32, 164.99, 164.84 (C^{24}), 154.22 (C^{23}/C^{28}), 154.15 (C^{23}/C^{28}), 145.38 (C^{7}/C^{18}), 145.00 (C^{7}/C^{18}), 139.71, 137.79, 133.95, 133.70, 133.12, 131.85, 131.42, 131.26 (C^{25}/C^{30}), 131.20 (C^{25}/C^{30}), 130.31, 128.59, 128.53, 128.45, 122.05, 121.72 (C^{24}/C^{29}), 121.64 (C^{24}/C^{29}), 120.59, 119.83 (C^{4}), 71.99, 71.92, 70.74, 70.67, 70.63, 70.53, 69.23, 65.22, 64.57, 61.21 (O*C*H$_2$CH$_3$), 61.17 (O*C*H$_2$CH$_3$), 59.13, 59.05, 14.41 (OCH$_2$*C*H$_3$), 14.36 (OCH$_2$*C*H$_3$).

ESI-MS: m/z calcd. for $C_{102}H_{100}O_{31}N_{12}Na$ $[M+H]^+$ 2011.65096, found: 2011.65445.

Compound 3.9XB (AB)



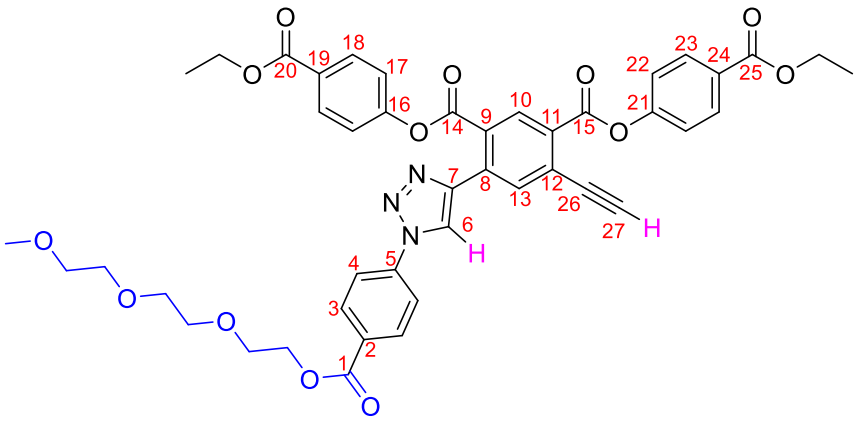
General procedure for amidation of active esters was used to react **3.7XB** (68 mg, 0.0342 mmol) and **3.8** (56 mg, 0.342 mmol). The product was purified by silica gel column chromatography (3-6% MeOH/DCM) to provide **3.9XB** (44 mg, 0.0222 mmol, 65%) as an off-white solid.

^{1}H NMR: (500 MHz, $CDCl_3$): δ 8.29 (3H, s, H^{21} + H^{25}), 8.22 (4H, d, J = 8.2 Hz, H^{3}), 8.01 – 7.94 (3H, m, H^{10} + H^{23}), 7.74 (2H, s, H^{13}), 7.71 (4H, d, J = 8.1 Hz, H^{4}), 7.41 (2H, s, H^{15}/H^{17}), 7.28 (2H, s, H^{15}/H^{17}), 4.52 – 4.48 (4H, m, TEG-CH_2), 3.84 (4H, t, J = 4.8 Hz, TEG-CH_2), 3.75 – 3.37 (70H, m, TEG-CH_2), 3.34 (6H, s, TEG-CH_3), 3.23 (6H, s, TEG-CH_3), 3.18 (6H, s, TEG-CH_3).

^{13}C NMR: (126 MHz, $CDCl_3$): δ 167.84 (C^{14}/C^{16}), 167.75 (C^{14}/C^{16}), 165.38 (C^{1}), 165.06 (C^{24}), 150.34 (C^{7}, C^{18}), 140.35 (C^{5}), 137.58 (C^{8}/C^{12}), 137.42 (C^{20}), 137.22 (C^{8}/C^{12}), 133.94 (C^{13}), 131.62 (C^{2}), 130.90 (C^{3}), 130.08 (C^{9}/C^{11}), 129.78 (C^{9}/C^{11}), 129.13 (C^{10}), 126.65 (C^{21}), 126.22 (C^{4}), 125.92 (C^{23}), 82.46 (C^{6}/C^{19}), 81.53 (C^{6}/C^{19}), 71.97, 71.86, 71.76, 70.74, 70.71, 70.66, 70.56, 70.42, 70.36, 70.15, 70.09, 69.46, 69.40, 69.16, 64.70, 60.11, 59.12, 58.96, 58.89, 39.99.

ESI-MS: m/z calcd. for $C_{90}H_{119}O_{28}N_{17}I_4$ $[M+2H]^{2+}$ 1197.23260, found: 1197.23133.

Compound 3.6HB (AB)



Compound **3.13** (236 mg, 0.36 mmol) and AgF (109 mg, 0.86 mmol) were added to dry ACN. Reaction was stirred for 8 h at rt, added to 1M HCl and stirred for 5 min. The aqueous suspension was then extracted with Et_2O, organic fractions washed with water (2x), dried with anhydrous Na_2SO_4, filtered and concentrated *in vacuo*. The residue was passed through a short silica gel column (DCM). This afforded deprotected alkyne (127 mg, 0.25 mmol) which was combined with **3.16** (64 mg, 0.21 mmol) in dry DCM. TBTA (11 mg, 0.021 mmol) and $Cu(CH_3CN)_4PF_6$ (7.7 mg, 0.021 mmol) were then added. The mixture was stirred at rt under Ar for 20 h and loaded directly onto a silica gel column (5-9% acetone/DCM) to provide **3.6HB** (84 mg, 0.102 mmol, 49%) as a white solid.

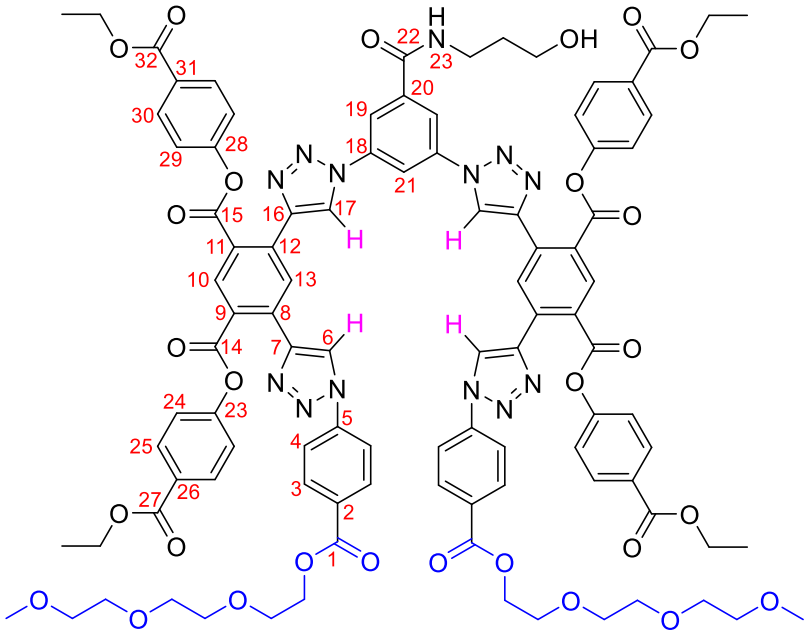
^{1}H NMR: (400 MHz, $CDCl_3$): δ 8.81 (1H, s, H^{10}), 8.62 (1H, s, H^6), 8.28 (1H, s, H^{13}), 8.19 (2H, d, J = 8.4 Hz, H^3), 8.10 (4H, dd, J = 8.6, 6.9 Hz, H^{18} + H^{23}), 7.85 (2H, d, J = 8.5 Hz, H^4), 7.33 (4H, dd, J = 14.5, 8.5 Hz, H^{17} + H^{22}), 4.49 (2H, t, J = 4.7 Hz, TEG-CH_2), 4.42 – 4.29 (4H, m, OCH_2CH$_3$),

3.84 (2H, t, *J* = 4.8 Hz, TEG-CH_2), 3.75 – 3.58 (7H, m, TEG-CH_2, H^{17}), 3.52 (2H, dd, *J* = 5.8, 3.5 Hz, TEG-CH_2), 3.33 (3H, s, TEG-CH_3), 1.37 (6H, q, *J* = 7.1 Hz, OCH$_2$CH_3).

^{13}C NMR: (101 MHz, $CDCl_3$): δ 165.75 (C^{20}/C^{25}), 165.67 (C^{20}/C^{25}), 165.27 (C^{14}/C^{15}), 164.65 (C^{14}/C^{15}), 162.53, 154.03 (C^{16}/C^{21}), 154.02 (C^{16}/C^{21}), 144.40 (C^{7}), 139.71 (C^{5}), 136.94 (C^{13}), 134.44 (C^{8}), 133.41 (C^{10}), 131.53 (C^{3}), 131.31 (C^{18}/C^{23}), 131.25 (C^{18}/C^{23}), 130.56, 128.63, 128.49, 127.31, 122.14 (C^{6}), 121.64 (C^{17}/C^{22}), 121.61 (C^{17}/C^{22}), 120.02 (C^{4}), 86.95 (C^{26}), 80.62 (C^{27}), 71.94, 70.71, 70.68, 70.63, 69.14, 64.62, 61.22 (OCH$_2$CH$_3$), 59.08, 14.37 (OCH$_2$$CH_3$).

ESI-MS: m/z calcd. for $C_{44}H_{41}O_{13}N_3Na$ $[M+Na]^+$ 842.25316, found: 842.25292.

<u>Compound 3.7HB</u> (AB)



Compound **3.6HB** (172 mg, 0.210 mmol) and **3.5** (26 mg, 0.100 mmol) were added to dry DCM. Cu(CH$_3$CN)$_4$PF$_6$ (7.5 mg, 0.02 mmol), TBTA (10.6 mg, 0.02 mmol) and DIPEA (7 µL, 0.04

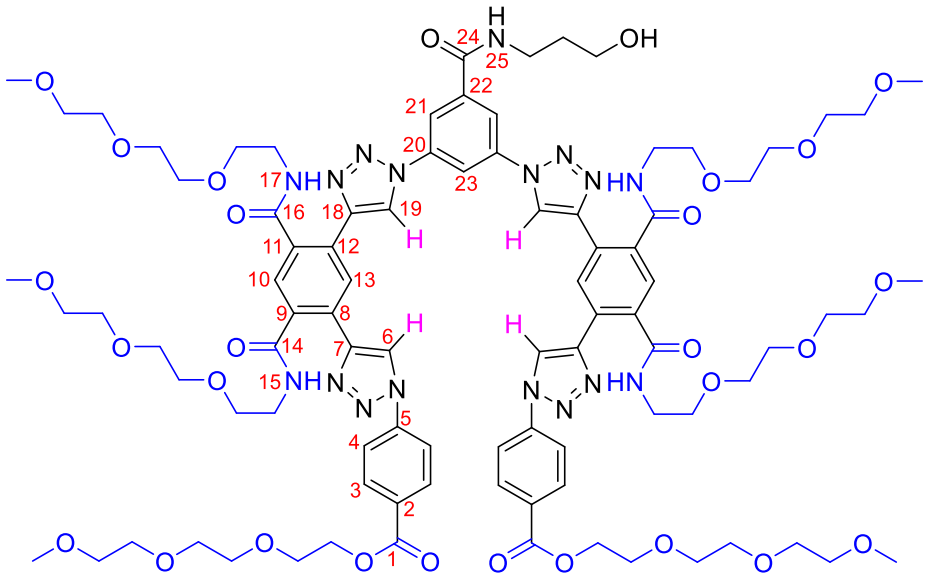
mmol). The reaction was stirred under Ar atmosphere for 1 d. It was then diluted with DCM, washed with aqueous Na_2EDTA solution, dried with anhydrous Na_2SO_4, decanted and concentrated *in vacuo*. The product was purified by silica gel column chromatography (3–4.5% MeOH/DCM) to provide **3.7HB** (168 mg, 0.0884 mmol, 88%) as an off-white solid.

^{1}H NMR: (500 MHz, $CDCl_3$): δ 8.88 – 8.67 (4H, m), 8.53 (2H, s), 8.36 (2H, s), 8.23 (1H, s, H^{21}), 8.11 (2H, s), 8.04 (8H, d, J = 8.1 Hz, H^3 + H^{25}/H^{30}), 7.94 (4H, d, J = 8.1 Hz, H^{25}/H^{30}), 7.84 (1H, s, H^{23}), 7.74 (4H, d, J = 8.2 Hz, H^4), 7.29 (4H, d, J = 8.2 Hz, H^{24}/H^{29}), 7.26 – 7.18 (4H, m, H^{24}/H^{29}), 4.45 (4H, t, J = 4.7 Hz, TEG-CH_2), 4.37 (4H, q, J = 7.1 Hz, OCH_2CH$_3$), 4.28 (4H, q, J = 7.1 Hz, OCH_2CH$_3$), 3.82 (4H, t, J = 4.8 Hz, TEG-CH_2), 3.79 – 3.54 (18H, m, TEG-CH_2), 3.51 (4H, dd, J = 5.8, 3.6 Hz, TEG-CH_2), 3.32 (6H, s, TEG-CH_3), 1.39 (6H, t, J = 7.1 Hz, OCH$_2$CH_3), 1.31 (6H, t, J = 7.1 Hz, OCH$_2$CH_3).

^{13}C NMR: (126 MHz, $CDCl_3$): δ 165.75 (C^{14}/C^{16}), 165.65 (C^{14}/C^{16}), 165.26, 164.89 164.86, 154.15 (C^{23}/C^{28}), 154.04 (C^{23}/C^{28}), 145.24 (C^7/C^{16}), 144.73 (C^7/C^{16}), 139.58 (C^5), 138.17, 137.45, 133.97, 133.51, 133.25, 131.44, 131.31, 131.23, 130.40, 128.64, 128.55, 128.26, 127.97, 122.46, 122.22, 121.72, 121.62, 119.76, 118.04, 72.01, 70.78, 70.75, 70.69, 69.20, 64.64, 61.29, 60.72, 59.13, 31.57, 14.45 (OCH$_2$*C*H$_3$), 14.39 (OCH$_2$*C*H$_3$).

ESI-MS: m/z calcd. for $C_{98}H_{94}N_{13}NaO_{28}$ $[M+H+Na]^{2+}$ 961.81145, found: 961.81183.

Compound 3.9HB (AB)



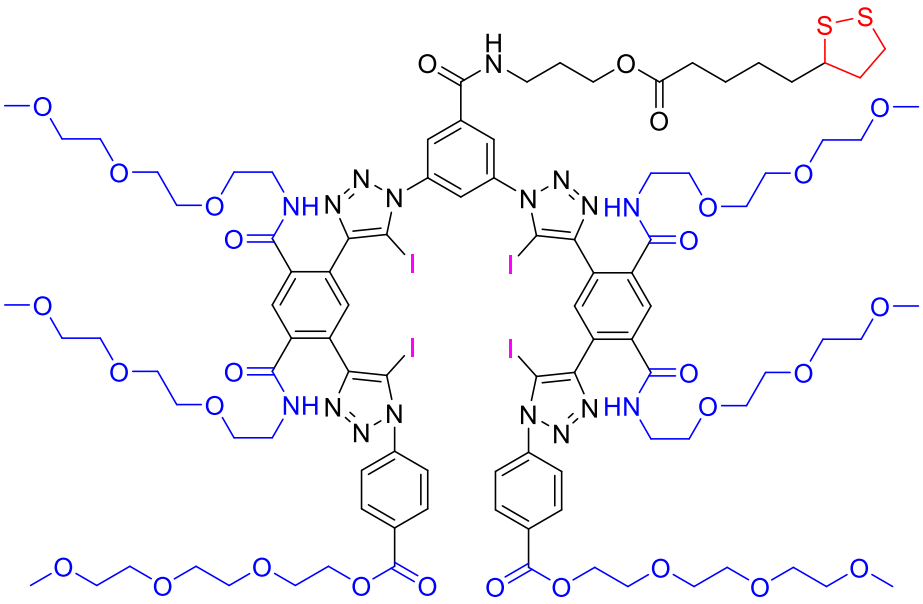
General procedure for amidation of reactive esters was used to react **3.7HB** (161 mg, 0.0848 mmol) and **3.8** (111 mg, 0.678 mmol). The product was purified by silica gel column chromatography (5-8% MeOH/DCM) followed by preparative TLC (7% MeOH/$CHCl_3$) to provide **3.9HB** (44 mg, 0.0238 mmol, 28%) as a white solid.

^{1}H NMR: (500 MHz, $CDCl_3$): δ 8.81 – 8.38 (4H, m), 8.38 – 7.63 (m, 17H), 7.62 – 7.30 (3H, m), 4.49 (4H, s), 4.01 – 2.90 (87H, m), 2.72 (3H, s), 1.35 – 1.11 (2H, m).

^{13}C NMR: (126 MHz, $CDCl_3$): δ 169.47, 169.18, 165.46, 145.14, 139.90, 137.73, 137.30, 134.62, 134.25, 133.17, 131.38, 130.11, 128.49, 128.27, 121.21, 120.62, 119.71, 117.44, 72.02, 71.88, 71.72, 70.77, 70.69, 70.57, 70.45, 70.29, 70.07, 69.89, 69.32, 69.22, 64.59, 59.84, 59.14, 58.97, 58.78, 39.80, 37.65, 32.00, 29.78.

ESI-MS: m/z calcd. for $C_{90}H_{123}N_{17}O_{28}$ $[M+2H]^{2+}$ 944.93562, found: 944.93554.

Disulfide-appended tetra-iodotriazole foldamer 3.1XB (RH)



Compound **3.9XB** (30 mg, 0.0125 mmol), lipoic acid (7.8 mg, 0.0375 mmol), N,N'-dicyclohexylcarbodiimide (7.8 mg, 0.0375 mmol) and a catalytic amount of 4-dimethylaminopyridine were dissolved in 8 mL dry DCM. After stirring under N_2 in the dark for 18 h the product was isolated by preparative TLC (DCM/MeOH/acetone 8:1:1) as an off-white solid (14 mg, 0.0054 mmol, 43%).

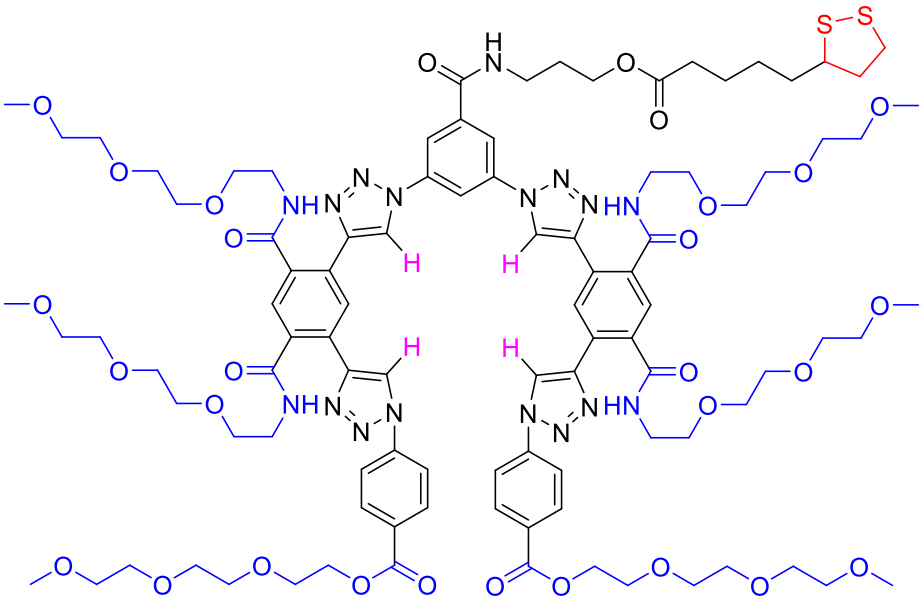
^{1}H NMR: (500 MHz, $CDCl_3$): δ 8.40 (2H, d, *J* = 2.0 Hz), 8.26 (4H, d, *J* = 8.3 Hz), 8.09 (3H, m), 7.82 (2H, s), 7.74 (4H, d, *J* = 8.3 Hz), 7.16 (2H, m), 7.10 (2H, m), 4.53 (4H, t, *J* = 4.8 Hz), 4.21 (2H, t, *J* = 6.1 Hz), 3.87 (4H, t, *J* = 4.8 Hz), 3.76 – 3.71 (4H, m), 3.70 – 3.67 (4H, m), 3.67 – 3.51 (52H, m), 3.47 (20H, m), 3.37 (6H, s), 3.26 (6H, s), 3.22 (6H, s), 3.20 – 3.04 (2H, m), 2.44 (1H, m), 2.33 (2H, t, *J* = 7.4 Hz), 1.99 (1H, q, *J* = 6.5 Hz), 1.94 – 1.85 (1H, m), 1.74 – 1.55 (4H, m), 1.46 (2H, m).

^{13}C NMR: (126 MHz, $CDCl_3$): δ 173.71, 167.52, 165.32, 164.51, 150.56, 150.37, 140.26, 137.66, 137.62, 137.27, 134.14, 131.65, 130.88, 130.10, 129.75, 129.23, 126.71, 126.13,

71.93, 71.82, 71.71, 70.70, 70.67, 70.62, 70.54, 70.50, 70.38, 70.36, 70.11, 70.01, 69.44, 69.13, 64.66, 61.89, 59.08, 58.92, 58.84, 56.43, 56.37, 50.86, 40.27, 40.24, 39.95, 39.82, 38.54, 37.32, 34.58, 34.05, 33.50, 28.77, 28.73, 28.62, 24.68, 24.54.

ESI-MS: m/z calcd. for $C_{98}H_{131}O_{29}N_{17}I_4S_2$ $[M+2H]^{2+}$ 1290.74539, found: 1290.74512.

Disulfide-appended tetra-iodotriazole foldamer 3.1HB (RH)



Compound **3.9HB** (20 mg, 0.0106 mmol), lipoic acid (6.6 mg, 0.0318 mmol), N,N'-dicyclohexylcarbodiimide (6.6 mg, 0.0318 mmol) and a catalytic amount of 4-dimethylaminopyridine were dissolved in 7 mL dry DCM. After stirring under N_2 in the dark for 18 h the product was isolated by preparative TLC (DCM/MeOH/acetone 11:1:1) as a white solid (16 mg, 0.0077 mmol, 73 %).

^{1}H NMR: (500 MHz, $CDCl_3$): δ 8.67 (4H, d, *J* = 15.8 Hz), 8.42 (3H, s), 8.30 – 8.13 (6H, m), 8.04 (1H, s), 7.94 (4H, d, *J* = 8.2 Hz), 7.82 (1H, s), 7.57 (4H, s), 4.52 (4H, t, *J* = 4.7 Hz), 4.27 (2H, t, *J* = 6.4 Hz) 3.88 (4H, t, *J* = 4.8 Hz), 3.82 (4H, s), 3.77 – 3.49 (60H, m), 3.48 – 3.40 (10H, m), 3.38 (6H, s), 3.32 (4H, m), 3.23 (6H, s), 3.18 – 3.04 (10H, m), 2.49 – 2.3 (4H, m), 2.09 (2H, m), 1.88 (10H, m), 1.67 (4H, m), 1.48 (2H, m).

^{13}C NMR: (101 MHz, $CDCl_3$): δ 173.64, 169.21, 168.99, 165.40, 145.15, 144.95, 139.91, 137.57, 134.70, 134.46, 131.39, 130.14, 128.68, 128.37, 121.26, 120.92, 119.82, 117.88, 71.94, 71.79, 71.63, 70.70, 70.68, 70.62, 70.53, 70.47, 70.34, 70.23, 70.03, 69.79, 69.30, 69.20, 69.15, 64.53, 62.21, 59.06, 58.86, 58.68, 56.36, 40.25, 40.22, 39.78, 39.69, 38.49, 37.48, 34.61, 34.07, 33.20, 28.79, 28.73, 28.71, 24.70, 24.51.

ESI-MS: m/z calcd. for $C_{98}H_{131}O_{29}N_{17}I_4S_2$ $[M+2H]^{2+}$ 1038.95210, found: 1038.94983.

7.5.3 Synthesis for Chapter 4

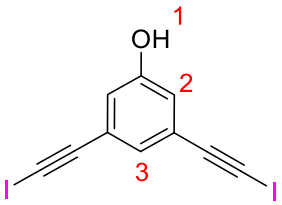
The synthetic route towards **4.4XB/HB** is shown in Scheme 4.1. The synthesis and characterisation of all compounds was carried out by Andrew Docker.

3,5-diethynyl phenol **4.6a**[378] and azido-*N*-Boc-*L*-serine methyl ester **4.8**[341] were prepared according to literature procedures.

General Procedure A:

$Cu(CH_3CN)_4PF_6$ (0.2 equiv.) and TBTA (0.2 equiv.) were dissolved in degassed CH_2Cl_2 (≈2 mL) and left to stir for 10 minutes under an atmosphere of N_2. The respective azides (3 equiv.) and alkynes (1 equiv.) were subsequently added to a solution of the copper complex. The resultant mixtures were left to stir at rt and were monitored by TLC analysis until full conversion of the respective alkyne and the mono-triazole intermediates to the bis-triazole products was observed. The resultant mixtures were diluted with CH_2Cl_2 (10 mL) and the organic layer washed with aqueous 0.01 M NH_4OH/ EDTA solution (10 mL). The resultant aqueous layer was back extracted with CH_2Cl_2 (2 x 10 mL), the combined organic phases were dried over $MgSO_4$ and concentrated *in vacuo* to obtain the crude product mixture, and the product isolated by silica gel column chromatography.

3,5-bis(iodoethynyl)phenol 4.6b (AD)



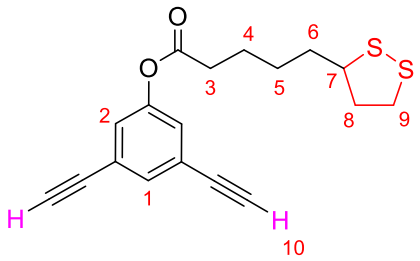
3,5-diethynyl phenol **4.6a** (500 mg, 3.52 mmol), *N*-Iodomorpholine hydriodide (3.61 g, 10.6 mmol) and CuI (67 mg , 0.352 mmol) were dissolved in anhydrous THF (22 ml) and left to stir excluded from the presence of light for 4 h at rt. After which the reaction mixture was diluted with CH_2Cl_2 (100 ml) and filtered through a CH_2Cl_2 saturated alumina pad, the organic phase subsequently washed with 0.01 M NH_4OH/EDTA solution, dried over $MgSO_4$ filtered and solvent removed *in vacuo*. The crude material was subjected to silica gel column chromatography and isolated as a white solid (792 mg, 2.01 mmol, 57%).

^{1}H NMR: (400 MHz, $CDCl_3$): δ 7.08 (1H, t, *J* = 1.4 Hz, H^3), 6.86 (2H, d, *J* = 1.4 Hz, H^2), 5.22 (1H, s, H^1).

^{13}C NMR: (101 MHz, $CDCl_3$): δ 155.19, 129.13, 124.84, 119.92, 92.91, 7.95.

ESI-MS: m/z calcd. for $C_{10}H_3OI_2$ $[M-H]^-$ 392.82787, found: 392.82748.

Compound 4.7a (AD)



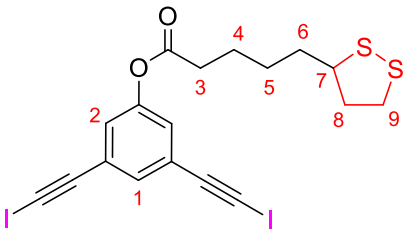
3,5-diethynyl phenol **4.6a** (100 mg, 0.704 mmol), lipoic acid (174 mg, 0.845 mmol), dicyclohexylcarbodiimide (192 mg, 0.930 mmol) and a spatula tip of DMAP were dissolved in anhydrous CH_2Cl_2 (20 ml) and left to stir at rt. After 2 h the mixture was diluted with CH_2Cl_2 (10 ml) filtered and the resultant filtrate was concentrated *in vacuo*. The crude residue was subjected to silica gel column chromatography and isolated as a yellow solid (233 mg, 0.704 mmol, quantitative).

^{1}H NMR: (500 MHz, $CDCl_3$): δ 7.46 (1H, s, H^1), 7.23 – 7.18 (2H, m, H^2), 3.65 – 3.53 (1H, m, H^7), 3.25 – 3.03 (4H, m, H^9 + H^{10}), 2.57 (2H, t, J = 7.5 Hz, H^3), 2.52 – 2.42 (1H, m, H^8), 2.00 – 1.85 (1H, m, H^8), 1.84 – 1.66 (4H, m, H^4 + H^6), 1.64 – 1.50 (2H, m, H^5).

^{13}C NMR: (126 MHz, $CDCl_3$): δ 171.49, 150.34, 133.22, 125.94, 123.81, 81.78, 78.92, 56.37, 40.36, 38.65, 34.70, 34.13, 28.78, 24.67.

ESI-MS: m/z calcd. for $C_{18}H_{19}O_2S_2$ $[M+H]^+$ 331.08210, found: 331.08228.

Compound 4.7b (AD)



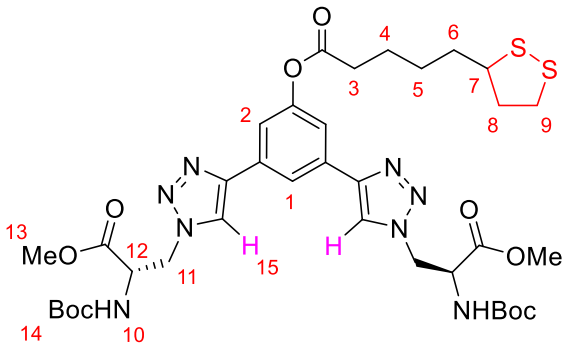
4.6b (200 mg, 0.508 mmol), lipoic acid (126 mg, 0.609 mmol), dicyclohexylcarbodiimide (115 mg, 0.558 mmol) and a spatula tip of DMAP were dissolved in anhydrous CH_2Cl_2 (20 ml) and left to stir at rt. After 2 h the mixture was diluted with CH_2Cl_2 (10 ml) filtered and the resultant filtrate was concentrated *in vacuo*. The crude residue was subjected to silica gel column chromatography and isolated as a yellow solid (266 mg, 0.457 mmol, 90%).

^{1}H NMR: (400 MHz, $CDCl_3$): δ 7.35 (1H, t, *J* = 1.4 Hz, H^1), 7.12 (2H, d, *J* = 1.4 Hz, H^2), 3.66 – 3.53 (1H, m, H^7), 3.26 – 3.06 (2H, m, H^9), 2.56 (2H, t, *J* = 7.4 Hz, H^3), 2.48 (1H, m, H^8), 1.93 (1H, m, H^8), 1.74 (4H, m, $H^4 + H^6$), 1.60 (2H, m, H^5).

^{13}C NMR (101 MHz, $CDCl_3$) δ 171.46, 150.17, 133.65, 126.15, 124.88, 92.34, 56.40, 40.40, 38.68, 34.74, 34.16, 28.81, 24.71, 9.24.

ESI-MS: m/z calcd. for $C_{18}H_{17}O_2I_2S_2$ $[M+H]^+$ 582.87538, found: 582.87521.

Compound 4.4HB (AD)



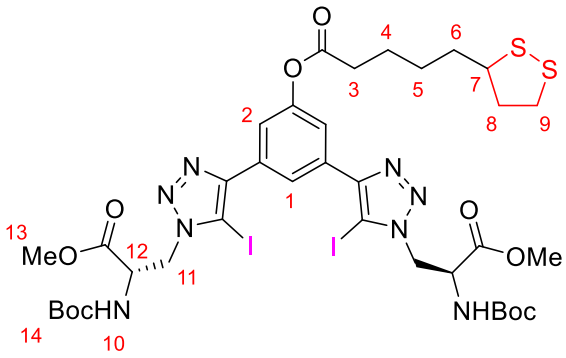
Synthesised according to General Procedure A: **4.7a** (70 mg, 0.212 mmol), azido-*N*-Boc-*L*-serine methyl ester (155 mg, 0.636 mmol), $Cu(CH_3CN)_4PF_6$ (16 mg, 0.042 mmol), TBTA (23 mg, 0.042 mmol). **4.4HB** isolated as brown solid (132 mg, 0.161 mmol, 76%).

^{1}H NMR: (400 MHz, $CDCl_3$): δ 8.06 (1H, s, H^1), 7.83 (2H, s, H^{15}), 7.52 (2H, d, J = 1.5 Hz, H^2), 5.62 – 5.41 (2H, m, H^{11}), 5.00 – 4.64 (6H, m, H^{10}+ H^{11} + H^{12}), 3.80 (6H, s, H^{13}), 3.71 – 3.52 (1H, m, H^7), 3.27 – 3.04 (2H, m, H^9), 2.62 (2H, t, J = 7.4 Hz, H^3), 2.55 – 2.43 (1H, m, H^8), 2.04 – 1.87 (1H, m, H^8), 1.86 – 1.69 (4H, m, H^4 + H^6), 1.64 – 1.52 (2H, m, H^5), 1.44 (18H, s, H^{14}).

^{13}C NMR: (101 MHz, $CDCl_3$): δ 171.96, 169.65, 155.35, 151.76, 146.67, 132.45, 121.62, 120.31, 118.78, 80.99, 56.44, 53.89, 53.31, 51.34, 40.40, 38.68, 34.75, 34.29, 28.87, 28.38, 24.82.

ESI-MS: m/z calcd. for $C_{36}H_{51}O_{10}N_8S_2$ $[M+H]^+$ 819.31641, found: 819.31653.

Compound 4.4XB (AD)



Synthesised according to General Procedure A: **4.7b** (70 mg, 0.120 mmol), azido-*N*-Boc-*L*-serine methyl ester (88 mg, 0.36 mmol), $Cu(CH_3CN)_4PF_6$ (9 mg, 0.024 mmol), TBTA (13 mg, 0.024mmol). **4.4XB** isolated as brown solid (94 mg, 0.0876 mmol, 73%).

^{1}H NMR: (400 MHz, $CDCl_3$): δ 8.49 (1H, t, *J* = 1.6 Hz, H^1), 7.77 (2H, d, *J* = 1.6 Hz, H^2), 5.58 – 5.38 (2H, m, H^{11}), 5.00 – 4.76 (6H, m, H^{10}+ H^{11} + H^{12}), 3.81 (6H, s, H^{13}), 3.67 – 3.53 (1H, m, H^7), 3.28 – 3.06 (2H, m, H^9), 2.63 (2H, t, *J* = 7.3 Hz, H^3), 2.56 – 2.42 (1H, m, H^8), 2.03 – 1.87 (1H, m, H^8), 1.89 – 1.69 (4H, m, H^4 + H^6), 1.62 – 1.53 (2H, m, H^5), 1.42 (18H, s, H^{14}).

^{13}C NMR: (101 MHz, $CDCl_3$): δ 171.83, 169.56, 155.17, 151.11, 148.46, 131.93, 123.25, 120.89, 80.84, 78.79, 56.51, 53.39, 53.32, 51.51, 40.40, 38.66, 34.71, 34.29, 28.82, 28.46, 24.82.

ESI-MS: m/z calcd. for $C_{36}H_{49}O_{10}N_8I_2S_2$ $[M+H]^+$ 1071.10969, found: 1071.10974.

Sodium salts of chiral anions (RH)

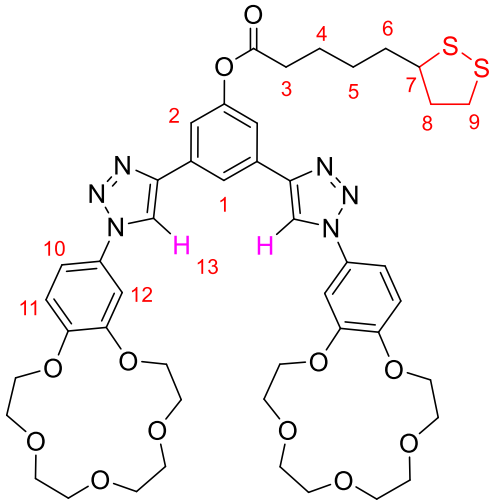
BINOL-PO_4Na as well as the sodium salts of the Boc-AAs were prepared by dissolving approx. 1 g of enantiopure acid in a minimal amount of MeOH/H_2O (≈4:1 v/v) to which 1 equiv. of NaOH dissolved in water was added under stirring. The solutions were stirred overnight and then reduced *in vacuo*. The salts were then dried at 60 °C *in vacuo* for at least 1 d. The hereby obtained solid sodium salts were subsequently used without further characterisation.

7.5.4 Synthesis for Chapter 5

The synthetic route towards **5.5XB/HB** is shown in Scheme 5.1. The synthesis and characterisation of all compounds was carried out by Andrew Docker.

4'- azidobenzo 15-crown-5 **5.6** was synthesised according to a reported procedure.[350]

Compound 5.5HB (AD)



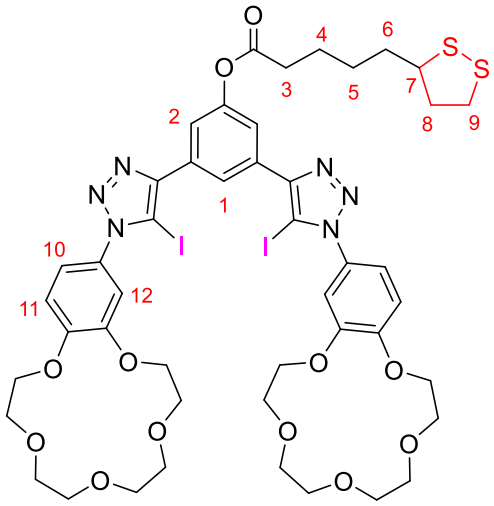
Synthesised according to General Procedure A: **4.7a** (70 mg, 0.212 mmol), Azido-benzo 15-crown-5 **5.6** (197 mg, 0.636 mmol), $Cu(CH_3CN)_4PF_6$ (16 mg, 0.042 mmol), TBTA (23 mg, 0.042 mmol). **5.5HB** isolated as brown solid (72 mg, 0.076 mmol, 36%).

^{1}H NMR: (400 MHz, $CDCl_3$): δ 8.48 (2H, s, H^{13}), 8.28 (1H, s, H^1), 7.70 (2H, d, J = 1.5 Hz, H^2), 7.40 (2H, d, J = 2.4 Hz, H^{12}), 7.30 (2H, dd, J = 8.7, 2.4 Hz, H^{10}), 6.92 (2H, d, J = 8.7 Hz, H^{11}), 4.32 – 4.18 (4H, m), 4.18 – 4.10 (4H, m), 3.99 – 3.85 (8H, m), 3.82 – 3.69 (16H, m), 3.69 – 3.60 (1H, m, H^7), 3.28 – 3.09 (2H, m, H^9), 2.64 (2H, t, J = 7.4 Hz, H^3), 2.58 – 2.41 (1H, m, H^8), 2.05 – 1.90 (1H, m, H^8), 1.88 – 1.71 (4H, m, $H^4 + H^6$), 1.69 – 1.53 (2H, m, H^5).

^{13}C NMR: (126 MHz, $CDCl_3$): δ 172.06, 151.95, 147.14, 132.62, 131.01, 120.60, 118.96, 118.72, 113.81, 112.95, 106.62, 70.89, 70.25, 69.20, 68.99, 56.51, 40.42, 38.72, 34.77, 34.34, 28.90, 24.85.

ESI-MS: m/z calcd. for $C_{46}H_{56}O_{12}N_6NaS_2$ $[M+Na]^+$ 971.32898, found: 971.32886.

Compound 5.5XB (AD)



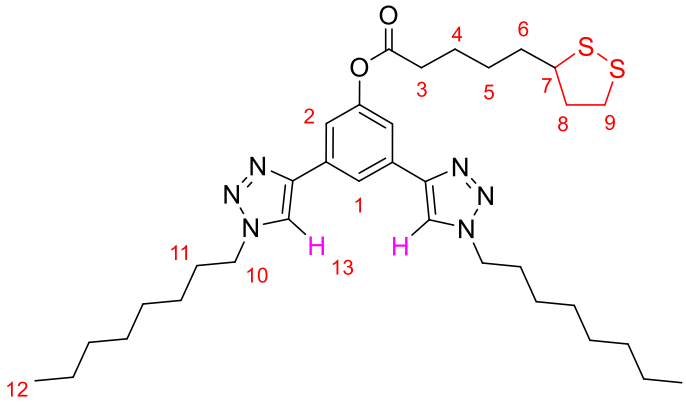
Synthesised according to General Procedure A: **4.7b** (150 mg, 0.381 mmol), 4'- azidobenzo 15-crown-5 **5.6** (354 mg, 1.14 mmol), $Cu(CH_3CN)_4PF_6$ (28 mg, 0.076 mmol), TBTA (40 mg, 0.076 mmol). **5.5XB** isolated as brown solid (110 mg, 0.091 mmol, 24%).

^{1}H NMR: (500 MHz, $CDCl_3$): δ 8.63 (1H, s, H^1), 7.87 (2H, d, J = 1.6 Hz, H^2), 7.12 – 7.05 (2H, m, H^{10}), 7.05 – 6.95 (4H, m, H^{11} + H^{12}), 4.25 – 4.15 (8H, m), 4.02 – 3.90 (8H, m), 3.82 – 3.75 (16H, m), 3.68 – 3.57 (1H, m, H^7), 3.27 – 3.05 (2H, m, H^9), 2.65 (2H, t, J = 7.3 Hz, H^3), 2.50 (1H, m, H^8), 1.95 (1H, m, H^8), 1.89 – 1.72 (4H, m, H^4 + H^6), 1.61 (2H, m, H^5).

^{13}C NMR: (126 MHz, $CDCl_3$): δ 171.85, 151.21, 150.74, 149.45, 148.92, 132.07, 130.13, 123.59, 121.10, 119.70, 113.20, 112.35, 71.29, 70.55, 69.51, 69.41, 69.27, 69.23, 56.53, 40.42, 38.69, 34.74, 34.35, 28.85, 24.86.

ESI-MS: m/z calcd. for $C_{46}H_{55}O_{12}N_6I_2S_2$ $[M+H]^+$ 1201.14032, found: 1201.13953.

Compound 5.6HB (AD)



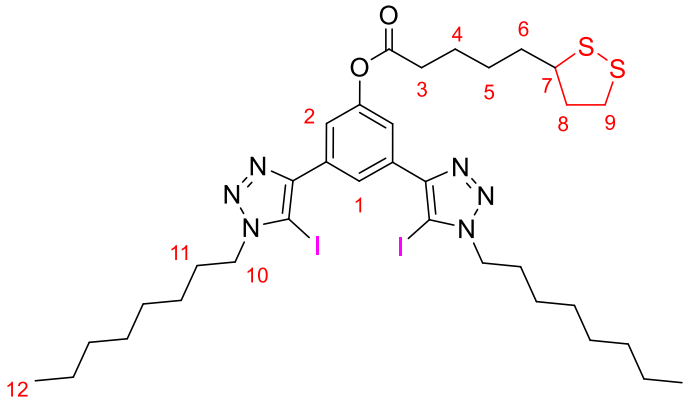
Synthesised according to General Procedure A: **4.7a** (70 mg, 0.212 mmol), octyl-azide (99 mg, 0.636 mmol), $Cu(CH_3CN)_4PF_6$ (16 mg, 0.042 mmol), TBTA (23 mg, 0.042 mmol). **5.6HB** isolated as brown solid (153 mg, 0.171 mmol, 81%).

^{1}H NMR: (400 MHz, $CDCl_3$): δ 8.16 (1H, s, H^1), 7.84 (2H, s, H^{13}), 7.55 (2H, s, H^2), 4.39 (4H, t, J = 7.2 Hz, H^{10}), 3.76 – 3.49 (1H, m, H^7), 3.32 – 2.95 (2H, m, H^9), 2.61 (2H, t, J = 7.4 Hz, H^3), 2.54 – 2.42 (1H, m, H^8), 2.01 – 1.85 (5H, m, $H^8 + H^{11}$), 1.87 – 1.64 (4H, m, $H^4 + H^6$), 1.67 – 1.50 (2H, m, H^5), 1.41 – 1.19 (20H, m) 0.87 (6H t, J = 6.6 Hz, H^{12}).

^{13}C NMR: (101 MHz, $CDCl_3$): δ 171.96, 151.75, 146.73, 132.85, 120.20 (d, *J* = 3.5 Hz), 118.46, 56.47, 50.67, 40.38, 38.68, 34.74, 34.29, 31.83, 30.43, 29.82, 29.16, 29.10, 28.85, 26.61, 24.82, 22.72, 14.18.

ESI-MS: m/z calcd. for $C_{34}H_{53}O_2N_6S_2$ $[M+H]^+$ 641.36659, found: 641.36646.

<u>Compound 5.6XB</u> (AD)



Synthesised according to General Procedure A: **4.7b** (70 mg, 0.120 mmol), octyl-azide (56 mg, 0.36 mmol), $Cu(CH_3CN)_4PF_6$ (9 mg, 0.024 mmol), TBTA (13 mg, 0.024 mmol). **5.6XB** isolated as white solid (75 mg, 0.084 mmol, 70%).

^{1}H NMR: (500 MHz, $CDCl_3$): δ 8.49 (1H, s, H^1), 7.77 (2H, s, H^2), 4.44 (4H, t, *J* = 7.4 Hz, H^{10}), 3.67 – 3.55 (1H, m, H^7), 3.24 – 3.03 (2H, m, H^9), 2.62 (2H, t, *J* = 7.4 Hz, H^3), 2.56 – 2.40 (1H, m, H^8), 2.02 – 1.88 (5h, m, H^8 + H^{11}), 1.88 – 1.67 (4H, m, H^4 + H^6), 1.67 – 1.50 (2H, m, H^5), 1.45 – 1.16 (20H, m), 0.88 (6H, t, *J* = 6.7 Hz, H^{12}).

^{13}C NMR: (126 MHz, $CDCl_3$): δ 171.82, 151.09, 148.54, 132.20, 123.26, 120.69, 56.51, 51.15, 40.39, 38.66, 34.71, 34.30, 31.85, 30.04, 29.18, 29.11, 28.82, 26.53, 24.82, 22.74, 14.21.

ESI-MS: m/z calcd. for $C_{34}H_{51}O_2N_6I_2S_2$ $[M+H]^+$ 893.15988, found: 893.15985.

Chapter 8

References

Chapter 8: References

1. P. M. Quinton, *FASEB J.*, **1990**, 4, 2709-2717.
2. F. Delange, *Thyroid*, **1994**, 4, 107-128.
3. V. H. Smith and D. W. Schindler, *Trends Ecol. Evol.*, **2009**, 24, 201-207.
4. E. A. Katayev, G. V. Kolesnikov and J. L. Sessler, *Chem. Soc. Rev.*, **2009**, 38, 1572-1586.
5. P. D. Beer and P. A. Gale, *Angew. Chem. Int. Ed.*, **2001**, 40, 486-516.
6. J. Pflugrath and F. Quiocho, *Nature*, **1985**, 314, 257.
7. H. Luecke and F. A. Quiocho, *Nature*, **1990**, 347, 402.
8. F. Hofmeister, *Arch. Exp. Pathol. Phar*, **1888**, 24, 247-260.
9. U. Mayer, *Coord. Chem. Rev.*, **1976**, 21, 159-179.
10. D. J. Cram, *Angew. Chem. Int. Ed.*, **1988**, 27, 1009-1020.
11. Y. Li and A. H. Flood, *Angew. Chem. Int. Ed.*, **2008**, 47, 2649-2652.
12. S. J. Grabowski, *Hydrogen bonding: new insights*, Springer, **2006**.
13. L. M. Eytel, H. A. Fargher, M. M. Haley and D. W. Johnson, *Chem. Commun.*, **2019**, 55, 5195-5206.
14. L. C. Gilday, S. W. Robinson, T. A. Barendt, M. J. Langton, B. R. Mullaney and P. D. Beer, *Chem. Rev.*, **2015**, 115, 7118-7195.
15. A. Brown and P. D. Beer, *Chem. Commun.*, **2016**, 52, 8645-8658.
16. J. Pancholi and P. D. Beer, *Coord. Chem. Rev.*, **2020**, 416, 213281.
17. M. Novák, C. Foroutan-Nejad and R. Marek, *Phys. Chem. Chem. Phys.*, **2015**, 17, 6440-6450.
18. J. Y. C. Lim and P. D. Beer, *Chem*, **2018**, 4, 731-783.
19. B. L. Schottel, H. T. Chifotides and K. R. Dunbar, *Chem. Soc. Rev.*, **2008**, 37, 68-83.
20. O. B. Berryman, F. Hof, M. J. Hynes and D. W. Johnson, *Chem. Commun.*, **2006**, 506-508.
21. M. Mascal, *Angew. Chem. Int. Ed.*, **2006**, 45, 2890-2893.
22. S. Guha and S. Saha, *J. Am. Chem. Soc.*, **2010**, 132, 17674-17677.
23. T. Lizal and V. Sindelar, *Isr. J. Chem.*, **2018**, 58, 326-333.
24. F. Biedermann, W. M. Nau and H.-J. Schneider, *Angew. Chem. Int. Ed.*, **2014**, 53, 11158-11171.

25. S. L. Tobey, B. D. Jones and E. V. Anslyn, *J. Am. Chem. Soc.*, **2003**, 125, 4026-4027.

26. C. R. Wade, A. E. J. Broomsgrove, S. Aldridge and F. P. Gabbaï, *Chem. Rev.*, **2010**, 110, 3958-3984.

27. G. Park, D. J. Brock, J.-P. Pellois and F. P. Gabbaï, *Chem*, **2019**, 5, 2215-2227.

28. P. D. Beer and J. Cadman, *Coord. Chem. Rev.*, **2000**, 205, 131-155.

29. E. Bakker and M. Telting-Diaz, *Anal. Chem.*, **2002**, 74, 2781-2800.

30. E. Bakker, P. Bühlmann and E. Pretsch, *Chem. Rev.*, **1997**, 97, 3083-3132.

31. E. Bakker, P. Bühlmann and E. Pretsch, *Electroanalysis*, **1999**, 11, 915-933.

32. P. Bühlmann and L. D. Chen, *Ion-Selective Electrodes With Ionophore-Doped Sensing Membranes*, Wiley, **2012**.

33. G. A. Crespo, *Electrochim. Acta*, **2017**, 245, 1023-1034.

34. K. N. Mikhelson, *Ion-selective electrodes*, Springer, **2013**.

35. E. Pretsch, *TrAC, Trends Anal. Chem.*, **2007**, 26, 46-51.

36. E. Zdrachek and E. Bakker, *Anal. Chem.*, **2019**, 91, 2-26.

37. J. Bobacka, A. Ivaska and A. Lewenstam, *Chem. Rev.*, **2008**, 108, 329-351.

38. J. Sabek, L. Adriaenssens, T. Guinovart, E. J. Parra, F. X. Rius, P. Ballester and P. Blondeau, *Chem. Eur. J.*, **2015**, 21, 448-454.

39. R. S. Hutchins, P. Molina, M. Alajarin, A. Vidal and L. G. Bachas, *Anal. Chem.*, **1994**, 66, 3188-3192.

40. R. S. Hutchins, P. Bansal, P. Molina, M. Alajarín, A. Vidal and L. G. Bachas, *Anal. Chem.*, **1997**, 69, 1273-1278.

41. C. M. Carey and W. B. Riggan, *Anal. Chem.*, **1994**, 66, 3587-3591.

42. S. Daunert and L. G. Bachas, *Anal. Chem.*, **1989**, 61, 499-503.

43. S. Nishizawa, P. Bühlmann, K. P. Xiao and Y. Umezawa, *Anal. Chim. Acta*, **1998**, 358, 35-44.

44. K. P. Xiao, P. Bühlmann, S. Nishizawa, S. Amemiya and Y. Umezawa, *Anal. Chem.*, **1997**, 69, 1038-1044.

45. M. M. G. Antonisse and D. N. Reinhoudt, *Electroanalysis*, **1999**, 11, 1035-1048.

46. P. Bühlmann, E. Pretsch and E. Bakker, *Chem. Rev.*, **1998**, 98, 1593-1688.

47. V. K. Gupta, L. P. Singh, S. Chandra, S. Kumar, R. Singh and B. Sethi, *Talanta*, **2011**, 85, 970-974.

48. D.-C. Jeong, H.-K. Lee and S.-W. Jeon, *Bull. Korean Chem. Soc.*, **2006**, 27, 1985-1988.

49. A. S. Watts, V. G. Gavalas, A. Cammers, P. S. Andrada, M. Alajarín and L. G. Bachas, *Sens. Actuators B Chem.*, **2007**, 121, 200-207.

50. M. Fibbioli, M. Berger, F. P. Schmidtchen and E. Pretsch, *Anal. Chem.*, **2000**, 72, 156-160.

51. S. Amemiya, P. Bühlmann, Y. Umezawa, R. C. Jagessar and D. H. Burns, *Anal. Chem.*, **1999**, 71, 1049-1054.

52. H.-K. Lee, K.-j. Song, H.-R. Seo and S.-w. Jeon, *Bull. Korean Chem. Soc.*, **2002**, 23, 1409-1412.

53. H. K. Lee, K. Song, H. R. Seo and S. Jeon, *Talanta*, **2004**, 62, 293-297.

54. V. K. Gupta, R. N. Goyal and R. A. Sharma, *Talanta*, **2008**, 76, 859-864.

55. L. Mendecki, T. Fayose, K. A. Stockmal, J. Wei, S. Granados-Focil, C. M. McGraw and A. Radu, *Anal. Chem.*, **2015**, 87, 7515-7518.

56. A. K. Jain, V. K. Gupta and J. R. Raisoni, *Talanta*, **2006**, 69, 1007-1012.

57. M. Cuartero, J. A. Ortuño, M. S. García, G. Sánchez, M. Más-Montoya and D. Curiel, *Talanta*, **2011**, 85, 1876-1881.

58. M. Cuartero, M. Más-Montoya, M. S. García, D. Curiel and J. A. Ortuño, *Talanta*, **2014**, 123, 200-206.

59. K. Martin, S. A. Kadam, U. Mattinen, J. Bobacka and I. Leito, *Electroanalysis*, **2019**, 31, 1061-1066.

60. M. J. Berrocal, A. Cruz, I. H. Badr and L. G. Bachas, *Anal. Chem.*, **2000**, 72, 5295-5299.

61. J. A. Ortuño, R. Expósito, C. Sánchez-Pedreño, M. I. Albero and A. Espinosa, *Anal. Chim. Acta*, **2004**, 525, 231-237.

62. N. Pankratova, M. Cuartero, L. A. Jowett, E. N. W. Howe, P. A. Gale, E. Bakker and G. A. Crespo, *Biosens. Bioelectron.*, **2018**, 99, 70-76.

63. V. K. Gupta, R. Ludwig and S. Agarwal, *Anal. Chim. Acta*, **2005**, 538, 213-218.

64. H. K. Lee, H. Oh, K. C. Nam and S. Jeon, *Sens. Actuators B Chem.*, **2005**, 106, 207-211.

65. B. Schazmann and D. Diamond, *New J. Chem.*, **2007**, 31, 587-592.

66. J. N. Babu, V. Bhalla, M. Kumar, R. Mahajan and R. K. Puri, *Tetrahedron Lett.*, **2008**, 49, 2772-2775.

67. J. N. Babu, V. Bhalla, M. Kumar, R. K. Puri and R. K. Mahajan, *New J. Chem.*, **2009**, 33, 675-681.

68. T. V. Shishkanova, D. Sýkora, J. L. Sessler and V. Král, *Anal. Chim. Acta*, **2007**, 587, 247-253.

69. E. M. Zahran, Y. Hua, Y. Li, A. H. Flood and L. G. Bachas, *Anal. Chem.*, **2010**, 82, 368-375.

70. E. M. Zahran, E. M. Fatila, C.-H. Chen, A. H. Flood and L. G. Bachas, *Anal. Chem.*, **2018**, 90, 1925-1933.

71. E. M. Zahran, Y. Hua, S. Lee, A. H. Flood and L. G. Bachas, *Anal. Chem.*, **2011**, 83, 3455-3461.

72. Z. Jarolímová, J. Bosson, G. M. Labrador, J. Lacour and E. Bakker, *Electroanalysis*, **2018**, 30, 1378-1385.

73. X. Xie, J. Zhai and E. Bakker, *J. Am. Chem. Soc.*, **2014**, 136, 16465-16468.

74. M. Parrilla, M. Cuartero and G. A. Crespo, *TrAC, Trends Anal. Chem.*, **2019**, 110, 303-320.

75. J. Hu, A. Stein and P. Bühlmann, *Angew. Chem. Int. Ed.*, **2016**, 55, 7544-7547.

76. B. Lou, C. Chen, Z. Zhou, L. Zhang, E. Wang and S. Dong, *Talanta*, **2013**, 105, 40-45.

77. E. Zdrachek and E. Bakker, *Anal. Chem.*, **2018**, 90, 7591-7599.

78. P. D. Beer, P. A. Gale and G. Z. Chen, *Coord. Chem. Rev.*, **1999**, 185, 3-36.

79. P. D. Beer, P. A. Gale and G. Z. Chen, *J. Chem. Soc., Dalton Trans.*, **1999**, 1897-1910.

80. S. R. Miller, D. A. Gustowski, Z. H. Chen, G. W. Gokel, L. Echegoyen and A. E. Kaifer, *Anal. Chem.*, **1988**, 60, 2021-2024.

81. R. Oliveira, S. Groni, C. Fave, M. Branca, F. Mavre, D. Lorcy, M. Fourmigue and B. Schollhorn, *Phys. Chem. Chem. Phys.*, **2016**, 18, 15867-15873.

82. R. Sun, L. Wang, H. Yu, Z.-u.-. Abdin, Y. Chen, J. Huang and R. Tong, *Organometallics*, **2014**, 33, 4560-4573.

83. P. D. Beer, Z. Chen, A. J. Goulden, A. Graydon, S. E. Stokes and T. Wear, *J. Chem. Soc., Chem. Commun.*, **1993**, 1834-1836.

84. P. D. Beer and A. D. Keefe, *J. Organomet. Chem.*, **1989**, 375, C40-C42.

85. D. Canevet, M. Sallé, G. Zhang, D. Zhang and D. Zhu, *Chem. Commun.*, **2009**, 2245-2269.

86. M. Biesaga, K. Pyrzyńska and M. Trojanowicz, *Talanta*, **2000**, 51, 209-224.

87. B. Kaur, C. A. Erdmann, M. Daniëls, W. Dehaen, Z. Rafiński, H. Radecka and J. Radecki, *Anal. Chem.*, **2017**, 89, 12756-12763.

88. M. Nicolas, B. Fabre, J. Chapuzet, J. Lessard and J. Simonet, *J. Electroanal. Chem.*, **2000**, 482, 211-216.

89. T. Ghosh, B. G. Maiya and M. W. Wong, *J. Phys. Chem. A*, **2004**, 108, 11249-11259.

90. P. Organic lettersAnzenbacher, M. A. Palacios, K. Jursíková and M. Marquez, *Org. Lett.*, **2005**, 7, 5027-5030.

91. A. Satheshkumar, R. Manivannan and K. P. Elango, *J. Organomet. Chem.*, **2014**, 750, 98-106.

92. A. C. Fahrenbach, S. C. Warren, J. T. Incorvati, A.-J. Avestro, J. C. Barnes, J. F. Stoddart and B. A. Grzybowski, *Adv. Mater.*, **2013**, 25, 331-348.

93. P. D. Beer, P. A. Gale and Z. Chen, *Electrochemical recognition of charged and neutral guest species by redox-active receptor molecules*, Academic Press, **1999**.

94. P. D. Beer, J. Cadman, J. M. Lloris, R. Martínez-Máñez, J. Soto, T. Pardo and M. D. Marcos, *J. Chem. Soc., Dalton Trans.*, **2000**, 1805-1812.

95. P. D. Beer and P. V. Bernhardt, *J. Chem. Soc., Dalton Trans.*, **2001**, 1428-1431.

96. P. V. Bernhardt and N. L. Creevey, *Dalton Trans.*, **2004**, 914-920.

97. O. Reynes, C. Bucher, J.-C. Moutet, G. Royal, E. Saint-Aman and E.-M. Ungureanu, *J. Electroanal. Chem.*, **2005**, 580, 291-299.

98. L.-J. Kuo, J.-H. Liao, C.-T. Chen, C.-H. Huang, C.-S. Chen and J.-M. Fang, *Org. Lett.*, **2003**, 5, 1821-1824.

99. X. Huang, B. Wu, C. Jia, B. P. Hay, M. Li and X. J. Yang, *Chem. Eur. J.*, **2013**, 19, 9034-9041.

100. L. O. Abouderbala, W. J. Belcher, M. G. Boutelle, P. J. Cragg, J. W. Steed, D. R. Turner and K. J. Wallace, *Proc. Natl. Acad. Sci. U. S. A.*, **2002**, 99, 5001.

101. O. Reynes, F. Maillard, J.-C. Moutet, G. Royal, E. Saint-Aman, G. Stanciu, J.-P. Dutasta, I. Gosse and J.-C. Mulatier, *J. Organomet. Chem.*, **2001**, 637, 356-363.

102. C. Li, L. Wang, L. Deng, H. Yu, J. Huo, L. Ma and J. Wang, *J. Phys. Chem. B*, **2009**, 113, 15141-15144.

103. F. Zapata, A. Caballero, A. Espinosa, A. Tárraga and P. Molina, *J. Org. Chem.*, **2008**, 73, 4034-4044.

104. M. Alfonso, A. Espinosa Ferao, A. Tárraga and P. Molina, *Inorg. Chem.*, **2015**, 54, 7461-7473.

105. M. Alfonso, A. Tárraga and P. Molina, *Inorg. Chem.*, **2013**, 52, 7487-7496.

106. F. Zapata, A. Caballero, A. Tárraga and P. Molina, *J. Org. Chem.*, **2010**, 75, 162-169.

107. M. Alfonso, A. Tárraga and P. Molina, *Dalton Trans.*, **2016**, 45, 19269-19276.

108. N. H. Evans, C. J. Serpell, K. E. Christensen and P. D. Beer, *Eur. J. Inorg. Chem.*, **2012**, 2012, 939-944.

109. L. Deng, L. Wang, J. Huo, Q. Tan, Q. Yang, H. Yu, H. Gao and J. Wang, *J. Phys. Chem. B*, **2008**, 112, 5333-5337.

110. F. Otón, A. Espinosa, A. Tárraga, I. Ratera, K. Wurst, J. Veciana and P. Molina, *Inorg. Chem.*, **2009**, 48, 1566-1576.

111. D. Nieto, A. M. González-Vadillo, S. Bruña, C. J. Pastor, A. E. Kaifer and I. Cuadrado, *Chem. Commun.*, **2011**, 47, 10398-10400.

112. F. Otón, A. Espinosa, A. Tárraga, C. R. de Arellano and P. Molina, *Chem. Eur. J.*, **2007**, 13, 5742-5752.

113. A. Sola, R. A. Orenes, M. Á. García, R. M. Claramunt, I. Alkorta, J. Elguero, A. Tárraga and P. Molina, *Inorg. Chem.*, **2011**, 50, 4212-4220.

114. P. A. Gale, M. B. Hursthouse, M. E. Light, J. L. Sessler, C. N. Warriner and R. S. Zimmerman, *Tetrahedron Lett.*, **2001**, 42, 6759-6762.

115. D.-S. Guo, Z.-P. Liu, J.-P. Ma and R.-Q. Huang, *Tetrahedron Lett.*, **2007**, 48, 1221-1224.

116. B. Tomapatanaget, T. Tuntulani and O. Chailapakul, *Org. Lett.*, **2003**, 5, 1539-1542.

117. A. J. Evans, S. E. Matthews, A. R. Cowley and P. D. Beer, *Dalton Trans.*, **2003**, 4644-4650.

118. E. Métay, M. C. Duclos, S. Pellet-Rostaing, M. Lemaire, J. Schulz, R. Kannappan, C. Bucher, E. Saint-Aman and C. Chaix, *Eur. J. Org. Chem.*, **2008**, 2008, 4304-4312.

119. B. Shaabani and Z. Shaghaghi, *Appl. Organomet. Chem.*, **2011**, 25, 317-322.

120. K. A. Nielsen, J. O. Jeppesen, E. Levillain and J. Becher, *Angew. Chem. Int. Ed.*, **2003**, 42, 187-191.

121. H. Lu, W. Xu, D. Zhang and D. Zhu, *Chem. Commun.*, **2005**, 4777-4779.

122. H. Lu, W. Xu, D. Zhang, C. Chen and D. Zhu, *Org. Lett.*, **2005**, 7, 4629-4632.

123. J. Xiong, L. Sun, Y. Liao, G.-N. Li, J.-L. Zuo and X.-Z. You, *Tetrahedron Lett.*, **2011**, 52, 6157-6161.

124. C. Bejger, J. S. Park, E. S. Silver and J. L. Sessler, *Chem. Commun.*, **2010**, 46, 7745-7747.

125. M. H. Lee, Q.-Y. Cao, S. K. Kim, J. L. Sessler and J. S. Kim, *J. Org. Chem.*, **2011**, 76, 870-874.

126. Z. Shi, Q.-H. Han, X.-Y. Li, M.-Y. Shao, Q.-Y. Zhu and J. Dai, *Dalton Trans.*, **2011**, 40, 7340-7347.

127. Z. Shi, Z.-J. Lu, Q.-Y. Zhu, L.-B. Huo, Q.-H. Han, G.-Q. Bian and J. Dai, *J. Phys. Chem. B*, **2011**, 115, 3020-3026.

128. P. D. Beer, M. G. B. Drew and R. Jagessar, *J. Chem. Soc., Dalton Trans.*, **1997**, 881-886.

129. D. P. Cormode, S. S. Murray, A. R. Cowley and P. D. Beer, *Dalton Trans.*, **2006**, 5135-5140.

130. D. P. Cormode, M. G. B. Drew, R. Jagessar and P. D. Beer, *Dalton Trans.*, **2008**, 6732-6741.

131. A. L. Schumacher, J. P. Hill, K. Ariga and F. D'Souza, *Electrochem. Commun.*, **2007**, 9, 2751-2754.

132. J. P. Clare, A. Statnikov, V. Lynch, A. L. Sargent and J. W. Sibert, *J. Org. Chem.*, **2009**, 74, 6637-6646.

133. C. Bhaumik, D. Saha, S. Das and S. Baitalik, *Inorg. Chem.*, **2011**, 50, 12586-12600.

134. C. Bhaumik, D. Maity, S. Das and S. Baitalik, *Polyhedron*, **2013**, 52, 890-899.

135. D. Maity, C. Bhaumik, D. Mondal and S. Baitalik, *Inorg. Chem.*, **2013**, 52, 13941-13955.

136. A. Das, P. Mondal, M. Dasgupta, N. Kishore and G. K. Lahiri, *Dalton Trans.*, **2016**, 45, 2605-2617.

137. J. Lehr, T. Lang, O. A. Blackburn, T. A. Barendt, S. Faulkner, J. J. Davis and P. D. Beer, *Chem. Eur. J.*, **2013**, 19, 15898-15906.

138. P. D. Beer, F. Szemes, V. Balzani, C. M. Salà, M. G. B. Drew, S. W. Dent and M. Maestri, *J. Am. Chem. Soc.*, **1997**, 119, 11864-11875.

139. P. D. Beer, N. G. Berry, A. R. Cowley, E. J. Hayes, E. C. Oates and W. W. Wong, *Chem. Commun.*, **2003**, 2408-2409.

140. N. G. Berry, M. D. Pratt, O. D. Fox and P. D. Beer, *Supramol. Chem.*, **2001**, 13, 677-682.

141. P. D. Beer, N. Berry, M. G. Drew, O. D. Fox, M. E. Padilla-Tosta and S. Patell, *Chem. Commun.*, **2001**, 199-200.

142. J.-L. Thomas, J. Howarth, K. Hanlon and D. McGuirk, *Tetrahedron Lett.*, **2000**, 41, 413-416.

143. T.-Q. Weng, Y.-F. Huang, L.-S. Xue, J. Cheng, S. Jin, S.-H. Liu, D.-Y. Wu and G. Z. Chen, *Molecules*, **2019**, 24, 238.

144. J.-B. Zhuo, C.-X. Lin, Q. Wan, L.-L. Xie and Y.-F. Yuan, *J. Organomet. Chem.*, **2015**, 791, 289-297.

145. J.-B. Zhuo, X.-X. Zhu, C.-X. Lin, S. Bai, L.-L. Xie and Y.-F. Yuan, *J. Organomet. Chem.*, **2014**, 770, 85-93.

146. J.-B. Zhuo, C.-Y. Zhang, C.-X. Lin, S. Bai, L.-L. Xie and Y.-F. Yuan, *J. Organomet. Chem.*, **2014**, 763, 34-43.

147. D. Kong, T. Weng, W. He, B. Liu, S. Jin, X. Hao and S. Liu, *J. Organomet. Chem.*, **2013**, 727, 19-27.

148. A. Caballero, N. G. White and P. D. Beer, *CrystEngComm*, **2014**, 16, 3694-3698.

149. V. Amendola, M. Boiocchi, B. Colasson, L. Fabbrizzi, E. Monzani, M. J. Douton-Rodriguez and C. Spadini, *Inorg. Chem.*, **2008**, 47, 4808-4816.

150. Y. Hua and A. H. Flood, *Chem. Soc. Rev.*, **2010**, 39, 1262-1271.

151. T. Romero, A. Caballero, A. Tárraga and P. Molina, *Org. Lett.*, **2009**, 11, 3466-3469.

152. Q.-Y. Cao, T. Pradhan, S. Kim and J. S. Kim, *Org. Lett.*, **2011**, 13, 4386-4389.

153. Q.-Y. Cao, T. Pradhan, M. H. Lee, D. H. Choi and J. S. Kim, *Tetrahedron Lett.*, **2012**, 53, 4917-4920.

154. T. Romero, R. A. Orenes, A. Tarraga and P. Molina, *Organometallics*, **2013**, 32, 5740-5753.

155. N. G. White and P. D. Beer, *Beilstein J. Org. Chem.*, **2012**, 8, 246.

156. C.-T. Li, Q.-Y. Cao, J.-J. Li, Z.-W. Wang and B.-N. Dai, *Inorg. Chim. Acta*, **2016**, 449, 31-37.

157. R. Hosseinzadeh, F. Maliji, H. Golchoubian and A. Bekhradnia, *ChemistrySelect*, **2019**, 4, 3914-3920.

158. J. Y. C. Lim, M. J. Cunningham, J. J. Davis and P. D. Beer, *Chem. Commun.*, **2015**, 51, 14640-14643.

159. J. Y. C. Lim and P. D. Beer, *Eur. J. Inorg. Chem.*, **2017**, 2017, 220-224.

160. F. Zapata, A. Caballero and P. Molina, *Eur. J. Inorg. Chem.*, **2017**, 2017, 237-241.

161. R. Oliveira, S. Groni, A. Vacher, F. Barrière, D. Lorcy, M. Fourmigué, E. Maisonhaute, B. Schöllhorn and C. Fave, *ChemistrySelect*, **2018**, 3, 8874-8880.

162. B. R. Mullaney, M. J. Cunningham, J. J. Davis and P. D. Beer, *Polyhedron*, **2016**, 116, 20-25.

163. C. Dusemund, K. S. Sandanayake and S. Shinkai, *J. Chem. Soc., Chem. Commun.*, **1995**, 333-334.

164. C. Bresner, J. K. Day, N. D. Coombs, I. A. Fallis, S. Aldridge, S. J. Coles and M. B. Hursthouse, *Dalton Trans.*, **2006**, 3660-3667.

165. A. E. Broomsgrove, D. A. Addy, C. Bresner, I. A. Fallis, A. L. Thompson and S. Aldridge, *Chem. Eur. J.*, **2008**, 14, 7525-7529.

166. A. Thakur, D. Mandal, S. Sao and S. Ghosh, *J. Organomet. Chem.*, **2012**, 715, 129-135.

167. Z.-M. Su, C.-X. Lin, Y.-T. Zhou, L.-L. Xie and Y.-F. Yuan, *J. Organomet. Chem.*, **2015**, 788, 17-26.

168. J. Li, G. Zhang, D. Zhang, R. Zheng, Q. Shi and D. Zhu, *J. Org. Chem.*, **2010**, 75, 5330-5333.

169. K. Mulla and Y. Zhao, *Tetrahedron Lett.*, **2014**, 55, 382-386.

170. B. Fabre, U. Lehmann and A. Schlüter, *Electrochim. Acta*, **2001**, 46, 2855-2861.

171. M. Nicolas, B. Fabre and J. Simonet, *Electrochim. Acta*, **2001**, 46, 1179-1190.

172. C. R. Wade and F. o. P. Gabbaï, *Inorg. Chem.*, **2010**, 49, 714-720.

173. M. Melaïmi, S. Solé, C.-W. Chiu, H. Wang and F. P. Gabbaï, *Inorg. Chem.*, **2006**, 45, 8136-8143.

174. C. L. Dorsey, P. Jewula, T. W. Hudnall, J. D. Hoefelmeyer, T. J. Taylor, N. R. Honesty, C.-W. Chiu, M. Schulte and F. P. Gabbaï, *Dalton Trans.*, **2008**, 4442-4450.

175. O. Reynes, C. Bucher, J.-C. Moutet, G. Royal and E. Saint-Aman, *Chem. Commun.*, **2004**, 428-429.

176. O. Reynes, J.-C. Moutet, J. Pecaut, G. Royal and E. Saint-Aman, *New J. Chem.*, **2002**, 26, 9-12.

177. C. Bucher, C. H. Devillers, J.-C. Moutet, G. Royal and E. Saint-Aman, *New J. Chem.*, **2004**, 28, 1584-1589.

178. M. J. Chmielewski, J. J. Davis and P. D. Beer, *Org. Biomol. Chem.*, **2009**, 7, 415-424.

179. M. J. Langton and P. D. Beer, *Acc. Chem. Res.*, **2014**, 47, 1935-1949.

180. A. Caballero, F. Zapata and P. D. Beer, *Coord. Chem. Rev.*, **2013**, 257, 2434-2455.

181. N. H. Evans and P. D. Beer, *Org. Biomol. Chem.*, **2011**, 9, 92-100.

182. N. H. Evans, C. J. Serpell, N. G. White and P. D. Beer, *Chem. Eur. J.*, **2011**, 17, 12347-12354.

183. N. H. Evans, C. J. Serpell and P. D. Beer, *Chem. Commun.*, **2011**, 47, 8775-8777.

184. N. H. Evans, H. Rahman, A. V. Leontiev, N. D. Greenham, G. A. Orlowski, Q. Zeng, R. M. J. Jacobs, C. J. Serpell, N. L. Kilah, J. J. Davis and P. D. Beer, *Chem. Sci.*, **2012**, 3, 1080-1089.

185. J. Y. C. Lim, M. J. Cunningham, J. J. Davis and P. D. Beer, *Dalton Trans.*, **2014**, 43, 17274-17282.

186. J. Y. C. Lim and P. D. Beer, *Eur. J. Org. Chem.*, **2019**, 2019, 3433-3441.

187. A. Brown and P. D. Beer, *Dalton Trans.*, **2012**, 41, 118-129.

188. D. Astruc, E. Boisselier and C. Ornelas, *Chem. Rev.*, **2010**, 110, 1857-1959.

189. D. Astruc and J. Ruiz, *J. Inorg. Organomet. Polym. Mater.*, **2015**, 25, 2-11.

190. D. Astruc, C. Deraedt, R. Djeda, C. Ornelas, X. Liu, A. Rapakousiou, J. Ruiz, Y. Wang and Q. Wang, *Molecules*, **2018**, 23, 966.

191. C. Valério, J.-L. Fillaut, J. Ruiz, J. Guittard, J.-C. Blais and D. Astruc, *J. Am. Chem. Soc.*, **1997**, 119, 2588-2589.

192. A. Callegari, M. Marcaccio, D. Paolucci, F. Paolucci, N. Tagmatarchis, D. Tasis, E. Vázquez and M. Prato, *Chem. Commun.*, **2003**, 2576-2577.

193. C. Ornelas, J. Ruiz Aranzaes, E. Cloutet, S. Alves and D. Astruc, *Angew. Chem. Int. Ed.*, **2007**, 46, 872-877.

194. M. C. Daniel, J. Ruiz, J. C. Blais, N. Daro and D. Astruc, *Chem. Eur. J.*, **2003**, 9, 4371-4379.

195. M.-C. Daniel, J. Ruiz and D. Astruc, *J. Am. Chem. Soc.*, **2003**, 125, 1150-1151.

196. M.-C. Daniel, F. Ba, J. R. Aranzaes and D. Astruc, *Inorg. Chem.*, **2004**, 43, 8649-8657.

197. J. Camponovo, J. Ruiz, E. Cloutet and D. Astruc, *Chem. Eur. J.*, **2009**, 15, 2990-3002.

198. R. Djeda, A. Rapakousiou, L. Liang, N. Guidolin, J. Ruiz and D. Astruc, *Angew. Chem. Int. Ed.*, **2010**, 49, 8152-8156.

199. C. Villena, J. Losada, P. García-Armada, C. M. Casado and B. Alonso, *Organometallics*, **2012**, 31, 3284-3291.

200. C. Valério, J. Ruiz, J.-L. Filiaux and D. Astruc, *C. R. Acad. Sci., Ser. IIc: Chim.*, **1999**, 2, 79-83.

201. A. Rapakousiou, Y. Wang, C. Belin, N. l. Pinaud, J. Ruiz and D. Astruc, *Inorg. Chem.*, **2013**, 52, 6685-6693.

202. J. R. Aranzaes, C. Belin and D. Astruc, *Angew. Chem. Int. Ed.*, **2006**, 45, 132-136.

203. A. Labande and D. Astruc, *Chem. Commun.*, **2000**, 1007-1008.

204. A. Labande, J. Ruiz and D. Astruc, *J. Am. Chem. Soc.*, **2002**, 124, 1782-1789.

205. M.-C. Daniel, J. Ruiz, S. Nlate, J. Palumbo, J.-C. Blais and D. Astruc, *Chem. Commun.*, **2001**, 2000-2001.

206. J. Ruiz Aranzaes, C. Belin and D. Astruc, *Chem. Commun.*, **2007**, 3456-3458.

207. R. C. Major and X. Y. Zhu, *J. Am. Chem. Soc.*, **2003**, 125, 8454-8455.

208. S. Zhang, C. M. Cardona and L. Echegoyen, *Chem. Commun.*, **2006**, 4461-4473.

209. E. Alonso, A. Labande, L. Raehm, J.-M. Kern and D. Astruc, *C. R. Acad. Sci., Ser. IIc: Chim.*, **1999**, 2, 209-213.

210. P. D. Beer, J. J. Davis, D. A. Drillsma-Milgrom and F. Szemes, *Chem. Commun.*, **2002**, 1716-1717.

211. O. Reynes, C. Bucher, J.-C. Moutet, G. Royal and E. Saint-Aman, *Inorg. Chim. Acta*, **2008**, 361, 1784-1788.

212. D. P. Cormode, A. J. Evans, J. J. Davis and P. D. Beer, *Dalton Trans.*, **2010**, 39, 6532-6541.

213. C. H. Devillers, D. Boturyn, C. Bucher, P. Dumy, P. Labbé, J.-C. Moutet, G. Royal and E. Saint-Aman, *Langmuir*, **2006**, 22, 8134-8143.

214. S. R. Bayly, T. M. Gray, M. J. Chmielewski, J. J. Davis and P. D. Beer, *Chem. Commun.*, **2007**, 2234-2236.

215. K. V. Gobi and T. Ohsaka, *J. Electroanal. Chem.*, **2000**, 485, 61-70.

216. P. Gołębiewski, B. Puciłowski, F. Sommer, S. Kubik, M. Daniels, W. Dehaen, U. Sivasankaran, K. G. Kumar, H. Radecka and J. Radecki, *Sens. Actuators B Chem.*, **2019**, 285, 536-545.

217. L. G. Jensen, K. A. Nielsen, T. Breton, J. L. Sessler, J. O. Jeppesen, E. Levillain and L. Sanguinet, *Chem. Eur. J.*, **2009**, 15, 8128-8133.

218. L. Faour, C. Adam, C. Gautier, S. Goeb, M. Allain, E. Levillain, D. Canevet and M. Sallé, *Chem. Commun.*, **2019**, 55, 5743-5746.

219. H. Hijazi, A. Vacher, S. Groni, D. Lorcy, E. Levillain, C. Fave and B. Schollhorn, *Chem. Commun.*, **2019**, 55, 1983-1986.

220. C. Lopez, J.-C. Moutet and E. Saint-Aman, *J. Chem. Soc., Faraday Trans.*, **1996**, 92, 1527-1532.

221. O. Reynes, T. Gulon, J.-C. Moutet, G. Royal and E. Saint-Aman, *J. Organomet. Chem.*, **2002**, 656, 116-119.

222. I. del Peso, B. Alonso, F. Lobete, C. M. Casado, I. Cuadrado and J. L. del Barrio, *Inorg. Chem. Commun.*, **2002**, 5, 288-291.

223. O. Reynes, G. Royal, E. Chaînet, J. C. Moutet and E. Saint-Aman, *Electroanalysis*, **2003**, 15, 65-69.

224. O. Reynes, J.-C. Moutet, G. Royal and E. Saint-Aman, *Electrochim. Acta*, **2004**, 49, 3727-3735.

225. F. J. Martínez, B. González, B. Alonso, J. Losada, M. P. García-Armada and C. M. Casado, *J. Inorg. Organomet. Polym. Mater.*, **2008**, 18, 51-58.

226. M. Takeuchi, T. Shioya and T. M. Swager, *Angew. Chem. Int. Ed.*, **2001**, 40, 3372-3376.

227. A. Aydogan, A. Koca, M. K. Şener and J. L. Sessler, *Org. Lett.*, **2014**, 16, 3764-3767.

228. M. Nicolas, B. Fabre, G. Marchand and J. Simonet, *Eur. J. Org. Chem.*, **2000**, 2000, 1703-1710.

229. R. Villoslada, B. Alonso, C. M. Casado, P. García-Armada and J. Losada, *Organometallics*, **2009**, 28, 727-733.

230. C. M. Casado, I. Cuadrado, B. Alonso, M. Morán and J. Losada, *J. Electroanal. Chem.*, **1999**, 463, 87-92.

231. C. Ornelas, J. Ruiz, C. Belin and D. Astruc, *J. Am. Chem. Soc.*, **2008**, 131, 590-601.

232. C. Ornelas, J. Ruiz and D. Astruc, *Organometallics*, **2009**, 28, 4431-4437.

233. Q. Xu and J. J. Davis, *Electroanalysis*, **2014**, 26, 1249-1258.

234. R. Ebdelli, A. Rouis, R. Mlika, I. Bonnamour, N. Jaffrezic-Renault, H. B. Ouada and J. Davenas, *J. Electroanal. Chem.*, **2011**, 661, 31-38.

235. S. Flink, B. A. Boukamp, A. Van Den Berg, F. C. Van Veggel and D. N. Reinhoudt, *J. Am. Chem. Soc.*, **1998**, 120, 4652-4657.

236. S. Flink, F. C. Van Veggel and D. N. Reinhoudt, *J. Phys. Chem. B*, **1999**, 103, 6515-6520.

237. N. Wanichacheva, E. R. Soto, C. R. Lambert and W. G. McGimpsey, *Anal. Chem.*, **2006**, 78, 7132-7137.

238. S. Zhang and L. Echegoyen, *J. Am. Chem. Soc.*, **2005**, 127, 2006-2011.

239. S. Zhang, A. Palkar and L. Echegoyen, *Langmuir*, **2006**, 22, 10732-10738.

240. F. Zhi, X. Lu, J. Yang, X. Wang, H. Shang, S. Zhang and Z. Xue, *J. Phys. Chem. C*, **2009**, 113, 13166-13172.

241. J. Wei, Z. Guo, X. Chen, D.-D. Han, X.-K. Wang and X.-J. Huang, *Anal. Chem.*, **2015**, 87, 1991-1998.

242. F. Bettazzi, D. Voccia, A. Bencini, C. Giorgi, I. Palchetti, B. Valtancoli and L. Conti, *Eur. J. Inorg. Chem.*, **2018**, 2018, 2675-2679.

243. M. P. Sanz, *Chem. Commun.*, **2007**, 5010-5012.

244. R. K. Shervedani and S. Pourbeyram, *Biosens. Bioelectron.*, **2009**, 24, 2199-2204.

245. S. Qiu, S. Gao, Q. Liu, Z. Lin, B. Qiu and G. Chen, *Biosens. Bioelectron.*, **2011**, 26, 4326-4330.

246. L. Torsi, M. Magliulo, K. Manoli and G. Palazzo, *Chem. Soc. Rev.*, **2013**, 42, 8612-8628.

247. P. Bergveld, *Sens. Actuators B Chem.*, **2003**, 88, 1-20.

248. C. Jimenez-Jorquera, J. Orozco and A. Baldi, *Sensors*, **2010**, 10, 61-83.

249. T. Minami, T. Minamiki and S. Tokito, *Chem. Commun.*, **2015**, 51, 9491-9494.

250. S. J. Choi, B. Yoon, J. D. Ray, A. Netchaev, L. C. Moores and T. M. Swager, *Adv. Funct. Mater.*, **2020**, 30, 1907087.

251. T. K. Mole, W. E. Arter, I. Marques, V. Félix and P. D. Beer, *J. Organomet. Chem.*, **2015**, 792, 206-210.

252. J. Yoo, M.-S. Kim, S.-J. Hong, J. L. Sessler and C.-H. Lee, *J. Org. Chem.*, **2009**, 74, 1065-1069.

253. K. Ghosh and A. R. Sarkar, *Tetrahedron Lett.*, **2009**, 50, 85-88.

254. T. A. Barendt, L. Ferreira, I. Marques, V. Félix and P. D. Beer, *J. Am. Chem. Soc.*, **2017**, 139, 9026-9037.

255. T. A. Barendt, A. Docker, I. Marques, V. Félix and P. D. Beer, *Angew. Chem. Int. Ed.*, **2016**, 55, 11069-11076.

256. L. Yang, Y. Wang, Y. Che and H. Jiang, *Org. Biomol. Chem.*, **2017**, 15, 7747-7752.

257. J. Y. C. Lim, I. Marques, V. Félix and P. D. Beer, *Chem. Commun.*, **2018**, 54, 10851-10854.

258. B. Chowdhury, S. Sinha and P. Ghosh, *Chem. Eur. J.*, **2016**, 22, 18051-18059.

259. M. J. Langton, I. Marques, S. W. Robinson, V. Félix and P. D. Beer, *Chem. Eur. J.*, **2016**, 22, 185-192.

260. J. M. Mercurio, A. Caballero, J. Cookson and P. D. Beer, *RSC Adv.*, **2015**, 5, 9298-9306.

261. B. R. Mullaney, A. L. Thompson and P. D. Beer, *Angew. Chem. Int. Ed.*, **2014**, 53, 11458-11462.

262. J. Du, M. Hu, J. Fan and X. Peng, *Chem. Soc. Rev.*, **2012**, 41, 4511-4535.

263. K. Kaur, R. Saini, A. Kumar, V. Luxami, N. Kaur, P. Singh and S. Kumar, *Coord. Chem. Rev.*, **2012**, 256, 1992-2028.

264. S. Groni, T. Maby-Raud, C. Fave, M. Branca and B. Schöllhorn, *Chem. Commun.*, **2014**, 50, 14616-14619.

265. G. Creste, S. Groni, C. Fave, M. Branca and B. Schöllhorn, *Faraday Discuss.*, **2017**, 203, 301-313.

266. S. Jin, D. Wang, X. Jin and G. Z. Chen, *ChemPhysChem*, **2004**, 5, 1623-1629.

267. D. Bao, B. Millare, W. Xia, B. G. Steyer, A. A. Gerasimenko, A. Ferreira, A. Contreras and V. I. Vullev, *J. Phys. Chem. A*, **2009**, 113, 1259-1267.

268. D. Bao, S. Ramu, A. Contreras, S. Upadhyayula, J. M. Vasquez, G. Beran and V. I. Vullev, *J. Phys. Chem. B*, **2010**, 114, 14467-14479.

269. A. L. Eckermann, D. J. Feld, J. A. Shaw and T. J. Meade, *Coord. Chem. Rev.*, **2010**, 254, 1769-1802.

270. N. H. Evans, H. Rahman, J. J. Davis and P. D. Beer, *Anal. Bioanal. Chem*, **2012**, 402, 1739-1748.

271. C. Adam, L. Faour, V. Bonnin, T. Breton, E. Levillain, M. Sallé, C. Gautier and D. Canevet, *Chem. Commun.*, **2019**, 55, 8426-8429.

272. N. H. Evans, H. Rahman, A. V. Leontiev, N. D. Greenham, G. A. Orlowski, Q. Zeng, R. M. Jacobs, C. J. Serpell, N. L. Kilah and J. J. Davis, *Chem. Sci.*, **2012**, 3, 1080-1089.

273. R. Mishra, S. Pandey, S. Trivedi, S. Pandey and P. S. Pandey, *RSC Adv.*, **2014**, 4, 33478-33488.

274. P. Fortgang, E. Maisonhaute, C. Amatore, B. Delavaux-Nicot, J. Iehl and J. F. Nierengarten, *Angew. Chem. Int. Ed.*, **2011**, 50, 2364-2367.

275. S. Zhang, Y. Chen, J. Wang, Y. Pan, Z. Xu and C.-H. Tung, *Org. Chem. Front.*, **2015**, 2, 578-585.

276. W. S. Brotherton, R. J. Clark and L. Zhu, *J. Org. Chem.*, **2012**, 77, 6443-6455.

277. J. Y. C. Lim, I. Marques, L. Ferreira, V. Félix and P. D. Beer, *Chem. Commun.*, **2016**, 52, 5527-5530.

278. S. W. Robinson, C. L. Mustoe, N. G. White, A. Brown, A. L. Thompson, P. Kennepohl and P. D. Beer, *J. Am. Chem. Soc.*, **2015**, 137, 499-507.

279. G. P. López, D. G. Castner and B. D. Ratner, *Surf. Interface Anal.*, **1991**, 17, 267-272.

280. S. Ciampi, T. Böcking, K. A. Kilian, M. James, J. B. Harper and J. J. Gooding, *Langmuir*, **2007**, 23, 9320-9329.

281. G. Zorn, L.-H. Liu, L. Árnadóttir, H. Wang, L. J. Gamble, D. G. Castner and M. Yan, *J. Phys. Chem. C*, **2014**, 118, 376-383.

282. C. D. Bain, H. A. Biebuyck and G. M. Whitesides, *Langmuir*, **1989**, 5, 723-727.

283. D. G. Castner, K. Hinds and D. W. Grainger, *Langmuir*, **1996**, 12, 5083-5086.

284. J. Lehr, J. R. Weeks, A. Santos, G. T. Feliciano, M. I. G. Nicholson, J. J. Davis and P. R. Bueno, *Physical Chemistry Chemical Physics*, **2017**, 19, 15098-15109.

285. M. D. Porter, T. B. Bright, D. L. Allara and C. E. D. Chidsey, *J. Am. Chem. Soc.*, **1987**, 109, 3559-3568.

286. H. Li, Q. Zheng and C. Han, *Analyst*, **2010**, 135, 1360-1364.

287. D. D. Popenoe, R. S. Deinhammer and M. D. Porter, *Langmuir*, **1992**, 8, 2521-2530.

288. R. Prins, A. R. Korswagen and A. G. T. G. Kortbeek, *J. Organomet. Chem.*, **1972**, 39, 335-344.

289. G. Valincius, G. Niaura, B. Kazakevičienė, Z. Talaikytė, M. Kažemėkaitė, E. Butkus and V. Razumas, *Langmuir*, **2004**, 20, 6631-6638.

290. L. Zhang, L. A. Godínez, T. Lu, G. W. Gokel and A. E. Kaifer, *Angewandte Chemie International Edition in English*, **1995**, 34, 235-237.

291. A. Kütt, T. Rodima, J. Saame, E. Raamat, V. Mäemets, I. Kaljurand, I. A. Koppel, R. Y. Garlyauskayte, Y. L. Yagupolskii, L. M. Yagupolskii, E. Bernhardt, H. Willner and I. Leito, *J. Org. Chem.*, **2011**, 76, 391-395.

292. M. J. Langton, C. J. Serpell and P. D. Beer, *Angew. Chem. Int. Ed.*, **2016**, 55, 1974-1987.

293. K. M. Bąk, K. Porfyrakis, J. J. Davis and P. D. Beer, *Mater. Chem. Front.*, **2020**, 4, 1052-1073.

294. J. Y. C. Lim and P. D. Beer, *Chem. Commun.*, **2015**, 51, 3686-3688.

295. S. P. Cornes, M. R. Sambrook and P. D. Beer, *Chem. Commun.*, **2017**, 53, 3866-3869.

296. A. Borissov, I. Marques, J. Y. C. Lim, V. Félix, M. D. Smith and P. D. Beer, *J. Am. Chem. Soc.*, **2019**, 141, 4119-4129.

297. M. J. Langton, S. W. Robinson, I. Marques, V. Félix and P. D. Beer, *Nat. Chem.*, **2014**, 6, 1039-1043.

298. T. Bunchuay, PhD thesis, University of Oxford, **2018**.

299. J. Piccoli, R. Hein, A. H. El-Sagheer, T. Brown, E. M. Cilli, P. R. Bueno and J. J. Davis, *Anal. Chem.*, **2018**, 90, 3005-3008.

300. A. Santos, P. R. Bueno and J. J. Davis, *Biosens. Bioelectron.*, **2018**, 100, 519-525.

301. P. R. Bueno, *Analytical Chemistry*, **2018**, 90, 7095-7106.

302. B. L. Garrote, A. Santos and P. R. Bueno, *ACS Sensors*, **2019**, 4, 2216-2227.

303. A. C. Ion, J.-C. Moutet, A. Pailleret, A. Popescu, E. Saint-Aman, E. Siebert and E. M. Ungureanu, *J. Electroanal. Chem.*, **1999**, 464, 24-30.

304. J. Lehr, F. C. B. Fernandes, P. R. Bueno and J. J. Davis, *Anal. Chem.*, **2014**, 86, 2559-2564.

305. P. Kanyong, A. V. Patil and J. J. Davis, *Annu. Rev. Anal. Chem.*, **2020**, 13, 183-200.

306. M. A. Herranz, B. Colonna and L. Echegoyen, *Proc. Natl. Acad. Sci. U. S. A.*, **2002**, 99, 5040-5047.

307. K. Morita, A. Yamaguchi and N. Teramae, *J. Electroanal. Chem.*, **2004**, 563, 249-255.

308. A. Borissov, J. Y. C. Lim, A. Brown, K. E. Christensen, A. L. Thompson, M. D. Smith and P. D. Beer, *Chem. Commun.*, **2017**, 53, 2483-2486.

309. K. Helttunen, R. Annala, A. Suhonen, J. Iloniemi, E. Kalenius, G. Aragay, P. Ballester, H. M. Tuononen and M. Nissinen, *Chem.: Asian J*, **2019**, 14, 647-654.

310. B. Zhu, T. Eurell, R. Gunawan and D. Leckband, *J. Biomed. Mater. Res.*, **2001**, 56, 406-416.

311. S. K. Das, C. Dickinson, F. Lafir, D. F. Brougham and E. Marsili, *Green Chem.*, **2012**, 14, 1322-1334.

312. T. Mahmoudi, Y. Wang and Y.-B. Hahn, *ACS Energy Lett.*, **2019**, 4, 235-241.

313. W. A. Volkert and T. J. Hoffman, *Chem. Rev.*, **1999**, 99, 2269-2292.

314. B. Wakoff and K. L. Nagy, *Environ. Sci. Technol.*, **2004**, 38, 1765-1771.

315. C. Jiang, G. Wang, R. Hein, N. Liu, X. Luo and J. J. Davis, *Chem. Rev.*, **2020**, 120, 3852-3889.

316. E. Boubour and R. B. Lennox, *J. Phys. Chem. B*, **2000**, 104, 9004-9010.

317. N. Darwish, P. K. Eggers, S. Ciampi, Y. Zhang, Y. Tong, S. Ye, M. N. Paddon-Row and J. J. Gooding, *Electrochem. Commun.*, **2011**, 13, 387-390.

318. M. S. Goes, H. Rahman, J. Ryall, J. J. Davis and P. R. Bueno, *Langmuir*, **2012**, 28, 9689-9699.

319. P. R. Bueno and J. J. Davis, *Anal. Chem.*, **2014**, 86, 1337-1341.

320. P. R. Bueno, *The Nanoscale Electrochemistry of Molecular Contacts*, Springer, **2018**.

321. P. R. Bueno, R. Hein, A. Santos and J. J. Davis, *Phys. Chem. Chem. Phys.*, **2020**, 22, 3770-3774.

322. D. A. Miranda and P. R. Bueno, *J. Phys. Chem. C*, **2019**, 123, 21213-21223.

323. A. Hutt and S. Tan, *Drugs*, **1996**, 52, 1-12.

324. R. Noyori, *Angew. Chem. Int. Ed.*, **2002**, 41, 2008-2022.

325. M. S. Taylor and E. N. Jacobsen, *Angew. Chem. Int. Ed.*, **2006**, 45, 1520-1543.

326. K. Manoli, M. Magliulo and L. Torsi, *Chiral sensor devices for differentiation of enantiomers*, Springer, **2013**.

327. G. A. Hembury, V. V. Borovkov and Y. Inoue, *Chem. Rev.*, **2008**, 108, 1-73.

328. S. Bartoli, T. Mahmood, A. Malik, S. Dixon and J. D. Kilburn, *Org. Biomol. Chem.*, **2008**, 6, 2340-2345.

329. D. Curiel, M. Más-Montoya and G. Sánchez, *Coord. Chem. Rev.*, **2015**, 284, 19-66.

330. J. Y. C. Lim, I. Marques, V. Félix and P. D. Beer, *Angew. Chem. Int. Ed.*, **2018**, 57, 584-588.

331. R. L. Sutar, E. Engelage, R. Stoll and S. M. Huber, *Angew. Chem. Int. Ed.*, **2020**, 59, 6806-6810.

332. J. Y. C. Lim, I. Marques, V. Félix and P. D. Beer, *J. Am. Chem. Soc.*, **2017**, 139, 12228-12239.

333. A. Berthod, *Anal. Chem.*, **2006**, 78, 2093-2099.

334. P. Laurent, H. Miyaji, S. R. Collinson, I. Prokeš, C. J. Moody, J. H. Tucker and A. M. Slawin, *Org. Lett.*, **2002**, 4, 4037-4040.

335. Y. Willener, K. M. Joly, C. J. Moody and J. H. R. Tucker, *J. Org. Chem.*, **2008**, 73, 1225-1233.

336. L. Challier, F. o. Mavré, J. Moreau, C. Fave, B. Schöllhorn, D. Marchal, E. Peyrin, V. Noël and B. Limoges, *Anal. Chem.*, **2012**, 84, 5415-5420.

337. Y. Huang, D. Guo, Q. Zhang, L. Guo, Y. Chen and Y. Fu, *RSC Adv.*, **2014**, 4, 33457-33461.

338. I. Pandey and R. Kant, *Biosens. Bioelectron.*, **2016**, 77, 715-724.

339. J. Yang, Z. Li, W. Tan, D. Wu, Y. Tao and Y. Kong, *Electrochem. Commun.*, **2018**, 96, 22-26.

340. Q. Zhao, J. Yang, J. Zhang, D. Wu, Y. Tao and Y. Kong, *Anal. Chem.*, **2019**, 91, 12546-12552.

341. D. Shetty, J. M. Jeong, C. H. Ju, Y. J. Kim, J.-Y. Lee, Y.-S. Lee, D. S. Lee, J.-K. Chung and M. C. Lee, *Biorg. Med. Chem.*, **2010**, 18, 7338-7347.

342. P. M. Sherwood, *J. Chem. Soc., Faraday Trans. 2*, **1976**, 72, 1805-1820.

343. D. Jagleniec, Ł. Dobrzycki, M. Karbarz and J. Romański, *Chem. Sci.*, **2019**, 10, 9542-9547.

344. A. V. Koulov, J. M. Mahoney and B. D. Smith, *Org. Biomol. Chem.*, **2003**, 1, 27-29.

345. S. K. Kim and J. L. Sessler, *Chem. Soc. Rev.*, **2010**, 39, 3784-3809.

346. A. J. McConnell and P. D. Beer, *Angew. Chem. Int. Ed.*, **2012**, 51, 5052-5061.

347. Q. He, G. I. Vargas-Zúñiga, S. H. Kim, S. K. Kim and J. L. Sessler, *Chem. Rev.*, **2019**, 119, 9753-9835.

348. J. M. Mahoney, A. M. Beatty and B. D. Smith, *J. Am. Chem. Soc.*, **2001**, 123, 5847-5848.

349. A. Brown, K. M. Mennie, O. Mason, N. G. White and P. D. Beer, *Dalton Trans.*, **2017**, 46, 13376-13385.

350. T. Bunchuay, A. Docker, U. Eiamprasert, P. Surawatanawong, A. Brown and P. D. Beer, *Angew. Chem.*, **2020**, 10.1002/anie.202001125.

351. A. Mele, P. Metrangolo, H. Neukirch, T. Pilati and G. Resnati, *J. Am. Chem. Soc.*, **2005**, 127, 14972-14973.

352. R. Tepper, B. Schulze, P. Bellstedt, J. Heidler, H. Görls, M. Jäger and U. S. Schubert, *Chem. Commun.*, **2017**, 53, 2260-2263.

353. Y.-H. Kim and J.-I. Hong, *Chem. Commun.*, **2002**, 512-513.

354. A. P. de Silva, G. D. McClean and S. Pagliari, *Chem. Commun.*, **2003**, 2010-2011.

355. P. D. Beer, Z. Chen and M. I. Ogden, *J. Chem. Soc., Faraday Trans.*, **1995**, 91, 295-302.

356. A. S. Wendji, M. Lutter, C. Dietz, V. Jouikov and K. Jurkschat, *Organometallics*, **2013**, 32, 5720-5730.

357. N. Nerngchamnong, B. Chailap, P. Leeladee, O. Chailapakul, C. Suksai and T. Tuntulani, *Tetrahedron Lett.*, **2011**, 52, 2914-2917.

358. M. Alfonso, A. Tárraga and P. Molina, *Org. Lett.*, **2011**, 13, 6432-6435.

359. F. Otón, A. Tárraga, M. D. Velasco and P. Molina, *Dalton Trans.*, **2005**, 1159-1161.

360. C. Suksai, P. Leeladee, D. Jainuknan, T. Tuntulani, N. Muangsin, O. Chailapakul, P. Kongsaeree and C. Pakavatchai, *Tetrahedron Lett.*, **2005**, 46, 2765-2769.

361. M. Alfonso, A. Sola, A. Caballero, A. Tárraga and P. Molina, *Dalton Trans.*, **2009**, 9653-9658.

362. M. Zaleskaya, D. Jagleniec, M. Karbarz, Ł. Dobrzycki and J. Romański, *Inorg. Chem. Front.*, **2020**, 7, 972-983.

363. M. Alfonso, A. Espinosa, A. Tárraga and P. Molina, *Org. Lett.*, **2011**, 13, 2078-2081.

364. S. Flink, H. Schönherr, G. J. Vancso, F. A. Geurts, K. G. van Leerdam, F. C. van Veggel and D. N. Reinhoudt, *J. Chem. Soc., Perkin Trans. 2*, **2000**, 2141-2146.

365. N. Ayawei, A. N. Ebelegi and D. Wankasi, *J. Chem.*, **2017**, 2017, 3039817.

366. H. Swenson and N. P. Stadie, *Langmuir*, **2019**, 35, 5409-5426.

367. G.-F. Zhang, J.-Y. Zhan and H.-B. Li, *Org. Lett.*, **2011**, 13, 3392-3395.

368. N. Feng, H. Zhao, J. Zhan, D. Tian and H. Li, *Org. Lett.*, **2012**, 14, 1958-1961.

369. P. Xu, J. Quan, W. Chen, J. Zhang, H. Yan, Y. Liu, S. Tan, X. Zeng, H. Li and G. Yang, *ChemPlusChem*, **2019**, 84, 907-912.

370. Y.-x. Sun, J.-h. He, J.-w. Huang, Y. Sheng, D. Xu, M. Bradley and R. Zhang, *J. Electroanal. Chem.*, **2020**, 865, 114130.

371. P. Thordarson, *Chem. Soc. Rev.*, **2011**, 40, 1305-1323.

372. J. Tkac and J. J. Davis, *J. Electroanal. Chem.*, **2008**, 621, 117-120.

373. J. S. Daniels and N. Pourmand, *Electroanalysis*, **2007**, 19, 1239-1257.

374. B.-Y. Chang and S.-M. Park, *Annu. Rev. Anal. Chem.*, **2010**, 3, 207-229.

375. B.-Y. Lee, S. R. Park, H. B. Jeon and K. S. Kim, *Tetrahedron Lett.*, **2006**, 47, 5105-5109.

376. Y. Shi, T. Suguri, C. Dohi, H. Yamada, S. Kojima and Y. Yamamoto, *Chem. Eur. J.*, **2013**, 19, 10672-10689.

377. M. J. Langton, Y. Xiong and P. D. Beer, *Chem. Eur. J.*, **2015**, 21, 18910-18914.

378. S.-H. Hwang, C. N. Moorefield, H.-C. Cha, P. Wang and G. R. Newkome, *Des. Monomers Polym.*, **2006**, 9, 413-424.

Appendices

Appendices

A2: Supplementary Information for Chapter 2

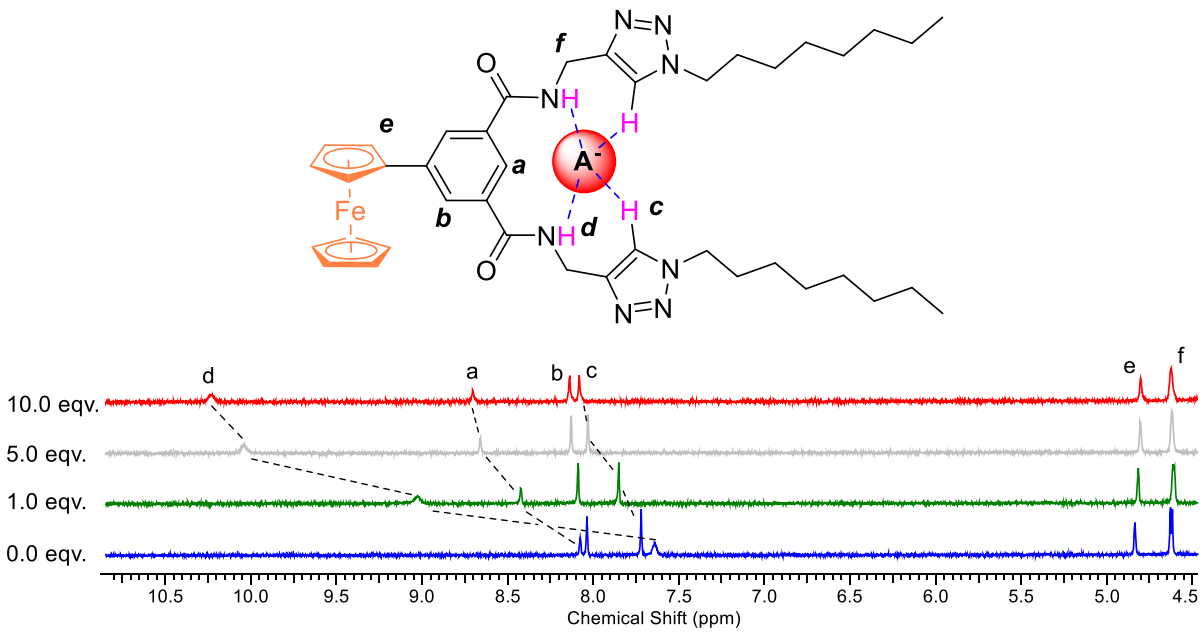


Figure A2.1. Partial ^{1}H NMR spectra of receptor **2.1HB** in CD_3CN in the presence of 0.0, 1.0, 5.0 and 10.0 equivalents of $TBAH_2PO_4$ (400 MHz, 298 K).

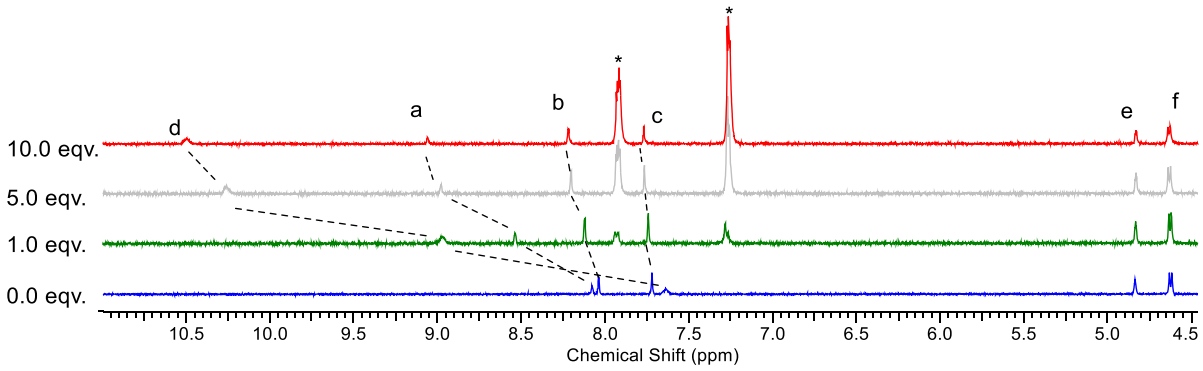


Figure A2.2. Partial ^{1}H NMR spectra of receptor **2.1HB** in CD_3CN in the presence of 0.0, 1.0, 5.0 and 10.0 equivalents of TBAOBz (400 MHz, 298 K, *aromatic signals of benzoate).

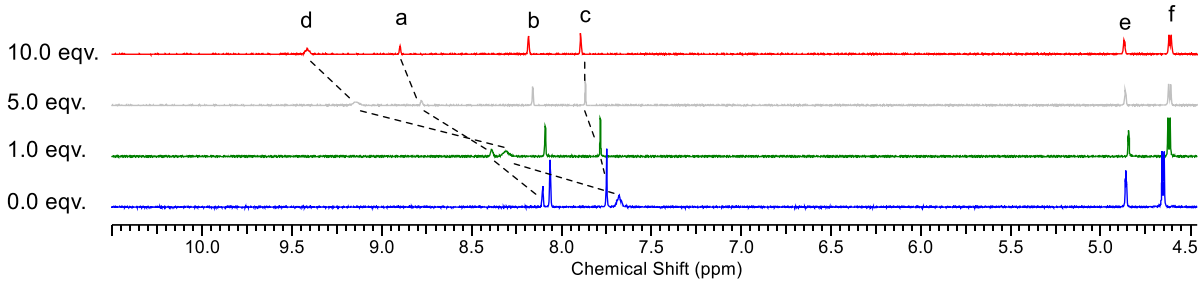


Figure A2.3. Partial ^{1}H NMR spectra of receptor **2.1HB** in CD_3CN in the presence of 0.0, 1.0, 5.0 and 10.0 equivalents of TBACl (400 MHz, 298 K).

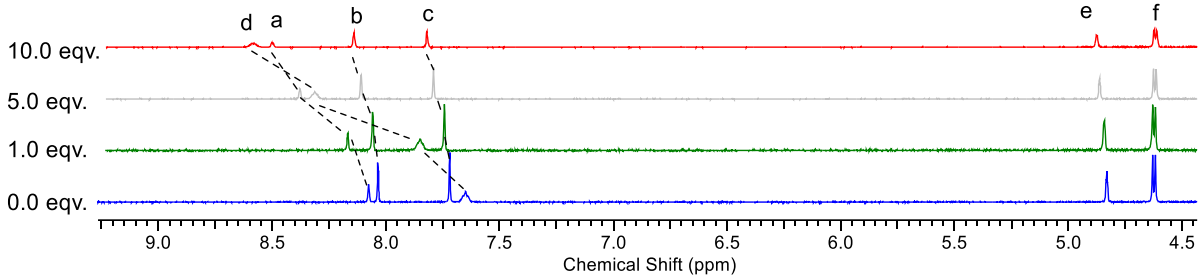


Figure A2.4. Partial ^{1}H NMR spectra of receptor **2.1HB** in CD_3CN in the presence of 0.0, 1.0, 5.0 and 10.0 equivalents of TBABr (400 MHz, 298 K).

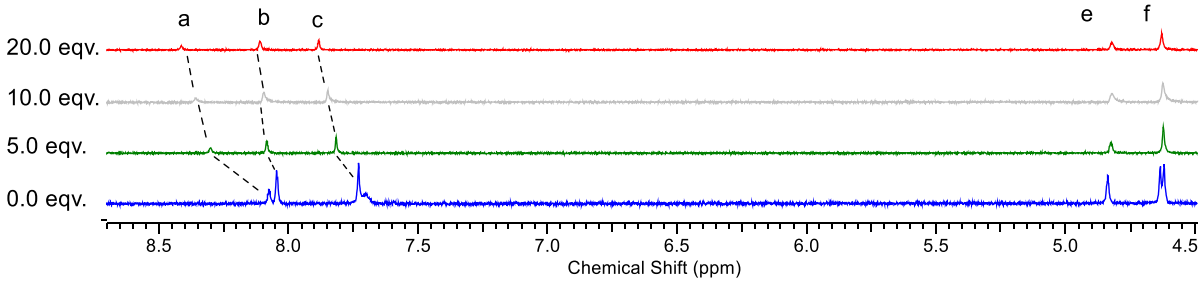


Figure A2.5. Partial ^{1}H NMR spectra of receptor **2.1HB** in CD_3CN/D_2O (99:1 *v*/*v*) in the presence of 0.0, 1.0, 5.0 and 10.0 equivalents of $TBAH_2PO_4$ (400 MHz, 298 K).

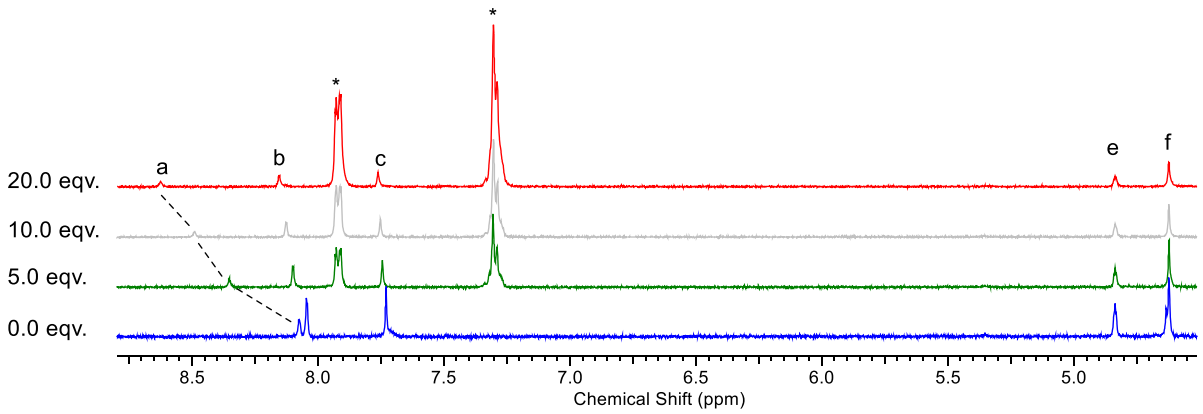


Figure A2.6. Partial ^{1}H NMR spectra of receptor **2.1HB** in CD_3CN/D_2O (99:1 *v*/*v*) in the presence of 0.0, 1.0, 5.0 and 10.0 equivalents of TBAbenzoate (400 MHz, 298 K, *aromatic signals of benzoate).

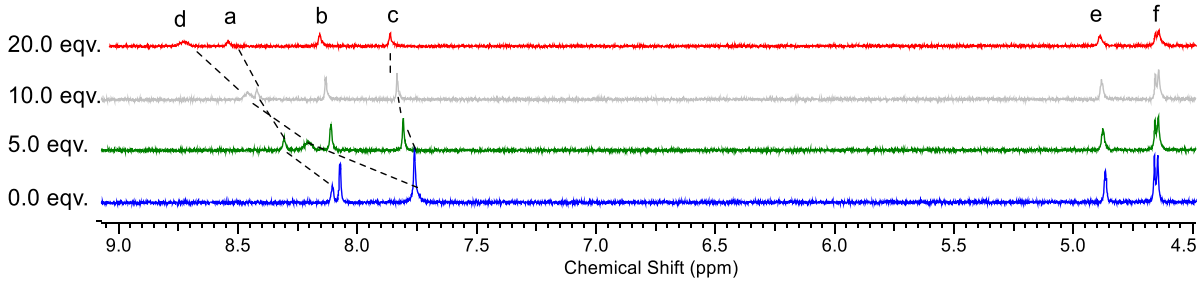


Figure A2.7. Partial ^{1}H NMR spectra of receptor **2.1HB** in CD_3CN/D_2O (99:1 *v*/*v*) in the presence of 0.0, 1.0, 5.0 and 10.0 equivalents of TBACl (400 MHz, 298 K).

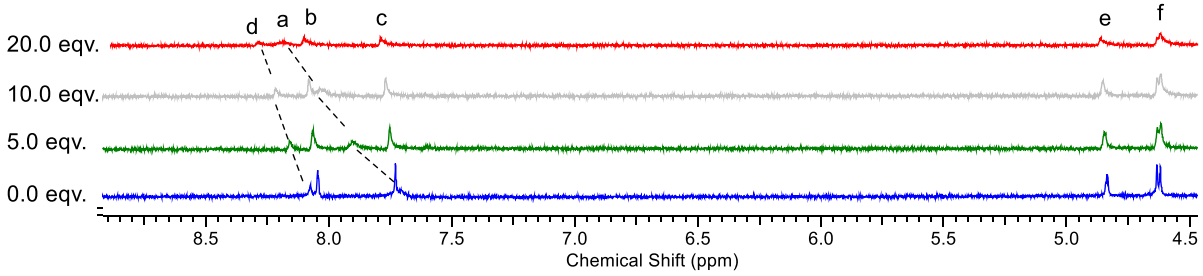


Figure A2.8. Partial ^{1}H NMR spectra of receptor **2.1HB** in CD_3CN/D_2O (99:1 *v*/*v*) in the presence of 0.0, 1.0, 5.0 and 10.0 equivalents of TBABr (400 MHz, 298 K).

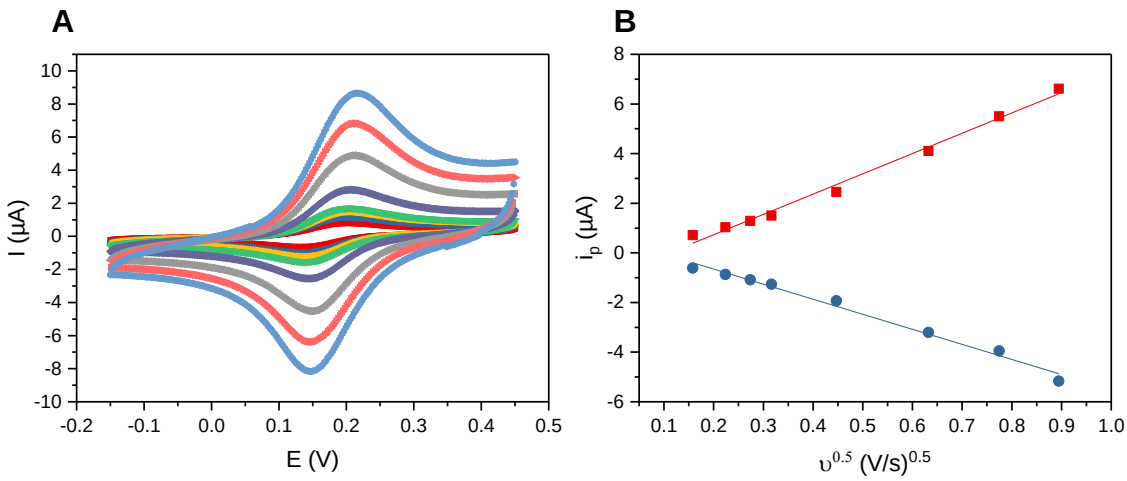


Figure A2.9. A) CVs at varying scan rate of 0.1 mM **2.1XB** in ACN, 100 mM $TBAClO_4$. B) The associated anodic and cathodic peak currents as a function of the square-root of the scan rate including linear fits.

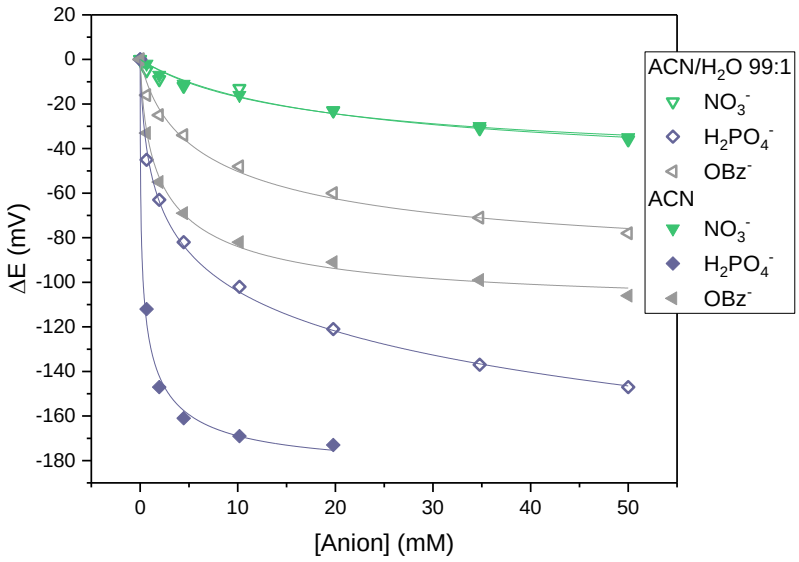


Figure A2.10. Cathodic voltammetric shifts of **2.1XB** in ACN (filled symbols) or ACN/H_2O 99:1 (empty symbols) upon titration with NO_3^-, $H_2PO_4^-$ or OBz^-. Solid lines represent fits to the 1:1 host-guest Nernst model (eqn. 2.2).

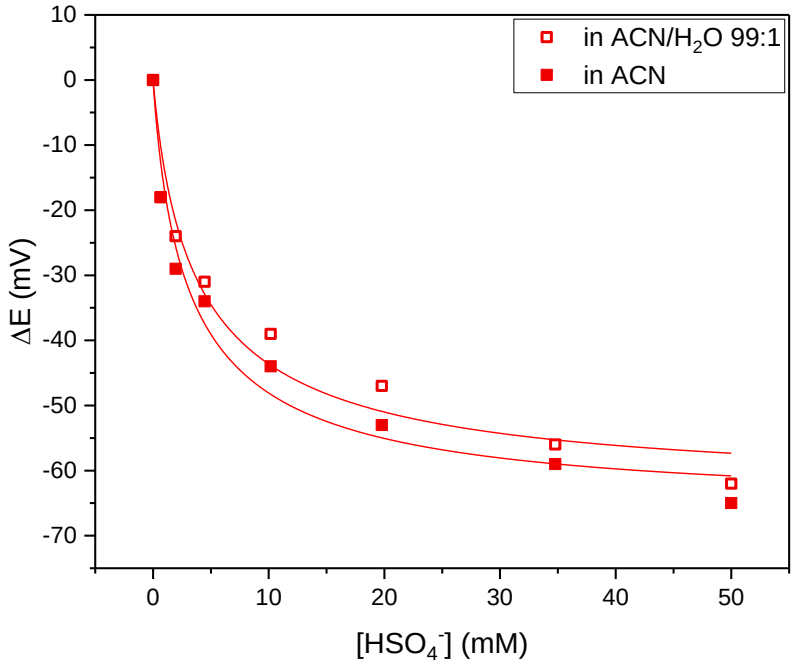


Figure A2.11. Cathodic voltammetric shifts of **2.1XB** in ACN (filled symbols) or ACN/H_2O 99:1 (empty symbols) upon titration with HSO_4^-. Solid lines represent fits to the 1:1 host-guest Nernst model (eqn. 2.2).

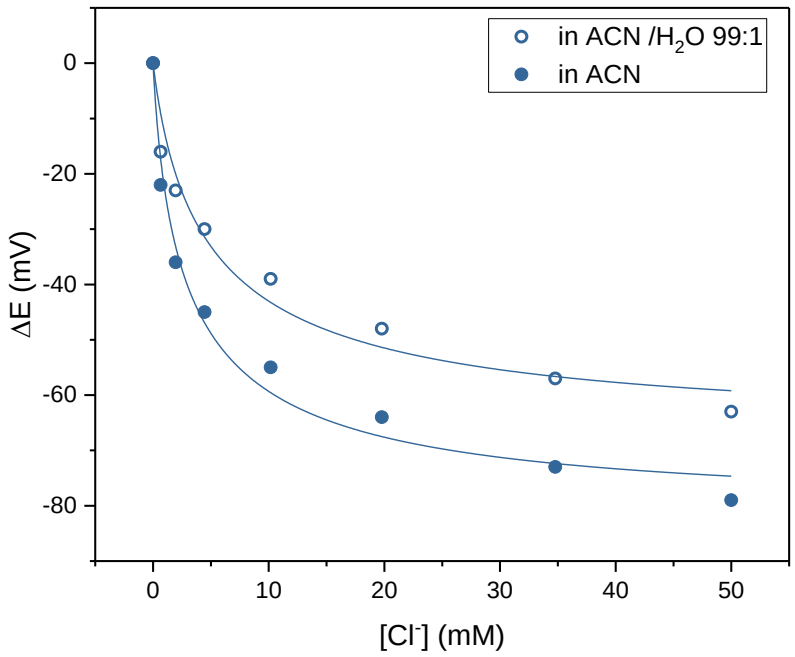


Figure A2.12. Cathodic voltammetric shifts of **2.1XB** in ACN (filled symbols) or ACN/H_2O 99:1 (empty symbols) upon titration with Cl^-. Solid lines represent fits to the 1:1 host-guest Nernst model (eqn. 2.2).

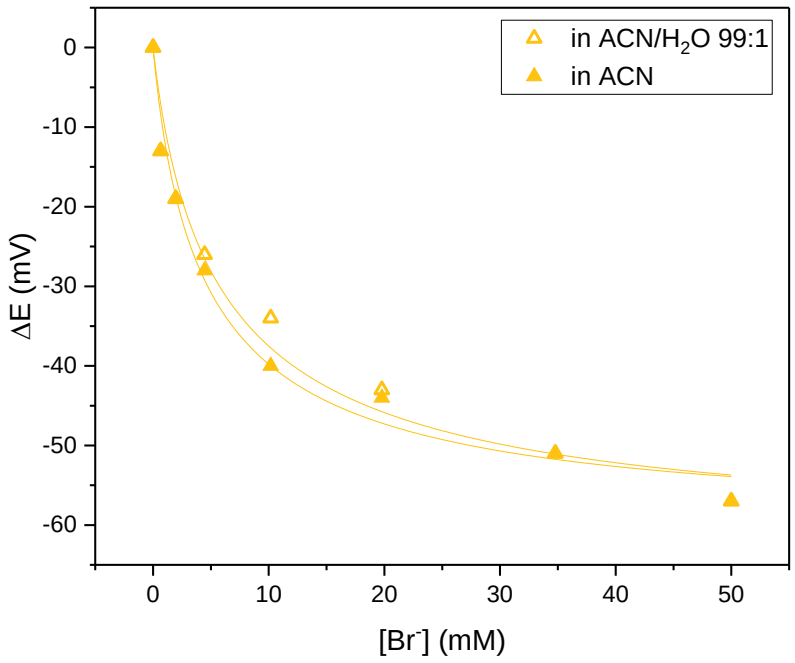


Figure A2.13. Cathodic voltammetric shifts of **2.1XB** in ACN (filled symbols) or ACN/H_2O 99:1 (empty symbols) upon titration with Br^-. Solid lines represent fits to the 1:1 host-guest Nernst model (eqn. 2.2).

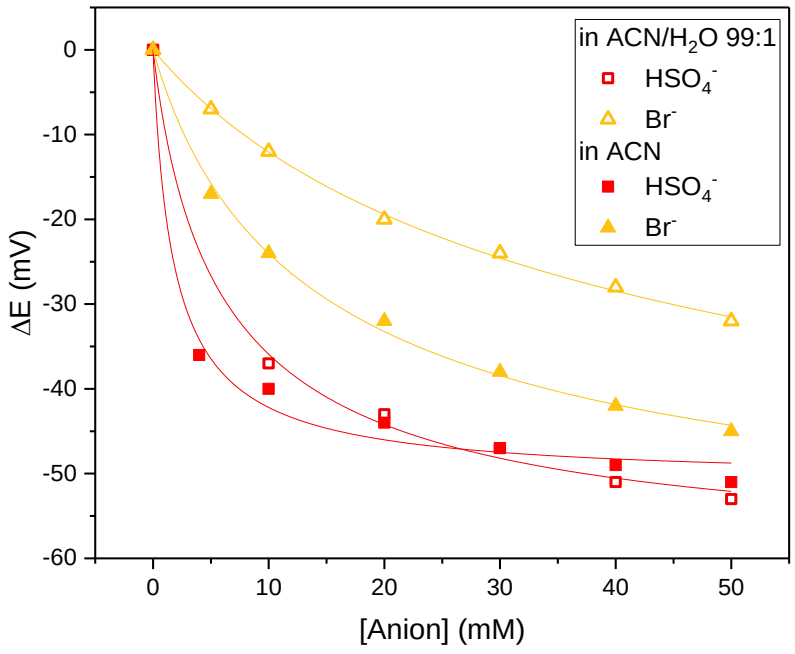


Figure A2.14. Cathodic voltammetric shifts of **2.1HB** in ACN (filled symbols) or ACN/H_2O 99:1 (empty symbols) upon titration with HSO_4^- or Br^-. Solid lines represent fits to the 1:1 host-guest Nernst model (eqn. 2.2).

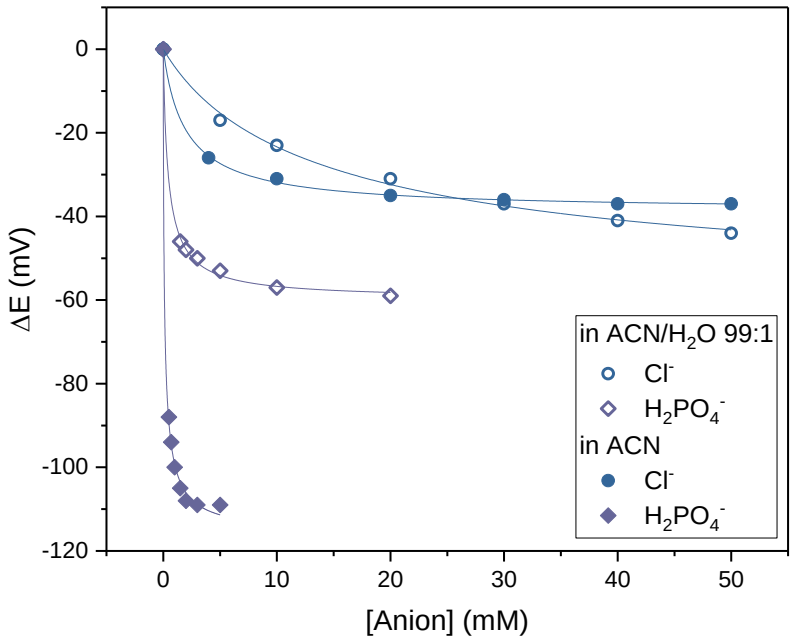


Figure A2.15. Cathodic voltammetric shifts of **2.1HB** in ACN (filled symbols) or ACN/H_2O 99:1 (empty symbols) upon titration with $H_2PO_4^-$ or Cl^-. Solid lines represent fits to the 1:1 host-guest Nernst model (eqn. 2.2).

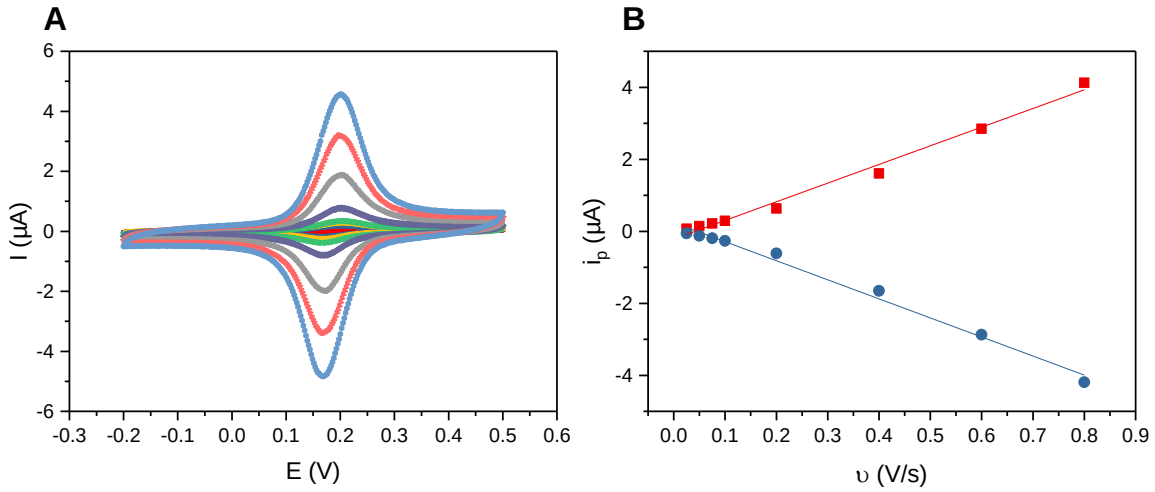


Figure A2.16. A) CVs at varying scan rate of **2.2XB$_{SAM}$** in ACN/H_2O 99:1, 100 mM $TBAClO_4$. B) The associated anodic and cathodic peak currents as a function of the scan rate including linear fits.

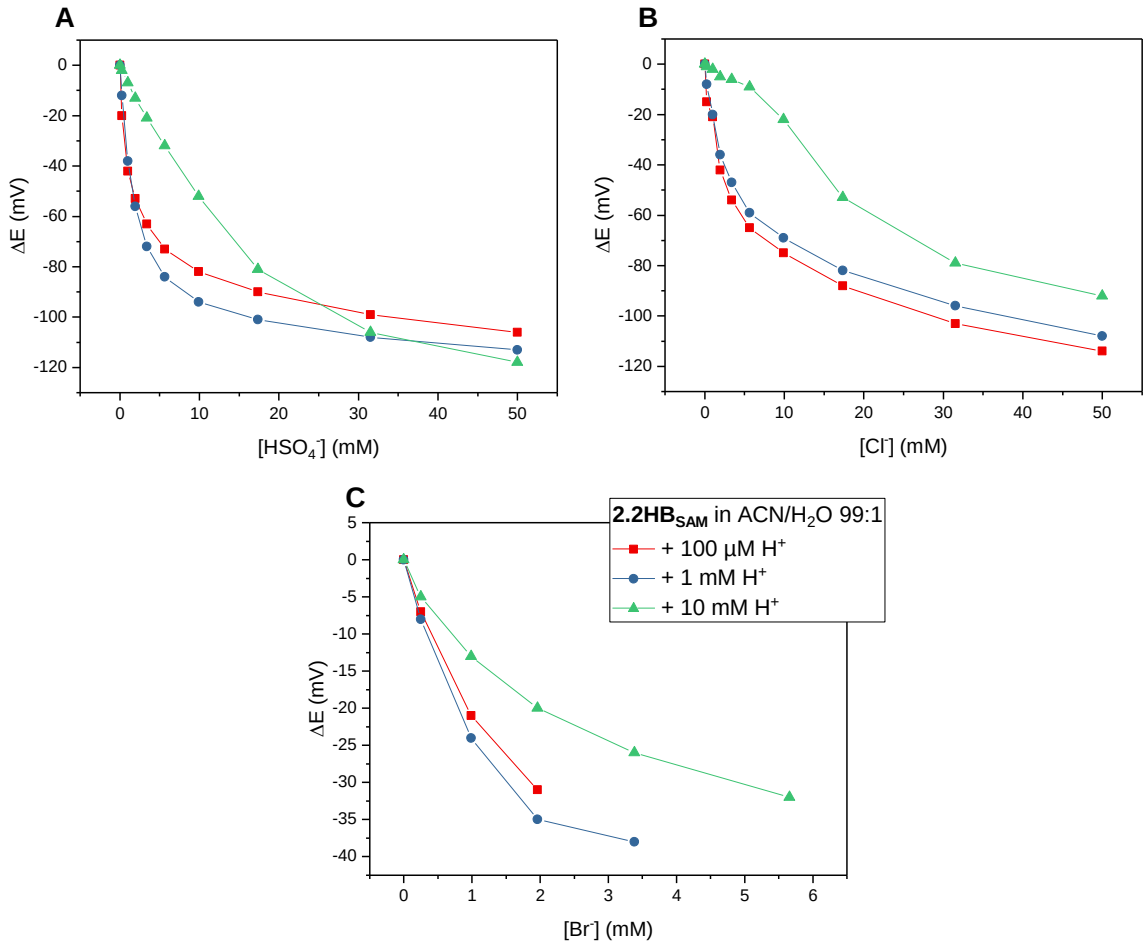


Figure A2.17. Cathodic voltammetric shifts of **2.2HB$_{SAM}$** upon titration with HSO_4^-, Cl^- and Br^- in ACN/H_2O 99:1 and various concentrations of acid. Solid lines do not represent any fits and are only meant to guide the eye.

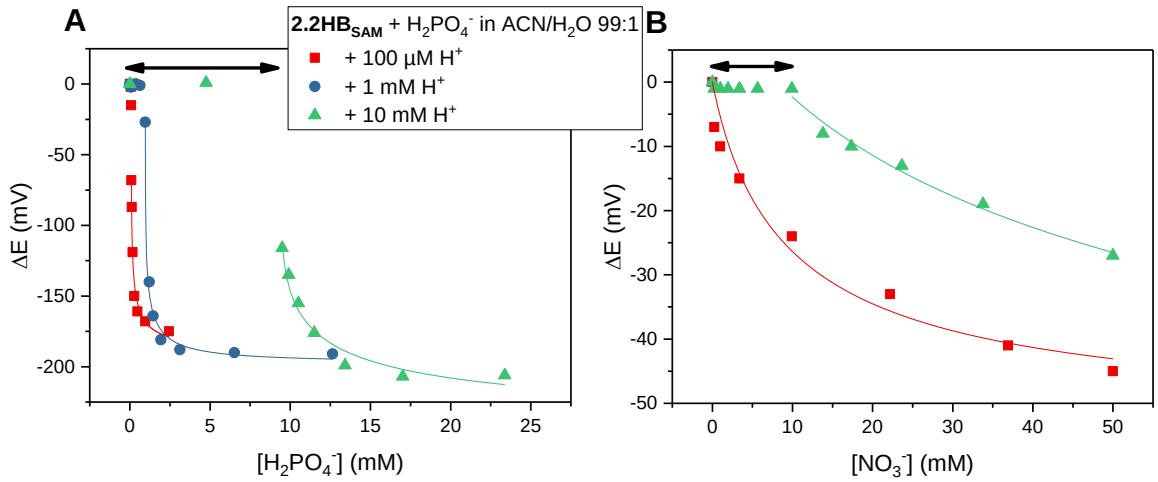


Figure A2.18. Cathodic voltammetric shifts of **2.2HB$_{SAM}$** upon titration with the basic anions $H_2PO_4^-$ and NO_3^- in ACN/H_2O 99:1 and various concentrations of acid. Solid lines represent fits to the 1:1 Nernst model with an offset (eqn. 2.3). The offset (*i.e.* "delayed" response) of the binding isotherm in the presence of 10 mM acid is shown by the black arrows.

Table A2.1. Maximum fluorescence emission enhancement of **2.7** and **2.8** in ACN in the presence of various anions.

	2.7	**2.8**
Cl^-	45%	82%
Br^-	13%	33%
I^-	1%	3%
SO_4^{2-}	152%	213%

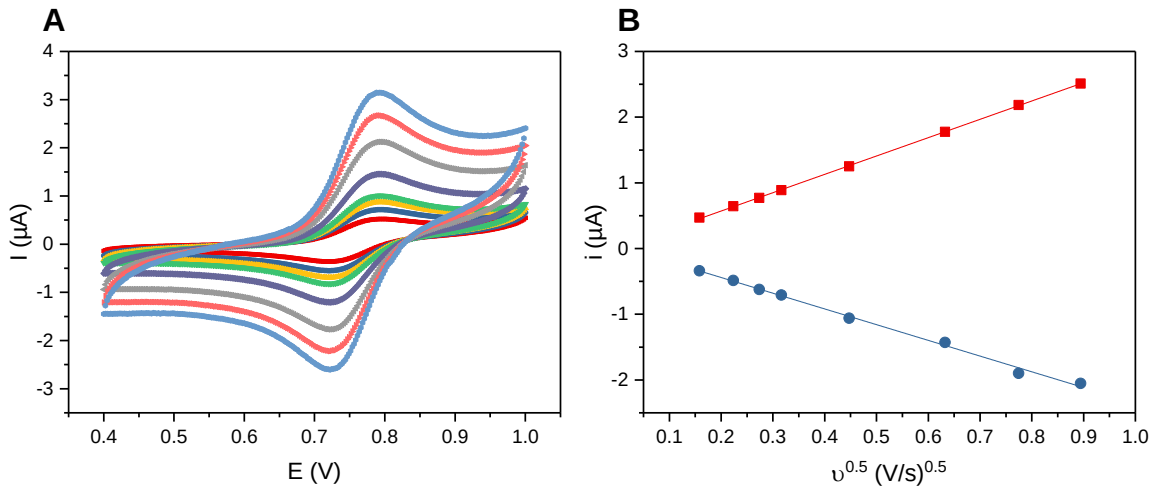


Figure A2.19. CVs (A) and anodic and cathodic peak currents (B) of 0.15 mM **2.7** in H_2O, 100 mM $NaNO_3$ at varying scan rates.

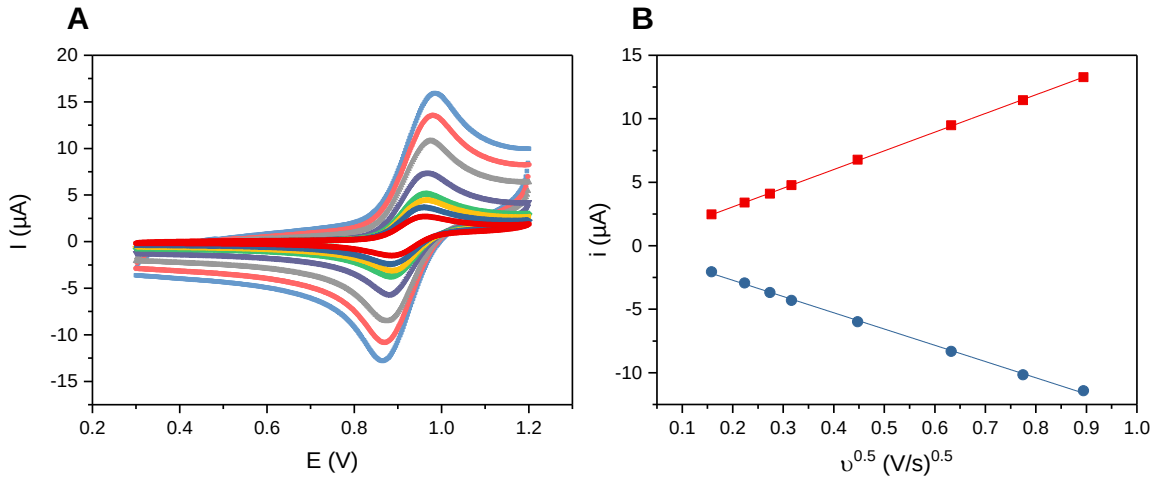


Figure A2.20. CVs (A) and anodic and cathodic peak currents (B) of 0.3 mM **2.7** in MeOH, 50 mM $TBAPF_6$ at varying scan rates.

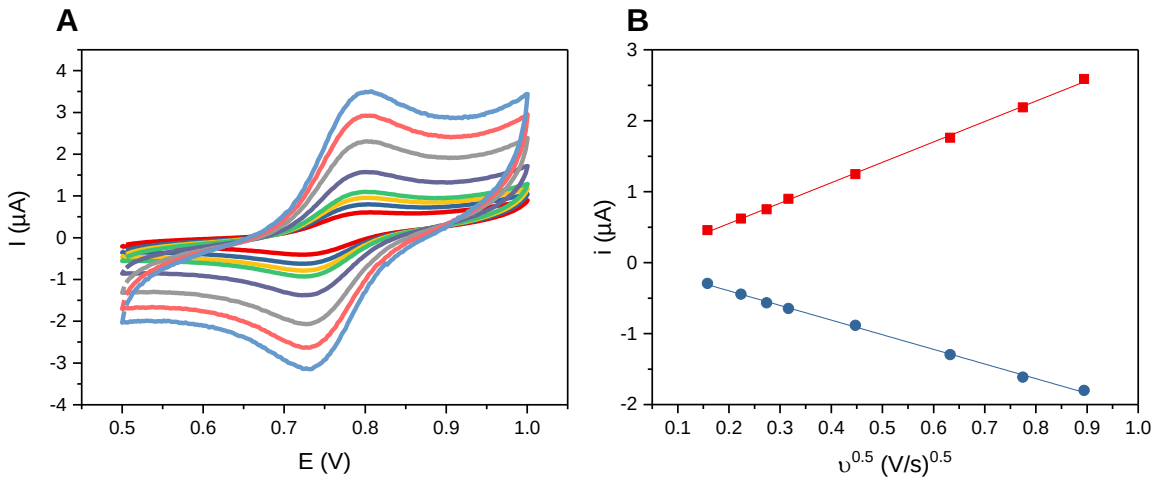


Figure A2.21. CVs (A) and anodic and cathodic peak currents (B) of 0.15 mM **2.8** in H_2O, 100 mM $NaNO_3$ at varying scan rates.

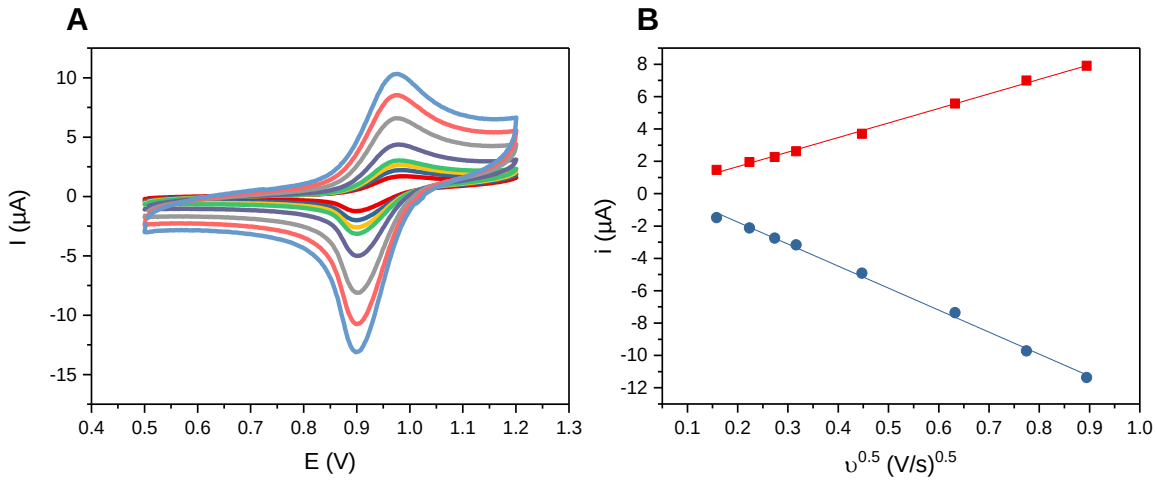


Figure A2.22. CVs (A) and anodic and cathodic peak currents (B) of 0.3 mM **2.8** in MeOH, 50 mM $TBAPF_6$ at varying scan rates.

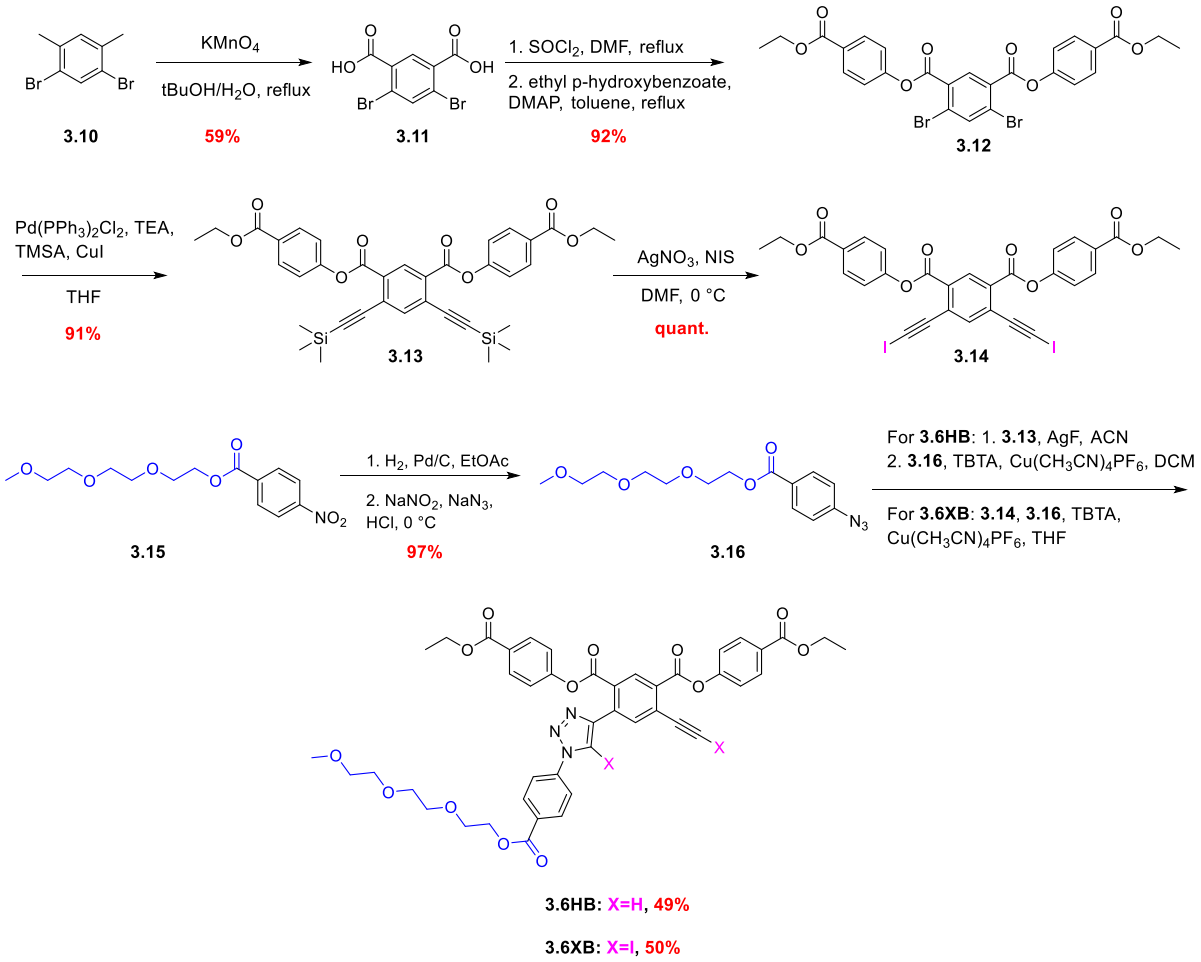
A3: Supplementary Information for Chapter 3

Table A3.1. Binding constants of various anions to **3.2XB** in water as determined by ITC, errors in parentheses. $\beta_2 = K_1 * K_2$. Anions were added as Na^+ salt.

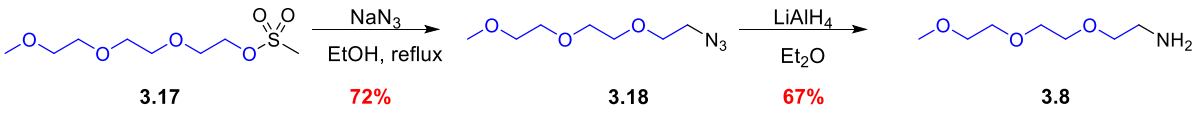
	β_2 (M^{-2})	K_1 (M^{-1})	K_2 (M^{-1})
I^-	1.45 (0.04) × 10^{10}	3.16 (0.05) × 10^4	4.59 (0.14) × 10^5
ReO_4^-	6.66 (0.55) × 10^8	4.91 (0.18) × 10^4	1.35 (0.07) × 10^4
SCN^-	3.40 (0.16) × 10^7	5.38 (0.20) × 10^3	6.33 (0.51) × 10^3
Br^-	3.43 (0.47) × 10^6	1.03 (0.11) × 10^3	3.34 (0.42) × 10^3
ClO_4^-	1.21 (0.13) × 10^5	5.55 (0.63) × 10^1	2.19 (0.08) × 10^3

Table A3.2. Binding constants of various anions to **3.2HB** in water as determined by ITC, errors in parentheses. Anions were added as Na^+ salt.

	K (M^{-1})
I^-	3876 (21)
SCN^-	346 (14)
ClO_4^-	2000 (14)



Scheme A3.1. Synthetic route towards **3.6XB/HB**.



Scheme A3.2. Synthetic route towards **3.8**.

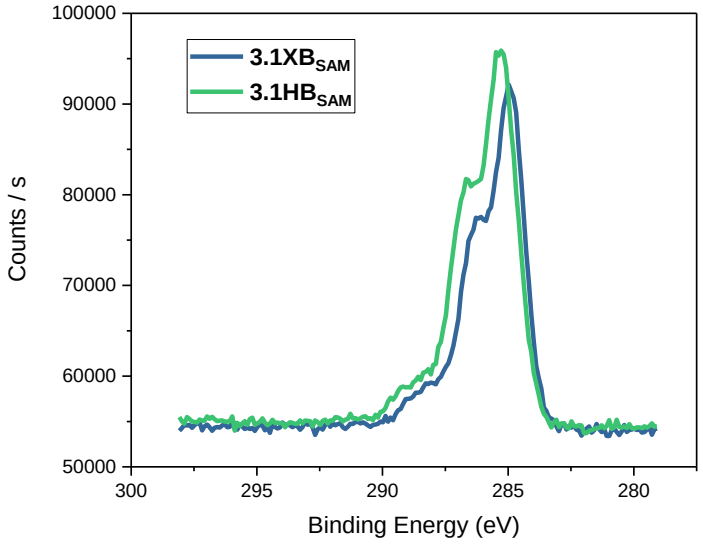


Figure A3.1. High resolution C 1s XPS spectra of **3.1XB/HB$_{SAM}$**.

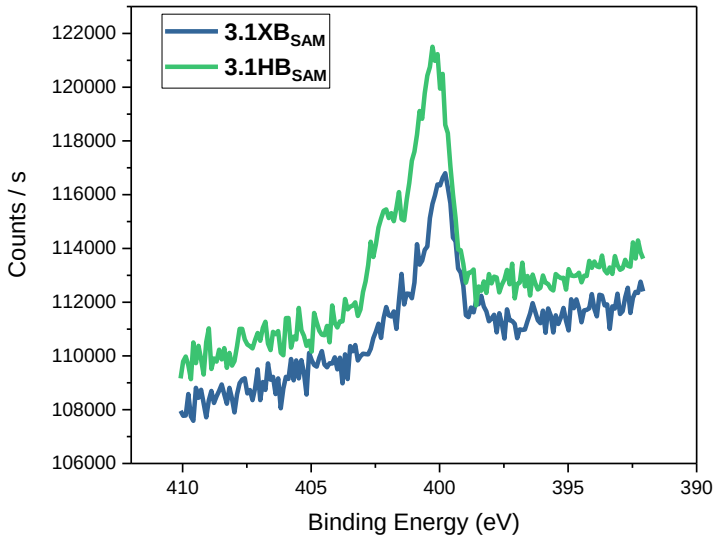


Figure A3.2. High resolution N 1s XPS spectra of **3.1XB/HB$_{SAM}$**.

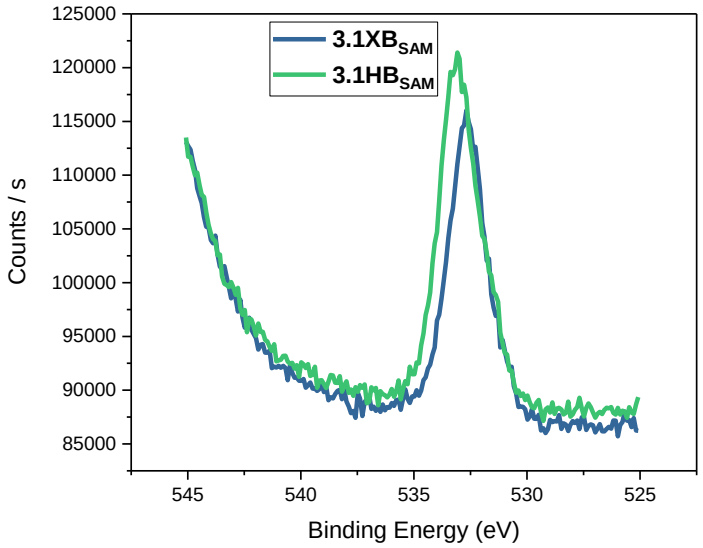


Figure A3.3. High resolution O 1s XPS spectra of **3.1XB/HB$_{SAM}$**.

Table A3.3. High resolution XPS peak data and atomic composition of **3.1XB$_{SAM}$**. Errors represent one standard deviation of triplicate measurements. BE = binding energy. The remaining atomic % arise from the underlying gold substrate.

Peak	Start BE (eV)	Peak BE (eV)	End BE (eV)	Atomic %
C 1s	293.41 ± 0.76	285.66 ± 0.26	278.91 ± 0.29	49.31 ± 4.56
N 1s	407.42 ± 2.52	400.31 ± 0.15	393.75 ± 0.29	8.74 ± 1.79
O 1s	537.08 ± 0.50	532.77 ± 0.13	526.41 ± 2.08	13.38 ± 1.31
S 2p	166.55 ± 1.16	163.44 ± 0.13	159.84 ± 1.10	1.05 ± 0.24
I 3d	625.41 ± 0.58	620.28 ± 0.77	614.75 ± 1.523	1.86 ± 0.13

Table A3.4. High resolution XPS peak data and atomic composition of **3.1HB$_{SAM}$**. Errors represent one standard deviation of triplicate measurements. BE = binding energy. The remaining atomic % arise from the underlying gold substrate.

Peak	Start BE (eV)	Peak BE (eV)	End BE (eV)	Atomic %
C 1s	296.08 ± 1.73	286.08 ± 0.20	278.08 ± 1.73	53.22 ± 2.70
N 1s	408.08 ± 0.50	400.91 ± 0.31	393.25 ± 3.55	8.71 ± 0.66
O 1s	537.08 ± 0.50	532.94 ± 0.11	524.75 ± 1.53	14.80 ± 0.66
S 2p	168.31 ± 2.39	163.13 ± 0.25	159.00 ± 0.00	1.19 ± 0.21

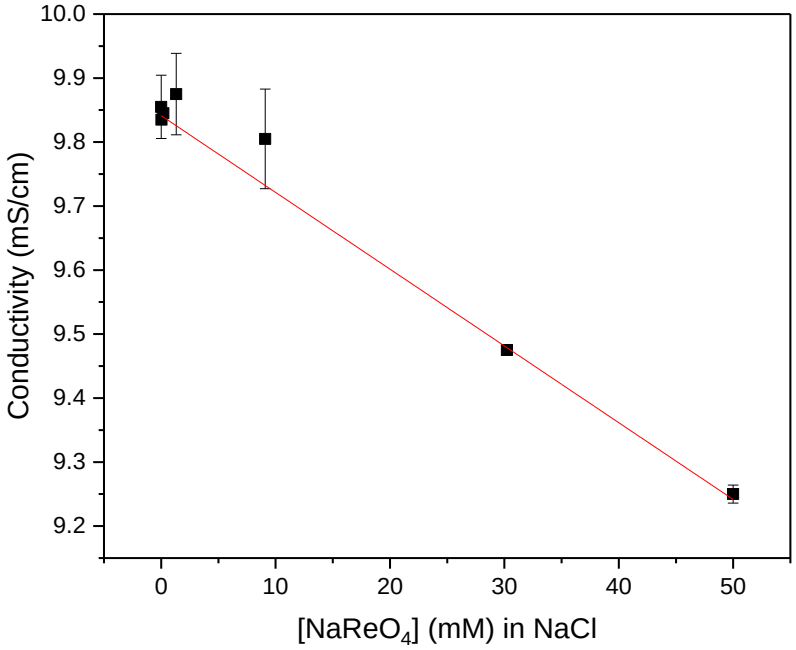


Figure A3.4. Conductivity of electrolyte solutions as used for all capacitive measurements. [Electrolyte] = 100 mM.

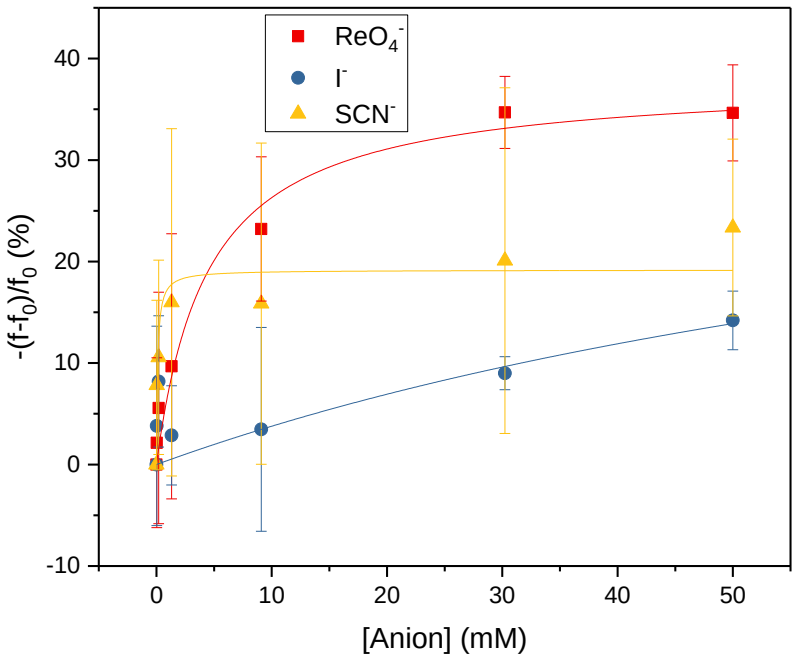


Figure A3.5. Normalised changes of f_t of **3.1XB$_{SAM}$** as a function of anion concentration. Error bars represent one standard deviation of three independent measurements. Solid lines represent fits to the Langmuir model (eqn. 3.1).

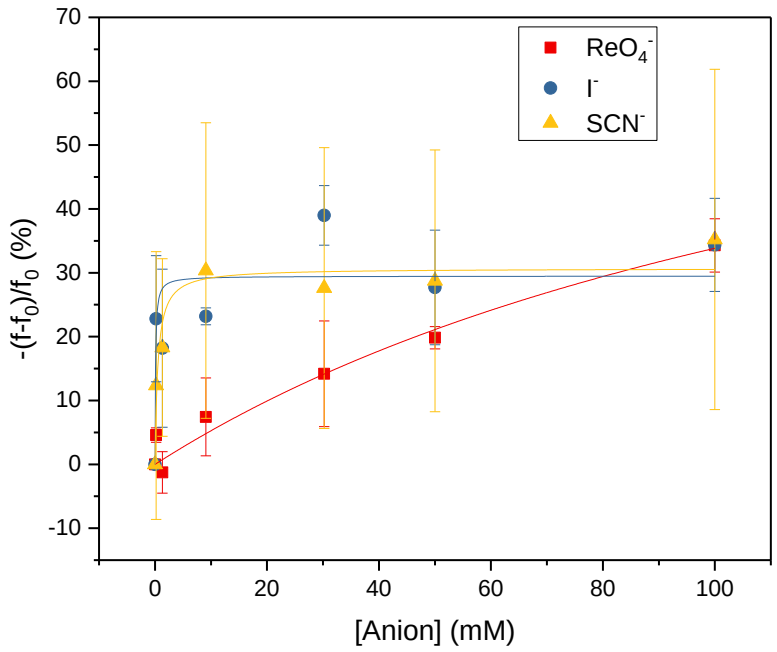


Figure A3.6. Normalised changes of f_t for **3.1HB$_{SAM}$** as a function of anion concentration. Error bars represent one standard deviation of three independent measurements. Solid lines represent fits to the Langmuir model (eqn. 3.1).

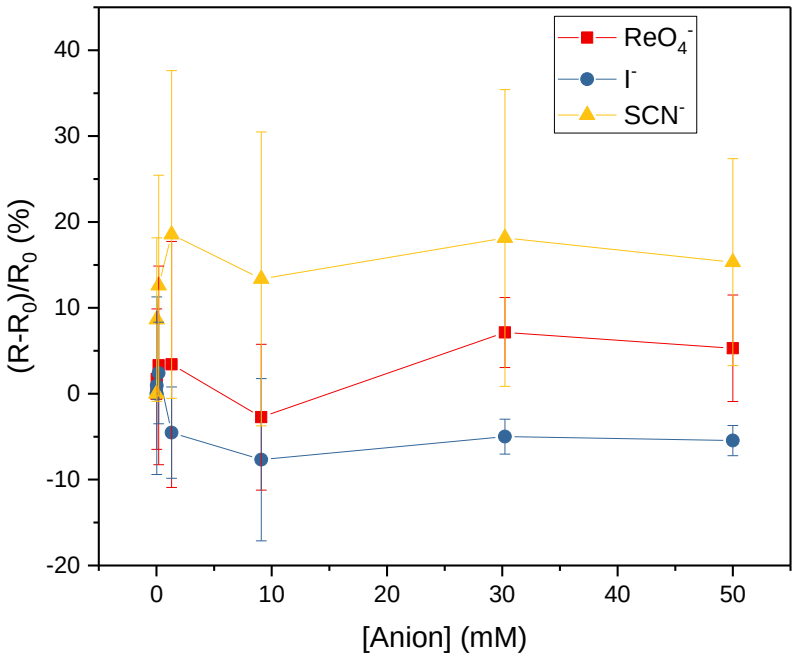


Figure A3.7. Normalised changes of R_t for **3.1XB$_{SAM}$** as a function of anion concentration. Error bars represent one standard deviation of three independent measurements. Solid lines do not represent any fits and are only meant to guide the eye.

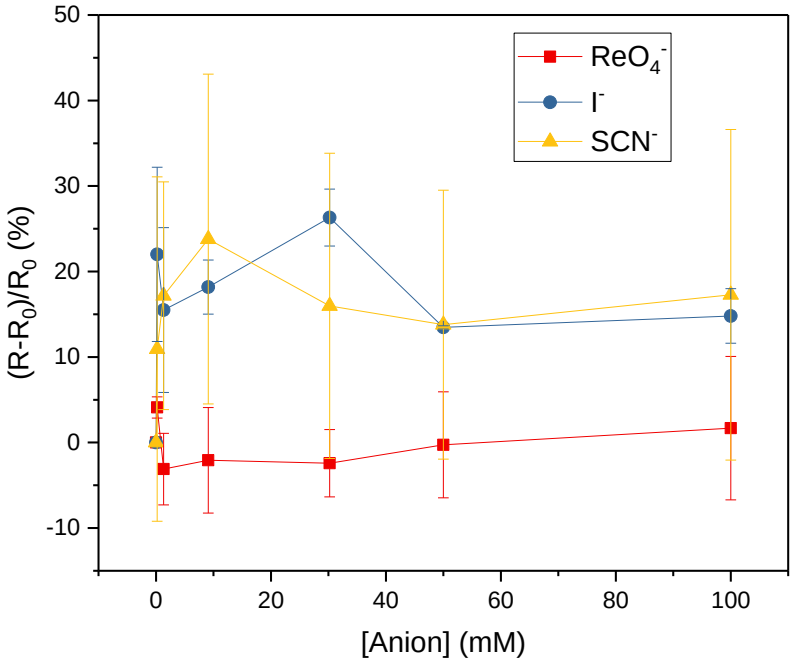


Figure A3.8. Normalised changes of R_t for **3.1HB$_{SAM}$** as a function of anion concentration. Error bars represent one standard deviation of three independent measurements. Solid lines do not represent any fits and are only meant to guide the eye.

A4: Supplementary Information for Chapter 4

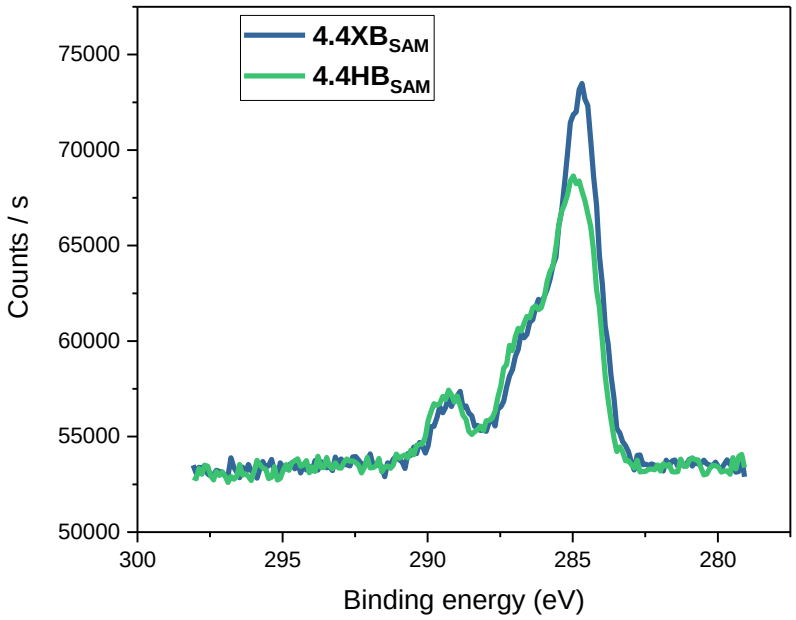


Figure A4.1. High resolution C 1s XPS spectra of **4.4XB/HB$_{SAM}$**.

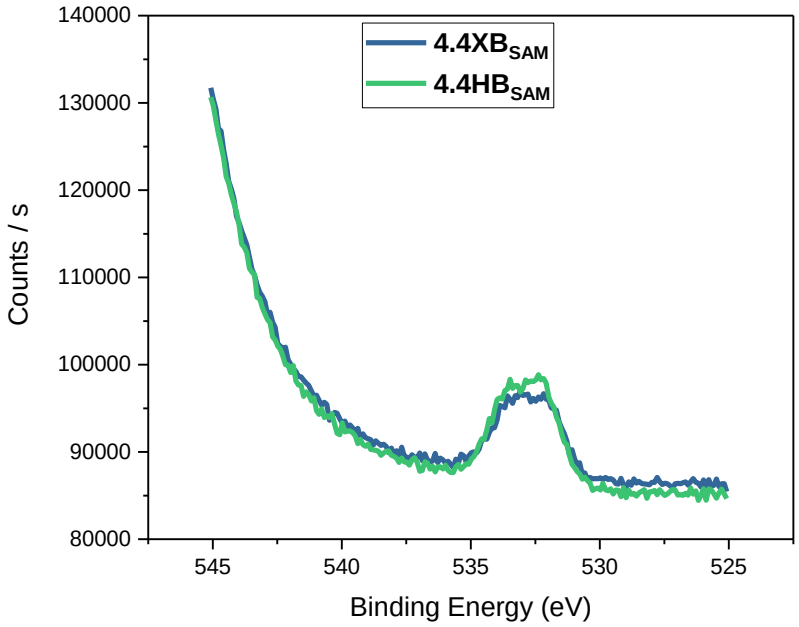


Figure A4.2. High resolution O 1s XPS spectra of **4.4XB/HB$_{SAM}$**.

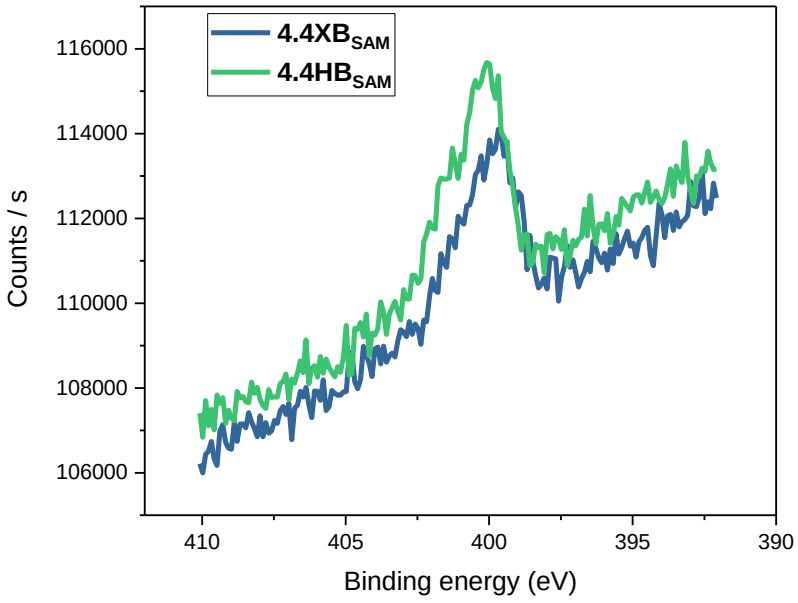


Figure A4.3. High resolution N 1s XPS spectra of **4.4XB/HB$_{SAM}$**.

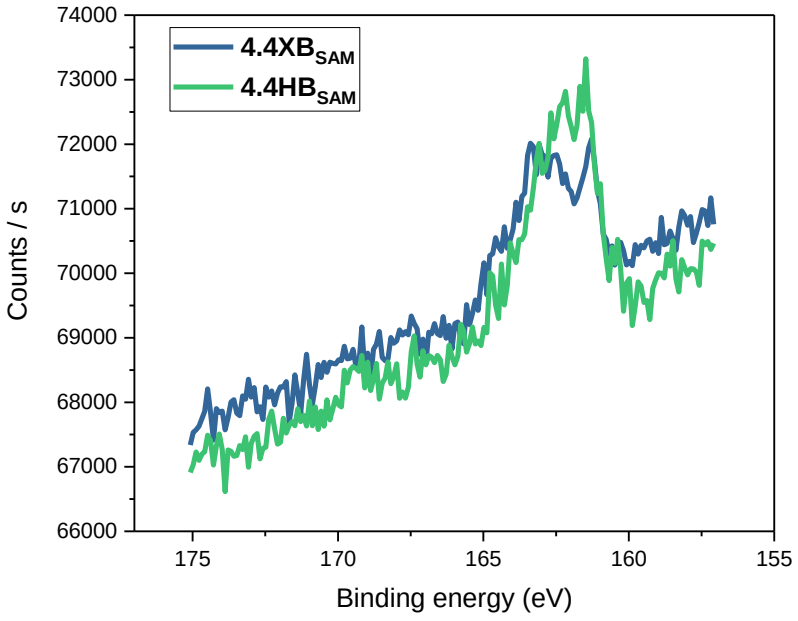


Figure A4.4. High resolution S 2p XPS spectra of **4.4XB/HB$_{SAM}$**.

Table A4.1. High resolution XPS peak data and atomic composition of **4.4XB$_{SAM}$**. Errors represent one standard deviation of triplicate measurements. BE = binding energy. The remaining atomic % arise from the underlying gold substrate.

Peak	Start BE (eV)	Peak BE (eV)	End BE (eV)	Atomic %
C 1s	295.23 ± 2.87	285.33 ± 0.12	278.76 ± 1.19	36.11 ± 4.36
N 1s	408.58 ± 1.32	400.55 ± 0.39	394.74 ± 2.02	9.29 ± 1.86
O 1s	536.58 ± 0.50	532.73 ± 0.36	527.41 ± 0.29	7.67 ± 0.31
S 2p	167.63 ± 2.07	162.74 ± 0.51	159.43 ± 0.38	1.40 ± 0.48
I 3d	626.19 ± 1.64	620.96 ± 0.10	615.41 ± 2.08	1.64 ± 0.16

Table A4.2. High resolution XPS peak data and atomic composition of **4.4HB$_{SAM}$**. Errors represent one standard deviation of triplicate measurements. BE = binding energy. The remaining atomic % arise from the underlying gold substrate.

Peak	Start BE (eV)	Peak BE (eV)	End BE (eV)	Atomic %
C 1s	292.48 ± 0.06	285.62 ± 0.19	281.31 ± 0.46	34.84 ± 0.18
N 1s	406.77 ±1.40	400.82 ± 0.05	395.88 ± 1.13	6.75 ± 0.20
O 1s	536.75 ± 0.29	532.96 ± 0.02	528.35 ± 0.08	9.27 ± 0.46
S 2p	167.93 ± 0.47	162.91 ± 0.06	158.74 ± 0.33	3.27 ± 0.14

In Figure A4.5B it is apparent that in NaCl BINOL-PO_4^- binding does not induce a shift in the frequency of C''_{max}. Within the equivalent circuit model that was developed in Section 3.5 this would indicate a sensor response that is not purely reflective of only a change in the capacitance of the film but also other circuit elements (*e.g.* R_t). However, as highlighted in Section 4.2, the structure of **4.4XB$_{SAM}$** is not only inherently different in comparison to **3.1XB/HB$_{SAM}$** but is also significantly altered by anion binding. A more detailed analysis of the capacitive in analogy to that carried out in Section 3.5 would thus need to take these factors into account.

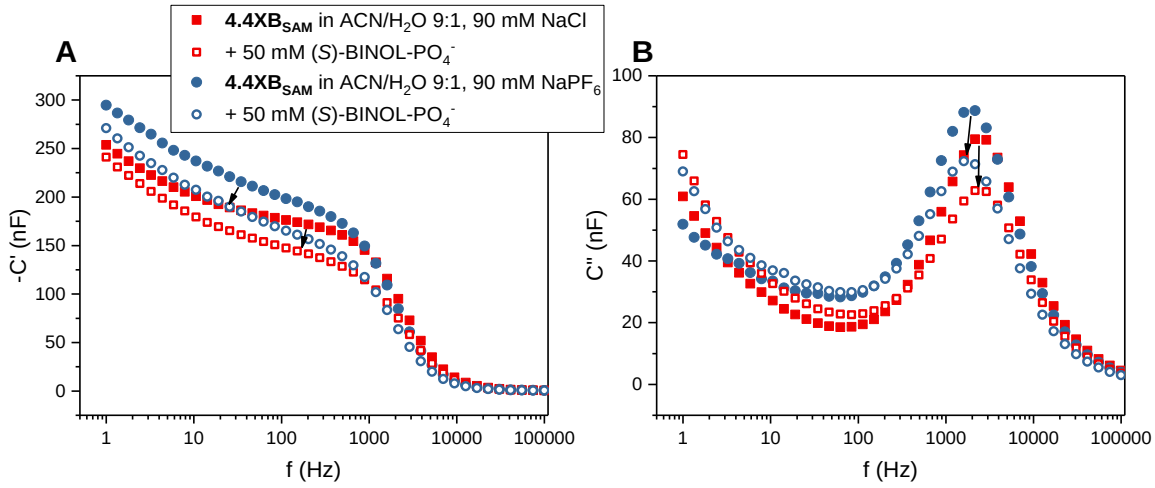


Figure A4.5. Bode plots of real capacitance C' (A) and imaginary capacitance C'' (B) of **4.4XB$_{SAM}$** in H_2O/ACN 9:1, 90 mM $NaPF_6$ (blue circles) or 90 mM NaCl (red squares) in the presence (empty symbols) and absence (filled symbols) of 45 mM (*S*)-BINOL-PO_4^-.

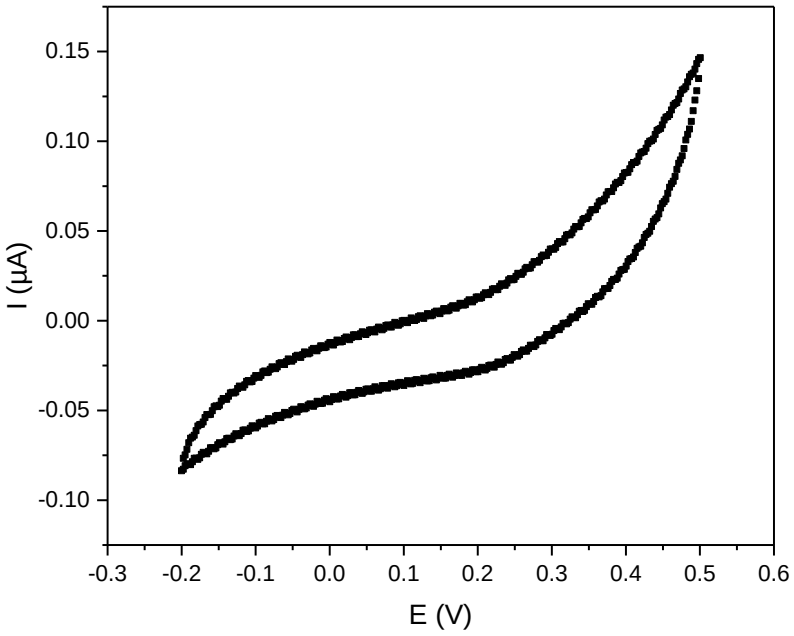


Figure A4.6. CV of **4.4XB$_{SAM}$** in H_2O/ACN 9:1, 2 mM $[Fe(CN)_6]^{3-/4-}$, 100 mM NaCl.

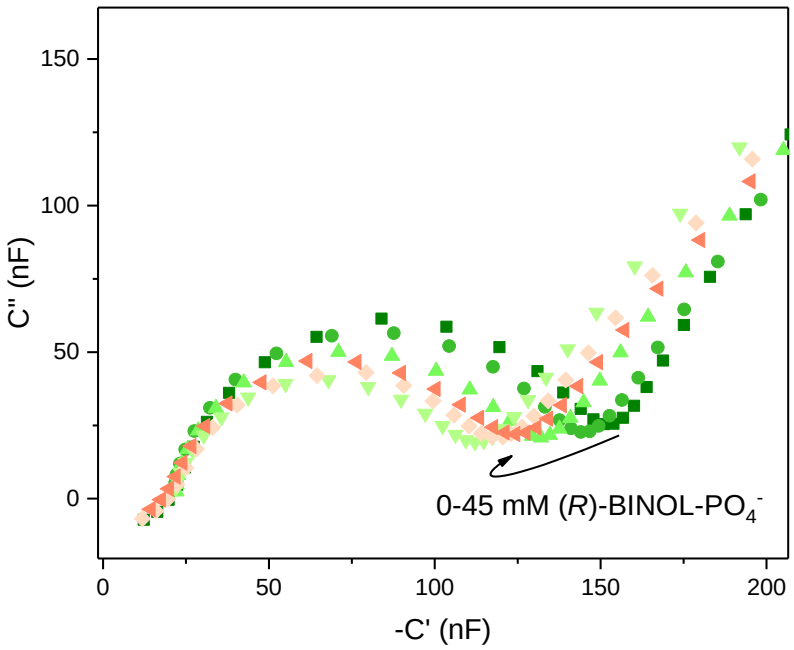


Figure A4.7. Capacitive Nyquist plots of **4.4XB$_{SAM}$** in H_2O/ACN 9:1, 9 mM $[Fe(CN)_6]^{3-/4-}$, 90 mM NaCl in the presence of increasing concentrations of (*R*)-BINOL-PO_4^-.

A5: Supplementary Information for Chapter 5

Table A5.1. High resolution XPS peak data and atomic composition of **5.5XB$_{SAM}$**. Errors represent one standard deviation of triplicate measurements. BE = binding energy. The remaining atomic % arise from the underlying gold substrate.

Peak	Start BE (eV)	Peak BE (eV)	End BE (eV)	Atomic %
C 1s	296.7 ± 1.3	285.9 ± 0.1	280.2 ± 1.0	46.1 ± 2.3
N 1s	408.4 ± 1.1	400.4 ± 0.3	394.4 ± 1.5	6.4 ± 2.0
O 1s	536.9 ± 0.3	533.0 ± 0.0	527.2 ± 2.3	11.1 ± 1.2
S 2p	166.3 ±1.3	162.5 ± 0.4	159.2 ± 0.9	1.3 ± 0.4
I 3d	625.8 ± 0.7	620.7 ± 0.2	615.7 ± 0.2	1.8 ± 0.3

Table A5.2. High resolution XPS peak data and atomic composition of **5.5HB$_{SAM}$**. Errors represent one standard deviation of triplicate measurements. BE = binding energy. The remaining atomic % arise from the underlying gold substrate.

Peak	Start BE (eV)	Peak BE (eV)	End BE (eV)	Atomic %
C 1s	294.7 ± 1.4	286.0 ± 0.0	279.1 ± 1.8	46.8 ± 1.8
N 1s	409.4 ± 1.2	400.8 ± 0.4	393.4 ± 2.9	8.8 ± 2.6
O 1s	536.7 ± 0.3	533.1 ± 0.0	523.8 ± 0.6	13.0 ± 1.1
S 2p	165.7 ± 0.4	162.5 ± 0.8	159.1 ± 0.9	1.2 ± 0.3

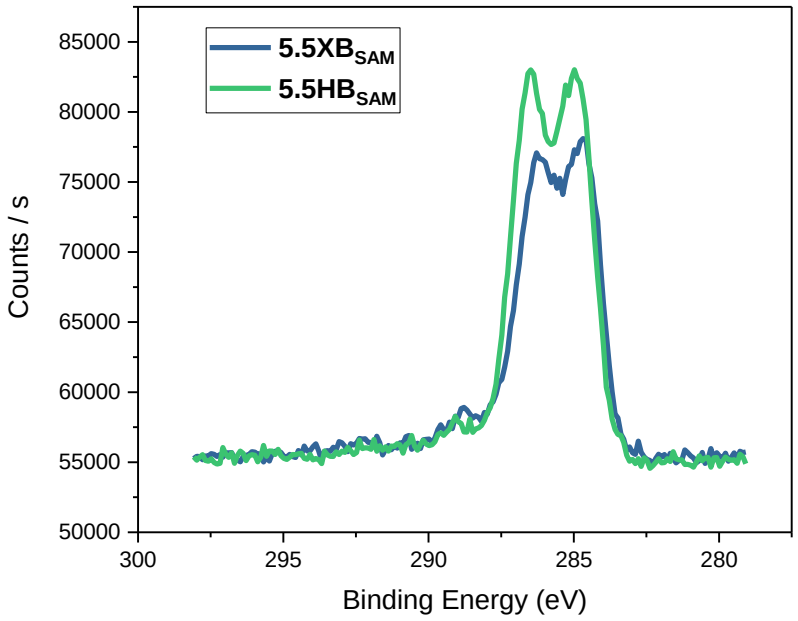


Figure A5.1. High resolution C 1s XPS spectra of **5.5XB/HB$_{SAM}$**.

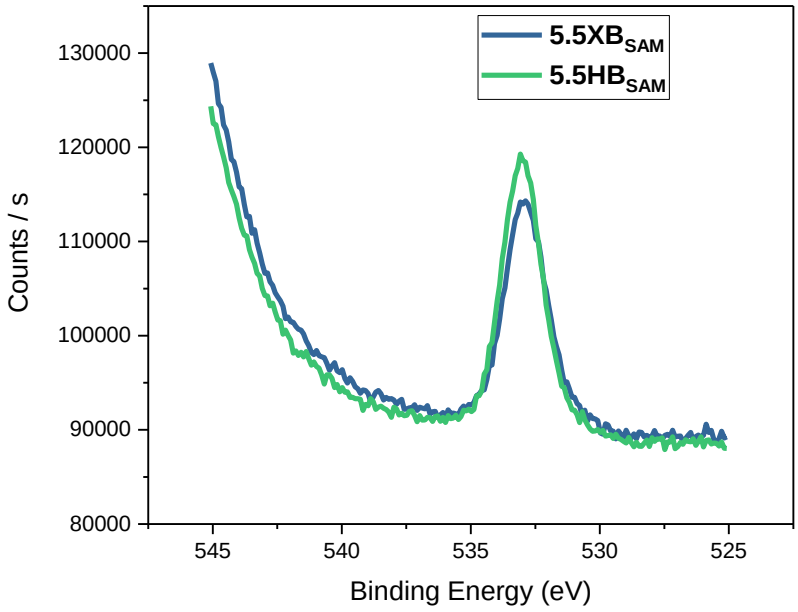


Figure A5.2. High resolution O 1s XPS spectra of **5.5XB/HB$_{SAM}$**.

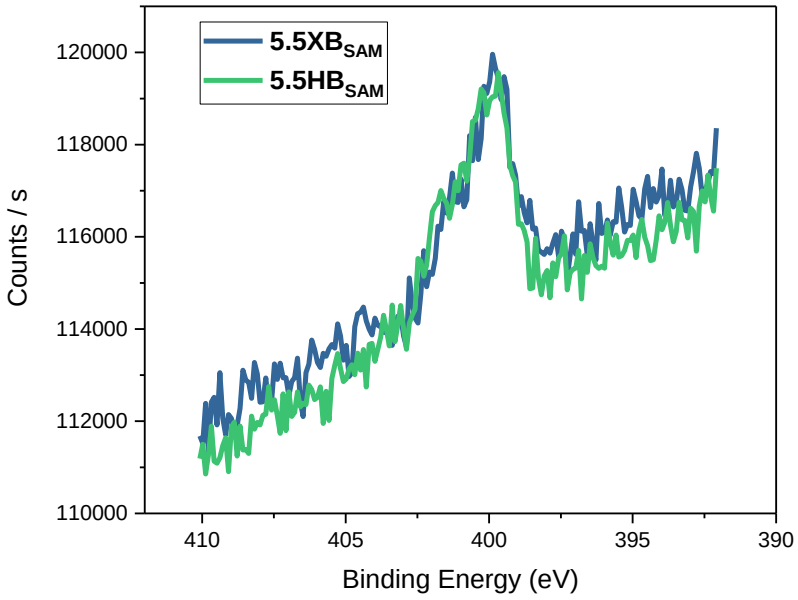


Figure A5.3. High resolution N 1s XPS spectra of **5.5XB/HB$_{SAM}$**.

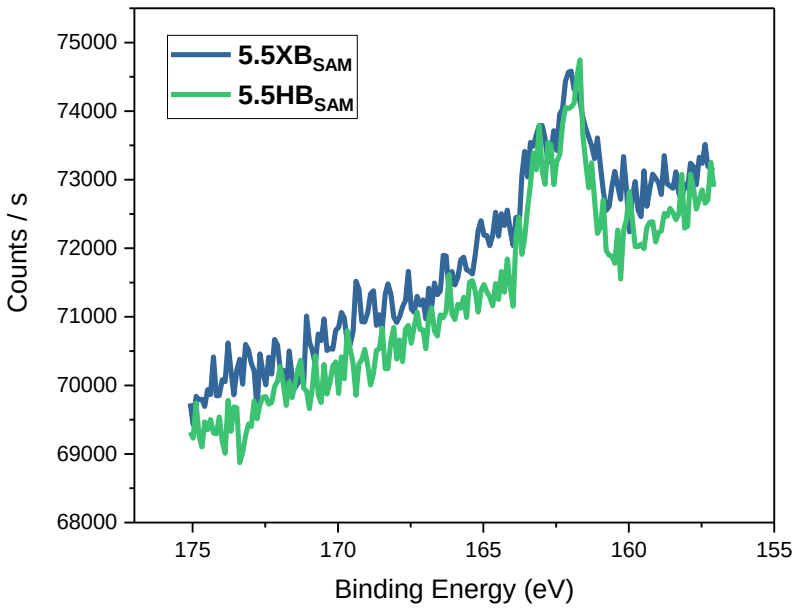


Figure A5.4. High resolution S 2p XPS spectra of **5.5XB/HB$_{SAM}$**.

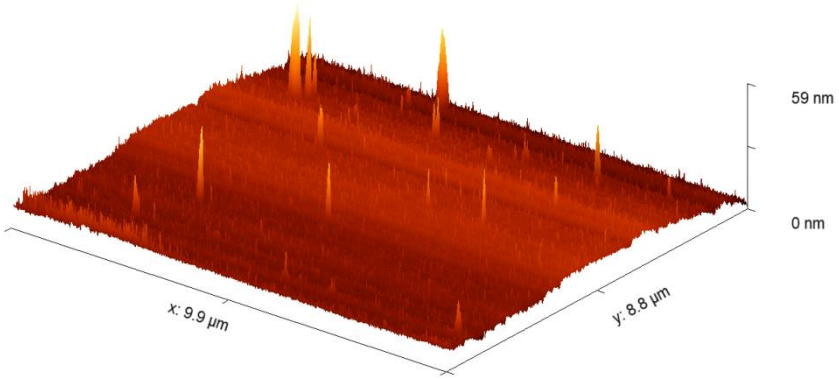


Figure A5.5. Low resolution AFM image of **5.5XB$_{SAM}$**.

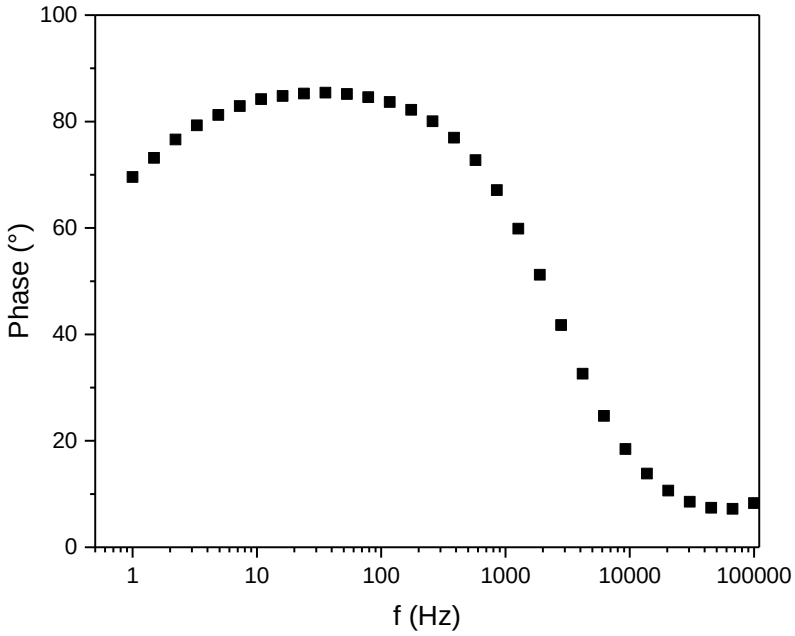


Figure A5.6. Bode phase plot of **5.5XB$_{SAM}$** in H_2O 100 mM $TBANO_3$.

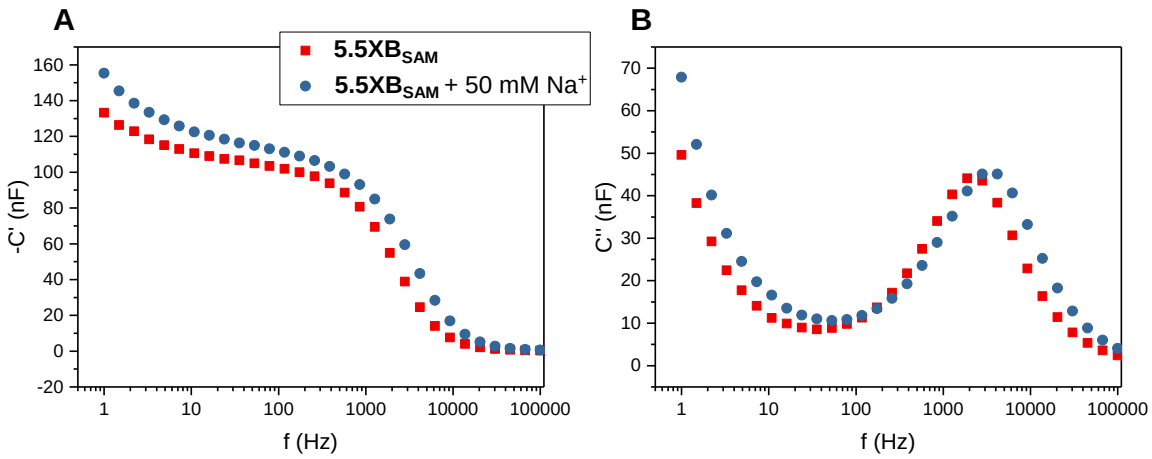


Figure A5.7. Bode plots of real capacitance C' (A) and imaginary capacitance C'' (B) of **5.5XB$_{SAM}$** in H_2O 100 mM $TBANO_3$ in the presence (blue circles) and absence (red squares) of 50 mM Na^+.

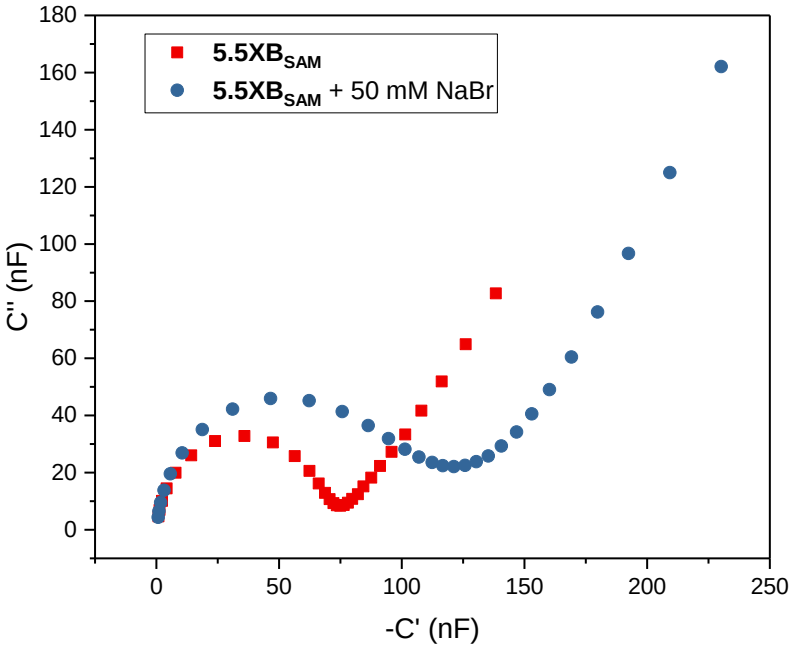


Figure A5.8. Capacitive Nyquist plots of **5.5XB$_{SAM}$** in the presence (blue circles) and absence (red squares) of 50 mM NaBr. Measurements were carried out at OCP in ACN/H_2O 9:1, 100 mM $TBAPF_6$.

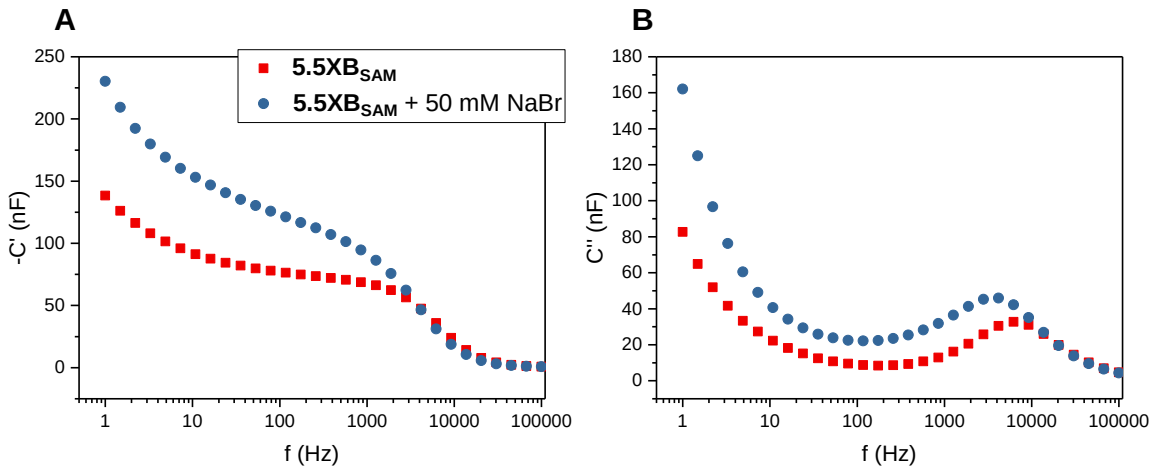


Figure A5.9. Bode plots of real capacitance C' (A) and imaginary capacitance C'' (B) of **5.5XB$_{SAM}$** in the presence (blue circles) and absence (red squares) of 50 mM NaBr. Measurements were carried out at OCP in ACN/H_2O 9:1, 100 mM $TBAPF_6$.

Table 5.6. K, maximum capacitive response (ΔC_{max}) and n values of **5.5XB/HB$_{SAM}$** upon exposure to NaBr in ACN/H_2O 9:1, 100 mM $TBAPF_6$. The data was obtained by isotherm fitting (Figure 5.18) according to the Langmuir-Freundlich model (eqn. 5.1).

	5.5XB$_{SAM}$	**5.5HB$_{SAM}$**
K (M^{-1})	388	185
ΔC_{max} (%)	56.7	61.1
n	0.571	0.464
R^2	0.9933	0.9910